



Waves and vibrations in inhomogeneous structures bandgaps and optimal designs

Jensen, Jakob Søndergaard

Publication date:
2011

Document Version
Publisher's PDF, also known as Version of record

[Link back to DTU Orbit](#)

Citation (APA):
Jensen, J. S. (2011). *Waves and vibrations in inhomogeneous structures: bandgaps and optimal designs*. DTU Mechanical Engineering.

General rights

Copyright and moral rights for the publications made accessible in the public portal are retained by the authors and/or other copyright owners and it is a condition of accessing publications that users recognise and abide by the legal requirements associated with these rights.

- Users may download and print one copy of any publication from the public portal for the purpose of private study or research.
- You may not further distribute the material or use it for any profit-making activity or commercial gain
- You may freely distribute the URL identifying the publication in the public portal

If you believe that this document breaches copyright please contact us providing details, and we will remove access to the work immediately and investigate your claim.

WAVES AND VIBRATIONS IN
INHOMOGENEOUS STRUCTURES
bandgaps and optimal designs

Jakob Søndergaard Jensen
DTU Mechanical Engineering
Technical University of Denmark

Title of the thesis:

Waves and Vibrations in Inhomogeneous Structures – bandgaps and optimal designs

Author:

Jakob Søndergaard Jensen

E-mail: jsj@mek.dtu.dk

Address:

Department of Mechanical Engineering

Technical University of Denmark

Nils Koppels Allé, Building 404

DK-2800 Kgs. Lyngby, Denmark

Copyright © 2011 Jakob Søndergaard Jensen

ISBN 978-87-90416-48-5



Denne afhandling er af Danmarks Tekniske Universitet antaget til forsvar for den tekniske doktorgrad. Antagelsen er sket efter bedømmelse af den foreliggende afhandling.

Kgs. Lyngby, den 2. marts 2011

Lars Pallesen
Rektor

/Martin P. Bendsøe
Dekan

This thesis has been accepted by the Technical University of Denmark for public defence in fulfilment of the requirements for the degree of Doctor Technices. The acceptance is based on an evaluation of the present dissertation.

Kgs. Lyngby, 2 March 2011

Lars Pallesen
Rector

/Martin P. Bendsøe
Dean

Preface

The work collected in this thesis has been carried out during my employment at the Technical University of Denmark, Department of Mechanical Engineering in the period from September 2001 to February 2010.

I am indebted to my colleague Ole Sigmund for suggesting to me to return to the scientific environment at the University and coming up with the initial idea to the project that started it all. Also I would like to give my sincere thanks to Jon Juel Thomsen who as my PhD-supervisor gave me my scientific upbringing and has continued to influence me through discussions and project cooperations.

I would like to thank all the various members of the TopOpt group who has responded to many ideas and come up with many suggestions and comments in group meetings and at informal events.

The staff and students at the section for Solid Mechanics have always provided a friendly and relaxed working atmosphere and have done their best to take my mind off scientific issues by engaging in lively conversations and discussions about daily life.

Finally, I would like to thank the two girls in my life, Teresa and Jana, for always putting my work in the proper perspective.

Kgs. Lyngby, February 22, 2010
Jakob Søndergaard Jensen

List of Thesis Papers

- [1] J. S. Jensen 2003 *Journal of Sound and Vibration* **266**(5), 1053–1078. Phononic band gaps and vibrations in one- and two-dimensional mass-spring structures.
- [2] J. S. Jensen, O. Sigmund, J. J. Thomsen and M. P. Bendsøe 2002 Design of multi-phase structures with optimized vibrational and wave-transmitting properties. In E. Lund, N. Olhoff and J. Stegmann (eds.), Institute of Mechanical Engineering, Aalborg University, Denmark, 63–66, 15th Nordic Seminar on Computational Mechanics.
- [3] B. S. Lazarov and J. S. Jensen 2007 *International Journal of Non-Linear Mechanics* **42**(10), 1186–1193. Low-frequency band gaps in chains with attached non-linear oscillators.
- [4] O. Sigmund and J. S. Jensen 2003 *Philosophical Transactions of the Royal Society of London Series A-Mathematical Physical and Engineering Sciences* **361**(1806), 1001–1019. Systematic design of phononic band-gap materials and structures by topology optimization.
- [5] S. Halkjær, O. Sigmund and J. S. Jensen 2005 *Zeitschrift für Kristallographie* **220**(9–10), 895–905. Inverse design of phononic crystals by topology optimization.
- [6] J. S. Jensen 2007 *Journal of Sound and Vibration* **301**(1–2), 319–340. Topology optimization problems for reflection and dissipation of elastic waves.
- [7] J. S. Jensen and N. L. Pedersen 2006 *Journal of Sound and Vibration* **289**(4–5), 967–986. On maximal eigenfrequency separation in two-material structures: the 1D and 2D scalar cases.
- [8] A. A. Larsen, B. Laksafoss, J. S. Jensen and O. Sigmund 2009 *Structural and Multidisciplinary Optimization* **37**(6), 585–594. Topological material layout in plates for vibration suppression and wave propagation control.
- [9] J. S. Jensen and O. Sigmund 2005 Systematic design of acoustic devices by topology optimization. In J. L. Bento Coelho and D. Alarcão (eds.), International Institute of Acoustics and Vibration, 12th International Congress on Sound and Vibration.
- [10] J. S. Jensen and O. Sigmund 2004 *Applied Physics Letters* **84**(12), 2022–2024. Systematic design of photonic crystal structures using topology optimization: Low-loss waveguide bends.

- [11] J. S. Jensen and O. Sigmund 2005 *Journal of the Optical Society of America B-Optical Physics* **22**(6), 1191–1198. Topology optimization of photonic crystal structures: a high-bandwidth low-loss T-junction waveguide.
- [12] P. I. Borel, A. Harpøth, L. H. Frandsen, M. Kristensen, P. Shi, J. S. Jensen and O. Sigmund 2004 *Optics Express* **12**(9), 1996–2001. Topology optimization and fabrication of photonic crystal structures.
- [13] L. H. Frandsen, A. Harpøth, P. I. Borel, M. Kristensen, J. S. Jensen and O. Sigmund 2004 *Optics Express* **12**(24), 5916–5921. Broadband photonic crystal waveguide 60° bend obtained utilizing topology optimization.
- [14] P. I. Borel, L. H. Frandsen, A. Harpøth, M. Kristensen, J. S. Jensen and O. Sigmund 2005 *Electronics Letters* **41**(2), 69–71. Topology optimised broadband photonic crystal Y-splitter.
- [15] J. S. Jensen, O. Sigmund, L. H. Frandsen, P. I. Borel, A. Harpøth and M. Kristensen 2005 *IEEE Photonics Technology Letters* **17**(6), 1202–1204. Topology design and fabrication of an efficient double 90° photonic crystal waveguide bend.
- [16] P. I. Borel, B. Bilenberg, L. H. Frandsen, T. Nielsen, J. Fage-Pedersen, A. V. Lavrinenko, J. S. Jensen, O. Sigmund and A. Kristensen 2007 *Optics Express* **15**(3), 1261–1266. Imprinted silicon-based nanophotonics.
- [17] J. S. Jensen and O. Sigmund 2005 Topology optimization of building blocks for photonic integrated circuits. In J. Herskovits, S. Mazorche and A. Canelas (eds.), International Society for Structural and Multidisciplinary Optimization, 6th World Congress on Structural and Multidisciplinary Optimization.
- [18] J. S. Jensen 2007 *International Journal for Numerical Methods in Engineering* **72**(13), 1605–1630. Topology optimization of dynamics problems with Padé approximants.
- [19] J. S. Jensen and B. S. Lazarov 2008 Optimization of non-linear mass damper parameters for transient response. In B. R. Andrievsky and A. L. Fradkov (eds.), European Mechanics Society, 6th EUROMECH Nonlinear Dynamics Conference.
- [20] J. S. Jensen 2009 *Computer Methods in Applied Mechanics and Engineering* **198**(5–8), 705–715. Space-time topology optimization for one-dimensional wave propagation.
- [21] J. S. Jensen 2010 *Control & Cybernetics* **39**(3), 599–614. Optimization of space-time material layout for 1D wave propagation with varying mass and stiffness parameters.

Contents

Preface	i
List of Thesis Papers	iii
Contents	v
1 Introduction	1
2 The bandgap phenomenon	7
2.1 Band diagram and forced vibrations	8
2.2 Structural damping	10
2.3 Experimental demonstration	11
2.4 Low-frequency bandgaps	12
2.5 Nonlinearities	12
3 Bandgap structures as optimal designs	17
3.1 Vibration-quenching structures	18
3.2 Maximizing wave reflection	20
3.3 Eigenfrequency separation	22
3.4 Maximizing wave dissipation	23
3.5 Plate structures	26
3.6 Acoustic design	28
4 Optimization of photonic waveguides	31
4.1 Waveguide bends and junctions	32
4.2 Photonic crystal building blocks	35
4.3 Advanced functionalities	38
4.4 Ridge waveguides	39
5 Advanced optimization procedures	43
5.1 Padé approximants	44
5.2 Nonlinear transients	46
5.3 Space-time topology optimization	47
6 Conclusions	53
References	54

Chapter 1

Introduction

This thesis is devoted to waves and vibrations in inhomogeneous structures and specifically to the investigation of bandgap phenomena and optimization of bandgap structures. The effect of a bandgap on the propagation of waves is illustrated in Fig. 1.1 for a simple one-dimensional structure. A single *inclusion* in an otherwise homogeneous structure reflects a part of the wave pulse (shown in the three figures to the left). A sequence of equidistantly spaced inclusions (4 inclusions in this example) causes *in-phase reflections* which lead to a larger part of the wave being reflected (shown in the three plots to the right). In order for in-phase reflections to occur and a *bandgap condition* to be created, the spacing between the inclusions must match certain conditions. These conditions are governed by the main frequency/wavelength of the wave pulse and also by the contrast between the material properties of the inclusions and the background material. This usually results in a few inclusions per wavelength. If the bandgap condition is fulfilled the amplitude of the *transmitted* wave decays exponentially with the number of inclusions and if an infinite number of inclusions were present (a *periodic material*) the incoming wave will, in theory, be totally reflected.

In the following the background and motivation for the work leading to this thesis will be outlined.

Phononic and photonic bandgaps

The research on bandgap materials and structures has had a rather peculiar history during the last century. To the author's knowledge the first report on the bandgap phenomenon was made in 1887 by Lord Rayleigh (Rayleigh, 1887) who found that in-phase reflections from certain periodic arrangements of different elastic materials may lead to frequency ranges for which waves will be totally reflected. However, Lord Rayleigh did not use the term bandgap to describe this effect. Neither did Brillouin in his book on wave propagation in lattice structures (Brillouin, 1953). Instead the terms *passband* and *stopband* were used to describe the frequency ranges for which waves either could or could not propagate. With his pioneering work, Brillouin paved the way for much of today's research in the field of bandgaps with his treatment of symmetry conditions and the concept of Brillouin zones. These concepts are nowadays an integrated part of the description of wave propagation through periodic materials through the use of the *band diagrams*.

A band diagram for a certain periodic material is illustrated in Fig. 1.2. The solid lines in the plot indicate propagating modes with the frequency of the wave

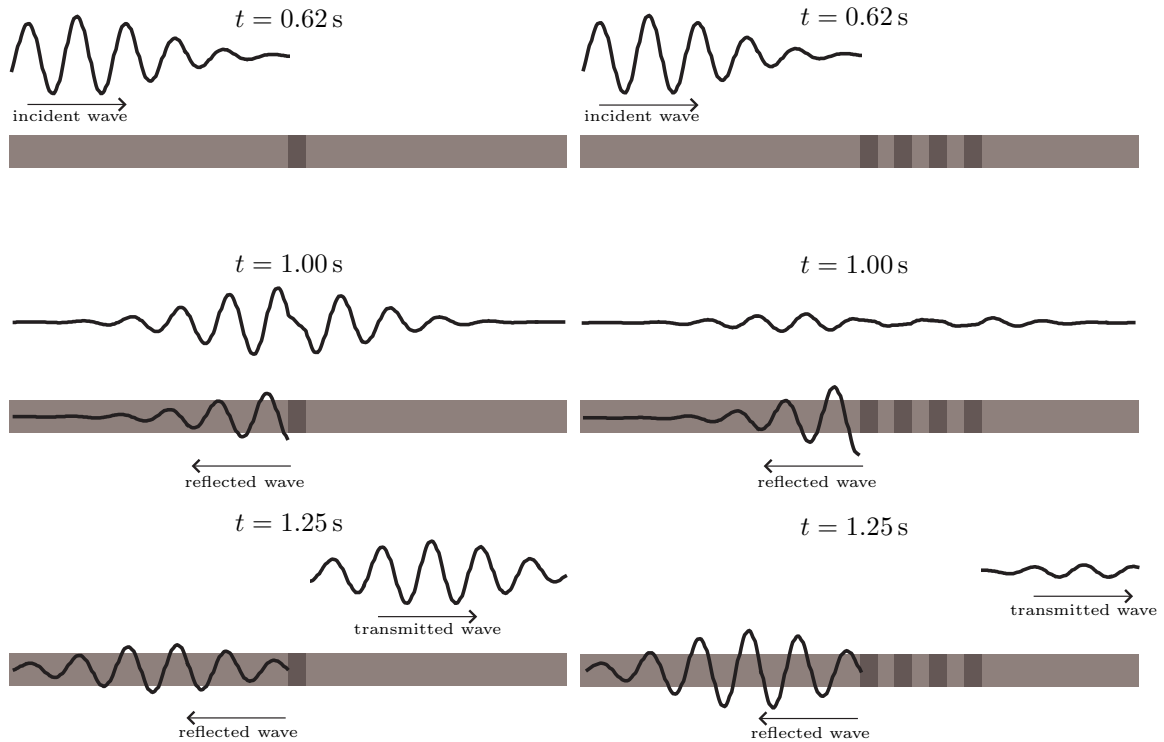


Figure 1.1 Illustration of the bandgap phenomenon for wave propagation in a one-dimensional layered structure. The plots show the incident/transmitted wave pulses as well as the reflected wave pulse at three different time instances. Left plots: a single inclusion with different material properties. Right plots: Four equidistantly placed inclusions, where the distance between the inclusions combined with the material properties leads to in-phase reflections of the incident wave. With infinitely many inclusions present, a complete reflection of the wave will occur – known as the bandgap phenomenon.

given along the vertical axis and the *reduced wave vector* given along the horizontal axis. A frequency range appears for which no modes exist. In this gap (the bandgap) waves cannot propagate regardless of the direction. The small inserted figure shows the *irreducible Brillouin zone* (Brillouin, 1953) spanned by the triangle $\Gamma-X-M-\Gamma$. The zone relates to the smallest repetitive unit in the periodic material – the *unit cell* (it is here a quadratic cell) – as well as its symmetry properties. The irreducible Brillouin zone indicates the wave vectors which are necessary to investigate in order to completely describe wave propagation through the material. It turns out to be sufficient to examine the wave vectors corresponding to the triangular path ¹.

About half a century later, in 1987, the discovery of the bandgap phenomenon for optical waves – *photonic bandgaps* – by John (1987) and Yablonovitch (1987) marks a major breakthrough in the field of electromagnetics. This finding had

¹In principle the entire triangular area must be examined, but it is commonly accepted that it is sufficient to examine the wavevectors on the exterior triangular path. To the author's knowledge no proof of this has been presented yet.

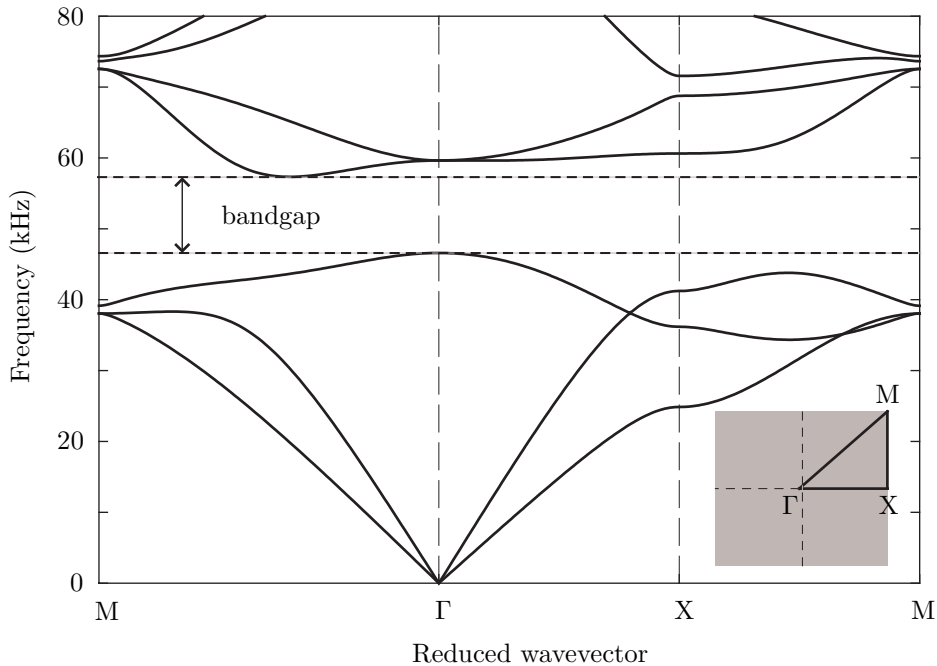


Figure 1.2 A band diagram for an infinite periodic material. The solid lines show propagating modes with the wave frequency along the vertical axis and the reduced wave vector (property of wave length and propagation direction) along the horizontal axis. A bandgap appears as a frequency range for which no waves can propagate through the material regardless of its direction. The inserted figure shows the irreducible Brillouin zone for the periodic material which is spanned by the triangle $\Gamma - X - M - \Gamma$. The wave propagation can be completely described by analyzing the wavevectors corresponding to the triangular path.

a significant impact and intensive research on the photonic bandgap phenomenon continues today in connection with applications in photonic crystal fibres and possible future applications in integrated optical circuits. Many books and papers have been published on the subject, e.g. the monograph by Joannopoulos et al. (1995) who provide a comprehensive set of band diagrams for different configurations of photonic bandgap materials – also known as *photonic crystals*.

The discovery of photonic bandgaps led to a "rediscovery" of the bandgap phenomenon for elastic waves. Band diagrams were produced and bandgaps found for many different periodic material configurations in 1D, 2D and 3D, see e.g. Sigalas and Economou (1992), Kushwaha (1996) and Suzuki and Yu (1998). Gaps in the band diagrams were now often referred to as *phononic bandgaps* or sometimes acoustic or sonic bandgaps. Parallel to this work, research on structures with a periodic-like nature was carried out including the works by Elachi (1976) and Mead (1996). Here, the main focus was not on the bandgap properties of an infinite periodic material but instead on the effect of the periodicity on the dynamic performance of engineering

structures.

The first paper of this thesis (paper [1]) intends to couple the analysis of the bandgap phenomenon for elastic waves in a periodic material with the corresponding dynamic behavior of a finite structure made from this periodic material. Furthermore, this paper attempts to provide an increased understanding of the *applicability* of bandgap structures in mechanical structures by studying the influence of boundaries, damping and disorder. Paper [1] was followed by other papers that investigate different aspects of the bandgap phenomenon.

Optimal material distribution – topology optimization

In past research bandgap materials in 2D and 3D are almost exclusively found in the form of circular or spherical inclusions. For the static behavior of mechanical structures it has been long known that circular or spherical holes are rarely optimal with respect to structural performance, but similar conclusions for elastic or optical waves are not widely known. In two papers, Cox & Dobson used a numerical material distribution method to optimize the distribution of air and dielectric material in a photonic bandgap material and maximized the size of the gap (Cox and Dobson, 1999, 2000). They found that circular holes were not optimal. Sigmund (2001) used *topology optimization* to maximize phononic bandgaps for elastic materials and arrived at a similar conclusion.

The method of topology optimization is widely applied in this thesis. Topology optimization of mechanical structures was introduced by Bendsøe and Kikuchi (1988) in order to optimize the material distribution and obtain maximum stiffness. Paper [4]² attempts to apply the topology optimization method to design phononic bandgap structures, i.e. to find the distribution of two elastic materials that optimizes the performance of the structure. This could be to minimize the vibrational response in a certain part of the structure. The basic hypothesis is that the optimal material distribution in certain cases should have a periodic appearance – a *bandgap structure*.

The work in paper [4] was later extended and topology optimization applied to design a number of different bandgap structures. The design methodology used in this thesis follows the outline schematically illustrated in Fig. 1.3. The top left figure shows a part of an original structure with two different materials (here the darkest color represents air holes and the two shades of gray represent a dielectric material). The top right figure shows a corresponding finite element (FE) model which is parameterized with a single *continuous design variable* x_e assigned to each element. With a suitable interpolation scheme, see e.g. Bendsøe and Sigmund (1999), it is ensured that $x_e = 0$ corresponds to air (illustrated as light gray) and $x_e = 1$ corresponds to dielectric material (black). A gradient-based iterative algorithm is then applied to find the set of design variables that optimizes a specified performance

²In the author's contribution to the paper.

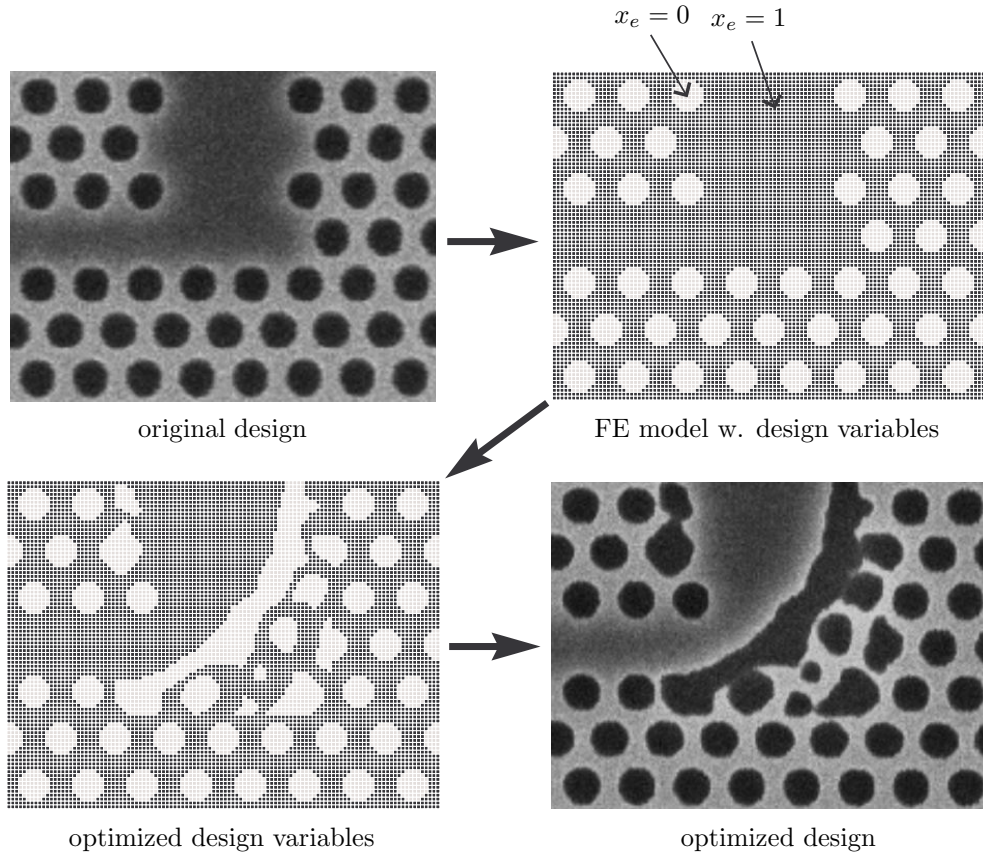


Figure 1.3 Illustration of the topology optimization method for optimizing the distribution of two materials in a bandgap structure. Top left: the original design with the dark color indicating air holes and light/dark gray indicating a dielectric material. Top right: finite element (FE) model with one continuous design variable x_e per element, for which $x_e = 0$ represent air (light gray) and $x_e = 1$ represent dielectric material (black). Bottom left: FE model with an optimized set of design variables taking either the value 0 or 1. Bottom right: the fabricated optimized design.

measure (objective function), e.g. maximizes the wave transmission through the structure. This procedure is based on the use of analytically computed gradients (the sensitivity of the objective function wrt. the design variables) and the use of a mathematical programming tool, as e.g. Krister Svanberg’s MMA (Svanberg, 1987). The bottom left figure shows the FE model with the optimized element design variables corresponding to a new distribution of the two materials. Finally, the bottom right figure shows the fabricated optimized structure.

As a general feature of topology optimization certain numerical techniques must be applied in order to generate usable optimized structures. *Penalization* is used to avoid design variables in the final design with intermediate values ($0 < x_e < 1$) that do not correspond to any of the specified materials. *Regularization* is applied to

convert ill-posed optimization problems into well-posed problems. *Filtering* is used to solve problems with mesh-dependency of the designs and also problems with small structural details that are not amenable to fabrication. For an overview of these tools and their application see e.g. the monograph by Bendsøe and Sigmund (2003). In this thesis new techniques have been developed to deal with issues specifically relevant to the optimization problems treated here.

Structure of the thesis

The four following chapters present the main results obtained in the thesis papers [1]–[21].

Chapter 2 is dedicated to the analysis of the bandgap phenomenon. The analysis is based on simple mass-spring structures and the results highlight the effect of finite dimensions, damping, nonlinearities, and type of bandgap material on the behavior of structures made from a bandgap material. Experimental support of the performance of bandgap structures is provided as well.

Chapter 3 introduces the method of topology optimization as a design tool for bandgap structures. The methodology is used to design structures that quench structural vibrations, minimize the transmission of elastic and acoustic waves and maximize the dissipation of waves. Furthermore, the chapter demonstrates that bandgap structures can be created by maximizing the separation of structural eigenfrequencies.

Chapter 4 illustrates the optimization method used to design photonic waveguide structures. Photonic crystal waveguide bends and splitters with low loss in large frequency ranges are designed. The method is also applied to design a wavelength splitter and splitters for waves in photonic ridge waveguides. The theoretical results are supplemented by fabricated devices and experimental testing of the performance.

Chapter 5 presents new advanced optimization procedures that are developed to design bandgap structures and are applicable to a broader range of problems as well. It illustrates an efficient method to optimize the performance of structures in finite frequency ranges by the use of Padé approximants. A transient topology optimization formulation is formulated to deal with a nonlinear bandgap structure and finally the chapter presents an extension of the transient topology optimization method to allow for optimized structures that vary in time as well as in space.

In each of the chapters a general brief introduction is followed by a summary of the contents of the relevant thesis papers and key references to original works in the area. Then comes a description of the main results from the papers and the chapters are concluded by references to the recent advances made in the research field since the publication of the thesis papers.

A concluding chapter summarizes the main contributions of the thesis.

Chapter 2

The bandgap phenomenon

In order to understand complex phenomena it is always useful to look at the simplest possible structure that displays the behavior of interest. This obvious observation fully applies to the phenomenon of the formation of gaps in the band structure for periodic materials. A system of simple masses connected by linear springs is particularly useful because it produces simple equations often amenable to analytical predictions. Additionally, visualization of the dynamic behavior is straightforward and this aids immensely in the process of grasping the mechanisms involved.

All theoretical results presented in this chapter are obtained using simple mass-spring models. This chapter intends to provide a fundamental understanding of the bandgap phenomenon and pinpoint the factors that have significant impact on the performance of engineering structures that integrate bandgap materials.

Thesis papers [1]–[3]

Paper [1] presents an analysis of the interaction between bandgaps and forced vibrations for 1D and 2D mass-spring systems. The focus is on these issues: the effects of the finite dimensions of structures created from a bandgap material, the effect of non-idealities such as damping and disorder and the possibility of creating waveguides in bandgap structures. These effects are analyzed for different types of bandgap materials. One of these offers the possibility of creating low-frequency bandgaps.

Paper [2] demonstrates experimentally the bandgap phenomenon for longitudinal vibrations in an elastic rod composed of sections of aluminum and PMMA (plastic). The experimental results are compared to predictions based on the mass-spring model studied in paper [1]. Paper [2] contains preliminary optimization results for bandgap structures which are relevant to the results presented in Chapter 3.

Paper [3] analyzes the bandgap behavior and wave transmission in a finite nonlinear structure using analytical and numerical tools. It focuses on a one-dimensional mass-spring system with nonlinear resonators attached with respect to low-frequency bandgaps. Special attention is given to the effect of the nonlinearities on the wave transmission through the chain. Furthermore, the paper includes a discussion of the possibilities of utilizing a non-uniform distribution of nonlinearities to reduce the wave transmission.

Main references

The main inspiration to paper [1] is the pioneering work by Brillouin (1953) who contributed significantly to the understanding of wave propagation in periodic lattice structures in 1D, 2D and 3D including the formation of bandgaps. It was influenced also by the work of Martinsson and Movchan (2003) who studied bandgaps in 2D lattice structures and looked at low-frequency bandgaps created by local resonating structures. However, the major contribution to the investigation of local resonators in mechanical structures was made previously by Liu et al. (2000) who introduced the concept of *locally resonant material*.

The effect of nonlinearities on bandgaps was only subjected to a few studies such as by Marathe and Chatterjee (2006). They examined the effect of weak nonlinear damping on the propagation characteristics of a periodic mass-spring structure.

2.1 Band diagram and forced vibrations

The band diagram reveals the fundamental characteristics of wave propagation through a periodic material. Fig. 2.1 shows the basic building block of a periodic material – the unit cell¹ and the corresponding band diagram. Propagating modes (indicated with solid lines in Fig. 2.1b) do not exist in the frequency range $\approx 46.6 - 57.3$ kHz for this particular configuration and set of parameters values. This implies that no waves in this range can propagate through the material regardless of the direction of propagation.

Thus, the band diagram provides useful information about propagation of waves in an infinite material. To fully understand the potential for applying bandgap materials in engineering structures the forced vibration response of a *finite structure* made from such a material is investigated. Fig. 2.2a displays a finite structure with simple supports and periodic loading with frequency Ω . The structure is composed of a number of identical unit cells (M_x cells horizontally and M_y vertically). Fig. 2.2b shows the forced vibration response of point A located in the middle position of the bottom structural boundary. There is a correlation between the bandgap frequency range (indicated by vertical dashed lines) and a low vibration response in point A. If the structure is composed of many unit cells (such as 15×15 or more), the response dips exactly when the forcing frequency exceeds the lower bandgap frequency limit. This response dip is significant and more pronounced with more unit cells. When waves cannot propagate in the material a high steady-state vibration level cannot build which explains this correlation. Instead the vibration level decays exponentially away from the point of excitation. With fewer unit cells (say 7×7 or less) the boundary effects become more dominant and resonance peaks appear within the bandgap frequency range close to the lower bandgap frequency limit.

¹The unit cell is defined as the smallest repetitive unit in a periodic configuration. The periodic material is understood as an infinite assembly of such unit cells.

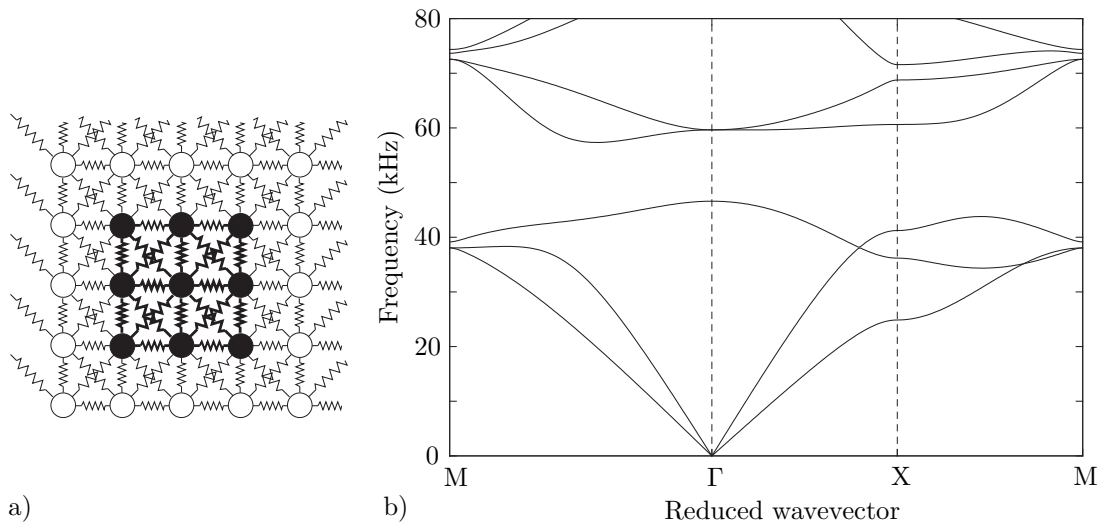


Figure 2.1 a) A 2D unit cell consisting of an inclusion with 3×3 masses and connecting springs (in bold) surrounded by a matrix material with additional masses and springs, b) The corresponding band diagram showing the frequency of propagating modes versus the reduced wavevector (indicating wavelength and direction of propagation). From paper [1].

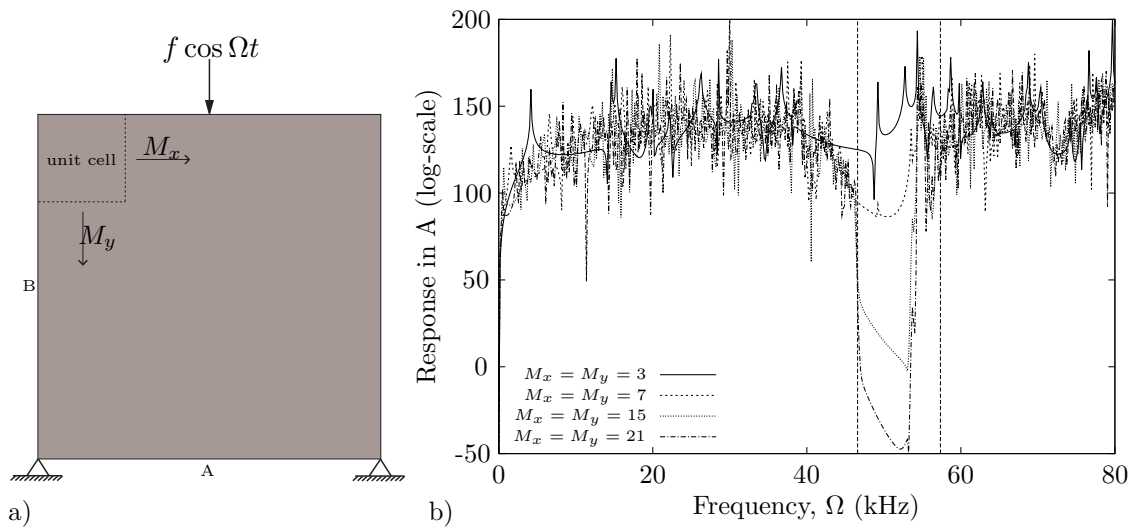


Figure 2.2 a) A simply supported structure with $M_x \times M_y$ unit cells subjected to a periodic load $f \cos \Omega t$, b) The acceleration response in point A with different numbers of unit cells in the structure. From paper [1].

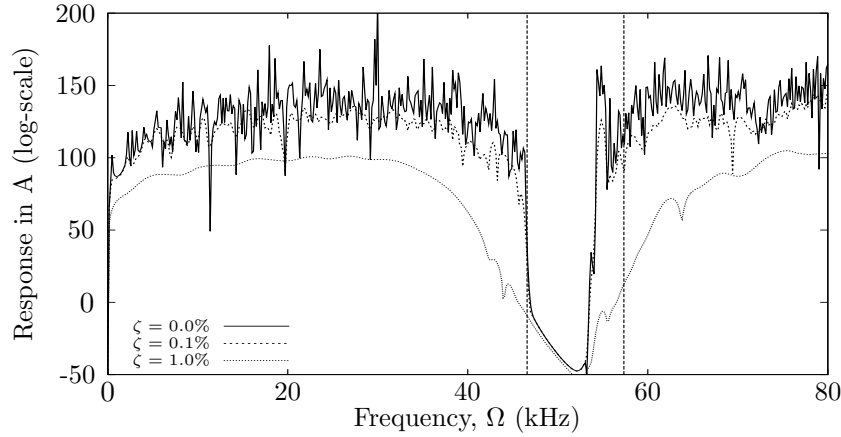


Figure 2.3 The influence of added viscous damping characterized by the damping ratio ζ of the individual masses. From paper [1].

At first glance the correlation seems to fail near the upper limit of the bandgap frequency range. Here, many resonance peaks and thus high vibration levels are found within the gap – also with many unit cells in the structure. However, unit cells near the boundary of the structure behave differently due the presence of a free edge and actually allow waves to propagate for these frequencies. Therefore it is possible for waves to propagate from the point of excitation to point A and to create high vibration levels.

2.2 Structural damping

Thus, it is clear that the dimensions of a bandgap structure and the presence of boundaries have a great influence on the bandgap footprint observed in a structure made from a periodic material. Another important factor that affects the vibrational behavior is the presence of structural damping.

Fig. 2.3 shows the response (measured in point A) of the structure shown in Fig. 2.2a with 21×21 unit cells. Curves indicate the undamped response as well as the response computed with linear viscous damping added to the masses. The damping corresponds to levels of 0.1% and 1.0% relative to critical damping of the individual masses. The expected effect of damping is clearly noted outside the bandgap frequency range where damping reduces the magnitude of resonance peaks and anti-resonance dips. The result is a more smooth response curve. Within the gap the apparent effect of damping is small. Hence, the vibration suppression from the bandgap effect dominates the suppression effect from damping. Only a high level of damping (1.0%) results in a slightly increased vibration reduction.

The results also indicate that the bandgap effect is retained even if all resonance effects away from the bandgap frequency range are smoothed by strong viscous damping. This result turns out to be very useful for optimizing bandgap structures (cf. Chapter 3).

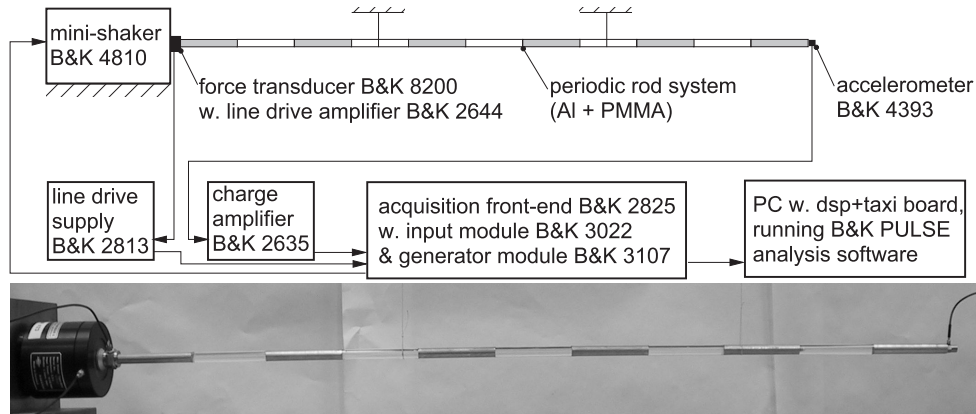


Figure 2.4 Experimental setup and part of the setup showing (from left to right) the vibration exciter, force transducer, periodic bar system with supporting threads, and accelerometer. From paper [2].

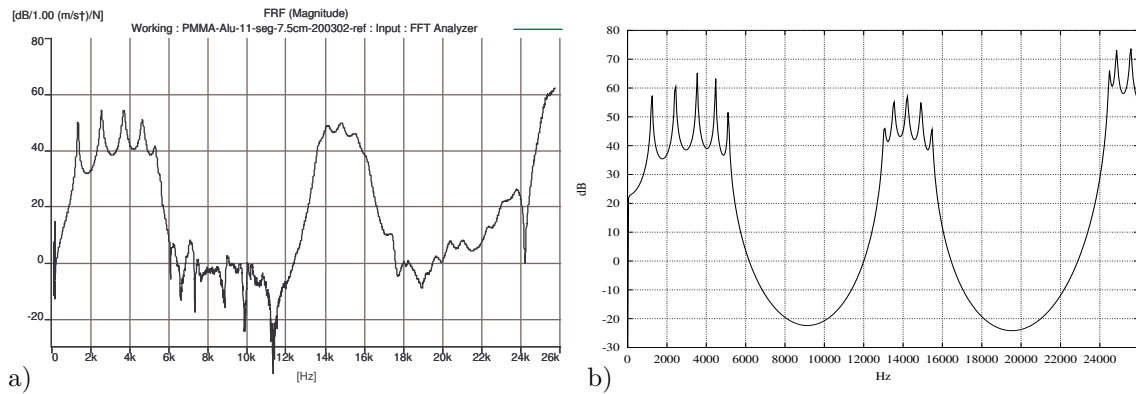


Figure 2.5 Response curves showing the acceleration response at the end of the bar versus the excitation frequency. Left: experimental data and right: corresponding theoretical predictions. From paper [2].

2.3 Experimental demonstration

The theoretical predictions are based on simple mass-spring models. Thus, it is here especially important to support observations and conclusions experimentally. In this way it can be documented that the bandgap phenomenon manifests itself in a realistic setup and is not merely the product of an overly simplified model.

Fig. 2.4 illustrates a schematic and experimental setup for measuring the forced vibration response of an elastic rod composed of alternating sections of aluminum and PMMA (a plastic material). The rod is subjected to periodic forcing imposed by a shaker in one end and the acceleration is recorded in the other end using an accelerometer. Fig. 2.5 shows plots of the measured response and the response predicted by a mass-spring model fitted to the actual material parameters including a single fitted viscous damping parameter.

The model predicts two frequency ranges with a low vibration level due to bandgaps in the band diagram for the corresponding periodic structure. The two gaps are computed to be located at $\approx 5.5 - 13$ kHz and $\approx 15.5 - 24.5$ kHz. The low vibration levels observed in the simulations are confirmed by the experiment. The non-smooth response within the bandgap frequency ranges is ascribed to background noise in the experimental setup (cables etc.).

2.4 Low-frequency bandgaps

The required spatial periodicity is a fundamental characteristic of a bandgap material. It also sets an important limitation for using bandgap materials as components in engineering structures. For example, compressional elastic waves/vibrations in steel at 200 Hz correspond to a wavelength of approximately 30 m. With a periodicity required at approximately the same order of magnitude, this naturally leads to finite structures of impractical large dimensions.

A way to circumvent this fundamental limitation is to use another type of unit cell. This is illustrated in Fig. 2.6b that shows a forced response curve for a corresponding finite structure (with loading and boundary conditions as in Fig. 2.2a) shown in Fig. 2.6a. The unit cell consists of a stiff and dense inclusion (the center 2×2 masses and connecting springs) which is suspended by flexible springs (a coating layer) and embedded in a matrix material. A bandgap emerges near a frequency in the vicinity of the fundamental natural frequency for rigid body motion. This frequency is primarily influenced by the total mass of the inclusion and the equivalent stiffness of the coating layer. Thus, with a suitable choice of parameters the bandgap can be moved to a low frequency range. This would otherwise require a unit cell of much larger dimensions.

It should be emphasized that the mechanism that causes this bandgap is fundamentally different from the previous examples. The prohibition of wave propagation is not caused by in-phase reflections but by a coupling to resonant motion of the inclusion. Hence, the structure behaves as if multiple added-mass vibration dampers were attached to it. The difference is also reflected in the forced vibration curve that shows a low vibration level only near the lower bandgap frequency limit (corresponding to the rigid body natural frequency). Additionally, it can be observed that the response is fairly insensitive to the positioning of the inclusions. This supports the conclusion that this phenomenon is not relying on a periodicity of the structure which is otherwise a key feature of the "normal" bandgap phenomenon.

2.5 Nonlinearities

For practical applications of bandgap materials the extension to the low-frequency range is promising. This section further investigates the effect of nonlinearities on low-frequency bandgap behavior. Fig. 2.7 shows a one-dimensional mass-spring

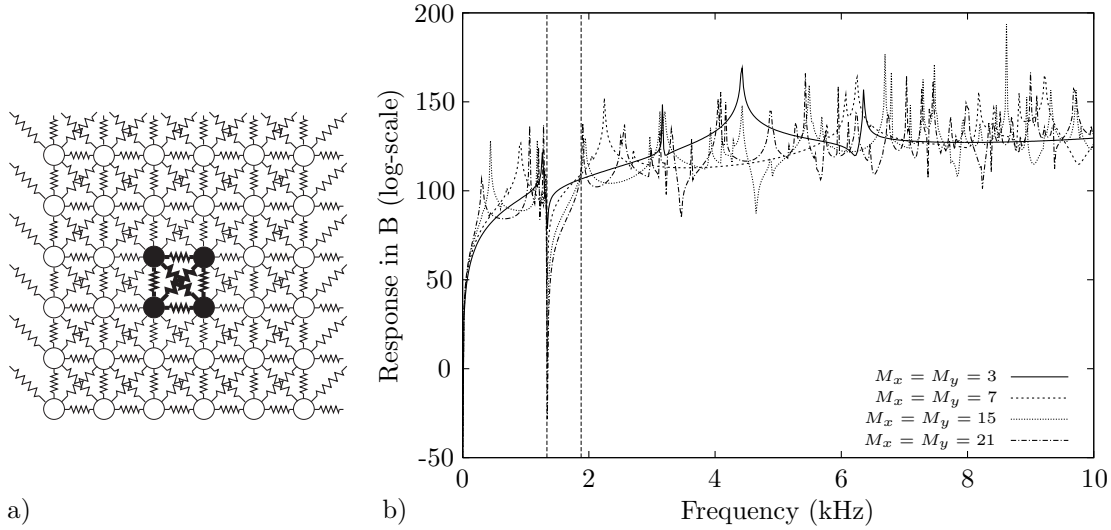


Figure 2.6 a) A 6×6 mass-spring unit cell that models a heavy stiff resonator (center 2×2 masses and springs) in soft suspension (surrounding springs) connected to a surrounding matrix material, b) The acceleration response in point B (cf. Fig. 2.2) with different numbers of unit cells included in the structure. From paper [1].

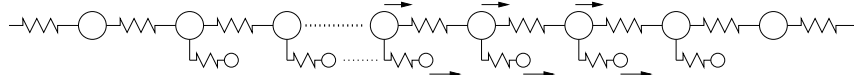


Figure 2.7 Linear mass-spring chain with local oscillators attached to the masses via linear or nonlinear spring (as well as linear viscous dampers). From paper [3].

structure with identical oscillators attached to the masses in the main structure. The structure behaves in a similar manner as the two-dimensional structure described in Section 2.4. Consequently, the corresponding periodic material has a bandgap near the eigenfrequency of the local oscillators.

If the local oscillators are attached to the main masses via nonlinear springs, the bandgap behavior is significantly modified. Cubic hardening springs make the attached system stiffer for high vibration amplitudes and therefore move the bandgap up in the frequency range. As a result, the bandgap becomes a local property as its location in the frequency spectrum depends on the local vibration amplitude of the attached oscillator. The resulting complex behavior is illustrated in the transmission of waves through a finite chain². Fig. 2.8 shows the transmission of a harmonic wave through a chain with 2000 attached oscillators (each having a normalized linear eigenfrequency of 1). For linear oscillators (Fig. 2.8a) the bandgap behavior is noticed with a low wave transmission in a well defined frequency range. With cubic hardening nonlinear oscillators the low transmission region is moved up in the fre-

²The chain is finite, but absorbing boundaries conditions are added to both ends in order to simulate wave transmission.

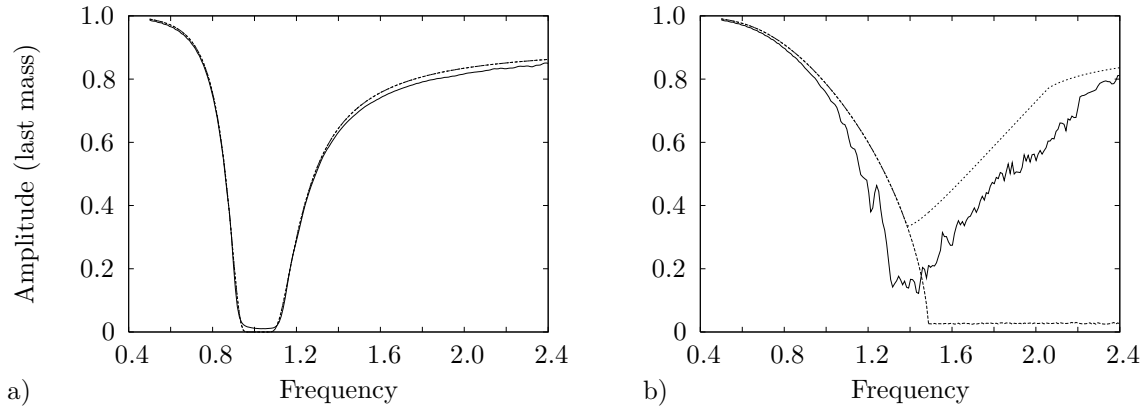


Figure 2.8 Amplitude of last mass (relative to the first mass) for a one-dimensional mass-spring structure with 2000 attached oscillators. a) Linear oscillators, b) Nonlinear oscillators. Solid lines: numerical simulation, dotted lines: analytical predictions of upper and lower amplitude bounds. From paper [3].

quency range and the behavior is much more complex due to the varying bandgap behavior along the structure and the nonlinear wave interaction. However, it can be observed that the amplitude reduction is smaller than for the linear case, but the frequency range with a significant reduction of the amplitude is slightly broader. The figures also illustrate upper and lower bounds for the response predicted analytically.

The perspectives for using a non-homogeneous distribution of nonlinearities along the chain is illustrated in Fig. 2.9 for the case of 400 attached oscillators. The solid line represents the wave transmission when the nonlinear parameter is increased along the chain according to a prescribed exponential function. This is done to compensate for the reduced wave amplitude and the resulting decrease in the bandgap frequency. The transmission is also shown with three different constant values of the nonlinear parameter. These values correspond to the minimum, maximum and the average value of the exponential parameter variation. It is seen that the non-homogeneous distribution opens up the possibilities of further wave propagation suppression. These findings have prompted the work on optimization of local oscillator parameters as presented in Section 5.2.

Relations to recent work

The research on bandgaps has continued with increasing intensity and a large number of papers have appeared since the publication of paper [1].

Paper [1] contributed to the basic understanding of the bandgap phenomenon by studying simple mass-spring systems. Other researchers have continued this work up until the present date. An incomplete compilation of recent theoretical papers on mass-spring systems include the work by Avila and Reyes (2008) on phonon propagation through 1D atomic structures, by Zalipaev et al. (2008) on waves in

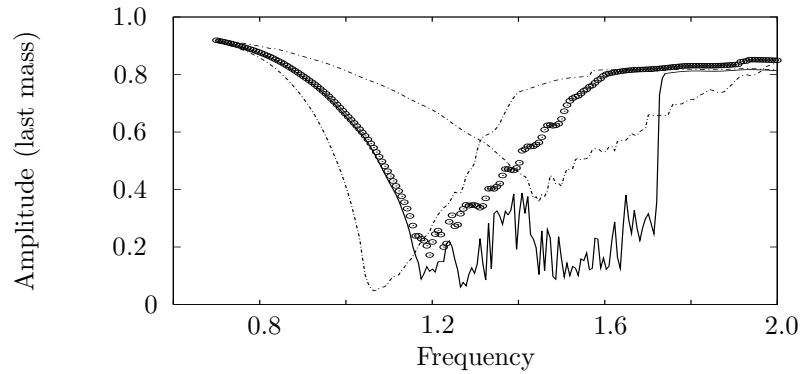


Figure 2.9 Relative amplitude of the last mass for non-homogeneous nonlinearity (solid line) for a structure with 400 attached oscillators. The circular dots and the two dashed lines show the amplitude for fixed nonlinearities of 0.3, 0.12 and 0.88 corresponding to the average, lowest and the highest value used for the chain with varying non-linearities. From paper [3].

2D lattices with defects, and by Yan et al. (2009) on localized modes for 1D elastic waves. Recently, experimental work has been carried out by Hladky-Hennionne and de Billy (2007) who investigated bandgaps in 1D diatomic structures and by Yao et al. (2008) who examined a structure with local resonators.

A large amount of recent papers concentrate on the creation of low-frequency bandgaps using local oscillators – often referred to as locally resonant materials. The research has focused on the use of local oscillators in different types of mechanical structures such as beams, plates and rotating shafts (Wang et al., 2006; Yu et al., 2006a,b; Liu et al., 2007). The connection between locally resonant materials and multiple added mass-dampers was recently investigated in a conference paper by the author and Boyan Lazarov (Jensen and Lazarov, 2007). Furthermore, the link between locally resonant materials and *electromagnetic metamaterials* was pointed out recently by Huang et al. (2009) and Zhou and Hu (2009).

Chapter 3

Bandgap structures as optimal designs

It can be concluded from the study of simple mass-spring structures that a large reduction of the vibration level can be obtained if the structure is created from a periodic material – a bandgap structure. One question then naturally arises: "Are bandgap structures then optimal for quenching vibrations?". The answer is in many cases yes and *periodic-like* structures often appear as optimal designs. Whether this is the case depends on the contrast of the material properties and the dimensions of the structure relative to the frequency of vibrations.

This chapter presents optimized designs for different types of mechanical and acoustic structures. All results are based on FE continuum models combined with gradient-based topology optimization.

Thesis papers [4]–[9]

Paper [4] presents a study of the optimal layout of two elastic materials in a planar two-dimensional continuum structure that is subjected to forced in-plane vibrations. The author's contribution to the paper focuses on design of structures that quench vibrations. Special emphasis is put on an investigation of how the optimized material layout depends on the contrast between material properties and the effect of different loading conditions. Additionally, the possibility of creating elastic waveguiding structures is explored.

Paper [5] also deals with optimization of the layout of two elastic materials in a planar two-dimensional structure. Here, the structure is subjected to a steady-state pressure or shear wave propagating in multiple directions. Special focus is put on investigating how the material layout depends on the wavelength of the wave relative to the dimensions of the structure.

Paper [6] follows up on the work initiated in paper [5]. Two-dimensional material layouts are obtained for the case of multi-frequency pressure and shear waves. Moreover, the optimization algorithm is extended to allow for distributing three materials in the structure. The paper also considers the design of structures that maximize the absorption of waves with two or three materials available.

Paper [7] considers the problem of vibration quenching from another perspective. Instead of minimizing vibration levels or wave amplitudes, the eigenfrequencies of the structure are explored. The paper demonstrates that bandgap structures can be created by maximizing the separation of two adjacent eigenfrequencies. The connection between the material properties and the maximum possible separation of eigenfrequencies is investigated as well.

In paper [8] the optimization problem is extended to the case of transverse vibrations and waves in moderately thick plates. The paper deals with optimizing the distribution of two elastic materials in order to suppress forced vibrations or guide elastic waves in designated paths in the plate.

Paper [9] studies a closely related problem in a quite different physical setting. Solid material is distributed in an acoustic chamber in order to minimize the transmission of acoustic waves through the chamber. The problem is considered for waves in a finite frequency range.

Main references

The design of phononic bandgap structures using a material distribution optimization method is believed to be a novel contribution of this thesis. Topology optimization methods had previously been used to design structures subjected to forced vibrations in the lower frequency range by Ma et al. (1993) for 2D elastic problems and by Soto and Diaz (1993) for plate structures. Tcherniak (2002) considered optimization of resonating structures and Jog (2002) optimized plates for minimum dynamic compliance by considering the dissipated energy. Optimization problems related to maximization and minimization of eigenfrequencies had also been considered using topology optimization, e.g. by Diaz and Kikuchi (1992) for 2D elastic structures and by Pedersen (2000) for plates. Ma et al. (1994) and Osher and Santosa (2001) considered the problem of separating eigenfrequencies. However, here the separation of low order eigenfrequencies was examined with no special consideration to bandgap structures.

Topology optimization of plate structures for maximum bandgaps was first explored by the author, Ole Sigmund and Søren Halkjær (Halkjær et al., 2006). Diaz et al. (2005) had previously studied maximization of bandgaps in similar beam grillage structures.

The problem of using topology optimization to design acoustic structures was proposed in two conference papers by the author, Ole Sigmund and co-workers (Sigmund and Jensen, 2003; Sigmund et al., 2004).

3.1 Vibration-quenching structures

The primary optimization problem is:

What is the optimal distribution of two elastic materials in a structure so that the forced vibration response is minimized?

Fig. 3.1a shows the model used to create the optimized structures. A free planar two-dimensional structure (plane-strain condition) is subjected to forced vibrations by a harmonic load (with frequency Ω) acting along a free edge. The vibration response is minimized along the opposite edge. Fig. 3.1b illustrates the optimized distribution of

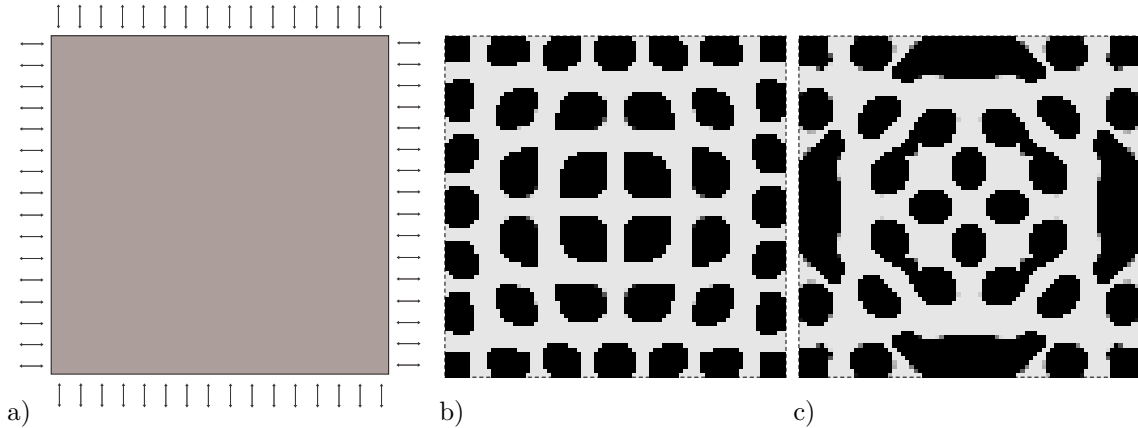


Figure 3.1 Optimized distribution of two elastic materials in a 2D structure (12×12 cm) for creating minimum response at 63 kHz. a) Structural domain and loading, b) Optimized distribution for a high material contrast, c) Optimized distribution for a low material contrast. In four considered scenarios, the load acts on one edge and the response is minimized on the opposite edge. From paper [4].

two materials with a high contrast between their material properties (mass density and Young’s modulus). Fig. 3.1c shows the distribution of the materials if the contrast is smaller. Four different loading scenarios are considered (with loading on each boundary) so that symmetrical structures are obtained.

For the high contrast case the structure appears periodic-like. However, it must be observed that the periodicity is irregular and changes near the free edges of the structure. This is not surprising, considering the results obtained in Section 2.1 which demonstrate that waves propagate differently along the structural boundary due to the presence of a free edge. Thus, along a free edge a different periodicity is needed to quench the vibrations. If the contrast is smaller, the structure cannot be characterized as periodic-like – although periodic substructures are observed. This is due to the fact that for the low contrast no bandgaps can be created for the infinite material¹ and consequently a periodic-like finite structure does not emerge.

Fig. 3.2 shows the vibration response curves for the two optimized structures. It is noticed that the response for the high contrast case has been significantly reduced. A clear bandgap footprint is observed with a well-defined low response frequency range. The vibration reduction is not nearly as pronounced for the low contrast case. It resembles more the low response obtained at the anti-resonances that distributed throughout the displayed frequency range. Furthermore, the figures show the response computed with a large amount of mass-proportional damping present. The significance of the damping is explained in the following.

The first attempts to find optimized material distributions for the structure in Fig. 3.1 were unsuccessful. A messy material distribution was obtained with no clear

¹A contribution from co-author Ole Sigmund.

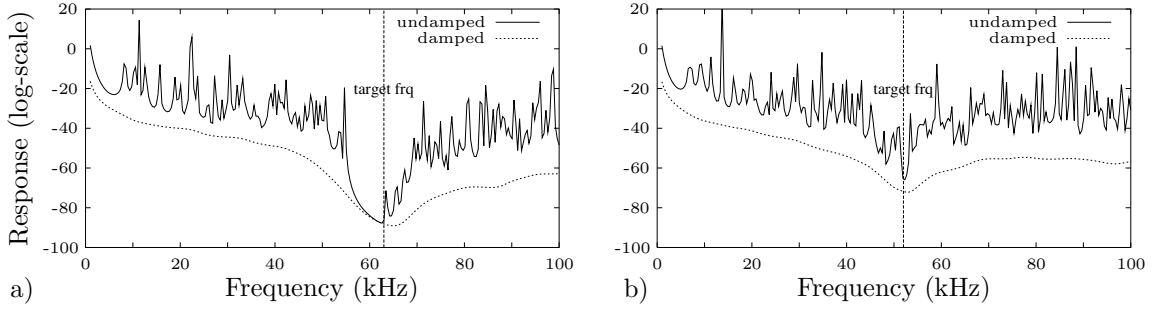


Figure 3.2 Vibration response for the two optimized material distributions in Fig. 3.1 showing the average response at the right boundary when subjected to loading at the left boundary. Target frequency for the optimization is indicated. a) High contrast case, b) Low contrast case. Curves shown with and without the added mass-proportional damping used in the optimization procedure. From paper [4].

definition of the two material constituents (black and light gray). It must be assumed that the multitude of resonance peaks and anti-resonance dips in the vicinity of the target frequency caused the optimization algorithm to find local optima with poor performance. Inspired by the work on mass-spring structures (Section 2.2) the optimization was then repeated with strong artificial damping added. This removes the peaks and dips in the response curves and results in the well-defined optimized structures shown in Fig. 3.1. The approach of using strong artificial damping in the optimization procedure has been applied successfully to most optimization problems in this thesis.

3.2 Maximizing wave reflection

The previous section showed optimized designs of structures subjected to forced vibrations. Their appearance could be explained with the connection between the bandgap phenomenon and vibrations of finite structures made from a periodic material as illustrated in Chapter 2. This section studies the closely related problem of optimizing planar two-dimensional structures subjected to propagation of harmonic steady-state waves.

Fig. 3.3 (top) illustrates the computational model used to create optimized designs for this type of problems. The design domain is indicated with length d_x and height d_y . Periodic boundary conditions are specified in the vertical direction in order to model a structure that stretches infinitely in the y -direction. The design domain (shown in dark gray) is surrounded by a homogeneous material and the optimized distribution of this material and a material with different elastic properties is to be identified. Using appropriate boundary conditions, a steady-state wave is simulated to propagate through the domain from left to right².

²As described in several thesis papers the study of wave propagation in finite structures relies

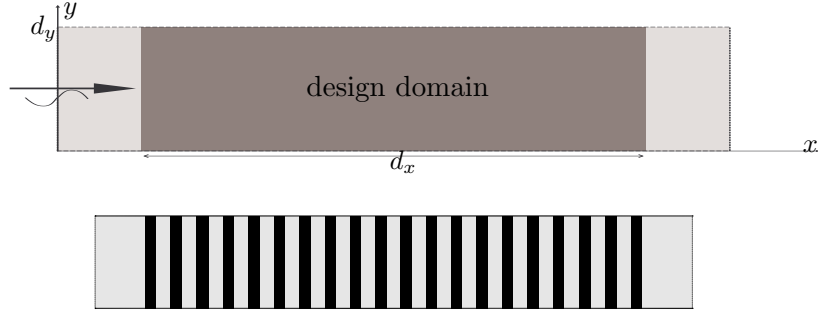


Figure 3.3 Top: computational model for obtaining optimized distributions of two different elastic materials in order to minimize wave transmission, bottom: the optimized design for a plane shear wave propagating in the structure. Design domain dimensions, length: $d_x = 10 \times \text{wavelength}$ and height: $d_y = 1/10$ of the length. From paper [5].

Fig. 3.3 (bottom) shows a typical optimized structure for the case of a normal incident shear wave. The wavelength is small compared to the dimensions of the structure ($\lambda \ll d_x$). In this case the optimal material distribution becomes a one-dimensional bandgap structure – also known as a *Bragg grating*.

Qualitatively different designs are obtained when the dimensions of the structure are reduced. This is also the case when different types of waves are considered simultaneously and when more wave frequencies are included. Fig. 3.4 illustrates two different examples of optimized designs along with the corresponding reflection curves. The curves show the reflected wave energy relative to the input energy versus the wave frequency. It is seen from a comparison with the structure in Fig. 3.3 that reduced structural dimensions result in fewer inclusions in the design. The particular design in Fig. 3.4a is created so that the transmission for *both* a shear and a pressure wave is minimized in a $\pm 10\%$ frequency range around 788 Hz. This condition results in a Bragg grating with uneven spacing between the three inclusion layers. Fig. 3.4b depicts the corresponding reflectance curves indicating a large reflection of both wave types. If the frequency range is extended to $\pm 25\%$, the optimized material distribution changes qualitatively and attains an intricate two-dimensional character (Fig. 3.4c and Fig. 3.4d).

Fig. 3.5 illustrates the effect of restricted dimensions of the structural domain combined with the effects of the angle of incidence and wave type. The structure is optimized for minimum transmission for a single frequency but with a variety of propagation directions. This is facilitated by considering a number of different loading conditions. For each loading condition a wave propagates from different small sections of the boundary. This ensures that the structure is able to reflect waves coming from different directions.

The dimensions of the structure are small so that $d_x \approx \lambda$. The three figures

on adding absorbing boundary conditions that allow waves to exit the structural domain without being reflected. One such type of boundary condition is the use of Perfectly Matched Layers (PML).

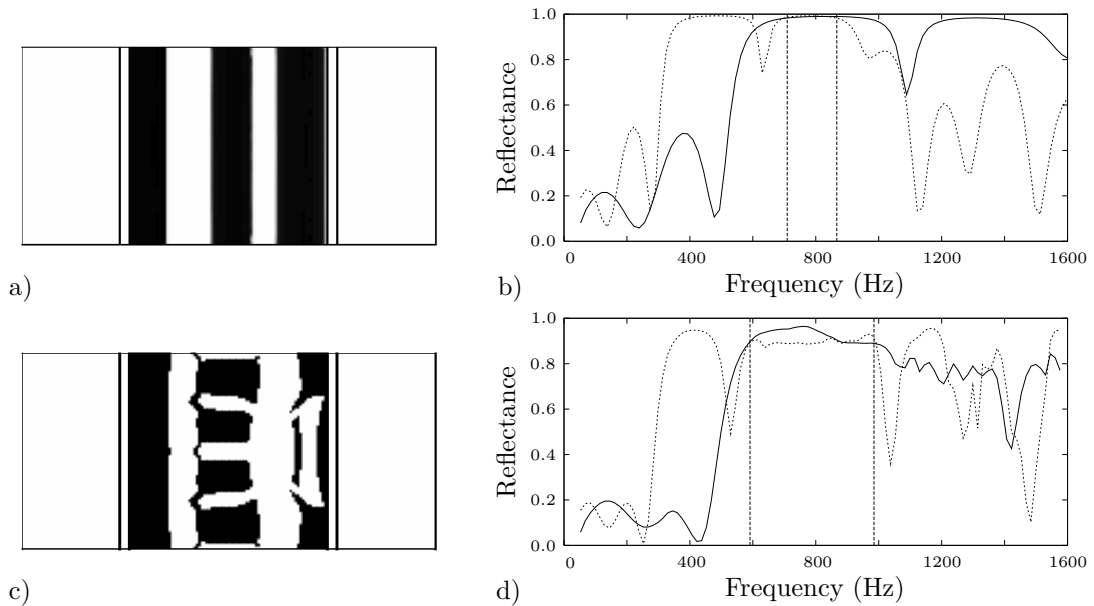


Figure 3.4 Optimized distribution of scattering (black) and host material (white) for maximum reflectance in a frequency interval around 788 Hz and reflectance curves for the optimized designs for pressure (solid line) and shear waves (dashed line). a,b) $\pm 10\%$ frequency interval, c,d) $\pm 25\%$ frequency interval. From paper [6].

are given for a pressure wave (a), a shear wave (b) and for both a shear and a pressure wave (c). The appearance of the structures reflects the multi-angle wave incidence that provokes the two-dimensional nature of the material distribution. The restricted spatial dimension also gives the structures appearances that are not regularly periodic.

The results show that adding a third material to the design problem has no beneficial effect on reducing the transmission of waves. In all reported cases the best performance is obtained for a structure that is composed of the two materials having the largest contrast between their material properties. For a further discussion of this observation see the comments in the last paragraph of this chapter.

3.3 Eigenfrequency separation

The optimized structures strongly depend on the specific location of the input force and/or the direction of the incoming wave. Hence, a unidirectional wave usually results in a one-dimensional structure (Bragg grating) optimized for exactly this form of excitation. Other excitation types as in the form of multi-directional waves result in different structures. If the structure is to be optimized for all relevant loading conditions, the problem of how to specify these loading conditions arises. An alternative to this approach is to consider the structural eigenfrequencies. If frequency ranges with no eigenfrequencies can be created, then no loading condition

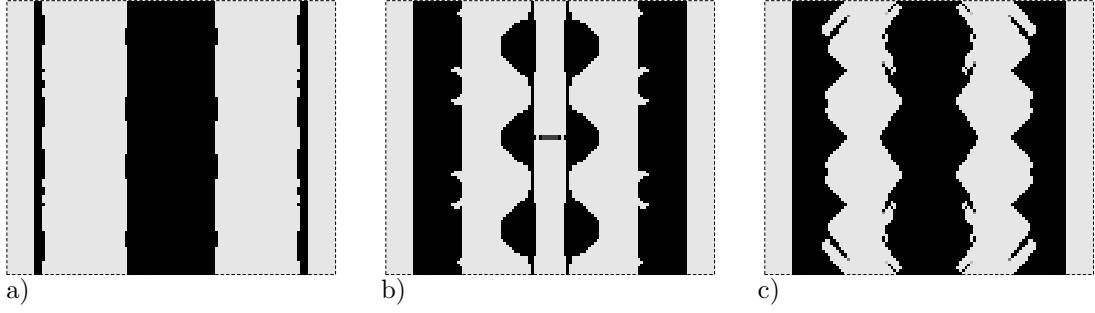


Figure 3.5 Optimized designs for the case of multi-directional wave input with a design domain length of twice the wavelength of a shear wave. The design domain height equals the length. Designs obtained for a) Pressure wave, b) Shear wave, c) Both pressure and shear wave. From paper [5].

can excite high vibration levels.

Fig. 3.6 shows two examples of optimized distribution of two materials in a 1D elastic bar and the corresponding vibration response. The response is recorded in one end of the bar when the structure is subjected to a periodic load in the other end³. The structures are obtained by formulating the optimization problem so that the separation of two adjacent eigenfrequencies is maximized. The resulting structures are clearly periodic-like bandgap structures with alternating sections of the two materials corresponding to the design variables taking the values 0 and 1. It is also evident that there exists a direct relation between the modes that are separated and the number of material sections in the optimized structure.

Additionally, it turns out that there is a direct connection between a single material contrast parameter and the maximum eigenfrequency separation that can be obtained. Here, the separation is quantified as the *ratio* between two adjacent eigenfrequencies. Fig. 3.7 shows the eigenfrequency separation for the optimized structures versus the mode numbers that are separated. Depending only on the contrast parameter $\beta = \rho_2 E_2 / (\rho_1 E_1)$, an asymptotic limit is found for how much the eigenfrequencies can be separated. Here, E and ρ denote Young's modulus and mass density, respectively.

It can also be shown that the fraction occupied by each of the two materials in the optimized structure relates directly to the contrast parameter $\alpha = \rho_1 E_2 / (\rho_2 E_1)$. For instance, it is observed that if $\alpha = 1$ then the two materials are equally represented in the optimized design.

3.4 Maximizing wave dissipation

All results presented so far have focused on the ability of bandgap (or periodic-like) structures to quench vibrations or to reflect waves. However, another interesting

³The 1D problem is supplemented by a similar problem in 2D in paper [7]. This is the contribution of the co-author Niels L. Pedersen.

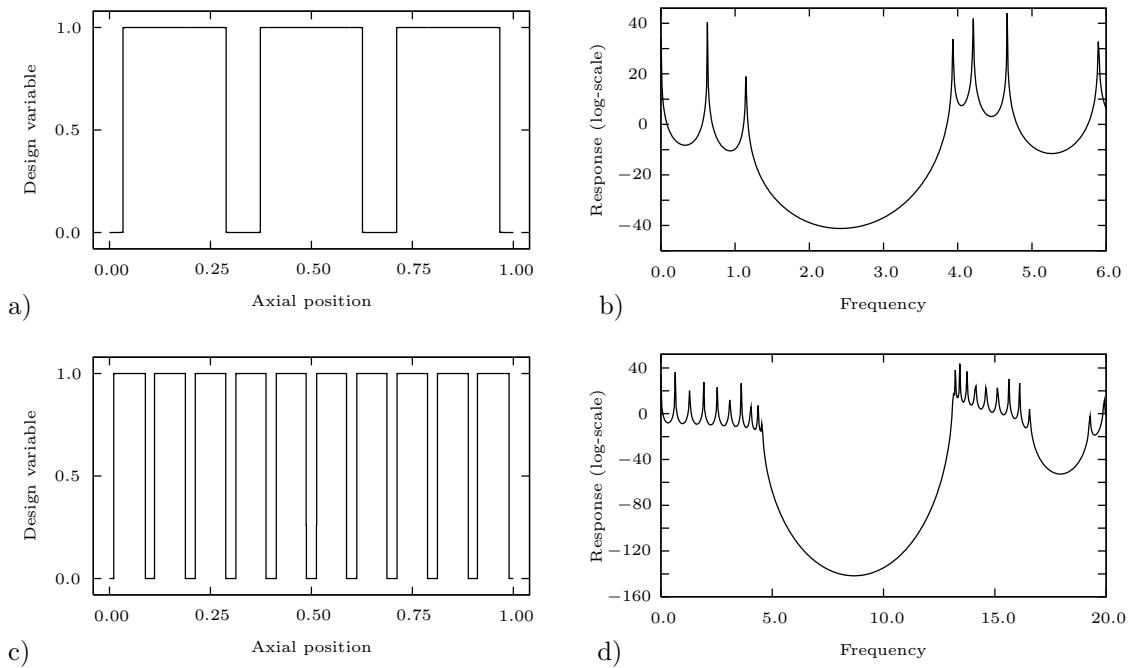


Figure 3.6 Optimized element design variables for maximum separation of two adjacent eigenfrequencies and the corresponding forced response curve for the optimized designs. a,b) Separation of eigenfrequency number 2 and 3, c,d) Separation of eigenfrequency 9 and 10. From paper [7].

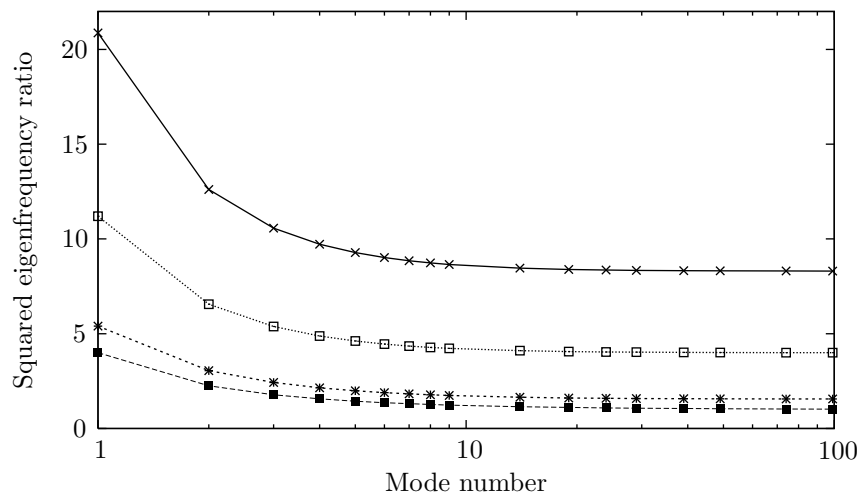


Figure 3.7 The squared eigenfrequency ratio for a series of optimized designs versus the optimization mode number. Curves are bottom-up for: a homogeneous rod (no optimization) and for increasing values of the material parameter $\beta = \rho_2 E_2 / (\rho_1 E_1)$ that characterizes the contrast between the two materials. From paper [7].

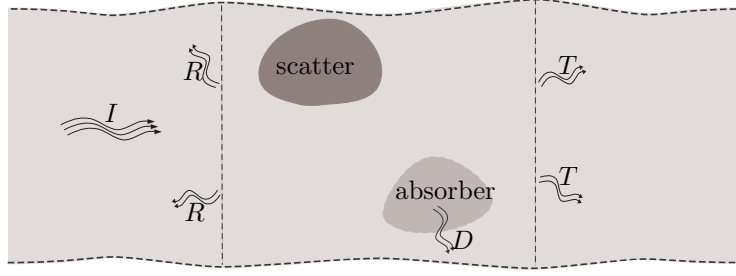


Figure 3.8 Basic setup for the problem of maximizing the dissipation of an incoming wave by optimizing the distribution of dissipating material (absorber) and possibly an extra reflecting material (scatter) in the background material. Incident wave power is I , transmitted and reflected powers T and R , and the dissipated power is D . From paper [6].

phenomenon is noticed if the dissipation of vibrations or waves is computed for a bandgap structure with added material damping. High energy dissipation occurs for frequencies near (but outside) bandgap frequency ranges where the eigenfrequencies are closely spaced in the frequency domain. This numerical observation leads to the question if periodic-like structures are also optimal for maximizing dissipation or, if not, which kind of structures are?

Fig. 3.8 shows the setup for studying maximization of the dissipation of elastic waves propagating through a two-dimensional section of material. The distribution of a background material and up to two additional materials is optimized. One of these materials is absorbing (and also slightly reflecting) and the other is a reflecting material (which is both denser and stiffer than the background material). Special focus is on investigating whether optimizing the distribution of both the absorbing and a reflecting material can increase the possible dissipation in the structure compared to distributing only absorbing material.

Fig. 3.9 depicts two examples of optimized material distributions. In Fig. 3.9a two materials are available: background (white) and absorbing (black) and in Fig. 3.9b the extra reflecting material is present (gray is the absorbing material and black is the reflecting material). Fig. 3.9a shows a clear distribution of the absorbing material. The structure is clearly not periodic-like, however, the distribution of inclusions inside the domain causes a large amount of wave reflection that leads to increased dissipation in the inclusions. Additionally, the thin strip of absorbing material near the inlet (left) causes an impedance match and a high transmission of the wave into the domain. The thicker material strip at the outlet (right) creates maximum wave reflection back into the domain. If the additional reflecting material is available (as shown in Fig. 3.9b), it replaces the outlet strip to increase the reflection of waves back into the absorbing domain. The distribution of the absorbing material inside the domain is different, too.

Fig. 3.9c illustrates the corresponding dissipation curve that depicts the fraction

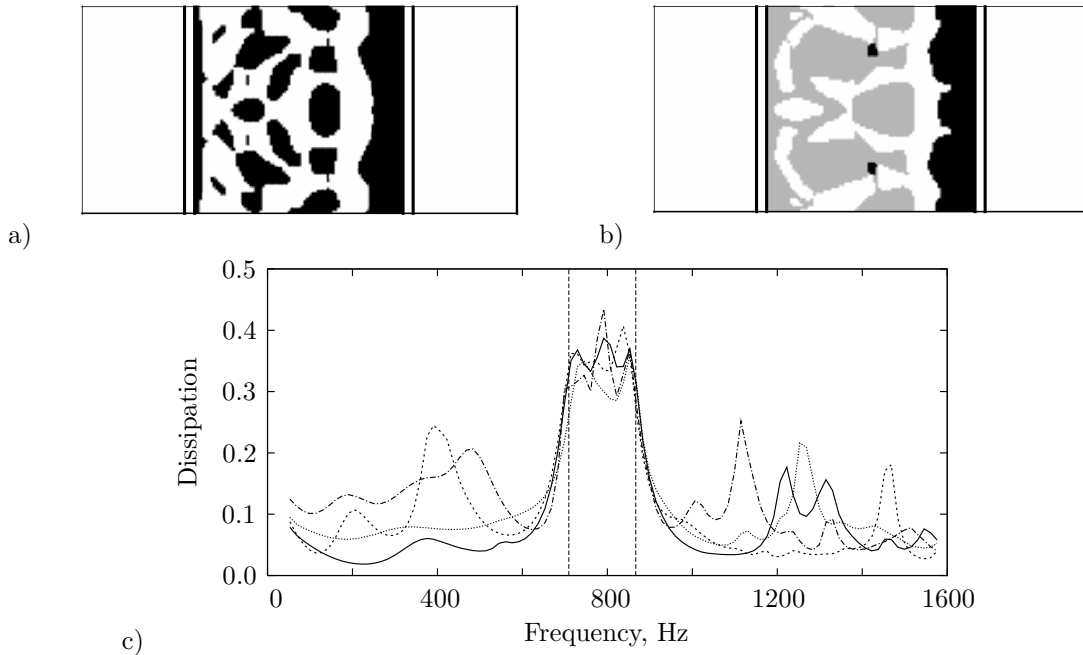


Figure 3.9 Optimized material distributions for maximum dissipation in a $\pm 10\%$ frequency interval around 788 Hz. a) Two materials: absorptive material (black) and loss-free background material (white), b) Three materials: absorptive material (gray), background material (white), reflecting material (black), c) Corresponding dissipated energy (relative to input energy) of pressure and shear waves. Pressure wave – 3 materials (solid), shear wave – 3 materials (dash), pressure wave – 2 materials (dot), shear wave – 2 materials (dashdot). From paper [6].

of the input wave energy that is dissipated versus the wave frequency. Plots for both pressure and shear waves are given. The curves in Fig. 3.9c show that the dissipation for both structures is about 40%, and the added benefit on the extra reflecting material is marginal. It should be noted that the dissipation is a factor two larger than the case in which the whole domain is filled with absorbing material. Structures that are efficient for absorbing wave energy could be of interest in components for which both transmission *and* reflection of incident waves is undesired or for energy harvesting purposes.

3.5 Plate structures

Plate structures are important for industrial applications in mechanics. The bandgap phenomenon can also be observed for bending waves and vibrations in plates. Such a wave type is typically of major interest for plates due to the corresponding low eigenfrequencies that often coincide with major emitters of waves and vibrations in mechanical structures. This section demonstrates how the material distribution in

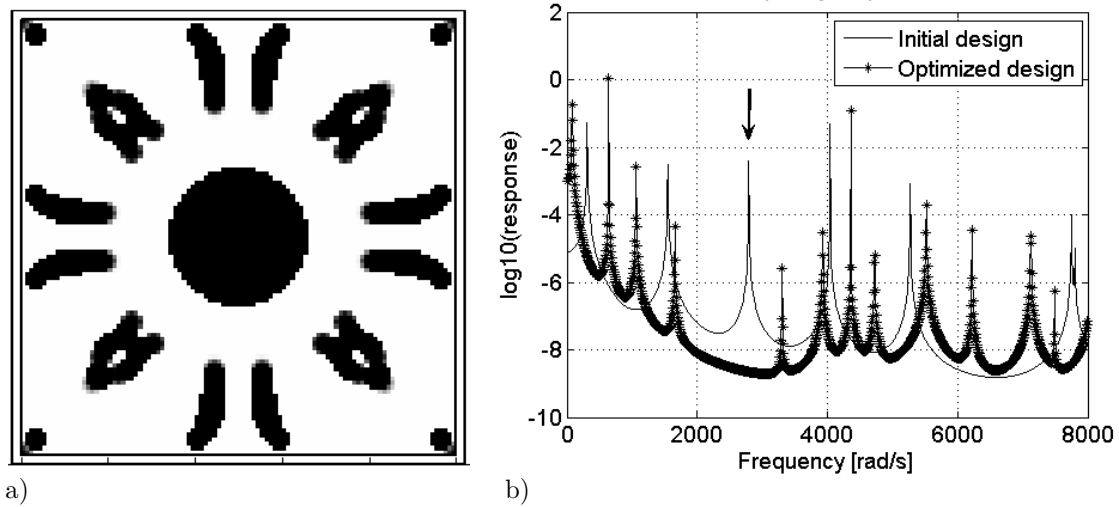


Figure 3.10 Minimization of the dynamic response of a simply supported plate subjected to a harmonic point load in the plate center. a) Optimized material distribution (black: steel, light gray: polycarbonate), b) Frequency responses for the optimized and initial (homogeneous) plate. The arrow in the frequency response indicates the optimization frequency. From paper [8].

plates can be optimized in order to quench vibrations and create advanced wave-guiding structures.

Fig. 3.10a shows an example of the optimized distribution of two elastic materials in a square plate of dimensions 30×30 cm with a thickness of 3 mm. The two materials are polycarbonate and steel and a maximum of 25 % of the material is allowed to be steel. The plate is simply supported along the rim and is subjected to a transverse harmonic load in the center. The optimized structure is seen to have a periodic-like distribution of steel inclusions near the rim of the plate combined with a large centrally placed circular inclusion. Fig. 3.10b illustrates the corresponding frequency response plot. It is seen how the vibration level (measured as the total kinetic energy of the plate) has been significantly reduced compared to the initial design – a homogeneous plate of equivalent mass.

The optimization algorithm can also be used to design structures with more advanced functionalities, as presented in Fig. 3.11a. Instead of minimizing the response, a plate is designed that transports wave energy in a circular path and thereby creating a ring wave device⁴. The wave is initiated by exciting the plate with two out-of-phase harmonic forces.

The wave vector plot in Fig. 3.11c shows that the desired functionality is obtained with reasonable success. The main part of the wave is guided anti-clockwise through the designated regions. The optimization setup could be refined by adding more energy evaluation points in the domain and consequently a better performance could

⁴Ring wave devices have several applications such as in small ultrasonic motors for cameras.

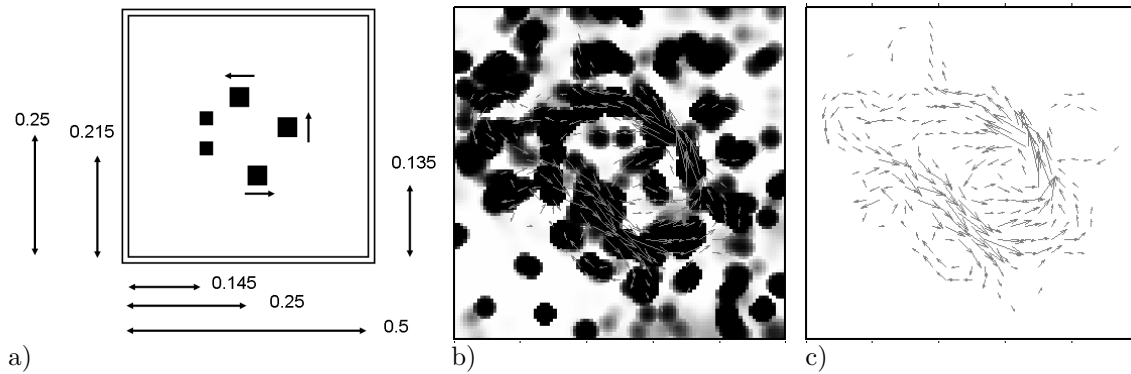


Figure 3.11 a) Sketch of optimization problem for creating a ring wave in a simply supported plate. The black parts indicate fixed steel regions and the arrows indicate in which direction the energy transport is maximized. The two small steel areas indicate where the out-of-phase harmonic forces are applied, b) Optimized material distribution, c) Energy transport in the optimized structure (only vectors larger than 10% of the maximum vector are shown). From paper [8].

be obtained. However, the present setup displays the basic principle. Fig. 3.11b shows the corresponding distribution of the two materials which indicate a relatively well defined structure consisting of steel inclusions (black) in a polycarbonate plate (light gray). Some dark gray areas indicate that design variables with intermediate values exist in the optimized design. The inclusions are observed to act partly to reflect the waves so that they do not propagate toward the edges of the plate and partly so that the waves are guided in the correct direction.

3.6 Acoustic design

This chapter is concluded with an example taken from a quite different physical setting. However, optimization of acoustic wave propagation can be performed using the same optimization scheme that was presented for elastic waves. This can be facilitated merely by changing the material parameters in order to model acoustic instead of elastic media.

Fig. 3.12 shows a (half) model of an acoustic reflection chamber. An optimized distribution of reflecting material and air is found in the design domain so that the transmission of steady-state acoustic waves is minimized. Fig. 3.12 presents an example of an optimized material distribution obtained by minimizing the transmission in a finite frequency range. Three inclusions of reflecting material are placed approximately with equal spacing in the design domain which causes reflection of a large part of the incoming wave. This is illustrated in the corresponding transmission plot in Fig. 3.13 showing that a transmission of less than 5% is obtained in the (non-dimensional) frequency range of interest from 0.15 – 0.20.

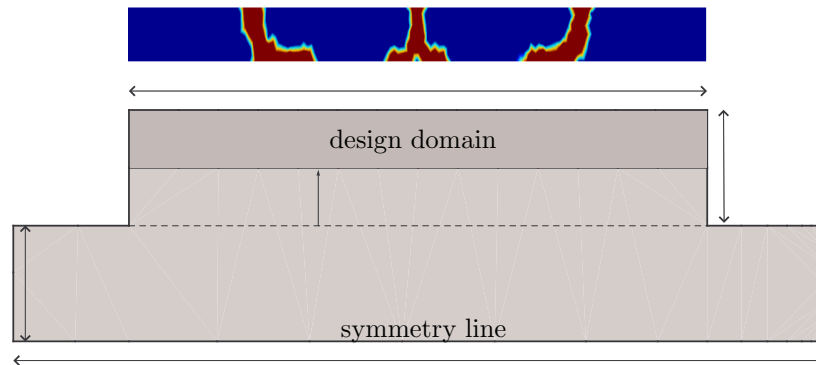


Figure 3.12 Bottom: Half model of a channel with two symmetrically placed reflection chambers, Top: Optimized topology in the chamber. Blue: air, red: solid material. From paper [9].

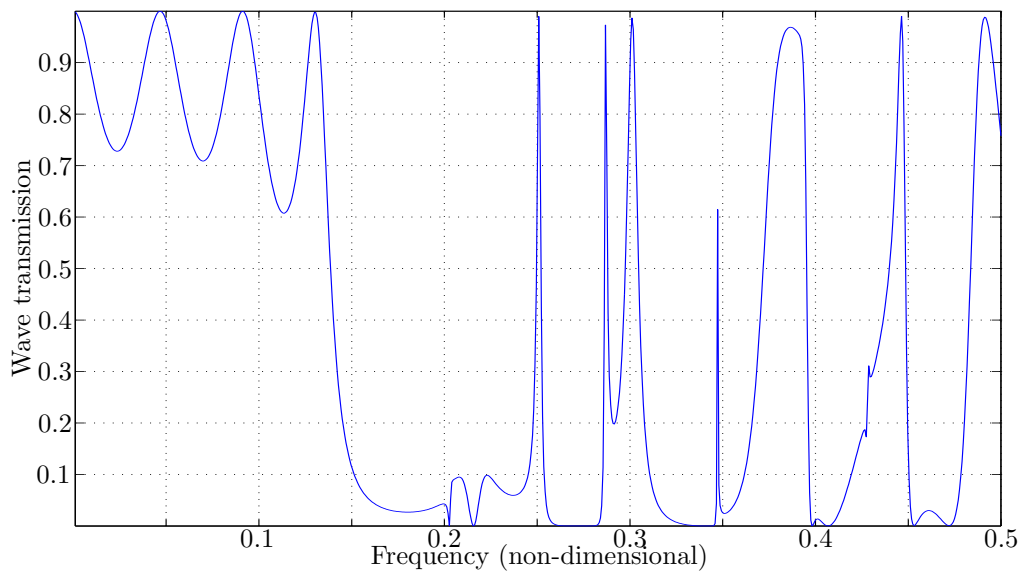


Figure 3.13 Transmission curve for the optimized design corresponding to an optimization frequency range from 0.15 – 0.20 (non-dimensional frequency). From paper [9].

Relations to recent work

Paper [4] was to the author's best knowledge the first that applied a numerical material distribution algorithm to the design of mechanical (or phononic) bandgap structures. This work has later been followed by a number of optimization studies on elastic structures for wave reflection, guiding and control purposes such as by Hussein et al. (2007b) for 1D banded materials, Hussein et al. (2007a) for 2D phononic crystals, by Rupp et al. (2007) who designed surface waveguides using 3D modeling, by Evgrafov et al. (2008) who optimized 2D tunable waveguides and by Du and Olhoff (2007a, 2010) who minimized and controlled sound radiation from vibrating structures. The separation of eigenfrequencies was also recently considered by Du and Olhoff (2007b,c) using topology optimization.

The conference paper [9] dealing with the acoustic design problem was later extended to a journal publication in cooperation with Maria Dühning (Dühning et al., 2008) where also 3D problems were analyzed as well the planar problem of optimization of sound barriers. The acoustic problem has later been studied using topology optimization by Wadbro and Berggren (2006) who considered optimal design of an acoustic horn, by Lee and Kim (2009) who optimized holes in a cavity partition in order to control eigenfrequencies. Duhamel (2006) used a genetic algorithm to design sound barriers. Related to this problem is also the study on topology optimization of acoustic-structure interaction by the author, Ole Sigmund and Gil Ho Yoon (Yoon et al., 2007).

In optimization problems where a large reflection of waves is required, well defined structures seem to appear "automatically". Thus there is no need for penalization of intermediate design variables (between 0 and 1). In most other applications of topology optimization such a penalization is essential. This phenomenon is related to the fact that intermediate design variables reduce the contrast between the materials and thus lead to a reduced wave reflection. Mathematically, this issue has been studied by Bellido and Donoso (2007) who proved that "classical solutions" (pure 0–1 designs) are optimal under certain conditions.

Chapter 4

Optimization of photonic waveguides

Bandgap materials for optical waves are known as photonic crystals. Technological applications have appeared in photonic crystal fibers for telecommunication purposes, for example, but also for waveguides in planar photonic crystals which are believed to have an important role in future integrated optical circuits. Thus, there has been a large interest in optimizing the performance of such components especially with respect to efficiency bottlenecks such as sharp waveguide bends.

Chapter 3 introduced a design methodology for phononic bandgap structures using topology optimization based on FE analysis. Chapter 4 applies the same methodology to the case of planar photonic waveguides. Although the two problems relate to very different physical settings (and magnitude of physical dimensions), the governing equations are similar so that the methodology can be adapted quite easily. However, important differences exist. When photonic crystal waveguides are concerned, the focus is often on designing only small parts of the structure where the problems occur instead of the entire structure. Additionally, it is necessary to modify the optimization formulation in several ways in order to overcome new problems such as the appearance of intermediate material properties in the optimized design.

Thesis papers [10]–[17]

Papers [10] and [11] present the first numerical results for the optimal design of photonic crystal waveguide bends and junctions using topology optimization. The material distribution in a 90-degree bend and in a T-junction of a waveguide are optimized in order to maximize the power flow through the components. Both examples use a two-dimensional model for E-polarized optical waves. Furthermore, paper [11] proposes a method for efficient optimization of the performance in a frequency range using Padé approximants. It also introduces a novel method for eliminating intermediate material properties in the optimized designs by using an artificial damping method.

In papers [12]–[15] a number of different photonic crystal waveguide components are optimized, fabricated and tested experimentally¹. The components form the basic building blocks for photonic crystal waveguide devices in the form of a 120-degree, 60-degree and a 90-degree bend and a wave splitter.

¹These papers are the result of a fruitful collaboration between the author, colleague Ole Sigmund, and a number of people at the Photonics department at the Technical University of Denmark (now DTU fotonik).

Paper [16] presents an example of an optimized, fabricated and experimentally tested photonic crystal component with a more advanced functionality. The λ -splitter splits an incoming wave by channeling shorter waves in one output direction and longer waves in another output direction. The component is fabricated with a nano-imprint lithography technique that facilitates an accurate reproduction of fine structural details.

In paper [17] the design methodology is applied to a similar problem of the design of a T-junction in a photonic ridge waveguide. Numerical results are presented for E- and H-polarized waves and the importance of the size of the design domain as well as the chosen frequency range for the optimization procedure are discussed.

Main references

The contributions in this thesis are believed to be the first that use a numerical material distribution optimization method to design photonic crystal waveguide bends and splitters.

Earlier optimization studies for photonic crystal waveguides were mostly based on simple geometrical variations such as the movement of one or several holes in the structure, as found in Mekis et al. (1996), Moosburger et al. (2001), Chutinan et al. (2002), and Olivier et al. (2002). Smajic et al. (2003) and Jiang et al. (2003) used genetic algorithms with relatively few design variables to optimize similar structures. Geremia et al. (2002) marked an exception by optimizing the material distribution in photonic crystal structures using a mathematical inversion technique. Optimization of ridge waveguide splitters was considered previously using a combination of numerical analysis and analytical considerations by Manolatou et al. (1999) and by Sakai et al. (2002).

Closely related is the application of topology optimization to the design of electromagnetic antenna structures as was demonstrated in the work by Kiziltas et al. (2003).

4.1 Waveguide bends and junctions

Fig. 4.1 shows two models used for the fundamental study of the optimization of bends and junctions in photonic crystal waveguides. Both structures are built around a 2D photonic bandgap material for E-polarized optical waves. The unit cell is squared with a circular inclusion of a dielectric material placed in air (light gray indicates air and black indicates dielectric). The bandgap is located in the (non-dimensional) frequency range from $\omega = 0.302 - 0.443$. A single line of dielectric inclusions is removed which creates a waveguide that allows a wave to propagate with frequencies in the range from $\omega = 0.312 - 0.443$. The aim of the optimization study is to redistribute air and dielectric in the vicinity of the bend or junction so that the power transmission through the components is maximized. Hereby the loss

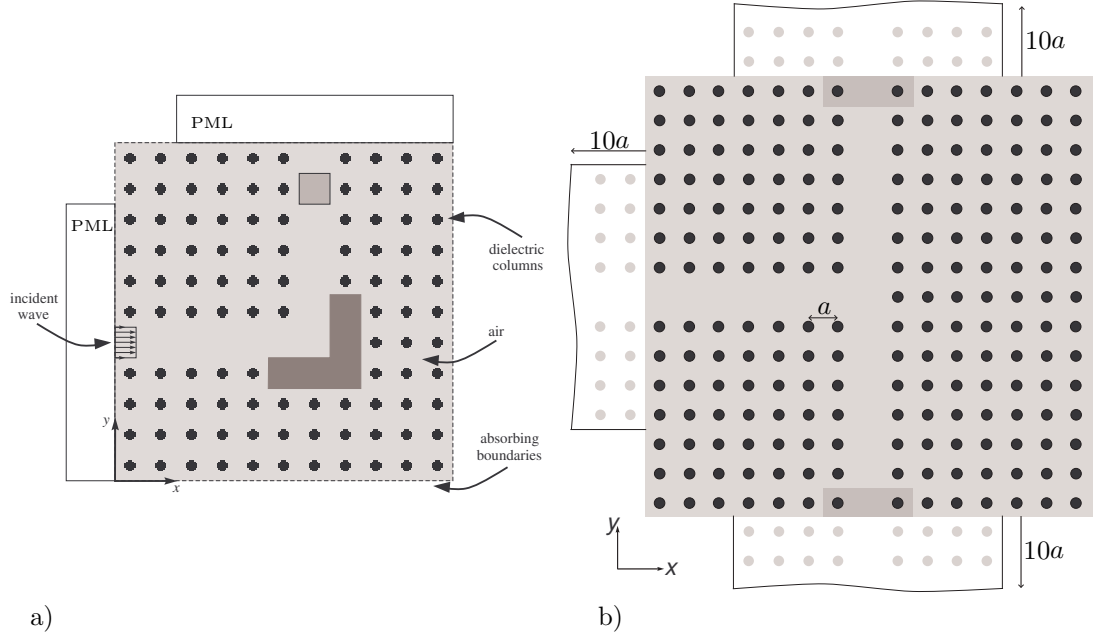


Figure 4.1 Topology optimization of the material distribution in photonic crystal waveguides, a) 90-degree bend, b) T-junction. Black: dielectric material with $\varepsilon = 11.56$, light gray: air. The design domain for the 90-degree bend is indicated in dark gray and the energy transmission in the structures is evaluated in the gray regions close to the output ports. Unwanted reflections from the waveguide boundaries are eliminated by using PML (Perfectly Matched Layers). From papers [10] and [11].

that otherwise occurs due to reflections at the waveguide discontinuities is reduced.

Fig. 4.2b shows the optimized material distribution for the 90-degree bend. The design is obtained by optimizing the sum of the transmitted power for the three frequencies $\omega = 0.34$, $\omega = 0.38$ and $\omega = 0.42$. The resulting structure has a non-intuitive appearance very different from structures reported in precedent studies (such as the one shown in Fig. 4.2a taken from Mekis et al. (1996)). More importantly, the structure also outperforms previously reported structures significantly by having a very low loss in a broad frequency range. Fig. 4.2c shows the performance of the structures. A bend loss of less than 0.3% in the frequency range from $\omega = 0.325 - 0.440$ is obtained for the optimized structure. This can be compared to the structure in Fig. 4.2a that has a similar low loss only in narrow frequency band around $\omega \approx 0.35$. The circular dots in Fig. 4.2c correspond to transmission losses for a post-processed optimized design in which the (few) elements with intermediate values of the design variable that appear in Fig. 4.2b are forced to either 0 or 1. The plot shows negligible discrepancy between the performance of two structures.

Fig. 4.1b illustrates the related design problem of a T-junction. A set of optimized material distributions is presented in Fig. 4.3a-c plotted together with the electric field amplitude for $\omega = 0.38$. The structures are all optimized for maxi-

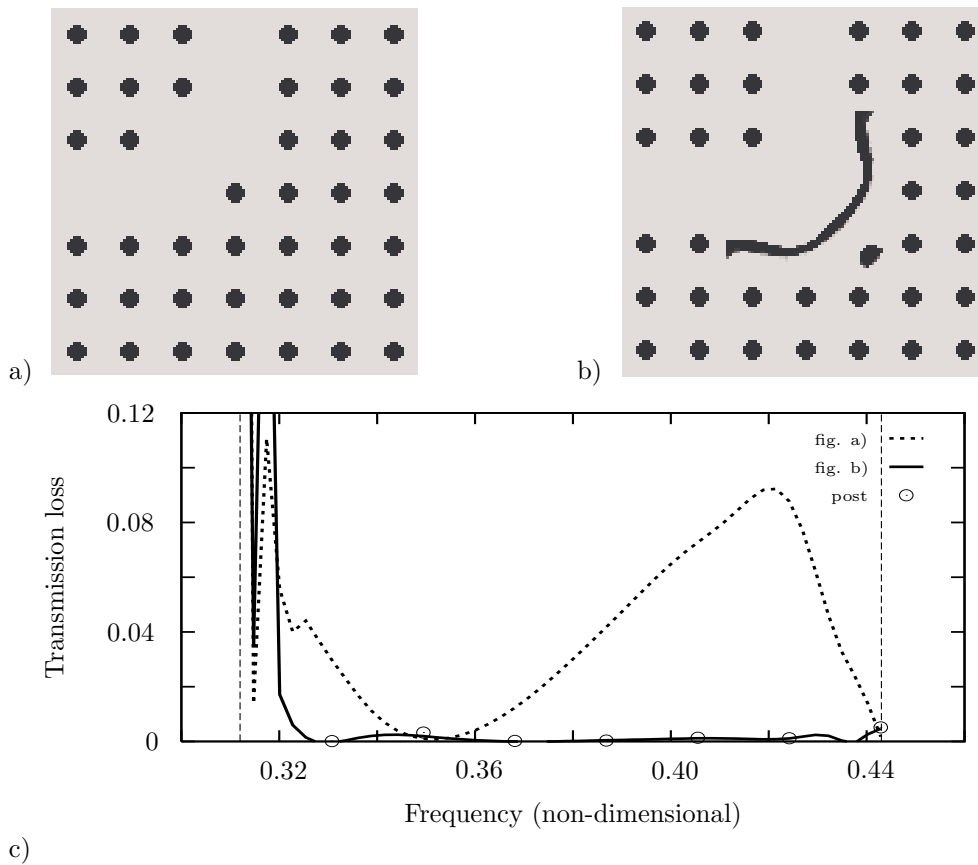


Figure 4.2 a) Bend design from Mekis et al. (1996), b) Topology optimized bend design, c) Transmission losses for the two designs and a post-processed topology optimized design with all intermediate design variables forced to either 0 or 1. From paper [10].

imum power transmission through the output channels. In Fig. 4.3a the structure is optimized for a single frequency ($\omega = 0.38$) whereas Fig. 4.3b,c show structures for which the entire frequency range from $\omega = 0.32 - 0.44$ is considered. The two latter structures differ merely in the chosen design domains. Fig. 4.3d depicts the transmission through the output channels and illustrates the difference between the performance of the three structures. The transmission for Fig. 4.3a is best (very close to the theoretical maximum value of 0.5) for $\omega = 0.38$, whereas a better broadband performance is seen for the other structures. The structure obtained for the larger design domain is seen to perform slightly better especially near the extremes of the frequency range.

An active set strategy is used to make the optimization procedure for an entire frequency range more efficient. Initially, a number of target frequencies (up to 12) are spread out evenly in the interval. During the optimization iterations these frequencies are changed repeatedly to target the most critical frequencies with low transmission. An accurate identification of these critical frequencies requires the

computation of a transmission curve with high frequency resolution. The computational burden associated with this identification is reduced significantly by using Padé approximants²

An extension of the optimization formulation is necessary in order to obtain the well defined distribution of dielectric material near the T-junction in Fig. 4.3c. The first attempts resulted in intermediate design variables near the corners of the junction and thus a well defined structure with air and dielectric material was not obtained. However, if a penalization of the intermediate design variables using artificial damping is introduced, the problem is resolved. Linear viscous damping is added in each element with the damping being proportional to $\epsilon x_e(1-x_e)$ in which ϵ is a positive constant and x_e is the element design variable. Thus if $x_e = 0$ or $x_e = 1$ no damping is present, but if x_e has an intermediate value, energy is dissipated and the power transmission reduced. Thus, to avoid unwanted dissipation of energy, x_e is forced toward either 0 or 1. The effect is clear as a well defined structure is obtained if ϵ is chosen sufficiently large. This method has later been applied successfully to other optimization problems as well.

4.2 Photonic crystal building blocks

A collaboration with a photonic crystal research group allowed for fabrication and experimental testing of optimized photonic crystal waveguide components. However, the components illustrated in Section 4.1 are optimized for E-polarized waves and are not easily fabricated due their realization as dielectric pillars placed in air. Instead a number of optimized designs for H-polarized waves were generated and fabricated. These basically consist of air holes in the dielectric material placed in a triangular pattern. This configuration is more amenable to fabrication and also less prone to out-of-plane losses.

Fig. 4.4 shows a compound photonic crystal structure that integrates three of the optimized building blocks (dark regions represent air and gray regions represent silicon). These building blocks allow for control and manipulation of the flow of light in the crystal. With optimized bends and splitters this can be done with minimum loss of energy. Specifically, the structure contains a 120-degree, a 60-degree bend and a splitter that separates a wave into two. All components are optimized separately by maximizing the power transmission through a simpler structure for given frequency ranges. This is carried out using the procedure described in Section 4.1. It is seen from the figure that holes of irregular sizes and shapes are obtained. The structures are hence qualitatively different than what could have been created using intuitive trial-and-error design methods and also regular parameter/size optimization. The performance of the individual components in Fig. 4.4 is very satisfactory with low loss over a broad frequency range. In all cases a significant improvement of the

²This procedure was the inspiration for the new method of frequency-range optimization using Padé approximants described in Section 5.1.

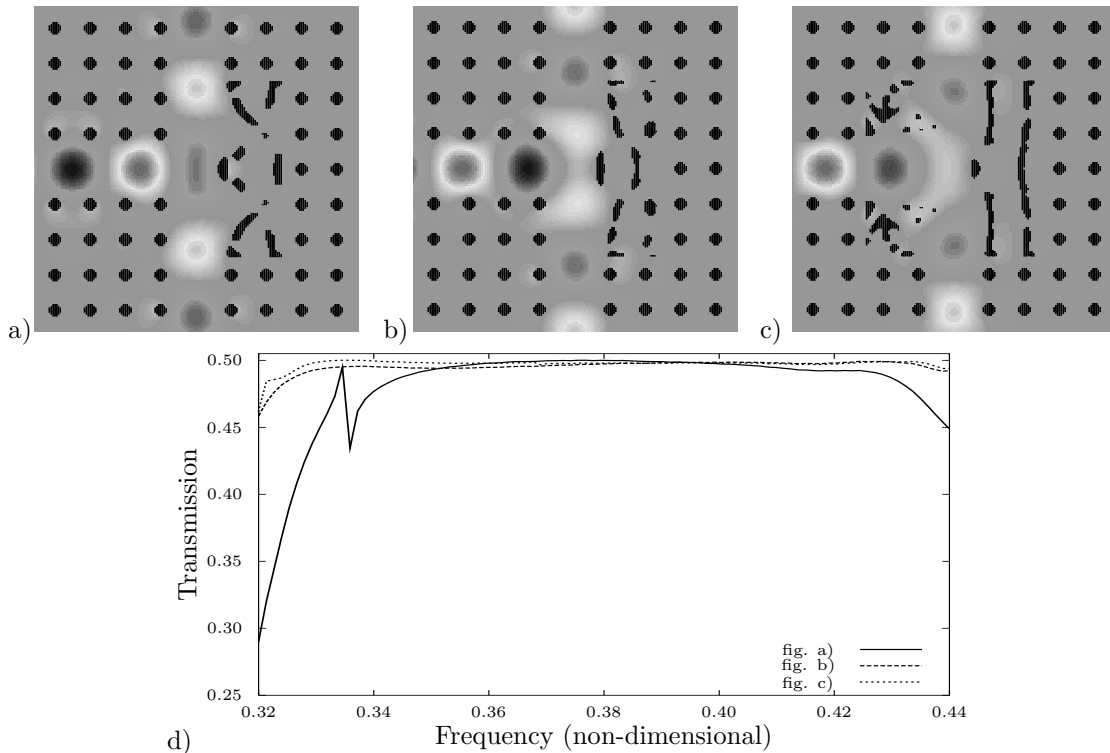


Figure 4.3 Optimized T-junction material distribution for: a) Target frequency 0.38, b,c) Frequency range 0.32 – 0.44 (non-dimensional frequencies), d) Transmission spectra for the three optimized designs. The designs in b) and c) differ in the extent of the chosen design domain. From paper [11].

performance is seen when compared to previously suggested structures.

Fig. 4.5b shows an optimized 90-degree bend. This is an unusual and rather awkward component due to the triangular hole configuration of the photonic crystal that does not readily facilitate a 90-degree bend. However, it demonstrates what can be achieved when the design freedom is greater by allowing larger parts of the structure to be optimized. Fig. 4.5c illustrates the measured performance for the optimized bend compared to the un-optimized generic 90-degree bend shown in Fig. 4.5a. As noted the optimization results in a large improvement of the performance.

For these building blocks the optimization techniques described earlier are applied. This means that penalization with artificial damping is introduced as described in Section 4.1. This was important especially for the 90-degree bend in order to obtain a well defined structure. Furthermore, the procedure of using a high value of added damping (as described in Section 3.1) has been used successfully. This technique is further developed here in that more damping is added to the air than to the dielectric which facilitates a reduction of the amount of air in the structure. This is beneficial for the performance of the structures since it is known that large out-of-plane losses occur in the air holes. Additionally, it is observed that adding

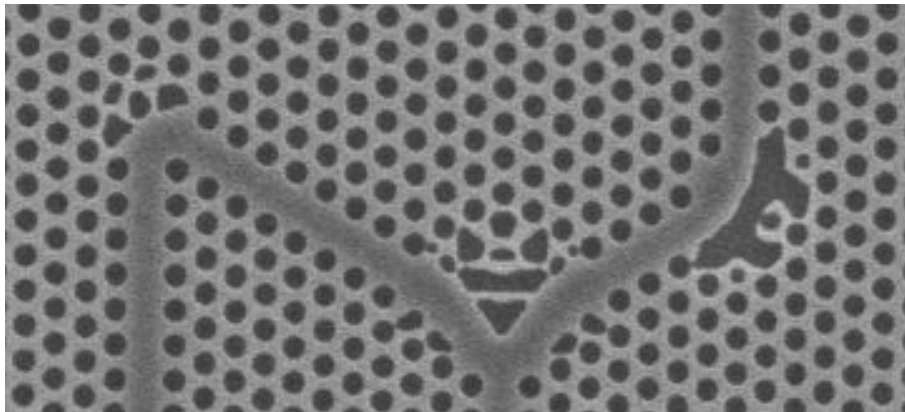


Figure 4.4 Compound structure illustrating the optimized building blocks for photonic crystal waveguides optimized in papers [12]–[14]. From left to right are seen: a 120-degree bend with 5 optimized holes near the outer bend region, a Y-splitter and a 60-degree bend.

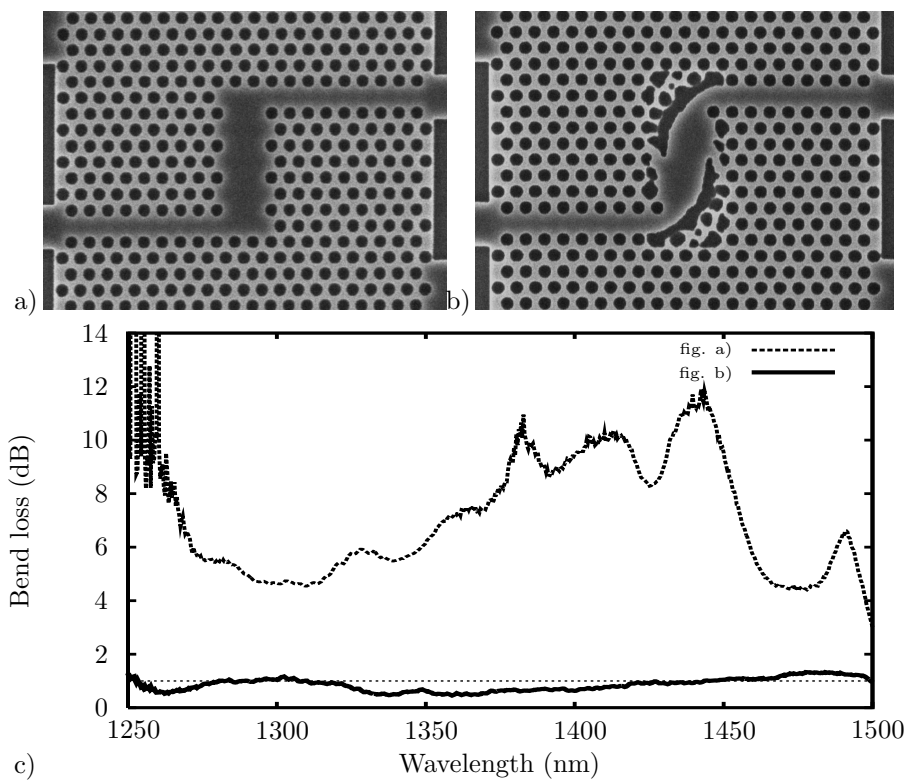


Figure 4.5 a) Fabricated un-optimized structure, b) Topology optimized (double) 90-degree photonic crystal waveguide bend, c) Measured bend loss for the two structures. From paper [15].

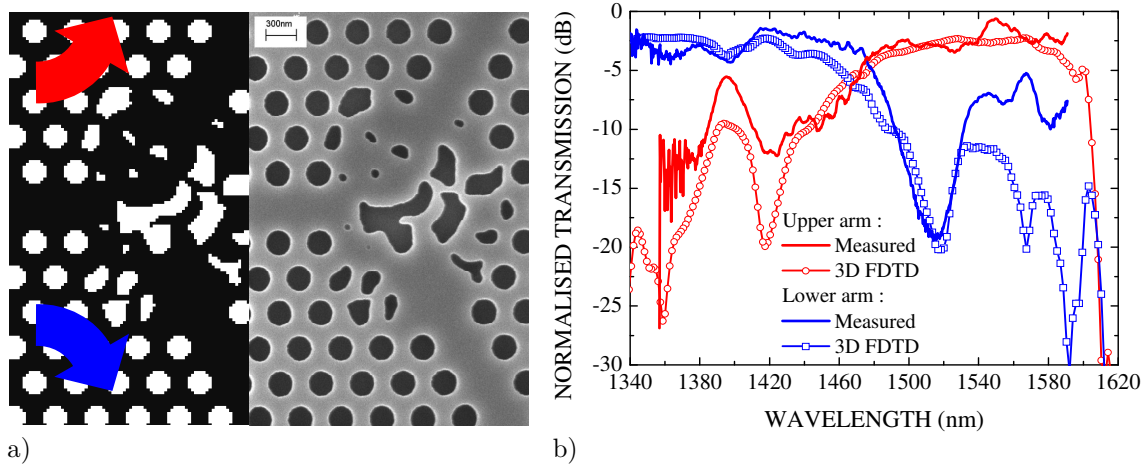


Figure 4.6 a) The optimized and fabricated design. Light enters the component from the left side and is split into the two arms dependent on the wavelength, b) Normalized measured transmission. Also shown are 3D FDTD calculations for the transmission that have been shifted by 0.5 % to match the experimental wavelength scale. From paper [16].

extra damping to the air quite accurately mimics the true 3D performance of the component. This is verified by comparisons with 3D FDTD calculations performed by colleagues at the Photonics department at the Technical University of Denmark.

4.3 Advanced functionalities

The optimized photonic crystal building blocks may be useful in future integrated photonic circuits. Additionally, components with more advanced functionality are relevant and can be designed with the developed methodology.

Fig. 4.6a shows one such advanced component. The optimization problem is apparently similar to the wave-splitter in Fig. 4.4 in so far as a wave is to be split up into two waves with a minimum of loss. However, here the wave is to be split so we have maximum transmission of shorter waves (below 1480 nm) through the lower output waveguide whereas longer waves (above 1480 nm) should propagate through the upper output waveguide. The optimized design is quite complicated with fine details³. Fig. 4.6b illustrates the corresponding transmission plot. The desired functionality is obtained with reasonable success but a noticeable loss of around 2 – 3 dB occurs in both channels. The loss is caused by the inherent difficulty of the problem and it is unlikely that a better performance can be obtained with the proposed setup.

³The fabrication of this device was performed with nano-imprint lithography which nicely reproduces the small features in the design.

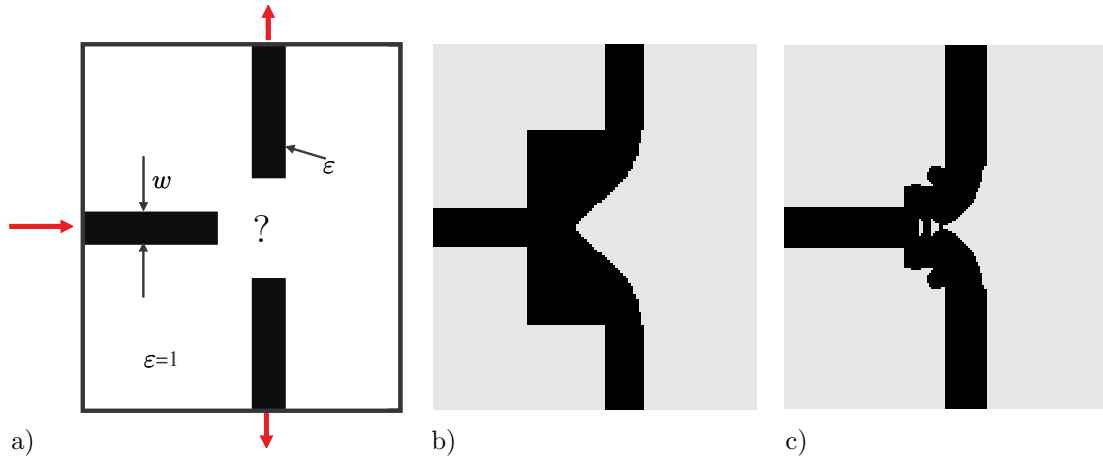


Figure 4.7 a) Design problem for a 2D model of a photonic ridge waveguide splitter. The objective is to distribute 50% of the input energy into the top and bottom output ports and thus avoid reflection and radiation at the T-junction, b) optimized design for E-polarized waves, c) optimized design for H-polarized waves. Black: dielectric material, light gray: air. From paper [17].

4.4 Ridge waveguides

The examples of optimized waveguide components are all based on waveguides carved out in photonic crystal structures. This provides a basis for confinement of the light which is very useful for waveguiding purposes. However, another type of waveguides, denoted strip or ridge waveguides, are applicable to photonic circuits as well. These consist of dielectric strips with a rectangular cross section placed on a substrate and surrounded by air. Such strips may provide perfect waveguiding for straight guides. However, the problems at bends and junctions are even more severe than for photonic crystal waveguides in that the waves are no longer confined to the guide and thus additional in-plane scattering losses may be induced.

Nevertheless, the same design procedure can be applied as for the photonic crystal waveguide components. Fig. 4.7a shows an optimization problem for the design of a T-junction in a 2D model of a ridge waveguide. The optimized junctions in Fig. 4.7b,c correspond to the case of E- and H-polarized waves, respectively. In both cases the optimization is performed for waves with a wavelength close to 1550 nm which is relevant for telecommunication purposes⁴.

For both optimized junctions the obtained efficiency is close to 100% near the wavelength 1550 nm, yet, the required junction area is larger (relative to the strip width w) for the case of the E-polarized waves (Fig. 4.7b). This is due to the wavelength/strip width ratio being larger for this polarization. If a smaller design domain is used, the efficiency is reduced accordingly. Fig. 4.7c illustrates also that

⁴It should be noted that the two different polarizations correspond to two different values of the strip width w and dielectric constant ε .

the optimized design for the case of H-polarized waves is more complicated with air holes inside the waveguide area.

Relations to recent work

The use of topology optimization for the design of photonic devices continues to be applied by different research groups. Different waveguide optimization studies have been performed recently e.g. by Frei et al. (2005) who optimized a photonic crystal waveguide termination for maximum directivity, by Tsuji et al. (2006), Hirayama et al. (2007) and Tsuji and Hirayama (2008) who considered various planar photonic waveguide optimization problems and by Nomura et al. (2009) who optimized the periodic microstructure of electromagnetic materials. Design of other photonic crystal components such as high-Q cavities have been considered e.g. by Dobson and Santosa (2004) using a material distribution method and also by Frei et al. (2007) and Frei et al. (2008) using related geometry-projection/level set methods. Similar optimization problems have been analyzed out using different numerical optimization techniques such as simulated annealing (Kim and O'Brien, 2004) and genetic algorithms (Smajic et al., 2004).

Some publications have elaborated directly on the optimized structures presented in this thesis. This includes a study on the optimized 60-degree bend by Miao et al. (2004). The structures optimized in papers [12]–[15] have also been further examined and subjected to additional experimental investigation by Tetu et al. (2005).

Furthermore, a number of optimized structures have been created by other researchers using the software developed by the author and co-workers. This has been facilitated by an executable code and a graphical user interface (GUI) which have been made accessible to colleagues in Denmark and Japan. Fig. 4.8 shows a snapshot of the GUI. The structures created with the use of the software include a waveguide crossing, a waveguide taper and waveguide bends (Ikeda et al., 2006; Watanabe et al., 2006, 2007, 2008; Asakawa et al., 2006; Yang et al., 2007).

The appearance of very small details in the optimized designs can be a major challenge with respect to fabrication and often these details cannot be reproduced exactly causing a deterioration of the performance. This problem is not addressed in this thesis. However, new work in this area (Sigmund, 2007, 2009) is expected to facilitate optimized structures that are robust to fabrication tolerances and uncertainties.

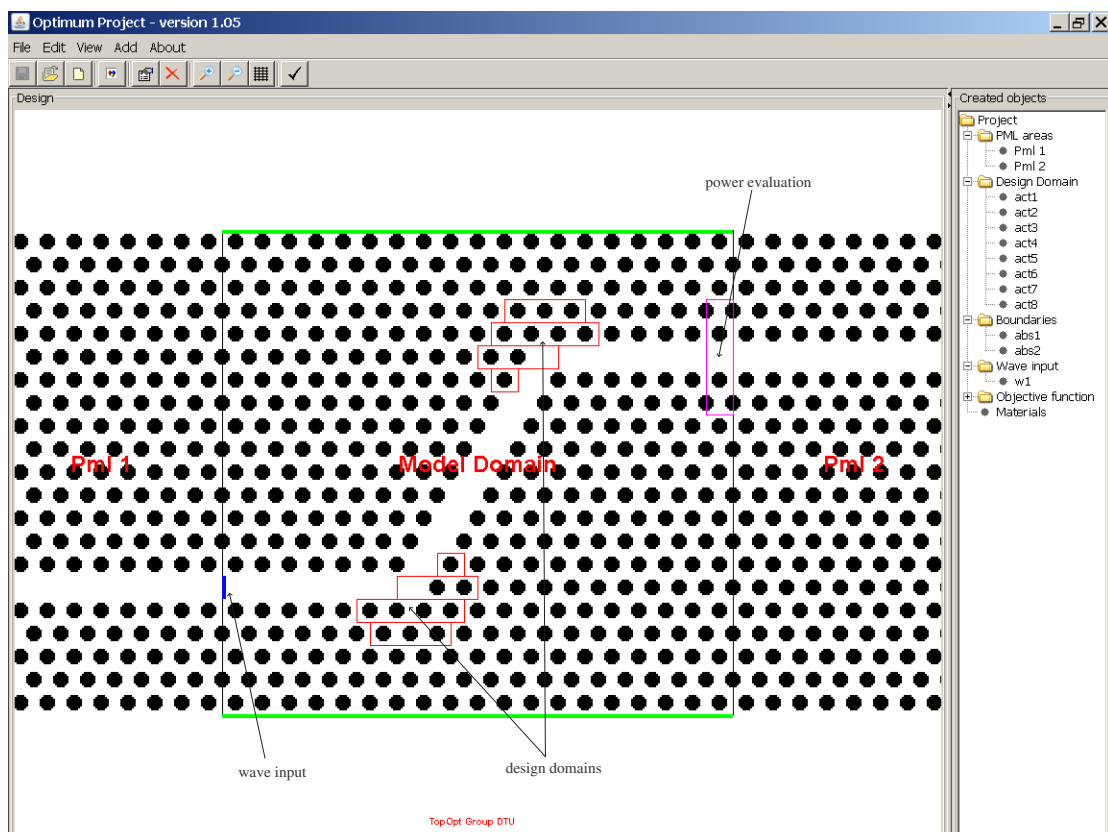


Figure 4.8 Screenshot from the GUI interface to the developed topology optimization software for the design of photonic crystal waveguide components. The setup for the design of a 60-degree bend is shown with indications of wave input, design domains and power evaluation area.

Chapter 5

Advanced optimization procedures

As mentioned in the previous chapters the optimization studies on phononic and photonic bandgap structures have inspired the development of new optimization procedures. This chapter will highlight three such procedures which can be identified as independent contributions. As a common feature they have been used to optimize bandgap structures but are also applicable to a broader class of problems that deal with the optimization of dynamic systems either based on steady-state or transient computations.

Thesis papers [18]–[21]

Paper [18] introduces an efficient scheme for optimization of dynamical systems in finite frequency ranges based on the use of Padé approximants. A detailed derivation of the computation of Padé approximants is provided along with derivation of the design sensitivities. The method is demonstrated on topology optimization of two dynamical structures subjected to forced vibrations with the aim to create frequency ranges with a low vibrational response.

In paper [19] the one-dimensional mass-spring structure with attached nonlinear oscillators is reconsidered (the same system was analyzed in paper [3]). Here, the four independent oscillator parameters, natural frequency, mass, damping ratio, and nonlinear stiffness, are individually optimized in order to reduce the transmission of waves through the chain. The optimization procedure is based on a transient optimization formulation for a nonlinear system.

In papers [20] and [21] the transient topology optimization method is extended to allow for optimized structures where the material distributions vary in time. In these papers, the necessary methodology is developed and expressions for the design sensitivities are derived. Paper [21] also demonstrates the importance of choosing the proper time-integration scheme. The papers present examples in which dynamic bandgap structures and pulse shaping structures are designed.

Main references

Optimization of the frequency response using Padé approximants has not received much attention. Webb (2002) marks an exception. Here an electromagnetic component, parameterized by a few design variables, was optimized.

Transient topology optimization has previously been used for the design of dynamic systems, e.g. by Min et al. (1999) for applications in structural mechanics,

by Nomura et al. (2007) for a 3D electromagnetics problem, and by the author, Ole Sigmund and Jonas Dahl (Dahl et al., 2008) who applied transient topology optimization to 1D wave propagation problems. The extension to a nonlinear wave propagation problem in paper [19] is believed to be a novel contribution of this thesis.

Optimal design based on a transient simulation with system parameters that vary in time was considered by Chambolle and Santosa (2002) for a single parameter in a one-dimensional structure. The optimization problem was for the first time treated as a material distribution problem in space and time in the work by Maestre et al. (2007) and Maestre and Pedregal (2009). However, it should be emphasized that the problem of finding the optimal time-evolution of parametrized systems has also been studied in the context of optimal control problems.

5.1 Padé approximants

As described earlier in this thesis, it is often important to optimize the performance for ranges of excitation frequencies rather than for single frequencies. This can be accomplished by considering several frequencies simultaneously, but this is usually computationally costly. Another drawback is that the performance between the target frequencies may be poor even with many frequencies considered. This can partly be resolved by tracking the worst-case frequencies during the optimization iterations as described in Section 4.1 using Padé approximants.

Another and more efficient approach is to use the Padé approximant directly in the optimization process. With Padé approximants the frequency response can be approximated as:

$$\mathbf{u}(\Omega) \approx \frac{\mathbf{u}(\Omega_0) + \sum_{i=1}^N \mathbf{a}_i (\Omega - \Omega_0)^i}{1 + \sum_{i=1}^N b_i (\Omega - \Omega_0)^i} \quad (5.1)$$

in which the unknown coefficients b_i and \mathbf{a}_i are determined based on the computation of first and higher order derivatives $d^n \mathbf{u} / d\Omega^n$ at a chosen expansion frequency Ω_0 . An accurate approximation for $\mathbf{u}(\Omega)$ can be obtained with a proper choice of the number of expansion functions N . Only one system matrix factorization is needed (for the center frequency Ω_0) and the computational overhead in addition to factorizing the system matrix is usually small. Additionally, the frequency resolution can be chosen arbitrarily fine without significant extra computational cost.

Fig. 5.1 illustrates an optimization example that illustrates an application of the optimization scheme. In Fig. 5.1a is shown a 2D structure subjected to forced vibrations. Two elastic materials are distributed in the structure in order to minimize the vibrational response in point A.

Fig. 5.1c-e show three examples of optimized distributions of the two materials. The structure is optimized for a single frequency ($\Omega = 1$) and for two different frequency intervals ($\Omega = 0.8-1.2$ and $\Omega = 0.7-1.3$). For both frequency intervals the optimization procedure is performed with seven expansion functions ($N = 7$) and a

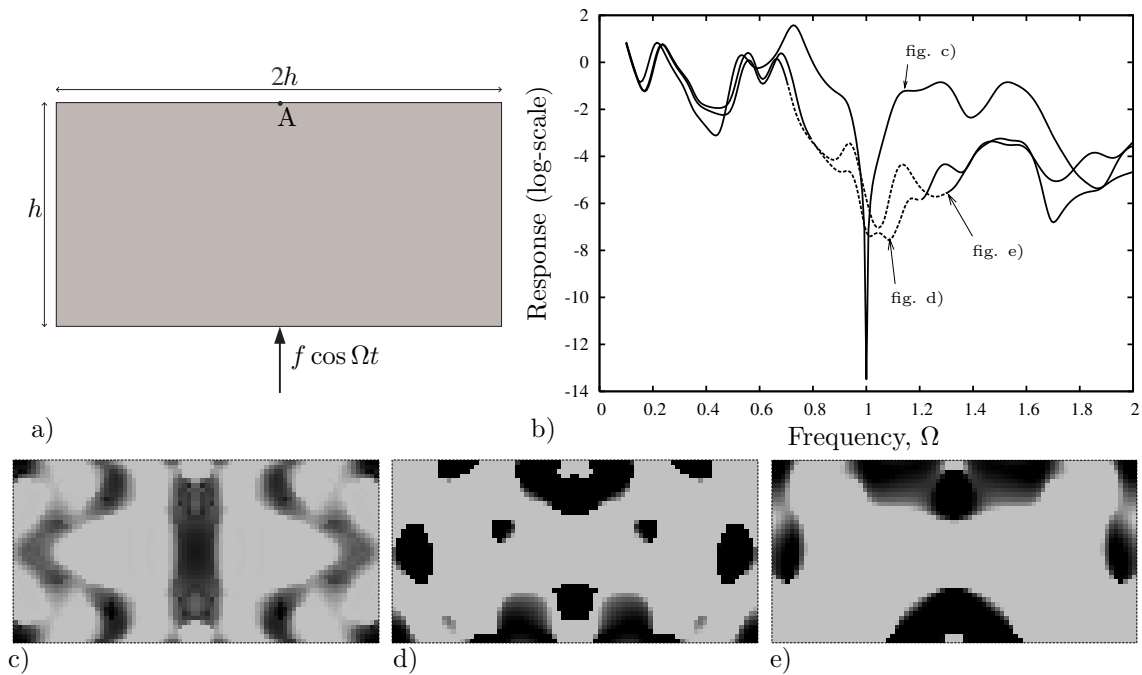


Figure 5.1 a) An unsupported 2D elastic body (plane stress) subjected to a harmonic load, b) Response in point A for the three optimized structures in c,d,e). Dashed lines indicate the optimization frequency intervals with the structure in c) optimized for the single frequency $\Omega = 1$ only. From paper [18].

resolution of the frequency range corresponding to 100 points. Fig. 5.1b displays the response of the structures. A difference in the performance for the three structures is seen; a very low response can be obtained for a single frequency but the response is very sensitive to the excitation frequency and just a small frequency de-tuning will result in a significantly higher response. With frequency range optimization a much more robust performance is obtained. Furthermore, it also results in much more well defined structures with fewer design variables with intermediate values between 0 and 1. The reason for this is, however, not fully understood.

Numerical problems arise if the number of expansion functions is too high. The coefficients are computed on the basis of derivatives at the expansion frequency and more functions require higher order derivatives. This puts a large demand on the numerical precision. This is illustrated in Fig. 5.2 which is based on a 1D model. The error in the b_i -coefficients is here plotted versus the precision used in the numerical scheme. Double precision, which is the standard in most numerical libraries (corresponding to 16 significant digits), yields unacceptable high errors if e.g. $N = 7$ is chosen (for this particular example). Quad-precision numerics (32 significant digits) would, in this case, yield acceptable accuracy.

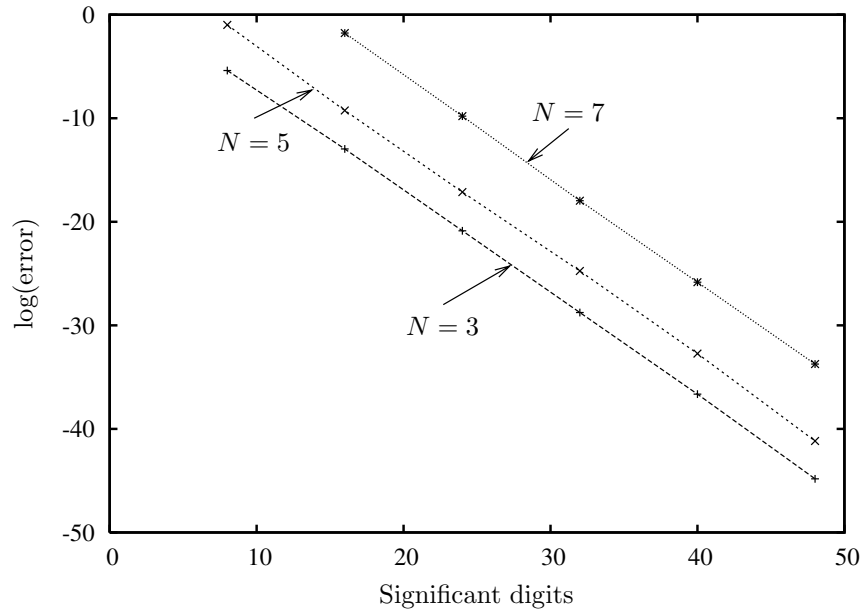


Figure 5.2 Error of the b_i -coefficients in the computation of the Padé approximant versus the numerical precision (significant digits) used in the computations. From paper [18].

5.2 Nonlinear transients

Section 2.5 analyzes the performance of a mass-spring structure with attached oscillators. The results indicate that it could be beneficial to optimize the parameters of each oscillator, including the nonlinear stiffness parameter, in order to minimize the transmission of waves through the structure.

The steady-state formulation used in Chapter 3 and Chapter 4 is not directly applicable to this system due to the presence of nonlinearities that add higher-order harmonics to the response. Instead, a time-domain optimization formulation can be applied which is based on transient simulation of the wave propagation through the system. The method is adapted to the present nonlinear system which turns out to pose no significant complications with regards to simulation and sensitivity analysis.

Fig. 5.3 shows the considered system with a one-dimensional mass-spring structure with a number of oscillators attached to the masses by linear viscous dampers and nonlinear springs. The design variables in the system are the mass ratio for each oscillator (relative to the mass it is attached to), the natural frequency, the viscous damping ratio and the nonlinear stiffness parameter. Thus, we have four design variables per attached oscillator and all oscillators may possess different parameters. A propagating steady-state wave pulse is simulated by adding a sinusoidal time-dependent force at the first mass and absorbing boundaries in the form of properly tuned viscous dampers at both ends.

Fig. 5.4 shows an example of the optimized distribution of the natural frequency,

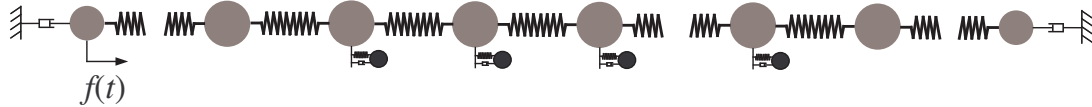


Figure 5.3 Finite one-dimensional mass-spring structure consisting of a number of masses with attached nonlinear oscillators. Viscous dampers are added in the ends to simulate absorbing boundaries. From paper [19].

mass ratio and nonlinear stiffness in a structure with 25 attached oscillators. The damping ratio is not shown since it is found it should always attain the minimum possible value in order to minimize the transmission of the waves. In this way the attached oscillators maximize their motion and have the largest possible effect on the system. The remaining parameters attain optimized values which do not immediately offer a physical interpretation. However, the nonlinear stiffness parameter increases along the length of the structure, which in Section 2.5 was shown to be beneficial for reducing the wave transmission. Notice, that the mass ratio is constrained so that the mean value must not exceed 0.1. If this constraint is omitted, the mass parameters attain their maximum value in order to maximize the effect of the attached oscillators.

5.3 Space-time topology optimization

Usual applications of topology optimization produce static material distributions also for dynamic problems. However, as demonstrated here, the methodology can be extended to create designs in which the optimized material distribution also change in time. With time-dependent designs additional functionalities can be obtained such as further enhancement of vibration and wave quenching or tailoring of the dynamic response of structures.

The extension of the design procedure is facilitated by adding the discretized time as an extra dimension to the existing design space. This implies that if a one-dimensional structure is to be designed the procedure results in a two-dimensional design grid. Since the time dimension is included in the procedure the optimization formulation is based on a transient simulation of the model equations. The sensitivity analysis is extended without great difficulties and importantly it can be performed as efficiently as for a standard "static" optimization procedure based on transient simulation.

An application of the method is illustrated by the example shown in Fig. 5.5. A one-dimensional elastic structure is subjected to a propagating Gauss-modulated sinusoidal pulse. The aim of the optimization procedure is to distribute two elastic materials in the design domain so that the transmission of the pulse through the domain is minimized. In this case the optimal *static* structure is a composite with 5 inclusion layers of the stiffer (but with equal density) material – thus resulting in

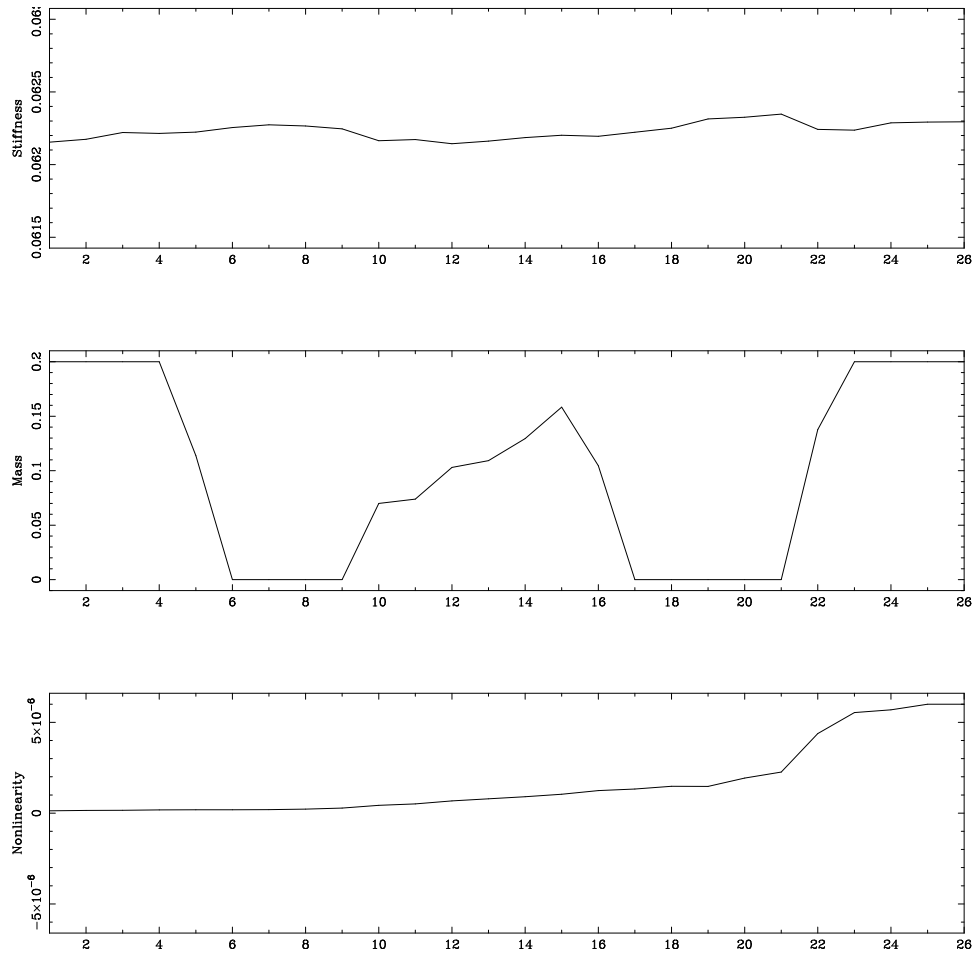


Figure 5.4 Optimized distribution of the 25 oscillator's parameters for maximum reflection of a steady-steady sinusoidal wave, top) Natural frequency, middle) Mass ratio, bottom) Nonlinear stiffness. From paper [19].

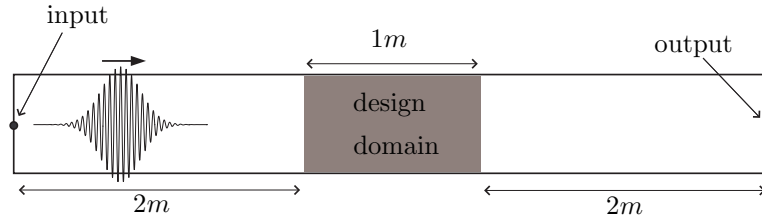


Figure 5.5 Design problem for the space-time topology optimization example. The transmission of a Gauss-modulated sinusoidal pulse is to be minimized by finding an optimized distribution of two materials in a space-time design domain. From paper [20].

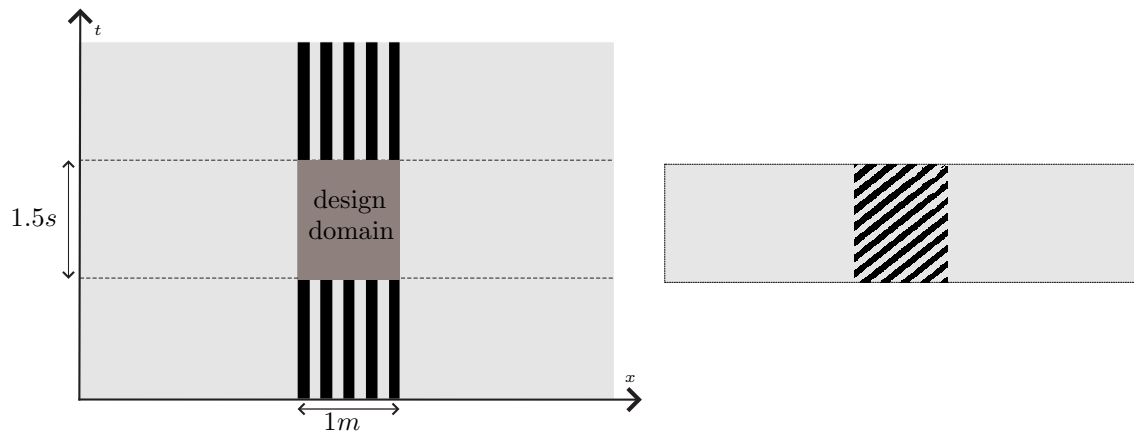


Figure 5.6 Left) Indication of the position-time design domain for the optimization problem, right) Optimized distribution of the two materials. From paper [20].

a one-dimensional bandgap structure (a so-called Bragg grating).

The optimized static structure is used as a basis for the space-time optimization as illustrated in Fig. 5.6(left). The static bandgap structure is retained in the simulation before the pulse enters the design domain and after the main part of the signal is transmitted through the domain. For a time interval of 1.5s for which the main part of the pulse propagates through the design domain the material is allowed to change in space and time using a corresponding two-dimensional design grid. Fig. 5.6(right) shows the material distribution in a space-time design variable plot. The black (stiffer) material is still distributed in layers but now arranged with a slope in space-time.

Fig. 5.7 illustrates the type of dynamic bandgap structure which is created. The plots show the instantaneous material distribution along with the wave motion for two separate time instances. The layered structure moves together with the wave with a speed matching the effective speed of the wave pulse (this speed can be computed from the slope in the space-time design plot in Fig. 5.6). The transmitted wave energy is reduced by approximately a factor three by this dynamic design

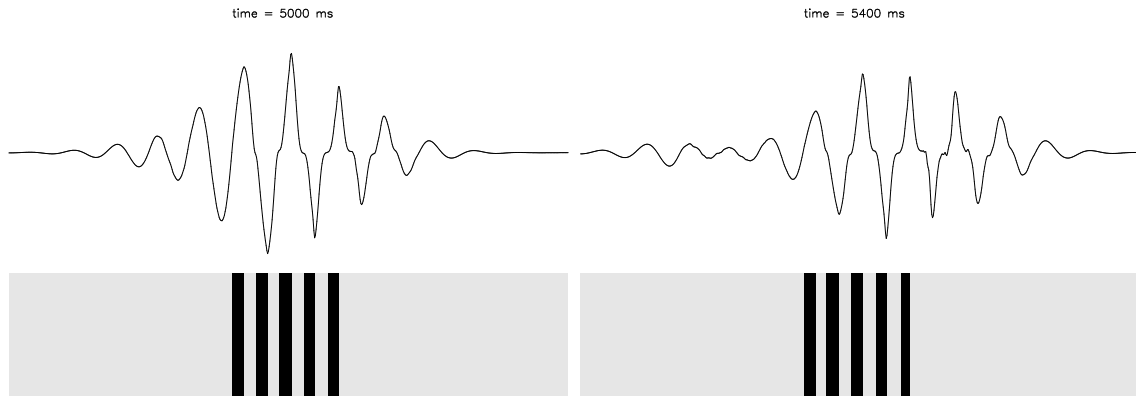


Figure 5.7 Instantaneous material distribution and wave motion for the optimized structure at $t = 5.0$ s and $t = 5.4$ s. From paper [20].

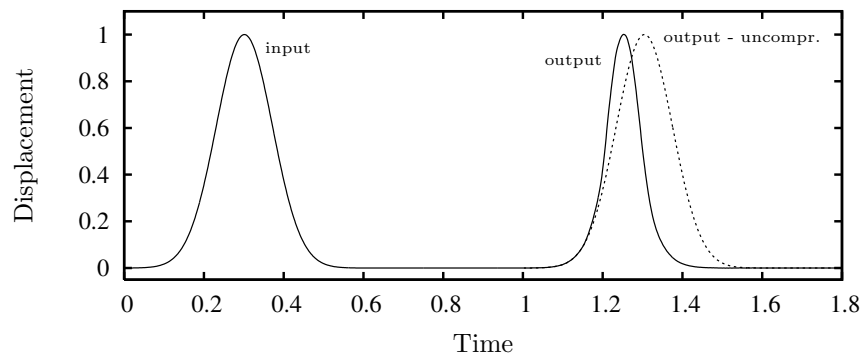


Figure 5.8 Input wave pulse and compressed wave pulse for an optimized structure. For comparison the uncompressed output wave pulse is shown too. From paper [21].

compared to the optimized static design. Interestingly, this improvement is not facilitated by an increased reflection. On the contrary, the reflected wave energy is reduced from 17% to only 1%. Instead wave energy is extracted from the system by the action of the external forces that must be present in order to change the stiffness at each structural position in time.

Other possibilities for wave manipulation appear when it is possible to change the structural properties in time as well as in space. In the second example the aim of the optimization procedure is to minimize the difference between the output pulse and a specified target output. Fig. 5.8 shows an example of the compression of a Gaussian pulse when it propagates through an optimized dynamic structure. Shown for comparison are also the input wave pulse and an uncompressed output wave pulse. It should be noted that for a static linear structure such a compression is not possible, since it involves changing the frequency contents of the pulse.

A further illustration of the compression of the pulse along with instantaneous plots of the material distribution is shown in Fig. 5.9. The compression of the pulse is created by the stiffer material moving along with the rear tail of the wave. In this case the design variables generally attain intermediate optimized values. However,

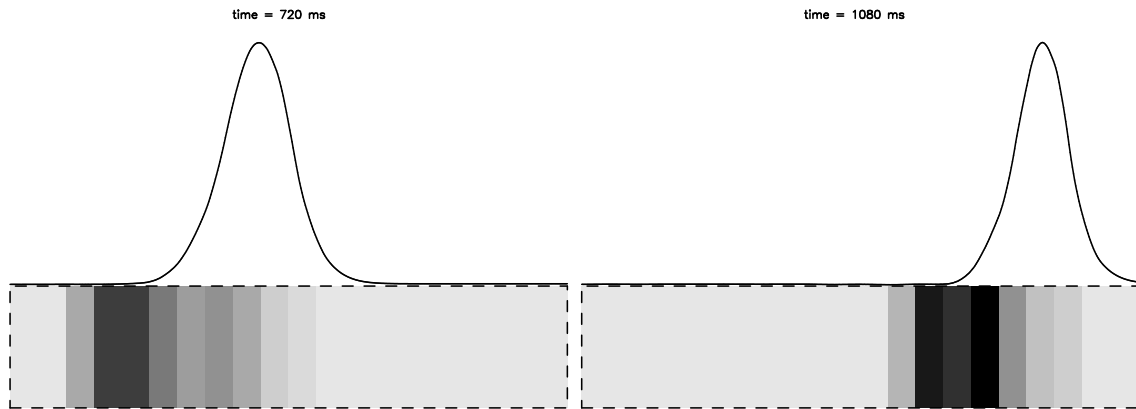


Figure 5.9 Illustration of the compression of the pulse as it propagates through a space-time optimized structure. From paper [21].

these can be partly removed if an explicit penalization term is added to the objective function, although this generally causes the output pulse to deviate more from the target output.

It turns out that if the two involved materials have different stiffness *and* mass density the possibility for manipulating the wave is greater. This however depends on the specific values of the parameters. An additional complication arises if the mass density varies in time. Then it becomes necessary to use a more sophisticated time-integration routine that is able to handle time-discontinuous velocity fields.

Relations to recent work

Optimization of dynamic systems in finite frequency ranges with Padé approximants was recently used by Donoso and Sigmund (2009). They considered the distribution of piezo-electric material in order to optimize the dynamic response of a mechanical structure.

The system of non-linear oscillators studied in paper [19] has been further examined by Rothos and Vakakis (2009) who studied wave interaction in the case of *essentially nonlinear* oscillators. They did not consider optimization.

Chapter 6

Conclusions

In the first five chapter of this thesis the main findings of papers [1]–[21] are summarized. Chapter 2 contains contributions to the basic understanding of the bandgap phenomenon, exemplified in simple one- and two-dimensional mass-spring structures. Chapter 3 demonstrates how the method of topology optimization can be applied to design various elastic and acoustic bandgap structures. Chapter 4 extends the topology optimization method to deal with photonic waveguide components and in Chapter 5 three advanced optimization methods and algorithms for the optimization of dynamical systems are presented.

The main contributions of this thesis are:

- Analysis of the connection between the band diagram for a periodic material and the forced vibration response for a finite structure made from this material.
- Analysis of the effect of nonlinearities on the bandgap effect of a mass-spring system with attached oscillators.
- Design of phononic bandgap structures using a material layout optimization method.
- Design of key components of photonic crystal waveguides using topology optimization.
- Development of new techniques based on artificial damping for using topology optimization to design bandgap structures
- Design of acoustic structures using topology optimization.
- Development of an efficient methodology for optimizing the performance of dynamic system using Padé approximants.
- Topology optimization for transient wave propagation problems with nonlinearities.
- Development of a space-time topology optimization formulation to design structures with optimized material distributions that can vary in time.

References

- K. Asakawa, Y. Sugimoto, Y. Watanabe, N. Ozaki, A. Mizutani, Y. Takata, Y. Kitagawa, H. Ishikawa, N. Ikeda, K. Awazu, X. M. Wang, A. Watanabe, S. Nakamura, S. Ohkouchi, K. Inoue, M. Kristensen, O. Sigmund, P. I. Borel, and R. Baets. Photonic crystal and quantum dot technologies for all-optical switch and logic device. *New Journal of Physics*, 8:208, 2006.
- A. Avila and D. Reyes. Phonon multiplexing through 1d chains. *Brazilian Journal of Physics*, 38(4):604–609, 2008.
- J. C. Bellido and A. Donoso. An optimal design problem in wave propagation. *Journal of Optimization Theory and Applications*, 134(2):339–352, 2007.
- M. P. Bendsøe and N. Kikuchi. Generating optimal topologies in structural design using a homogenization method. *Computer Methods in Applied Mechanics and Engineering*, 71(2):197–224, 1988.
- M. P. Bendsøe and O. Sigmund. Material interpolations in topology optimization. *Archive of Applied Mechanics*, 69:635–654, 1999.
- M. P. Bendsøe and O. Sigmund. *Topology Optimization - Theory, Methods and Applications*. Springer Verlag, Berlin Heidelberg, 2003.
- L. Brillouin. *Wave propagation in periodic structures*. Dover Publications, 2 edition, 1953.
- A. Chambolle and F. Santosa. Control of the wave equation by time-dependent coefficient. *ESAIM-Control Optimisation And Calculus Of Variations*, 8:375–392, 2002.
- A. Chutinan, M. Okano, and S. Noda. Wider bandwidth with high transmission through waveguide bends in twodimensional photonic crystal slabs. *Applied Physics Letters*, 80:1698–1700, 2002.
- S. J. Cox and D. C. Dobson. Maximizing band gaps in two-dimensional photonic crystals. *SIAM Journal on Applied Mathematics*, 59(6):2108–2120, 1999.
- S. J. Cox and D. C. Dobson. Band structure optimization of two-dimensional photonic crystals in h -polarization. *Journal of Computational Physics*, 158(2):214–224, 2000.

- J. Dahl, J. S. Jensen, and O. Sigmund. Topology optimization for transient wave propagation problems in one dimension. *Structural and Multidisciplinary Optimization*, 36:585–595, 2008.
- A. R. Diaz and N. Kikuchi. Solution to shape and topology eigenvalue optimization problems using a homogenization method. *International Journal for Numerical Methods in Engineering*, 35:1487–1502, 1992.
- A. R. Diaz, A. G. Haddow, and L. Ma. Design of band-gap grid structures. *Structural and Multidisciplinary Optimization*, 29(6):418–431, 2005.
- D. C. Dobson and F. Santosa. Optimal localization of eigenfunctions in an inhomogeneous medium. *SIAM Journal on Applied Mathematics*, 64(3):762–774, 2004.
- A. Donoso and O. Sigmund. Optimization of piezoelectric bimorph actuators with active damping for static and dynamic loads. *Structural And Multidisciplinary Optimization*, 38(2):171–183, 2009.
- J. Du and N. Olhoff. Minimization of sound radiation from vibrating bi-material structures using topology optimization. *Structural and Multidisciplinary Optimization*, 33:305–321, 2007a.
- J. Du and N. Olhoff. Topological design of freely vibrating continuum structures for maximum values of simple and multiple eigenfrequencies and frequency gaps. *Structural and Multidisciplinary Optimization*, 34:91–110, 2007b.
- J. Du and N. Olhoff. Erratum: Topological design of freely vibrating continuum structures for maximum values of simple and multiple eigenfrequencies and frequency gaps. *Structural and Multidisciplinary Optimization*, 34:545, 2007c.
- J. Du and N. Olhoff. Topological design of vibrating structures with respect to optimum sound pressure characteristics in a surrounding acoustic medium. *Structural and Multidisciplinary Optimization*, 42:43–54, 2010.
- D. Duhamel. Shape optimization of noise barriers using genetic algorithms. *Journal of Sound and Vibration*, 297(1–2):432–443, 2006.
- M. B. Dühring, J. S. Jensen, and O. Sigmund. Acoustic design by topology optimization. *Journal of Sound and Vibration*, 317(3–5):557–575, 2008.
- C. Elachi. Waves in active and passive periodic structures: a review. *Proceedings of the IEEE*, 64(12):1666–1698, 1976.
- A. Evgrafov, C. J. Rupp, M. L. Dunn, and K. Maute. Optimal synthesis of tunable elastic wave-guides. *Computer Methods in Applied Mechanics and Engineering*, 198(2):292–301, 2008.

- W. R. Frei, D. A. Tortorelli, and H. T. Johnson. Optimization of photonic nanostructures. *Applied Physics Letters*, 86(11):111114, 2005.
- W. R. Frei, D. A. Tortorelli, and H. T. Johnson. Geometry projection method for optimizing photonic nanostructures. *Optics Letters*, 32(1):77–79, 2007.
- W. R. Frei, H. T. Johnson, and D. A. Tortorelli. Optimization of photonic nanostructures. *Computer Methods in Applied Mechanics and Engineering*, 197(41–42):3410–3416, 2008.
- J. M. Geremia, J. Williams, and H. Mabuchi. Inverse-problem approach to designing photonic crystals for cavity qed experiments. *Physics Review E*, 66:066606, 2002.
- S. Halkjær, O. Sigmund, and J. S. Jensen. Maximizing band gaps in plate structures. *Structural and Multidisciplinary Optimization*, 32:263–275, 2006.
- K. Hirayama, Y. Tsuji, T. Nomura, K. Sato, and S. Nishiwaki. Application of topology optimization to h-plane waveguide component. *IEICE Transactions on Electronics*, E90C(2):282–287, 2007.
- A.-C. Hladky-Hennionne and M. de Billy. Experimental validation of band gaps and localization in a one-dimensional diatomic phononic crystal. *Journal of the Acoustical Society of America*, 122(5):2594–2600, 2007.
- H. H. Huang, C. T. Sun, and G. L. Huang. On the negative effective mass density in acoustic metamaterials. *International Journal Of Engineering Science*, 47(4):610–617, 2009.
- M. I. Hussein, K. Hamza, G. M. Hulbert, and K. Saitou. Optimal synthesis of 2d phononic crystals for broadband frequency isolation. *Waves in Random and Complex Media*, 17(4):491–510, 2007a.
- M. I. Hussein, G. M. Hulbert, and R. A. Scott. Dispersive elastodynamics of 1d banded materials and structures: Design. *Journal of Sound and Vibration*, 307(3–5):865–893, 2007b.
- N. Ikeda, Y. Sugimoto, Y. Watanabe, N. Ozaki, A. Mizutani, Y. Takata, J. S. Jensen, O. Sigmund, P. I. Borel, M. Kristensen, and K. Asakawa. Topology optimised photonic crystal waveguide intersections with high-transmittance and low crosstalk. *Electronics Letters*, 42(18):1031–1033, 2006.
- J. S. Jensen and B. S. Lazarov. Topology optimization of distributed mass dampers for low-frequency vibration suppression. In M. Papadrakakis, D.C. Charmpis, N.D. Lagaros, and Y. Tsompanakis, editors, *Proceedings of ECCOMAS Thematic Conference on Computational Methods in Structural Dynamics and Earthquake Engineering*, pages CD–rom, Rethymno, Crete, Greece, 2007.

- J. Jiang, J. Cai, G. P. Nordin, and L. Li. Parallel microgenetic algorithm design for photonic crystal and waveguide structures. *Optics Letters*, 28(23):2381–2383, 2003.
- J. D. Joannopoulos, R. D. Meade, and J. N. Winn. *Photonic Crystals*. Princeton University Press, New Jersey, 1995.
- C. S. Jog. Topology design of structures subjected to periodic loading. *Journal of Sound and Vibration*, 253(3):687–709, 2002.
- S. John. Strong localization of photons in certain disordered dielectric superlattices. *Physical Review Letters*, 58(23):2486–2489, 1987.
- W. J. Kim and J. D. O’Brien. Optimization of a two-dimensional photonic-crystal waveguide branch by simulated annealing and the finite element method. *J. Opt. Soc. Am. B*, 21(2):289–295, 2004.
- G. Kiziltas, D. Psychoudakis, J. L. Volakis, and N. Kikuchi. Topology design optimization of dielectric substrates for bandwidth improvement of a patch antenna. *International Journal of Modern Physics*, 51(10):2732–2743, 2003.
- M. S. Kushwaha. Classical band structure of periodic elastic composites. *International Journal of Modern Physics*, 10(9):977–1094, 1996.
- J. W. Lee and Y. Y. Kim. Optimal distribution of holes in a partition interfacing two cavities for controlling the eigenfrequencies by acoustical topology optimization. *Computer Methods in Applied Mechanics and Engineering*, 198(27–29):2175–2189, 2009.
- Y. Z. Liu, D. L. Yu, L. Li, H. G. Zhao, J. H. Wen, and X. S. Wen. Design guidelines for flexural wave attenuation of slender beams with local resonators. *Physics Letters A*, 362(5–6):344–347, 2007.
- Z. Liu, X. Zhang, Y. Mao, Y. Y. Zhu, Z. Yang, C. T. Chan, and P. Sheng. Locally resonant sonic materials. *Science*, 289:1734–1736, 2000.
- Z.-D. Ma, N. Kikuchi, and I. Hagiwara. Structural topology and shape optimization for a frequency response problem. *Computational Mechanics*, 13:157–174, 1993.
- Z.-D. Ma, H.-C. Cheng, and N. Kikuchi. Structural design for obtaining desired eigenfrequencies by using the topology and shape optimization method. *Computing Systems in Engineering*, 5(1):77–89, 1994.
- F. Maestre and P. Pedregal. Dynamic materials for an optimal design problem under the two-dimensional wave equation. *Discrete and Continuous Dynamical Systems - Series A*, 23:973–990, 2009.

- F. Maestre, A. Münch, and P. Pedregal. A spatio-temporal design problem for a damped wave equation. *SIAM Journal of Applied Mathematics*, 68:109–132, 2007.
- C. Manolatu, S. G. Johnson, S. Fan, P. R. Villeneuve, H. A. Haus, and J. D. Joannopoulos. High-density integrated optics. *Journal of Lightwave Technology*, 17(9):1682–1692, 1999.
- A. Marathe and A. Chatterjee. Wave attenuation in nonlinear periodic structures using harmonic balance and multiple scales. *Journal of Sound and Vibration*, 289: 871–888, 2006.
- P. G. Martinsson and A. B. Movchan. Vibrations of lattice structures and phononic band gaps. *The Quarterly Journal of Mechanics and Applied Mathematics*, 56(1): 45–64, 2003.
- D. J. Mead. Wave propagation in continuous periodic structures: Research contributions from southampton, 1964–1995. *Journal of Sound and Vibration*, 190(3): 495–524, 1996.
- A. Mekis, J. C. Chen, I. Kurland, S. Fan, P. R. Villeneuve, and J. D. Joannopoulos. High transmission through sharp bends in photonic crystal waveguides. *Physical Review Letters*, 77(18):3787–3790, 1996.
- B. Miao, C. Chen, S. Shi, J. Murakowski, and D. W. Prather. High-efficiency broad-band transmission through a double-60° bend in a planar photonic crystal single-line defect waveguide. *IEEE Photonics Technology Letters*, 16(11):2469–2471, 2004.
- S. Min, N. Kikuchi, Y. C. Park, S. Kim, and S. Chang. Optimal topology design of structures under dynamic loads. *Structural Optimization*, 17:208–218, 1999.
- J. Moosburger, M. Kamp, A. Forchel, S. Olivier, H. Benisty, C. Weisbuch, and U. Oesterle. Enhanced transmission through photonic-crystal-based bent waveguides by bend engineering. *Applied Physics Letters*, 79(22):3579–3581, 2001.
- T. Nomura, K. Sato, K. Taguchi, T. Kashiwa, and S. Nishiwaki. Structural topology optimization for the design of broadband dielectric resonator antennas using the finite difference time domain technique. *Applied Physics Letters*, 71(11):1261–1296, 2007.
- T. Nomura, S. Nishiwaki, K. Sato, and K. Hirayama. Topology optimization for the design of periodic microstructures composed of electromagnetic materials. *Finite Elements In Analysis And Design*, 45(3):210–226, 2009.
- S. Olivier, H. Benisty, C. Weisbuch, C. J. M. Smith, T. F. Krauss, R. Houdré, and U. Oesterle. Improved 60° bend transmission of submicron-width waveguides

- defined in two-dimensional photonic crystals. *Journal of Lightwave Technology*, 20(7):1198–1203, 2002.
- S. Osher and F. Santosa. Level set methods for optimization problems involving geometry and constraints i. frequencies of a two-density inhomogeneous drum. *Journal of Computational Physics*, 171:272–288, 2001.
- N. L. Pedersen. Maximization of eigenvalues using topology optimization. *Structural and Multidisciplinary Optimization*, 20:2–11, 2000.
- Lord Rayleigh. On the maintenance of vibrations by forces of double frequency, and on the propagation of waves through a medium endowed with a periodic structure. *Philosophical Magazine*, 24:145–159, 1887.
- V. M. Rothos and A. F. Vakakis. Dynamic interactions of traveling waves propagating in a linear chain with a local essentially nonlinear attachment. *Wave Motion*, 46(3):174–188, 2009.
- C. J. Rupp, A. Evgrafov, K. Maute, and M. L. Dunn. Design of phononic materials/structures for surface wave devices using topology optimization. *Structural and Multidisciplinary Optimization*, 34(2):111–121, 2007.
- A. Sakai, T. Fukazawa, and T. Baba. Low loss ultra-small branches in a silicon photonic wire waveguide. *IEICE Transactions on Electronics*, E85C(4):1033–1038, 2002.
- M. M. Sigalas and E. N. Economou. Elastic and acoustic wave band structure. *Journal of Sound and Vibration*, 158(2):377–382, 1992.
- O. Sigmund. Microstructural design of elastic band gap structures. In G. D. Cheng, Y. Gu, S. Liu, and Y. Wang, editors, *Proceedings of the Fourth World Congress of Structural and Multidisciplinary Optimization WCSMO-4*, pages CD–rom, Dalian, China, 2001.
- O. Sigmund. Morphology-based black and white filters for topology optimization. *Structural and Multidisciplinary Optimization*, 33(4–5):401–424, 2007.
- O. Sigmund. Manufacturing tolerant topology optimization. *ACTA Mechanica Sinica*, 25(2):227–239, 2009.
- O. Sigmund and J. S. Jensen. Design of acoustic devices by topology optimization. In C. Cinquini, M. Rovati, P. Venini, and R. Nascimbene, editors, *Short papers of the 5th World Congress on Structural and Multidisciplinary Optimization WCSMO5*, pages 267–268, Lido de Jesolo, May 19–23, 2003, 2003. Italian Polytechnic Press, Milano.

- O. Sigmund, J. S. Jensen, A. Gersborg-Hansen, and R. B. Haber. Topology optimization in wave-propagation and flow problems. In T. Lewiński, O. Sigmund, J. Sokołowski, and A. Żochowski, editors, *Optimal shape design and modeling*, pages 45–54, Warszawa, 2004. Akademicka Oficyna Wydawnicza EXIT.
- J. Smajic, C. Hafner, and D. Erni. Design and optimization of an achromatic photonic crystal bend. *Optics Express*, 11(12):1378–1384, 2003.
- J. Smajic, C. Hafner, and D. Erni. Optimization of photonic crystal structures. *J. Opt. Soc. Am. A*, 21(11):2223–2232, 2004.
- C. A. Soto and A. R. Diaz. Layout of plate structures for improved dynamic response using a homogenization method. *Advances in Design Automation*, 1:667–674, 1993.
- T. Suzuki and P. K. L. Yu. Complex elastic wave band structures in three-dimensional periodic elastic media. *Journal of the Mechanics and Physics of Solids*, 46(1):115–138, 1998.
- K. Svanberg. The method of moving asymptotes - a new method for structural optimization. *International Journal for Numerical Methods in Engineering*, 24: 359–373, 1987.
- D. Tcherniak. Topology optimization of resonating structures using simp method. *International Journal for Numerical Methods in Engineering*, 54:1605–1622, 2002.
- A. Tetu, M. Kristensen, L. H. Frandsen, A. Harpøth, P. I. Borel, J. S. Jensen, and O. Sigmund. Broadband topology-optimized photonic crystal components for both te and tm polarizations. *Optics Express*, 13(21):8606–8611, 2005.
- Y. Tsuji and K. Hirayama. Design of optical circuit devices using topology optimization method with function-expansion-based refractive index distribution. *IEEE Photonics Technology Letters*, 20(9–12):982–984, 2008.
- Y. Tsuji, K. Hirayama, T. Nomura, K. Sato, and S. Nishiwaki. Design of optical circuit devices based on topology optimization. *IEEE Photonics Technology Letters*, 18(5–8):850–852, 2006.
- E. Wadbro and M. Berggren. Topology optimization of an acoustic horn. *Computer Methods in Applied Mechanics and Engineering*, 196(1–3):420–436, 2006.
- G. Wang, X. S. Wen, J. H. Wen, and Y. Z. Liu. Quasi-one-dimensional periodic structure with locally resonant band gap. *Journal of Applied Mechanics – Transactions of the ASME*, 73(1):167–170, 2006.

- Y. Watanabe, Y. Sugimoto, N. Ikeda, N. Ozaki, A. Mizutani, Y. Takata, Y. Kitagawa, and K. Asakawa. Broadband waveguide intersection with lowcrosstalk in two-dimensional photonic crystal circuits by using topology optimization. *Optics Express*, 14(20):9502–9507, 2006.
- Y. Watanabe, N. Ikeda, Y. Sugimoto, Y. Takata, Y. Kitagawa, A. Mizutani, N. Ozaki, and K. Asakawa. Topology optimization of waveguide bends with wide, flat bandwidth in air-bridge-type photonic crystal slabs. *Journal of Applied Physics*, 101(11):113108, 2007.
- Y. Watanabe, N. Ikeda, Y. Takata, Y. Kitagawa, N. Ozaki, Y. Sugimoto, and K. Asakawa. Topology optimization of a wavelength-selective y-junction for 2d photonic crystal waveguides. *Journal of Physics D-Applied Physics*, 41(17):175109, 2008.
- J. P. Webb. Design sensitivity of frequency response in 3-d finite-element analysis of microwave devices. *IEEE Transactions on Magnetism*, 38:1109–1112, 2002.
- E. Yablonovitch. Inhibited spontaneous emission in solid-state physics and electronics. *Physical Review Letters*, 58(20):2059–2062, 1987.
- Z. Z. Yan, C. Z. Zhang, and Y. S. Wang. Analysis of wave propagation and localization in periodic/disordered layered composite structures by a mass-spring model. *Applied Physics Letters*, 94(16):161909, 2009.
- L. Yang, A. V. Lavrinenko, L. H. Frandsen, P. I. Borel, A. Tetu, and J. Fage-Pedersen. Topology optimisation of slow light coupling to photonic crystal waveguides. *Electronics Letters*, 43(17):923–924, 2007.
- S. S. Yao, X. M. Zhou, and G. K. Hu. Experimental study on negative effective mass in a 1d mass-spring system. *New Journal of Physics*, 10:043020, 2008.
- G. H. Yoon, J. S. Jensen, and O. Sigmund. Topology optimization of acoustic-structure interaction using mixed finite elements. *International Journal for Numerical Methods in Engineering*, 70:1049–1075, 2007.
- D. L. Yu, Y. Z. Liu, G. Wang, L. Cai, and J. Qiu. Low frequency torsional vibration gaps in the shaft with locally resonant structures. *Physics Letters A*, 348(3–6):410–415, 2006a.
- D. L. Yu, G. Wang, Y. Z. Liu, J. H. Wen, and J. Qiu. Flexural vibration band gaps in thin plates with two-dimensional binary locally resonant structures. *Chinese Physics*, 15(2):266–271, 2006b.
- V. V. Zalipaev, A. B. Movchan, and I. S. Jones. Waves in lattices with imperfect junctions and localized defect modes. *Proceedings of the Royal Society A – Mathematical Physical and Engineering Sciences*, 464(2096):2037–2054, 2008.

- X. M. Zhou and G. K. Hu. Analytic model of elastic metamaterials with local resonances. *Physical Review B*, 79(19):195109, 2009.

Dansk resumé

Dansk titel: Bølger og vibrationer i inhomogene strukturer: båndgab og optimale design

Denne afhandling omhandler bølger og vibrationer i inhomogene strukturer med speciel fokus på undersøgelse af båndgabsfænomenet og optimering af båndgabsstrukturer. Afhandlingen består af 21 artikler, hvoraf 17 er publiceret i internationale tidsskrifter og 4 er publiceret i conferenceproceedings. Afhandlingen indledes med en sammenfatning af de vigtigste resultater fra artiklerne. Denne sammenfatning består af en indledning fulgt af fire kapitler, der beskriver de opnåede resultater inden for områderne: båndgabsfænomenet, båndgab som optimal design, optimering af fotoniske bølgeledere og avancerede optimerings procedurer. Sammenfatningen afrundes med en kort opsummerende konklusion.

Et båndgab er et fænomen der optræder i periodiske materialer, f.eks. i en lagdelt elastisk stang eller i en to-dimensional fotonisk krystal bestående af cirkulære huller placeret i et hexagonalt eller kvadratisk mønster i et dielektrisk materiale. Ordet båndgab referer til et specifikt frekvensinterval, hvor bølger ikke kan udbrede sig igennem materialet.

I denne afhandling klarlægges bl.a., hvorledes mekaniske strukturer, der er opbygget af et båndgabsmateriale, opfører sig, når de påvirkes af en harmonisk belastning. Dette gøres ved at modellere systemerne som simple masse-fjeder strukturer. Det vises, hvorledes dimensionerne af konstruktionen, randbetingelser samt dæmpning og imperfektioner har en indflydelse på opførslen, og det demonstreres, at båndgabsstrukturer generelt er effektive mht. at dæmpe vibrationer. En eksperimentel demonstration af båndgabsfænomenet er ligeledes inkluderet. I afhandlingen analyseres desuden en speciel type af båndgabsstrukturer baseret på resonante svingninger af lokale resonatorer. Disse vises at være effektive til at dæmpe lavfrekvente svingninger. Desuden undersøges det, hvorledes ikke-lineariteter i form af ikke-lineære fjedre influerer transmissionen af bølger igennem simple masse-fjeder systemer.

Topologioptimering er en effektiv metode til at designe materialefordelingen i en struktur for at opnå ønskede egenskaber. I denne afhandling anvendes og videreudvikles metoden til at designe båndgabsstrukturer. Det vises, at hvis en struktur optimeres for at opnå et minimalt vibrationsniveau, vil den genererede materialefordeling ofte have en periodisk lignende struktur – en båndgabsstruktur. Det demonstreres dog yderligere, at materialefordelingen i den optimerede struktur hænger nøje sammen med dimensionerne af strukturen og af belastningssituation. Det vises også at båndgabsstrukturer kan genereres ved at maksimere separationen af egenfrekvenser

i strukturen. En række forskellige problemstillinger analyseres: materialefordelingen i pladestrukturer optimeres for at opnå minimalt vibrationsniveau eller for at generere en ringbølge i pladen, akustiske strukturer optimeres for minimal transmission af trykbølger, og endelig optimeres elastiske strukturer så de absorberer bølgeenergi maksimalt.

Et vigtigt resultat i afhandlingen er anvendelsen af optimeringsmetoden til at designe bøj og splittere i bølgeledere baseret på fotoniske krystaller. Optimeringen af disse strukturer medfører store forbedringer mht. signaltab og båndbredde. Desuden vises det ofte at resultere i nye designs, der er meget anderledes end de sædvanlige strukturer, der tidligere har været benyttet. Desuden demonstreres det at metoden kan anvendes til at designe mere komplicerede komponenter som f.eks. en bølgelængde splitter, og metoden anvendes yderligere til at designe splittere i fotoniske strip bølgeledere.

I forbindelse med anvendelsen af topologioptimering til at designe båndgabsstrukturer er der benyttet nye strategier til at opnå gode designs. Stærk dæmpning viser sig at være særdeles nyttig i optimeringsproceduren med henblik på at opnå strukturer med gode egenskaber. Desuden benyttes dæmpning til at eliminere grå designs, der ikke kan fabrikere med de specificerede materialer.

Til slut demonstreres nye optimeringsprocedurer der er udviklet til at designe båndgabsstrukturer. Disse kan dog også finde anvendelser inden for en bredere vifte af problemer relateret til optimering af dynamiske strukturer. Først demonstreres en effektiv metode til at optimere strukturers dynamiske opførsel i et frekvensbånd. Dette gøres ved at bruge de såkaldte Padé funktioner. Topologioptimering baseret på transient simulering af strukturers dynamiske opførsel bruges til at optimere et system af ikke-lineære resonatorer for at minimere transmissionen af bølger gennem et masse-fjeder system. Til sidst demonstreres det, hvorledes transient topologioptimering kan udvides, således at man kan finde optimale materialefordelinger, der kan variere i tiden. Fordelen ved et tidsvarierende optimeret design demonstreres i forbindelse med generering af en-dimensionale båndgabsstrukturer og strukturer, der kan komprimere en bølgepuls.

ACADEMIC
PRESSAvailable online at www.sciencedirect.com

SCIENCE @ DIRECT®

Journal of Sound and Vibration 266 (2003) 1053–1078

JOURNAL OF
SOUND AND
VIBRATIONwww.elsevier.com/locate/jsvi

Phononic band gaps and vibrations in one- and two-dimensional mass–spring structures

J.S. Jensen*

*Department of Mechanical Engineering, Section for Solid Mechanics, Technical University of Denmark Nils Koppels Allé,
Building 404, DK-2800 Kgs. Lyngby, Denmark*

Received 1 July 2002; accepted 1 October 2002

Abstract

The vibrational response of finite periodic lattice structures subjected to periodic loading is investigated. Special attention is devoted to the response in frequency ranges with gaps in the band structure for the corresponding infinite periodic lattice. The effects of boundaries, viscous damping, and imperfections are studied by analyzing two examples; a 1-D filter and a 2-D wave guide. In 1-D the structural response in the band gap is shown to be insensitive to damping and small imperfections. In 2-D the similar effect of damping is noted for one type of periodic structure, whereas for another type the band gap effect is nearly eliminated by damping. In both 1-D and 2-D it is demonstrated how the free structural boundaries affect the response in the band gap due to local resonances. Finally, 2-D wave guides are considered by replacing the periodic structure with a homogeneous structure in a straight and a 90° bent path, and it is shown how the vibrational response is confined to the paths in the band gap frequency ranges.

© 2003 Elsevier Science Ltd. All rights reserved.

1. Introduction

In the last decade the interest in photonic band gap crystals has been great. Periodic structures of two materials with different di-electric properties may exhibit stop bands in the band structure where light waves cannot propagate—thus, photonic crystals can be constructed that effectively inhibit light at certain frequencies to be transmitted through them. Numerous research papers have appeared on the subject, see e.g., Refs. [1,2] and possible industrial applications have emerged such as e.g., wave guides, antennas, and lasers.

*Tel.: +45-45-25-4280; fax: +45-45-93-1475.

E-mail address: jsj@mek.dtu.dk (J.S. Jensen).

The work on photonic band gaps has led to a renewed interest in elastic wave propagation in periodic materials and especially the existence of the so-called phononic band gaps—i.e., stop bands in the band structure for propagation of elastic waves. However, the existence of frequency ranges where propagating wave solutions do not exist has already been demonstrated by Rayleigh [3]. Comprehensive reviews of earlier work on wave propagation and band gaps in periodic structures can be found in Refs. [4–6]. New research has focussed on theoretical predictions as well as experimental documentation of gaps in the band structure. Studies of periodic structures in one dimension include the experimental and theoretical analysis of string–mass chains [7], microtapered optical fibers [8], and theoretical work on band structures in locally periodic media governed by the wave equation [9]. In 2- and 3-D periodic structures gaps in the elastic band structure have been predicted using a variety of computational methods such as plane-wave expansion e.g., Refs. [10,11], finite elements (FEM) e.g., Refs. [12,13], the multiple scattering-theory (MST) e.g., Refs. [14,15], and a related Rayleigh method [16]. An extensive review of newer research in band structures of periodic materials can be found in Ref. [17], and frequently updated reference lists on phononic and photonic band gaps can be found at <http://www.pbglink.com>.

Unlike e.g., photonic crystals to the author's knowledge no direct applications of phononic band gap structures and materials have appeared. Little work has been published on analyzing the behavior of band gap materials in engineering structures, where the effects of the finite dimension, boundaries, damping, and imperfections must be addressed. Two recent exceptions are the studies of surface states and localization phenomena in periodic structures with defects [18,19]. It is the aim of this work to add knowledge that can be exploited in the development towards future applications. An extension of this work is the application of topology optimization techniques in the design of materials and structures with phononic band gaps [20,21].

In this work simple mass–spring models are used to demonstrate the dynamical behavior of periodic structures. The mass–spring models provide a convenient setting for the realization and visualization of periodic structures, for including damping and imperfections, and qualitatively they fully capture the phenomena involved. In Section 2 the mass–spring models of the *unit cells* are presented. The unit cells describe the repetitive units in the periodic structure. Band structures are calculated for the corresponding infinite lattices and for special cases approximate analytical frequency bounds for the gaps are obtained. Two examples are then provided in Section 3 in order to analyze the vibrational response of the periodic structures subjected to periodic loading in the band gap frequency ranges.

The first example deals with a 1-D structure with filtering properties (Section 3.2). Two different sizes of masses and springs are used in the structure, chosen so that it corresponds to a discrete model of aluminum and PMMA (acrylplastic) with filtering of longitudinal waves. It is shown how the response in the band gap frequency range depends on the number of unit cells in the structure and also how the response in the band gap is insensitive to moderate amounts of viscous damping and to small imperfections in the periodic structure.

The second example deals with a 2-D structure that can be utilized as a wave guide (Section 3.3). The structure is considered with two different types of unit cells, with masses and springs chosen to make the lattice correspond to a structure with a stiff aluminum inclusion in an epoxy matrix (type 1), or a heavy resonator of copper suspended in a flexible layer of silicone rubber in an epoxy matrix (type 2). With type 1 unit cells the response in the band gap depends only weakly on damping, whereas with type 2 unit cells damping almost eliminates the band gap effect. It is

shown for 2-D, as well as for the 1-D example, how the presence of boundaries creates local resonances that affect the response in the band gap. Finally, two wave guide structures are created by replacing the periodic structure with a homogeneous structure in a straight and in a 90° bent path. It is demonstrated how the vibrational response is confined to these paths when the frequency of the periodic loading is within the band gap.

2. Model: the unit cell—infinite lattices

The periodic structures to be considered are made up of a finite number of identical *unit cells*. These unit cells are the repetitive units that are used to describe the micro-structure (or material). If the unit cells are inhomogeneous, i.e., made up of different masses and/or springs, the corresponding structure is periodic, whereas with a homogeneous unit cell the structure is also homogeneous.

In the following, dispersion relations are obtained for wave propagation in infinite periodic lattices. Results are presented in form of band structures relating the frequency of the propagating waves to the wavenumber or wavevector.

2.1. The one-dimensional case—longitudinal waves

Fig. 1a shows the 1-D unit cell. Within the cell N masses m_j are connected by linear elastic springs with stiffness coefficients k_j . The small-amplitude displacement of the $(p + j)$ th mass is governed by

$$m_j \ddot{u}_{p+j} = k_j(u_{p+j+1} - u_{p+j}) - k_{j-1}(u_{p+j} - u_{p+j-1}), \tag{1}$$

where p is an arbitrary integer.

Wave propagation through an infinite number of connected unit cells is considered and thus a travelling wave solution is assumed as

$$u_{p+j} = A_j e^{i((p+j)\gamma - \omega t)}, \tag{2}$$

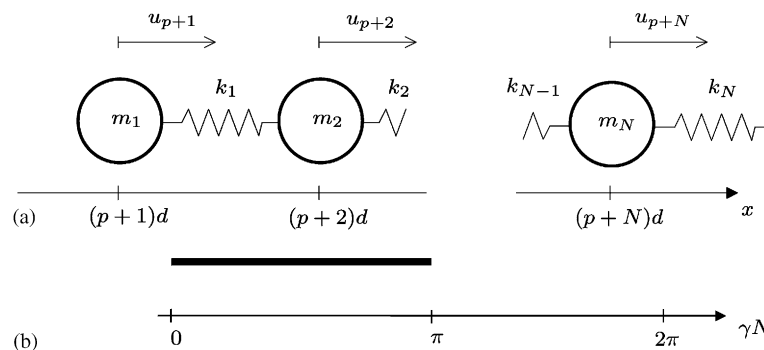


Fig. 1. (a) The 1-D unit cell with N masses m_j and springs k_j , and (b) the corresponding irreducible Brillouin zone indicating the range of the wavenumber γ evaluated when constructing the complete band structure from Eq. (8).

where A_j is the wave amplitude, γ the wavenumber, and ω is the wave frequency. Inserting Eq. (2) into Eq. (1) yields N linear complex equations

$$(\omega_j^2 - \omega^2)A_j = c_j^2 e^{i\gamma} A_{j+1} + (\omega_j^2 - c_j^2) e^{-i\gamma} A_{j-1}, \quad j = 1, \dots, N, \quad (3)$$

where the following non-dimensional parameters have been introduced:

$$\omega_j^2 = \frac{k_j + k_{j-1}}{m_j}, \quad (4)$$

$$c_j^2 = \frac{k_j}{m_j}. \quad (5)$$

An infinite number of identical unit cells is considered and the following periodic boundary conditions can thus be applied:

$$A_{j-1} = A_N, \quad j = 1, \quad (6)$$

$$A_{j+1} = A_1, \quad j = N. \quad (7)$$

Eq. (3) forms with Eqs. (6) and (7) a standard complex eigenvalue problem

$$(\mathbf{S}(\gamma) - \omega^2 \mathbf{I})\mathbf{A} = \mathbf{0}, \quad (8)$$

that can be solved to construct the band structure of wave frequencies ω for known wavenumber γ .

It is not necessary to solve Eq. (8) for all values of γ . Due to the periodicity all propagating modes are captured by restricting the wavenumber to the irreducible Brillouin zone as shown in Fig. 1b [4]. The two end points in the zone, $\gamma N = 0$ and π , correspond to the masses in two neighboring unit cells moving in phase and in anti-phase, respectively.

2.1.1. Wave propagation for an inhomogeneous unit cell

As it is well known no gaps exist in the band structure for the homogeneous infinite lattice, i.e., waves of all frequencies are allowed to propagate. However, with an inhomogeneous unit cell gaps emerge in the band structure for the corresponding periodic infinite lattice. An example of an inhomogeneous unit cell is shown in Fig. 2a. This unit cell consists of four masses with the center masses and springs representing a material with lower stiffness to mass ratio (lower wave speed).

For the four-mass system ($N = 4$) the masses and springs are chosen as

$$m_1 = m_4 = 3.98 \text{ kg},$$

$$m_2 = m_3 = 1.69 \text{ kg},$$

$$k_1 = k_4 = 70.9 \times 10^9 \text{ kg/s}^2,$$

$$k_2 = k_3 = 5.28 \times 10^9 \text{ kg/s}^2 \quad (9)$$

which makes the mass–spring system correspond to a discrete model of a 0.15 m rod with the middle 50% of PMMA and the two ends of aluminum.¹

¹Material data: $E_{alu} = 70.9 \text{ GPa}$, $\rho_{alu} = 2830 \text{ kg/m}^3$, $E_{pmma} = 5.28 \text{ GPa}$, $\rho_{pmma} = 1200 \text{ kg/m}^3$.

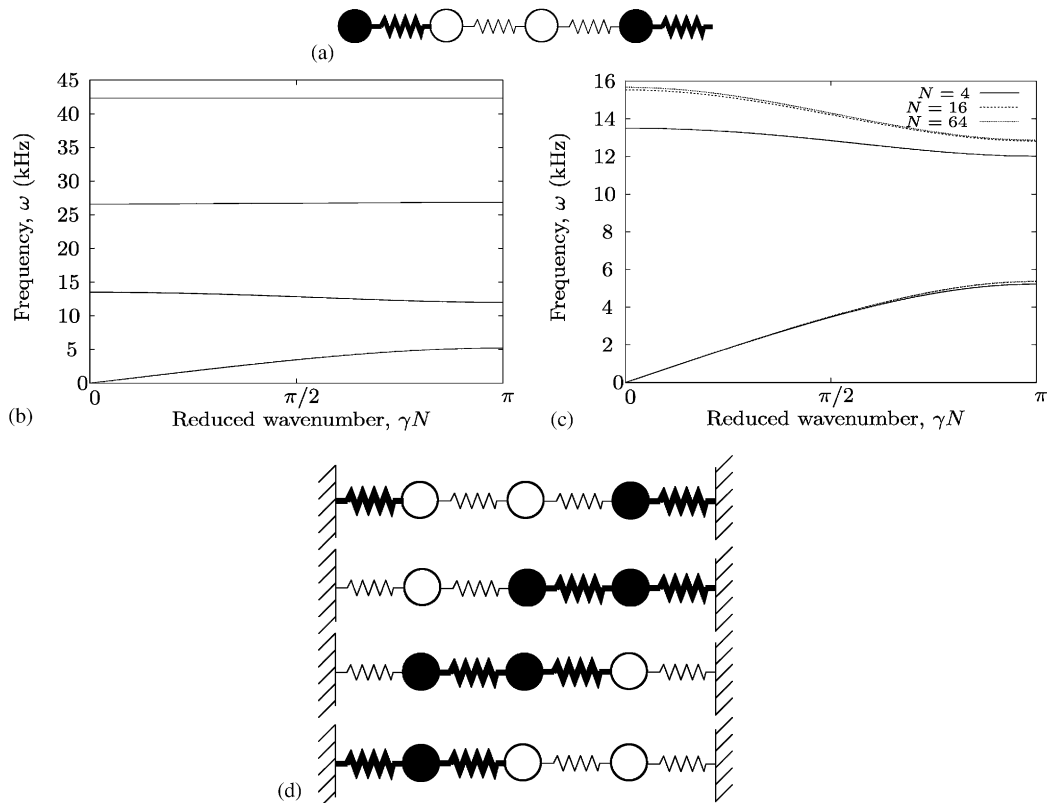


Fig. 2. (a) The unit cell with $N = 4$ (sizes of masses and springs given in the text), (b) band structure for wave propagation in the infinite periodic lattice, (c) close-up of the first gap including curves computed for $N = 16$ and 64 , and (d) the four possible isolated systems with a single mass in the unit cells fixed.

As shown in Fig. 2b three large gaps appear in the band structure for $\omega \approx 5.2\text{--}12.0$, $13.5\text{--}26.6$, and $26.8\text{--}42.3$ kHz. In these frequency ranges no waves can propagate through the infinite periodic lattice. In Fig. 2c is shown a close-up of the lowest band gap including curves computed for higher values of N (a finer discretization of the unit cell with the middle $N/2$ masses and springs of PMMA). The band structure converges with increasing N towards the corresponding continuum model, but as appears the simple model with $N = 4$ gives a good estimation of the first band gap. For the other gaps the difference between the simple model and the continuum model is naturally larger.

The upper and lower frequency bounds for the first band gap can be accurately estimated by considering a simplified system (Fig. 2d). For wave propagation in the first pass band the four masses move in phase, corresponding to the fundamental mode of propagation. The first band gap appears when $\gamma N = \pi$ (Fig. 2a) for which the wave amplitude of one of the masses in the unit cells vanishes. Fig. 2d shows the four possible system configurations with a single mass in the unit cell fixed (replaced by a support in the figure). It is now possible to estimate the lower and upper frequency bound of the band gap by identifying the lowest and highest fundamental eigenfrequency for the four configurations. The system third from top in Fig. 2d has the lowest

fundamental eigenfrequency $\omega = 5.2$ kHz which matches the lower band gap frequency well, and the system at the top has the highest fundamental eigenfrequency found as $\omega = 12.0$ kHz giving a good estimation of the upper band gap frequency.

In the band gaps, instead of propagating modes, solutions exist for purely imaginary wavenumbers. Introducing the imaginary wavenumber $\gamma \rightarrow i\gamma$ into the solution form (2) yields

$$u_{p+j} = A_j e^{-(p+j)\gamma} e^{-i\omega t} \tag{10}$$

showing that the solution is a standing wave with an amplitude of vibration that is exponentially decaying spatially.

2.2. The 2-D case—in-plane elastic waves

A 2-D unit cell is shown in Fig. 3a. Within the cell $N \times N$ masses are arranged in a square configuration with each mass connected to eight neighboring masses with springs. The four springs connected to the j, k th mass in the $0^\circ, 45^\circ, 90^\circ,$ and 135° directions from the x -axis are denoted $k_{j,k,1}, k_{j,k,2}, k_{j,k,3},$ and $k_{j,k,4}$.

The equations of motion governing the small-amplitude displacements of the $(p + j), (q + k)$ th mass in the x and y directions (u, v) are given as:

$$\begin{aligned} m_{j,k} \ddot{u}_{p+j,q+k} = & k_{j,k,1}(u_{p+j+1,q+k} - u_{p+j,q+k}) \\ & + \frac{1}{2} k_{j,k,2}(u_{p+j+1,q+k+1} - u_{p+j,q+k} + v_{p+j+1,q+k+1} - v_{p+j,q+k}) \\ & + \frac{1}{2} k_{j,k,4}(u_{p+j-1,q+k+1} - u_{p+j,q+k} - v_{p+j-1,q+k+1} + v_{p+j,q+k}) \\ & + k_{j-1,k,1}(u_{p+j-1,q+k} - u_{p+j,q+k}) \\ & + \frac{1}{2} k_{j-1,k-1,2}(u_{p+j-1,q+k-1} - u_{p+j,q+k} + v_{p+j-1,q+k-1} - v_{p+j,q+k}) \\ & + \frac{1}{2} k_{j+1,k-1,4}(u_{p+j+1,q+k-1} - u_{p+j,q+k} - v_{p+j+1,q+k-1} + v_{p+j,q+k}), \end{aligned} \tag{11}$$

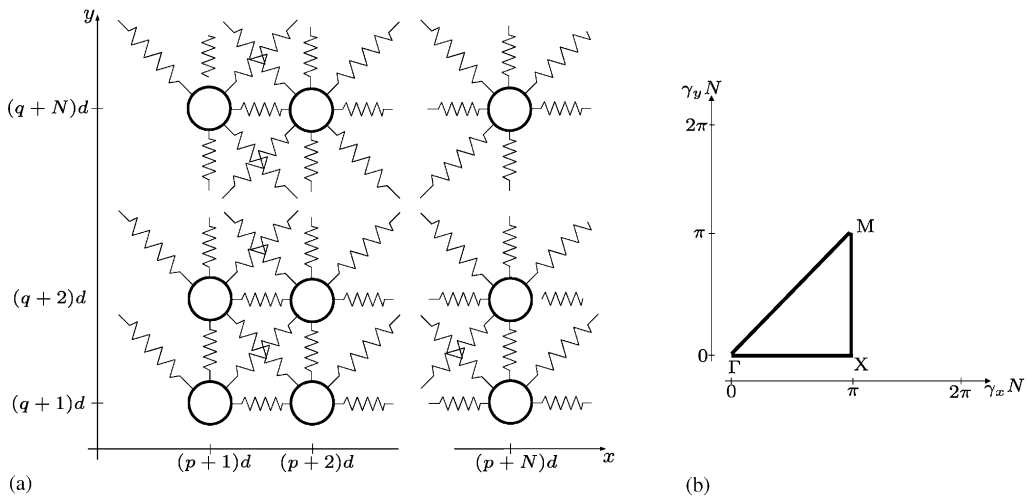


Fig. 3. (a) The 2-D square unit cell with $N \times N$ masses and corresponding $4 \times N \times N$ springs, and (b) the corresponding irreducible Brillouin zone indicating the triangular path on which the wavevector γ should be evaluated in Eq. (21).

$$\begin{aligned}
 m_{j,k} \ddot{v}_{p+j,q+k} = & k_{j,k,3}(v_{p+j,q+k+1} - v_{p+j,q+k}) \\
 & + \frac{1}{2} k_{j,k,2}(v_{p+j+1,q+k+1} - v_{p+j,q+k} + u_{p+j+1,q+k+1} - u_{p+j,q+k}) \\
 & + \frac{1}{2} k_{j,k,4}(v_{p+j-1,q+k+1} - v_{p+j,q+k} - u_{p+j-1,q+k+1} + u_{p+j,q+k}) \\
 & + k_{j,k-1,3}(v_{p+j,q+k-1} - v_{p+j,q+k}) \\
 & + \frac{1}{2} k_{j-1,k-1,2}(v_{p+j-1,q+k-1} - v_{p+j,q+k} + u_{p+j-1,q+k-1} - u_{p+j,q+k}) \\
 & + \frac{1}{2} k_{j+1,k-1,4}(v_{p+j+1,q+k-1} - v_{p+j,q+k} - u_{p+j+1,q+k-1} + u_{p+j,q+k}),
 \end{aligned} \tag{12}$$

where p and q are arbitrary.

As in the 1-D case a travelling wave solution is assumed in the infinite lattice

$$u_{p+j,q+k} = A_{j,k} e^{i((p+j)\gamma_x + (q+k)\gamma_y - \omega t)}, \tag{13}$$

$$v_{p+j,q+k} = B_{j,k} e^{i((p+j)\gamma_x + (q+k)\gamma_y - \omega t)}, \tag{14}$$

where $A_{j,k}$ and $B_{j,k}$ are the wave amplitudes, ω the wave frequency, and γ_x and γ_y are the two components of the wavevector γ .

With the following non-dimensional constants defined:

$$\omega_{x,j,k}^2 = \frac{k_{j,k,1} + k_{j-1,k,1} + \frac{1}{2}(k_{j,k,2} + k_{j,k,4} + k_{j-1,k-1,2} + k_{j+1,k-1,4})}{m_{j,k}}, \tag{15}$$

$$\omega_{y,j,k}^2 = \frac{k_{j,k,3} + k_{j,k-1,3} + \frac{1}{2}(k_{j,k,2} + k_{j,k,4} + k_{j-1,k-1,2} + k_{j+1,k-1,4})}{m_{j,k}}, \tag{16}$$

$$\tilde{k}_{j,k} = \frac{\frac{1}{2}(k_{j,k,2} - k_{j,k,4} + k_{j-1,k-1,2} - k_{j+1,k-1,4})}{m_{j,k}}, \tag{17}$$

$$c_{j,k}^2 = \frac{k_{j,k}}{m_{j,k}}, \tag{18}$$

Eqs. (11) and (12) become

$$\begin{aligned}
 (\omega_{x,j,k}^2 - \omega^2)A_{j,k} + \tilde{k}_{j,k}B_{j,k} = & c_{j,k,1}^2 e^{i\gamma_x} A_{j+1,k} \\
 & + \frac{1}{2} c_{j,k,2}^2 (e^{i(\gamma_x + \gamma_y)} A_{j+1,k+1} + e^{i(\gamma_x + \gamma_y)} B_{j+1,k+1}) \\
 & + \frac{1}{2} c_{j,k,4}^2 (e^{i(\gamma_y - \gamma_x)} A_{j-1,k+1} - e^{i(\gamma_y - \gamma_x)} B_{j-1,k+1}) \\
 & + c_{j-1,k,1}^2 e^{-i\gamma_x} A_{j-1,k} \\
 & + \frac{1}{2} c_{j-1,k-1,2}^2 (e^{-i(\gamma_x + \gamma_y)} A_{j-1,k-1} + e^{-i(\gamma_x + \gamma_y)} B_{j-1,k-1}) \\
 & + \frac{1}{2} c_{j+1,k-1,4}^2 (e^{i(\gamma_x - \gamma_y)} A_{j+1,k-1} - e^{i(\gamma_x - \gamma_y)} B_{j+1,k-1}),
 \end{aligned} \tag{19}$$

$$\begin{aligned}
(\omega_{y,j,k}^2 - \omega^2)B_{j,k} + \tilde{k}_{j,k}A_{j,k} = & c_{j,k,3}^2 e^{i\gamma_y} B_{j,k+1} \\
& + \frac{1}{2} c_{j,k,2}^2 (e^{i(\gamma_x+\gamma_y)} B_{j+1,k+1} + e^{i(\gamma_x-\gamma_y)} A_{j+1,k+1}) \\
& + \frac{1}{2} c_{j,k,4}^2 (e^{i(\gamma_y-\gamma_x)} B_{j-1,k+1} - e^{i(\gamma_y+\gamma_x)} A_{j-1,k+1}) \\
& + c_{j,k-1,3}^2 e^{-i\gamma_y} B_{j-1,k} \\
& + \frac{1}{2} c_{j-1,k-1,2}^2 (e^{-i(\gamma_x+\gamma_y)} B_{j-1,k-1} + e^{-i(\gamma_x-\gamma_y)} A_{j-1,k-1}) \\
& + \frac{1}{2} c_{j+1,k-1,4}^2 (e^{i(\gamma_x-\gamma_y)} B_{j+1,k-1} - e^{i(\gamma_x+\gamma_y)} A_{j+1,k-1}) \quad (20)
\end{aligned}$$

with periodic boundary conditions applied using a 2-D equivalent of Eqs. (6) and (7).

The corresponding eigenvalue problem is set up

$$(\mathbf{S}(\gamma_x, \gamma_y) - \omega^2 \mathbf{I})\mathbf{A} = \mathbf{0} \quad (21)$$

and solved for the wave frequency ω for known wavevector components γ_x and γ_y . As in the 1-D case it is not necessary to analyze Eq. (21) for all γ_x and γ_y . In Fig. 3b the irreducible Brillouin zone in two dimensions is shown, [4], where the analysis can be restricted to the triangular zone if the unit cell is square and symmetrical. Furthermore, it is only necessary to search the zone on the exterior boundary, i.e., along the path $\Gamma - X - M - \Gamma$, since the extremums of the wave frequencies are always found on the zone boundary.²

2.2.1. Band gaps for a stiff inclusion: type 1 unit cell

The homogeneous unit cell produces a band structure without gaps, as was also the case for the 1-D problem.

A unit cell with a band gap is shown in Fig. 4a with the corresponding band structure shown in Fig. 4b. A cell with 5×5 masses and connecting springs is chosen where the center 3×3 masses and corresponding springs represent a heavy and stiff inclusion and the remaining masses and springs are the lighter and more flexible matrix material.

The values of masses and springs are

$$\begin{aligned}
m_{mat} &= 1.82 \times 10^{-2} \text{ kg}, \\
m_{inc} &= 4.53 \times 10^{-2} \text{ kg}, \\
k_{mat,1} = k_{mat,3} &= 2 \times k_{mat,2} = 2 \times k_{mat,4} = 4.10 \times 10^9 \text{ kg/s}^2, \\
k_{inc,1} = k_{inc,3} &= 2 \times k_{inc,2} = 2 \times k_{inc,4} = 70.9 \times 10^9 \text{ kg/s}^2. \quad (22)
\end{aligned}$$

The values in Eq. (22) are chosen so that the model corresponds to a $0.02 \text{ m} \times 0.02 \text{ m}$ unit cell of epoxy matrix with an aluminum inclusion. By choosing the springs $k_{2,}$ and $k_{4,}$ to be half the size of the springs $k_{1,}$ and $k_{3,}$ as in Eq. (22), a good qualitative agreement is obtained between the mass-spring model and a plane-strain 2-D continuum model of materials with the Poisson ratio near $\nu = 0.3$.

²To the author's knowledge no proof of this has been published. However, it appears to be generally accepted and in the numerical examples presented in this paper this is indeed so.

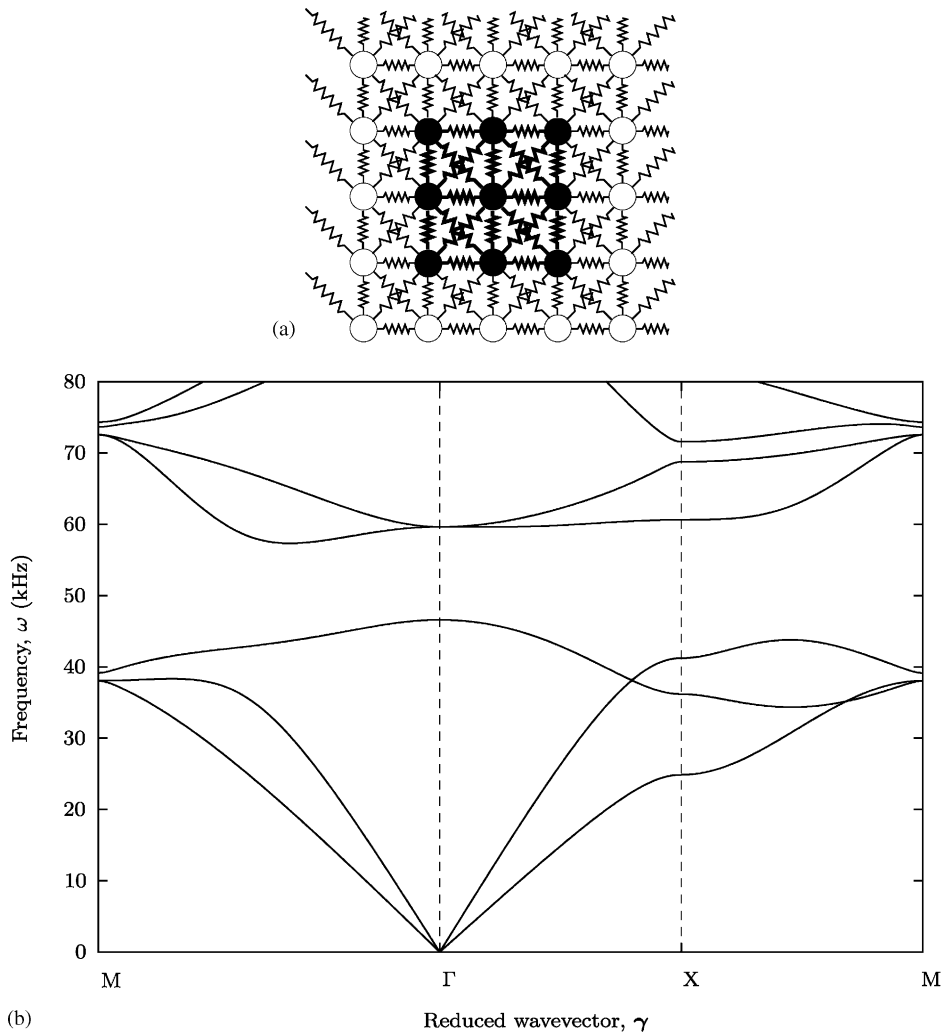


Fig. 4. (a) The 5×5 mass–spring unit cell (denoted type 1) modelling a stiff inclusion (center 3×3 masses and springs) in a surrounding matrix, and (b) the corresponding band structure for wave propagation in the infinite periodic lattice structure.

As appears from Fig. 4b a gap appears in the band structure for $\omega \approx 46.6\text{--}57.3$ kHz between the third and fourth bands. In this frequency range waves cannot propagate in the infinite lattice regardless of the direction of propagation. The band gap calculated for this mass-spring unit cell model corresponds qualitatively to the band gap found for the corresponding continuum model, see e.g., Refs. [15,20].

2.2.2. Band gaps for a heavy resonator: type 2 unit cell

Alternatively, band gaps can be obtained in the lower frequency range by placing a heavy inclusion in soft suspension with a surrounding matrix material. The heavy inclusion acts as a

local resonator and splits up the band structure. Recently, band gaps for such structures were demonstrated in Refs. [14,22], with the former pointing out a possible application in noise reduction due to the low band gap frequency range.

Fig. 5a shows the unit cell and the corresponding band structure is shown in Fig. 5b. The masses and springs in the model have been chosen as

$$\begin{aligned} m_{mat} &= 1.27 \times 10^{-2} \text{ kg}, \\ m_{inc} &= 9.93 \times 10^{-2} \text{ kg}, \\ k_{mat,1} = k_{mat,3} &= 2 \times k_{mat,2} = 2 \times k_{mat,4} = 4.10 \times 10^9 \text{ kg/s}^2, \\ k_{inc,1} = k_{inc,3} &= 2 \times k_{inc,2} = 2 \times k_{inc,4} = 118 \times 10^9 \text{ kg/s}^2, \\ k_{susp,1} = k_{susp,3} &= 2 \times k_{susp,2} = 2 \times k_{susp,4} = 4.00 \times 10^6 \text{ kg/s}^2. \end{aligned} \quad (23)$$

With the parameters in Eq. (23) the model corresponds to a 0.02 m × 0.02 m unit cell of an epoxy matrix with a copper inclusion suspended in a thin massless layer of silicone rubber.³

The band gap frequency range can be accurately predicted. The local resonance of the heavy inclusion in the soft suspension splits up the band structure and determines the lower bound for the band gap

$$\omega_1 \approx \sqrt{\frac{K_{susp}}{M_{inc}}} = \sqrt{\frac{7k_{susp}}{4m_{inc}}} \approx 1.34 \text{ kHz}. \quad (24)$$

The first possible propagation mode above the band gap is when the inclusion and the matrix material can move essentially rigidly in anti-phase. With the matrix motion denoted x and the motion of the inclusion y , the rigid motion is governed by the 2-d.o.f. system

$$M_{mat}\ddot{x} = K_{susp}(y - x), \quad (25)$$

$$M_{inc}\ddot{y} = K_{susp}(x - y), \quad (26)$$

that yields the upper bound frequency

$$\omega_2 \approx \sqrt{\frac{K_{susp}(M_{inc} + M_{mat})}{M_{inc}M_{mat}}} = \sqrt{\frac{7k_{susp}(4m_{inc} + 32m_{mat})}{4m_{inc}32m_{mat}}} \approx 1.88 \text{ kHz} \quad (27)$$

as well as the ratio of amplitudes at the upper frequency bound

$$\frac{y}{x} = 1 - \omega_2^2 \frac{M_{mat}}{K_{susp}} = -\frac{M_{mat}}{M_{inc}} = -\frac{32m_{mat}}{4m_{inc}} \approx -1.02. \quad (28)$$

It is noted that the frequency bounds in Eqs. (24) and (27) correspond well to the gap frequencies shown in the inset in Fig. 5b.

³Material data: $E_{epo} = 4.1 \text{ GPa}$, $\rho_{epo} = 1140 \text{ kg/m}^3$, $E_{cop} = 118 \text{ GPa}$, $\rho_{cop} = 8940 \text{ kg/m}^3$, $E_{rub} = 4 \text{ MPa}$.

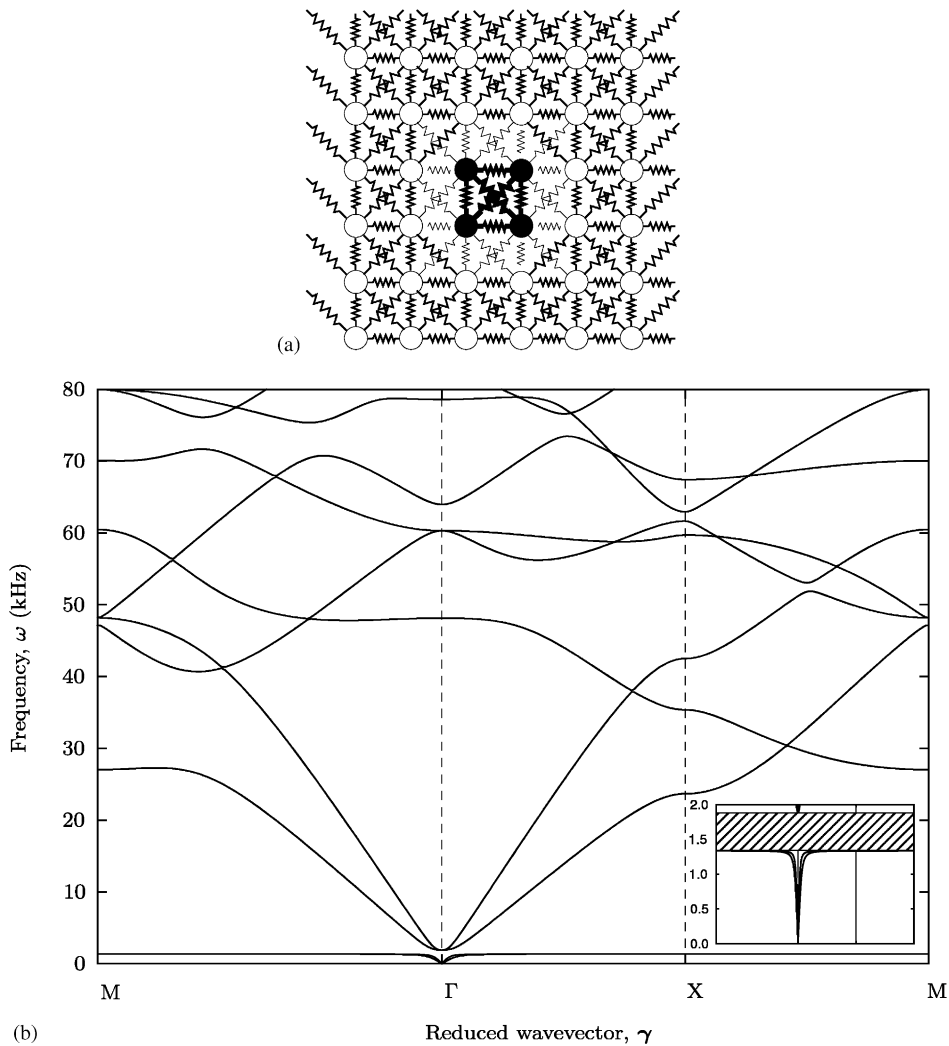


Fig. 5. (a) The 6×6 mass-spring unit cell (denoted type 2) modelling a heavy stiff resonator (center 2×2 masses and springs) in soft suspension (surrounding springs) connected to a surrounding matrix, and (b) the corresponding band structure for wave propagation in the infinite periodic lattice. The inset shows a magnification of the band structure from $\omega = 0$ –2 kHz with the band gap shown hatched.

3. Finite lattice structures

Wave propagation in infinite, undamped, periodic lattices was analyzed in Section 2. In this section the behavior of finite periodic structures subjected to periodic loading is considered in order to study the effects of boundaries, damping, and imperfections in the periodic structure.

The finite structures are treated by two examples: A 1-D-periodic structure that acts as a filter and a 2-D-periodic structure that can be used to guide waves.

3.1. Model equations

A finite number of 1-D or 2-D unit cells are considered. The displacement vector $\mathbf{u}(t) = \{u_1 u_2 \dots u_{N_{tot}}\}^T$ is introduced where N_{tot} is the total number of degrees of freedom in the model. In 1-D the vector takes the form: $\mathbf{u}(t) = \{u_1 \dots u_N u_{N+1} \dots u_{MN}\}^T$, where M is the number of unit cells. In 2-D the vector is given as $\mathbf{u}(t) = \{u_{1,1} v_{1,1} \dots u_{1,M_y N} v_{1,M_y N} \dots u_{M_x N, M_y N} v_{M_x N, M_y N}\}^T$, where M_x and M_y is the number of unit cells in the x and y directions, respectively.

The model equations that govern the small-amplitude displacement of the masses can now be taken directly from Eq. (1) or (11)–(12) and written as

$$\mathbf{M}\ddot{\mathbf{u}} + \mathbf{C}\dot{\mathbf{u}} + \mathbf{K}\mathbf{u} = \mathbf{f}e^{i\Omega t}, \quad (29)$$

where \mathbf{M} and \mathbf{K} is the assembled mass- and stiffness-matrices, respectively, \mathbf{C} is an added viscous damping matrix, and \mathbf{f} is a vector of forces of frequency Ω .

A diagonal damping matrix is used to model the viscous damping with the components c_i expressed in terms of the actual to critical damping ratio ζ_i from the relation

$$\zeta_i = \frac{c_i}{2\sqrt{m_i \bar{k}_i}}, \quad (30)$$

where m_i is the mass corresponding to the i th dof and \bar{k}_i is an equivalent stiffness defined as $m_i \omega_i^2$, cf. Eq. (4) in 1-D and Eqs. (15) and (16) in 2-D.

With the time dependency of the displacement vector

$$\mathbf{u}(t) = \mathbf{a}e^{i\Omega t} \quad (31)$$

inserted into Eq. (29), the linear set of equations to be solved for the amplitudes \mathbf{a} is given as

$$(-\Omega^2 \mathbf{M} + i\Omega \mathbf{C} + \mathbf{K})\mathbf{a} = \mathbf{f}. \quad (32)$$

3.2. Example 1: a 1-D filter

An application for band gaps in a 1-D lattice is as pass- or stop-band filters. In theory, for an infinite, and perfectly periodic lattice without damping, perfect filtering properties exist with alternating pass bands and complete stop bands. The properties of finite lattice structures subjected to periodic loading is here considered by analyzing the effect of the number of unit cells in the structure, viscous damping, and imperfections in the periodic structure.

The unit cell considered in Section 2.1 with four masses and springs is used to describe the periodic structure. As previously stated, this can be seen as a discrete model of a 0.15 m unit cell consisting of 50% aluminum and 50% PMMA. In Section 2.1 it was shown that for the infinite lattice this unit cell displays a band gap between approximately 5.2–12 kHz. Another band gap appears above 13.5 kHz but the focus is here put on the response in the first gap.

Fig. 6a shows the model of the structure with M unit cells. The structure is subjected to a periodic loading $f \cos \Omega t$ at the left end. Fig. 6b shows the corresponding computational mass-spring model with 10 unit cells ($M = 10$) and the four mass unit cell ($N = 4$).

In the following sections, the filtering properties of this structure are analyzed for different choice of system parameters. The response of the structure is typically given for the last mass in the lattice and presented as frequency response functions (FRF) showing the acceleration of the

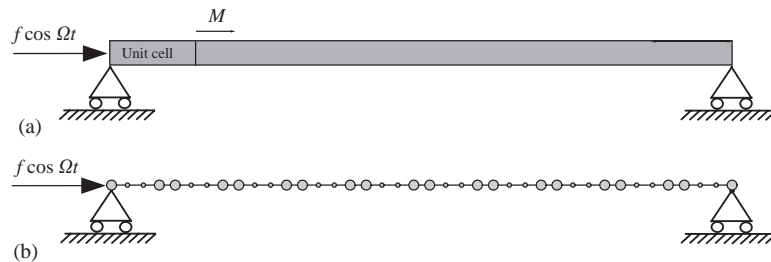


Fig. 6. (a) Structure made of M unit cells with a periodic loading $f \cos \Omega t$ acting in one end, and (b) the corresponding computational mass–spring model with $M = 10$ and the unit cell with 4 masses ($N = 4$).

mass for a reference force amplitude. The FRF curves are computed by solving the full set of linear equations (32) for each frequency Ω .

3.2.1. The number of unit cells

An important parameter in the performance of the filter is of course the number of unit cells used. If only a few unit cells are used the potential attenuation of the signal in the band gap frequency range is lower than if more unit cells are used.

Fig. 7a displays the FRF for the last mass in the lattice structure when it is subjected to a periodic loading of the first mass. Curves are shown for $M = 2, 5, 10$, and for comparison the band gap boundaries calculated for the infinite lattice are shown with vertical dashed lines.

For $M = 2$ the band gap is detectable from the curve but the drop in response inside the band gap is not much larger than the response drops between other resonance frequencies. With more unit cells included the gap clearly appears—resonances are clustered outside the gap, the response is reduced significantly inside the gap, and the steepness of curves increases at the band gap boundaries. With even more unit cells included the steepness of the response curves near these boundaries can, in principle, be as large as desired.

When M is large the computed band gap boundaries for the infinite lattice are seen to correspond well with the band gap detectable from the FRF. However, a small discrepancy is noted near the first gap $\Omega \approx 5.3$ kHz where resonance peaks appear just inside the gap boundary. The resonance here is associated with a local eigenmode located near the boundary of the structure where the boundary conditions are different.

This boundary effect is displayed in Fig. 7b. Here, the response of all masses in the structure is shown for four frequencies. The short-dashed line for $\Omega = 5.27$ kHz corresponds to the boundary mode frequency. The two curves for frequencies inside the band gap (i.e., $\Omega = 5.27$ and 6.00 kHz) display an exponentially decreasing amplitude away from the point of excitation as predicted from Eq. (10), but the boundary mode is seen as an increase in the response towards the end of the structure. The curves for the two other frequencies outside the band gap correspond to excitation of a low and a high vibration mode.

3.2.2. Viscous damping and imperfections

Fig. 8a shows FRF-curves for the considered structure with $M = 10$ without damping and with three different amounts of viscous damping characterized by the damping ratios $\zeta = 0.1\%$, 1.0%, and 5.0% added.

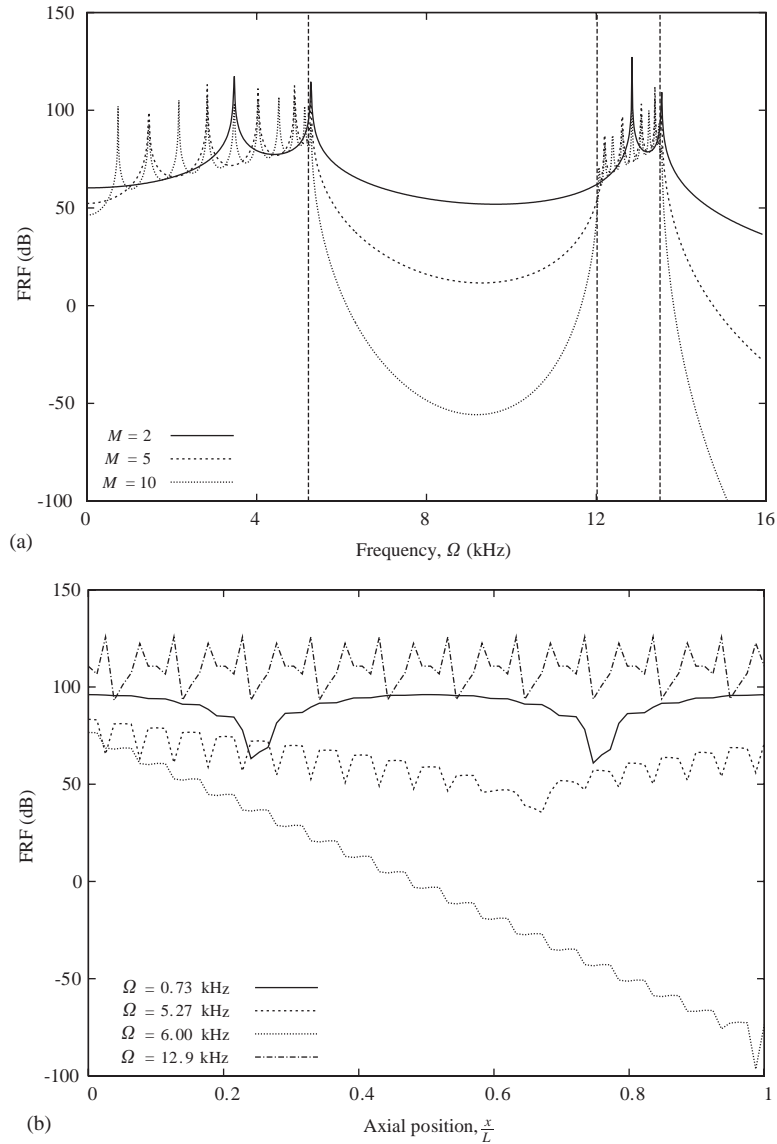


Fig. 7. (a) FRF-curves for the last mass in the lattice for different numbers of unit cells in the structure. Vertical dashed lines indicate the band gap boundaries calculated for the infinite periodic structure, and (b) the response for all masses for $M = 10$ for four different frequencies.

For low values of damping the response resembles that of the undamped structure, except that the peaks at resonance are reduced, i.e., a normal effect of added damping. In the band gap the responses are hardly changed by small amounts of damping. Only with strong damping added ($\zeta = 5\%$) is the response inside the gap affected.

Like with damping it can be expected that some imperfection in the periodic structure is present. Fig. 8b shows the effect of adding some level of disorder to the perfect periodic structure.

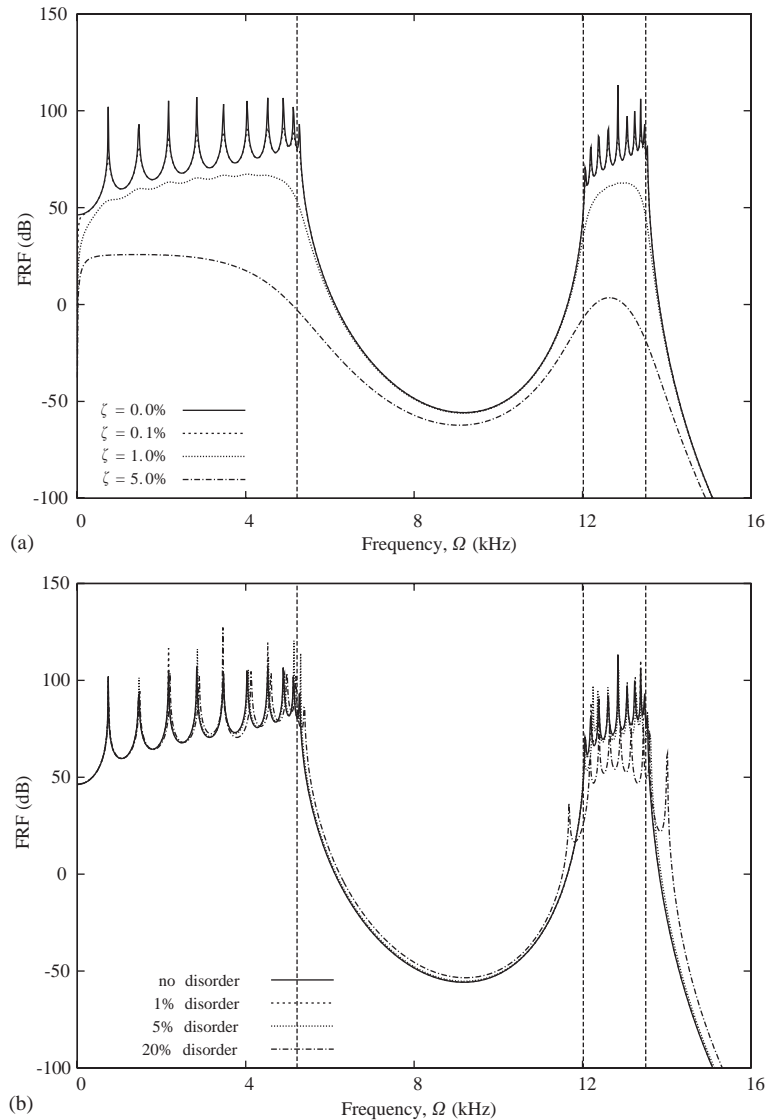


Fig. 8. (a) The influence on the response of the last mass of added viscous damping characterized by the actual to critical damping ratio ζ of the individual masses, and (b) the influence of random disorder of the sizes of the individual masses. For all curves $M = 10$.

The imperfections are simulated by adding a random variation to each mass size. The variation is indicated by a disorder percentage representing the maximum variation of the mass relative to its nominal value.

Fig. 8b shows that the response is insensitive to the presence of small imperfections. Only if the structure deviates significantly from the perfect periodic (20% disorder) is the response inside the band gap noticeably changed by e.g., the presence of local resonances. But even with this high level of imperfection the band gap is still clearly seen in the response.

3.3. Example 2: a 2-D waveguide

In Sections 2.2.1 and 2.2.2 it was shown how two different inhomogeneous unit cells have gaps in the band structure for 2-D in-plane waves. In this section the vibrational response of periodic structures with these two types of unit cells are analyzed when it is subjected to periodic loading. The effects of the number of unit cells, viscous damping, and boundary effects are considered and it is shown also how a structure with band gap unit cells can act as a wave guide.

Fig. 9a displays a model of the structure composed of a number of unit cells, M_x in one direction and M_y in the other. A periodic loading $f \cos \Omega t$ is applied centrally on the upper boundary and the structure is simply supported at the two lower corners. Fig. 9b shows the corresponding computational mass–spring model for $M_x = M_y = 7$ with type 1 unit cell.

3.3.1. Type 1 unit cells

Fig. 10 shows FRF-curves for the structure with type 1 unit cells (5×5 masses corresponding to a $0.02 \text{ m} \times 0.02 \text{ m}$ epoxy matrix with a square aluminum inclusion). Indicated in the figure with vertical dashed lines are the band gap boundaries for the infinite periodic lattice, as seen in Fig. 5. Fig. 10a shows the response in the bottom of the structure (point A in Fig. 9a), and Fig. 10b on the side of the structure (point B). For $M_x = M_y = 3$ the band gap is not clearly detectable from the response, with e.g., several resonance peaks appearing inside the band gap boundaries. With more unit cells the response clearly drops inside the gap. However for all curves resonance peaks and a high response are seen from $\Omega \approx 55 \text{ kHz}$ and up to the upper boundary frequency. These resonance peaks are associated with local resonances for the boundary elements, as in the 1-D case.

Fig. 11 shows contour plots of the response in the structure for two frequencies. The response in Fig. 11a is calculated for $\Omega = 52.1 \text{ kHz}$, corresponding to a point in the middle of the band gap and shows clearly how the response is localized near the point of excitation. For $\Omega = 54.8 \text{ kHz}$ a high response is seen to be localized near the boundary of the structure. This frequency is inside the band gap range but appears as waves can still propagate along the boundary elements.

3.3.2. Type 2 unit cells

The type 2 unit cell also displays a band gap, but in a lower frequency range than type 1 unit cell. This unit cell corresponds to a $0.02 \text{ m} \times 0.02 \text{ m}$ epoxy matrix with a copper inclusion in a soft suspension of silicon rubber.

Fig. 12 shows the FRF-curves and the corresponding band gap frequency range in points A and B. As expected, the response drops inside the band gap, but a significant reduction is seen only very locally near the lower band gap frequency boundary, i.e. the local resonance frequency of the inclusions.

A contour plot of the response for $\Omega = 1.34 \text{ kHz}$ is shown in Fig. 13a, the frequency where the response drops to a minimum. The vibrations are seen to be localized near the point of excitation with the inclusions vibrating with a higher amplitude than the surrounding masses throughout the whole structure.

Fig. 13b shows the response for $\Omega = 1.90 \text{ kHz}$, i.e., slightly above the upper band gap frequency. Here, the response is seen to be nearly constant over most of the domain except near

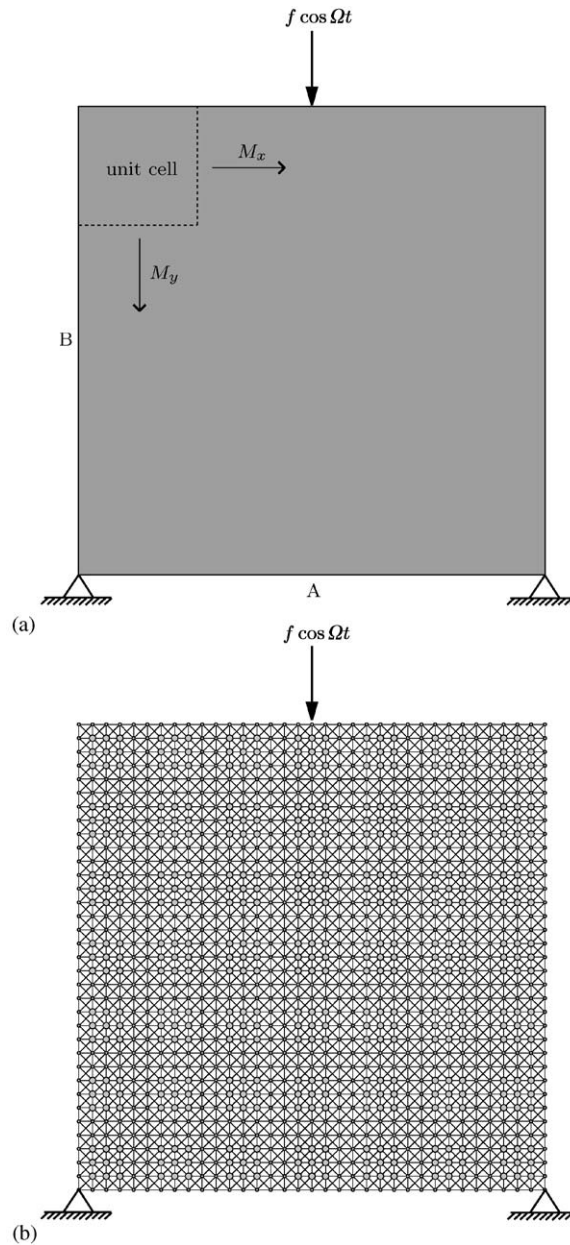


Fig. 9. (a) The structure with $M_x \times M_y$ unit cells with a periodic loading $f \cos \Omega t$ acting centrally at the top boundary and simple supports at the bottom corners, and (b) the corresponding computational model for $M_x = M_y = 7$ and type 1 unit cells.

the supports. This corresponds well to the motion predicted by Eq. (28), where the inclusions and the matrix material are predicted to move essentially rigidly in anti-phase with nearly identical amplitudes.

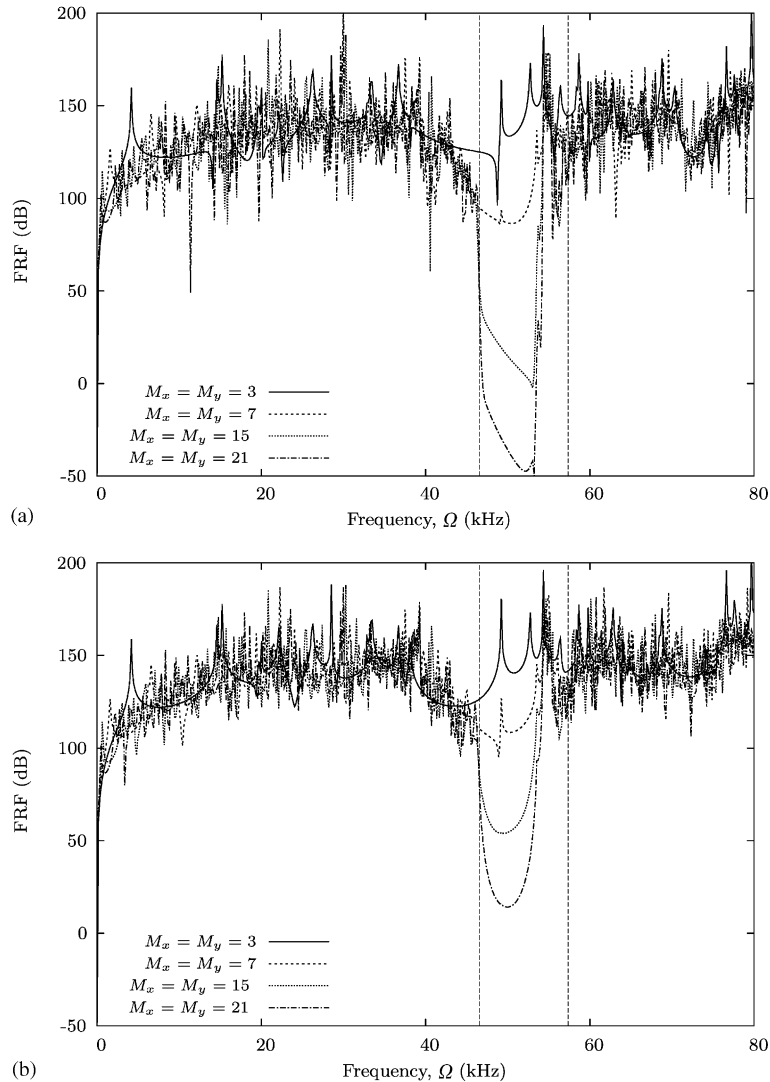


Fig. 10. The structural response with $M_x \times M_y$ type 1 unit cells included in the structure, (a) shows the response in point A and (b) in point B.

3.3.3. Viscous damping

Fig. 14a shows the effect of adding damping to the structure with $M_x = M_y = 21$ and type 1 unit cells. The undamped FRF curve is shown for comparison together with curves for damping ratios of $\zeta = 0.1\%$ and 1.0% . Fig. 14b shows the corresponding curves with type 2 unit cells.

Clearly, with type 1 unit cells the band gap is still noticeable with damping present, even when the damping is so strong that all resonance peaks have nearly disappeared from the response. However, with type 2 unit cells in the structure the band gap practically disappears for strong

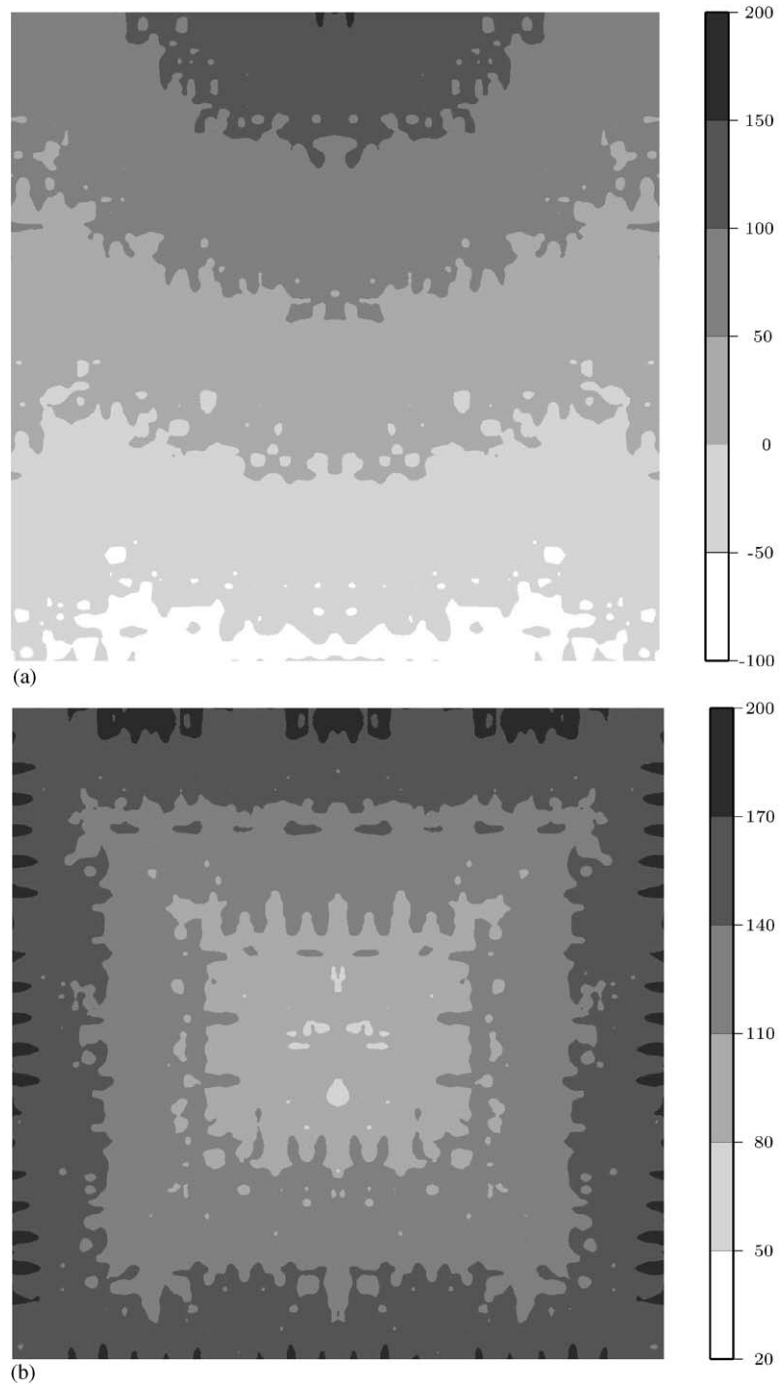


Fig. 11. (a) Contour plot of the structural response (in dB) for $\Omega = 52.1$ kHz, and (b) for $\Omega = 54.8$ kHz. Type 1 unit cells with $M_x = M_y = 21$.

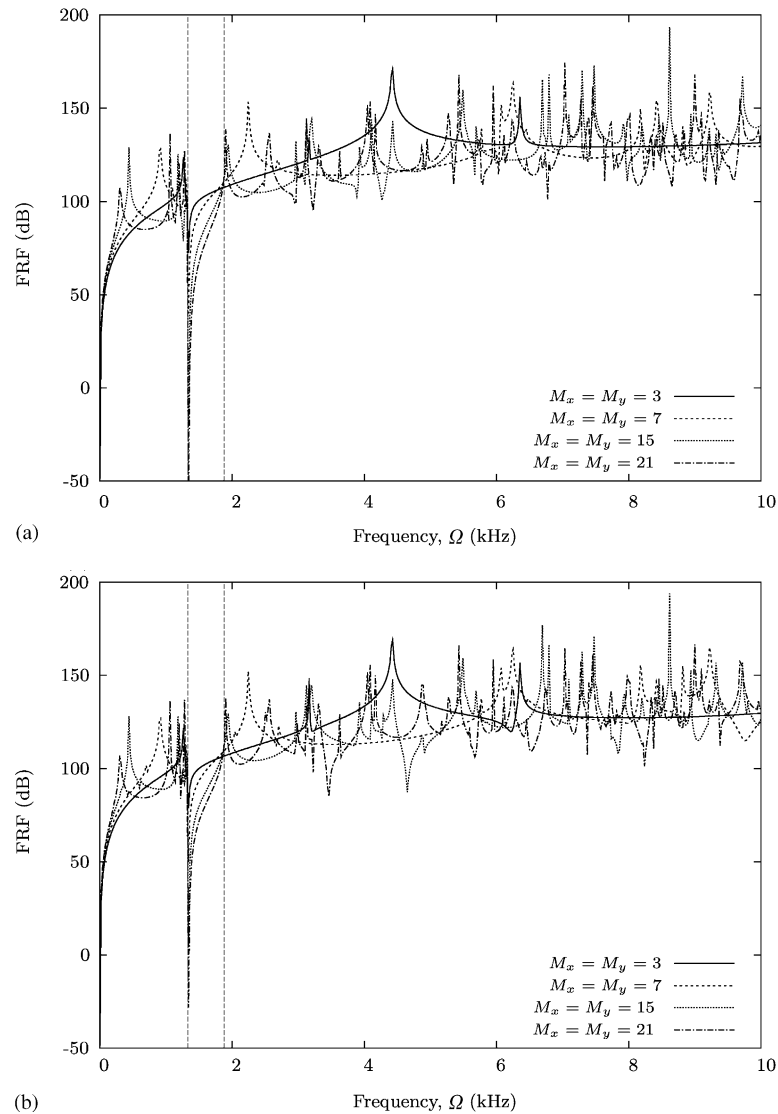


Fig. 12. The structural response with $M_x \times M_y$ type 2 unit cells included in the structure, (a) shows the response in point A and (b) in point B.

damping, and although for $\zeta = 0.1\%$ a drop in the response is noticed near the gap it is hardly distinguishable from other response drops between resonances.

3.3.4. Wave guides

It has been demonstrated how structures assembled from unit cells with band gaps may exhibit a large reduction in the structural response away from the point of excitation when subjected to

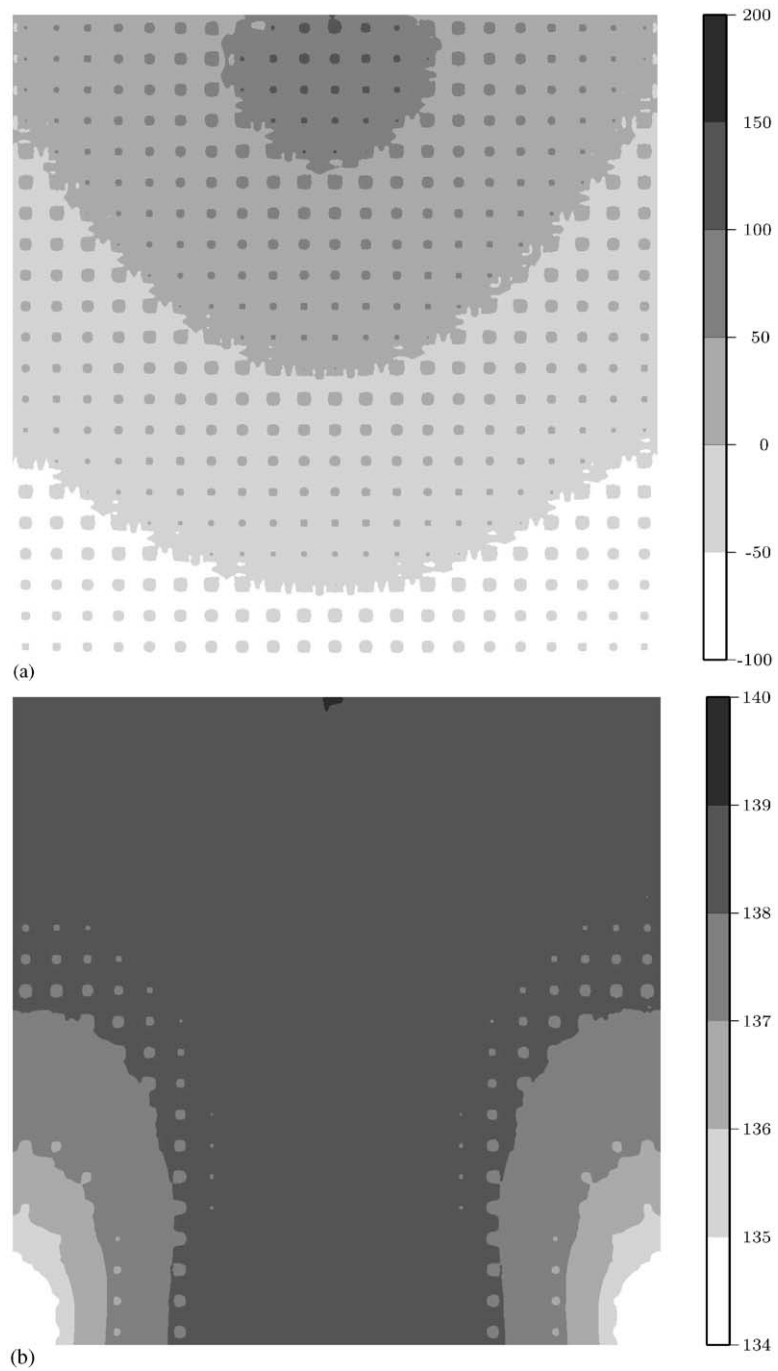


Fig. 13. (a) Contour plot of the structural response (in dB) for $\Omega = 1.34$ kHz, and (b) for $\Omega = 1.90$ kHz. Type 2 unit cells with $M_x = M_y = 21$.

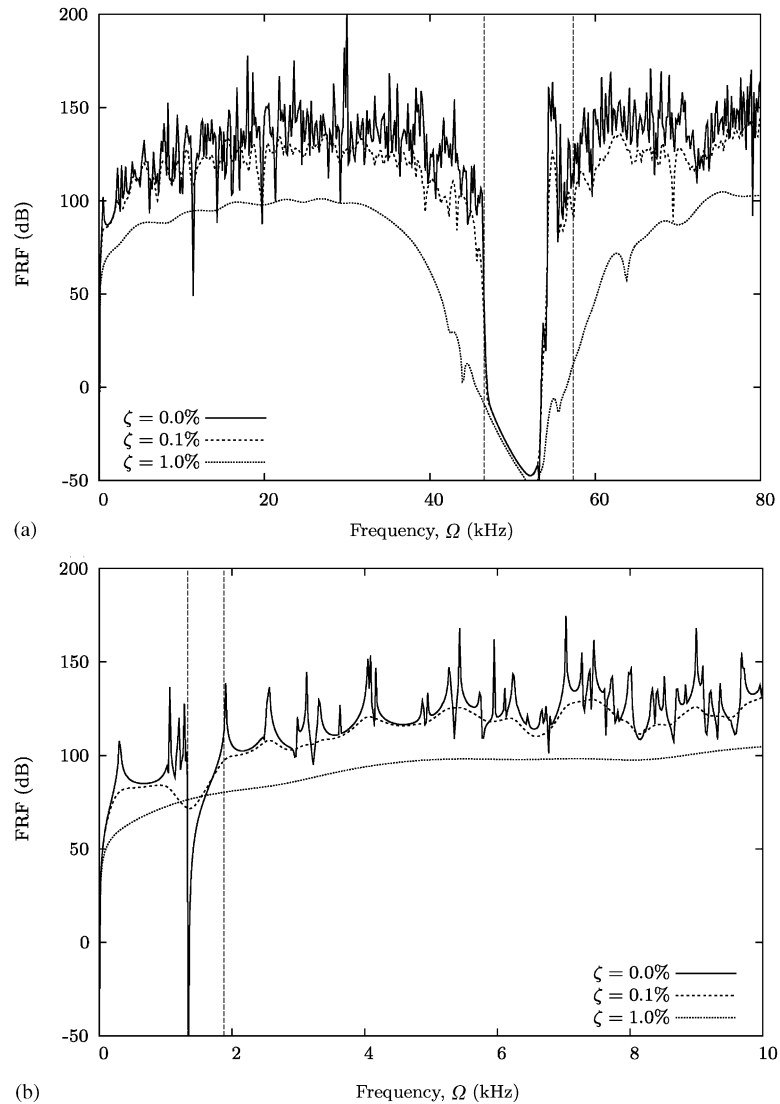


Fig. 14. The influence on the response of added viscous damping characterized by the actual to critical damping ratio ζ of the individual masses, (a) for type 1 unit cells, and (b) type 2 unit cells. In both figures $M_x = M_y = 21$.

periodic loading at certain frequency ranges. By introducing defects in the periodicity this effect can now be utilized to construct wave guides.

Type 1 unit cells are used in the following with $M_x = M_y = 21$. The defect is introduced by removing the inclusions from the unit cells in a path from the point of excitation in either a straight path to the bottom of the structure (point A) or in a 90° bent path to the side of the structure (point B).

Fig. 15a shows the response with a straight path of defects through the structure. It is seen that as for the perfect periodic structure the response in point B drops significantly in the band gap,

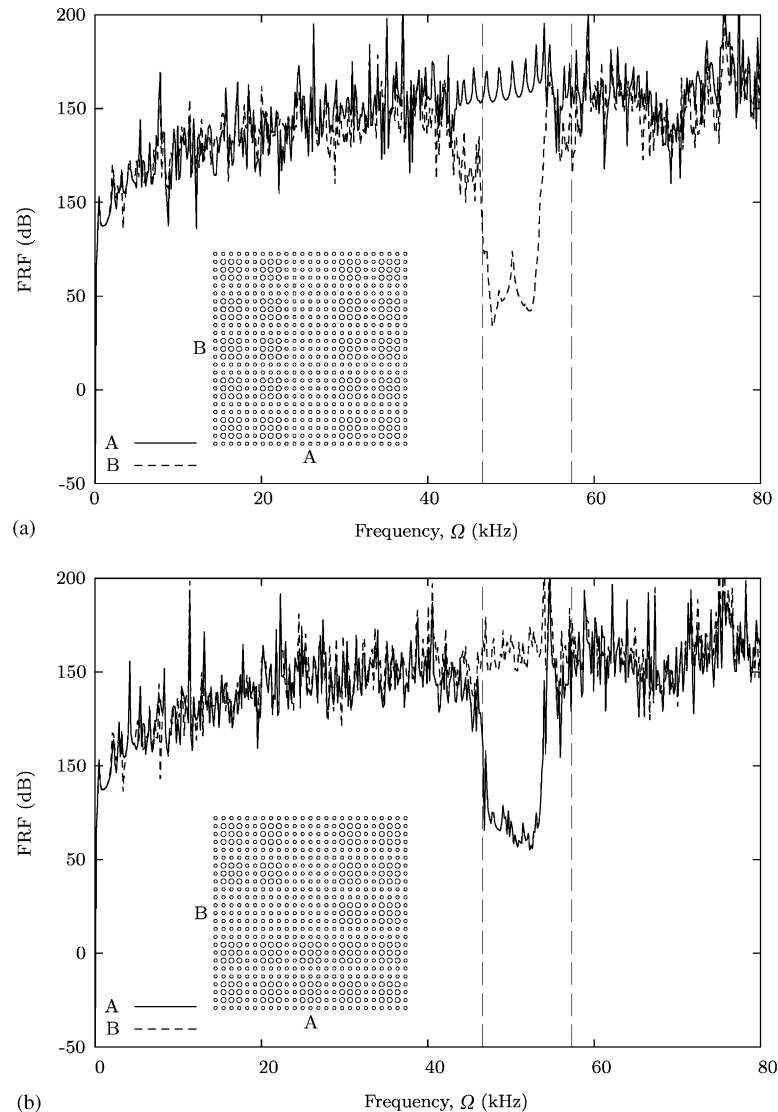


Fig. 15. The response in points A and B with a path of defects in the periodic structure for a the structure, (a) for vertical path, and (b) for a corner path. The insets show schematics of the paths. Type 1 unit cells with $M_x = M_y = 21$.

whereas in point A the response remains high indicating that the signal is now confined to the path. Fig. 15b shows the response for the bent path leading to point B. The response is now seen to be normalized in B inside the band gap, whereas in point A the response drops.

Contour plots of the response for the two lattice structures with paths are shown in Figs. 16a and b, respectively. The frequency of excitation for both figures is $\Omega = 52.1$ kHz, i.e., inside the band gap. The figure shows how the paths of defects in the periodic structures effectively isolates the vibrations to the path regions and thus “leads” the vibrations to the structural point A or B, whereas away from the paths the response drops rapidly with distance.

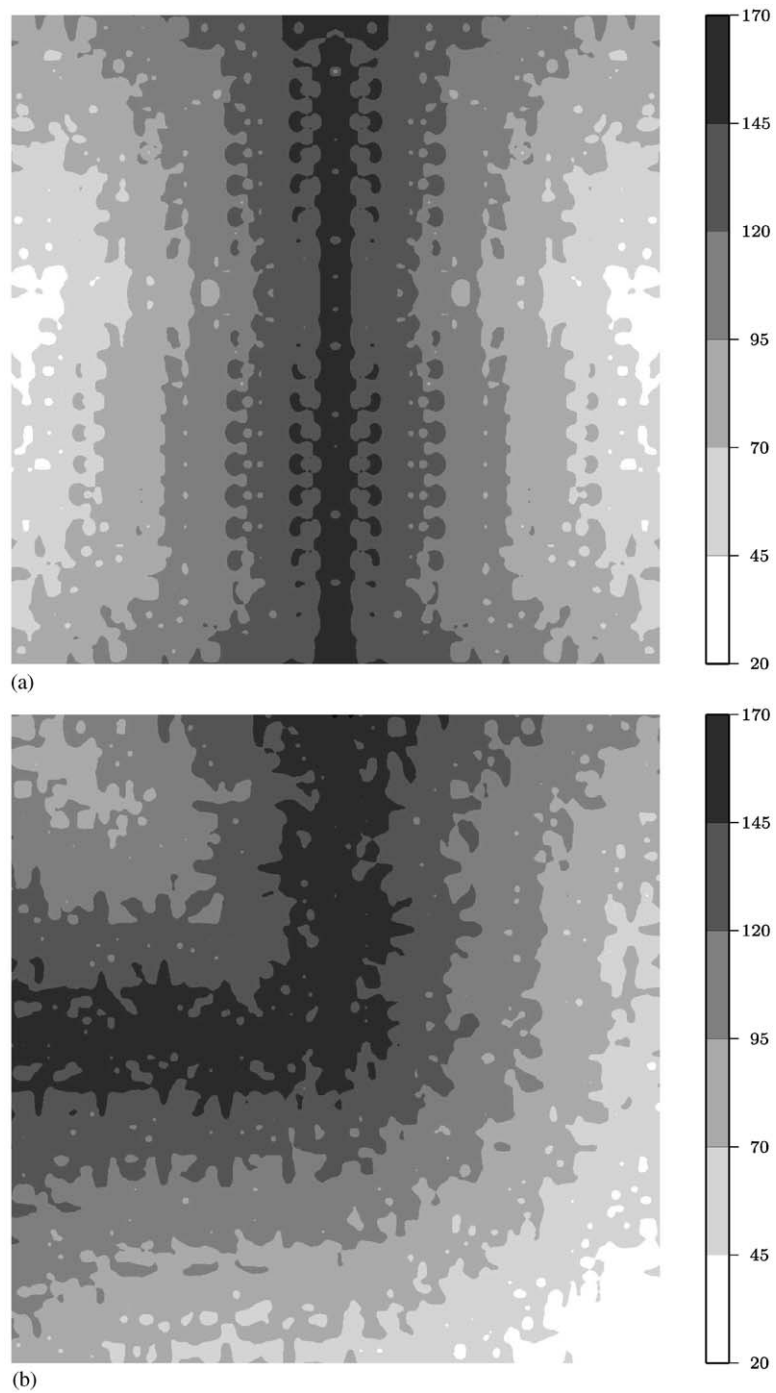


Fig. 16. Contour plot of the response for $\Omega = 52.1$ kHz, (a) for a vertical path of defects, and (b) for a corner path of defects. Type 1 unit cells with $M_x = M_y = 21$.

4. Conclusions

In order to use phononic band gap materials in mechanical structures that utilize the selective wave blocking abilities of these materials, the effects associated with the boundaries, damping, and imperfections need to be taken into account.

In this work the vibrational response of 1-D and 2-D mass–spring structures subjected to periodic loading has been investigated. The focus has been put on analyzing structures with a periodic micro-structure (unit cells) with gaps in the band structure for the corresponding infinite periodic lattice. Two examples were used to demonstrate the effect on the response of boundaries, viscous damping, and imperfections—a 1-D structure acting as a wave filter, and wave guiding in 2-D structures.

It was shown how the response in the band gap frequency range depends on the number of unit cells in the structure. In 1-D and for one of the two types of unit cells analyzed in 2-D, it was seen how the response in the band gap is insensitive to moderate amounts of viscous damping, whereas for the other 2-D unit cell analyzed, the band gap effect almost disappears with strong damping added. In the 1-D example it was shown also that the response in the band gap is insensitive to small imperfections in the periodic structure. It was demonstrated in both the 1-D and 2-D example, that the free boundaries cause local resonances that affect the response in the band gap. Two 2-D wave guides were analyzed, created by replacing the periodic structure with a homogeneous structure in a straight and a 90° bent path. It was shown how the vibrational response is confined to these paths in the band gap frequency ranges.

Further work deals with the formulation and solution of optimization problems that can be used to design of applications of phononic band gap materials and structures.

Acknowledgements

This work was supported by the Danish Research Council through the project “Phononic bandgap materials: Analysis and optimization of wavetransmission in periodic materials”. The author would like to thank Jon Juel Thomsen, Ole Sigmund, and Martin P. Bendsøe for valuable comments and suggestions.

References

- [1] J.D. Joannopoulos, R.D. Meade, J.N. Winn, *Photonic Crystals, Molding the Flow of Light*, Princeton University Press, Princeton, NJ, 1995.
- [2] E. Yablonovitch, Photonic crystals: semiconductors of light, *Scientific American* 285 (2001) 34–41.
- [3] Lord Rayleigh, On the maintenance of vibrations by forces of double frequency, and on the propagation of waves through a medium endowed with a periodic structure, *Philosophical Magazine* 24 (1887) 145–159.
- [4] L. Brillouin, *Wave Propagation in Periodic Structures*, Dover Publications Inc, New York, 1953.
- [5] C. Elachi, Waves in active and passive periodic structures: a review, *Proceedings of the IEEE* 64 (1976) 1666–1698.
- [6] D.J. Mead, Wave propagation in continuous periodic structures: research contributions from Southampton, 1964–1995, *Journal of Sound and Vibration* 190 (1996) 495–524.
- [7] S. Parmley, T. Zobrist, T. Clough, A. Perez-miller, M. Makela, R. Yu, Phononic band structure in a mass chain, *Applied Physics Letters* 67 (1995) 777–779.

- [8] A. Diez, G. Kakarantzas, T.A. Birks, P.St.J. Russel, Acoustic stop-bands in periodically microtapered optical fibers, *Applied Physics Letters* 76 (2000) 3481–3483.
- [9] D.J. Griffiths, C.A. Steinke, Waves in locally periodic media, *American Journal of Physics* 69 (2001) 137–154.
- [10] M.M. Sigalas, E.N. Economou, Elastic and acoustic wave band structure, *Journal of Sound and Vibration* 158 (1992) 377–382.
- [11] T. Suzuki, P.K.L. Yu, Complex elastic wave band structures in three-dimensional periodic elastic media, *Journal of the Mechanics of Physics and Solids* 46 (1998) 115–138.
- [12] P. Langlet, A.-C. Hladky-hennion, J.-N. Decarpigny, Analysis of the propagation of plane acoustic waves in passive periodic materials using the finite element method, *Journal of the Acoustical Society of America* 98 (1995) 2792–2800.
- [13] W. Axmann, P. Kuchment, An efficient finite element method for computing spectra of photonic and acoustic band-gap materials, *Journal of Computational Physics* 150 (1999) 468–481.
- [14] Z. Liu, X. Zhang, Y. Mao, Y.Y. Zhu, Z. Yang, C.T. Chan, P. Sheng, Locally resonant sonic materials, *Science* 289 (2000) 1734–1736.
- [15] J.O. Vasseur, P.A. Deymier, G. Frantziskonis, G. Hong, B. Djafari-rouhani, L. Dobrzynski, Experimental evidence for the existence of absolute acoustic band gaps in two-dimensional periodic composite media, *Journal of Physics: Condensed Matter* 10 (1998) 6051–6064.
- [16] C.G. Poulton, A.B. Movchan, R.C. McPhedran, N.A. Nicorovici, Y.A. Antipov, Eigenvalue problems for doubly periodic elastic structures and phononic band gaps, *Proceedings of the Royal Society of London A* 456 (2000) 2543–2559.
- [17] M.S. Kushwaha, Classical band structure of periodic elastic composites, *International Journal of Modern Physics* 10 (1996) 977–1094.
- [18] M. Torres, F.R. Montero de Espinosa, D. García-Pablos, N. García, Sonic band gaps in finite elastic media: surface states and localization phenomena in linear and point defects, *Physical Review Letters* 82 (1999) 3054–3057.
- [19] I.E. Psarobas, N. Stefanou, A. Modinos, Phononic crystals with planar defects, *Physical Review B* 62 (2000) 5536–5540.
- [20] O. Sigmund, Microstructural design of elastic band gap structures, in: G.D. Cheng, Y. Gu, S. Liu, Y. Wang (Eds.), *Proceedings of the Second World Congress of Structural and Multidisciplinary Optimization*, CD-rom, Liaoning Electronic Press, Dalian, China, 2001.
- [21] O. Sigmund, J.S. Jensen, Topology optimization of phononic band gap materials and structures, *Fifth World Congress on Computational Mechanics*, Vienna, Austria, 2002, available at <http://wccm.tuwien.ac.at>.
- [22] P.G. Martinsson, A.B. Movchan, Vibrations of lattice structures and phononic band gaps 56 (2003) 45–64.

Design of multi-phase structures with optimized vibrational and wave-transmitting properties

Jakob S. Jensen*, Ole Sigmund and Jon J. Thomsen

Department of Mechanical Engineering, Solid Mechanics
Technical University of Denmark, Lyngby, Denmark
e-mail: jsj@mek.dtu.dk

Martin P. Bendsøe

Department of Mathematics
Technical University of Denmark, Lyngby, Denmark

Summary In this paper we show the status of a research project dealing with optimization of vibration and wave-propagation in multi-phase structures. We present experimental and theoretical results and point out directions for further research.

Introduction

Band gap materials have received considerable attention in the last decade, see e.g. [1]. A periodic arrangement of materials with different physical properties may cause *gaps* to appear in the classical *band structures*—corresponding to ranges of frequencies for which waves cannot propagate. The waves may be electromagnetic or elastic, with the corresponding band gap materials referred to as *photonic* and *phononic*, respectively.

Structures made from a band gap material have several interesting applications, e.g. as parts of mechanical filters and resonators and in optical wave guides and lasers. A FE-program has been developed to analyze steady-state vibration and/or wave-propagation in periodic structures. As an example we show the vibrational behavior of an elastic band gap structure shown in Fig. 1. The periodic material has here been designed so that a band gap exists in the frequency range around 40 kHz and the corresponding frequency response is seen to be significantly reduced near this frequency. Currently, the computational model is being extended to cover also 3D structures and has also been used to study the behavior of periodic mass-spring structures [2].

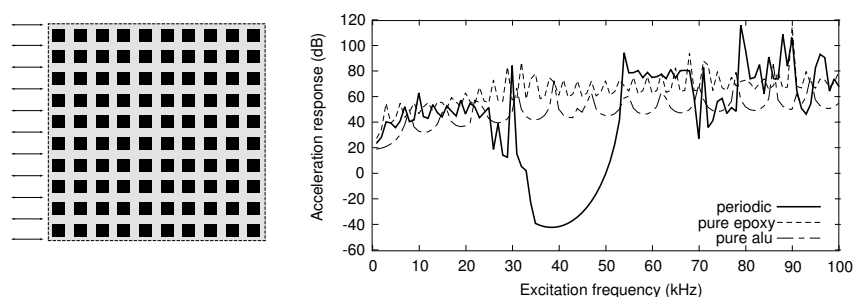


Figure 1: A structure composed of 10×10 square aluminum inclusions in epoxy subjected to periodic loading at the left boundary and the corresponding frequency response at the right boundary.

To facilitate the design of *optimized* structures a topology optimization code has been developed. Recently the topology optimization technique was applied successfully to the design of band gap *materials* [3], and the first results for designing *structures* with optimized wave-reflecting and

wave-guiding properties show promising results [4, 5, 6]. This paper presents a status of the research project dealing with the design of optimized structures and provides an outlook on further research.

Vibrations in an elastic bar: Theory and experiments

To test the computational model and study the basic phenomenon a simple experiment has been performed. The theoretical predictions of frequency responses were checked experimentally using a laboratory model of an elastic bar and the setup shown in Fig. 2. Here, an input signal is fed to a vibration shaker, which transmits vibrations to the bar across a force transducer. Elastic waves then propagate through the bar, where end movements are picked up by an accelerometer.

We tested elastic bars made of periodic sections of Brass-PMMA or Aluminium-PMMA, both exhibiting band gaps. The results described here are for the bar shown in Fig. 2, made of five-and-a-half repetitions of a base section consisting of two bars of circular cross section, one of Aluminium and one of PMMA, both having diameter 10 mm and length 75 mm, and with bar pieces glued end-to-end using Araldite 2011 epoxy structural adhesive.

Fig. 3(left) is a typical frequency response for this periodic bar, showing two pronounced band gaps with a response drop-off about 40 dB compared with the non-resonant, low-level response outside the band gaps. Fig. 3(right) shows the corresponding theoretical predictions from the computational program. Reasonable agreement is noted, both with regards to the resonance tops but more importantly with respect to the response drop in the band gap frequency ranges. The noise in the experimental curves in the band gaps originates in the noise limit of the experimental setup.

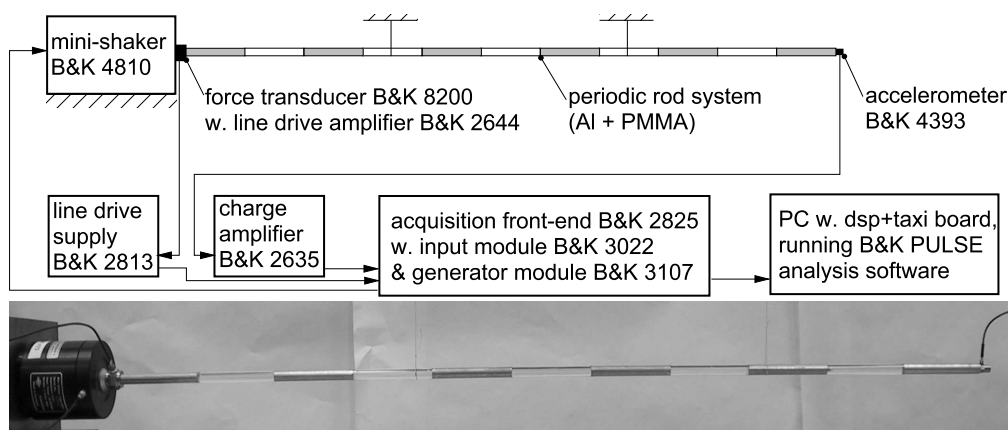


Figure 2: Experimental setup and part of the setup showing (from left to right) the vibration exciter, force transducer, periodic bar system with supporting threads, and accelerometer.

Additional experiments are planned in order to study the vibrational response of 2D periodic and optimized structures as well as of micro-size structures.

The topology optimization method

The topology optimization technique, see e.g. [7], can with advantage be used to design multi-phase structures with optimized vibrational and wave-transmitting properties. Using this method for the *steady-state* dynamical problem involves, in addition to e.g. a compliance problem, additional difficulties due the complex FE equations, possible wave-transmitting boundary conditions, and/or structural damping.

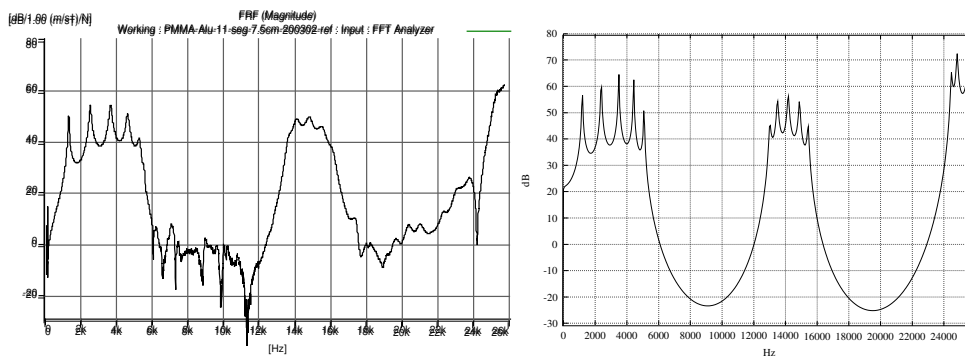


Figure 3: Response curves showing the acceleration response at the end of the bar as a function of the excitation frequency, left: experimental data and right: corresponding theoretical predictions.

With the objective of e.g. *minimizing* the structural response in a certain part of the structure we can formulate a topology optimization problem as

$$\begin{aligned} \min_{\mathbf{x}} \quad & |\mathbf{a}|^T \mathbf{L} |\mathbf{a}| \\ \text{s.t. :} \quad & (\mathbf{K} + i\Omega\mathbf{C} - \Omega^2\mathbf{M}) \mathbf{a} = \mathbf{f} \\ & 0 \leq x_e \leq 1, \quad e = 1, \dots, N \end{aligned} \quad (1)$$

where \mathbf{K} , \mathbf{C} , \mathbf{M} are the stiffness-, damping-, and mass-matrix, \mathbf{f} , \mathbf{a} the forcing and vibration/wave amplitude and \mathbf{L} is a zero matrix with ones at the diagonal elements corresponding to the degrees of freedom of the nodes, lines, or areas to be damped. A design variable x_e is assigned to each of the N finite elements and the element properties are interpolated as:

$$p(x_e) = (1 - x_e)p_1 + x_ep_2 \quad (2)$$

where the subscripts 1 and 2 here correspond to two different material phases and p is a relevant physical property, e.g. mass density and two stiffness parameters in the elastic case.

Design of optimized structures

In the following, we present some examples of two-phase material structures with optimized wave-reflecting and wave-guiding properties. In all examples the structural domain is 20×20 cm, out-of-plane waves/vibrations are considered, and the two materials are epoxy and aluminum. The figures show the optimized topology and the frequency response to the corresponding periodic loading.

In Fig. 4(a) the structure is optimized for a minimum vibration response along each edge of the structure when it is subjected to a periodic load at 40 kHz along the *opposite* edge. All boundaries are free. The frequency response from Fig. 1 is shown for comparison. In Fig. 4(b) the structure is optimized for maximum wave amplitude at the center of the right edge with a 40 kHz load acting on most of the left edge. The boundaries are all wave-transmitting and for comparison the wave-amplitudes are also shown for the structures made of the pure materials.

Further research is currently focused around design of wave-guide structures with the aim of comparing the response of optimized designs to existing wave-guide structures.

Concluding remarks

By using multiple material phases it is possible to design structures that have specific wave-reflecting/vibration-damping and wave-guiding properties. The basic phenomenon used in the de-

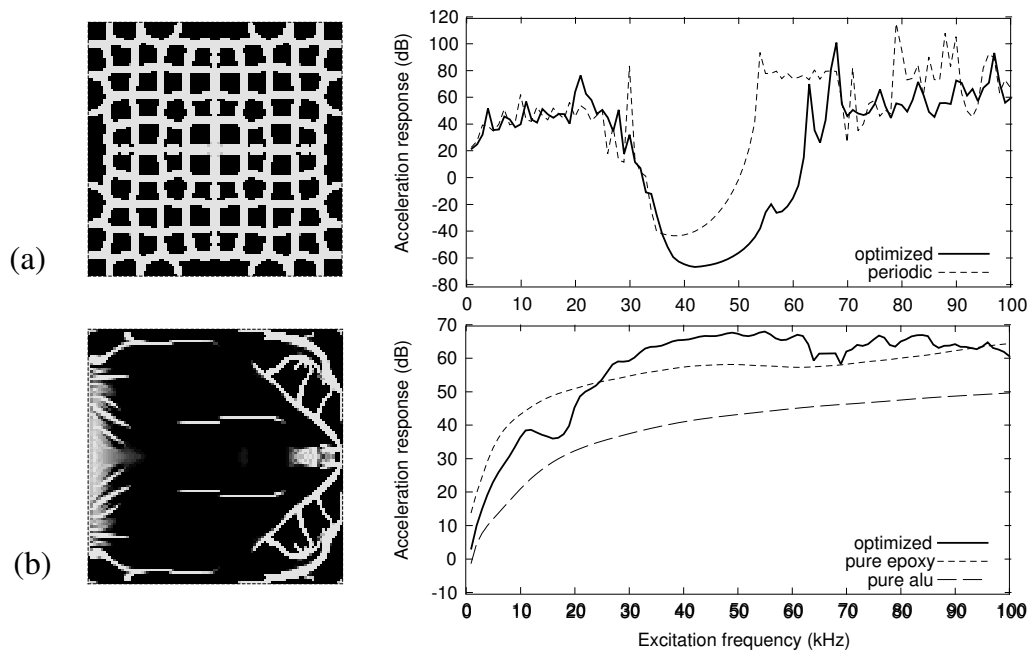


Figure 4: Optimized topologies (left) and frequency responses (right) for 2D structures designed for minimum/maximum wave/vibration amplitude, (a) wave-reflecting structure, (b) wave-guide structure.

sign process is band gaps, representing certain frequency ranges for which waves cannot propagate through a multi-phase periodic material. Topology optimization enables us to systematically design structures that have optimized properties. This paper has presented some recent results and also a simple experiment validating the theory and illustrating the basic physical phenomenon.

References

- [1] J.D. Joannopoulos, R.D. Meade and J.N. Winn. *Photonic Crystals*. Princeton, NJ: Princeton University Press, (1995).
- [2] J.S. Jensen. Phononic band gaps and vibrations in one- and two-dimensional mass-spring structures. Accepted for publication in *J. Sound. Vibr.*, (2002).
- [3] O. Sigmund. Microstructural design of elastic band gap structures. In *Proc. 4th WCSMO*, Dalian, June 4–8, (2001).
- [4] O. Sigmund and J.S. Jensen. Systematic design of phononic band gap materials and structures by topology optimization. Submitted, (2002).
- [5] J.S. Jensen and O. Sigmund. Phononic band gap structures as optimal designs. To appear in *Proc. IUTAM symp. on asymptotics, singularities, and homogenization in problems of mechanics*, Liverpool, July 8–12, (2002).
- [6] O. Sigmund and J.S. Jensen. Topology optimization of phononic band gap materials and structures. In *Proc. Fifth world congress on computational mechanics, WCCM V*, Vienna, July 7–12, (2002).
- [7] M.P. Bendsøe and O. Sigmund. *Topology Optimization – Theory, Methods and Applications*. Springer Verlag, Berlin Heidelberg, (2003) (to appear).



Low-frequency band gaps in chains with attached non-linear oscillators

B.S. Lazarov*, J.S. Jensen

Department of Mechanical Engineering, Solid Mechanics, Nils Koppels Alle, Technical University of Denmark, Building 404, 2800 Kgs. Lyngby, Denmark

Received 17 July 2007; received in revised form 31 August 2007; accepted 18 September 2007

Abstract

The aim of this article is to investigate the wave propagation in one-dimensional chains with attached non-linear local oscillators by using analytical and numerical models. The focus is on the influence of non-linearities on the filtering properties of the chain in the low frequency range. Periodic systems with alternating properties exhibit interesting dynamic characteristics that enable them to act as filters. Waves can propagate along them within specific bands of frequencies called pass bands, and attenuate within bands of frequencies called stop bands or band gaps. Stop bands in structures with periodic or random inclusions are located mainly in the high frequency range, as the wavelength has to be comparable with the distance between the alternating parts. Band gaps may also exist in structures with locally attached oscillators. In the linear case the gap is located around the resonant frequency of the oscillators, and thus a stop band can be created in the lower frequency range. In the case with non-linear oscillators the results show that the position of the band gap can be shifted, and the shift depends on the amplitude and the degree of non-linear behaviour.

© 2007 Elsevier Ltd. All rights reserved.

Keywords: Non-linear wave propagation; Local resonators; Low-frequency band gaps

1. Introduction

The filtering properties of periodic structures with alternating characteristics have been investigated by many authors by using analytical, numerical and experimental methods. Such systems possess interesting filtering properties. Waves can propagate unattenuated along these structures within specific bands of frequencies called propagation or pass bands, and attenuate within bands of frequencies called stop bands, attenuation zones or band gaps. Band gaps in linear systems can also be created by introducing random inclusions or geometric disturbances. External excitation in such structures results in localised response surrounding the external input. The majority of the texts consider linear systems [1–3]. Localisation phenomena can also be observed in perfectly periodic non-linear structures [4–7], where spring–mass chains are studied and the non-linear behaviour is introduced either in the spring between the two neighbour masses, or by adding non-linear springs

between the ground and the masses. The applications of these filtering phenomena are mainly in the high frequency range, as the distance between the inclusions has to be comparable with the wavelength.

In the beginning of the twentieth century Frahm discovered the vibration absorber as a very efficient way to reduce the vibration amplitude of machinery and structures by adding a spring with a small mass to the main oscillatory body [8]. The additional spring–mass system is tuned to be in resonance with the applied load. When the natural frequency of the attached absorber is equal to the excitation frequency, the main structure does not oscillate at all, as the attached absorber provides force equal and with opposite sign to the applied one. The idea can be exploited further by attaching multiple absorbers on a waveguide. Waves are attenuated in a frequency band located around the resonant frequency of the local oscillators, and thus stop bands can be created in the lower frequency range, which is often more important in mechanical applications. The effect has been studied experimentally and analytically in [9–11].

If the attached oscillators are non-linear, the response displays a dependency between the amplitude and the frequency. Very little is known about the filtering properties of the

* Corresponding author.

E-mail addresses: bsl@mek.dtu.dk (B.S. Lazarov), jsj@mek.dtu.dk (J.S. Jensen).

systems in this case. Periodic spring–mass system with attached non-linear pendulums are investigated in [12]. The attached pendulums are considered to be stiffer than the main chain, and they do not introduce band gaps in the lower frequency range. The aim of this paper is to investigate the behaviour of one-dimensional infinite spring–mass chain with locally attached oscillators with linear or non-linear behaviour. The oscillators are considered to be relatively soft compared to the main chain, and to create band gaps in the lower frequency range. The non-linearities in the attached oscillators are considered to be cubic. First the mechanical system together with the equations of motion is presented. The appearance of band gaps is shown in the linear case, and in the case with non-linear attached oscillators the method of harmonic balance is utilised to obtain a system of equations for the wave amplitude, as well as an approximate expression for the wave propagation properties of the chain. The analytical results are compared with the ones obtained by numerical simulations, some of which are presented in [13].

2. Mechanical system and equations of motion

The considered spring–mass system with attached local oscillators is shown in Fig. 1. Using the dynamic equilibrium condition for mass j , the equations describing its motion together with the equation of motion of the attached oscillator can be written as

$$(m + M) \frac{d^2 u_j}{d\tau^2} + 2ku_j - ku_{j-1} - ku_{j+1} + M \frac{d^2 q_j}{d\tau^2} = 0, \quad (1)$$

$$M \frac{d^2 q_j}{d\tau^2} + c\dot{q}_j + k^l f(q_j) = 0, \quad (2)$$

where k is the spring stiffness between two masses, m is the mass at position $j = 0, 1, \dots, \infty$, M is the mass of the attached local oscillator, $k^l f(q_j)$ is its restoring force and c is a viscous damping coefficient. u_j is the displacement of mass j , with positive direction shown in Fig. 1, and q_j is the relative displacement of the local oscillator. Both u_j and q_j are functions of the time and their positions j . The function $f(q_j)$ is assumed to be in the form

$$f(q_j) = q_j + \gamma_j q_j^3, \quad (3)$$

where γ_j is a parameter controlling the degree of non-linearity. By introducing normalised time $t = \omega_0 \tau$, where $\omega_0 = \sqrt{k/m}$, the coefficients $\beta = M/m$ and $\alpha = k^l/k$, Eqs. (1) and (2) can be written as

$$\ddot{u}_j + 2u_j - u_{j-1} - u_{j+1} - \beta\kappa^2 f(q_j) - 2\beta\zeta\kappa\dot{q}_j = 0, \quad (4)$$

$$\ddot{q}_j + 2\zeta\kappa\dot{q}_j + \kappa^2 f(q_j) + \ddot{u}_j = 0, \quad (5)$$

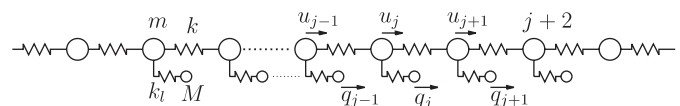


Fig. 1. Spring mass system with attached local oscillators.

where $\kappa = \sqrt{\alpha/\beta}$ and $\ddot{(\)}$ denotes the second derivative with respect to the normalised time t .

3. Band gaps in spring–mass chains with attached oscillators

3.1. Linear undamped oscillators

Using the idea for the vibration absorber, an efficient filter for waves propagating along a spring–mass chain can be created by attaching multiple absorbers to the chain as shown in Fig. 1. The equations of motion are given by (4) and (5), where the non-linear parameter γ and the damping parameter ζ are set to zero. In order to study the transmission properties of the chain, the solution is sought in the form [1]

$$u_j = B e^{j\mu_u + i\omega t}, \quad (6)$$

where μ_u is the so-called wave propagation constant of harmonic wave with frequency ω , which is equal to the wave number multiplied by the distance between the masses in the main chain, and j is the mass index. The displacements of the neighbour masses $j + 1$ and $j - 1$ become

$$u_{j+1} = e^{\mu_u} u_j, \quad u_{j-1} = e^{-\mu_u} u_j. \quad (7)$$

By inserting (6) and (7) into the equations of motion (4) and (5), and requiring the resulting equations to be valid at all time instances, the following relation between μ_u and ω is obtained:

$$\cosh(\mu_u) = 1 + \frac{1}{2} \frac{\omega^4 - (1 + \beta)\kappa^2 \omega^2}{\kappa^2 - \omega^2}. \quad (8)$$

Eq. (8) is also known as the dispersion relation. Plots of the real and the imaginary part of μ_u for different frequencies are shown in Fig. 2. Around the natural frequency of the attached oscillators there exists a frequency band where waves are attenuated. Outside the band gap, two neighbour masses j and $j + 1$ oscillate with phase difference $\text{Im}(\mu_u)$. Inside the band gap, below the natural frequency κ of the attached oscillators, two neighbour masses oscillate with an opposite phase $\text{Im}(\mu_u) = \pi$ and above κ they oscillate with phase difference $\text{Im}(\mu_u) = 0$. The real part $\text{Re}(\mu_u)$ gives the attenuation rate of the wave amplitude. At $\omega = \kappa$ the real part of μ_u is infinity and decreases to zero outside the band gap. It should be pointed out that the system studied in this section has no energy dissipation mechanism.

3.2. Non-linear local oscillators

A solution of the non-linear system of equations (4) and (5) is not known in a closed form. An approximate solution can be obtained by using the method of harmonic balance, the method of multiple scales or the method of averaging, e.g. [14,15]. Non-linear oscillators with third order non-linearities, as the one described by (5), are well studied in the literature. Based on these solutions the method of harmonic balance is applied here, in order to study the wave propagation along the chain with attached damped non-linear oscillators.

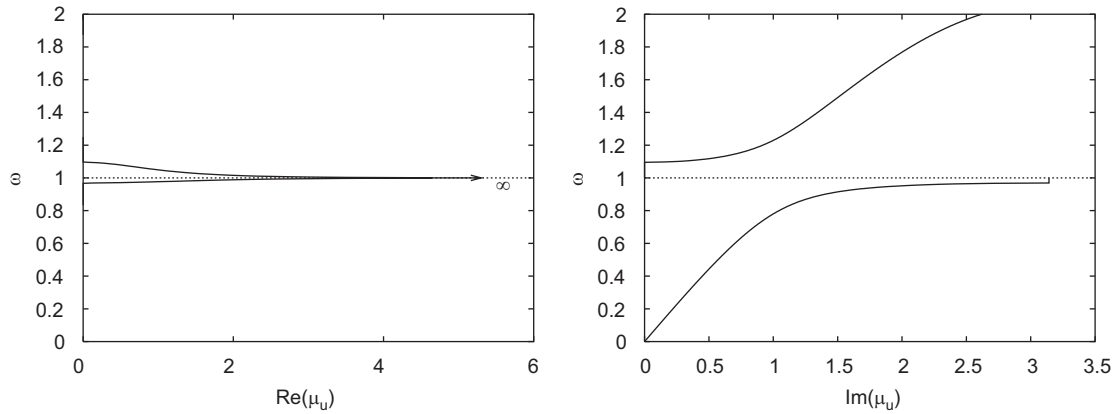


Fig. 2. Dispersion relation for $\kappa = 1.0$ and $\beta = 0.1$.

The time response of $q_j(t)$ is assumed to be periodic in the form of complex Fourier series

$$q_j(t) = \sum_k \varepsilon^{(k-1)/2} A_{k,j} e^{ik\omega t} + \varepsilon^{(k-1)/2} \bar{A}_{k,j} e^{-ik\omega t},$$

$$k = 1, 3, \dots, \tag{9}$$

where ε is a dimensionless bookkeeping parameter showing the order of the amplitude of the motion. By substituting (9) into (5) and integrating twice with respect to time, the following expression for the time response of mass j can be obtained:

$$u_j(t) = A_{1,j} \left(-1 + \frac{\kappa^2}{\omega^2} + 3\varepsilon \frac{\gamma_j \kappa^2}{\omega^2} A_{1,j} \bar{A}_{1,j} + \frac{2i\zeta\kappa}{\omega} \right) e^{i\omega t}$$

$$+ \varepsilon \left(-A_{3,j} + \frac{2}{3} \frac{i\zeta\kappa}{\omega} A_{3,j} + \frac{1}{9} \frac{\kappa^2}{\omega^2} A_{3,j} + \frac{1}{9} \frac{\gamma_j \kappa^2}{\omega^2} A_{1,j}^3 \right)$$

$$\times e^{i3\omega t} + \text{c.c.} + O(\varepsilon^2). \tag{10}$$

The expression in the above equation is obtained by truncating the time series and preserving only the first two terms. By substituting (10) and (9) into (4) and equating to zero the coefficients in front of $e^{ik\omega t}$, a system of algebraic equations for the amplitudes $A_{k,j}$ can be obtained

$$\left(2 \left(\frac{\kappa^2}{\omega^2} - 1 \right) + \omega^2 - \beta_1 \kappa^2 + 2i\zeta \frac{\kappa}{\omega} (2 - \beta_1 \omega^2) \right) A_{1,j}$$

$$+ 3\gamma_j \frac{\kappa^2}{\omega^2} (2 - \beta_1 \omega^2) A_{1,j}^2 \bar{A}_{1,j}$$

$$+ \left(1 - \frac{\kappa^2}{\omega^2} - 2i\zeta \frac{\kappa}{\omega} \right) (A_{1,j+1} + A_{1,j-1})$$

$$- 3\gamma_{j+1} \frac{\kappa^2}{\omega^2} A_{1,j+1}^2 \bar{A}_{1,j+1} - 3\gamma_{j-1} \frac{\kappa^2}{\omega^2} A_{1,j-1}^2 \bar{A}_{1,j-1} = 0, \tag{11}$$

$$\left(2 \left(\frac{\kappa^2}{\omega_3^2} - 1 \right) + \omega_3^2 - \beta_1 \kappa^2 + 2i\zeta \frac{\kappa}{\omega_3} (2 - \beta_1 \omega_3^2) \right) A_{3,j}$$

$$+ \left(2 \frac{\kappa^2}{\omega_3^2} - \beta_1 \kappa^2 \right) \gamma_j A_{1,j}^3 + \left(1 - \frac{\kappa^2}{\omega_3^2} - 2i\zeta \frac{\kappa}{\omega_3} \right)$$

$$\times (A_{3,j+1} + A_{3,j-1})$$

$$- \gamma_{j+1} \frac{\kappa^2}{\omega_3^2} A_{1,j+1}^3 - \gamma_{j-1} \frac{\kappa^2}{\omega_3^2} A_{1,j-1}^3 = 0, \tag{12}$$

where $\beta_1 = \beta + 1$ and $\omega_3 = 3\omega$. By specifying the amplitudes for two neighbour masses and, respectively, for the attached oscillators, a solvable system of equations for the response amplitudes of the attached oscillators can be obtained. The system is non-linear and there can be multiple solutions satisfying it in certain cases. The amplitude of the wave travelling along the main chain can be obtained by inserting the amplitude of the attached oscillators into (10).

The wave travelling along the spring–mass chain can also be investigated by using the wave number multiplied by the distance between the masses in the main chain μ_u . The displacements of the masses neighbour to mass j can be expressed as

$$u_{j\pm 1} = \sum_k B_{k,j} e^{\pm i\mu_u k} e^{ik\omega t} + \text{c.c.}, \tag{13}$$

where $B_{k,j}$ are the coefficients in front of $e^{ik\omega t}$ from Eq. (10). It can be clearly seen that the solution in the non-linear case consists of a zero order wave with frequency ω and additional high order waves. As the non-linearities are assumed to be small and the focus is on the filtering properties of the chain around the linear natural frequency of the attached oscillators, the contributions to the solution of the harmonics of order equal to and higher than $k = 3$ are neglected. Substituting (13) and (9) into (4), equating the coefficients in front of $e^{i\omega t}$ to zero and solving the resulting equation with respect to μ_u , the dispersion relation for the non-linear case is obtained in

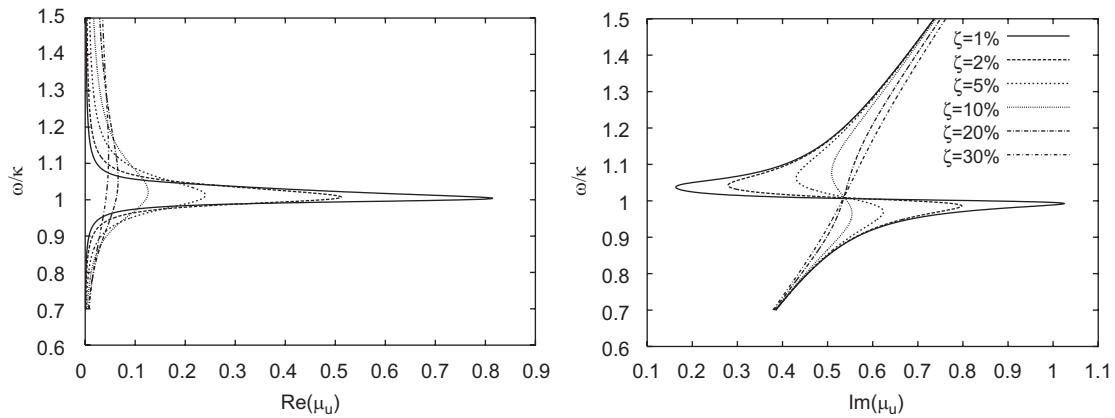


Fig. 3. Dispersion relation for $\beta = 0.1$, $\gamma = 0$ and different damping ratios.

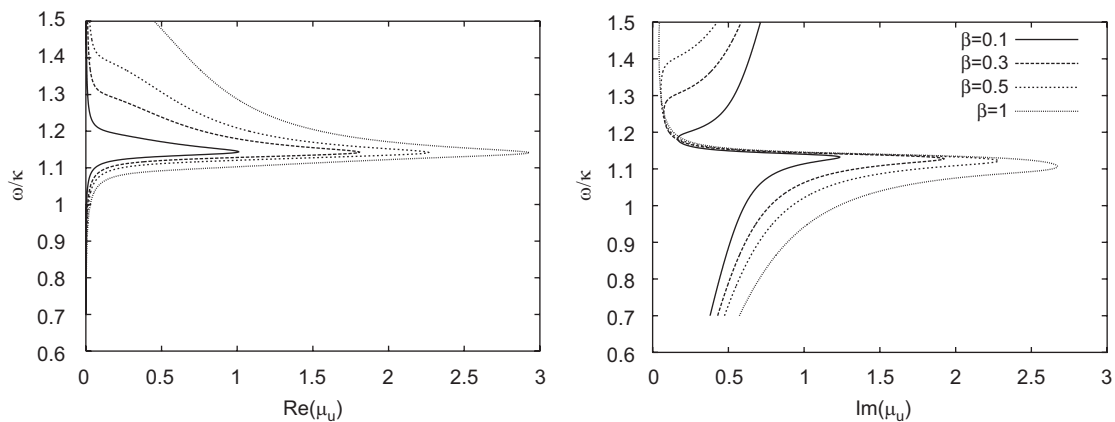


Fig. 4. Dispersion relation for $\zeta = 0.01$, $\gamma A_{1,j} \bar{A}_{1,j} = 0.1$ and different mass ratios.

the form

$$\cosh(\mu_u) = 1 - \frac{1}{2} \omega^2 - \frac{1}{2} \frac{\omega^2 \beta (\kappa^2 + 2i\zeta\kappa\omega + 3\kappa^2 \gamma_j A_{1,j} \bar{A}_{1,j})}{(\kappa^2 + 2i\zeta\kappa\omega + 3\kappa^2 \gamma_j A_{1,j} \bar{A}_{1,j} - \omega^2)}. \quad (14)$$

The dispersion relation for the linear case can be obtained from (14) by setting the non-linear parameter γ_j equal to zero and removing the damping in the attached oscillators. The influence of the damping parameter ζ on the dispersion relation in the linear case can be seen in Fig. 3. Den Hartog has shown in [8] that the introduction of viscous damping in the vibration absorber increases the frequency interval in which the device is effective. Similar behaviour can be observed for wave propagation problems. The maximal value of the attenuation rate decreases with increasing the damping in the attached oscillators, and for high values of ζ the band gap practically disappears. Similar behaviour is observed for two-dimensional wave propagation problems in [16]. The value of $\text{Im}(\mu_u)$ is always different from 0 or $\pm\pi$ in the damped case, and thus oscillatory behaviour in the spatial domain can always be observed. The influence of the mass ratio β on the band gap is shown in Fig. 4. The width of the stop band can be increased by increasing the attached mass.

For the non-linear spring–mass chain, μ_u depends on the amplitude of the attached oscillator at position j . Plots of the dispersion relation for different values of the non-linear parameter $\gamma A_{1,j} \bar{A}_{1,j}$ are shown in Fig. 5. As can be seen, the position of the maximal value of the attenuation rate varies with the value of the non-linear parameter. The maximum is shifted above the linear natural frequency of the attached oscillators, and the shift increases for larger values of the amplitude $A_{1,j}$. For a negative value of the non-linear parameter γ , the shift will occur in the opposite direction, below the linear natural frequency. As the wave propagates, the amplitude $A_{1,j}$ decreases, due to the reflections from the attached oscillators, as well as due to the damping in the system, and the position of the maximal value of $\text{Re}(\mu_u)$ moves toward $\omega/k = 1$. The amplitudes vary along the chain, and μ_u becomes a function of the spatial coordinate j . A fixed wave propagation constant cannot be defined in the non-linear case.

3.3. Transmission properties based on analytical calculations

For given values of the amplitudes $B_{1,j}$ and $A_{1,j}$ of mass j and the corresponding attached oscillator, the value of μ_u can be calculated using (14). The amplitude of the mass at position $j + 1$ is calculated as $B_{1,j+1} = e^{\mu_u} B_{1,j}$. The amplitude

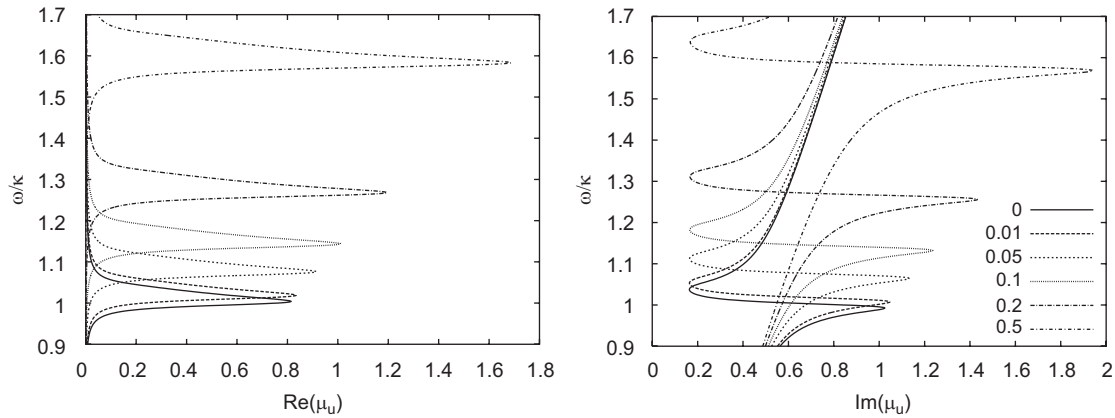


Fig. 5. Dispersion relation for $\beta = 0.1$, $\zeta = 0.01$ and different values of the non-linear parameter $\gamma A_{1,j} \bar{A}_{1,j}$.

$A_{1,j+1}$ of the attached oscillator can be calculated by solving the following equation:

$$B_{1,j+1} = A_{1,j+1} \left(-1 + \frac{\kappa^2}{\omega^2} + 3 \frac{\gamma_{j+1} \kappa^2}{\omega^2} A_{1,j+1} \bar{A}_{1,j+1} + \frac{2i\zeta\kappa}{\omega} \right) \tag{15}$$

which is obtained from (10) and (13) by equating the coefficients of $e^{i\omega t}$. Eq. (15) resembles the equation for the amplitude of the stationary response of externally excited Duffing oscillator. By using polar representation for the amplitudes $A_{1,j+1} = R_A(\cos(\psi) + i \sin(\psi))$ and $R_B = |B_{1,j+1}|$, (15) can be written as

$$9\gamma^2 r^4 R_A^6 + 6\gamma_{j+1} r^2 (r^2 - 1) R_A^4 + ((r^2 - 1)^2 + 4\zeta^2 r^2) R_A^2 - R_B^2 = 0, \tag{16}$$

where $r = \kappa/\omega$. Eq. (16) can be represented as a cubic equation with respect to R_A^2 . It has either one, or three real roots for R_A^2 . In the second case, two of the solutions are stable and one of them is unstable, which is well known property of the Duffing oscillator [14]. There are two values of μ_u corresponding to the two stable solutions of (16), and a unique value for $B_{1,j+2}$ cannot be obtained. The two solutions for $\mu_{u,j+1}$ can be ordered by the magnitude of their real part. The one with larger absolute real value, $\mu_{u,j+1}^l$, produces an amplitude with a smaller absolute value, and the other one, $\mu_{u,j+1}^u$, produces an amplitude with a larger absolute value. Continuing in this way, an estimate for the upper and the lower bounds of the absolute value of the wave amplitude can be obtained:

$$|B_{1,j+k}^u| = \left(\prod_{n=1 \dots k} e^{\text{Re}(\mu_{u,j+n}^u)} \right) |B_{1,j}^u|, \tag{17}$$

$$|B_{1,j+k}^l| = \left(\prod_{n=1 \dots k} e^{\text{Re}(\mu_{u,j+n}^l)} \right) |B_{1,j}^l|.$$

In the case where only a single real solution for R_A^2 exists, $\mu_{u,j+k}^l$ is equal to $\mu_{u,j+k}^u$ and $|B_{1,j+k}^u| = |B_{1,j+k}^l|$.

4. Numerical simulations

The theoretical analysis derived in the previous section is validated by using numerical simulations for finite spring–mass chain, as shown in Fig. 1. Absorbing boundary conditions are applied at each end of the chain by adding dash-pot with a damping constant $c = 1$. The damping constant corresponds to the exact absorbing boundary condition for a continuous rod with distributed mass $\rho A = 1$ and stiffness $EA = 1$, where ρ is the mass density, A is the section area and E is the elastic modulus. A wave travelling in the right direction is generated by applying a harmonic force with frequency ω and unit amplitude at the left end of the chain. The first and the last 10 masses in the chain are without attached oscillators. The wave travels undisturbed, until it reaches the part with the attached oscillators, where a part of it is reflected back, and a part of it propagates until it reaches the right end of the chain. The system is integrated numerically, until steady state is reached. The root-mean-squared (RMS) value of the response amplitude

$$[B_j] = \frac{1}{\sqrt{2}} \sqrt{\frac{1}{T} \int_t^{t+T} u_j^2(t) dt} \tag{18}$$

is calculated at the right end of the chain and is compared with the results obtained by using the analytical prediction derived in the previous section. The RMS value is calculated for a finite time interval $T = 20\lambda$, where $\lambda = 2\pi/\omega$ and ω is the frequency of the generated wave. The contribution of the higher order harmonics to the RMS value of the response amplitude is assumed to be small.

4.1. Influence of the non-linearities

The transmission properties of a chain with 2000 attached oscillators calculated by using numerical simulations, and the procedure in Section 3.3, are shown in Fig. 6. The non-linear coefficients $\gamma_j = \gamma$ are taken to be the same for all attached oscillators. The results are obtained for several values of γ . The linear normalised frequency κ of the attached oscillators is 0.05. For small values of the non-linear coefficient the estimated

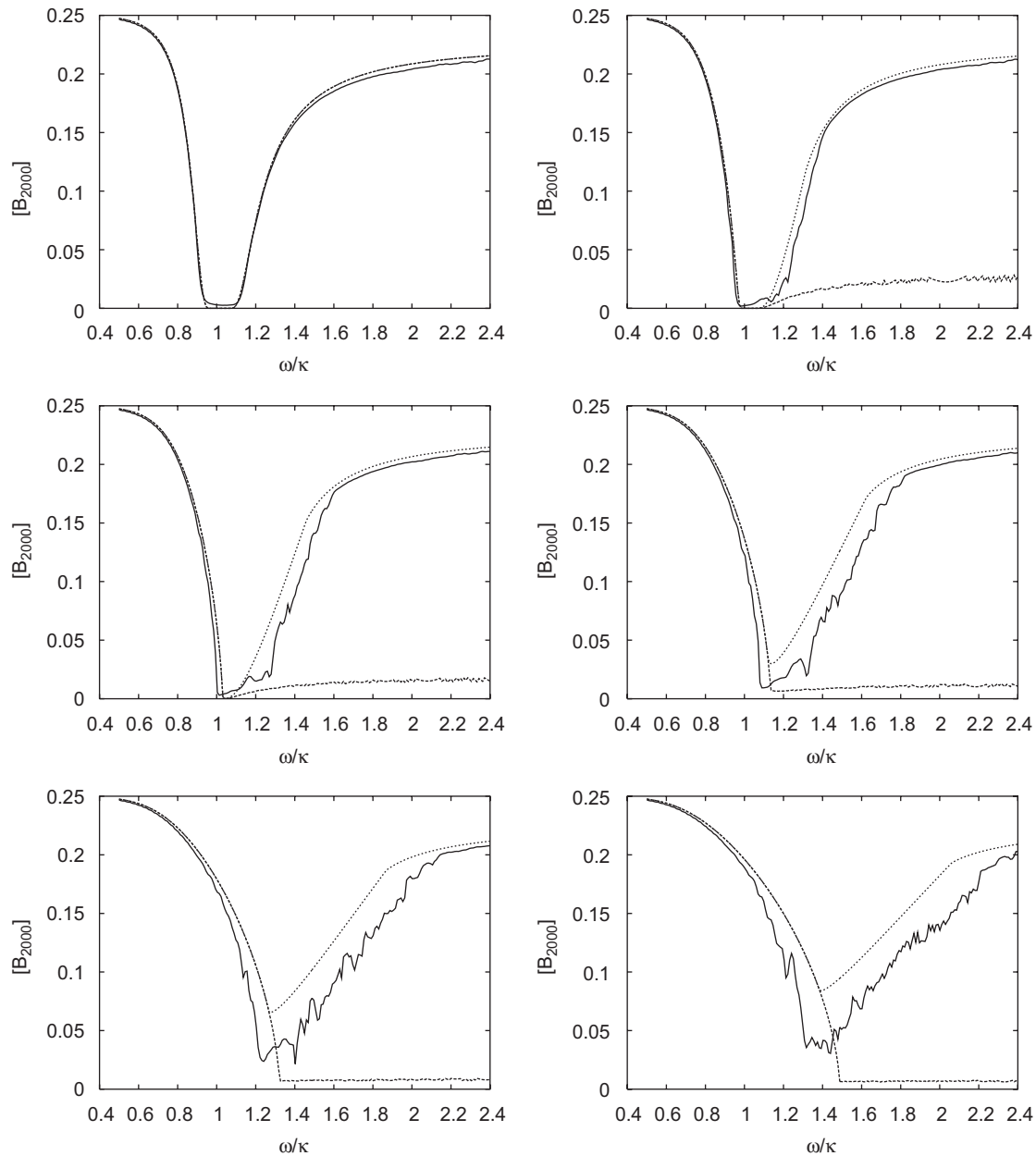


Fig. 6. Comparison of the theoretical prediction (dotted curves) of the transmitted amplitude with the one obtained by numerical integration for different values of $\gamma = 0.0, 0.1, 0.25, 0.5, 1.0, 1.5$, $\beta = 0.1$, $\zeta = 0.01$. The RMS value of the amplitude of the first mass is 0.25.

upper and lower values of the absolute value of the amplitude bound well the estimated RMS value of the amplitude from the numerical simulations. For large values of the non-linearity the results start to deviate. The frequency shift in the band gap can be clearly observed in all plots for $\gamma \neq 0$. In addition, the shape of the band gap changes, and the decaying rate decreases with increasing the non-linear coefficient.

4.2. Influence of the chain length

The results obtained by both numerical simulations and analytical calculations for chains with different number of the attached oscillators are shown in Fig. 7. The non-linear parameter $\gamma = 0.3$ is kept at a fixed value for all different spring-mass

chains, and is taken to be the same for all attached oscillators. As can be seen, for small number of the attached oscillators the frequency shift of the band gap is significant. The reduction of the transmitted amplitude is relatively small compared with the one obtained for larger number of the attached oscillators. As the wave propagates along the chain, the amplitude is decreasing leading to frequency shift of the band gap back towards the linear natural frequency. The effect can be clearly observed by studying the plots.

4.3. Chains with variable non-linear coefficients

If the wave frequency is located in the band gap, the amplitude is decaying fast, and the band gap is shifted back to

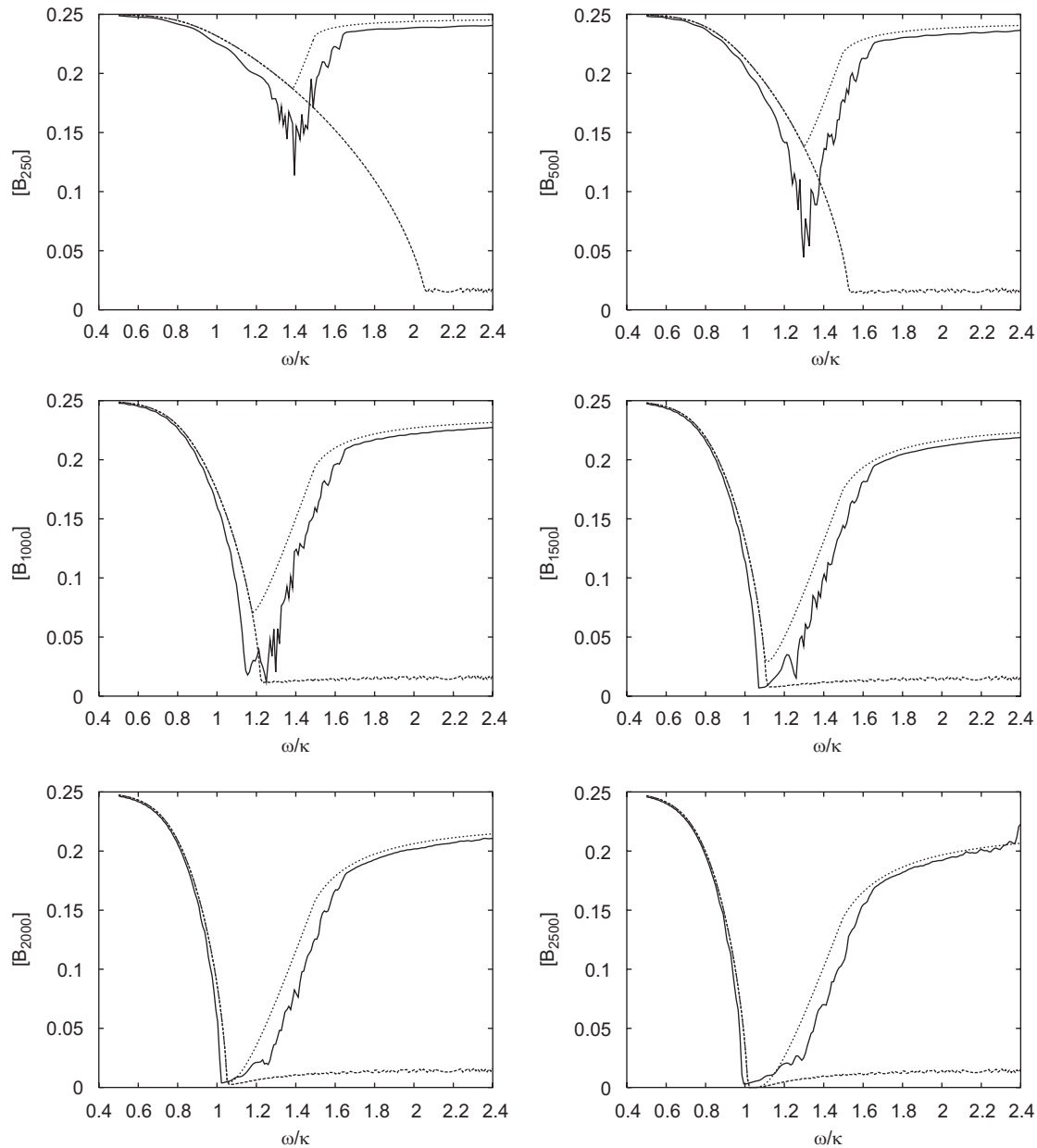


Fig. 7. Comparison of the theoretical prediction (dotted curve) of the transmitted amplitude with the one obtained by numerical integration for different numbers of the attached oscillators $n_l = 250, 500, 1000, 1500, 2000, 2500$ and $\gamma = 0.3$.

the one obtained for linear attached oscillators. The shift depends on the value of $\gamma_j A_{1,j} \bar{A}_{1,j}$. As the amplitude decreases along the chain, γ_j can be changed, in order to keep the shift of the band gap at a desirable frequency. For very small amplitudes the value of γ needs to be very large and thus, there will always be a wave with finite amplitude propagating after the part of the chain with attached oscillators. Plots of the transmitted amplitude for chains with 400 attached oscillators are shown in Fig. 8. A chain with variable non-linearities is chosen with γ equal to $0.12\sqrt{\exp((i-1)/100)}$, and for comparison the results for chains with constant $\gamma = 0.12$ corresponding to the minimal value of γ in the chain with variable non-linearities, $\gamma = 0.88$ (maximal value) and $\gamma = 0.3$ (intermediate value), are

shown in the figure. The input RMS value of the amplitude is equal to 0.25, the damping coefficient is $\zeta = 0.02$ and i is the number of the attached oscillators. The theoretical prediction is calculated by using the procedure in Section 3.3. In all cases with $\gamma \neq 0$, a shift in the stop band frequency can be clearly observed. The shift of the chain with variable γ is between the shift for the cases with $\gamma = 0.12$ and 0.88 , and close to the case with the intermediate value $\gamma = 0.3$. The theoretical prediction indicates better filtering properties in the case with variable γ and this result is also supported by the numerical simulations.

The expression for γ in the chain with variable non-linearities is obtained by trial and error. A systematic optimisation procedure can produce better results. More improvements are

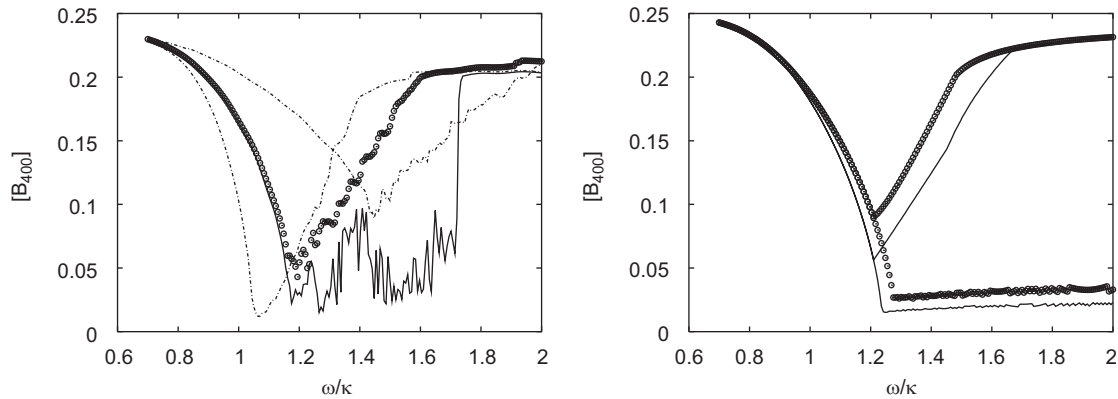


Fig. 8. Comparison of the transmitted amplitude for variable (solid line) and fixed (circular dots $\gamma = 0.3$) γ for chain with 400 attached oscillators. The two dashed lines show the transmitted amplitude for fixed γ (0.12, 0.88) equal to the lowest and the highest value used for the chain with varying non-linearities. The second plot is obtained by using the analytical calculations with variable γ and $\gamma = 0.3$.

possible if variation is allowed not only in the non-linearities but also in the linear stiffness coefficients, mass ratio and the damping. A study based on a topology optimisation approach for a similar linear continuous system is presented by the authors in [17]. An extension to the non-linear case is a subject for future work.

5. Conclusions

The focus in this article is on the influence of the non-linearities on the filtering properties of the chain around the linear natural frequency of the attached oscillators. The position of the band gap can be shifted by changing the degree of non-linearity of the oscillators, or by changes of the wave amplitude. A comparison with numerical simulations for a finite chain with attached oscillators shows that the analytical predictions match simulations well for small non-linearities, and start to deviate for large ones. Both estimations clearly show a shift in the band gap. The transmitted amplitude will always be different than zero for wave frequencies different than the linear natural frequency of the attached oscillators and for finite values of the non-linear parameter γ . The change in the position of the stop band can be utilised in the design of adjustable filters in the lower frequency range. The optimal distribution of the non-linearities, as well as the natural frequencies and the damping of the attached oscillators, is subject to further investigations.

Acknowledgements

This work was supported by Grant 274-05-0498 from the Danish Research Council for Technology and Production Sciences. The authors wish to thank Professor Jon Juel Thomsen for his suggestions and valuable discussions.

References

- [1] L. Brillouin, *Wave Propagation in Periodic Structures*, Dover Publications Inc., New York, 1953.

- [2] D.J. Mead, Wave-propagation and natural modes in periodic systems. 1. Mono-coupled systems, *J. Sound Vib.* 40 (1975) 1–18.
- [3] D.J. Mead, Wave-propagation and natural modes in periodic systems. 2. Multi-coupled systems, with and without damping, *J. Sound Vib.* 40 (1975) 19–39.
- [4] A.F. Vakakis, M.E. King, A.J. Pearlstein, Forced localization in a periodic chain of nonlinear oscillators, *Int. J. Non-linear Mech.* 29 (1994) 429–447.
- [5] G. Chakraborty, A.K. Mallik, Dynamics of a weakly non-linear periodic chain, *Int. J. Non-linear Mech.* 36 (2001) 375–389.
- [6] A. Marathe, A. Chatterjee, Wave attenuation in nonlinear periodic structures using harmonic balance and multiple scales, *J. Sound Vib.* 289 (2006) 871–888.
- [7] O. Richoux, C. Depollier, J. Hardy, Propagation of mechanical waves in a one-dimensional nonlinear disordered lattice, *Phys. Lett. E* 73 (2006) 026611.
- [8] J.P. Den Hartog, *Mechanical Vibrations*, 4th ed., McGraw-Hill, New York, 1956 (Reprinted by Dover Publications Inc., New York, 1985).
- [9] D.L. Yu, Y.Z. Liu, G. Wang, L. Cai, J. Qiu, Low frequency torsional vibration gaps in the shaft with locally resonant structures, *Phys. Lett. A* 348 (2006) 410–415.
- [10] Z. Liu, X. Zhang, Y. Mao, Y.Y. Zhu, Z. Yang, C.T. Chan, P. Sheng, Locally resonant sonic materials, *Science* 289 (2000) 1734–1736.
- [11] G. Wang, J. Wen, X. Wen, Quasi-one-dimensional phononic crystals studied using the improved lumped-mass method: application to locally resonant beams with flexural wave band gap, *Phys. Lett. B* 71 (2005) 104302.
- [12] I.T. Georgiou, A.F. Vakakis, An invariant manifold approach for studying waves in a one-dimensional array of non-linear oscillators, *Int. J. Non-linear Mech.* 31 (1996) 871–886.
- [13] B.S. Lazarov, J.S. Jensen, Band gap effects in spring–mass chains with attached local oscillators, in: *Proceedings of the ECCOMAS Thematic Conference of Computational Methods in Structural Dynamics and Earthquake Engineering*, Rethymno, Crete, Greece, 2007.
- [14] J.J. Thomsen, *Vibrations and Stability*, Springer, Berlin, Heidelberg, 2003.
- [15] A.H. Nayfeh, D.T. Mook, *Nonlinear Oscillations*, Wiley, New York, 1979.
- [16] J.S. Jensen, Phononic band gaps and vibrations in one- and two-dimensional mass–spring structures, *J. Sound Vib.* 266 (2003) 1053–1078.
- [17] J.S. Jensen, B.S. Lazarov, Topology optimization of distributed mass dampers for low-frequency vibration suppression, in: *Proceedings of the ECCOMAS Thematic Conference of Computational Methods in Structural Dynamics and Earthquake Engineering*, Rethymno, Crete, Greece, 2007.

Systematic design of phononic band-gap materials and structures by topology optimization

BY OLE SIGMUND AND JAKOB SØNDERGAARD JENSEN

*Department of Mechanical Engineering, Section for Solid Mechanics,
Nils Koppels Allé Building 404, 2800 Kgs. Lyngby, Denmark*

Published online 26 March 2003

Phononic band-gap materials prevent elastic waves in certain frequency ranges from propagating, and they may therefore be used to generate frequency filters, as beam splitters, as sound or vibration protection devices, or as waveguides. In this work we show how topology optimization can be used to design and optimize periodic materials and structures exhibiting phononic band gaps. Firstly, we optimize infinitely periodic band-gap materials by maximizing the relative size of the band gaps. Then, finite structures subjected to periodic loading are optimized in order to either minimize the structural response along boundaries (wave damping) or maximize the response at certain boundary locations (waveguiding).

Keywords: phononic band gaps; topology optimization; materials; structures

1. Introduction

A new application of the topology-optimization method is design of materials and structures subject to wave propagation. The wave may be elastic, acoustic or electromagnetic, but the phenomenon is the same: for some frequency bands it is possible to construct periodic materials or structures that hinder propagation. The phenomenon is a band gap.

The phenomenon of band gaps may be illustrated by the following example. Figure 1*a, b* shows a two-dimensional square domain subjected to a periodic loading at the left edge and with absorbing boundary conditions along all the edges. The frequency of excitation of the structure in figure 1*a* is lower than that for figure 1*b*. It is seen that waves propagate unhindered through the structures from left to right, damped only slightly at the top and bottom due to the absorbing boundary conditions. Now, if we introduce a periodic distribution of inclusions with different propagation speeds, the situation changes. For the structure subjected to a lower excitation frequency (figure 1*c*), there is still propagation, although the waves are significantly distorted by the reflection and refraction from the inclusions. However, for the structure subjected to a higher excitation frequency (figure 1*d*), there seems to be no propagation at all. This illustrates the band-gap phenomenon. For elastic and acoustic waves the materials are called *phononic band gap* materials, and for electromagnetic wave propagation the materials are called *photonic band gap* materials.

One contribution of 12 to a Theme 'Micromechanics of fluid suspensions and solid composites'.

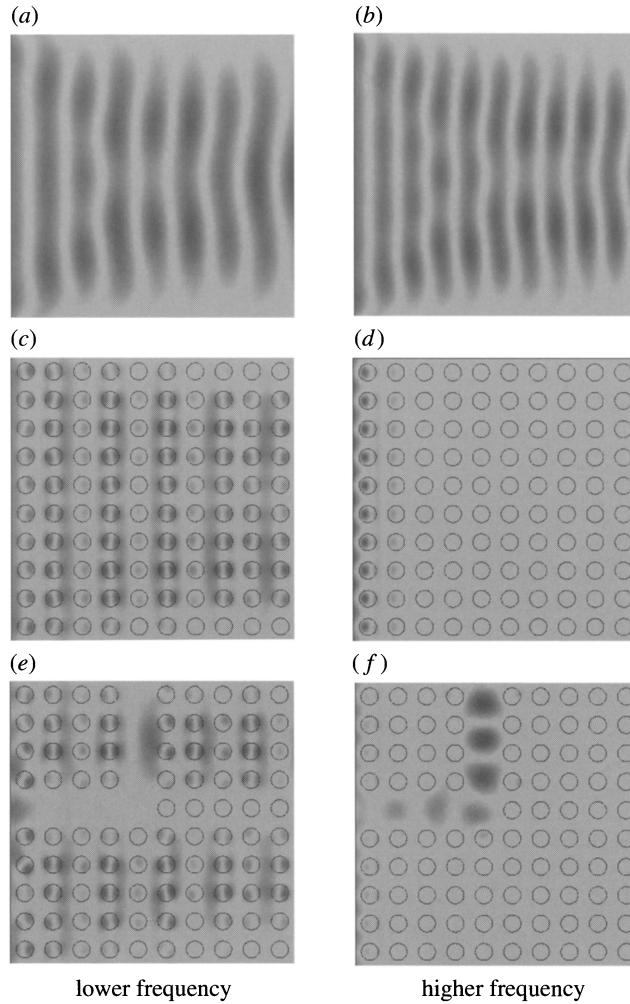


Figure 1. Scalar wave propagation in two-dimensional domains with absorbing boundary conditions and forced vibrations at the left edge. (a) Wave propagation through homogeneous structure; (b) wave propagation with higher frequency through a homogeneous structure; (c) wave propagation through a structure with periodic inclusions; (d) (no) wave propagation with higher frequency through a periodic structure; (e) wave propagation through a periodic structure with a defect; and (f) waveguiding a higher frequency through a periodic structure with a defect.

Interest in the *photonic band gap* materials and structures over the last decade has been large. Based on the theory developed (see, for example, Joannopoulos *et al.* 1995; Yablonovitch 2001), industrial applications such as improved waveguides (see figure 1*e, f*) and lasers have emerged. The work on photonic band gaps has caused a renewed interest in *phononic band gap* materials. The basic principles of wave propagation in elastic media are well established (e.g. Brillouin 1953; Elachi 1976), but more recent research in this field has focused on theoretical and experimental demonstration of band gaps in two-dimensional and three-dimensional periodic materials (e.g. Sigalas & Economou 1992; Vasseur *et al.* 1998; Liu *et al.* 2000; Kushwaha 1996).

However, unlike photonic crystals, phononic band-gap materials and structures have, to the authors' knowledge, not yet directly led to industrial applications, but have potentially rewarding applications in frequency filters with control of pass or stop bands, as beam splitters, as sound or vibration protection devices, as acoustic lasers (phasers), as perfect acoustic mirrors, or as elastic waveguides.

A comprehensive and frequently updated reference list for work on photonic and phononic band gaps can be found on <http://www.pbglink.com>.

Little work has been done on the systematic design of band-gap materials and structures. In the literature, the 'optimal' band-gap material is usually found by parameter studies based on fixed inclusion shapes (e.g. circular inclusions). A promising method for systematic design of band-gap materials and structures is the topology-optimization method (see Bendsøe & Sigmund (2003) and references therein). In topology optimization one discretizes the design domain (e.g. the periodic base cell) by a large number of elements (typically coinciding with the finite-element mesh) and allows the material density or type in each element to be a design variable. By defining proper objective functions and constraints, efficient and entirely new topologies defined as raster pictures may be obtained. Since its introduction in the late 1980s (Bendsøe & Kikuchi 1988), the topology-optimization method has been applied to a myriad of design problems ranging from simple compliance minimization for elastic structures over design of extremal materials with negative thermal expansion coefficients (Sigmund & Torquato 1997) to design of microelectromechanical systems (Sigmund 2001*a, b*). Topology-optimization methods have been applied to the design of photonic band-gap materials considering scalar fields in Cox & Dobson (1999, 2000), and preliminary results of the topology-optimization method applied to the design of phononic band-gap materials considering both scalar and coupled problems have been published in Sigmund (2001*c*) and Sigmund & Jensen (2002). To the authors' knowledge, no papers on topology optimization of band gap *structures* have been published, apart from some preliminary results presented in Sigmund & Jensen (2002).

The paper is organized as follows: after defining the basic equations, we briefly discuss the analysis of materials and structures in a standard finite-element-method (FEM) formulation and provide examples showing the typical behaviour of periodic materials and structures (§ 2). We then introduce the topology-optimization technique and apply it to design materials with maximum relative band-gap size and structures with optimized wave-damping or waveguiding properties (§ 3). Finally, we make some conclusions (§ 4).

2. Propagation of elastic waves

Vibrations and wave propagation in a three-dimensional elastic inhomogeneous medium are governed by

$$\rho \frac{\partial^2 u}{\partial t^2} = \frac{\partial}{\partial x} (\lambda \nabla \cdot \mathbf{u}) + \nabla \cdot \left(\mu \left(\nabla u + \frac{\partial \mathbf{u}}{\partial x} \right) \right), \quad (2.1)$$

$$\rho \frac{\partial^2 v}{\partial t^2} = \frac{\partial}{\partial y} (\lambda \nabla \cdot \mathbf{u}) + \nabla \cdot \left(\mu \left(\nabla v + \frac{\partial \mathbf{u}}{\partial y} \right) \right), \quad (2.2)$$

$$\rho \frac{\partial^2 w}{\partial t^2} = \frac{\partial}{\partial z} (\lambda \nabla \cdot \mathbf{u}) + \nabla \cdot \left(\mu \left(\nabla w + \frac{\partial \mathbf{u}}{\partial z} \right) \right), \quad (2.3)$$

where λ and μ are Lamé's coefficients, ρ is the material density, and $\mathbf{u} = \{uvw\}^T$ the displacement vector.

In the following we assume that any variation in the material parameters occurs in the (x, y) -plane only; thus we have $\lambda = \lambda(x, y)$, $\mu = \mu(x, y)$, and $\rho = \rho(x, y)$. Further, we restrict the analysis by only considering waves that propagate in the (x, y) -plane, so that $\partial\mathbf{u}/\partial z = 0$. Equations (2.1)–(2.3) can then be split into two coupled in-plane equations (governing the longitudinal and transverse modes) and an out-of-plane equation (the acoustic modes):

$$\rho \frac{\partial^2 u}{\partial t^2} = \frac{\partial}{\partial x} \left((2\mu + \lambda) \frac{\partial u}{\partial x} + \lambda \frac{\partial v}{\partial y} \right) + \frac{\partial}{\partial y} \left(\mu \left(\frac{\partial u}{\partial y} + \frac{\partial v}{\partial x} \right) \right), \quad (2.4)$$

$$\rho \frac{\partial^2 v}{\partial t^2} = \frac{\partial}{\partial x} \left(\mu \left(\frac{\partial v}{\partial x} + \frac{\partial u}{\partial y} \right) \right) + \frac{\partial}{\partial y} \left((2\mu + \lambda) \frac{\partial v}{\partial y} + \lambda \frac{\partial u}{\partial x} \right), \quad (2.5)$$

$$\rho \frac{\partial^2 w}{\partial t^2} = \frac{\partial}{\partial x} \left(\mu \frac{\partial w}{\partial x} \right) + \frac{\partial}{\partial y} \left(\mu \frac{\partial w}{\partial y} \right). \quad (2.6)$$

Equations (2.4)–(2.6) can be solved with the appropriate boundary conditions applied. For the design of waveguides we need to be able to simulate travelling waves, and for that purpose we introduce absorbing boundary conditions. In the scalar case, for normal incident waves on a flat boundary, the absorbing boundary condition can be written as (e.g. Krenk 2002)

$$\frac{\partial w}{\partial n} + \frac{1}{c} \frac{\partial w}{\partial t} = 0, \quad (2.7)$$

where \mathbf{n} is the outward-pointing normal vector and $c = \sqrt{\mu/\rho}$ is the local wave speed.

Further analysis is now split into two separate parts. First, the material problem is addressed by analysing base cells that are repeated infinitely, and then the structural problem is considered for finite-dimensional media with external loading. In both cases, equations (2.4)–(2.6), with the boundary conditions (2.7), are solved using a standard FEM procedure using four-noded bilinear quadrilateral elements for the discretization.

(a) The material problem

For the material problem, the wave equation may be solved as an eigenvalue problem for an infinitely periodic structure. We may solve the global problem by analysing the smallest repetitive unit, the base cell Y . We assume that the modes can be described by the expression

$$\mathbf{u}(\mathbf{y}, \mathbf{k}) = \tilde{\mathbf{u}}(\mathbf{y}) e^{i\mathbf{k}^T \mathbf{y}} e^{i\omega t}, \quad (2.8)$$

where $\tilde{\mathbf{u}}$ is a Y -periodic displacement field, $\mathbf{y} = (y_1, y_2)$ are the local cell coordinates and \mathbf{k} is the plane wave vector. For $\mathbf{k} = \mathbf{0}$, the solution mode $\mathbf{u}(\mathbf{y})$ will be Y -periodic, for $\mathbf{k} = \boldsymbol{\pi}$, the solution mode will be $2Y$ -periodic and for other \mathbf{k} , the solution modes can take any kind of periodicity in the plane. This kind of modelling is based on the so-called Floquet–Bloch wave theory (Mathews & Walker 1964; Kittel 1986).

Inserting (2.8) into either (2.4), (2.5) or (2.6), dropping the tilde, and converting to FEM notation yields

$$(\mathbf{K}(\mathbf{k}) - \omega^2 \mathbf{M}) \mathbf{u} = \mathbf{0}, \quad (2.9)$$

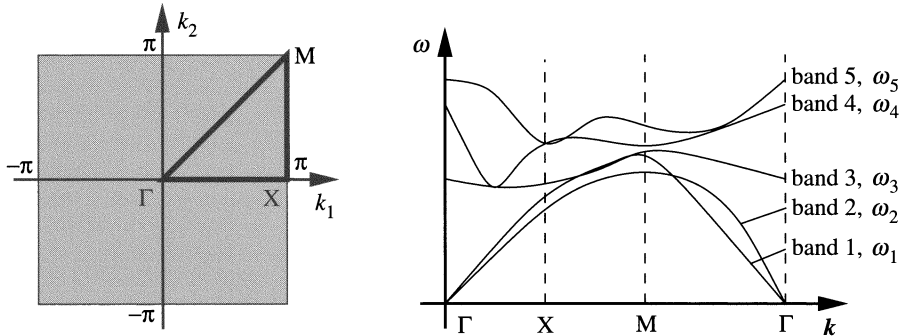


Figure 2. (a) The irreducible Brillouin zone indicating the wave vectors to be searched for the general two-dimensional case (grey area). For square symmetry, the wave equation only has to be calculated for \mathbf{k} -vector values along the curve Γ -X-M- Γ . (b) Sketch of band structure indicating lowest five eigenvalues for wave vectors along the line Γ -X-M- Γ in the irreducible Brillouin zone.

Table 1. Material parameters for the examples

contrast	ρ_1 (10^3 kg m^{-3})	ρ_2 (10^3 kg m^{-3})	E_1 (GPa)	E_2 (GPa)	ν
high	1	2	4	20	0.34
low	1	2	4	9	0.34

which is recognized as a complex eigenvalue problem with $\mathbf{K}(\mathbf{k})$ the stiffness matrix and \mathbf{M} the mass matrix. Equation (2.9) should be solved for any wave vector \mathbf{k} , but due to the periodicity we may restrict the wave vector to the first Brillouin zone $\mathbf{k} \in [-\pi, \pi]^d$, where d is the dimension (Brillouin 1953). Due to the square symmetry of the base cell, the area can be restricted further to the triangle defined by the lines $\Gamma \rightarrow X$, $X \rightarrow M$ and $M \rightarrow \Gamma$ (see figure 2a). In principle, the whole triangle should be searched, but, although unproven, many researchers claim that the information required can be obtained by searching points only on the boundary lines. Figure 2b shows a sketch of how the results of the FE analysis are presented in a band diagram for the coupled problem (2.4), (2.5) solved for the five lowest eigenvalues.

Throughout this paper we will use two sets of material parameters for the examples. They are denoted the ‘high-contrast’ and the ‘low-contrast’ cases (see table 1).

Band diagrams calculated for base cells of $2 \text{ cm} \times 2 \text{ cm}$ composed of two material phases (high-contrast) are shown in figure 3. First we show the band diagrams for the in-plane coupled modes (2.4) and (2.5) for pure material phases 1 and 2 in figure 3a and figure 3b, respectively. It is seen that, for these homogeneous materials, eigenmodes (i.e. propagation modes) exist for all frequencies. Figure 3c shows the band structure for square phase 2 cylinders in a matrix of phase 1. It is seen that in this case there is a range of frequencies with no corresponding eigenmodes, i.e. there is a band gap between the third and fourth bands (from 56 to 64 kHz, corresponding to a relative band-gap size of $\Delta f/f_0 = 0.14$). This means that no elastic waves with frequencies within the band gap may propagate through the structure. The band-gap zone is indicated with hatched regions in the diagram. Figure 3d shows the band-gap structure for the scalar case (2.6). Here there is a band gap between the first

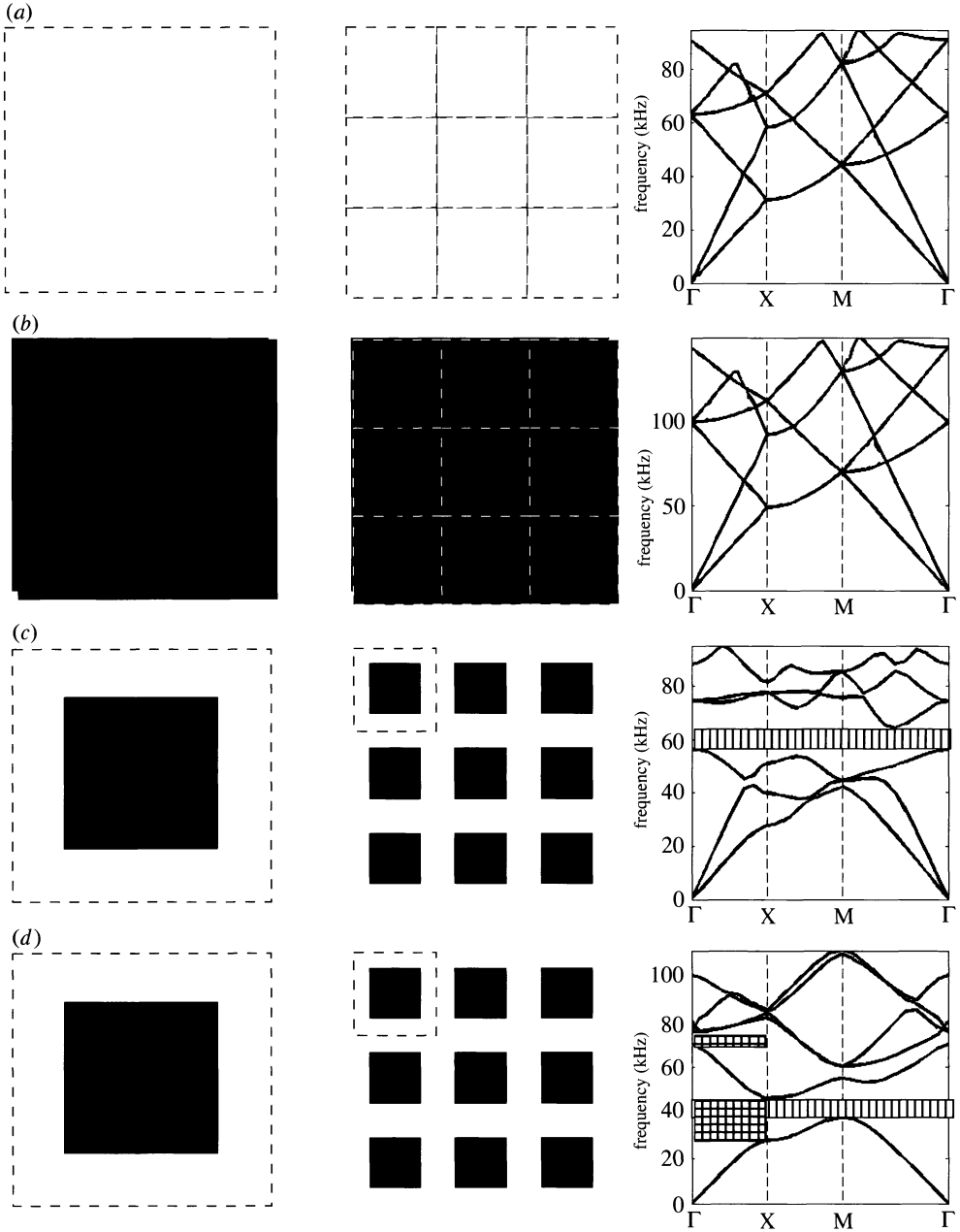


Figure 3. Left, single cell; middle, 3×3 arrays of cells; right, band diagram for coupled plane waves in (a) pure phase 1, (b) pure phase 2 and (c) square phase 2 cylinders in matrix of phase 1 (high-contrast case). Hatched areas denote band gaps. The horizontal axes denote values of the wave vector \mathbf{k} on the boundary of the irreducible Brillouin zone. The band diagrams are based on the solution of 30 eigenvalue problems with varying \mathbf{k} solved for the six lowest eigenvalues. (d) Band diagram for the scalar (out-of-plane) problem with the full band gap shown as a hatched region and two partial band gaps indicated by cross-hatched regions. The size of the base cells is $2 \text{ cm} \times 2 \text{ cm}$ and the discretization is 10×10 elements.

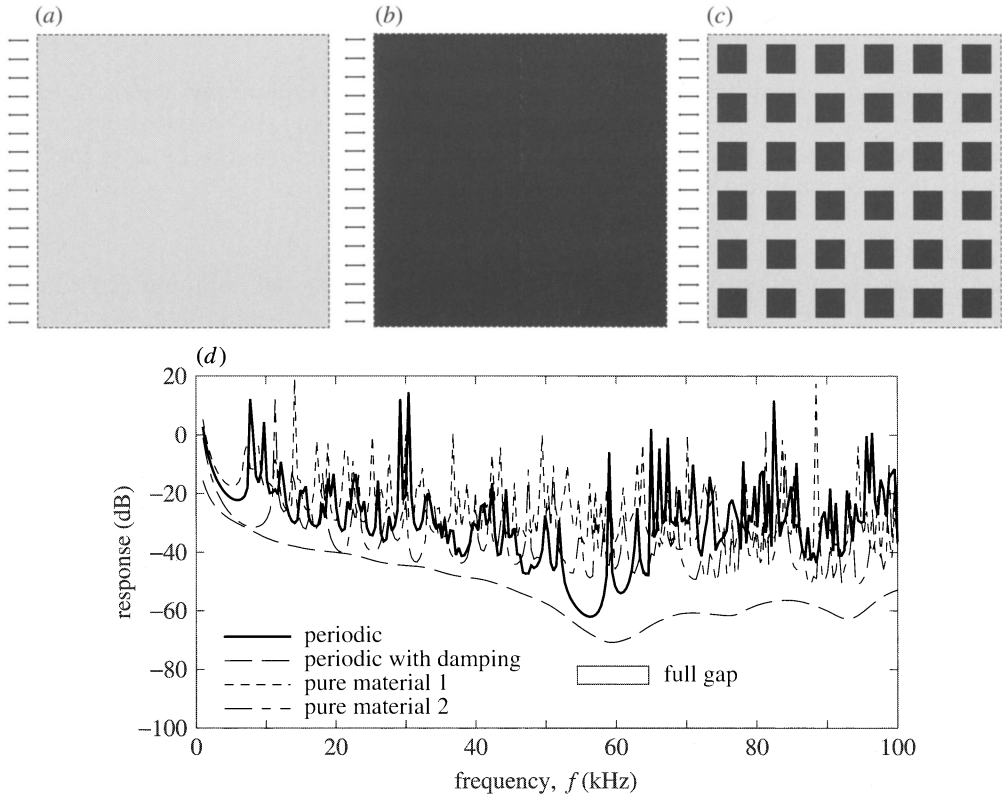


Figure 4. Response of a $12\text{ cm} \times 12\text{ cm}$ square structure subjected to periodic loading on the left boundary, (a) pure material 1, (b) pure material 2, and (c) a periodic structure of materials 1 and 2; (d) response calculated as the average amplitude on the right boundary for the structure of pure materials 1 and 2 without damping, and for the periodic structure with and without mass-proportional damping. High-contrast case.

and second bands (from 38 to 46 kHz, corresponding to a relative band-gap size of $\Delta f/f_0 = 0.20$). Furthermore, there are two partial band gaps (for modes propagating in the horizontal direction for the frequency ranges 28–46 kHz and 70–76 kHz (indicated by cross-hatched regions in the figure). Note that the calculations in this example are based on an extremely coarse discretization (10×10 elements). The coarse discretization is chosen in order to be able to compare the results with results for the finite-dimensional structures that cannot be modelled with an extremely fine grid due to computing-time limitations.

(b) The structural problem

For the structural problem with external harmonic loading, we assume a harmonic wave solution described as

$$\mathbf{u} = \hat{\mathbf{u}}e^{i\Omega t}, \quad (2.10)$$

where Ω is the driving frequency and $\hat{\mathbf{u}}$ is the amplitude. Substituting equation (2.10) into equations (2.4), (2.5) or equation (2.6), depending on whether in-plane or out-of-plane waves are considered, dropping the hat, and converting to FEM notation

we get

$$(\mathbf{K} + i\Omega\mathbf{C} - \Omega^2\mathbf{M})\mathbf{u} = \mathbf{f}, \quad (2.11)$$

where we have added boundary (harmonic) forces \mathbf{f} and a damping matrix \mathbf{C} stemming from absorbing boundaries (2.7) or structural damping. In this work we include absorbing boundaries only in the out-of-plane case. Structural damping is included in the form of standard Rayleigh damping,

$$\mathbf{C} = \alpha\mathbf{K} + \beta\mathbf{M}, \quad (2.12)$$

with α the stiffness-proportional and β the mass-proportional damping constants.

Figure 4 shows three different structures and the corresponding steady-state responses when subjected to harmonic loading at the left boundary. In-plane vibrations are considered for the high-contrast case and the response is calculated as the average amplitude along the right boundary. The structure in figure 4c is made from a periodic material consisting of a matrix of material 1 (grey) with 36 square inclusions of material 2 (black) (the inclusions cover 36% of the base cells, corresponding to the periodic material in figure 3c). From figure 3c it was found that the infinitely periodic material has a band gap between the third and the fourth propagation modes around $f = 60$ kHz. Figure 4d shows the corresponding response of the finite structure when subjected to the external loading. The band gap is identified from the drop in response around the gap frequency, but the drop is not as large as might have been expected and there are two peaks in the middle of the interval. This can partly be ascribed to the small number of base cells (6×6) included in the structure, but more importantly to resonance effects due to the reflections from the non-absorbing boundaries.

Figure 4d also shows the response calculated with mass-proportional damping included ($\alpha = 0$, $\beta = 50 \times 10^3$). The damping is seen to remove the resonance peaks in the response, but the reduction in response near the band gap is still seen and the peaks inside the band-gap range have been removed. This effect of smoothing of the response by including damping will be used later in the optimization procedure. The responses for the structures made of pure material 1 and material 2, respectively, are shown in figure 4d for comparison.

A response diagram for the structure in figure 4c but modelling the out-of-plane case and including absorbing boundary conditions on the left and right edges is shown in figure 5. Compared with the response curve for the in-plane and non-absorbing boundary case from figure 4, the response is seen to be much cleaner and free from local peaks. Also, the band gap is seen to correspond very well to the partial band gaps from figure 3d.

From the results shown in figures 3 and 4, two optimization problems naturally emerge. For the *material problem* the size of the band gaps should be maximized to increase the frequency range for which waves cannot propagate through the material. For the *structural problem*, the response of the structure may be minimized for a given frequency, or alternatively maximized in certain structural areas to create wave-damping or wave-guiding structures, respectively.

3. Topology optimization

We follow the standard approach to topology optimization (cf. Bendsøe 1995; Bendsøe & Sigmund 2003). The topology-optimization problem consists of distribut-

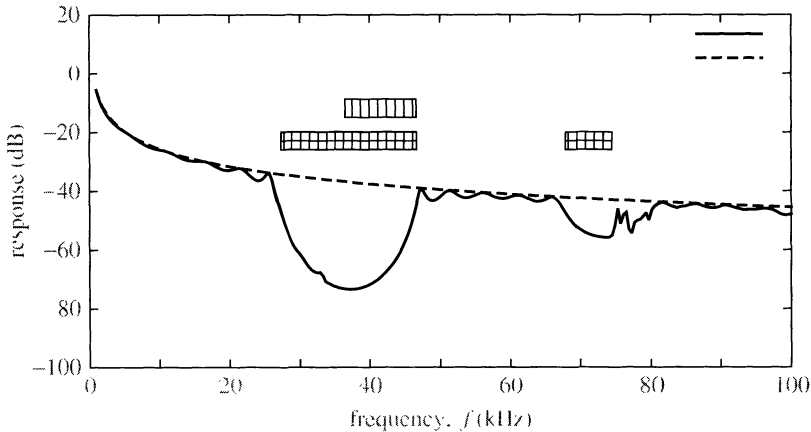


Figure 5. Response of a 12 cm \times 12 cm square structure subjected to periodic loading on the left boundary, absorbing boundary conditions on the left and right edges and out-of-plane modelling. High-contrast case.

ing two material phases in the design domain such that an objective function is extremized subject to a number of constraints. The design variables are material ‘densities’ $x_e \in [0, 1]$ that interpolate the material properties for each element used to discretize the structure. If the design variable takes a zero value we should have pure phase 1 material, and if the design variable takes a value of one we should have pure phase 2 material in the element. We choose a linear interpolation between the phases, given as

$$\rho(x_e) = (1 - x_e)\rho_1 + x_e\rho_2, \quad (3.1)$$

$$\mu(x_e) = (1 - x_e)\mu_1 + x_e\mu_2, \quad (3.2)$$

$$\lambda(x_e) = (1 - x_e)\lambda_1 + x_e\lambda_2, \quad (3.3)$$

where subscripts ‘1’ and ‘2’ denote the properties in materials 1 and 2, respectively.

The choice of linear interpolation stems from the observation that there appears to be no need for penalizing intermediate ‘densities’, i.e. values of x_e other than zero or one in the final design. The reason for this is believed to originate in the nature of the band-gap phenomenon, where large contrasts between the involved material phases is favoured.

(a) Material optimization

An obvious goal for the optimization of band-gap materials is to maximize the relative band-gap size. In this way the range of prohibited frequencies will be wider and more signals may be sent through a waveguide based on defects in the band-gap material.

The goal of the optimization is to maximize the relative band-gap size between bands j and $j+1$, i.e. maximize the lowest value of the overlying bands and minimize the maximum value of the underlying bands. This can be written as a (double) max–min objective

$$\max_x : c(x) = \frac{\Delta\omega^2(x)}{\omega_0^2(x)} = 2 \frac{\min_{\mathbf{k}} \omega_{j+1}^2(\mathbf{k}, x) - \max_{\mathbf{k}} \omega_j^2(\mathbf{k}, x)}{\min_{\mathbf{k}} \omega_{j+1}^2(\mathbf{k}, x) + \max_{\mathbf{k}} \omega_j^2(\mathbf{k}, x)}. \quad (3.4)$$

This is a ‘dirty’ objective function in the sense that it is a max–min problem with varying critical points (the \mathbf{k} -vector(s) for the critical frequencies may change during the optimization) and it may have several multiple eigenvalues. Interestingly, however, there is no need for a volume fraction constraint in the problem, since pure phase 1 will give no band gap and pure phase 2 will give no band gap (cf. figure 3*a, b*). Somewhere in between there must be a volume fraction that results in the biggest band gap.

The optimization problem may be written as

$$\max_x \frac{\Delta\omega^2(x)}{\omega_0^2(x)} \quad \text{s.t.: } (\mathbf{K}(\mathbf{k}) - \omega^2\mathbf{M}) \mathbf{u} = \mathbf{0}, \quad \mathbf{k} \in [\Gamma\text{-X-M-}\Gamma],$$

$$0 \leq x_e \leq 1, \quad e = 1, \dots, N, \quad (3.5)$$

where N is the number of elements used to discretize the design domain. The optimization problem may efficiently be solved by use of the mathematical programming ‘method of moving asymptotes’ (MMA) (Svanberg 1987, 1998).† As mentioned, the sensitivity analysis is somewhat complicated, since it involves sensitivities of multiple eigenvalues; methods to avoid this problem are described in Seyranian *et al.* (1994).

An interesting observation can be made by studying the results of both the material optimization problem and the structural optimization problem (see below). In conventional topology-optimization problems with the goal of minimizing elastic compliance, the optimal solution does not exist in the sense that a finer discretization will result in a topology with a more complicated microgeometry and a better compliance. In the wave-propagation examples considered in this paper, this mesh-dependency is not encountered. This may be attributed to the finite length-scales imposed by the wavelengths. Nevertheless, in order to convexify the problems during initial iterations, we use the filter method suggested by Sigmund (1997). However, the filter is removed before the final convergence.

(i) Results for out-of-plane waves

The resulting topologies for maximization of the band gap between the first and the second bands, considering out-of-plane modelling for the two material cases, are shown in figure 6. For the high-contrast case the relative band-gap size is 0.225, and for the low-contrast case it is 0.025. It is seen that, for the high-contrast case, the optimized topology is a square inclusion of phase 2 material with slightly rounded corners. For the low-contrast case, the optimized topology approaches a circular inclusion with a lower volume fraction of phase 2 material. For comparison, a square inclusion with relative size 0.7 would result in relative band-gap sizes of 0.225 and 0.010, respectively. This means that, at least for the high-contrast case, the simplest and optimal solution is the square inclusion.

(ii) Results for in-plane waves

The resulting topologies for in-plane waves are seen in figure 7. For both the high-contrast and low-contrast cases, the optimized topologies are seen to be square

† A modified version of the code (Svanberg 1998) that allows for solving of the min–max problem (3.5) can be obtained from Svanberg (free for academic purposes).

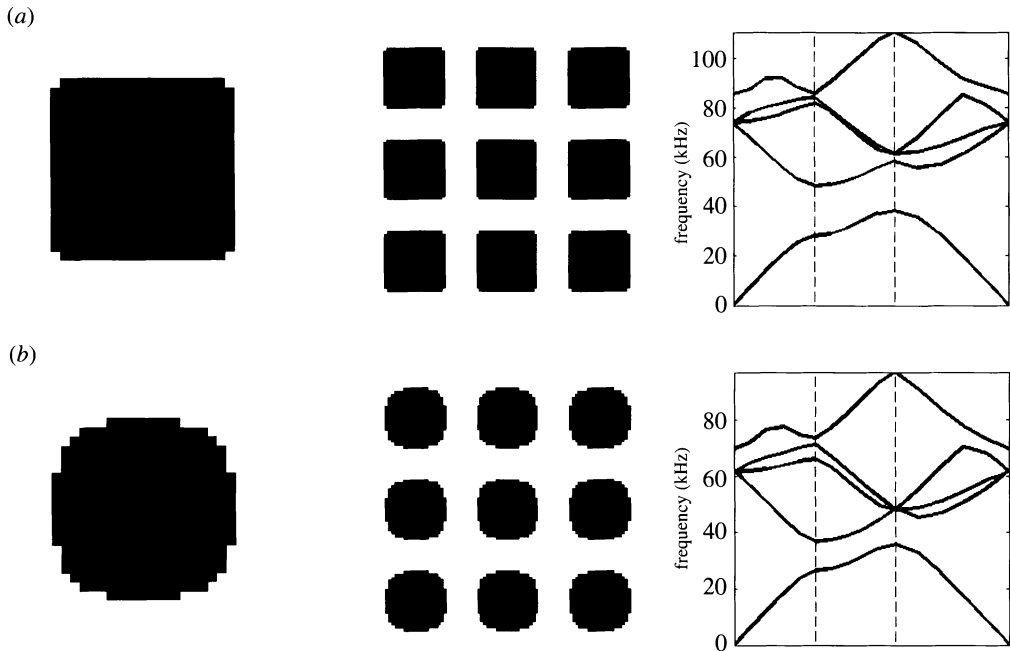


Figure 6. Material optimization based on out-of-plane modelling. Optimized topologies for maximization of relative size of the band gap between the first and the second bands: (a) high-contrast case; (b) low-contrast case. In both cases the base cell was discretized by 30×30 bilinear finite elements.

inclusions with small ‘ears’ almost independent of the phase contrast. The relative band-gap sizes are 0.21 for the high-contrast case and 0.001 (i.e. hardly a band gap) for the low-contrast case. For comparison, the relative band-gap sizes for perfect square inclusions with relative sizes 0.17 are 0.19 and -0.001 , respectively. In this case, it therefore cannot be concluded that the perfectly square inclusion is the optimal solution.

(b) Structural optimization

The material design problem in the previous subsection assumed infinite periodicity of the material. This means that neither the influence of boundaries nor the defects in the periodic structure could be modelled. In order to model finite domains, we use the wave equation (2.11) and the objective function here may be to minimize the magnitude of the wave at the boundaries (hinder wave propagation) or to maximize the wave magnitude at certain points in the structure (waveguiding).

An optimization problem solving the problem of minimizing the wave magnitude at a point, a line, or an area of a structure subjected to periodic loading with frequency Ω can be written as

$$\min_{\mathbf{x}} |\mathbf{u}|^T \mathbf{L} |\mathbf{u}| \quad \text{s.t.}: (\mathbf{K} + i\Omega \mathbf{C} - \Omega^2 \mathbf{M}) \mathbf{u} = \mathbf{f}, \quad 0 \leq x_e \leq 1, \quad e = 1, \dots, N, \quad (3.6)$$

where \mathbf{L} is a zero matrix with ones at the diagonal elements corresponding to the degrees of freedom of the nodes, lines or areas to be damped. Due to the complex

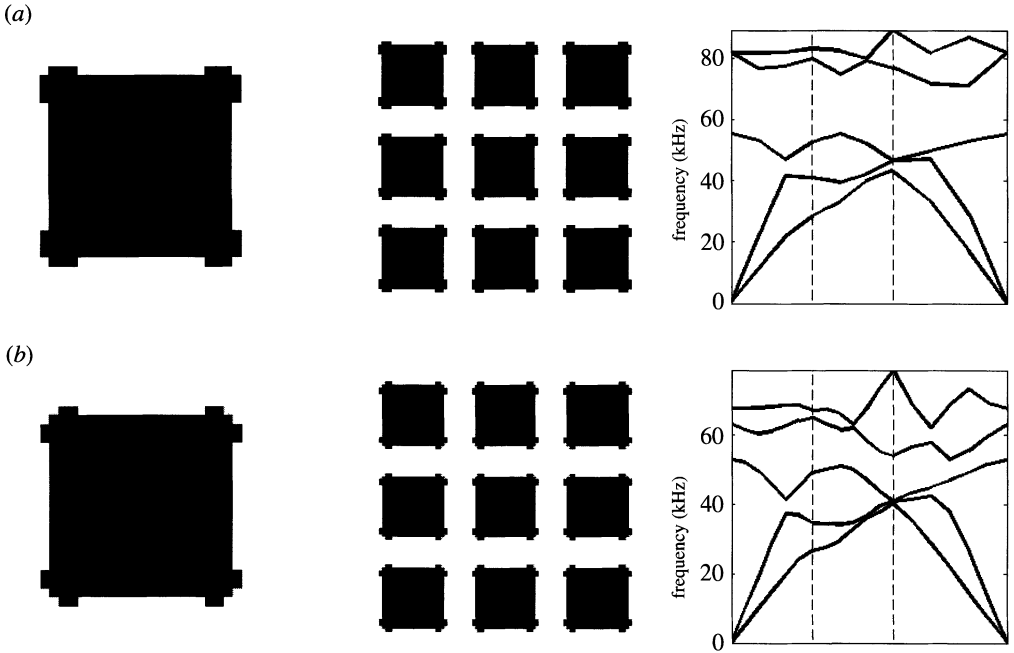


Figure 7. Material optimization based on in-plane modelling. Optimized topology for maximization of relative size of the band gap between the third and fourth bands: (a) high-contrast case; (b) low-contrast case.

damping term $i\Omega C$, the solution of (2.11) may be complex and, therefore, one must consider the magnitude of the output displacement in the objective function.

The sensitivities of the objective function can by the adjoint method be found to be

$$\frac{dc}{dx_e} = 2 \operatorname{Re} \left(\boldsymbol{\lambda}^T \left[\frac{d\mathbf{K}}{dx_e} + i\Omega \frac{d\mathbf{C}}{dx_e} - \Omega^2 \frac{d\mathbf{M}}{dx_e} \right] \mathbf{u} \right), \quad (3.7)$$

where $\operatorname{Re}(\cdot)$ means the real part and $\boldsymbol{\lambda}$ is the solution to

$$(\mathbf{K} + i\Omega \mathbf{C} - \Omega^2 \mathbf{M})^T \boldsymbol{\lambda} = -\mathbf{L}\bar{\mathbf{u}}, \quad (3.8)$$

where the overbar denotes the complex conjugate. As for the material problem, the MMA (Svanberg 1987) is applied to solve the optimization problem. The advantage of the adjoint sensitivity formulation is that only one extra load case needs to be solved (equation (3.8)) in order to obtain the sensitivity of the objective function for each design iteration.

As seen in figure 4, the undamped structural response, especially in the in-plane case, has a number of resonance peaks that must be attributed to reflections from the boundaries. This causes ill-convergence of the optimization algorithm. Therefore, we introduce material damping in all our design problems in order to filter away the reflecting waves and other disturbances. After the design process, we remove the damping and analyse the undamped structure. The resulting topologies using this approach are, in our experience, always better than the topologies obtained without damping.

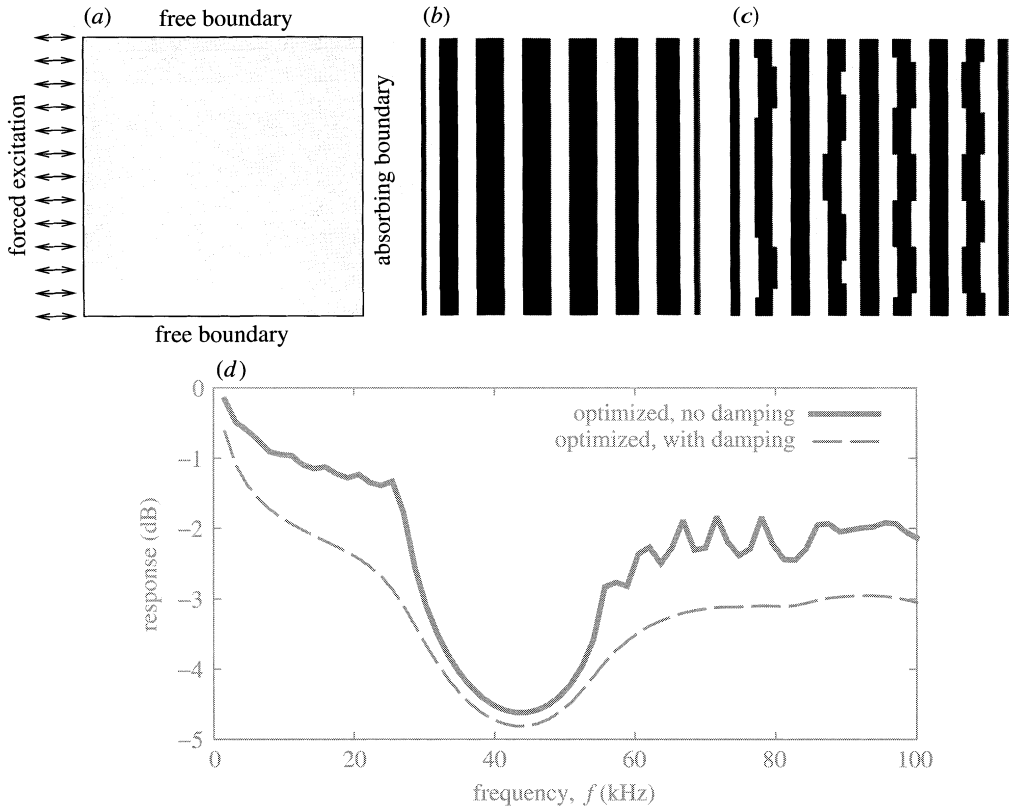


Figure 8. Damping of wave propagation in a quadratic plate for $f = 41$ kHz. (a) Design domain and boundary conditions; (b) optimized structure for high-contrast case; (c) optimized structure for low-contrast case; (d) frequency response for the high-contrast case. Dashed line, $\alpha = 0$, $\beta = 25 \times 10^3$; solid line, $\alpha = \beta = 0$.

In the following we show a number of examples with different combinations of object, boundary condition and out-of-plane/in-plane modelling. The examples are selected for illustrative purposes, and any other combinations of the above can be solved by simple changes in an input file.

(i) Results for out-of-plane waves

Figure 8 shows an example where the suggested optimization procedure is used to minimize wave propagation through a square plate. The left edge is subjected to forced vibrations with frequency $f = 41$ kHz (corresponding to the centre frequency of the gap of figure 3d); the left and right edges have absorbing boundary conditions, and the top and bottom edges are free. The objective is to minimize the average amplitude at the right edge. The resulting topologies are, not unexpectedly, a grid of alternating phase 1 and phase 2 materials corresponding to Bragg gratings. This structure is known to reflect one-dimensional (horizontally propagating) waves. The frequency response for the high-contrast case is shown in figure 8d. It is seen that there is a large band gap around the excitation frequency $f = 41$ kHz. Compared with the response of the square-inclusion structure from figure 5, where the input

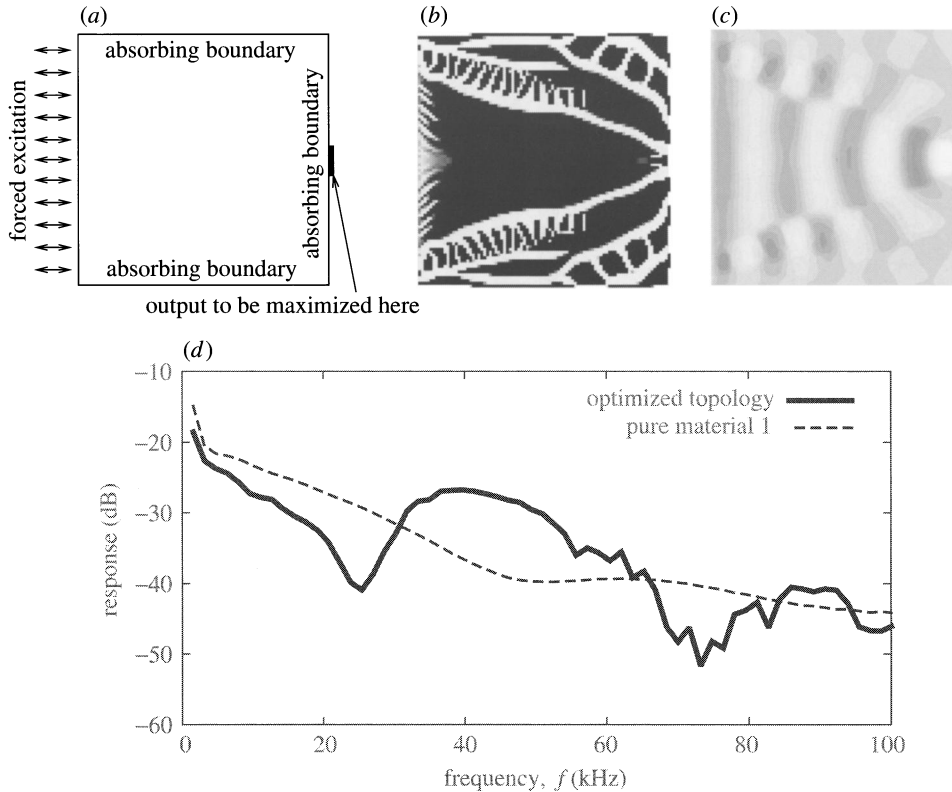


Figure 9. Optimization of waveguidance in a quadratic plate for $f = 41$ kHz. (a) Design domain and boundary conditions; (b) optimized structure in the high-contrast case; (c) the wave field; (d) frequency response of the structure ($\alpha = 0$, $\beta = 25 \times 10^3$).

signal was damped by 35 dB, the optimized Bragg-like topology damps the input signal by 70 dB. The resulting topology for the low-contrast case is seen in figure 8c. Again, the optimized topology is a Bragg-like grating but with a smaller volume fraction of phase 2 than in the high-contrast case.

The problem formulation may also be used to design waveguides (3.6) as shown in figure 9. Here, all edges have absorbing boundary conditions. The left edge is subjected to forced vibrations and the objective function is to *maximize* the wave magnitude at a small fixed vertical line around the centre of the right edge. The resulting structure is intriguing. Apparently, the wave is guided towards the output point through a cone of material 2. The cone is surrounded by a periodic structure that prevents the waves from escaping. It is seen from the wave picture (figure 9c) that the mode at the output port has been magnified by *ca.* 10 dB compared with that of a pure material 1 structure.

(ii) Results for in-plane waves

Figure 10 shows the results of the optimization of the high-contrast case for in-plane periodic modelling. We consider a $12 \text{ cm} \times 12 \text{ cm}$ structure and wish to distribute material 1 and material 2 such that the response is minimized for $f = 63$ kHz

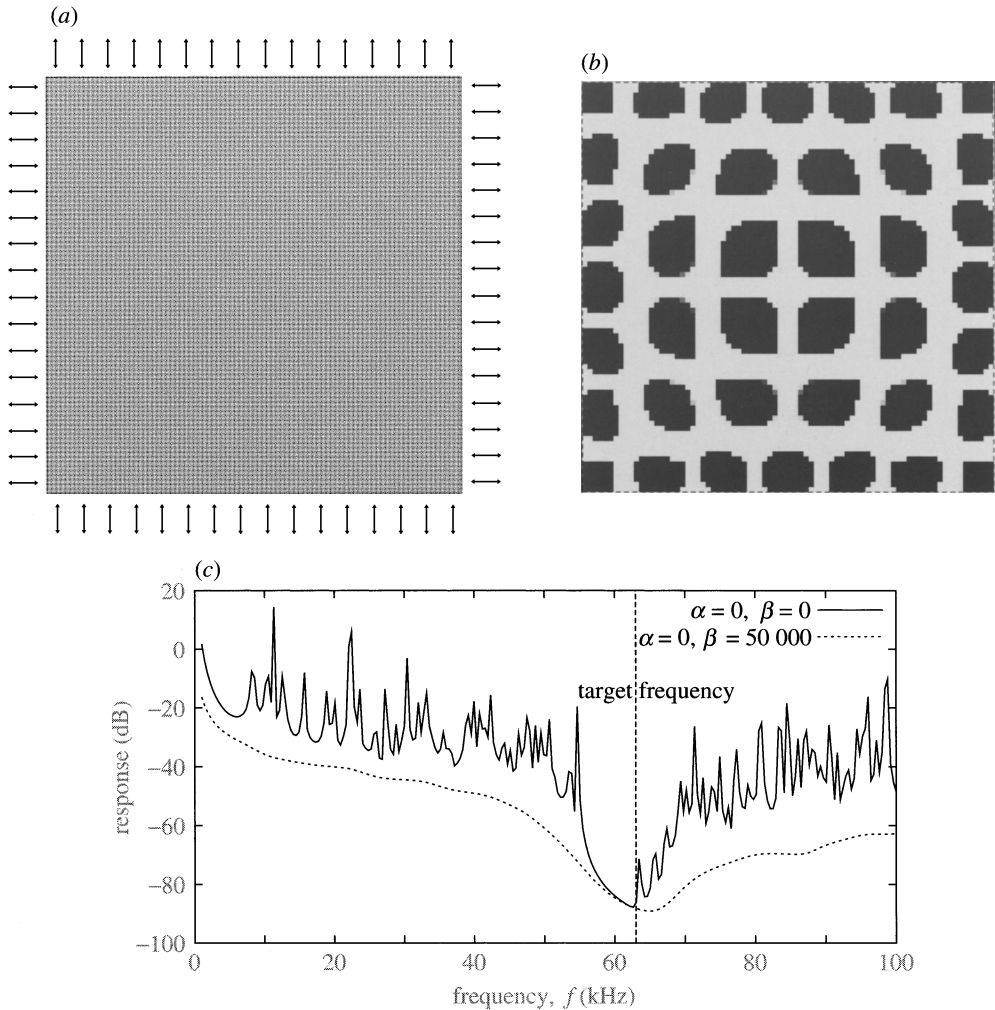


Figure 10. Optimization of structure for minimum response at $\Omega = 63$ kHz. (a) Structural domain and periodic boundary loading in the optimization procedure; (b) optimized topology; (c) average response at the right boundary when subjected to loading at the left boundary. Dashed line, $\alpha = 0, \beta = 50 \times 10^3$; solid line, $\alpha = \beta = 0$. High-contrast case.

(corresponding to the centre frequency of the optimized gap of figure 7b). In order to obtain square symmetry of the resulting structure, we this time solve a multi-load problem. The structure is subjected to periodic excitation at the four edges independently, and we then minimize the sum of responses at the opposing edges. The optimization is performed with strong damping added ($\alpha = 0, \beta = 50 \times 10^3$) in order to remove resonance peaks and ensure stable convergence.

Figure 10b shows the optimized structure. The topology is quasi-periodic and closely resembles the periodic band-gap structure in figure 4c. The largest difference between the two topologies is seen at the boundaries, where the finite structure has inclusions touching the boundaries and with a different periodicity. This prevents waves from propagating along the boundaries: a phenomenon that cannot be

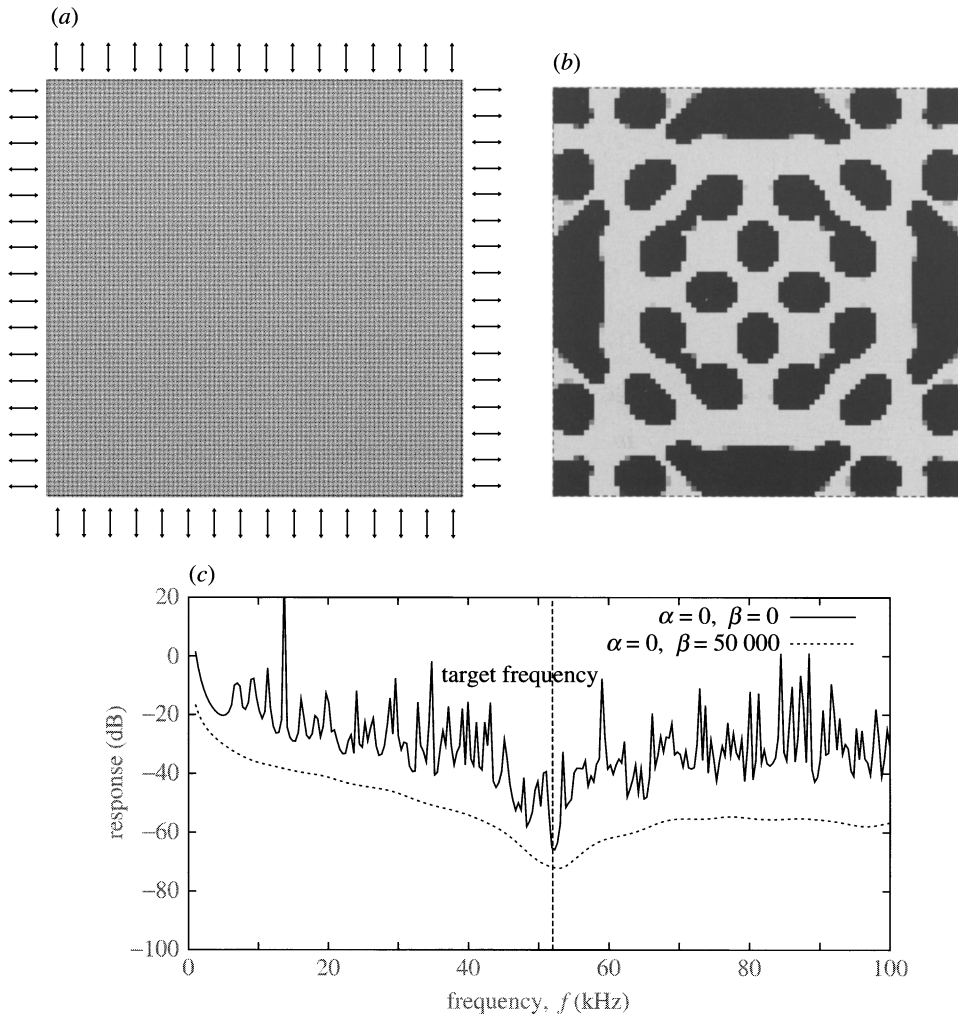


Figure 11. Optimization of structure for minimum response at $\Omega = 52$ kHz. (a) Structural domain and periodic boundary loading in the optimization procedure; (b) optimized topology; (c) average response at the right boundary when subjected to loading at the left boundary. Dashed line, $\alpha = 0, \beta = 50 \times 10^3$; solid line, $\alpha = \beta = 0$. Low-contrast case.

modelled in the material case. The corresponding response is seen in figure 10c. The response with strong damping is shown by the dashed line and that without damping by the solid line. Although the optimization was carried out with damping included, it is also seen that when the damping is removed there is a large drop in the response, due to the band gap. We have tried to continue the optimization with the topology in figure 10b as a starting guess but without damping. However, this does not result in a significant improvement of the objective function. This finding justifies our idea of stabilizing the optimization procedure by including (artificial) damping.

Next, we try to optimize the structure for the low-contrast case. In this case, there is no longer a gap in the band structure for the corresponding periodic material (cf.

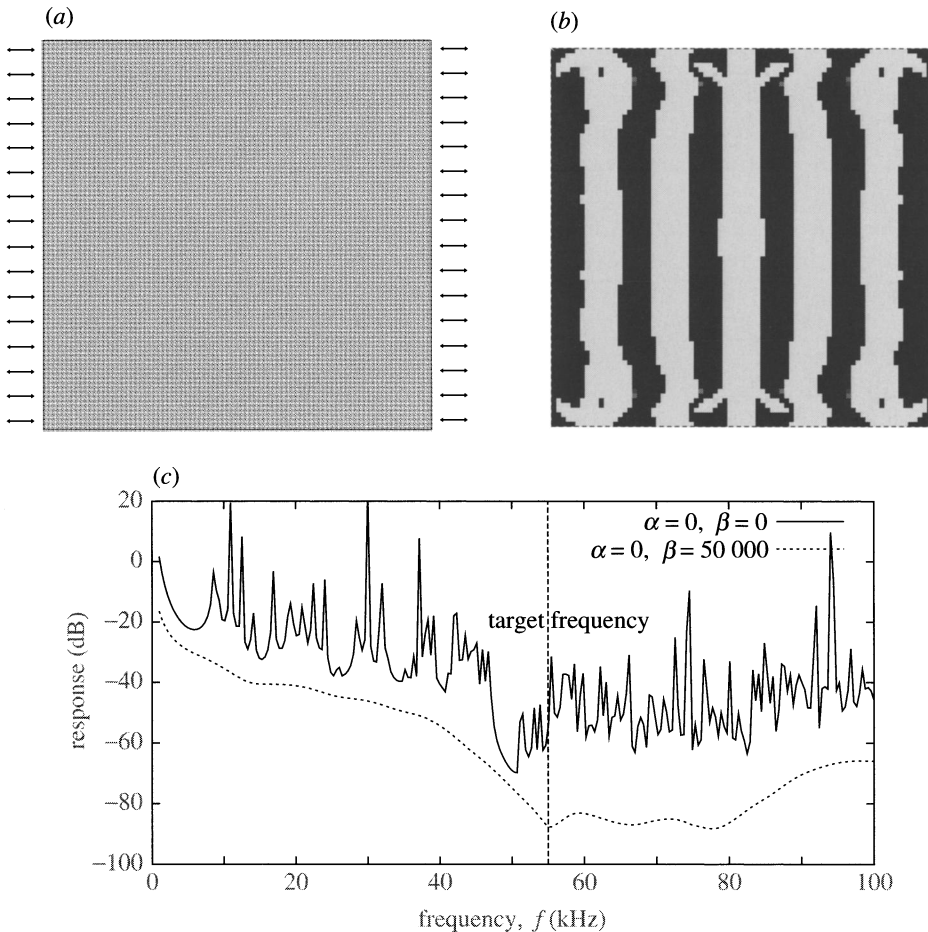


Figure 12. Optimization of structure for minimum response at $\Omega = 55$ kHz. (a) Structural domain and periodic boundary loading in the optimization procedure; (b) optimized topology; (c) average response at the right boundary when subjected to loading at the left boundary. Dashed line $\alpha = 0, \beta = 50 \times 10^3$; solid line, $\alpha = \beta = 0$. High-contrast case.

figure 7b). As a result, the optimized topology obtained for $f = 52$ kHz is no longer periodic (see figure 11b). The response shown in figure 11c only has a small reduction in the response when the damping is removed. Since we tried several different starting guesses that always led to the same conclusion, this example strongly indicates that design of a band gap for the low-contrast case and in-plane modelling is not possible.

Figure 12 shows the result of an optimization problem resembling the one in figure 8. Here the structure is subjected to loading at only two opposite boundaries (modelled as two separate loading cases). The optimized topology (figure 12b) is now seen to resemble a one-dimensional Bragg grating with some modifications near the boundaries. The response obtained with damping included (figure 12c) shows a reduction in response for a large frequency range (up to more than 80 kHz). However, the response with the damping removed is dominated by resonance peaks due to reflections at the boundaries.

4. Conclusion

We have demonstrated that topology optimization is an efficient tool for the design of materials and structures with band gaps. We have formulated two optimization problems: one for the maximization of band-gap sizes for infinitely periodic structures and the other for the design of finite structures with wave-stopping or waveguiding behaviours.

The proposed optimization formulations were used to design periodic band-gap materials with maximum relative band-gap size, and it was found that, at least for the scalar (out-of-plane) case, the optimum inclusion shape depends on the contrast in material properties between the material phases. For the structural problem we have demonstrated that the optimum band-gap materials for the finite case are close to periodic, although the inclusions close to the boundaries should be touching the rim in order to prevent surface modes from propagating along the boundaries. We have also shown an example of the design of a waveguide that concentrates a wide incoming wave to a narrow and magnified output wave. The size of problems solved was limited by MATLAB storage requirements. For future work we are rewriting the code to FORTRAN 90, which allows for larger problems. In MATLAB, typical computing times for an 80×80 element out-of-plane problem (such as figure 9) is *ca.* 5–6 h for 500 iterations. This time is expected to be significantly reduced by using the FORTRAN 90 code.

The issue of multiple local minima was not addressed in this paper, but, in the structural case, several optimized designs can be obtained by varying the initial value of the design variables. These designs will have different periodicities corresponding to different band gaps. However, in our experience, topologically different solutions obtained from different starting guesses usually have very similar objective function values.

The analysis was restricted to deal with the uncoupled problem of in-plane and out-of-plane waves. In the case where this decoupling cannot be performed, e.g. due to inclusions with out-of-plane misalignments or waves not initially propagating strictly in the plane, fully three-dimensional modelling is required. The effect of out-of-plane scattering and the design of three-dimensional structures are subjects for further work. In future work we will additionally consider improved objective functions and more advanced waveguiding problems.

This work received support from Denmark's Technical Research Council through the Talent/THOR Program 'Design of microelectromechanical systems (MEMS)' and the Research Project 'Phononic bandgap materials: analysis and optimization of wave transmission in periodic materials'. The authors express their gratitude to Professors Martin P. Bendsøe and Jon J. Thomsen, Technical University of Denmark, for valuable discussions and inspiration.

References

- Bendsøe, M. P. 1995 *Optimization of structural topology, shape and material*. Springer.
- Bendsøe, M. P. & Kikuchi, N. 1988 Generating optimal topologies in structural design using a homogenization method. *Comput. Meth. Appl. Mech. Engng* **71**, 197–224.
- Bendsøe, M. P. & Sigmund, O. 2003 *Topology optimization: theory, methods and applications*. Springer.
- Brillouin, L. 1953 *Wave propagation in periodic structures*, 2nd edn. New York: Dover.

- Cox, S. J. & Dobson, D. C. 1999 Maximizing band gaps in two-dimensional photonic crystals. *SIAM J. Appl. Math.* **59**, 2108–2120.
- Cox, S. J. & Dobson, D. C. 2000 Band structure optimization of two-dimensional photonic crystals in *H*-polarization. *J. Computat. Phys.* **158**, 214–224.
- Elachi, C. 1976 Waves in active and passive periodic structures: a review. *Proc. IEEE* **64**, 1666–1698.
- Joannopoulos, J. D., Meade, R. D. & Winn, J. N. 1995 *Photonic crystals*. Princeton, NJ: Princeton University Press.
- Kittel, C. 1986 *Solid state physics*. Wiley.
- Krenk, S. 2002 Unified formulation of radiation conditions for the wave equation. *Int. J. Numer. Meth. Engng* **53**, 275–295.
- Kushwaha, M. S. 1996 Classical band structure of periodic elastic composites. *Int. J. Mod. Phys. B* **10**, 977–1094.
- Liu, Z., Zhang, X., Mao, Y., Zhu, Y., Yang, Z., Chan, C. & Sheng, P. 2000 Locally resonant sonic materials. *Science* **289**, 1734–1736.
- Mathews, J. & Walker, R. 1964 *Mathematical methods of physics*. Addison-Wesley.
- Seyranian, A. P., Lund, E. & Olhoff, N. 1994 Multiple eigenvalues in structural optimization problems. *Struct. Optimiz.* **8**, 207–227.
- Sigalas, M. & Economou, E. 1992 Elastic and acoustic wave band structure. *J. Sound Vib.* **158**, 377–382.
- Sigmund, O. 1997 On the design of compliant mechanisms using topology optimization. *Mech. Struct. Mach.* **25**, 493–524.
- Sigmund, O. 2001a Design of multiphysics actuators using topology optimization. I. One-material structures. *Comput. Meth. Appl. Mech. Engng* **190**, 6577–6604.
- Sigmund, O. 2001b Design of multiphysics actuators using topology optimization. II. Two-material structures. *Comput. Meth. Appl. Mech. Engng* **190**, 6605–6627.
- Sigmund, O. 2001c Microstructural design of elastic band gap structures. In *WCSMO-4, Proc. 2nd World Cong. Structural and Multidisciplinary Optimization, Dalian, China*. Liaoning, China: Liaoning Electronic Press. (On CD-ROM.)
- Sigmund, O. & Jensen, J. S. 2002 Topology optimization of phononic band gap materials and structures. In *Proc. 5th World Congress on Computational Mechanics, Vienna, Austria* (ed. H. A. Mang, F. G. Rammerstorfer and J. Eberhardsteiner). (<http://wccm.tuwien.ac.at>.) Vienna University of Technology.
- Sigmund, O. & Torquato, S. 1997 Design of materials with extreme thermal expansion using a three-phase topology optimization method. *J. Mech. Phys. Solids* **45**, 1037–1067.
- Svanberg, K. 1987 The method of moving asymptotes: a new method for structural optimization. *Int. J. Numer. Meth. Engng* **24**, 359–373.
- Svanberg, K. 1998 The method of moving asymptotes: modelling aspects and solution schemes. In *Advanced Topics in Structural Optimization*, Report S81. Danish Center for Applied Mathematics and Mechanics.
- Vasseur, J., Deymier, P., Frantzikonis, G., Hong, G., Djafari-Rouhani, B. & Dobrzynski, L. 1998 Experimental evidence for the existence of absolute acoustic band gaps in two-dimensional periodic composite media. *J. Phys. Condens. Matter* **10**, 6051–6064.
- Yablonoitch, E. 2001 Photonic crystals: semiconductors of light. *Scient. Am.* **285**, 34–41.

Inverse design of phononic crystals by topology optimization

Søren Halkjær, Ole Sigmund and Jakob S. Jensen*

Technical University of Denmark, Department of Mechanical Engineering 2800 Kgs. Lyngby, Denmark

Received July 13, 2004; accepted December 9, 2004

Phononic crystal / Band gaps / Inverse design / Topology optimization

Abstract. Band gaps, i.e. frequency ranges for which waves cannot propagate, can be found in most elastic structures if the material or structure has a specific periodic modulation of material properties. In this paper, we maximize phononic band gaps for infinite periodic beams modelled by Timoshenko beam theory, for infinite periodic, thick and moderately thick plates, and for finite thick plates. Parallels are drawn between the different optimized crystals and structures and several new designs obtained using the topology optimization method.

Introduction

Phononic or sonic crystals (SCs) [1] offer a great variety of interesting and important design problems, e.g. how do we design crystals for maximum size of band gaps, i.e. the frequency ranges for which waves cannot propagate through the crystals, or how many crystals are needed in order to obtain the desired properties of a phononic crystal structure. Such design problems can usually be formulated as inverse problems: find the crystal or structure that satisfies some specified requirements. Determination of SC characteristics in form of e.g. band structures involves complex computations which typically makes the inverse design problem non-trivial. Most examples of solving this problem are based on size optimization using a few design variables and typically using genetic algorithms or other heuristic approaches. In this paper we solve three inverse design problems by using the topology optimization method which is based on a gradient-based algorithm with a large number of design variables and practically unlimited design freedom.

Topology optimization has in the last decade evolved as a popular design tool in structural and material mechanics [2]. The first design problem to be solved was to find the optimal distribution of a restricted amount of material in a given domain that gives the stiffest possible structure [3]. Another design problem was to identify the material that has the lowest (negative!) Poisson's ratio [4]. The method is based on repeated material re-distributions

using a large number of continuous design variables, typically one for each element in the corresponding discretized model, and the use of computationally in-expensive analytical sensitivity analysis and advanced mathematical programming tools. Lately the method has been applied to other problems in alternative physics settings as well, ranging from MEMS and fluid dynamics to electromagnetics (see [2] for an overview).

In the closely related research area of photonic crystals (PhCs) inverse design methods have received an increased focus [5] due to the potential large application possibilities for using PhCs in optical circuits. Cox and Dobson [6] used a material distribution method to design two-dimensional square photonic crystals with maximum band gaps. The references [7, 8] applied the topology optimization method to design photonic crystal waveguides. More traditional studies of photonic crystal structures using a few design variables and optimization based on either numerical sensitivity analysis, genetic algorithms, simulated annealing or a combination of these are seen in Refs. [9, 10].

This study extends the results published in a recent paper [11] which presented some results for maximizing the band gap size of square lattice two-dimensional SCs and optimization of finite structures subjected to periodic loading. Here, we present results for maximizing the band gap size for bending and longitudinal waves in rods modelled by Timoshenko beam theory¹, we optimize 2D crystals with quadratic and hexagonal base cells for inplane and bending waves, and finally present examples of optimized finite-size structures subjected to in-plane polarized waves. In previous work [13] we have performed experiments on simple longitudinal waves propagating in a 1D SC composed of PMMA and Aluminum. Since we plan to extend these experiments to plate and shell structures, we will throughout this paper make use of these two materials. The results of this paper will be used in the planning of the experiments.

Inverse design by topology optimization

The topology optimization method is a gradient-based optimization algorithm that is used to find optimal material

* Correspondence author (e-mail: jsj@mek.dtu.dk)

¹ A modelling study has previously been performed based on Bernoulli-Euler beam theory [12].

distributions. The design variables are spatial material densities. By using analytical sensitivity analysis and mathematical programming tools it is possible efficiently to handle a large number of design variables. We base our implementation on Finite Element (FE) modelling and typically choose one continuous design variable per element or node:

$$\zeta_e \in \mathbb{R}, \quad e = 1, \dots, N, \quad (1)$$

where N is the number of finite elements or nodes in the design domain. It should be emphasized that the method can be used with a finite difference discretization just as easily and that more design variables can be assigned to each element in order to distribute more than two materials in the design domain.

The goal for the optimization algorithm is to distribute two materials in a domain such that some cost function is minimized (or maximized). The continuous design variables control the material distribution by defining the element-wise constant material properties in each element. If ϱ_e denotes an element-wise property we can write:

$$\varrho_e = (1 - \zeta_e) \varrho_1 + \zeta_e \varrho_2 \quad (2)$$

where subscript 1 and 2 refers to the properties of material 1 and material 2, respectively. In this case we let ζ_e vary continuously between 0 and 1, such that for $\zeta_e = 0$ the corresponding element takes the material properties of material 1 and for $\zeta_e = 1$ those of material 2.

Denoting the cost function Φ we can now formulate the optimization problem as follows:

$$\min_{\zeta} \Phi = \Phi(\omega, \mathbf{u}, \zeta), \quad (3)$$

$$\text{s.t.}: g_i(\zeta) \leq g_i^*, \quad (4)$$

$$0 \leq \zeta_e \leq 1, \quad e = 1, \dots, N, \quad (5)$$

$$(\mathbf{K} - \omega^2 \mathbf{M}) \mathbf{u} = \mathbf{f}, \quad (6)$$

where Eq. (6) is the discretized FE equation of the time-harmonic wave propagation problem. The vector \mathbf{u} contains the discretized nodal values of the complex amplitudes of the displacement field, and \mathbf{K} and \mathbf{M} are the stiffness and mass matrices, respectively. The load vector \mathbf{f} comes from external wave loading. In (4) a number of additional constraints can be specified, e.g. specifying a maximum amount of a single material component. For more details about computational procedures, sensitivity analysis and more, the reader is referred to [2].

The advantage of using continuous design variables is that it allows for the use of efficient gradient-based optimization algorithms. However, it also implies that we may end up with values of ζ_e that are neither 0 or 1, but an intermediate value that does not correspond to any of the two materials. There are several ways to penalize the appearance of intermediate density solutions (see e.g. [2]), however, it is our experience that intermediate densities seldomly remain in the optimized band gap designs since band gaps are favoured by maximum contrast in the material properties. Therefore we have not used any penalization techniques in this work.

As for all topology optimization problems with spatial material distribution the results depend on the mesh. How-

ever, as opposed to conventional stiffness design problems where the objective is improved with mesh-refinement, it appears that the finite length of the elastic waves imposes a length-scale for the present band gap design problems and thus we do usually not experience a significant mesh-dependence. Therefore, we do not use regularization techniques in this paper. For more discussions of this issue, the reader is referred to [2]. Concerning the convergence of the finite element model, we require discretizations that at least have 10 elements pr. wave-length. Due to the reasons discussed above, we do not expect to find significantly different design solutions if the mesh is further refined.

Design of 1D structures: the infinite periodic elastic beam

In this section, we study elastic wave propagation in a periodic beam of infinite length. The beam consists of an infinite number of copies of a *base cell* with a specific geometry and material distribution. The periodicity introduces frequency band gaps for both longitudinal and bending waves, preventing waves with frequencies in these gaps from propagating in the beam. In general, the band gap frequency ranges for the two wave types are different, but for certain geometries and material distributions of the base cell, band gaps for the two wave types overlap, preventing both of the two wave types from propagating in the beam. Such studies are relevant in design problems where vibration insulation and filtering are important objectives.

Theory

Let the beam axis be directed along the x -axis. Longitudinal wave propagation in the beam is described using the usual 1D theory

$$\frac{\partial}{\partial x} \left(E \frac{\partial u}{\partial x} \right) = \rho \frac{\partial^2 u}{\partial \tau^2} \quad (7)$$

where $u = u(x, \tau)$ denotes the displacement along the x -axis. ρ denotes the mass density and E is Young's modulus.

Bending waves in the beam are described by Timoshenko theory

$$\frac{\partial}{\partial x} \left(k_s GA \left(\frac{\partial w}{\partial x} + \theta \right) \right) = \rho A \frac{\partial^2 w}{\partial \tau^2}, \quad (8)$$

$$\frac{\partial}{\partial x} \left(EI \frac{\partial \theta}{\partial x} \right) - k_s GA \left(\frac{\partial w}{\partial x} + \theta \right) = \rho I \frac{\partial^2 \theta}{\partial \tau^2} \quad (9)$$

where $w = w(x, \tau)$ and $\theta = \theta(x, \tau)$ denote the transverse displacement and angle of rotation of the cross-section respectively. A , I , G and k_s denote the cross-sectional area, area moment of inertia, shear modulus and the shear correction coefficient, respectively. Here, we use $k_s = 6(1 + \nu)/(7 + 6\nu)$ [14] for a circular cross-section, where ν is the Poisson ratio. Timoshenko theory is used, as the ratio between considered wave length and cross-section dimension is smaller than the lower bound (≈ 20) for using the simpler Bernoulli-Euler theory.

While the above PDEs may be solved analytically for uniform and homogeneous beams, numerical methods like the FE Method must be resorted to when considering periodic in-homogeneous structures as will be the case here. Let a base cell of length d be divided into N finite elements. For longitudinal wave motion, the $N + 1$ degrees of freedom (d.o.f) are the nodal longitudinal displacements, while for bending waves the $2(N + 1)$ d.o.f. are the nodal transverse displacements and the rotation of the cross-section. For each of the two wave type problems, the global stiffness matrix \mathbf{K} and mass matrix \mathbf{M} for the base cell are assembled in the usual manner from the corresponding element matrices. For longitudinal waves the element matrices are 2×2 matrices using first order polynomials as shape function for u [15]. For bending waves, the element matrices are 4×4 matrices using third and second order polynomials as shape functions for w and θ respectively [14]. According to Bloch theory [16], the periodic boundary condition at the ends of the base cell becomes for longitudinal waves

$$u_N = u_1 e^{ik^B}$$

where $k^B = kd$ is the Bloch parameter and k the wave number. Due to reasons of periodicity, $0 \leq k^B \leq \pi$. Similarly for bending waves, the periodic boundary conditions become

$$\begin{aligned} w_N &= w_1 e^{ik^B}, \\ \theta_N &= \theta_1 e^{ik^B}. \end{aligned}$$

These boundary conditions must be incorporated into the corresponding stiffness matrices.

Assuming time harmonic motion with circular frequency ω the two eigenvalue problems become

$$\mathbf{K}_i(k^B) \mathbf{u}_i = \lambda_i \mathbf{M}_i \mathbf{u}_i, \quad \lambda_i = \omega_i^2, \quad i = L, B \quad (10)$$

where \mathbf{u}_i contains the nodal values of the variables, $L =$ longitudinal waves and $B =$ bending waves. The dependence on k^B is shown explicitly.

The stiffness and mass matrices \mathbf{K} and \mathbf{M} depend in general on the cross-sectional geometry, length of base cell and material parameters. Here we choose a fixed circular cross-section of radius $r = 0.5$ cm, such that we end up with only the longitudinally varying material properties and the cell length as design variables. As discussed in the previous section, the goal is to find the distribution of two *a priori* chosen materials in the base cell, that results in the largest band gaps as calculated by (10). We choose a continuous design variable $0 \leq \zeta_e \leq 1$, $\zeta_e = 1, \dots, N$ for each element, that interpolates between the two chosen materials. In our model (10), there are three material parameters E , ρ and ν introduced above. We thus have the following three material interpolation functions on the form (2)

$$\begin{aligned} E(\zeta_e) &= (1 - \zeta_e) E_1 + \zeta_e E_2, \\ \rho(\zeta_e) &= (1 - \zeta_e) \rho_1 + \zeta_e \rho_2, \\ \nu(\zeta_e) &= (1 - \zeta_e) \nu_1 + \zeta_e \nu_2. \end{aligned}$$

The subscript $i = 1, 2$ denotes one of the two materials.

Finally, we also let the base cell length d be a design parameter, such that the cell length can be optimized.

Table 1. Material properties for the two materials used in the numerical example.

Material	ρ [kg/m ³]	E [GPa]	ν
Aluminium	2830	70.9	0.34
PMMA	1200	5.28	0.40

The optimization problem

For each of the two wave type problems, we can state the problem of maximizing the relative band gap between frequency bands j and $j + 1$

$$\max_{\substack{\zeta \in [0, 1]^N \\ d \in [d_{\min}, d_{\max}]}} : \Phi(\zeta, d) = 2 \frac{\min_{k^B \in [0, \pi]} \omega_{j+1} - \max_{k^B \in [0, \pi]} \omega_j}{\min_{k^B \in [0, \pi]} \omega_{j+1} + \max_{k^B \in [0, \pi]} \omega_j}. \quad (11)$$

For 1D problems, finding the minimum/maximum of the involved frequencies over k^B in (11) can be avoided, since empirically it is known that the frequency bands are alternating monotonic (for the purpose of illustration, consult Fig. 1). Therefore the minimum band gap between two consecutive bands will occur at $k^B = \pi$ for $j = 1, 3, 5, \dots$ and at $k^B = 0$ for $j = 2, 4, 6, \dots$. The maximization problem (11) is solved iteratively using the method of moving asymptotes MMA [17], which is based on a gradient descent approach.

For the coupled problem of maximizing the overlap between band gaps for longitudinal and bending waves, the formulation becomes

$$\begin{aligned} \max_{\substack{\zeta \in [0, 1]^N \\ d \in [d_{\min}, d_{\max}]}} : \Phi(\zeta, d) \\ = 2 \frac{\min(\omega_{j+1}^L, \omega_{i+1}^B) - \max(\omega_j^L, \omega_i^B)}{\min(\omega_{j+1}^L, \omega_{i+1}^B) + \max(\omega_j^L, \omega_i^B)} \end{aligned} \quad (12)$$

where $i, i + 1$ denote the bending frequency bands and $j, j + 1$ denote the longitudinal frequency bands.

The FE problem (10) together with either (11) or (12) are the problem specific equivalents to (3) and (6) in the general formulation.

Numerical examples

We now study an actual maximization problem considering the two materials Aluminum (Material 1) and PMMA (Material 2) with material properties listed in Table 1. Comparing the two materials, Aluminum is the heavy and stiff material while PMMA is the light and soft material.

As a first example, the relative band gap between the first and second frequency band ($j = 1$) for longitudinal waves has been maximized. The resulting design is shown in Fig. 1. From (10) and (11) it can be shown, that the relative band gap sizes are independent of the base cell length. In the maximization algorithm this variable has been fixed at a value of $d = 8.70$ cm for reasons that will be explained later. It is seen that the algorithm has chosen the two extreme materials 1 and 2 (corresponding to $\zeta_e = 0, 1$ on the y -axis) instead of interpolations of the two. This is interpreted as favouring high contrast in the

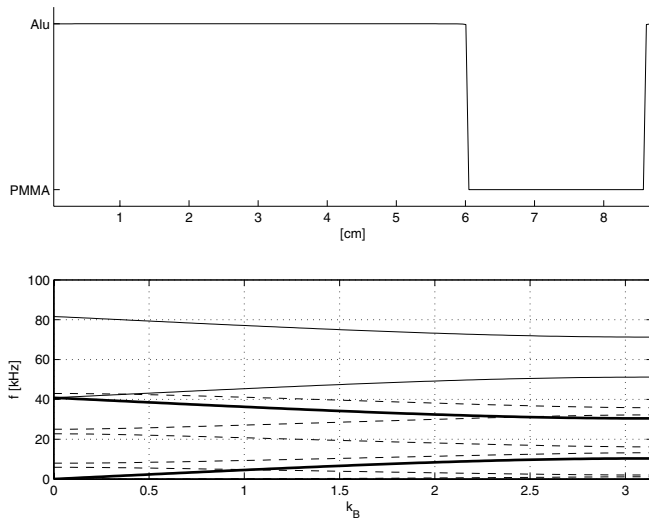


Fig. 1. Final design corresponding to maximum relative band gap between first and second band (thick lines) for longitudinal waves. Full lines: Longitudinal waves. Dashed lines: Bending waves.

Table 2. Extreme frequency band values for longitudinal waves in Figure 1. Unit is kHz.

	$k^B = 0$	$k^B = \pi$
f_1	0	10.367
f_2	40.798	30.452
f_3	40.844	51.191
f_4	81.603	71.283

design. It should be noted, that if another base cell length was chosen, no qualitative change would be observed and the ratio of the two material lengths would be the same. With this said, PMMA occupies approximately a fraction of 0.29 of the base cell length. That is, the larger part of the base cell is made up of the heavy and stiff material while a smaller part is occupied by the light and soft material. Figure 1 (bottom) also shows the lowest frequency bands for both longitudinal and bending waves, the latter just to indicate their position. The extreme edge values of the bands are listed in Table 2. The first three relative band gap sizes are listed in Table 6 (second column). The symbols in the first column denote band gap number and wave type considered, e.g. Φ_{12}^L denotes the band gap between the first and second frequency band and L indicates, that longitudinal waves are considered.

As a second example the relative band gap between the third and fourth band for bending waves has been maximized. The resulting design and frequency bands are shown in Fig. 2. In this case, increasing or decreasing the base cell length results in an increasing relative band gap size mainly due to vertical displacements of the frequency bands. This effect has been excluded by choosing the same constant base cell length as in the previous case $d = 8.70$ cm. This design problem appears to have many local minima, some of which result in designs consisting of mixtures of the two materials (i.e. $\zeta_e \neq 0, 1$), depending on the starting point. The design shown in Fig. 2 has the largest relative band gap of several trials and furthermore

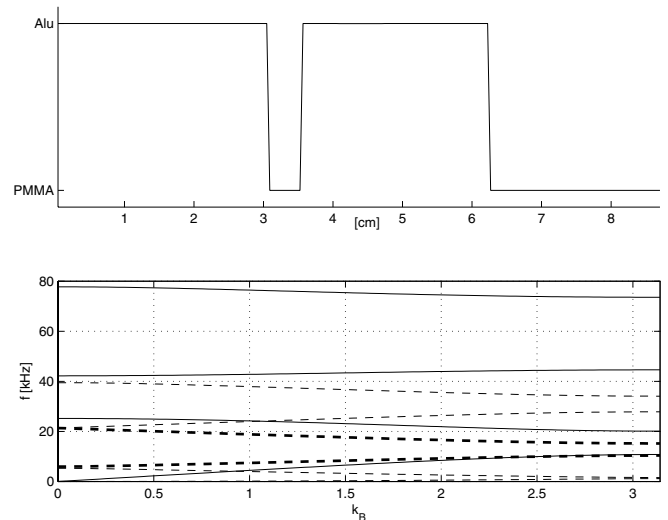


Fig. 2. Final design corresponding to maximum relative band gap between third and fourth band (thick lines) for bending waves. Full lines: Longitudinal waves. Dashed lines: Bending waves.

Table 3. Extreme frequency band values for bending waves in Fig. 2. Unit is kHz.

	$k^B = 0$	$k^B = \pi$
f_1	0	1.1508
f_2	5.2781	1.5692
f_3	5.9316	10.363
f_4	21.302	15.194
f_5	21.415	27.832
f_6	39.457	34.075

has a pure 0/1 design. The majority of the cell is again occupied by the heavy and stiff material while a smaller part (around a fraction of 0.33) is occupied by the light and soft material. However, this time the light material is distributed in two different parts. The extreme frequency band values are listed in Table 3. The first three relative band gaps are listed in Table 6 (third column).

As the last optimization example, the design resulting from maximizing the overlap between the first and second longitudinal band and the third and fourth bending band is shown in Fig. 3 together with the frequency bands. These band gaps are chosen because they have overlaps initially. An optimized base cell length of $d = 8.70$ cm is found by the algorithm in this case (which is the reason for choosing this value in the previous two cases). The unique solution is a result of the frequency bands for the two wave types moving in the same direction but with different speeds as a function of base cell length. The design is quite similar to the design in the bending case. A larger part of the light material occupies the same amount of the cell as in the bending case, while the narrow part has decreased compared to the bending case. The extreme values for the different frequency bands are tabulated in Table 4. The relative band gaps for the separate wave types as well as for the combined problem are shown in Table 6 (fourth column) with Φ denoting the overlapping band gap for the combined problem. As expected, the first longitudinal

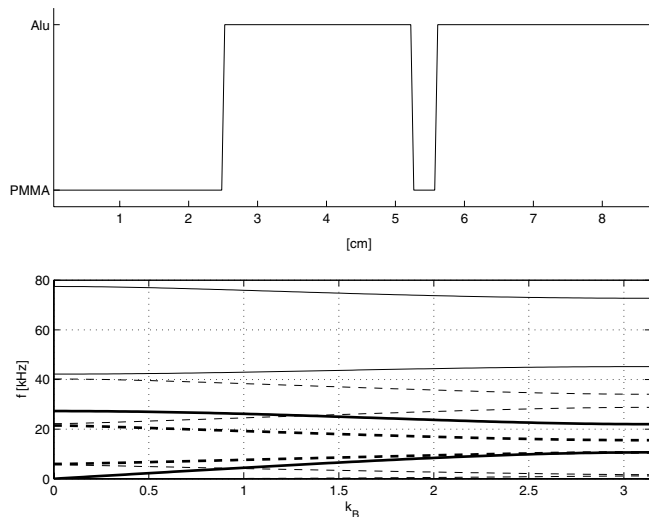


Fig. 3. Final design corresponding to maximum relative band gap between first and second band for longitudinal waves and third and fourth band for bending waves. Full lines: Longitudinal waves. Dashed lines: Bending waves.

Table 4. Extreme frequency band values for bending and longitudinal waves in Fig. 3. Unit is kHz.

	B waves		L waves	
	$k^B = 0$	$k^B = \pi$	$k^B = 0$	$k^B = \pi$
f_1	0	1.145	0	10.643
f_2	5.6165	1.6585	27.272	21.993
f_3	5.9774	10.643	42.172	45.188
f_4	21.454	15.534	77.451	72.706

band gap is smaller than the corresponding first (optimized) relative band gap for the single longitudinal case, while the second and third are actually larger. Also, the third relative band gap for bending waves is smaller (but not much) than the corresponding third (optimized) relative band gap for the single bending case. The similarity between this design and the bending case design (they are almost each other's mirrors) is also reflected in their performances, which are very close (relative band gaps of 0.374 and 0.378).

Torsion waves in a beam are described by the same differential equation as for longitudinal waves, but with the factor $\frac{E}{2(1+\nu)} \frac{K}{I}$ replacing E . Here I is the area moment of inertia as before and K is the torsion stiffness cross-sectional factor. For a circular cross-section $K = I$ and it may be seen that the torsional frequencies are lower than the longitudinal frequencies by a factor of $\sqrt{2(1+\nu)} \approx 1.6$. Comparing the torsional frequency bands with the bands in Fig. 3 for the optimized design in the combined case shows that there is a band gap between 10.6–13.2 kHz (relative band gap 0.43) for all three wave types, i.e. in this interval all three wave types are prevented from propagating in the beam.

Since for all geometries $\frac{K}{I} \leq 1$ (with “=” only for circular cross-sections), it is not possible to obtain $\frac{K}{I} = 2(1+\nu)$ which would result in perfectly coinciding

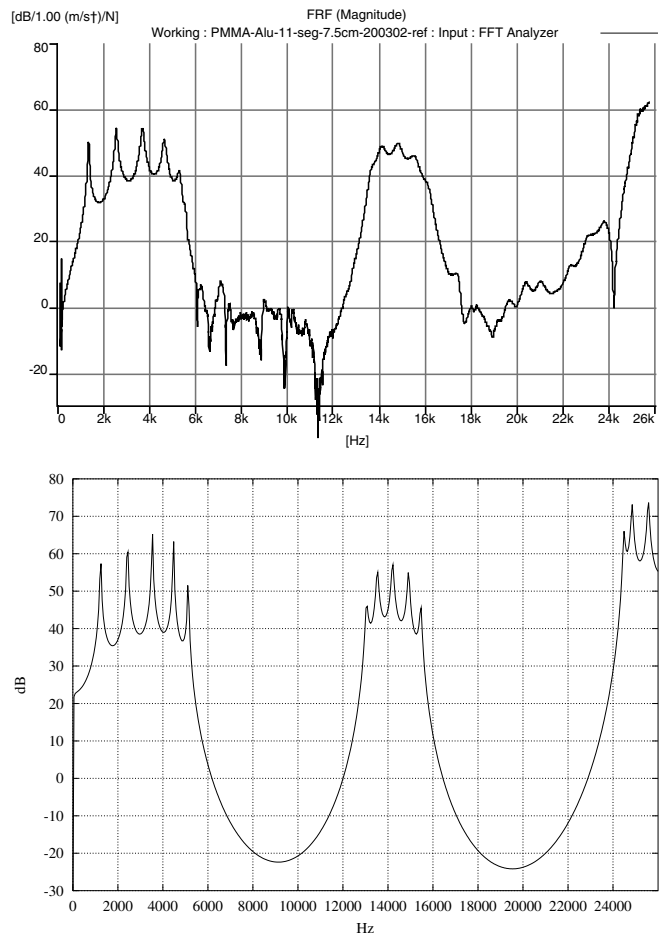


Fig. 4. Frequency response curves from [13]. Top: Experimental. Bottom: Theoretical.

Table 5. Frequency band gaps in Fig. 4 determined by inspection. Unit is kHz.

f_1^{\min}	f_1^{\max}	f_2^{\min}	f_2^{\max}
5.1	13.1	15.4	24.3

torsional and longitudinal bands. To increase the common gap size, one may consider lowering the mid-gap values between higher torsional modes. This can be obtained by decreasing the ratio $\frac{K}{I}$ which can be achieved by choosing a non-circular cross-section. This aspect will be investigated in future work.

In the following, the above results are compared with the experimental results presented in [13]. Here, the set-up is a (non-optimized) bar made up of five-and-a-half repetitions of a base section consisting of two bars glued together with circular cross-sections with diameter 1 cm and made of PMMA and Aluminum respectively, as in the above case. Each bar is 7.5 cm resulting in a base cell with a length of 15 cm. An experimental response curve showing the acceleration response at the end of the bar as a function of the longitudinal vibration excitation frequency applied to the opposite end is shown in Fig. 4 (upper) with a corresponding theoretical prediction shown below. The 40 dB horizontal line has been used to identify

Table 6. Relative band gap sizes for the three different beam maximization problems and [13] (non-optimized rod with equal volume fractions of Aluminium and PMMA). Gaps with numbers in bold have been optimized.

	L	B	LB	L [13]
Φ_{12}^L	0.9841		0.6956	0.8791
Φ_{23}^L	0.0011		0.4291	0.4484
Φ_{34}^L	0.3281		0.4668	
Φ_{12}^B		0.3076	0.3663	
Φ_{23}^B		0.1166	0.0623	
Φ_{34}^B		0.3781	0.3737	
Φ			0.3737	

the beginning and end of the two pronounced band gaps in the figure. Their values are listed in Table 5. The relative band gaps are shown in Table 6 (fifth column).

An infinite periodic beam with this base cell was analysed using (10) and the frequency bands and gaps were calculated to compare with the experimental results. Very good agreement was found.

The relative band gaps for the current problem are higher than those for the coupled problem in Fig. 3. Comparing with the longitudinal results in Fig. 1, the latter performs better for the first band gap as expected. Thus, the optimized design is superior to the non-optimized design for the first band gap considered.

Design of infinite 2D crystals

In this section we consider the design of infinite two dimensional crystals with maximum relative band gap sizes. We optimize the crystals for in-plane polarized elastic waves assuming very thick plates (i.e. plane strain assumption) and for bending waves assuming moderately thick plates (using Mindlin plate theory for the same reason as considering Timoshenko theory in the previous section).

In-plane polarized wave propagation in thick elastic plates is governed by the Navier equations

$$\frac{\partial}{\partial x} \left((\lambda + 2\mu) \frac{\partial u}{\partial x} + \lambda \frac{\partial v}{\partial y} \right) + \frac{\partial}{\partial y} \left(\mu \frac{\partial v}{\partial x} + \mu \frac{\partial u}{\partial y} \right) + \rho \omega^2 u = 0, \quad (13)$$

$$\frac{\partial}{\partial x} \left(\mu \frac{\partial u}{\partial y} + \mu \frac{\partial v}{\partial x} \right) + \frac{\partial}{\partial y} \left((\lambda + 2\mu) \frac{\partial v}{\partial y} + \lambda \frac{\partial u}{\partial x} \right) + \rho \omega^2 v = 0, \quad (14)$$

where u and v are the two amplitude components and λ , μ are the Lamé parameters, defined as $\lambda = E\nu/((1-2\nu)(1+\nu))$, $\mu = E/(2(1+\nu))$. The out-of-plane case is not considered here.

For bending waves in up to moderately thick plates the governing equations are

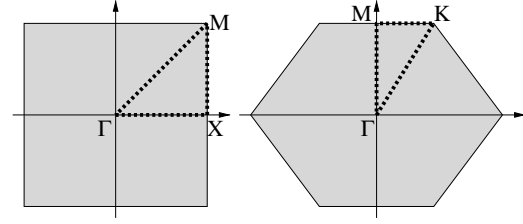


Fig. 5. Irreducible Brillouin zones for square and rhombic base cells.

$$\begin{aligned} & -\frac{\partial}{\partial x} \left(D \frac{\partial \Theta_x}{\partial x} \right) - \frac{\partial}{\partial y} \left((1-\nu) \frac{D}{2} \frac{\partial \Theta_x}{\partial y} \right) \\ & -\frac{\partial}{\partial x} \left(\nu D \frac{\partial \Theta_y}{\partial y} \right) - \frac{\partial}{\partial y} \left((1-\nu) \frac{D}{2} \frac{\partial \Theta_y}{\partial x} \right) \\ & - Gkt \left(\frac{\partial w}{\partial x} - \Theta_x \right) = \frac{\rho t^3}{12} \frac{d^2 \Theta_x}{dt^2}, \end{aligned} \quad (15)$$

$$\begin{aligned} & -\frac{\partial}{\partial y} \left(\nu D \frac{\partial \Theta_x}{\partial x} \right) - \frac{\partial}{\partial x} \left((1-\nu) \frac{D}{2} \frac{\partial \Theta_x}{\partial y} \right) \\ & -\frac{\partial}{\partial x} \left((1-\nu) \frac{D}{2} \frac{\partial \Theta_y}{\partial x} \right) - \frac{\partial}{\partial y} \left(D \frac{\partial \Theta_y}{\partial y} \right) \\ & - Gkt \left(\frac{\partial w}{\partial y} - \Theta_y \right) = \frac{\rho t^3}{12} \frac{d^2 \Theta_y}{dt^2}, \end{aligned} \quad (16)$$

$$\begin{aligned} & -\frac{\partial}{\partial x} \left(Gkt \frac{\partial w}{\partial x} \right) - \frac{\partial}{\partial y} \left(Gkt \frac{\partial w}{\partial y} \right) \\ & + \frac{\partial}{\partial x} (Gkt \Theta_x) + \frac{\partial}{\partial y} (Gkt \Theta_y) = \rho t \frac{d^2 w}{dt^2}, \end{aligned} \quad (17)$$

where t is the plate thickness and other values are defined previously. Θ_x denotes the angle between the x -axis and a cross-section in the yz -plane, and similarly for Θ_y . Here, in-plane modes are ignored. Note that for $\nu = 0$ and no variation in the y -direction, Eqs. (15) and (17) correspond exactly to the equations for Timoshenko beam theory (8) and (9).

In both cases, the periodicity conditions for the base cell are again given by Bloch theory, e.g.

$$w(\mathbf{r} + \mathbf{R}) = e^{i\mathbf{R} \cdot \mathbf{k}} w(\mathbf{r}) \quad (18)$$

and likewise for the other degrees of freedom. Here \mathbf{R} is a lattice vector and \mathbf{k} the (two-dimensional) wave vector. The dynamic response of the 2D crystals can be obtained by solving Eqs. (13)–(14) or (15)–(17) with boundary conditions (18) for wave vectors within the irreducible Brillouin zone. The irreducible Brillouin zones for quadratic and rhombic base cells are shown in Fig. 5. Assuming isotropic constituents and imposing 90 degree symmetry in the square cells and 60 degree symmetry in the rhombic cells, the irreducible zones can be further reduced to the triangles indicated in the figure. Finally, it is the experience that the size of the band gap can be measured by performing analyses only for wave vectors on the edge of the triangular zones thus saving significantly in CPU-time.

The analysis is performed using the commercial FE program FEMLAB which can be called from a MATLAB script that includes the optimization routine Method of Moving Asymptotes [17]. Triangular first order elements have been used in the FE analysis.

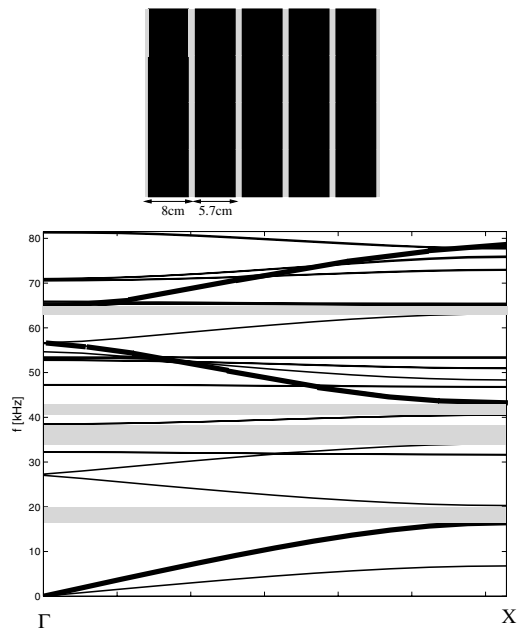


Fig. 6. Top: 5 by 4 unit cells of a simple slab-like crystal consisting of 71% Aluminum inclusions (black) in a PMMA material. Bottom: Dispersion diagram for in-plane polarized waves in a PMMA/Aluminum grating with Aluminum slab to cell width ratio of 0.71. The first 25 modes for propagation in the horizontal direction are shown and bold lines indicate longitudinal modes. The grey areas indicate band gaps.

Numerical examples

First we consider in-plane polarized elastic waves in a 2D elastic crystal with a square base cell size measuring 8 cm by 8 cm. To compare the results with the beam case, we initially perform an analysis of waves propagating along the x -axis through a grating consisting of alternating PMMA and Aluminum slabs with the slab to cell width ratios of 0.29 and 0.71, respectively, as given by the result from Fig. 1. The resulting dispersion diagram for the first 25 eigenvalues for horizontally propagating waves (i.e. wave vectors along the line $\Gamma - X$ in Fig. 5) is shown in Fig. 6. The thick lines indicate the longitudinal modes and the thin lines indicate in-plane elastic shear waves. The thick lines for longitudinal waves do not fully match the full lines for the beam longitudinal waves in Fig. 1 because of slightly different base cell sizes, and the Poisson's ratio effect. As opposed to the beam case, however, the dispersion diagram is "polluted" with in-plane elastic shear waves (thin lines) and there are only four narrow band gaps as indicated by the grey boxes. It is not obvious between which bands the gap will be largest for waves propagating along the x -axis. In order to optimize the structure, we first perform a simple parameter study where we vary the relative width of the Aluminum slabs and find the maximum band gap for the grating structure. The result of this study is that the largest gap is found between the 3rd and the 4th band for an Aluminum slab to cell width ratio of 0.42. The dispersion diagram for this structure is shown in Fig. 7 and the size of the relative band gap is 0.452. The dispersion diagram in Fig. 7 can be compared with the transmission diagram for the optimized finite periodic structure in Fig. 13.

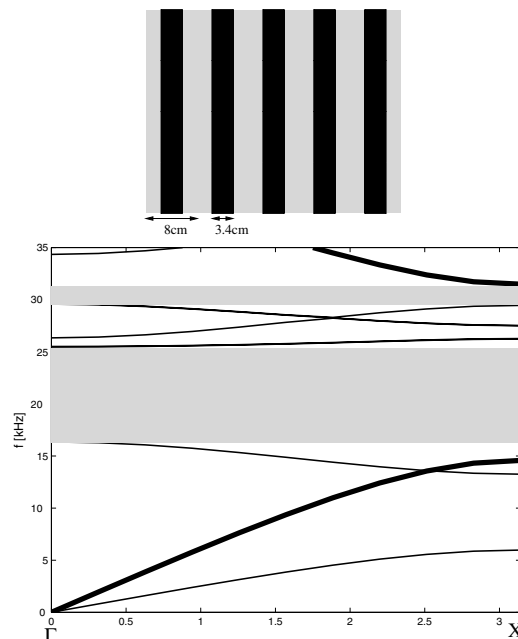


Fig. 7. Top: 5 by 4 unit cells of a simple optimized slab-like crystal consisting of 42% Aluminum inclusions (black) in a PMMA material. Bottom: Dispersion diagram for in-plane polarized waves propagating in the x -direction. The bold lines indicate longitudinal modes. The grey areas indicate band gaps and the relative size of the first band gap is 0.45.

Now one may ask the question whether it is possible to obtain a larger band gap for waves propagating in the x -direction if one allows the topology of the grating to vary? Indeed, this is possible. The result of a topology optimization process where no symmetry was imposed on the square base cell and the gap between the 3rd and the 4th bands was optimized is seen in Fig. 8. The optimization problem corresponded to Eq. (11), except that the design variables for this case were the 3364 nodal density variables in the FE mesh used to discretize the base cell. The obtained relative band gap size is 0.525, i.e. approximately 15% better than the simple grating from Fig. 7. The topology in Fig. 8 is an interesting variation of the simple grating that apparently raises the shear mode bands that define the upper edge of the gap.

If we want to create a band gap for all wave directions simultaneously, we have to optimize the band gap for all wave-vectors on the edges of the triangular areas indicated in Fig. 5. The results of this study for the square base cell is a square Aluminum inclusion with slightly rounded corners which has a relative band gap of 0.428. For the rhombic base cell the optimized topology is shown in Fig. 9. The bases cells were both discretized by 6728 triangular first order elements. The optimized relative band gap size is 0.505 for the rhombic base cell. Both values are, as expected, lower than for the directionally optimized topology in Fig. 7. It is seen that the topology with the largest complete band gap is a hexagonal array of PMMA matrix material with circular inclusions of Aluminum (Fig. 9). As discussed in Ref. [11], the optimal topology depends on the material properties and must therefore always be optimized for the particular materials considered.

Now we repeat the same study for bending waves.

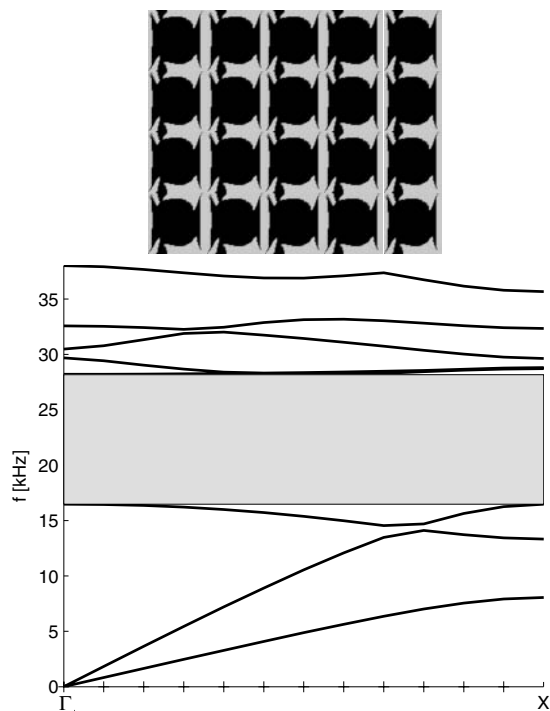


Fig. 8. Top: 5 by 4 unit cells of a topology optimized crystal structure consisting of Aluminum (black) in a PMMA material. Bottom: Dispersion diagram for in-plane polarized waves in the topology optimized crystal. The relative band gap is 0.525.

To compare the results with the beam case, we initially perform an analysis of bending waves propagating along the x -axis through a grating plate consisting of alternating PMMA and Aluminum slabs with the slab to cell width ratios of 0.29 and 0.71, respectively, as given by the result from Fig. 1. The base cell size is again 8 by 8 cm and the thickness of the cell is 1 cm. The resulting dispersion diagram for the first 15 eigenvalues for horizontally propagating waves is shown in Fig. 10. Note that all the shear wave bands are double modes. The thick dashed lines indicate the bending modes and the thin lines indicate torsional modes. The thick dashed lines for the bending waves do not fully match the full lines for the beam bending waves (dashed lines in Fig. 1) because of slightly different base cell size, Poisson's ratio effect and because the beam has a circular cross section. Compared to the beam case, the dispersion diagram for the lowest modes is similar, however, the higher bending modes are "polluted" with the torsional waves (thin lines). A parameter study where the Aluminum slab to cell width ratio is optimized reveals that the largest relative size of the first band gap is 0.53 and is obtained for Aluminum slab to cell width ratio of 0.2 and that the largest relative size of the second band gap is 0.42 and is obtained for Aluminum slab to cell width ratio of 0.44. In contrast to the in-plane case above, we did not find any non-symmetric cell topologies that could improve the size of the relative band gaps of the grating like structures for the first and second gaps. This can be explained by the fact that the first and second gaps only are controlled by the bending modes whereas for the in-plane case the upper boundary of the gaps were limited by a combination of longitudinal and shear wave modes.

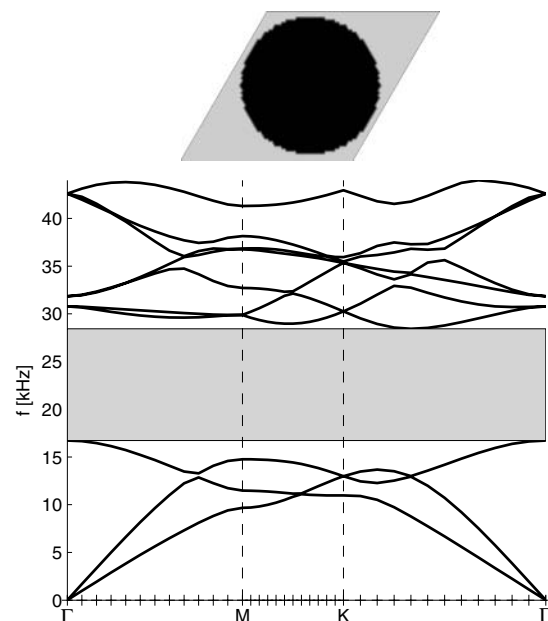


Fig. 9. Dispersion diagram and optimized topology for in-plane polarized waves for a rhombic base cell with waves propagating in all directions. The complete relative band gap size is 0.505.

To create a band gap for all wave directions simultaneously, we optimize the band gap for all wave-vectors on the edges of the triangular areas indicated in Fig. 5. We did not manage to open up a gap for the square cell case (for the considered materials and geometry) but a topology with a resulting relative band gap size of 0.02 (very small) for the rhombic base cell is shown in Fig. 11. It is seen that the optimized topology again is a hexagonal array of nearly circular Aluminum inclusions in a PMMA matrix, however, this time with a smaller radius than for the in-plane polarized case.

In future work we plan to study the case of combined bending and in-plane plane waves modelled by the plane stress assumption, i.e. the shell case.

Design of finite structures: 2D wavereflectors

In the previous two examples it was demonstrated how infinite phononic crystals can be optimized with respect to maximum band gap size. This can lead to a significant improvement of the performance of potential phononic crystal-based devices, such as e.g. mechanical filters and vibration insulators. However, the analysis of the crystals is based on the assumption of infinite media. Thus, if the dimensions of the device are small, approaching that of a single crystal, edge effects become important and must be considered.

In this example we consider wave propagation through a finite slab of elastic material and aim to design the slab for minimum transmission of longitudinal and shear waves. Figure 12 shows the model. We consider a wave (longitudinal or shear) propagating in a matrix material denoted 1 (material properties: E_1 , ρ_1 , ν_1). The goal is now to optimize the distribution of the matrix material and a scattering material (E_2 , ρ_2 , ν_2) in the slab (design domain) such that the wave energy transmitted through the

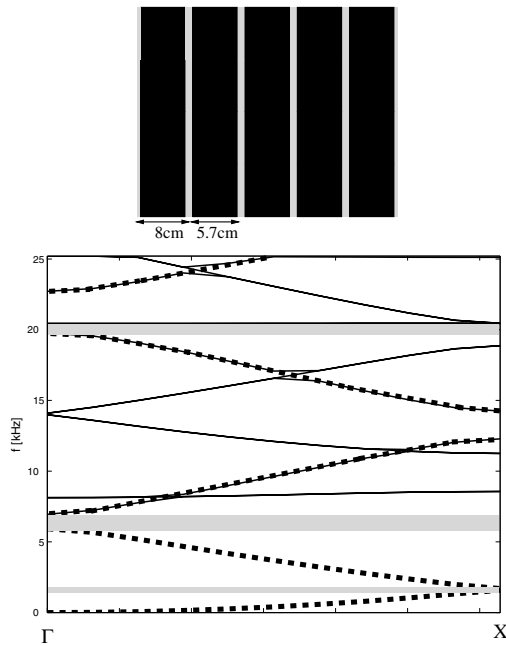


Fig. 10. Dispersion diagram for bending waves along the x -axis in a PMMA/Aluminum grating with Aluminum slab to cell width ratio of 0.71. The first 15 modes are shown and bold dashed lines indicate pure bending modes. The grey areas indicate band gaps.

slab is minimized. In this example, the material properties again correspond to PMMA and Aluminum, respectively.

As in Eqs. (13)–(14) we again consider in-plane polarized waves with the plane strain assumption for the following examples.

In order to avoid artificial reflections of waves propagating in the negative x direction at $x = 0$ and in the positive x direction at $x = L$, a Perfectly Matched Layer (PML) is added at $x < 0$ and $x > L$, respectively. Details of PML modelling for elastic waves can be found e.g. in [18].

The slab is modelled as being infinite in the y direction by using periodic boundary conditions:

$$u(x, d_y) = u(x, 0), \quad (19)$$

$$v(x, d_y) = v(x, 0). \quad (20)$$

The cost function Φ for the optimization problem is the squared amplitude of the transmitted wave evaluated at $x = L$:

$$\Phi = \frac{1}{d_y} \int_0^{d_y} (u(L, y)^2 + v(L, y)^2) dy, \quad (21)$$

thus, giving a measure of the average transmitted wave energy.

As in the previous examples we use a FE discretization of the governing equation:

$$(\mathbf{K} - \omega^2 \mathbf{M}) \mathbf{u} = \mathbf{f}, \quad (22)$$

where $\mathbf{u} = \{u_1, v_1, \dots, u_N, v_N\}$ are the discretized nodal values of the displacement field and where the stiffness matrix \mathbf{K} and the mass matrix \mathbf{M} are complex due to the added PML damping layers. The load vector \mathbf{f} specifies an incoming longitudinal or shear wave. Quadratic first order elements have been used in the FE analysis.

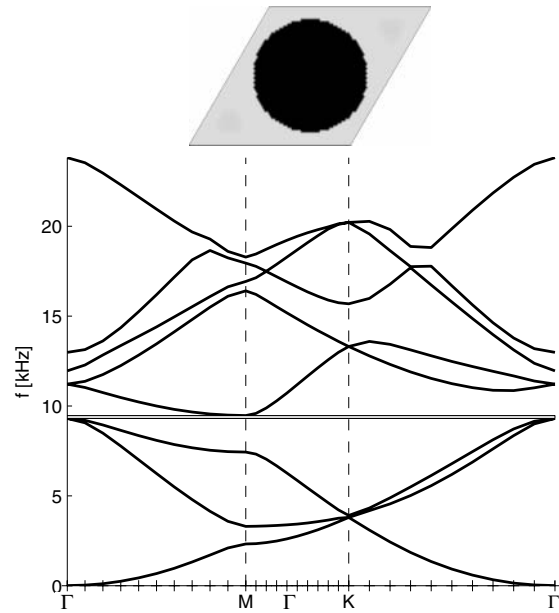


Fig. 11. Dispersion diagram and optimized topology for the bending case. The relative band gap size is 0.02 between the 3rd and the 4th bands.

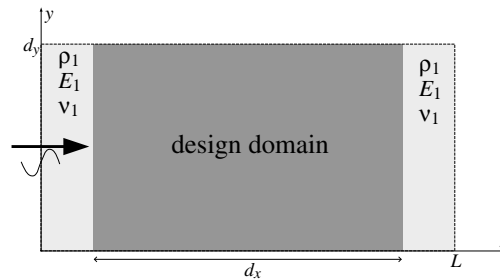


Fig. 12. Computational model. The inverse design problem is to find the optimal distribution of matrix and scattering material in the design domain in order to have the minimum wave transmission through the domain.

In the following examples PMMA is used as a matrix material and aluminum as the scattering material, with the material properties as in the previous examples.

Case of $d_x \gg \text{wavelength}$

We first consider the case where the slab dimension d_x is large compared to the wavelength in the matrix material, the wavelength being $2\pi c/\omega$ where c is the wave speed. Specifically, we consider a propagating shear wave and let $d_x = 10 \times 2\pi c_s/\omega$, where $c_s = \sqrt{\mu_1/\rho_1}$ is the shear wave velocity. Thus, the axial dimension of the design domain is 10 wavelengths in the matrix material. Additionally, we consider a thin slab ($d_y = 1/10 d_x$) in order to avoid any design variation in the y direction.

Figure 13 shows the optimized design obtained for a plane shear wave propagating from left to right. As appears, the design is periodic-like consisting of almost identical base cells. The bottom picture depicts the transmission spectrum, defined as the logarithm to the ratio between the squared incident and transmitted amplitudes, for a longitudinal and a shear wave propagation in the optimized struc-

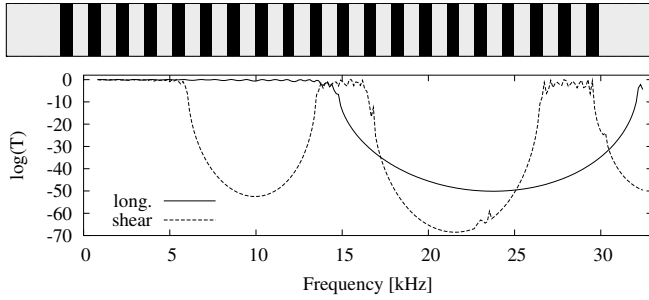


Fig. 13. Top: optimized design for a plane shear wave propagating from left to right. Design domain dimensions: $d_x = 10 \times 2\pi c_s/\omega$ and $d_y = d_x/10$. Bottom: corresponding transmission spectrum for a shear and a longitudinal wave (periodicity of the design chosen to be 8 cm).

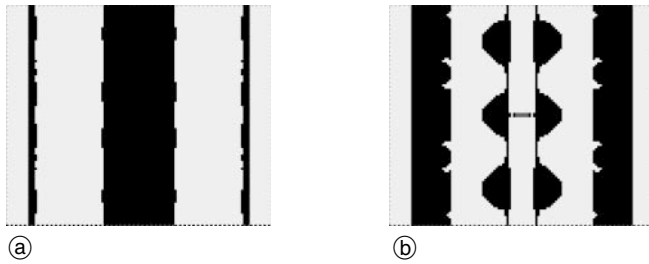


Fig. 14. Optimized designs for the case of $d_x = 2 \times 2\pi c_s/\omega$ and $d_y = d_x$. (a): longitudinal wave, (b): shear wave.

ture. Here, the periodicity of the structure has been chosen to be 8 cm which corresponds to $d_x \approx 1.546$ m. It is noted that the results compare well with the results obtained in the previous section for the 2D crystals. Studying the optimized topology in Fig. 13 reveals that the Aluminum to base cell size ratio is approximately 0.42 – exactly like the result obtained for an infinite periodic medium in Fig. 7. One may also compare the dispersion diagram in Fig. 7 and the transmission spectrum in Fig. 13 and find nearly perfect agreement as should be expected.

Case of $d_x \approx$ wavelength

The slab dimension is now reduced so that $d_x = 2 \times 2\pi c_s/\omega$, i.e. the axial dimension is just two wavelengths of a shear wave. The slab section height is doubled so that the design domain now is quadratic ($d_y = d_x$).

Instead of considering only a single plane wave, we now optimize the design for five different waves simultaneously. Each wave propagates from $x = 0$ but only from 1/5th of the section height. In this way we can ensure that the resulting design reflects incoming waves from multiple directions. Additionally, we treat waves propagating both from left to right and vice versa, so that a total of 10 load cases are treated.

Figure 14 shows the optimized designs obtained for a longitudinal wave and for a shear wave, separately. It is apparent that the designs are no longer periodic-like but are strongly influenced by the limited axial dimension. The wavelength of the longitudinal wave is longer than the shear wavelength ($c_c = \sqrt{(2 - 2\nu)/(1 - 2\nu)} c_s = \sqrt{6} c_s$ for material 1), which implies that d_x is less than a single

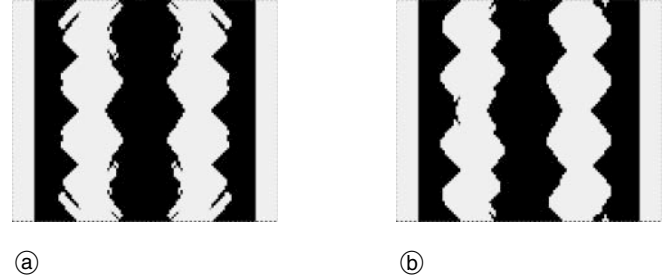


Fig. 15. Optimized design for the case of $d_x = 2 \times 2\pi c_s/\omega$ and $d_y = d_x$. (a): longitudinal and shear wave propagating in both directions, (b): longitudinal and shear wave propagating from left to right.

wavelength. This is reflected in the designs as well as in the performance. Due to the larger wavelength the longitudinal wave cannot be reflected very efficiently, and with an incoming plane wave we compute $\Phi \approx 0.27$, which is only a 1.5 dB improvement compared to the case where the whole design domain is filled with material 2. For the shorter shear wave the corresponding optimized design performs better, and with a plane wave we find $\Phi \approx 0.00071$ which is a 23 dB improvement compared to a completely scatter-filled design domain.

Finally, we try to design the slab so that it minimizes the transmission of longitudinal and shear waves simultaneously. Figure 15 shows the optimized designs. The design to the left was obtained for 10 load cases just as the previous examples, whereas the design to the right was obtained by considering only waves propagating from left to right. For the symmetric design we obtain $\Phi = 0.60$ for an incoming plane longitudinal wave and $\Phi = 0.00078$ for a shear wave, whereas we compute $\Phi = 0.58$ and $\Phi = 0.00081$ for the asymmetrical design.

In order to study the influence of the load cases, the optimization has been performed also with 10 wave load cases from each side instead of five, and using the previously obtained designs as a starting guess. This caused only very small changes of the optimized designs, which indicates that the designs are quite robust with respect to the angle of incidence of the incoming waves.

Conclusion and outlook

The topology optimization method has been used to design infinite periodic beams and plates as well as finite structures with maximum band gaps from two *a priori* chosen materials; one heavy and stiff (Aluminum), the other light and soft (PMMA).

For the beam case we have designed two beams, which prevent either longitudinal or bending waves with frequencies in certain intervals from propagating in them, while a third beam has been designed which prevents both wave types from propagating.

Producing 2d gratings from the optimized beam topologies is not feasible since in-plane shear modes and out-of-plane torsional modes “pollute” the band gaps. Instead, we have performed simple parameter studies as well as free material distribution by topology optimization in order to find the optimal cell geometries of infinite sonic crystals.

Finally we have compared the results obtained for the infinite 2d case with topology optimized finite 2d structures. When the size of the design domain is large (e.g. 10 wavelengths) we get full agreement with the infinite case whereas for design domain dimension comparable to one wavelength we get significantly different structures.

Although mixtures of the two materials are allowed, the optimized designs for the base cell are all binary designs. We interpret this as band gaps favouring high material contrast.

We believe that the found designs are feasible in the sense that they can be manufactured using machine or laser cutting.

Future work will include shell analysis and experiments.

Acknowledgments. This work was supported by the Danish Technical Research Council through the project “Designing band gap materials and structures with optimized dynamic properties”.

References

- [1] Sigalas, M. M.; Economou, E. N.: Elastic and acoustic wave band structure. *J. Sound Vib.* **158** (1992) 377–382.
- [2] Bendsøe, M. P.; Sigmund, O.: *Topology optimization – Theory, Methods and Applications*. Springer-Verlag, Berlin Heidelberg 2003.
- [3] Bendsøe, M. P.; Kikuchi, N.: Generating Optimal Topologies in Structural Design using a Homogenization Method. *Comput. Method. Appl. M.* **71** (1988) 197–224.
- [4] Larsen, U. D.; Sigmund, O.; Bouwstra, S.: Design and Fabrication of Compliant Micromechanisms and Structures with Negative Poisson’s Ratio. *IEEE J. Microelectromechanical Systems* **6** (1997) 99–106.
- [5] Burger, M.; Osher, S. J.; Yablonovitch, E.: Inverse problem techniques for the design of photonic crystals. *IEICE T. Electron.* **E87-C** (2004) 258–265.
- [6] Cox, S. J.; Dobson, D. C.: Maximizing band gaps in two-dimensional photonic crystals. *SIAM J. Appl. Math.* **59** (1999) 2108–2120.
- [7] Borel, P. I.; Harpøth, A.; Frandsen, L. H.; Kristensen, M.; Jensen, J. S.; Sigmund, O.: Topology optimization and fabrication of photonic crystal structures. *Opt. Expr.* **12** (2004) 1996–2001.
- [8] Jensen, J. S.; Sigmund, O.: Systematic design of photonic crystal structures using topology optimization: Low-loss waveguide bends. *Appl. Phys. Lett.* **84** (2004) 2022–2024.
- [9] Felici, T.; Gallagher, T. F. G.: Improved waveguide structures derived from new rapid optimization techniques. *Proc. SPIE* **4986** (2003) 375–385.
- [10] Kim, W. J.; O’Brien, J. D.: Optimization of a two-dimensional waveguide branch by simulated annealing and the finite element method. *J. Opt. Soc. Am.* **B21** (2004) 289–295.
- [11] Sigmund, O.; Jensen, J. S.: Systematic design of phononic band-gap materials and structures by topology optimization. *Phil. Trans. R. Soc. Lond.* **A361** (2003) 1001–1019.
- [12] Sorokin, S. V.; Ershova O. A.: Plane wave propagation and frequency band gaps in periodic plates and cylindrical shells with and without heavy fluid loading. *Y. Sound Vibration* **278** (2004) 501–526.
- [13] Jensen, J. S.; Sigmund, O.; Thomsen, J. J.; Bendsøe, M. P.: Design of multiphase structures with optimized vibrational and wave-transmitting properties. 15th Nordic Seminar on Computational Mechanics, 2002 (Eds. E. Lund, N. Olhoff, J. Stegmann) www.ime.auc.dk/nscm15
- [14] Friedman, Z.; Kosmatka, J. B.: An Improved Two-Node Timoshenko Beam Finite Element. *Comp. Struct.* **47** (1993) 473–481.
- [15] Cook, R. D.; Malkus, D. S.; Plesha, M. E.; Witt, R. J.: *Concepts and applications of finite Element Analysis*. John Wiley Sons, 4th ed. 2002.
- [16] Mathews, J.; Walker, R.: *Mathematical methods of physics*. Addison-Wesley, 1964.
- [17] Svanberg, K.: The method of moving asymptotes: a new method for structural optimization. *Int. J. Numer. Meth. Engng.* **24** (1987) 359–373.
- [18] Zheng, Y.; Huang, X.: Anisotropic perfectly matched layers for elastic waves in cartesian and curvilinear coordinates. MIT-report (2002) 18 pages.

Topology optimization problems for reflection and dissipation of elastic waves

Jakob S. Jensen

Department of Mechanical Engineering, Solid Mechanics, Technical University of Denmark, Nils Koppels Allé, Building 404, DK-2800 Kgs. Lyngby, Denmark

Received 29 August 2006; received in revised form 11 October 2006; accepted 11 October 2006
Available online 28 November 2006

Abstract

This paper is devoted to topology optimization problems for elastic wave propagation. The objective of the study is to maximize the reflection or the dissipation in a finite slab of material for pressure and shear waves in a range of frequencies. The optimized designs consist of two or three material phases: a host material and scattering and/or absorbing inclusions. The capabilities of the optimization algorithm are demonstrated with two numerical examples in which the reflection and dissipation of ground-borne wave pulses are maximized.

© 2006 Elsevier Ltd. All rights reserved.

1. Introduction

This work deals with two fundamental optimization problems encountered in the study of elastic wave propagation through a finite slab of material. Wave propagation can be suppressed if the wave reflection or the wave dissipation is maximized and in this work these two problems are addressed with the method of topology optimization. The method is used to find an optimized distribution of inclusions of scattering and/or absorbing material that maximizes the reflection and/or the dissipation, respectively.

Recently, much work has been devoted to highly reflecting materials and structures created with a periodic distribution of scattering inclusions—the so-called bandgap materials. If inclusions are distributed periodically a large reflection of propagating waves can occur due to destructive interference. For a comprehensive overview see e.g. the recent review paper by Sigalas et al. [1].

Bandgap structures are promising candidates as optimal wave reflecting structures. In Sigmund and Jensen [2] it was demonstrated that optimized designs are typically periodic-like structures with modifications near the boundaries that compensate for edge effects. A material optimization problem was also considered in which the topology of repetitive identical inclusions was optimized. Rupp et al. [3] studied similar problems with a topology optimization algorithm. Halkjær et al. [4] considered bending waves in beams and plates and structures with limited spatial dimensions that did not allow for a repetitive periodic structure. Hussein et al. [5] analyzed one-dimensional wave propagation through a layered medium and used a genetic algorithm to generate optimized structures.

E-mail address: jsj@mek.dtu.dk.

Optimization of the dissipation of elastic waves has been far less studied than the reflection/transmission problem. Planar structures that maximize dissipation of scalar waves was previously demonstrated by the author [6]. Razansky et al. [7] studied dissipation of acoustic waves and gave bounds for maximal dissipation in thin and thick dissipative layers. Work has also been done on optimal placement of dampers to reduce structural dynamic compliance [8,9]. Related work with the method topology optimization were seen in Jog [10] who studied the forced vibration problem and minimized the dissipated energy and in Wang and Chen [11] who maximized heat dissipation in cellular structures.

Closely related to this present work are optimization studies related to propagation of electromagnetic waves. Cox and Dobson [12] studied optimal design of infinite periodic structures with a material distribution method and maximized the optic (photonic) bandgaps and Jensen and Sigmund [13] studied a finite photonic bandgap structure and topology optimized the material distribution in a 90° bend so that the transmitted power through the bend was maximized.

This paper extends the work of Jensen [6] and considers dissipation of elastic waves (pressure and shear) for multiple frequencies instead of scalar waves at a single frequency. The work of Halkjær et al. [4] is extended to deal with the multiple frequency case. Furthermore, both optimization problems are extended to allow for the distribution of three material phases instead of two. The paper is organized as follows: first, the general model for elastic wave propagation is presented (Section 2), and the formulation of the two optimization problems are discussed in detail (Section 3). Section 4 describes the parametrization of the design domain with two continuous design fields, the material interpolation model, and the artificial damping penalization. In Section 5 the numerical implementation of the optimization problem is explained, including boundary conditions, FEM discretization, and a mathematical formulation of the problem. In Sections 6 and 7 two numerical examples are presented that demonstrate optimization of the material distribution for maximized reflection and dissipation of ground-borne wave pulses. Finally, main conclusions are given in Section 8.

2. Elastodynamic model

The computational model is based on the full 3D elastodynamic equations for an inhomogeneous medium. The 3D model is reduced to a 2D model under the assumption that the waves propagate in the plane and material properties vary in the same plane.

The 3D elastodynamic equations:

$$\rho \ddot{\mathbf{U}} = \nabla \cdot \boldsymbol{\Sigma}, \quad (1)$$

govern the displacements $\mathbf{U} = \{U(\mathbf{x}, t) \ V(\mathbf{x}, t) \ W(\mathbf{x}, t)\}^T$ of an elastic medium with position-dependent density $\rho = \rho(\mathbf{x})$. The position vector is denoted $\mathbf{x} = \{x \ y \ z\}^T$, and $\boldsymbol{\Sigma} = \boldsymbol{\Sigma}(\mathbf{x}, t)$ is the stress tensor.

Eq. (1) is transformed to complex form with the complex variable transformation $\mathbf{U} \rightarrow \tilde{\mathbf{U}}$ and $\boldsymbol{\Sigma} \rightarrow \tilde{\boldsymbol{\Sigma}}$, so that $\mathbf{U} = \text{Re}(\tilde{\mathbf{U}})$ and $\boldsymbol{\Sigma} = \text{Re}(\tilde{\boldsymbol{\Sigma}})$. Time-harmonic motion with frequency ω gives a steady-state solution to the complex version of Eq. (1):

$$\tilde{\mathbf{U}}(\mathbf{x}, t) = \mathbf{u}(\mathbf{x})e^{i\omega t}, \quad (2)$$

$$\tilde{\boldsymbol{\Sigma}}(\mathbf{x}, t) = \boldsymbol{\sigma}(\mathbf{x})e^{i\omega t}, \quad (3)$$

in which the displacement amplitude vector $\mathbf{u}(\mathbf{x})$ and the stress amplitude tensor $\boldsymbol{\sigma}(\mathbf{x})$ are generally complex. The solution forms (2) and (3) are inserted into the complex version of Eq. (1) to give the standard time-harmonic elastic wave equation:

$$\nabla \cdot \boldsymbol{\sigma} + \rho \omega^2 \mathbf{u} = 0. \quad (4)$$

With the appropriate boundary conditions Eq. (4) gives the displacement field used as the basis for the optimization problems introduced in the following section. With a specific solution to the complex equation (4) the instantaneous displacement and stresses are:

$$\mathbf{U}(\mathbf{x}, t) = \text{Re}(\mathbf{u}(\mathbf{x})e^{i\omega t}) = \mathbf{u}^r \cos \omega t - \mathbf{u}^i \sin \omega t, \quad (5)$$

$$\Sigma(\mathbf{x}, t) = \text{Re}(\boldsymbol{\sigma}(\mathbf{x})e^{i\omega t}) = \boldsymbol{\sigma}^r \cos \omega t - \boldsymbol{\sigma}^i \sin \omega t, \quad (6)$$

where superscripts r and i refer to the real and imaginary parts of the complex variable.

Eq. (4) is simplified by assuming the stresses to be invariant in a single direction (arbitrarily chosen as the z -direction) and can be written in component form as:

$$\frac{\partial \sigma_{xx}}{\partial x} + \frac{\partial \sigma_{yx}}{\partial y} + \rho \omega^2 u = 0, \quad (7)$$

$$\frac{\partial \sigma_{xy}}{\partial x} + \frac{\partial \sigma_{yy}}{\partial y} + \rho \omega^2 v = 0, \quad (8)$$

$$\frac{\partial \sigma_{xz}}{\partial x} + \frac{\partial \sigma_{yz}}{\partial y} + \rho \omega^2 w = 0, \quad (9)$$

with $\mathbf{u} = \{u(\mathbf{x}) \ v(\mathbf{x}) \ w(\mathbf{x})\}^T$. This assumption could be realized, e.g. with a uniform material distribution in the z -direction and waves that propagate strictly in the (x, y) -plane.

For a linear isotropic elastic medium the stress components are:

$$\sigma_{xx} = \frac{E}{(1+\nu)(1-2\nu)} \left((1-\nu) \frac{\partial u}{\partial x} + \nu \frac{\partial v}{\partial y} \right), \quad (10)$$

$$\sigma_{xy} = \sigma_{yx} = \frac{E}{2(1+\nu)} \left(\frac{\partial u}{\partial y} + \frac{\partial v}{\partial x} \right), \quad (11)$$

$$\sigma_{yy} = \frac{E}{(1+\nu)(1-2\nu)} \left((1-\nu) \frac{\partial v}{\partial y} + \nu \frac{\partial u}{\partial x} \right), \quad (12)$$

for the coupled in-plane problem, and

$$\sigma_{xz} = \frac{E}{2(1+\nu)} \frac{\partial w}{\partial x}, \quad (13)$$

$$\sigma_{yz} = \frac{E}{2(1+\nu)} \frac{\partial w}{\partial y}, \quad (14)$$

for the scalar out-of-plane problem. In the following the coupled problem will be considered. Various optimization results for the out-of-plane problem can be found e.g. in Refs. [2,6].

3. Optimization problems

Two optimization problems are considered in this paper. The basic setup is displayed in Fig. 1. A plane elastic wave propagates in a loss-free host material. Within the slab of material, indicated by the vertical dashed lines, a number of scattering and/or absorbing inclusions cause the incident wave to be partially reflected and/or possibly dissipated and partially transmitted through the slab. The power balance for the system is

$$\tilde{I} = \tilde{R} + \tilde{T} + \tilde{D}, \quad (15)$$

where \tilde{I} is the incident wave power, \tilde{T} and \tilde{R} is the transmitted and reflected power, respectively, and \tilde{D} is the power dissipated due to absorbing inclusions.

3.1. Maximizing reflection

The first optimization problem is to maximize the reflection of the propagating wave with an optimized distribution of inclusions of one or two scattering materials. Pressure and shear waves at multiple frequencies are treated but the analysis is restricted to plane waves with normal incidence.

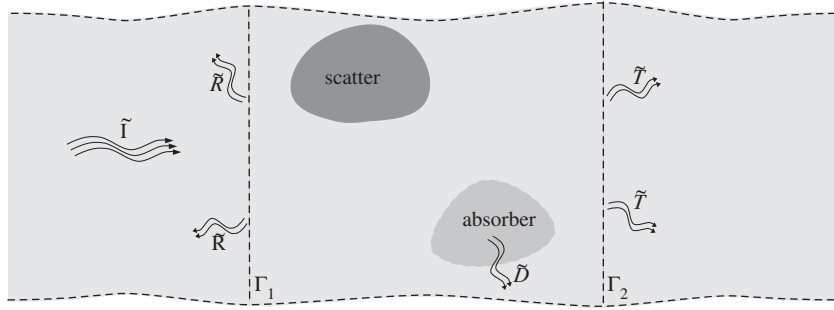


Fig. 1. Basic setup for the two optimization problems. Incident wave power is denoted \tilde{I} , transmitted and reflected power \tilde{T} and \tilde{R} , and the dissipated power is \tilde{D} .

The reflection of the wave is found indirectly from the transmitted power at the output boundary Γ_2 . The instantaneous transmitted power (Poynting vector) is defined as (e.g. Ref. [14, p. 133]):

$$\mathbf{p}(\mathbf{x}, t) = \{p_x(\mathbf{x}, t) \ p_y(\mathbf{x}, t)\}^T, \quad (16)$$

where

$$p_x(\mathbf{x}, t) = -\Sigma_{xx}\dot{U} - \Sigma_{yx}\dot{V}, \quad (17)$$

$$p_y(\mathbf{x}, t) = -\Sigma_{xy}\dot{U} - \Sigma_{yy}\dot{V}, \quad (18)$$

is the power in the x - and y -direction, respectively.

Expressions for $\dot{\mathbf{U}}$ and Σ , taken from Eqs. (5)–(6), are inserted into Eqs. (17)–(18) so that p_x and p_y are expressed in terms of the computed quantities \mathbf{u} and σ . Now, the time-averaged x - and y -components of the power can be computed as:

$$\langle p_x(\mathbf{x}, t) \rangle = \frac{\omega}{2\pi} \int_0^{2\pi/\omega} (-\Sigma_{xx}\dot{U} - \Sigma_{yx}\dot{V}) dt = \frac{1}{2}\omega \text{Re}(i\sigma_{xx}\bar{u} + i\sigma_{yx}\bar{v}), \quad (19)$$

$$\langle p_y(\mathbf{x}, t) \rangle = \frac{\omega}{2\pi} \int_0^{2\pi/\omega} (-\Sigma_{xy}\dot{U} - \Sigma_{yy}\dot{V}) dt = \frac{1}{2}\omega \text{Re}(i\sigma_{xy}\bar{u} + i\sigma_{yy}\bar{v}), \quad (20)$$

where the notation $\langle \cdot \rangle = \omega/2\pi \int_0^{2\pi/\omega} dt$ is introduced and will be used in the following. In Eqs. (19)–(20) the overbar denotes complex conjugation. The time-averaged power \tilde{T} transmitted through the output boundary is now found as:

$$\tilde{T} = \left\langle \int_{\Gamma_2} \mathbf{n} \cdot \mathbf{p} \, d\mathbf{x} \right\rangle = \int_{\Gamma_2} \langle p_x \rangle \, d\mathbf{x}, \quad (21)$$

in which $\mathbf{n} = \{1 \ 0\}^T$ is the outward pointing normal vector at Γ_2 .

Without dissipation the reflected power \tilde{R} is simply the difference between the time-averaged incident and transmitted power $\tilde{R} = \tilde{I} - \tilde{T}$ and the corresponding reflectance R is computed by scaling \tilde{R} with \tilde{I} :

$$R = \frac{\tilde{I} - \tilde{T}}{\tilde{I}} = 1 - T, \quad (22)$$

where $T = \tilde{T}/\tilde{I}$ is the transmittance and \tilde{I} is found by evaluating the Poynting vector at the input boundary Γ_1 :

$$\tilde{I}_p = \int_{\Gamma_1} \langle -\dot{U}\Sigma_{xx} \rangle \, d\mathbf{x}, \quad (23)$$

for a plane pressure (P) wave of normal incidence (pure horizontal motion) and

$$\tilde{I}_s = \int_{\Gamma_1} \langle -\dot{V} \Sigma_{yx} \rangle d\mathbf{x}, \quad (24)$$

for shear (S) wave (vertical motion). In Section 5 a set of boundary conditions are specified that ensure a unit magnitude incident wave that propagates away from Γ_1 in both directions. Eqs. (23)–(24) are evaluated with these boundary conditions (Eqs. (49)–(50)):

$$\tilde{I} = \frac{1}{2} h \omega^2 Z, \quad (25)$$

where h is the vertical dimension of the input boundary and Z is the wave impedance, given as $Z = Z_p$ for a P wave and $Z = Z_s$ for an S wave, in which:

$$Z_p = \sqrt{\frac{E_h \rho_h (1 - \nu_h)}{(1 + \nu_h)(1 - 2\nu_h)}}, \quad (26)$$

$$Z_s = \sqrt{\frac{E_h \rho_h}{2(1 + \nu_h)}}, \quad (27)$$

and the subscript h denotes host material which is fixed at the boundary Γ_1 . Thus, the final expression for the reflectance from the slab of material between Γ_1 and Γ_2 is

$$R = 1 - \frac{1}{h\omega Z} \int_{\Gamma_2} \text{Re}(i\sigma_{xx}\bar{u} + i\sigma_{yx}\bar{v}) d\mathbf{x}, \quad (28)$$

that takes the value 1 when the wave is fully reflected and 0 with full transmission. The reflectance R will be the first objective function in the optimization study.

3.2. Maximizing dissipation

An alternative optimization problem is now defined. Another way to hinder propagation of the wave is to maximize the dissipation of the wave within the slab. A benefit of this is that potential annoyance associated with the reflected wave can be eliminated.

Naturally, the dissipation of the wave energy is dependent on the damping model. A simple model is mass- and stiffness-proportional viscous damping. Reasonable agreement with experimental results can be obtained in large frequency ranges if a suitable combination of these two contributions are used. In this work smaller frequency ranges are considered and a simple mass-proportional damping model is chosen.

The mass-proportional viscous damping is added directly to the continuous Eq. (1):

$$\rho \ddot{\mathbf{U}} + \rho \eta_\rho \dot{\mathbf{U}} = \nabla \cdot \boldsymbol{\Sigma}, \quad (29)$$

where $\eta_\rho = \eta_\rho(\mathbf{x})$ is a position-dependent damping coefficient. Eq. (29) leads to a time-harmonic wave equation with a complex density:

$$\nabla \cdot \boldsymbol{\sigma} + \tilde{\rho} \omega^2 \mathbf{u} = 0, \quad (30)$$

$$\tilde{\rho} = \rho \left(1 - i \frac{\eta_\rho}{\omega} \right). \quad (31)$$

A power balance is obtained by multiplying both sides of Eq. (29) by the velocities:

$$\dot{\mathbf{U}} \cdot (\rho \ddot{\mathbf{U}}) + \dot{\mathbf{U}} \cdot (\rho \eta_\rho \dot{\mathbf{U}}) = \dot{\mathbf{U}} \cdot (\nabla \cdot \boldsymbol{\Sigma}). \quad (32)$$

The second term on the l.h.s. is the instantaneous point-wise dissipated power:

$$d(\mathbf{x}, t) = \rho \eta_\rho \dot{\mathbf{U}} \cdot \dot{\mathbf{U}}, \quad (33)$$

which averaged over a wave period yields the time-averaged dissipation:

$$\langle d(\mathbf{x}, t) \rangle = \frac{1}{2} \omega^2 \rho \eta_\rho (u\bar{u} + v\bar{v}). \quad (34)$$

The second objective function \tilde{D} is defined as the time-averaged dissipation $\langle d(\mathbf{x}, t) \rangle$ integrated over the total domain Ω . The relative dissipation D is obtained by scaling with the input power \tilde{I} :

$$D = \frac{\tilde{D}}{\tilde{I}} = \frac{1}{hZ} \int_{\Omega} \rho \eta_\rho (u\bar{u} + v\bar{v}) \, d\mathbf{x}. \quad (35)$$

4. Design variables and material interpolation

The design optimization is based on two continuous design fields q_1 and q_2 that are defined everywhere within the slab:

$$q_1(\mathbf{x}) \in \mathbb{R} \mid 0 \leq q_1 \leq 1, \quad (36)$$

$$q_2(\mathbf{x}) \in \mathbb{R} \mid 0 \leq q_2 \leq 1. \quad (37)$$

These two design fields are used to specify and control the point-wise material properties and can, in the present formulation, be used to distribute three different materials in the slab. For both problems one material is the host material through which the undisturbed wave propagates and the other two may be scattering and/or absorbing materials.

Any material property; E , ρ , v or η_ρ is found by a linear interpolation between the properties of the involved materials:

$$\alpha(\mathbf{x}) = (1 - q_1)\alpha_h + q_1((1 - q_2)\alpha_1 + q_2\alpha_2), \quad (38)$$

in which α is any of the properties. Subscript h denotes host material, and subscripts 1 and 2 refer to the two other materials. A material interpolation scheme such as Eq. (38) is a standard implementation for three-phase design. See e.g. Bendsøe and Sigmund [15, p. 120], for a similar implementation with two materials and void.

From Eq. (38) it can be seen that the design field q_1 is an indicator of host material (obtained for $q_1 = 0$) or inclusion (obtained for $q_1 = 1$). If an inclusion is specified by q_1 , the field q_2 then specifies the inclusion type. Hence, type 1 is found for $q_2 = 0$ ($q_1 = 1$) and type 2 for $q_2 = 1$ ($q_1 = 1$). Non 0 – 1 values of the design variables correspond to some intermediate material property that may not be physically realizable. This is not important in the optimization procedure, but it must be ensured that only 0 – 1 values remain in the finalized optimized design so that the material properties are well defined.

4.1. Penalization with artificial dissipation

In most implementations of material interpolation models, penalization factors are introduced (SIMP model) (e.g. Ref. [15, p. 5]). This is done so that the continuous design variables are likely to take only the extreme values 0 or 1 in the final design. The SIMP strategy is not used in this work since a constraint on the amount of one of the material phases is required and for this problem such a constraint is not natural. Moreover, previous studies on wave propagation problems have shown that maximum material contrasts are favored so that 0 – 1 optimized designs appear automatically [12,2,4]. However, in the dissipation example intermediate design variables appear especially with three material phases. In this case a penalization method is adapted that was originally introduced for optics problems.

In Jensen and Sigmund [16] it was suggested to use artificial damping to penalize intermediate design variables. An extra damping term was introduced:

$$\eta_{\text{art}} = \beta q(1 - q), \quad (39)$$

for the case of a single design field q . In Eq. (39) β is a damping coefficient and the product $q(1 - q)$ ensures that only intermediate design variables cause dissipation of energy. This penalization is similar to the explicit penalization method introduced by Allaire and Francfort [17]. A nice physical interpretation is possible by imagining the intermediate material as a sponge that soaks up energy.

Here, this approach is reused and expanded to deal with two design fields:

$$\eta_{\text{art}} = \beta_1 \varrho_1((1 - \varrho_1) + \beta_2 \varrho_2(1 - \varrho_2)), \tag{40}$$

where the two factors β_1 and β_2 allow for separate penalization of ϱ_1 and ϱ_2 (in the numerical examples $\beta_2 = 1$). The specific form of Eq. (40) is connected to the definition of the design fields, i.e. if $\varrho_1 = 0$ host material is obtained regardless of the value of ϱ_2 . Thus, only if $\varrho_1 \neq 0$ intermediate values of ϱ_2 should be penalized. The fraction of the input power that is dissipated due to the artificial damping is

$$D_{\text{art}} = \frac{\beta_1}{hZ} \int_{\Omega} \rho \varrho_1((1 - \varrho_1) + \beta_2 \varrho_2(1 - \varrho_2))(u\bar{u} + v\bar{v}) \, dx. \tag{41}$$

where ρ is given from Eq. (38).

It should be emphasized that the artificial damping approach penalizes intermediate design variables only if the optimization problem is of the maximization type. With a minimization problem, e.g. minimizing the reflection, a work-around could be either to reformulate the problem into a maximization problem (e.g. maximizing the transmission) or alternatively to use a negative artificial damping coefficient β_1 . The latter approach, however, lacks an appealing physical interpretation and has not been thoroughly tested.

5. Numerical implementation

The computational model is shown in Fig. 2. The design domain is defined with outer dimensions $L \times h$, input boundary Γ_1 at $x = 0$, and output boundary Γ_2 at $x = L + 2\delta$. Two perfectly matched layers (PMLs) are added to the computational domain to absorb waves propagating away from the design domain (at arbitrary angles) in the positive and/or negative x -direction, respectively. The reader is referred to Basu and Chopra [18] for a comprehensive treatment of PMLs for elastic waves.

5.1. Perfectly matched layers (PML)

PMLs generally ensure a low reflection for all angles of incidence for pressure and shear waves. A good performance of the absorbing boundary is important since the distribution of inclusions is not known a priori and a good optimization algorithm can be expected to exploit this. The good performance comes, however, at the expense of increased computational requirements due to the enlarged domain.

For the computational model in Fig. 2, the governing equations in the PMLs become:

$$\frac{1}{\varepsilon} \frac{\partial \tilde{\sigma}_{xx}}{\partial x} + \frac{\partial \tilde{\sigma}_{yx}}{\partial y} + \rho_h \omega^2 u = 0, \tag{42}$$

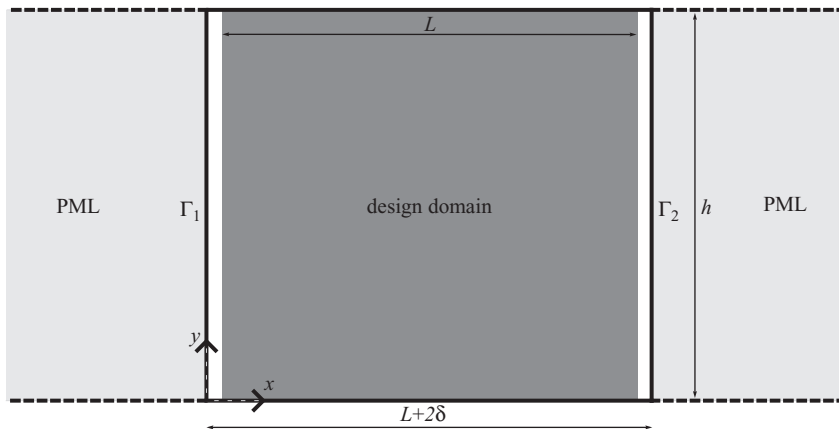


Fig. 2. Computational model used for numerical implementation of the optimization algorithm.

$$\frac{1}{\varepsilon} \frac{\partial \tilde{\sigma}_{xy}}{\partial x} + \frac{\partial \tilde{\sigma}_{yy}}{\partial y} + \rho_h \omega^2 v = 0, \quad (43)$$

where the modified stress components are:

$$\tilde{\sigma}_{xx} = \frac{E_h}{(1+v_h)(1-2v_h)} \left(\frac{1}{\varepsilon} (1-v_h) \frac{\partial u}{\partial x} + v_h \frac{\partial v}{\partial y} \right), \quad (44)$$

$$\tilde{\sigma}_{xy} = \tilde{\sigma}_{yx} = \frac{E_h}{2(1+v_h)} \left(\frac{1}{\varepsilon} \frac{\partial v}{\partial x} + \frac{\partial u}{\partial y} \right), \quad (45)$$

$$\tilde{\sigma}_{yy} = \frac{E_h}{(1+v_h)(1-2v_h)} \left((1-v_h) \frac{\partial v}{\partial y} + \frac{1}{\varepsilon} v_h \frac{\partial u}{\partial x} \right), \quad (46)$$

in which subscript h indicates that the material in the PMLs is host material. The complex variable ε is a function of x :

$$\varepsilon(x) = 1 - i\alpha \left(\frac{x-x^*}{L^*} \right)^2, \quad (47)$$

where x^* is the x -position of PML layer/real domain interface, and α is the absorption coefficient in the layer. The total length of the PML domain is L^* . Eq. (47) fulfills that $\varepsilon = 1$ for $x = x^*$, so that the PML equations (42)–(43) reduce to the normal wave equations at the interface. The imaginary part of ε ensures the dissipation of the wave. The choice of letting the imaginary part increase with square of the distance from the interface is empirical but has been shown to yield low reflection values [18]. The coefficient α should be chosen large enough so that the wave is fully absorbed in the PMLs, but not excessively large so that spurious reflections occur at the interface. Here, $L^* = L/2$ and $\alpha = 50$ have been used in the numerical examples.

5.2. Boundary conditions

A non-zero stress amplitude jump at Γ_1 specifies a stress wave propagating away from the boundary in both directions:

$$\mathbf{n} \cdot (\boldsymbol{\sigma}^+ - \boldsymbol{\sigma}^-) = 2i\omega \{Z_p U_0 \quad Z_s V_0\}^T, \quad (48)$$

where $\mathbf{n} = \{-1 \ 0\}^T$ is the normal vector pointing away from Ω , $(\boldsymbol{\sigma}^+ - \boldsymbol{\sigma}^-)$ is the stress jump and U_0 and V_0 are the amplitudes of the P and S wave. Thus for a P wave of unit magnitude:

$$-(\sigma_{xx}^+ - \sigma_{xx}^-) = 2i\omega Z_p, \quad (49)$$

and

$$-(\sigma_{xy}^+ - \sigma_{xy}^-) = 2i\omega Z_s, \quad (50)$$

gives a unit magnitude S wave that propagates away from Γ_1 .

The wave input boundary condition and the transition to the PMLs are simplified with constant material properties (host material) at the interface. This is accomplished by moving the design domain a small distance δ (Fig. 2) away from Γ_1 and Γ_2 . The transmitted power is averaged over the small domain instead of evaluated at the boundary:

$$T = \frac{1}{h\omega Z\delta} \int_{L+\delta}^{L+2\delta} \int_0^h \text{Re}(i\sigma_{xx}\bar{u} + i\sigma_{yx}\bar{v}) dy dx, \quad (51)$$

as this simplifies the numerical implementation of the sensitivities (Section 5.3).

A periodic boundary condition is applied for the amplitude fields on the upper boundary:

$$\mathbf{u}(x, h) = \mathbf{u}(x, 0), \quad (52)$$

as well as zero traction conditions at the outer PML boundaries.

5.3. FEM discretization and sensitivity analysis

The commercial finite element software package COMSOL is used to discretize the domain and to assemble and solve the discretized equations. The two displacement fields u, v as well as the two design fields q_1 and q_2 are discretized as follows:

$$u(\mathbf{x}) = \sum_{i=1}^N \psi_i^1 u_i, \quad v(\mathbf{x}) = \sum_{i=1}^N \psi_i^2 v_i, \quad (53)$$

$$q_1(\mathbf{x}) = \sum_{i=1}^M \phi_i^1 q_{1,i}, \quad q_2(\mathbf{x}) = \sum_{i=1}^M \phi_i^2 q_{2,i}, \quad (54)$$

in which $\psi_i^1, \psi_i^2, \phi_i^1, \phi_i^2$ are the basis functions, N is the number of nodal displacement variables, and M is the number of nodal design variables. Linear or quadratic basis functions are used for the displacement fields and linear basis functions are used for the design fields. A regular mesh with nearly quadratic elements is used in all examples.

The discretized version of Eq. (4) with boundary conditions and PMLs is

$$\mathbf{S}(\omega)\mathbf{d} = \mathbf{f}(\omega), \quad (55)$$

where

$$\mathbf{S} = \mathbf{K} + i\omega\mathbf{C} - \omega^2\mathbf{M}, \quad (56)$$

is the system matrix and $\mathbf{d} = \{u_1 \ u_2 \ \dots \ u_N \ v_1 \ v_2 \ \dots \ v_N\}^T$ are the discretized nodal amplitudes, \mathbf{K} , \mathbf{C} and \mathbf{M} is the stiffness, damping, and mass matrices, respectively, and \mathbf{f} is the frequency-dependent load vector.

The vector of design variables $\boldsymbol{\gamma} = \{q_{1,1} q_{1,2} \dots q_{1,M} q_{2,1} q_{2,2} \dots q_{2,M}\}^T$ is introduced and the sensitivities of the objective function with respect to these design variables are obtained. Let Φ be either of the two objective functions considered and let $' = d/d\gamma_i$ denote the derivative with respect to the i th design variable. The adjoint method (e.g. Ref. [19]) leads to the expression for the derivative of the augmented objective function Φ_0 :

$$\Phi'_0 = \Phi' + \boldsymbol{\lambda}^T \mathbf{R}' + \bar{\boldsymbol{\lambda}}^T \bar{\mathbf{R}}', \quad (57)$$

where Φ' is the derivative of the objective function, $\boldsymbol{\lambda}$ is a vector of Lagrangian multipliers, and \mathbf{R}' is the derivative of the residual of Eq. (55) that vanishes at equilibrium ($\mathbf{R} = \mathbf{R}' = \mathbf{0}$). Straightforward calculations lead to an equation for the Lagrangian multipliers:

$$\mathbf{S}^T \boldsymbol{\lambda} = - \left(\frac{\partial \Phi}{\partial \mathbf{d}'} - i \frac{\partial \Phi}{\partial \mathbf{d}^i} \right)^T, \quad (58)$$

so that the final expression for the sensitivities become:

$$\Phi' = \frac{\partial \Phi}{\partial \gamma_i} + \text{Re} \left(\boldsymbol{\lambda}^T \frac{\partial \mathbf{S}}{\partial \gamma_i} \mathbf{d} \right). \quad (59)$$

The implementation of the sensitivity analysis is facilitated by the use of the COMSOL software, that allows for an almost automated generation of the derivatives [20].

5.4. Optimization problem formulation

With artificial damping included the overall power balance can be written:

$$R = 1 - (T + D + D_{art}), \quad (60)$$

where T , D and D_{art} are defined in Eqs. (51), (35) and (41). From Eq. (60) it is seen that the artificial damping reduces R so that intermediate design variables are costly and likely to be penalized from the design.

In the example in Section 6 the wave reflection is maximized. Only scattering inclusions are considered so there is no real dissipation ($D = 0$). However, if material damping is added the convergence of the

optimization algorithm is enhanced and the risk of obtaining a local optimum is reduced [2]. The material damping is applied using a continuation method in which the optimization procedure is initiated with high damping which is then gradually removed as the optimization progresses. A reverse procedure is used with the artificial damping. The optimization is started with a small (or vanishing) artificial damping coefficient β_1 which is then increased slowly.

For the second optimization problem, the power balance (60) is rewritten as:

$$D = 1 - (T + R + D_{\text{art}}), \quad (61)$$

from which it is seen that artificial damping penalizes intermediate design variables also when D is maximized.

Both optimization problems are solved with Krister Svanberg's MMA routine [21] with multiple load cases that comprise several frequencies for pressure and shear waves. The implementation is based on the min–max approach [22] and the final optimization problem is written:

$$\begin{aligned} & \min_{\gamma} \max_{\omega_i} (\Phi_p(\omega_i), \Phi_s(\omega_i)) \\ & \text{subject to : } \mathbf{S}(\omega_i)\mathbf{d} = \mathbf{f}(\omega_i) \\ & \quad 0 \leq \gamma \leq 1, \end{aligned} \quad (62)$$

in which $\Phi = T + D + D_{\text{art}}$ for the reflection problem and $\Phi = 1 - D$ for the dissipation problem. The subscripts p and s refer to pressure and shear waves and ω_i is any of the frequencies that are considered. Thus, the formulation in Eq. (62) states that the maximum value of the objective function Φ for both wave types and all frequencies is to be minimized by an optimized set of design variables γ that fulfills the constraints.

6. Numerical example 1

In this first example the aim is to design a structure that reflects both P and S wave pulses. The wave pulse is assumed to be narrow-band with center frequency f_0 and the main frequency content in a finite frequency range near the center frequency. A possible application could be for isolation of structures from ground-borne waves, e.g. coming from underground train tunnels. The properties of the materials used in this example have been taken partly from studies of train-induced ground vibrations [23]. Table 1 lists the material properties of the three materials that are used.

The optimized design should be a compromise between having a sufficient reflection of waves but also a structure with manageable spatial dimensions. The length of the design domain slab, L_s , is chosen to be one wavelength for a P wave in the host material. With a center frequency of $f_0 = 788$ Hz this gives $L = 1$ m.

Before optimized designs are generated the reflectance is computed for two structures with inclusions of scattering material (scatter 1) placed periodically in the design domain. It is well known that periodically placed inclusions may cause bandgaps in the corresponding band structure which leads to high reflection. This occurs if the material contrast is sufficiently high and the wavelength is commensurable with the periodicity [1].

Fig. 3a shows a one-dimensional periodic structure, a Bragg-grating, and the corresponding reflectance (Fig. 3b). Large frequency bands with high reflectance exist for pressure and shear waves, but they are off-set due to the difference in wavelength. However, near the center frequency $f_0 = 788$ Hz high reflectance occurs for both wave types. For the two-dimensional periodic structure (Fig. 4a) frequency bands with high

Table 1
Material properties used for the reflection example

Material	ρ (kg/m ³)	E (MPa)	ν	η_p (s ⁻¹)
Host (ground)	1550	269	0.257	—
Scatter 1 (ground)	2450	2040	0.179	—
Scatter 2	775	134.5	0.257	—

The material data for the two ground types is taken from Ref. [23].

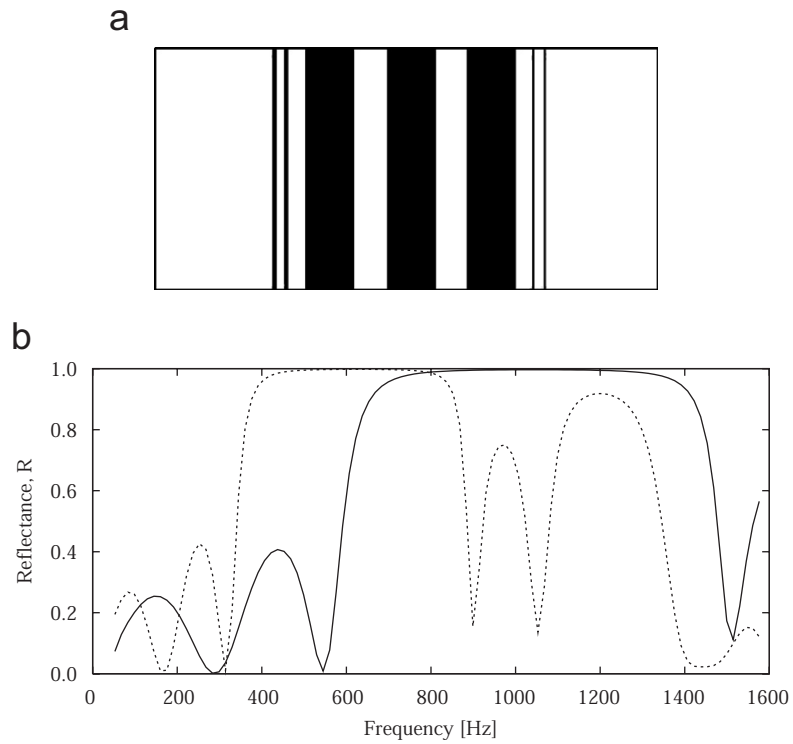


Fig. 3. (a) One-dimensional periodic structure (Bragg grating) with three inclusions of scatterer 1 (black) in the host ground material (white); (b) the corresponding reflected power R for P and S waves. P wave (solid line), S wave (dashed line).

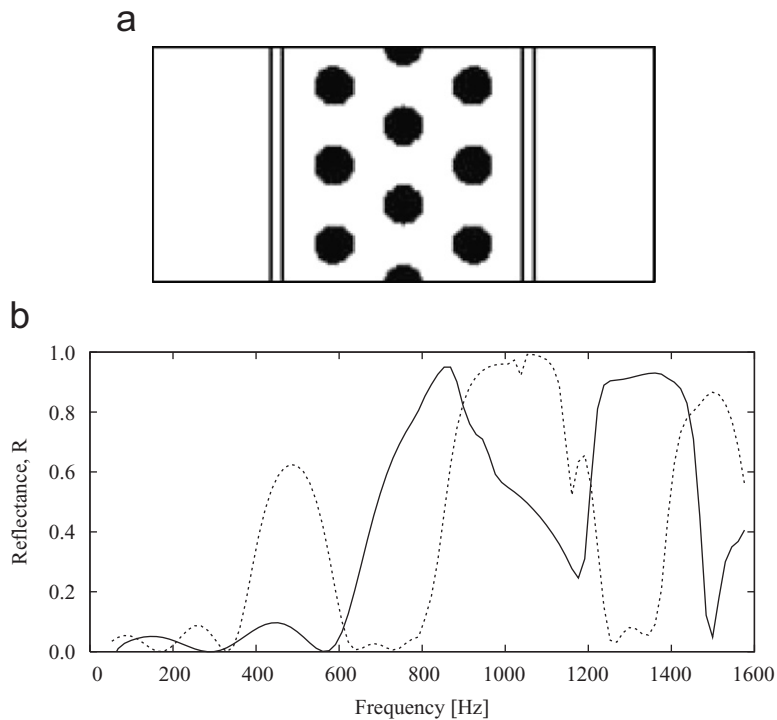


Fig. 4. (a) Two-dimensional triangular periodic structure with three rows of scatterer 1 inclusions (black) in the host ground material (white); (b) the corresponding reflected power R for P and S waves. P wave (solid line), S wave (dashed line).

reflectance are also seen (Fig. 4b) but the reflectance is generally lower than for a Bragg-grating with the same number of rows of inclusions. However, a 2D-structure is known better to reflect waves from different angles of incidence [1]. The size of the inclusions were chosen after a simple parameter study so that a large reflectance was obtained near $f_0 = 788$ Hz. It should be emphasized that a further improvement is possible by using repetitive cells with an optimized material distribution [2]. However, the improvement that can be obtained with further cell optimization is small due to the restricted design space.

6.1. Two-phase design

Thus, with two materials available a one-dimensional layered structure seems a good candidate as an optimal design. However, as will be shown in this section this depends on whether the frequency range is sufficiently small so that high reflectance bands for P and S waves can overlap. First the optimization is performed for a relative small frequency range $\pm 10\%$ away from the center frequency. Fig. 5 shows the optimized design and the reflectance curves for pressure and shear waves. The design is a one-dimensional structure with three inclusion layers of different thickness and with uneven spacing between them. Everywhere in the target frequency range a high reflectance is obtained.

The target frequency range is now extended to $\pm 25\%$ and Fig. 6a shows the optimized design (with 10 optimization frequencies in the target range). The design is no longer a one-dimensional layered structure since such a structure cannot reflect both wave types sufficiently in the entire frequency range. Instead a combination of a layered structure and a more intricate 2D material arrangement is seen. Fig. 6b shows that the reflectance is more than 90% in the entire optimization range. Fig. 7 shows the corresponding wave pattern for P and S waves at the center frequency and illustrates how wave amplitudes are attenuated in the structure.

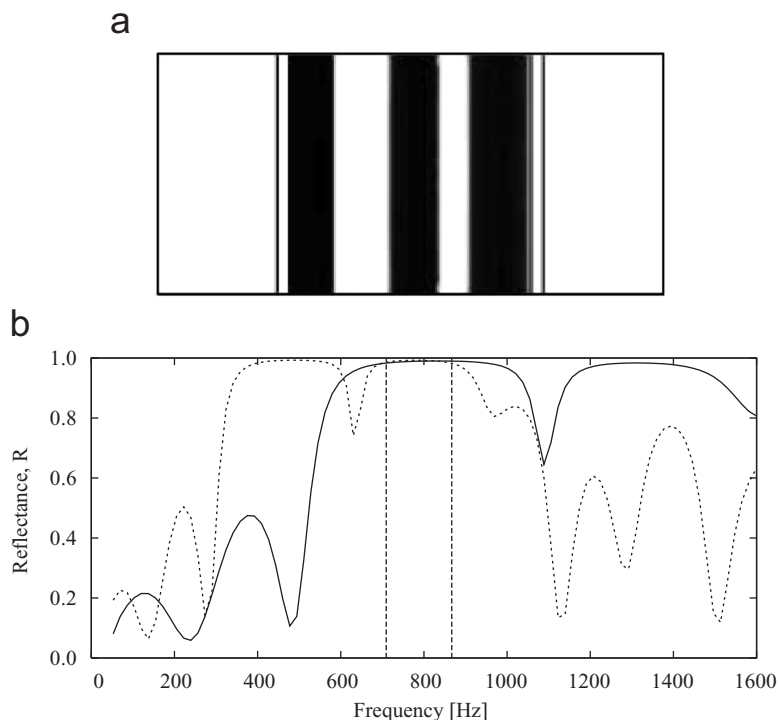


Fig. 5. (a) Optimized distribution of scatter 1 (black) and host material (white) for maximum reflectance in a $\pm 10\%$ frequency interval around the center frequency $f_0 = 788$ Hz; (b) resulting reflectance curves for P and S waves. P wave (solid line), S wave (dashed line).

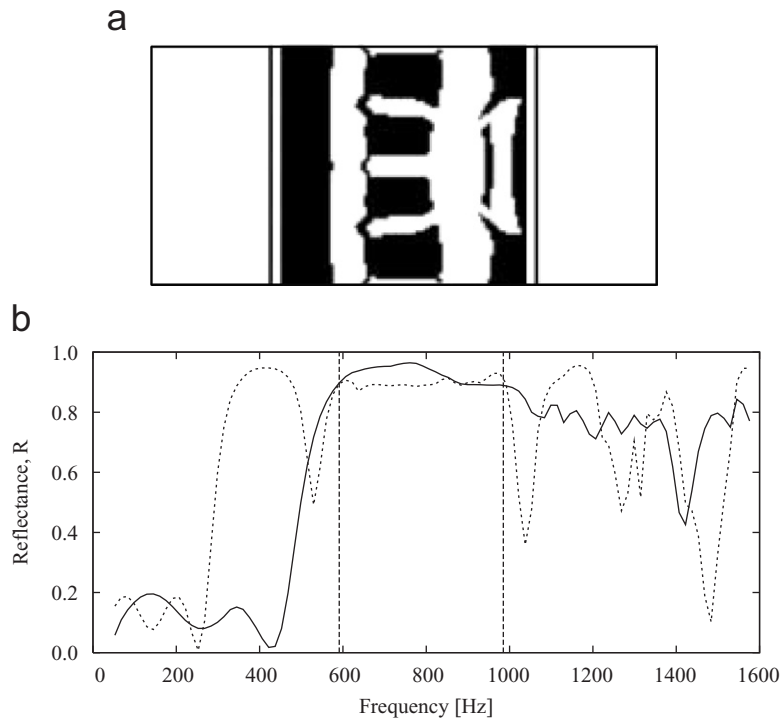


Fig. 6. (a) Optimized distribution of scatter 1 (black) and host material (white) for maximum reflectance in a $\pm 25\%$ frequency interval around the center frequency $f_0 = 788$ Hz; (b) resulting reflectance curves for P and S waves. P wave (solid line), S wave (dashed line).

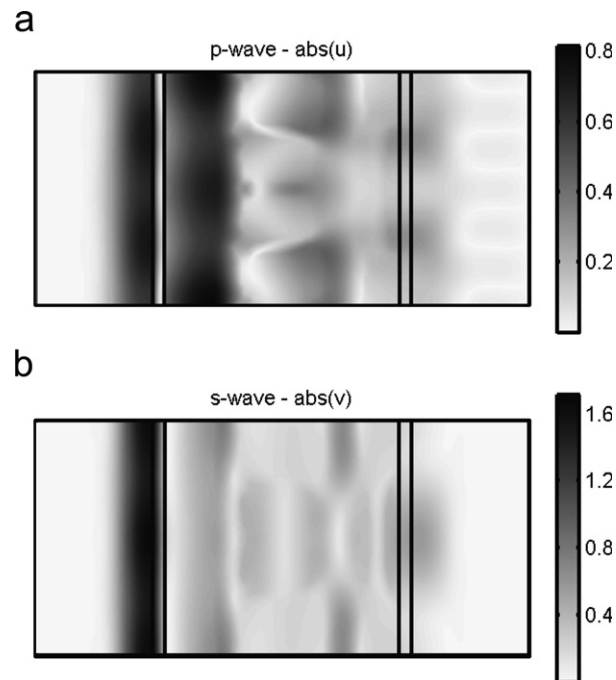


Fig. 7. Wave patterns for the optimized structure computed for the center frequency $f_0 = 788$ Hz: (a) $\text{abs}(u)$ for a P wave and (b) $\text{abs}(v)$ for an S wave.

It should be emphasized that other local optima can be found with different initial material distributions. The design shown in Fig. 6a is the best structure found after an extensive search but it is not guaranteed to be the global optimum. The problem with many local optima in wave-propagation problems is known and has to the author's knowledge not yet been solved. Genetic or other evolutionary algorithms are not easily applied to this problem due to the large number of design variables (5000 or more).

6.2. Three-phase design

A more effective wave-reflecting structure can be obtained if the design domain length L is increased. This allows for more inclusion layers in the structure and consequently higher reflectance. Also for larger L the optimized design has a combined layered/2D appearance (as in Fig. 6a) so that it is effective in the entire frequency range.

For situations where the spatial extent of the design domain is limited higher reflectance can be obtained with increased contrast between the inclusion material and the host. This contrast can be quantified as the ratio between the impedances (cf. Eq. (26)–(27)). Generally, the layout of the optimized designs is different for different contrasts.

However, an additional scattering material does not seem to increase the reflectance. Extensive numerical experiments showed in all cases that a design with those two materials having the highest contrast is always better than a three-phase design. This supports previous studies that indicate that maximum contrast is favorable for high wave reflection (cf. Section 4.1).

Fig. 8 illustrates this effect. A third material phase is introduced (Table 1) and the corresponding optimized design (Fig. 8a) consists mainly of scatter 1 (gray) and scatter 2 (black) as they have the largest material contrast. However, small areas of host material (white) are seen in the design. If these areas are replaced by scattering material (Fig. 8b), the reflectance (Fig. 8c) is almost identical as for the optimized 3-phase design and actually slightly better averaged over the target range. Thus, it can be concluded that the 3-phase optimized design is a local optimum.

Quadratic elements were used for the displacement fields in the last example to increase the convergence and stability of the optimization algorithm. However, although an improvement was noted the final design is still unsymmetrical which is an indication of the instabilities in the optimization procedure. The design is also dominated by small fragmented details. To remedy this problem, different filtering techniques could be applied (e.g. Ref. [15]). This has not been examined further in this work.

7. Numerical example 2

In this second example the setting from the first example is kept but now the goal is to maximize the fraction of the input power that is dissipated in the slab. An absorptive material phase with the properties of epoxy (Table 2) is introduced. The damping coefficient is chosen arbitrarily as $\eta_\rho = 0.05 \text{ s}^{-1}$ and the damping of the other material phases is neglected. The importance of η_ρ will be investigated for the optimized designs. A third material phase (scatter) is also introduced and it will be investigated how this can improve the performance of the design. The material properties of this material are chosen so that the density is twice and the stiffness 20 times that of the host material.

The dissipated power fraction D is computed for the situation with the entire design domain filled up with absorptive material. Fig. 9 shows the dissipation of a P and an S wave with $\eta_\rho = 0.05 \text{ s}^{-1}$ and also for higher values of η_ρ . Due to the impedance contrast between the two material phases a part of the incident wave is reflected directly at the input boundary and consequently not all input power is dissipated regardless of the magnitude of η_ρ .

Thus, merely filling up the domain with absorptive material is not optimal for maximum dissipation, although perhaps intuitively attractive. Instead, a good design must ensure a low direct reflection at the input boundary and additionally ensure that the wave is not transmitted but reflected inside the domain and then dissipated. The following sections demonstrate that such designs are generated by the optimization algorithm.

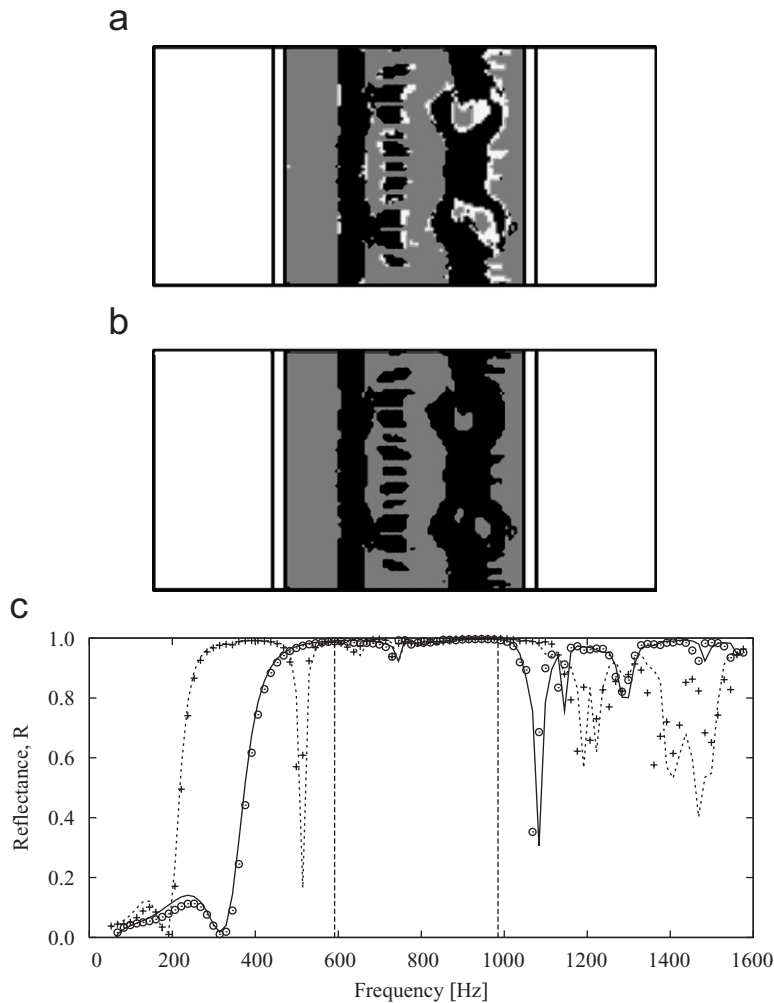


Fig. 8. (a) Optimized distribution of scatter 1 (gray), scatter 2 (black) and host (white); (b) 2-phase design with host replaced by scattering material; (c) resulting reflectance curves for P and S waves. P wave (solid line), S wave (dashed line), P wave-2 phase (discrete circles), S wave-2 phase (discrete crosses).

Table 2
Material properties for the materials used in the dissipation example

Material	ρ (kg/m ³)	E (MPa)	ν	η_ρ (s ⁻¹)
Host (ground)	1550	269	0.257	—
Epoxy	2000	4000	0.400	0.05
Scatter	3100	5380	0.350	—

The material data for the ground is taken from Ref. [23].

7.1. Two-phase design

In this section host and the absorptive material are used for the optimization. Fig. 10a shows an optimized design for shear and pressure waves in a $\pm 10\%$ frequency range near the center frequency with 10 optimization frequencies used. The optimized design is complicated but with characteristic features. A thin

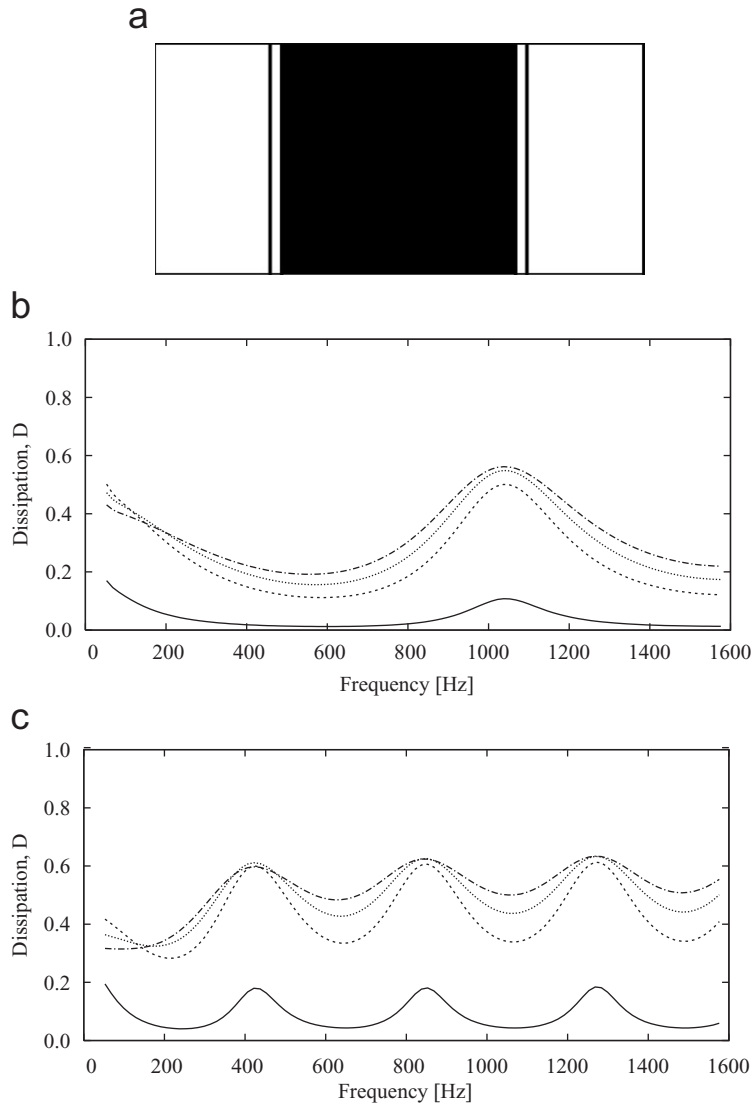


Fig. 9. (a) Design domain filled with absorptive material (epoxy), corresponding dissipated energy fraction D for (b) P and (c) S waves for four different values of η_ρ . $\eta_\rho = 0.05 \text{ s}^{-1}$ (solid), $\eta_\rho = 0.50 \text{ s}^{-1}$ (dash), $\eta_\rho = 0.75 \text{ s}^{-1}$ (dot), $\eta_\rho = 1.00 \text{ s}^{-1}$ (dash-dot).

inclusion slab at the input boundary modifies the effective impedance seen by the incident wave so that the direct reflection is minimized. The thicker slab at the output boundary maximizes the reflection of the wave that “escapes” through the domain. The inner parts of the domain are filled with strategically placed inclusions that dissipate the high amplitude waves.

Fig. 10b shows curves for the dissipated power fraction. The dissipation is significantly increased in the target range and is a factor 2–10 higher than for the case with the whole domain filled (Fig. 9). The dissipation is also plotted for the same structure with a higher value of η_ρ . It is noted that the dissipation approaches unity. This implies that the structure effectively reduces the direct reflection and the transmission through the domain to a minimum. This also indicates that the specific choice of η_ρ used in the optimization algorithm is not critical for the generation of the optimized design. Fig. 11 shows the point-wise distribution of the dissipated power for the two wave types computed at the center frequency. The dissipation of both wave types is seen to be localized and concentrated in a few absorptive inclusions near the input boundary and in the inner part of the domain.

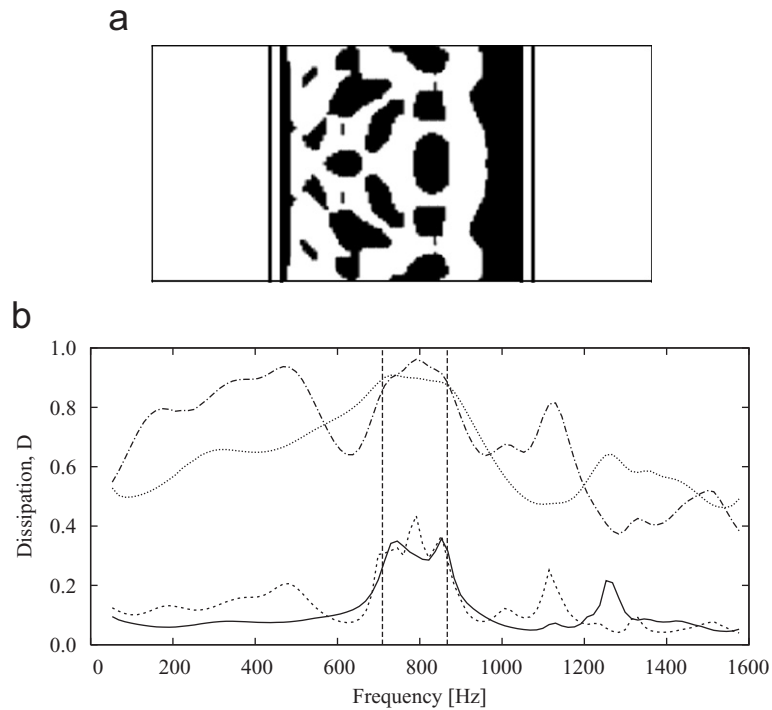


Fig. 10. (a) Optimized distribution of absorptive material (black) and loss-free host material (white) for maximum dissipation in a $\pm 10\%$ frequency interval around $f_0 = 788 \text{ Hz}$; (b) corresponding dissipation of P and S waves. P wave $\eta_p = 0.05 \text{ s}^{-1}$ (solid), S wave $\eta_p = 0.05 \text{ s}^{-1}$ (dash), P wave $\eta_p = 0.75 \text{ s}^{-1}$ (dot), S wave $\eta_p = 0.75 \text{ s}^{-1}$ (dash-dot).

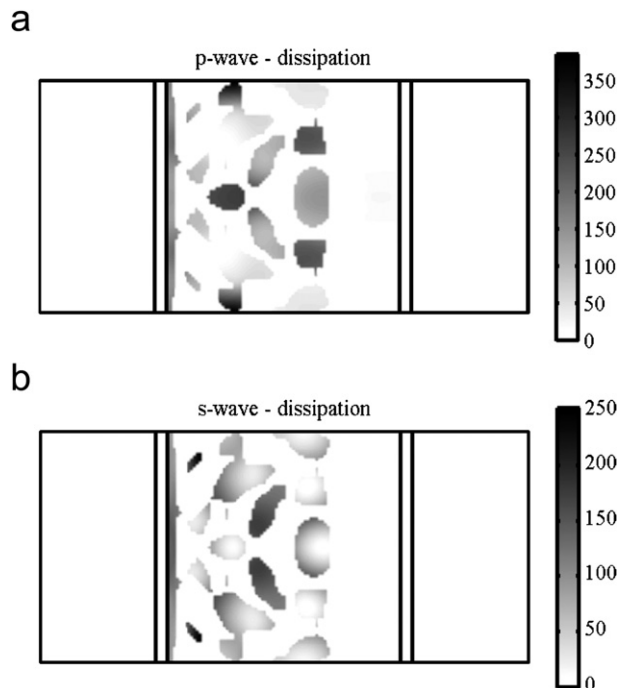


Fig. 11. Point-wise dissipated power for the optimized design for $f_0 = 788 \text{ Hz}$: (a) a P wave and (b) an S wave. $\eta_p = 0.05 \text{ s}^{-1}$.

7.2. Three-phase design

The extra scattering material is now included in an attempt to further improve the performance. The hypothesis is that with a highly reflecting material available a larger part of the wave can be reflected leading to higher wave amplitudes and higher dissipation. Fig. 12a shows the optimized design with gray as absorptive material and black as scattering material. Qualitatively, the design is similar to the two-phase design. The major difference is that the inclusion near the output boundary is made of the scattering material as the higher impedance contrast leads to increased reflection. Additionally, two small reflecting inclusions are seen in the inner part of the structure.

Fig. 12b shows the dissipated power fraction for the three-phase design. The improvement of the performance is quite limited (from about 32% to about 35% in average) and although the details of the two-phase and three-phase designs are different the performance in the target range is similar. Thus, it seems possible to create many good optimized designs (local optima) with similar overall features but with different structural details such as precise size and placement of the absorptive inclusions.

The effect of a refinement of the computational model and the use of higher-order finite elements is illustrated in Fig. 13. Fig. 13a shows the optimized design with quadratic elements for the displacement fields instead of linear elements. The higher-order elements stabilize the optimization algorithm (as for the reflection example) and the small asymmetries in the design in Fig. 12a vanish. Apart from this the two designs are very similar. Fig. 13b shows an optimized design with 100×100 linear elements in the design domain (80×80 used in the other examples) and with 15 optimization frequencies in the target range (instead of 10 used in the other examples). The overall features of the design are unchanged but the details are different. The numerical instabilities are more severe and lead to a very unsymmetrical design. However, as illustrated in Fig. 13c, these differences in the design are not reflected in the performance which is very similar in the target range.

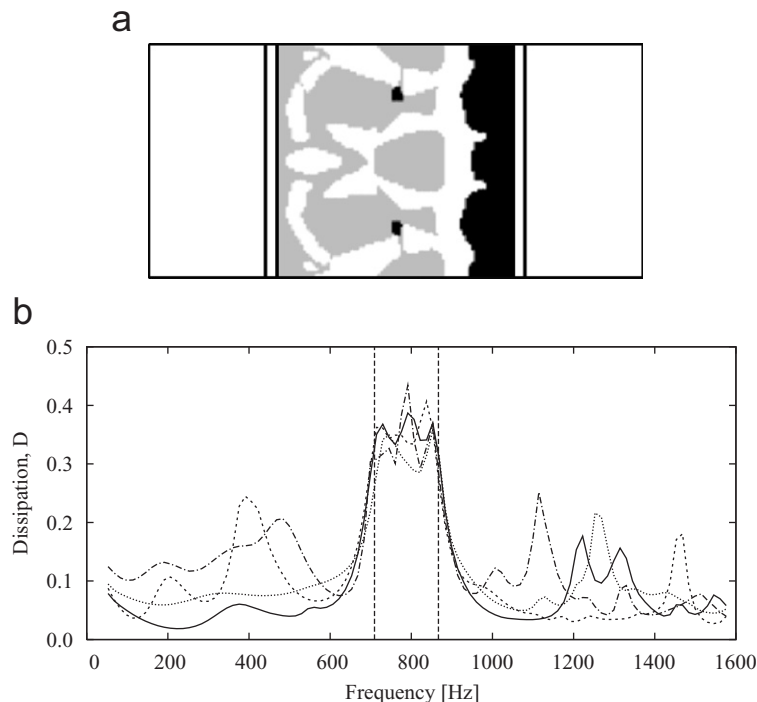


Fig. 12. (a) Optimized distribution of absorptive material (gray), host material (white), and scattering material (black) for maximum dissipation in a $\pm 10\%$ frequency interval around $f_0 = 788$ Hz; (b) corresponding dissipation of P and S waves compared to the two-phase design in Fig. 10. P wave-3 phase (solid), S wave-3 phase (dash), P wave-2 phase (dot), S wave-2 phase (dash-dot). $\eta_p = 0.05 \text{ s}^{-1}$.

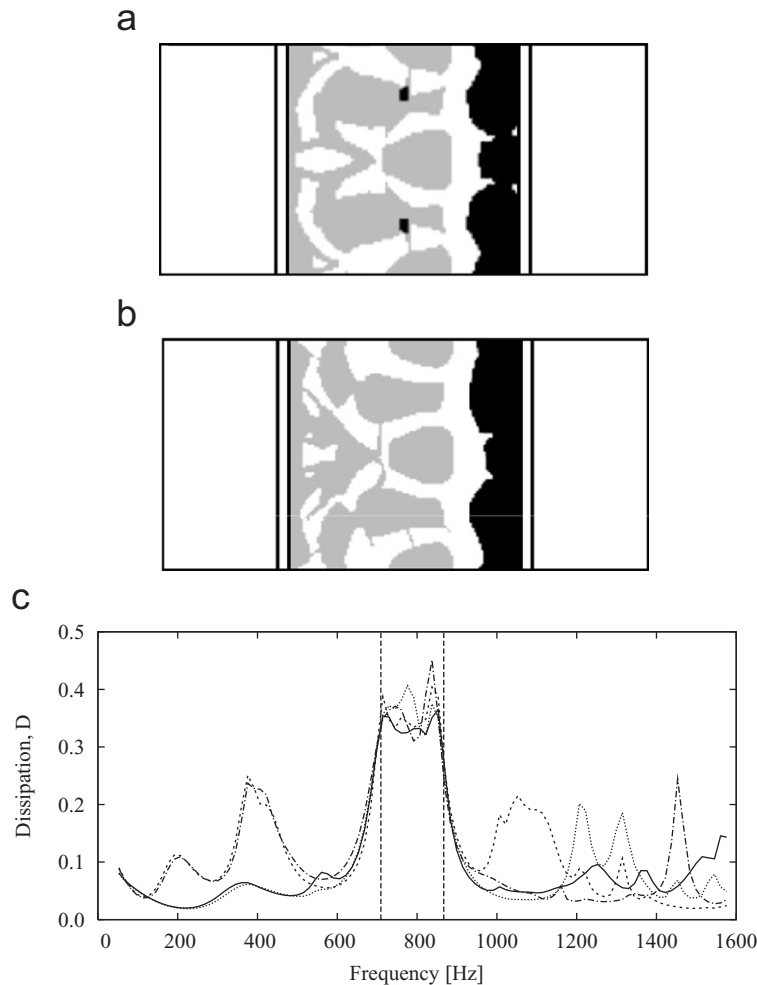


Fig. 13. (a) Optimized design obtained with quadratic elements for the displacement amplitudes; (b) design obtained with refined mesh and more optimization frequencies in the target range; (c) the corresponding dissipation for P and S waves. P wave-refined (solid), S wave-refined (dash), P wave-quadratic (dot), S wave-quadratic (dash-dot). $\eta_p = 0.05 \text{ s}^{-1}$.

Fig. 14 shows the point-wise dissipated power computed at the center frequency for the structure generated with quadratic elements for the displacement fields. The dissipation is fairly well distributed for the P wave and more localized near the input boundary for the S wave. The behavior of the optimized absorptive structure is further examined in Fig. 15. The dissipation (D), reflectance (R), and transmittance (T) are depicted for an S wave. As seen in Fig. 15a ($\eta_p = 0.05 \text{ s}^{-1}$) the increase in dissipation in the target range is accompanied by a large drop in R . However, the transmission T is relatively large due to the small dissipation in the absorptive inclusions. If a material with a larger damping coefficient is used ($\eta_p = 0.75 \text{ s}^{-1}$) the reflection R is again very small, but now almost all of the wave that propagates through the structure is dissipated and consequently the transmission T of the wave is almost reduced to zero. Similar behavior is seen for a P wave.

8. Conclusions

Two topology optimization problems for elastic wave propagation were considered. The objective of the optimization study was to optimize the distribution of two or three material phases in a slab of material so that

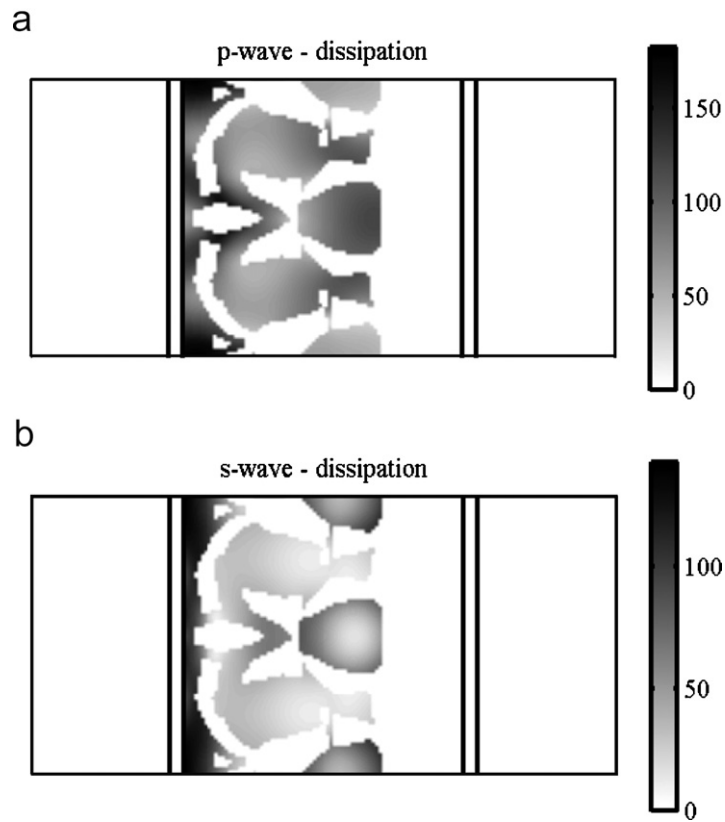


Fig. 14. Point-wise dissipated power for the optimized design for $f_0 = 788$ Hz: (a) a P wave and (b) an S wave. $\eta_p = 0.05 \text{ s}^{-1}$.

wave propagation was hindered. This was accomplished either by maximizing the reflection from the slab or the wave dissipation in the slab.

A design domain was defined and parameterized with two continuous design fields that control the material properties. With two design fields up to three different material phases could be distributed in the domain. A penalization method based on artificial damping was introduced. The penalization was employed to ensure well-defined material properties in the final design.

The optimization problems were formulated and discretized with a standard finite element method and implemented with the commercial software COMSOL. The optimization problem was solved with the aid of the mathematical programming software MMA, with analytical sensitivity analysis and a min-max formulation so that pressure and shear waves for multiple wave frequencies could be considered.

The use of the optimization algorithm was demonstrated by two application examples. The propagation of a ground-borne wave pulse was suppressed by optimizing the material distribution in a square design domain. In the first example scattering inclusions were distributed to maximize the wave reflection and in the second example the wave dissipation was maximized with an optimized distribution of absorbing and scattering inclusions.

The examples have demonstrated that large reflection of waves can be obtained by optimizing the distribution of two material phases but also that adding a third phase with intermediate material properties could not lead to further improvement. By optimizing the distribution of absorbing material the dissipation of waves can be significantly enhanced and it was shown that the dissipation could be further increased by including also a scattering material phase in the design optimization.

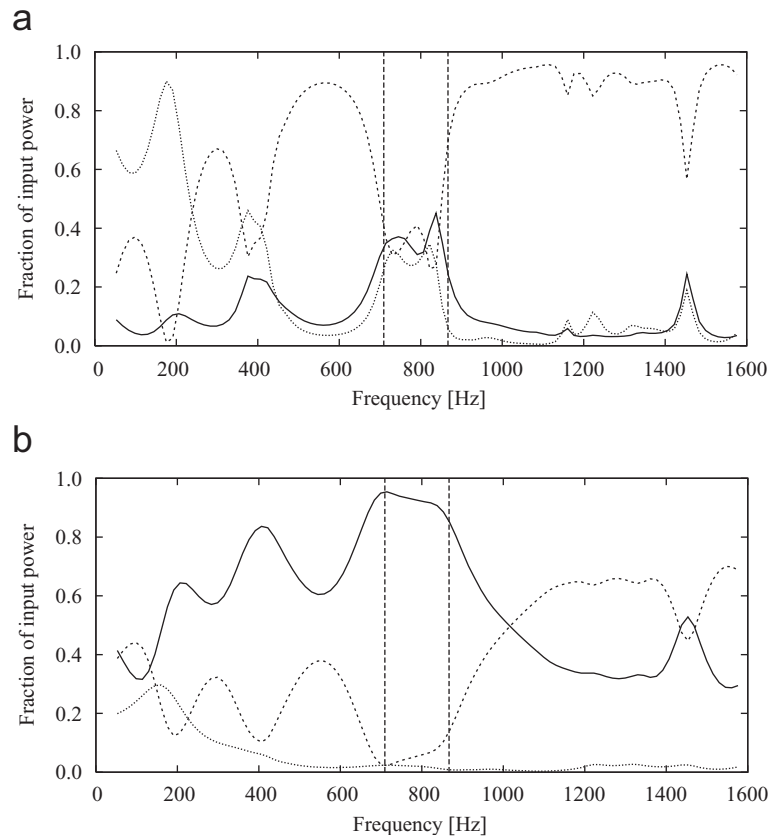


Fig. 15. Dissipation D , reflectance R , and transmittance T for the optimized three-phase design in Fig. 13a for an S wave, (a) $\eta_\rho = 0.05 \text{ s}^{-1}$ and (b) $\eta_\rho = 0.75 \text{ s}^{-1}$. Dissipation (solid), reflectance (dash), transmittance (dot).

Acknowledgements

The work was partially supported by the Danish Technical Research Council through the project “Designing bandgap materials and structures with optimized dynamic properties” and by the Danish Center for Scientific Computing (DCSC).

References

- [1] M. Sigalas, M.S. Kushwaha, E.N. Economou, M. Kafesaki, I.E. Psarobas, W. Steurer, Classical vibrational modes in phononic lattices: theory and experiment, *Zeitschrift für Kristallographie* 220 (2005) 765–809.
- [2] O. Sigmund, J.S. Jensen, Systematic design of phononic band-gap materials and structures by topology optimization, *Philosophical Transactions of the Royal Society London, Series A (Mathematical Physical and Engineering Sciences)* 361 (2003) 1001–1019.
- [3] C. Rupp, M. Frenzel, A. Evgrafov, K. Maute, M.L. Dunn, Design of nanostructures phononic materials, *Proceedings of IMECE2005, 2005 ASME International Mechanical Engineering Congress and Exposition*, Orlando, Florida, USA, 2005.
- [4] S. Halkjær, O. Sigmund, J.S. Jensen, Inverse design of phononic crystals by topology optimization, *Zeitschrift für Kristallographie* 220 (2005) 895–905.
- [5] M.I. Hussein, K. Hamza, G.M. Hulbert, R.A. Scott, K. Saitou, Multiobjective evolutionary optimization of periodic layered materials for desired wave dispersion characteristics, *Structural and Multidisciplinary Optimization* 31 (2006) 60–75.
- [6] J.S. Jensen, Optimal design of lossy bandgap structures, *Proceedings of XXI International Congress on Theoretical and Applied Mechanics*, pages on CD-rom, Warsaw, August 15–21, 2004.
- [7] D. Razansky, P.D. Einziger, D.R. Adam, Effectiveness of acoustic power dissipation in lossy layers, *Journal of the Acoustic Society of America* 116 (1) (2004) 84–89.
- [8] I. Takewaki, Optimal damper placement for planar building frames using transfer functions, *Structural and Multidisciplinary Optimization* 20 (2000) 280–287.

- [9] J.A. Bishop, A.G. Striz, On using genetic algorithms for optimum damper placement in space trusses, *Structural and Multidisciplinary Optimization* 28 (2004) 136–145.
- [10] C.S. Jog, Topology design of structures subjected to periodic loading, *Journal of Sound and Vibration* 253 (3) (2002) 687–709.
- [11] B. Wang, G. Chen, Design of cellular structures for optimum efficiency of heat dissipation, *Structural and Multidisciplinary Optimization* 30 (2005) 447–458.
- [12] S.J. Cox, D.C. Dobson, Maximizing band gaps in two-dimensional photonic crystals, *SIAM Journal for Applied Mathematics* 59 (6) (1999) 2108–2120 ISSN 00361399.
- [13] J.S. Jensen, O. Sigmund, Systematic design of photonic crystal structures using topology optimization: low-loss waveguide bends, *Applied Physics Letters* 84 (12) (2004) 2022–2024.
- [14] D. Royer, E. Dieulesaint, *Elastic Waves in Solids I*, Springer, Berlin, Heidelberg, 2000 ISBN 3-540-65932-3.
- [15] M.P. Bendsøe, O. Sigmund, *Topology Optimization—Theory, Methods and Applications*, Springer, Berlin, Heidelberg, 2003.
- [16] J.S. Jensen, O. Sigmund, Topology optimization of photonic crystal structures: a high-bandwidth low-loss T-junction waveguide, *Journal of the Optical Society of America B* 22 (6) (2005) 1191–1198.
- [17] G. Allaire, G.A. Francfort, A numerical algorithm for topology and shape optimization, in: M.P. Bendsøe, C.A. Mota Soares (Eds.), *Topology Optimization of Structures*, Kluwer Academic Publishers, Dordrecht, 1993, pp. 239–248.
- [18] U. Basu, A.K. Chopra, Perfectly matched layers for time-harmonic elastodynamics of unbounded domains: theory and finite-element implementation, *Computer Methods in Applied Mechanics and Engineering* 192 (2003) 1337–1375.
- [19] D.A. Tortorelli, P. Michaleris, Design sensitivity analysis: overview and review, *Inverse Problems in Engineering* 1 (1994) 71–105.
- [20] L.H. Olesen, F. Okkels, H. Bruus, A high-level programming-language implementation of topology optimization applied to steady-state navier-stokes flow, *International Journal for Numerical Methods in Engineering* 65 (2006) 975–1001.
- [21] K. Svanberg, The method of moving asymptotes—a new method for structural optimization, *International Journal for Numerical Methods in Engineering* 24 (1987) 359–373.
- [22] K. Svanberg, The method of moving asymptotes—modelling aspects and solution schemes, Lecture Notes for the DCAMM Course: advanced Topics in Structural Optimization, Lyngby, June 25–July 3, 1998.
- [23] D.V. Jones, M. Petyt, Ground vibration in the vicinity of a strip load: an elastic layer on an elastic half-space, *Journal of Sound and Vibration* 161 (1) (1993) 1–18.

Available online at www.sciencedirect.com

SCIENCE @ DIRECT®

Journal of Sound and Vibration 289 (2006) 967–986

JOURNAL OF
SOUND AND
VIBRATIONwww.elsevier.com/locate/jsvi

On maximal eigenfrequency separation in two-material structures: the 1D and 2D scalar cases

Jakob S. Jensen^{a,*}, Niels L. Pedersen^b^a*Department of Mechanical Engineering, Technical University of Denmark, Nils Koppels Allé,
Building 404, DK-2800 Kgs. Lyngby, Denmark*^b*Institute of Mechanical Engineering, Aalborg University, Pontoppidanstræde 101, DK-9220 Aalborg East, Denmark*

Received 1 March 2004; received in revised form 7 February 2005; accepted 1 March 2005

Available online 8 August 2005

Abstract

We present a method to maximize the separation of two adjacent eigenfrequencies in structures with two material components. The method is based on finite element analysis and topology optimization in which an iterative algorithm is used to find the optimal distribution of the materials. Results are presented for eigenvalue problems based on the 1D and 2D scalar wave equations. Two different objectives are used in the optimization, the difference between two adjacent eigenfrequencies and the ratio between the squared eigenfrequencies. In the 1D case, we use simple interpolation of material parameters but in the 2D case the use of a more involved interpolation is needed, and results obtained with a new interpolation function are shown. In the 2D case, the objective is reformulated into a double-bound formulation due to the complication from multiple eigenfrequencies. It is shown that some general conclusions can be drawn that relate the material parameters to the obtainable objective values and the optimized designs.

© 2005 Elsevier Ltd. All rights reserved.

1. Introduction

One strategy for the passive vibration control of mechanical structures is to design the structures so that eigenfrequencies lie as far away as possible from the excitation frequencies. This paper exploits the possibility for using the method of topology optimization to maximize the

*Corresponding author. Tel.: +45 45 25 4280; fax: +45 45 93 1475.

E-mail address: jsj@mek.dtu.dk (J.S. Jensen).

separation of two adjacent eigenfrequencies in structures with two material components. This study is restricted to 1D and 2D structures where the vibrations are governed by the scalar wave equation.

The method of topology optimization [1] has been used to optimize a number of different mechanical and physical systems [2]. The original formulation using a homogenization approach was applied by Diaz and Kikuchi [3] for eigenfrequency optimization. The problem was formulated as a reinforcement problem in which a given structure is reinforced in order to maximize eigenfrequencies. Soto and Diaz [4] considered optimal design of plate structures and they maximized higher-order eigenfrequencies and also two eigenfrequencies simultaneously. Ma et al. [5] used the same formulation to maximize the sums of a number of the lowest eigenfrequencies and also considered maximization of gaps between eigenfrequencies of low-order modes for structures with concentrated masses. Topology optimization using interpolation schemes (e.g. SIMP with penalization) or similar material interpolation models [6], was used by Kosaka and Swan [7] to optimize the sum of low-order eigenfrequencies. In Ref. [8] topology optimization was used to maximize eigenfrequencies of plates. Here, the problem was not formulated as a reinforcement problem and emphasis was laid on the use of an interpolation function different from SIMP. Recently, optimization of the lowest eigenfrequencies for plates subjected to pre-stress has been considered [9].

The separation of adjacent eigenfrequencies is closely related to the existence of gaps in the band structure characterizing wave propagation in periodic elastic materials [10], often referred to as phononic band gaps. This is illustrated by the 1D example in Fig. 1, showing an elastic rod subjected to time-harmonic longitudinal excitation. The rod is made from a periodic material with two components PMMA and aluminum. It can be shown that there are large gaps in the band structure corresponding to frequency ranges where longitudinal waves cannot propagate through the compound material. The implication for the corresponding structure is that no eigenfrequencies exist in these band gap frequency ranges, except possibly for localized modes

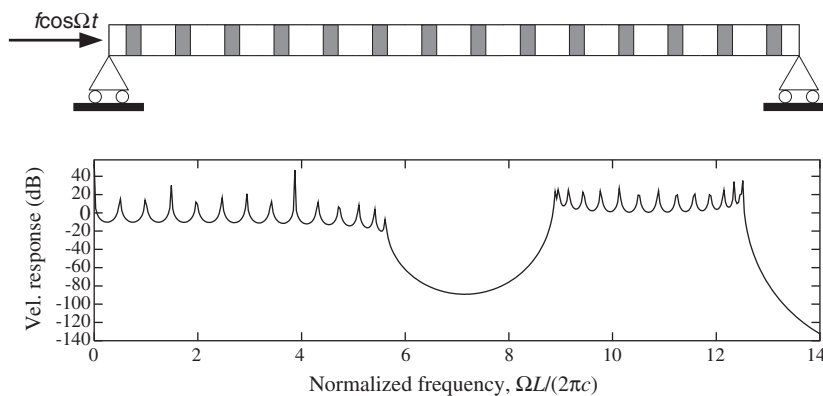


Fig. 1. Longitudinal vibrations of a PMMA rod with 14 periodically placed aluminum inclusions subjected to time-harmonic excitation at the left end. The bottom figure shows the velocity response at the right end versus the normalized excitation frequency $\Omega L/(2\pi c)$, where L is the rod length and c is the wave speed in PMMA. Material properties are $\rho_{\text{PMMA}} = 1200 \text{ kg/m}^3$, $\rho_{\text{alu}} = 2700 \text{ kg/m}^3$, $E_{\text{PMMA}} = 5.3 \text{ GPa}$ and $E_{\text{alu}} = 70 \text{ GPa}$.

near the boundaries [11]. The resulting gaps between two adjacent eigenfrequencies may be large, as seen from the frequency response curve in the figure, and the corresponding response in the gaps when subjected to time-harmonic excitation may be very low.

Topology optimization and related methods have previously been applied to maximize the band gaps in periodic materials for photonic band gaps, i.e. for electromagnetic waves [12,13] and by Sigmund [14] for phononic band gaps. Minimizing the response for band gap structures, i.e. creating a structure with a response as low as possible (cf. Fig. 1), was considered by Sigmund and Jensen [15]. Other works have considered minimizing the vibrational response of structures, such as Ma et al. [16] who used the homogenization approach for the optimal design of structures with low response and in Ref. [17] where structures subjected to time-harmonic loading were optimized with respect to dynamic compliance.

Osher and Santosa [18] used a level set method to study extremal eigenvalue problems for a two-material drum, considering also the case of maximizing the gap between the first and second eigenfrequencies. The present paper extends these results by considering the more general scalar wave equation problem and by systematically considering separation of eigenfrequencies of arbitrary order. We start by treating the simplest problem of structures for which the vibrations are governed by the 1D wave equation and present results for maximizing the gap between two eigenfrequencies and also for an alternative formulation that considers the ratio of adjacent eigenfrequencies. Then we consider the more complicated problem of 2D structures and show results for both optimization formulations. In the 2D case we introduce a new interpolation of the material parameters in order to ensure a final 0–1 design, i.e. a design with a clear separation of the use of the two materials. Additionally, we must treat multiple eigenfrequencies which are present in the optimized designs. The treatment of multiple eigenfrequencies is primarily related to the sensitivity calculation but we also reformulate the objective of the optimization into a double-bound formulation which gives stable convergence. Finally, we present some conclusions.

2. The 1D scalar problem

First, we treat the simplest problem of separating eigenfrequencies for the 1D scalar problem.

2.1. Model

Consider the 1D scalar time-reduced wave equation (Helmholtz equation):

$$(A(x)w')' + \omega^2 B(x)w = 0, \quad (1)$$

subjected to free–free boundary conditions at $x = 0$ and $x = L$.

Eq. (1) governs eigenvibrations of different mechanical systems depending on the choice of the coefficients A and B . For $A = 1$ and $B = \tilde{\rho}/T$ we can interpret the problem as that of transverse vibrations of a taut string with $\tilde{\rho}(x)$ and T being the string mass per length and the tensile force, respectively. For $A = E$ and $B = \rho$ we instead treat the problem of longitudinal vibrations of a uniform rod. In this case, $E(x)$ is Young's modulus and $\rho(x)$ is the density. Similarly, with another set of coefficients we can treat the problem of torsional vibrations of a rod.

To solve the wave equation with in-homogeneous coefficients we apply a standard Galerkin finite element discretization of Eq. (1) and the boundary conditions, which lead to the discrete eigenvalue problem:

$$\mathbf{K}\boldsymbol{\phi} = \omega^2\mathbf{M}\boldsymbol{\phi}, \quad (2)$$

which has $(\omega_i, \boldsymbol{\phi}_i)$ as the i th eigensolution (frequency and vector), and where \mathbf{M} and \mathbf{K} are system matrices given by

$$\mathbf{K} = \sum_{e=1}^N A_e \mathbf{k}_e, \quad \mathbf{M} = \sum_{e=1}^N B_e \mathbf{m}_e, \quad (3)$$

where the summations should be understood in the normal finite element sense, and \mathbf{k}_e and \mathbf{m}_e are element matrices defined as

$$\mathbf{k}_e = \int_{V_e} \frac{d\mathbf{N}^T}{dx} \frac{d\mathbf{N}}{dx} dV, \quad \mathbf{m}_e = \int_{V_e} \mathbf{N}^T \mathbf{N} dV, \quad (4)$$

where \mathbf{N} is the shape function vector for the chosen element type. In this work, we use simple elements, i.e. a 2-node linear element for the 1D case and later a 4-node bilinear quadratic element for the 2D case.

This finite element formulation for the problem is now the basis for the optimization procedure presented in the following.

2.2. Optimization

The basis of topology optimization with a material interpolation scheme is to assign constant material properties to each element in the finite element model and then associate these material properties with continuous design variables [2]. We choose one design variable per element and let it vary continuously between 0 and 1:

$$t_e \in \mathbb{R} \mid 0 \leq t_e \leq 1, \quad e \in [1, N], \quad (5)$$

where N is the number of finite elements in the model.

We now let the material properties in each element, A_e and B_e , be a specified interpolation function of this design variable. This is done so that the material properties for $t_e = 0$ correspond to material 1, i.e. A_1 and B_1 , and similarly for $t_e = 1$ they take the values of material 2, A_2 and B_2 . We emphasize the fundamental difference between this approach in which we use a continuous design variable that allows us to apply well-founded gradient-based optimization techniques, and the use of discrete design variables that requires integer-type algorithms.

Since t_e vary continuously between 0 and 1 we may expect that in the optimal design we can end up with material properties that do not correspond to either of the two materials, but instead with some intermediate values. In order to ensure a well-defined distribution of materials 1 and 2 in the structure, referred to as a 0–1 design, we can manipulate the interpolation functions [6]. Especially when dealing with eigenvalue problems the choice of the interpolation function is important [8]. However, for the 1D problem the choice is less critical and we choose the functions:

$$A_e(t_e) = A_1 + t_e(A_2 - A_1) = (1 + t_e(\mu_A - 1))A_1, \quad (6)$$

$$B_e(t_e) = \frac{B_1}{1 + t_e \left(\frac{B_1}{B_2} - 1 \right)} = \frac{B_1}{1 + t_e (\mu_B^{-1} - 1)}, \quad (7)$$

which correspond to the homogenized density (B_e) and stiffness (A_e) of an “effective” 1D material with two different material components. As will appear later this is sufficient to ensure the wanted 0–1 design. In Eqs. (6)–(7) the coefficient contrast parameters $\mu_A = A_2/A_1$ and $\mu_B = B_2/B_1$ have been introduced.

We now define the difference between two adjacent eigenfrequencies ω_n and ω_{n+1} as our objective for the optimization to maximize. This can be written as a standard optimization problem as follows:

$$\begin{aligned} \max_{t_e} \quad & J = \omega_{n+1} - \omega_n \\ \text{s.t.} \quad & \mathbf{K}\boldsymbol{\phi} = \omega^2 \mathbf{M}\boldsymbol{\phi} \\ & 0 \leq t_e \leq 1, \quad e \in [1, N]. \end{aligned} \quad (8)$$

The maximization problem in Eq. (8) is solved using an iterative procedure involving the following steps:

1. Choose n for the optimization problem.
2. Choose an initial design t_e , typically chosen as a homogeneous material distribution (e.g. $t_e = 0.5$ for all elements).
3. Calculate the M lowest eigenfrequencies ($M > n + 1$) from Eq. (2) and compute the objective function J .
4. Calculate the sensitivities dJ/dt_e .
5. Get a design update using an optimizing routine, e.g. MMA [19].
6. Repeat steps 3–5 until the design change between successive iterations is less than a specified tolerance.

The sensitivity of the objective function is calculated analytically

$$\frac{dJ}{dt_e} = \frac{d\omega_{n+1}}{dt_e} - \frac{d\omega_n}{dt_e}, \quad (9)$$

where the sensitivity of the n th eigenvalue is

$$\frac{d\omega_n}{dt_e} = \frac{\frac{dA_e}{dt_e} u_{\text{ela}} - \omega_n^2 \frac{dB_e}{dt_e} u_{\text{kin}}}{2\omega_n}, \quad (10)$$

where we assume that only A_e and B_e are functions of the design variable t_e on an element level. It is also assumed that the eigenvectors have been normalized so that $\boldsymbol{\phi}^T \mathbf{M}\boldsymbol{\phi} = 1$, and that

$$u_{\text{kin}} = (\boldsymbol{\phi}_e)_n^T \mathbf{m}_e(\boldsymbol{\phi}_e)_n, \quad (11)$$

$$u_{\text{ela}} = (\boldsymbol{\phi}_e)_n^T \mathbf{k}_e(\boldsymbol{\phi}_e)_n, \quad (12)$$

are the element-specific kinetic and elastic energies for the given mode of order n .

In the following section, we show results for a specific choice of the material coefficients. We consider free–free boundary conditions and enumerate the rigid body mode as $n = 0$.

2.3. Results—the elastic rod

In the example, we use the values $\mu_A = 13.21$ and $\mu_B = 2.25$. This corresponds to the ‘elastic rod’ problem of longitudinal vibrations with PMMA and aluminum as the two materials to be distributed. The objective of the optimization is to distribute the two materials in such a way that the eigenfrequency gap $\omega_{n+1} - \omega_n$ is maximized.

Results are shown in Fig. 2 for maximizing the gap for four different cases: $n = 1$, $n = 2$, $n = 9$, and $n = 24$. The figures on the left show the material distribution in the optimized designs with the relative element position indicated along the abscissa. The figures on the right are the results of subjecting the optimized structure to time-harmonic excitation at the left end and computing the velocity response at the right end. The curves show the response versus the normalized excitation frequency $\Omega L/(2\pi c)$, where L is the rod length and $c = \sqrt{A_1/B_1}$ is the wave speed in material 1. From these curves the discrete eigenfrequencies of the structure are easily identified by the peaks.

The most important result is that the designs consist of alternating sections of $t_e = 0$ (material 1) and $t_e = 1$ (material 2); thus the structures are well defined in terms of distribution of materials 1 and 2. Furthermore, there is a direct relation between the mode order n and the number of sections with material 2 (inclusions) that appear. The inclusions also appear to have a uniform size in the interior of the structure, and only near the rod ends the effect of the boundary conditions may be seen as a local modification of the material distribution. For high-order mode separation ($n = 9$ and 24) the optimized gap between mode n and $n + 1$ becomes significantly larger than the gaps between other adjacent modes, and a low-velocity response is noted in the maximized gap. For low-order modes ($n = 1$ and 2) the difference in gaps is smaller and the response drop in the maximized gap is hardly distinguishable compared to the drop in response between the other eigenfrequencies.

2.4. Maximizing the ratio of adjacent eigenfrequencies

Instead of maximizing the gap between two adjacent eigenfrequencies we now maximize the ratio between the two eigenfrequencies (or rather the square of the frequencies). The new objective function is

$$J = \frac{\omega_{n+1}^2}{\omega_n^2}, \quad (13)$$

and the corresponding expression for the sensitivities is given as

$$\frac{dJ}{dt_e} = 2 \frac{\omega_{n+1}}{\omega_n^2} \left(\frac{d\omega_{n+1}}{dt_e} - \frac{\omega_{n+1}}{\omega_n} \frac{d\omega_n}{dt_e} \right), \quad (14)$$

where $d\omega_n/dt_e$ and $d\omega_{n+1}/dt_e$ are found from Eq. (10).

In order to compare the designs obtained using this new objective function with the previous, results are shown with μ_A and μ_B as in Section 2.3 for two different modes, $n = 4$ and $n = 19$. The

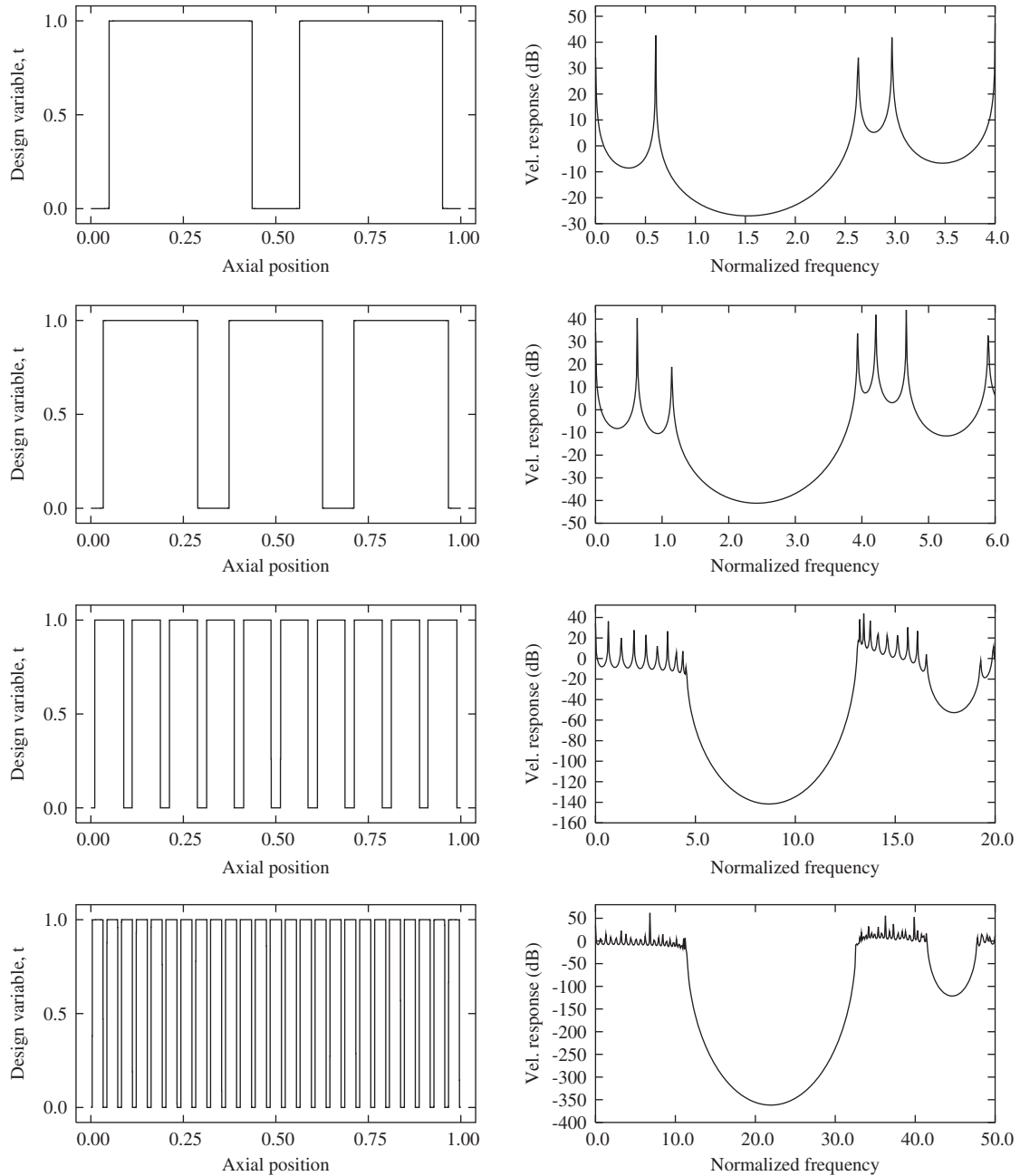


Fig. 2. Optimized design (left) and corresponding velocity response (right) for maximum separation of ω_{n+1} and ω_n . The material parameters correspond to the 'elastic rod case' with $\mu_A = 13.21$, $\mu_B = 2.25$. Results are given for four different values of n , from top to bottom: $n = 1, 2, 9, 24$.

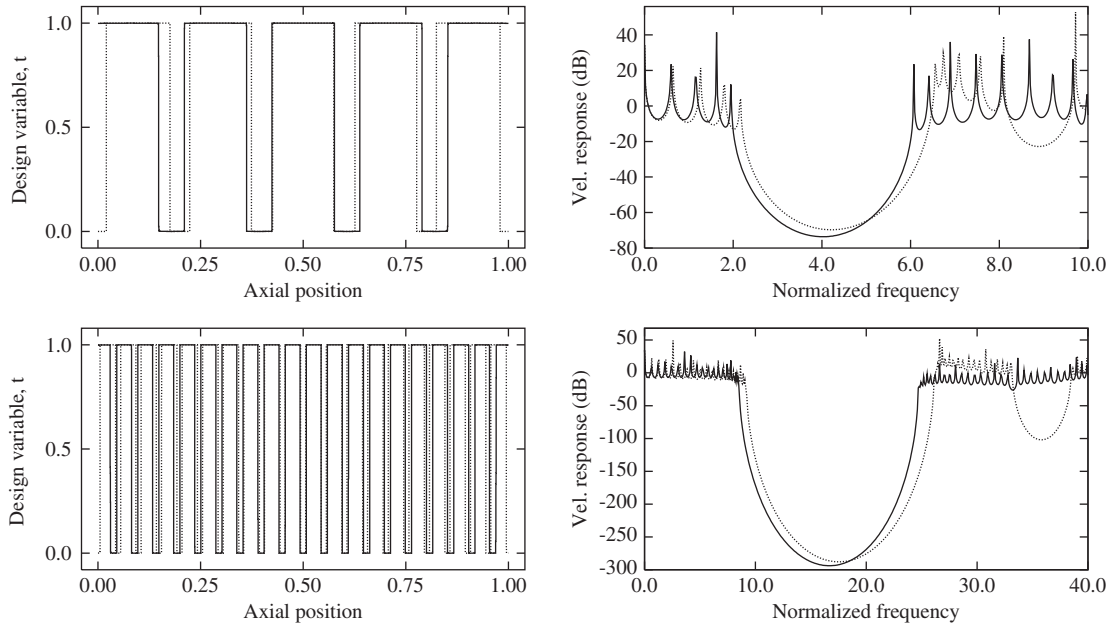


Fig. 3. Comparison of optimized design (left) and velocity response (right) for maximizing the eigenfrequency gap $\omega_{n+1} - \omega_n$ (dotted lines) and maximizing the eigenfrequency ratio $\omega_{n+1}^2/\omega_n^2$ (solid lines). Material parameters are as for Fig. 2 and results are given for $n = 4$ and 19.

comparison is shown in Fig. 3 with the results for the new objective function plotted with solid lines and for the old objective function with dotted lines.

The material distribution curves left show that the new objective function has caused a shift in the distribution between materials 1 and 2 and that the material in the end of the rods is now material 2 instead of material 1. Interestingly, the response curves on the right show that the response in the gaps optimized for maximum ratio drops lower in both examples even though the absolute gap size is smaller for these designs.

We now introduce a material parameter β that characterizes the contrast between materials

$$\beta = \mu_A \mu_B > 1, \tag{15}$$

where the last inequality condition just implies that if not fulfilled the enumeration of the two materials should be interchanged.

In Fig. 4, we show results for maximizing the ratio of eigenfrequencies for three different combinations of material coefficients but keeping $\beta = 4$. We vary μ_A and μ_B such that in the top figures $\mu_A = \mu_B$, in the middle figures $\mu_A = 4, \mu_B = 1$, and in the bottom figures $\mu_A = 1$ and $\mu_B = 4$. For all three combinations we maximize the ratio for $n = 4$ and find that the ratio for the optimized designs in all cases becomes 3.09. For other combinations of material coefficients and when optimizing for other n , we see that the maximum ratio between the adjacent eigenfrequencies obtainable for any mode order seems to depend only on the parameter β . However, as also seen in the figure, the material distribution varies and there is also a large difference in the response curves for the different combinations of material coefficients.

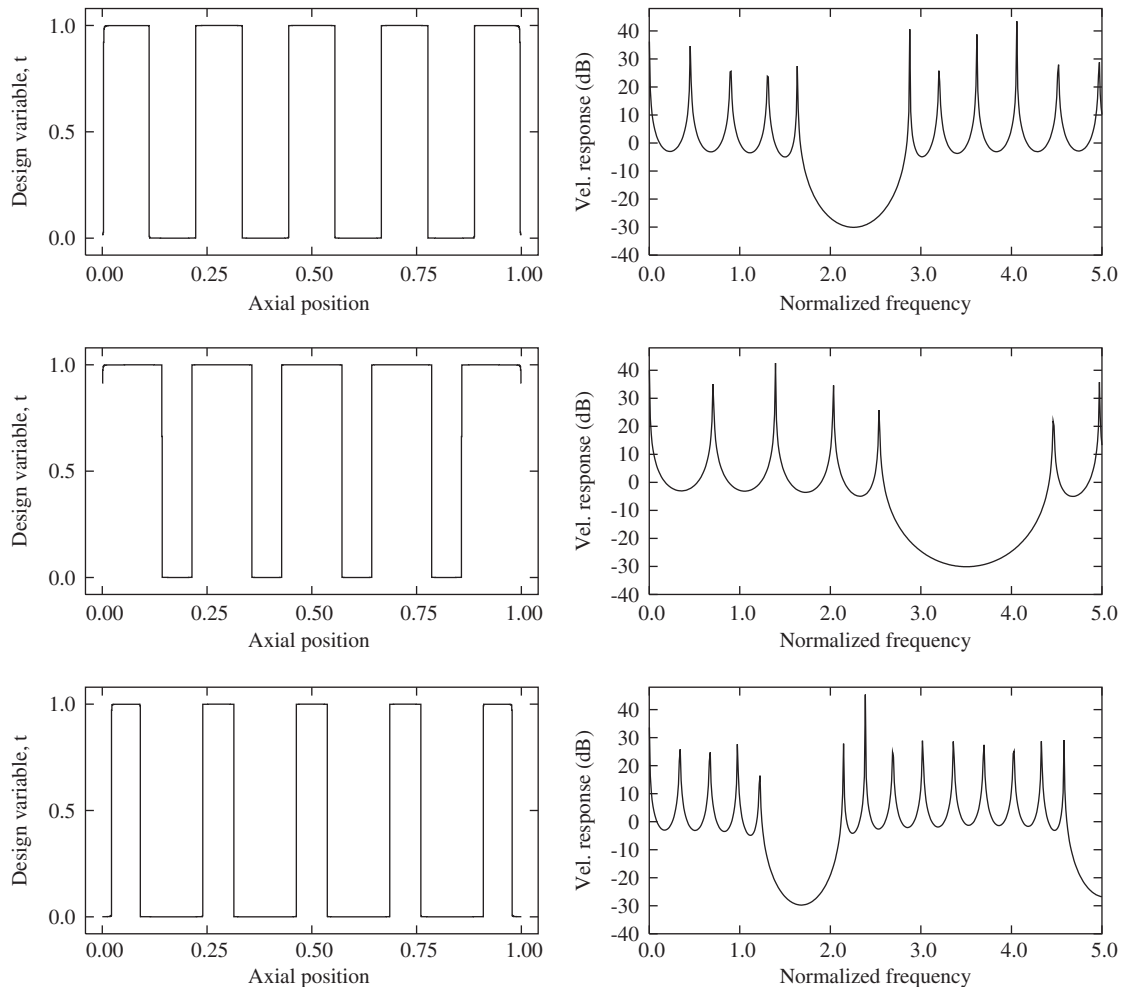


Fig. 4. Optimized design (left) and corresponding velocity response (right) for maximized eigenvalue ratio ω_5^2/ω_4^2 for three different choices of μ_A and μ_B , top: $\mu_A = \mu_B = 2$, middle: $\mu_A = 4$, $\mu_B = 1$, and bottom: $\mu_A = 1$, $\mu_B = 4$. The maximum ratio is (for $n = 4$ as shown) for all three cases equal to 3.09.

We now plot the maximum obtainable eigenfrequency ratio versus mode order n for different values of the parameter β . Fig. 5 shows the maximum ratio for three different values of β , corresponding to the combination of coefficients for the elastic rod ($\beta \approx 29.7$), as well as for $\beta = 2$ and $\beta = 9$. The ratio for a homogeneous structure which is given by the analytical expression $\omega_{n+1}^2/\omega_n^2 = (n+1)^2/n^2$ is also shown in the figure. Naturally, for higher contrast, i.e. higher values of β , the maximum ratio is higher. Also it appears that for high values of n this ratio attains a constant value.

Fig. 4 shows that although the eigenfrequency ratio for the optimal design depends only on the value of the parameter β , the material distribution depends on the chosen values of the material

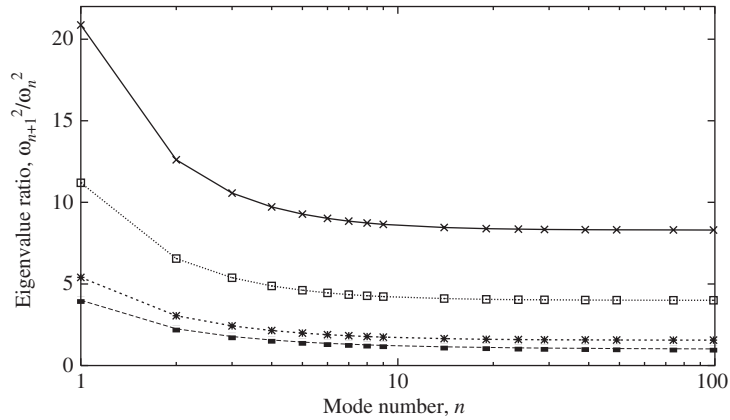


Fig. 5. The maximum eigenfrequency ratio $\omega_{n+1}^2/\omega_n^2$ as a function of the mode order n . Curves are presented for the homogeneous case (■) as well as for three values of $\beta = \mu_A\mu_B$: $\beta = 2$ (*), $\beta = 9$ (□), and $\beta = 29.7$ (×), the latter corresponding to the elastic rod case.

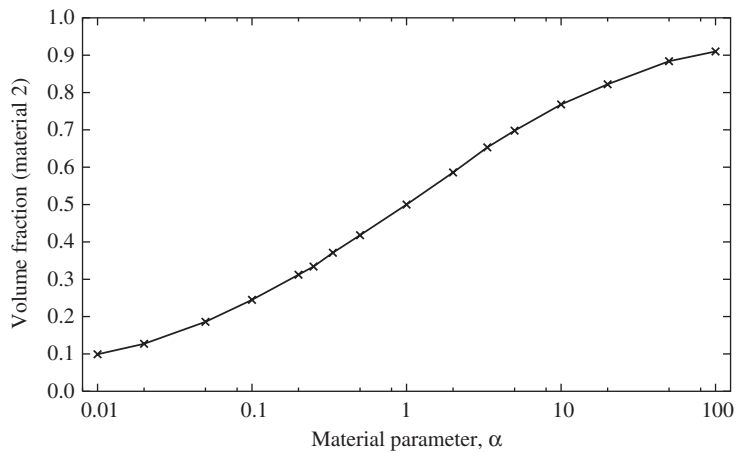


Fig. 6. Fraction of material 2 in the optimized design as a function of the material parameter $\alpha = \mu_A/\mu_B$. The fraction is calculated in the middle of the structure where the end effects do not play a role.

coefficients. In order to analyze this effect, a second material parameter is introduced:

$$\alpha = \frac{\mu_A}{\mu_B}. \tag{16}$$

We now optimize the ratio for different material coefficients but keep α constant. In this case the optimized material distribution is always the same, whereas the maximum eigenvalue ratio varies significantly. In Fig. 6, we plot the volume fraction of material 2 versus the value of α . The volume fraction is computed in the interior part of the domain where the boundary effects are not important. As seen, with $\alpha = 1$ the two materials are evenly distributed in the optimized design,

whereas if α is increased material 2 is dominating and for lower values of α material 1 is dominating. If $\mu_A = 1$ (e.g. a taut string) we have $\alpha = 1/\beta < 1$ which shows that material 1 (the lighter material) is always dominant in the optimized design for this special case.

3. The 2D scalar case

We now consider the more complex problem of the 2D scalar case.

3.1. Model

The 2D scalar time-reduced wave equation (Helmholtz equation) is given by

$$\nabla^T(A(x,y)\nabla w) + \omega^2 B(x,y)w = 0, \quad (17)$$

where the problem-dependent material coefficients A and B can now vary in the 2D plane (x, y) . As in the 1D case we apply a standard FEM discretization, which leads to the discrete eigenvalue problem stated in Eqs. (2)–(3). The element matrices are in the 2D case given by

$$\mathbf{k}_e = \int_{V_e} (\mathbf{\partial N})^T \mathbf{\partial N} dV, \quad \mathbf{m}_e = \int_{V_e} \mathbf{N}^T \mathbf{N} dV, \quad (18)$$

where

$$\mathbf{\partial} = \begin{bmatrix} \partial/\partial x & 0 \\ 0 & \partial/\partial y \end{bmatrix}. \quad (19)$$

Also in the 2D case we may study different structural vibration problems by changing the two coefficients A and B . Letting $A = 1$ and $B = \rho/T$ enables us to analyze the membrane problem where $\rho(x, y)$ is the density and T is the uniform tension (force per area). Alternatively with $A = E/(2(1 + \nu))$, where $E(x, y)$ is Young's modulus and $\nu(x, y)$ is Poisson's ratio, and with $B = \rho(x, y)$ being the density, Eq. (19) governs out-of-plane shear vibrations of a thick elastic body.

3.2. Optimization

When we optimize a 2D domain with respect to maximizing the gap between eigenfrequencies there are a number of extra difficulties we must deal with. The primary source of the difficulties is the possibility of multiple eigenfrequencies. The multiple eigenfrequencies can be calculated without difficulty using, e.g. the subspace iteration method [20].

The objective for the optimization is as in the 1D case given by

$$\text{maximize } J = \omega_{n+1} - \omega_n, \quad (20)$$

where the gap between the eigenfrequency of order $n + 1$ and n is maximized.

If the eigenfrequencies of order $n + 1$ and n are both distinct eigenpairs, with squared eigenfrequencies ω_{n+1}^2 and ω_n^2 and corresponding eigenvectors ϕ_{n+1} and ϕ_n , no problems arise and we use the objective (20) directly since the sensitivities of the squared eigenfrequency with respect

to a design parameter t_e are given by

$$\frac{d\omega^2}{dt_e} = \boldsymbol{\Phi}^T \left(\frac{d\mathbf{K}}{dt_e} - \omega^2 \frac{d\mathbf{M}}{dt_e} \right) \boldsymbol{\Phi}, \quad (21)$$

where it is assumed that the eigenvector has been normalized so that $\boldsymbol{\Phi}^T \mathbf{M} \boldsymbol{\Phi} = 1$. In the case of multiple eigenvalues we cannot use Eq. (21) to find the sensitivities. The extended method is presented in Ref. [21] and was used more recently in Ref. [22].

We elaborate on the case of a double eigenfrequency with two corresponding eigenvectors, $(\omega^2, \boldsymbol{\Phi}_1, \boldsymbol{\Phi}_2)$. It is assumed that the two eigenvectors are normalized with respect to the mass matrix as before and that the two eigenvectors are orthogonal, i.e.,

$$\boldsymbol{\Phi}_1^T \mathbf{M} \boldsymbol{\Phi}_2 = 0. \quad (22)$$

The problem is that any linear combination of the two eigenvectors is also an eigenvector with the same corresponding eigenfrequency:

$$\bar{\boldsymbol{\Phi}} = c_1 \boldsymbol{\Phi}_1 + c_2 \boldsymbol{\Phi}_2, \quad (23)$$

$$c_1^2 + c_2^2 = 1 \Rightarrow \bar{\boldsymbol{\Phi}}^T \mathbf{M} \bar{\boldsymbol{\Phi}} = 1. \quad (24)$$

Therefore, the sensitivities are not only related to the change in design space, given by the change in design parameter t_e , but also by the choice of the eigenvector. Only for two specific eigenvectors, depending on the design parameter, do the sensitivities have meaning, because only these two eigenvectors exist when t_e is changed. By inserting Eq. (23) in Eq. (21) we get

$$\frac{d\omega^2}{dt_e} = c_1^2 g_{11} + c_2^2 g_{22} + 2c_1 c_2 g_{12}, \quad (25)$$

$$g_{\alpha\beta} = \boldsymbol{\Phi}_\alpha^T \left(\frac{d\mathbf{K}}{dt_e} - \omega^2 \frac{d\mathbf{M}}{dt_e} \right) \boldsymbol{\Phi}_\beta. \quad (26)$$

The extreme values of $d\omega^2/dt_e$ are found by differentiating Eq. (25) with respect to the two constants c_1 and c_2 and setting this equal to zero

$$\begin{bmatrix} g_{11} & g_{12} \\ g_{12} & g_{22} \end{bmatrix} \begin{Bmatrix} c_1 \\ c_2 \end{Bmatrix} = \begin{Bmatrix} 0 \\ 0 \end{Bmatrix}, \quad (27)$$

and we now find the eigenvalues and the eigenvectors of the matrix in Eq. (27):

$$\left(g_a, \mathbf{c}_a = \begin{Bmatrix} c_{a1} \\ c_{a2} \end{Bmatrix} \right), \quad \left(g_b, \mathbf{c}_b = \begin{Bmatrix} c_{b1} \\ c_{b2} \end{Bmatrix} \right). \quad (28)$$

The sensitivities of the double eigenfrequency with respect to the design parameter t_e are given directly by g_a and g_b . The corresponding eigenvectors are given by Eq. (23) where the constants c_1 and c_2 are the values of the eigenvector \mathbf{c}_a or \mathbf{c}_b :

$$\frac{d\omega^2}{dt_e} = \begin{cases} g_a & \text{with eigenvector } \boldsymbol{\Phi}_a = c_{a1} \boldsymbol{\Phi}_1 + c_{a2} \boldsymbol{\Phi}_2, \\ g_b & \text{with eigenvector } \boldsymbol{\Phi}_b = c_{b1} \boldsymbol{\Phi}_1 + c_{b2} \boldsymbol{\Phi}_2. \end{cases} \quad (29)$$

For different design parameters the eigenvectors ϕ_a and ϕ_b vary, i.e. the sensitivities in Eq. (29) are given for two specific directions in the space spanned by the two originally determined eigenvectors (ϕ_1, ϕ_2). The derivation shown here is for a double eigenfrequency but the extension to a higher number of multiplicity is straightforward.

It is now possible to find the sensitivities of multiple eigenfrequencies. However, there is still a problem because the sensitivities are given for specific eigenvectors that vary for each design parameter. It is therefore difficult to solve the optimization problem as formulated in Eq. (20). As an alternative formulation we propose to use a double-bound formulation, as in Ref. [14]. The standard-bound formulation is used to reformulate a min–max problem; instead of minimizing the maximum value of a given quantity, a new variable is introduced which is minimized subject to the constraint that the value of the given quantity should be less than this variable. By using the double-bound formulation we do not need to identify the two eigenvectors corresponding to ω_n and ω_{n+1} in each iteration step of the optimization, which may change from iteration to iteration. This is an advantage when we have multiple eigenfrequencies. The optimization problem of maximizing the gap between two eigenfrequencies is thus reformulated as

$$\begin{aligned} \max_{t_e} \quad & J = C_1 - C_2 \\ \text{s.t.} \quad & \omega_{n+i} \geq C_1 \quad i \in [1, n_u] \\ & \omega_{n+1-j} \leq C_2 \quad j \in [1, n_l] \\ & \mathbf{K}\phi = \omega^2 \mathbf{M}\phi \\ & 0 \leq t_e \leq 1, \quad e \in [1, N], \end{aligned} \quad (30)$$

where the two extra variables introduced are C_1 and C_2 . The numbers n_u and n_l are chosen suitable in order to secure that all eigenfrequencies of order $n + 1$ and higher are greater than C_1 and all eigenfrequencies of order n and lower are less than C_2 .

In the practical implementation in each iteration step of the optimization we need to check if there are multiple eigenfrequencies and in this case calculate the sensitivities according to Eq. (29). It is important to note here that the sensitivities found for multiple eigenfrequencies are found for different eigenvectors for each design parameter. If the eigenfrequency of order n is a double eigenfrequency, which vector of sensitivities should we assign to the eigenfrequency of order n and which one to the eigenfrequency of order $n - 1$? For a specific design parameter it is natural to assign the lowest sensitivity (including the sign) to the lowest order eigenfrequency ($n - 1$) and the highest sensitivity to the highest order eigenfrequency (n). If we make the infinitesimal design change the actual values of the involved eigenfrequencies comply with the chosen allocation of the sensitivities.

3.3. Penalization

The simplest interpolation of the material coefficients A and B when using two materials is made using a linear approach:

$$A_e(t_e) = A_1 + t_e(A_2 - A_1) = (1 + t_e(\mu_A - 1))A_1, \quad (31)$$

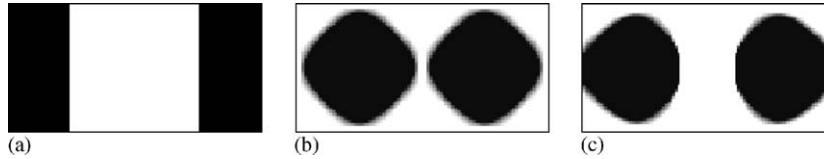


Fig. 7. Eigenfrequency optimization of a 2D domain with two different materials, the ratio of the side length is 2/1 and the domain have no supports (free boundary conditions). (a) The result when optimized for minimum first eigenfrequency, (b) the result when optimized for maximum second eigenfrequency, (c) the result when maximizing the gap between first and second eigenfrequency.

$$B_e(t_e) = B_1 + t_e(B_2 - B_1) = (1 + t_e(\mu_B - 1))B_1, \tag{32}$$

where t_e is the element design parameter which, we recall, takes values between 0 and 1.

As an illustrative example we start with a domain where the ratio between the side lengths of the domain is 2/1 and the domain has free boundary conditions, i.e, we find the free–free modes.

In Fig. 7, the result of three different optimizations are shown: Fig. 7(a) shows the result when minimizing the first eigenfrequency, in Fig. 7(b) the maximization of the second eigenfrequency is shown, and finally in, Fig. 7(c) the result of maximizing the gap between the second and first eigenfrequencies is shown. It should be noted that by the notation of first and second eigenfrequencies we have neglected the rigid body mode.

In Figs. 7(a–c) the black color corresponds to material 2 and the white color corresponds to material 1. From Fig. 7 we see that the maximization of the gap between first and second eigenfrequencies clearly is a compromise between the results of minimizing first eigenfrequency and maximizing second eigenfrequency. It should be noted that for the case of maximizing the second eigenfrequency, this second eigenfrequency is a double eigenfrequency, and in the case of maximizing the gap between the two eigenfrequencies the second eigenfrequency is also a double eigenfrequency. In Fig. 7(a) we have a 0–1 design, i.e. no intermediate values of t_e are present, whereas in Figs. 7(b–c) there are some remaining elements with intermediate values, so-called “gray” elements.

To explain the gray elements we must discuss the interpolation (in some case penalization) that is used. For the optimizations shown in Fig. 7 the linear interpolation in Eqs. (31) and (32) are used. In Ref. [8] it was noted that the important aspect is not the interpolation of the stiffness (here coefficient A) or the interpolation of the mass (here coefficient B), but the interpolation of the eigenfrequency. The squared eigenfrequency ω^2 is by the Rayleigh quotient given as “stiffness divided by mass”. Using Eqs. (31) and (32), we find

$$\frac{A_e}{B_e} = \frac{(1 + t_e(\mu_A - 1)) A_1}{(1 + t_e(\mu_B - 1)) B_1} = f(t_e) \frac{A_1}{B_1}. \tag{33}$$

The curvature of Eq. (33) is such that intermediate values are penalized when an eigenfrequency is minimized. To achieve this intermediate values are penalized when an eigenfrequency is maximized, the curvature of the interpolation function, $f(t_e)$ must have an opposite sign. This can be obtained in many ways and here it is chosen to let the interpolation be a second-order polynomial that goes through the three points

$$P_1 = (0, 1), \quad P_2 = (p_{2x}, p_{2y}), \quad P_3 = (1, \alpha).$$

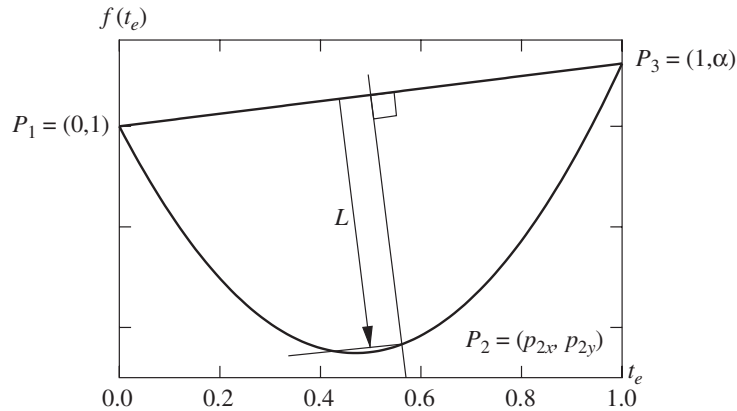


Fig. 8. Interpolation function of the squared eigenfrequency that simultaneously acts as a penalization function when eigenfrequencies are maximized.

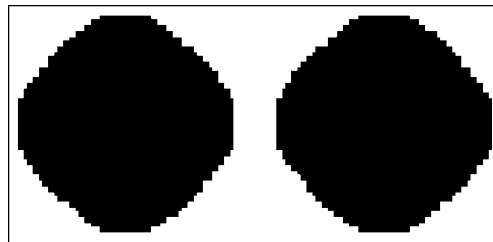


Fig. 9. Optimization of second eigenfrequency of a 2D domain with two different materials using interpolation (34), the ratio of the side lengths is 2/1 and the domain has no supports (free boundary conditions).

The three points are shown in Fig. 8. Point P_2 is at a distance L along a line that is perpendicular to the linear interpolation and intersects this line at the center. The parameter L can be used in a continuation setting where the value of L is slowly increased during optimization to ensure 0–1 design. The penalization of A is then given by

$$A_e = f(t_e)B_e = (k_1(t_e)^2 + k_2t_e + 1) \cdot (1 + t_e(\mu_B - 1))A_1, \tag{34}$$

where k_1 and k_2 are constants that depend on the specific value of L and B_e is the linear interpolation (32), which seems reasonable from a physical point of view.

Using the new penalization function (34) together with Eq. (32) we achieve the optimized design in Fig. 9, where it is clear that the gray elements have been removed. However, there is still a problem with regard to the interpolation functions when the objective is to maximize the gap between two eigenfrequencies. The interpolation function shown in Fig. 8 with positive values of L is suited for the maximization of eigenfrequencies, whereas for negative values of L it is suited for the minimization. In the maximization of the gap we need both so we apply the following approach: when calculating the sensitivities of the constraints in Eq. (30) with respect to the lower bound C_2 we calculate the eigenfrequencies and the sensitivities on the basis of the interpolation function (34) with $L < 0$. When we calculate the sensitivities of the constraints in Eq. (30) with

respect to the higher bound C_1 we calculate the eigenfrequencies and the sensitivities on the basis of the interpolation function (34) with $L > 0$. The cost of using this method is that we have to calculate the eigenfrequencies twice.

3.4. Results for a square design domain

In the first examples we use material parameters corresponding to

$$\mu_A = 2.25, \quad \mu_B = 2.$$

First, we maximize the gap between eigenfrequencies for a square domain. A square design inherently has double eigenfrequencies even with only one material. If we want to maximize the gap between the first and second eigenfrequencies it is not possible to start from an initial design where all of the design values have been assigned a uniform value (e.g. $t_e = 0.5$). To overcome this problem it is chosen to start from a design in which all design variables are assigned a finite value, e.g. $t_e = 0.5$, except for one element in which the value $t_e = 0$ is used. With this small variation, there are no initial double eigenfrequency and the optimization works. We apply a continuation scheme in which the optimization is started with $L = 0$ and the value of $|L|$ is then increased during the optimization to ensure a final 0–1 design. This scheme also reduces the possibility of ending in a local minimum. Additionally, we always perform the optimization with different initial designs in order to ensure that we converge to the same minimum.

In Fig. 10, the results of optimizing the gap between eigenfrequencies are shown for $n \in [1 : 12]$. The design domain is discretized in 100×100 elements. As it appears from the figure, the new penalization scheme has enabled us to obtain optimized structures with a well-defined distribution of the two materials. Only very few gray elements appear such as those near the corners for $n = 7$ and $n = 12$. For some modes it appears that the pattern observed in 1D is valid here as well, i.e. the optimal design is periodic like with the periodicity increasing with increasing mode order. For other modes ($n = 5, n = 10, n = 11$ and $n = 12$) the optimized design show a different topological distribution of the two materials.

3.5. Results for a rectangular design domain

In the next examples the same method of optimization has been used but in this case the design domain size is changed so that the ratio of the side length is 2/1. The results of the optimizations are shown in Fig. 11. The design domain is here discretized in 100×50 elements.

The results depicted in Fig. 11 are similar to the results for the square domain with some topologies being periodic like and others being qualitatively different. We now try to examine if the general results from 1D can be transferred to the 2D case.

3.6. Maximizing the ratio of adjacent eigenfrequencies

As in the 1D case we now change the objective function to that in Eq. (13) so that the ratio between adjacent eigenfrequencies is maximized, but we still use the double-bound formulation introduced in Eq. (30). We repeat the optimization for the rectangular domain for the case where $n = 7$, i.e. corresponding to the design in Fig. 11(g).

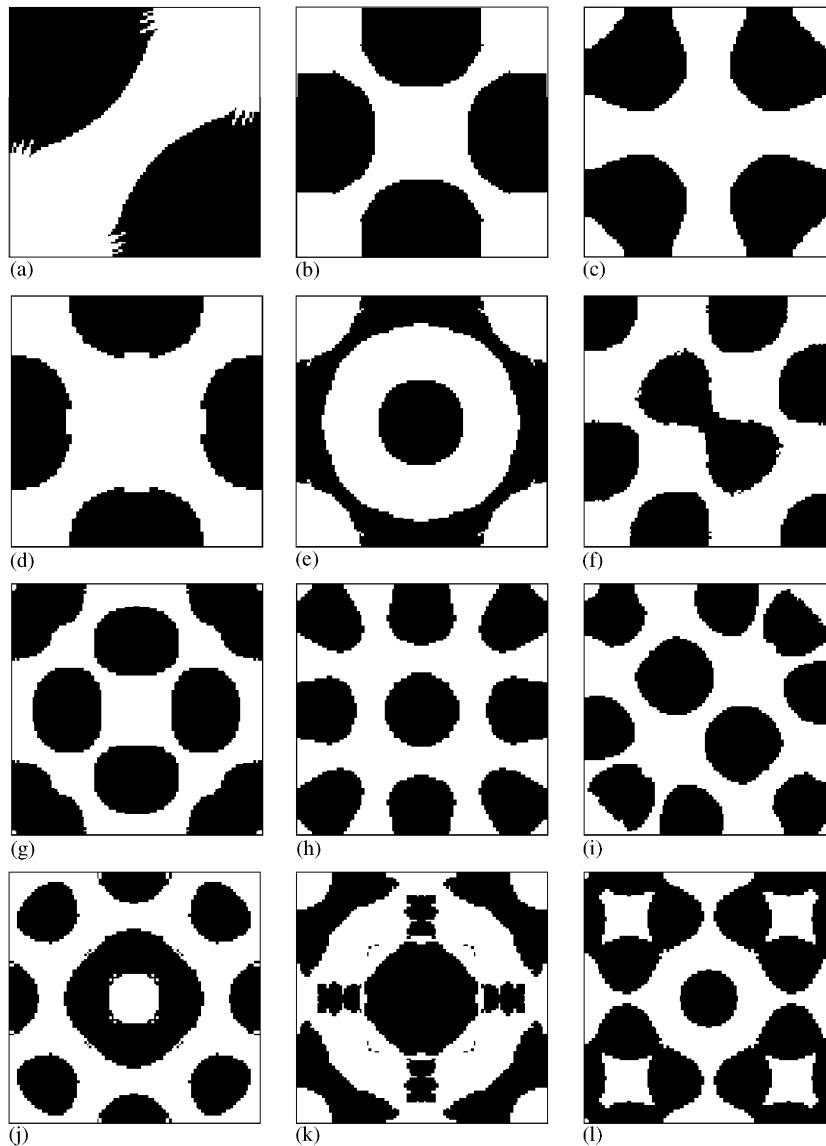


Fig. 10. Eigenfrequency optimization of a 2D domain with two different materials, the design domain is a square that has no supports (free boundary conditions). (a) The result when maximizing the gap between 1st and 2nd eigenfrequency ($n = 1$), (b) $n = 2$, (c) $n = 3$, (d) $n = 4$, (e) $n = 5$, (f) $n = 6$, (g) $n = 7$, (h) $n = 8$, (i) $n = 9$, (j) $n = 10$, (k) $n = 11$, (l) $n = 12$.

We change the values μ_A and μ_B so that the value of α is changed but the value of $\beta = 4.5$ is kept fixed. The results are shown in Fig. 12(a–c). The value of the objective, i.e. the ratio between the squared eigenfrequencies, does not vary significantly but is not exactly constant as in the 1D case. The value of ω_8^2/ω_7^2 is 2.12, 2.06 and 2.00 for Figs. 12(a–c), respectively.

When we compare Figs. 12(a–c) it is clear that although the value of the objective stays almost constant the design change is evident. In the final examples we fix the value of $\alpha = 1.125$ and

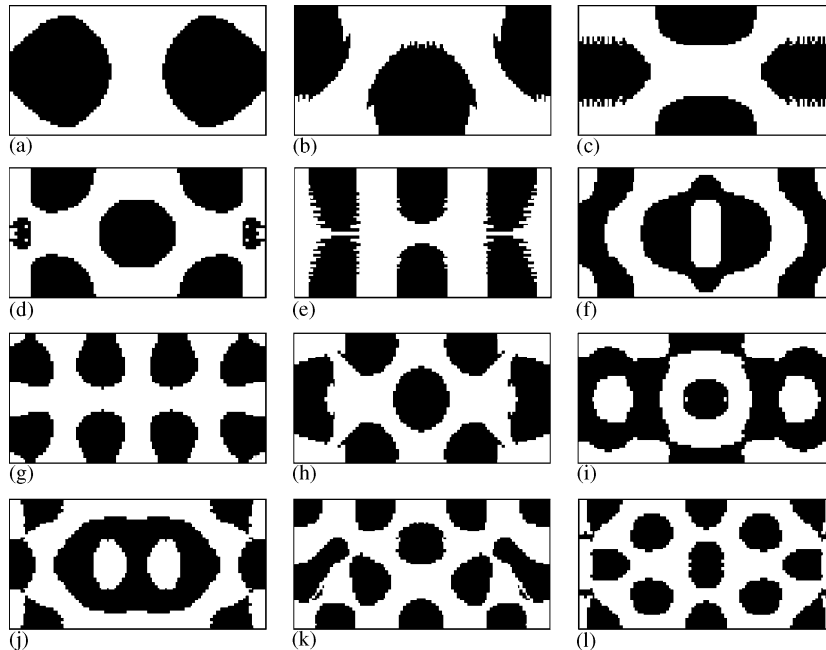


Fig. 11. Eigenfrequency optimization of a 2D domain with two different materials, the ratio of the side length is 2/1 and the domain has no supports (free boundary conditions). (a) $n = 1$, (b) $n = 2$, (c) $n = 3$, (d) $n = 4$, (e) $n = 5$, (f) $n = 6$, (g) $n = 7$, (h) $n = 8$, (i) $n = 9$, (j) $n = 10$, (k) $n = 11$, (l) $n = 12$.

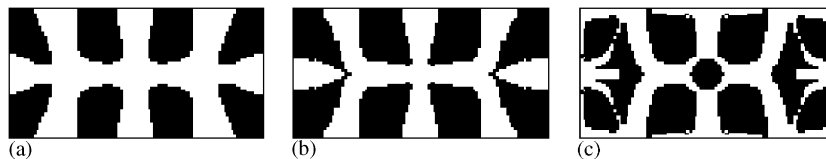


Fig. 12. Maximizing the separation of 7th and 8th eigenfrequencies ($n = 7$). Compared to Fig. 11 the objective is here the ratio between the squared eigenfrequencies and the value of α is changed but the value of $\beta = 4.5$ is kept fixed. (a) $\alpha = 2$, $\omega_8^2/\omega_7^2 = 2.12$, (b) $\alpha = 4$, $\omega_8^2/\omega_7^2 = 2.06$, (c) $\alpha = 8$, $\omega_8^2/\omega_7^2 = 2.00$.

instead vary the value of β . The results of the optimization are shown in Fig. 13(a–c) and the objective values are 2.99, 4.18 and 5.89, respectively. The figures show that we achieve the opposite result compared to when the value of α is changed; the objective value is changed considerably but the design stays more or less the same.

4. Conclusions

In this paper, we consider optimal design of 1D and 2D structures for which the vibrations are governed by the scalar wave equation. The method of topology optimization is used to maximize

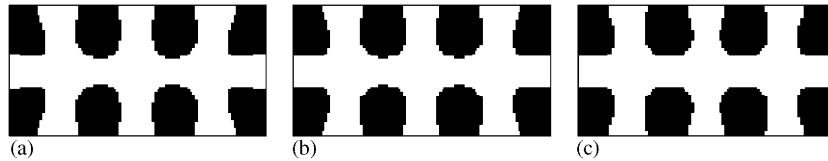


Fig. 13. Maximizing the separation of 7th and 8th eigenfrequencies ($n = 7$). Compared to Fig. 11 the objective is here the ratio between the squared eigenfrequencies and the value of β is changed but the value of $\alpha = 1.125$ is kept fixed. (a) $\beta = 9$, $\omega_8^2/\omega_7^2 = 2.99$, (b) $\beta = 18$, $\omega_8^2/\omega_7^2 = 4.18$, (c) $\beta = 36$, $\omega_8^2/\omega_7^2 = 5.89$.

the separation of two adjacent eigenfrequencies for structures with two different material components.

The optimization procedure is based on finite element analysis with a single continuous design variable assigned to each element. This design variable t_e is defined so that for $t_e = 0$ the material properties in that element are those of material 1 and for $t_e = 1$ the properties correspond to material 2. For intermediate values of t_e the material properties are also intermediate and a special interpolation formulation is introduced in the 2D case to ensure that only the two materials appear in the final optimized design. In the 2D case we treat multiple eigenfrequencies both in relation to the sensitivity calculations but also by reformulating the objective into a double-bound formulation.

Two different formulations are used for maximizing the separation of the eigenfrequencies. The first approach is to use the maximum difference in the frequencies as the optimization objective. For both the 1D and the 2D cases the optimized designs are well-defined 0–1 designs, i.e. no intermediate materials appear in the optimal designs. In 1D the optimized structures are periodic-like and there is a direct relation between the mode order and the number of alternating sections of materials 1 and 2. In the 2D case, square and rectangular domains are studied, and it is seen that the optimized designs for some modes consist of periodically placed inclusions as in 1D, whereas for other modes a quite different topology is obtained.

In the second optimization formulation we maximize the ratio of two adjacent eigenfrequencies. Two material parameters are introduced: α and β that are functions of the material coefficients of the two materials. In 1D it is shown that the material distribution in the final optimized design appears to depend only on α , whereas the maximum ratio for this design depends only on β . For 2D a similar relation appears, but unlike in 1D an exact correspondence is not seen. Additionally, it is seen that in 1D the maximum ratio that can be obtained between adjacent eigenfrequencies seems to be independent of the mode order n for high values of n . This phenomenon was not studied in 2D.

Acknowledgements

The work of Jakob S. Jensen was supported by the Danish Technical Research Council through the project “Designing bandgap materials and structures with optimized dynamic properties”.

References

- [1] M.P. Bendsøe, N. Kikuchi, Generating optimal topologies in structural design using a homogenization method, *Computer Methods in Applied Mechanics and Engineering* 71 (2) (1988) 197–224.
- [2] M.P. Bendsøe, O. Sigmund, *Topology Optimization—Theory, Methods and Applications*, Springer, Berlin, Heidelberg, 2003.
- [3] A. Diaz, N. Kikuchi, Solution to shape and topology eigenvalue optimization problems using a homogenization method, *International Journal for Numerical Methods in Engineering* 35 (1992) 1487–1502.
- [4] C.A. Soto, A.R. Diaz, Layout of plate structures for improved dynamic response using a homogenization method, *Advances in Design Automation* 1 (1993) 667–674.
- [5] Z.-D. Ma, H.-C. Cheng, N. Kikuchi, Structural design for obtaining desired eigenfrequencies by using the topology and shape optimization method, *Computing Systems in Engineering* 5 (1) (1994) 77–89.
- [6] M.P. Bendsøe, O. Sigmund, Material interpolations in topology optimization, *Archive of Applied Mechanics* 69 (1999) 635–654.
- [7] I. Kosaka, C.C. Swan, A symmetry reduction method for continuum structural topology optimization, *Computers and Structures* 70 (1999) 47–61.
- [8] N.L. Pedersen, Maximization of eigenvalues using topology optimization, *Structural and Multidisciplinary Optimization* 20 (2000) 2–11.
- [9] N.L. Pedersen, On topology optimization of plates with pre-stress, *International Journal of Numerical Methods in Engineering* 51 (2) (2001) 225–239.
- [10] M.M. Sigalas, E.N. Economou, Elastic and acoustic wave band structure, *Journal of Sound and Vibration* 158 (2) (1992) 377–382.
- [11] J.S. Jensen, Phononic band gaps and vibrations in one- and two-dimensional mass-spring structures, *Journal of Sound and Vibration* 266 (5) (2003) 1053–1078.
- [12] S.J. Cox, D.C. Dobson, Maximizing band gaps in two-dimensional photonic crystals, *SIAM Journal for Applied Mathematics* 59 (6) (1999) 2108–2120.
- [13] S.J. Cox, D.C. Dobson, Band structure optimization of two-dimensional photonic crystals in *h*-polarization, *Journal of Computational Physics* 158 (2) (2000) 214–224.
- [14] O. Sigmund, Microstructural design of elastic band gap structures, in: G.D. Cheng, Y. Gu, S. Liu, Y. Wang (Eds.), *Proceedings of the Fourth World Congress of Structural and Multidisciplinary Optimization WCSMO-4*, Dalian, China, 2001, CD-rom.
- [15] O. Sigmund, J.S. Jensen, Systematic design of phononic band-gap materials and structures by topology optimization, *Philosophical Transactions of the Royal Society London, Series A (Mathematical, Physical and Engineering Sciences)* 361 (2003) 1001–1019.
- [16] Z.-D. Ma, N. Kikuchi, I. Hagiwara, Structural topology and shape optimization for a frequency response problem, *Computational Mechanics* 13 (1993) 157–174.
- [17] C.S. Jog, Topology design of structures subjected to periodic loading, *Journal of Sound and Vibration* 253 (3) (2002) 687–709.
- [18] S. Osher, F. Santosa, Level set methods for optimization problems involving geometry and constraints i. frequencies of a two-density inhomogeneous drum, *Journal of Computational Physics* 171 (2001) 272–288.
- [19] K. Svanberg, The method of moving asymptotes—a new method for structural optimization, *International Journal for Numerical Methods in Engineering* 24 (1987) 359–373.
- [20] K.J. Bathe, *Finite Element Procedures*, second ed., Prentice-Hall, Englewood Cliffs, NJ, 1996.
- [21] A.P. Seyranian, E. Lund, N. Olhoff, Multiple eigenvalues in structural optimization problems, *Structural Optimization* 8 (4) (1994) 207–227.
- [22] N.L. Pedersen, A.K. Nielsen, Optimization of practical trusses with constraints on eigenfrequencies, displacements, stresses and buckling, *Structural and Multidisciplinary Optimization* 25 (2003) 436–445.

Topological material layout in plates for vibration suppression and wave propagation control

Anders A. Larsen · Bogi Laksafoss ·
Jakob S. Jensen · Ole Sigmund

Received: 13 August 2007 / Revised: 21 February 2008 / Accepted: 28 February 2008
© Springer-Verlag 2008

Abstract We propose a topological material layout method to design elastic plates with optimized properties for vibration suppression and guided transport of vibration energy. The gradient-based optimization algorithm is based on a finite element model of the plate vibrations obtained using the Mindlin plate theory coupled with analytical sensitivity analysis using the adjoint method and an iterative design update procedure based on a mathematical programming tool. We demonstrate the capability of the method by designing bi-material plates that, when subjected to harmonic excitation, either effectively suppress the overall vibration level or alternatively transport energy in predefined paths in the plates, including the realization of a ring wave device.

Keywords Mindlin plate · Topology design · Energy transport · Vibration response

1 Introduction

In this paper we use the method of topology optimization to design bi-material structures for suppressing the vibration response and for controlling the transport of vibration energy in moderately thick plates. Possible applications are for structural shielding and isolation of vibration in the audible frequency range and for the creation of devices that rely on guided transportation of vibrations e.g. for absorption or harvesting of energy.

Topology optimization (Bendsøe and Kikuchi 1988) is a systematic design methodology that allows to create material distributions of one or more materials that optimize a specified objective. Aside from its original application to structural optimization problems in mechanics, many recent extensions to other physics settings have appeared, e.g. in optics, fluid mechanics, electromagnetism, etc. (see e.g. Bendsøe and Sigmund (2003) for a recent comprehensive coverage of the method and its applications).

The idea of using topology optimization to design mechanical structures for passive control of the propagation of elastic waves was suggested in Sigmund and Jensen (2003), in which several examples dealing with wave shielding and wave guiding devices were given. The paper considered the material design problem, in which repetitive unit cells were designed and used for periodic wave-reflectors and also the corresponding structural optimization problem for finite structures to be used for both wave reflecting and wave guiding purposes. In the examples a 2D plane strain model of

Most of this work was performed while AAL was employed at the Department of Mechanical Engineering.

A. A. Larsen (✉)
Department of Mathematics,
Technical University of Denmark, Matematiktorvet,
Building 303S, 2800 Lyngby, Denmark
e-mail: a.a.larsen@mat.dtu.dk

B. Laksafoss
NKT Flexibles, 2605 Brøndby, Denmark
e-mail: bogi.laksafoss@nktflexibles.com

J. S. Jensen · O. Sigmund
Department of Mechanical Engineering,
Technical University of Denmark, Nils Koppels Allé,
Building 404, 2800 Lyngby, Denmark

J. S. Jensen
e-mail: jsj@mek.dtu.dk

O. Sigmund
e-mail: sigmund@mek.dtu.dk

a thick solid was considered. A few years earlier the use of a material distribution method was suggested by Cox and Dobson (1999) for optimizing repetitive unit cells for optical wave reflecting structures (photonic crystals).

The study in Sigmund and Jensen (2003) was extended in two papers (Halkjær et al. 2005, 2006) to deal with propagation of bending waves in moderately thick plates. The relatively low frequency of bending waves makes the plate structures attractive candidates for applications in the audible frequency range. The papers considered the optimization of repetitive unit cells and in Halkjær et al. (2005) bi-material designs were generated, whereas in Halkjær et al. (2006) designs with one material (and void) were generated. The latter paper included a comparison of the theoretical model with experimental results obtained for a specimen with 10 by 10 optimized unit cells.

Several related studies that deal with design of elastic structures for optimized wave propagation characteristics have appeared recently. Hussein et al. (2007) considered the design of 1D layered structures for longitudinal wave propagation and Rupp et al. (2007) considered design of 3D structures for optimized surface wave propagation. In these papers bi-material designs were generated for wave reflection and wave guiding. In Jensen (2007b) bi- and triple-material designs were generated for minimizing the transmission and absorption of elastic waves through slabs of material.

These papers build on numerous works that have considered topology optimization of steady-state forced vibrations of elastic structures. The problem was considered e.g. by Ma et al. (1995), Jog (2002) and recently by Du and Olhoff (2007), Olhoff and Du (2008) for plate structures.

The results in the present paper extends the work in Halkjær et al. (2005, 2006) on plates. Instead of considering the unit cell optimization problem, this paper considers the structural problem that was initiated in Sigmund and Jensen (2003) for a 2D plane strain model, in which the material in the entire plate can be distributed freely not relying on periodicity. Additionally, we consider the possibility to create novel wave propagation control in plates by directing the propagation of waves in certain directions and also the possibility of creating ring wave devices that function purely due to material contrast differences.

The paper is organized as follows: section two presents the plate model and the formulas describing energy transport in plates are presented in section three. In section four the problem is discretized and in section five the optimization problems are defined. Section six and seven show two examples: in the first

example the method is used to design structures with minimized vibrational response in finite frequency ranges and the second example demonstrates the generation of energy transporting devices.

2 Plate model

Plate models are well established but to provide the basis for the energy flow derivations presented in the next section we review the basic equations. The equilibrium equations for an infinitesimal small plate element

$$\frac{\rho h^3}{12} \frac{d^2 \psi_x}{dt^2} = T_x - \frac{\partial M_x}{\partial x} - \frac{\partial M_{xy}}{\partial y} \tag{1}$$

$$\frac{\rho h^3}{12} \frac{d^2 \psi_y}{dt^2} = T_y - \frac{\partial M_y}{\partial y} - \frac{\partial M_{xy}}{\partial x} \tag{2}$$

$$\rho h \frac{d^2 w}{dt^2} = \frac{\partial T_x}{\partial x} + \frac{\partial T_y}{\partial y} \tag{3}$$

govern the out-of-plane deflection w and the angles of rotation ψ_x and ψ_y (see Fig. 1). The moments are denoted M_x , M_y and M_{xy} , the shear forces T_x and T_y , and ρ is the mass density and h is the plate thickness.

We use the Mindlin plate theory to account for the transverse shear deformation introduced in moderately thick plates. Thus the moments and shear forces are defined in terms of the deflection and rotations as

$$\begin{Bmatrix} M_x \\ M_y \\ M_{xy} \\ T_x \\ T_y \end{Bmatrix} = -\mathbf{D} \begin{Bmatrix} \psi_{x,x} \\ \psi_{y,y} \\ \psi_{x,y} + \psi_{y,x} \\ \psi_x - w_{,x} \\ \psi_y - w_{,y} \end{Bmatrix} \tag{4}$$

where the subscript $()$, denotes differentiation with respect to the spatial variables and the stiffness matrix is defined as

$$\mathbf{D} = \begin{bmatrix} D & \nu D & 0 & 0 & 0 \\ \nu D & D & 0 & 0 & 0 \\ 0 & 0 & \frac{1-\nu}{2} D & 0 & 0 \\ 0 & 0 & 0 & kGh & 0 \\ 0 & 0 & 0 & 0 & kGh \end{bmatrix} \tag{5}$$

where $D = \frac{Eh^3}{12(1-\nu^2)}$ is the flexural rigidity, G is the shear modulus, ν is Poissons' ratio, and k is a shear correction factor which takes the value $\frac{5}{6}$ for the plate.

Assuming harmonic excitation of the form $f e^{i\omega t}$, with angular frequency ω , the resulting displacements

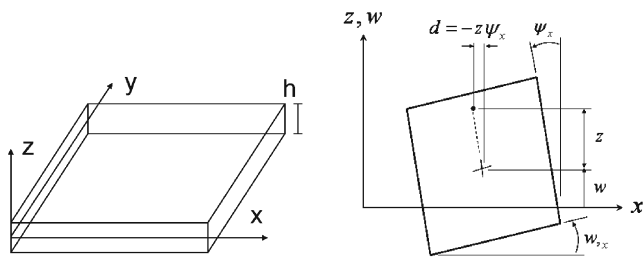


Fig. 1 Plate element showing rotations and translations. Coordinate system and dimensions

will also be harmonic. We use the following complex notation

$$\psi_x(x, y, t) = \Re \left(\tilde{\psi}_x(x, y) e^{i\omega t} \right) \tag{6}$$

$$\psi_y(x, y, t) = \Re \left(\tilde{\psi}_y(x, y) e^{i\omega t} \right) \tag{7}$$

$$w(x, y, t) = \Re \left(\tilde{w}(x, y) e^{i\omega t} \right) \tag{8}$$

where a tilde denotes the complex amplitudes and i is the imaginary unit. \Re symbolizes the real part of a complex quantity. Inserting (4)–(8), (1)–(3) can be rewritten in the complex form

$$\begin{aligned} & \left(D \left(\tilde{\psi}_{x,x} + \nu \tilde{\psi}_{y,y} \right) \right)_{,x} + \left(\frac{1-\nu}{2} D \left(\tilde{\psi}_{x,y} + \tilde{\psi}_{y,x} \right) \right)_{,y} \\ & + kGh \left(\tilde{w}_{,x} - \tilde{\psi}_x \right) + \omega^2 \frac{\rho h^3}{12} \tilde{\psi}_x = 0 \end{aligned} \tag{9}$$

$$\begin{aligned} & \left(D \left(\tilde{\psi}_{y,y} + \nu \tilde{\psi}_{x,x} \right) \right)_{,y} + \left(\frac{1-\nu}{2} D \left(\tilde{\psi}_{y,x} + \tilde{\psi}_{x,y} \right) \right)_{,x} \\ & + kGh \left(\tilde{w}_{,y} - \tilde{\psi}_y \right) + \omega^2 \frac{\rho h^3}{12} \tilde{\psi}_y = 0 \end{aligned} \tag{10}$$

$$\begin{aligned} & \left(kGh \left(\tilde{w}_{,x} - \tilde{\psi}_x \right) \right)_{,x} + \left(kGh \left(\tilde{w}_{,y} - \tilde{\psi}_y \right) \right)_{,y} \\ & + \omega^2 \rho h \tilde{w} = 0 \end{aligned} \tag{11}$$

in which the moments and forces have been written explicitly in terms of the complex deflection and rotation amplitudes.

The equations are solved using a standard finite element method implementation, but first we derive expressions for energy transport in the plate in continuous form.

3 Energy flow and the Poynting vector

The Poynting vector $\mathbf{P}(x, y, z, t)$ is a measure of the point-wise instantaneous power flow in the plate. The in-plane components are (Auld 1973)

$$P_x = -\sigma_{xx} \dot{d}_x - \sigma_{yx} \dot{d}_y - \sigma_{zx} \dot{d}_z \tag{12}$$

$$P_y = -\sigma_{xy} \dot{d}_x - \sigma_{yy} \dot{d}_y - \sigma_{zy} \dot{d}_z \tag{13}$$

where σ_{ij} are the stress components and $\{\dot{d}_x, \dot{d}_y, \dot{d}_z\}$ are the point-wise velocity components.

The velocity components are related to the plate model degrees-of-freedom in the following way

$$\dot{d}_x(x, y, z) = -z \dot{\psi}_x(x, y) \tag{14}$$

$$\dot{d}_y(x, y, z) = -z \dot{\psi}_y(x, y) \tag{15}$$

$$\dot{d}_z(x, y, z) = \dot{w}(x, y) \tag{16}$$

assuming that the out-of-plane (z -direction) velocity is constant through the plate thickness and the in-plane velocities depend linearly with the distance z from the mid-plane (see Fig. 1).

The total xy -plane power flow per unit area, denoted $\hat{\mathbf{P}}(x, y, t)$, is found by integrating \mathbf{P} through the plate thickness:

$$\hat{\mathbf{P}}(x, y, t) = \int_{-h/2}^{h/2} \mathbf{P}(x, y, z, t) dz \tag{17}$$

so that

$$\hat{P}_x = \int_{-h/2}^{h/2} (\sigma_{xx} z \dot{\psi}_x + \sigma_{yx} z \dot{\psi}_y - \sigma_{zx} \dot{w}) dz \tag{18}$$

$$\hat{P}_y = \int_{-h/2}^{h/2} (\sigma_{xy} z \dot{\psi}_x + \sigma_{yy} z \dot{\psi}_y - \sigma_{zy} \dot{w}) dz \tag{19}$$

The integrals can be expressed in terms of the defined moments and shear forces by using the relations

$$M_x = \int_{-h/2}^{h/2} \sigma_{xx} z dz, \quad M_y = \int_{-h/2}^{h/2} \sigma_{yy} z dz,$$

$$M_{xy} = \int_{-h/2}^{h/2} \sigma_{yx} z dz,$$

$$T_x = \int_{-h/2}^{h/2} \sigma_{zx} dz, \quad T_y = \int_{-h/2}^{h/2} \sigma_{zy} dz, \tag{20}$$

which give the following expressions for the Poynting vector integrated through the plate thickness

$$\hat{P}_x = M_x \dot{\psi}_x + M_{xy} \dot{\psi}_y - T_x \dot{w} \tag{21}$$

$$\hat{P}_y = M_{yx} \dot{\psi}_x + M_y \dot{\psi}_y - T_y \dot{w} \tag{22}$$

By inserting the expressions for the moments and shear forces we obtain

$$\begin{aligned} \hat{P}_x = & -D(\psi_{x,x} + \nu \psi_{y,y}) \dot{\psi}_x - \frac{1-\nu}{2} D(\psi_{x,y} + \psi_{y,x}) \dot{\psi}_y \\ & + kGh(\psi_x - w_{,x}) \dot{w} \end{aligned} \tag{23}$$

$$\begin{aligned} \hat{P}_y = & -\frac{1-\nu}{2} D(\psi_{x,y} + \psi_{y,x}) \dot{\psi}_x - D(\nu \psi_{x,x} + \psi_{y,y}) \dot{\psi}_y \\ & + kGh(\psi_y - w_{,y}) \dot{w} \end{aligned} \tag{24}$$

The above expressions provide instantaneous values of the power flow. The energy transported during a single period of excitation \mathcal{T} is defined as:

$$\mathbf{W} = \int_{\mathcal{T}} \hat{\mathbf{P}} dt \tag{25}$$

This measure of the energy transported by a travelling wave is considered as the optimization objective in our second application example. In the case of a standing wave considered in the first example, W vanishes since no energy is transported in this case.

The time-dependence of the solution from (6)–(8) is inserted into (23)–(24) and the integration is performed to yield the expressions

$$\begin{aligned} W_x &= \pi D \Re \left(i \left(\tilde{\psi}_{x,x} + \nu \tilde{\psi}_{y,y} \right) \tilde{\psi}_x^* \right) \\ &+ \frac{1-\nu}{2} \pi D \Re \left(i \left(\tilde{\psi}_{x,y} + \tilde{\psi}_{y,x} \right) \tilde{\psi}_y^* \right) \\ &- \pi k Gh \Re \left(i \left(\tilde{\psi}_x - \tilde{w}_{,x} \right) \tilde{w}^* \right) \end{aligned} \tag{26}$$

$$\begin{aligned} W_y &= \frac{1-\nu}{2} \pi D \Re \left(i \left(\tilde{\psi}_{x,y} + \tilde{\psi}_{y,x} \right) \tilde{\psi}_x^* \right) \\ &+ \pi D \Re \left(i \left(\nu \tilde{\psi}_{x,x} + \tilde{\psi}_{y,y} \right) \tilde{\psi}_y^* \right) \\ &- \pi k Gh \Re \left(i \left(\tilde{\psi}_y - \tilde{w}_{,y} \right) \tilde{w}^* \right) \end{aligned} \tag{27}$$

where the asterisk is used to denote the complex conjugate.

4 Discretized problem

A standard Galerkin FE approach is used to set up a set of discretized equations based on (9)–(11):

$$\left(-\omega^2 \mathbf{M} + i\omega \mathbf{C} + \mathbf{K} \right) \mathbf{d} = \mathbf{f} \tag{28}$$

in which \mathbf{M} , \mathbf{C} and \mathbf{K} are the mass-, damping- and stiffness matrices, respectively, \mathbf{d} is a vector containing the complex nodal variables and \mathbf{f} is a load vector. The matrices \mathbf{M} , \mathbf{C} and \mathbf{K} are collected in the system matrix $\mathbf{S} = -\omega^2 \mathbf{M} + i\omega \mathbf{C} + \mathbf{K}$.

\mathbf{M} and \mathbf{K} are assembled from the local element matrices in the usual way. These are based on the local shape functions defined as:

$$\begin{Bmatrix} \tilde{w} \\ \tilde{\psi}_x \\ \tilde{\psi}_y \end{Bmatrix} = \mathbf{N} \mathbf{d}^e = \begin{bmatrix} \mathbf{N}_1^T \\ \mathbf{N}_2^T \\ \mathbf{N}_3^T \end{bmatrix} \mathbf{d}^e \tag{29}$$

and from the \mathbf{B} matrix defined as:

$$\begin{Bmatrix} \tilde{\psi}_{x,x} \\ \tilde{\psi}_{y,y} \\ \tilde{\psi}_{x,y} + \tilde{\psi}_{y,x} \\ \tilde{\psi}_x - \tilde{w}_{,x} \\ \tilde{\psi}_y - \tilde{w}_{,y} \end{Bmatrix} = \mathbf{\partial} \mathbf{N} \mathbf{d}^e = \mathbf{B} \mathbf{d}^e = \begin{bmatrix} \mathbf{N}_{2,x}^T \\ \mathbf{N}_{3,y}^T \\ \mathbf{N}_{2,y}^T + \mathbf{N}_{3,x}^T \\ \mathbf{N}_2^T - \mathbf{N}_{1,x}^T \\ \mathbf{N}_3^T - \mathbf{N}_{1,y}^T \end{bmatrix} \mathbf{d}^e \tag{30}$$

In all examples presented in this paper we use rectangular 4-noded bilinear elements with dimensions $2a$ by $2b$.

Damping is not defined in the continuous problem but included in the discretized version in the form of proportional (Rayleigh) damping:

$$\mathbf{C} = \alpha \mathbf{M} + \beta \mathbf{K} \tag{31}$$

where α and β is the mass- and stiffness-proportional damping coefficients.

The load is specified in the examples and the load vector is assembled in the usual way.

Inserting the discretized displacements into the formulas for the energy transport we obtain

$$W_x = \pi \Re \left(i \left(\mathbf{d}^e \right)^T \mathbf{Q}_x^e \left(\mathbf{d}^e \right)^* \right) \tag{32}$$

$$W_y = \pi \Re \left(i \left(\mathbf{d}^e \right)^T \mathbf{Q}_y^e \left(\mathbf{d}^e \right)^* \right) \tag{33}$$

in which \mathbf{Q}_x^e and \mathbf{Q}_y^e are local element matrices defined in terms of the shape functions and their derivatives as:

$$\begin{aligned} \mathbf{Q}_x^e &= D(\mathbf{N}_{2,x} + \nu \mathbf{N}_{3,y}) \mathbf{N}_2^T + \frac{1-\nu}{2} D(\mathbf{N}_{2,y} + \mathbf{N}_{3,x}) \mathbf{N}_3^T \\ &- k Gh (\mathbf{N}_2 - \mathbf{N}_{1,x}) \mathbf{N}_1^T \end{aligned} \tag{34}$$

$$\begin{aligned} \mathbf{Q}_y^e &= D(\nu \mathbf{N}_{2,x} + \mathbf{N}_{3,y}) \mathbf{N}_3^T + \frac{1-\nu}{2} D(\mathbf{N}_{2,y} + \mathbf{N}_{3,x}) \mathbf{N}_2^T \\ &- k Gh (\mathbf{N}_3 - \mathbf{N}_{1,y}) \mathbf{N}_1^T \end{aligned} \tag{35}$$

The energy transport in the x - and y -direction through a single element is given as:

$$W_x^e = \int_e W_x dy, \quad W_y^e = \int_e W_y dx \tag{36}$$

By assuming uniform energy transport through an element we approximate this as

$$\begin{aligned} W_x^e &= \int_e \pi \Re \left(i \left(\mathbf{d}^e \right)^T \mathbf{Q}_x^e \left(\mathbf{d}^e \right)^* \right) dy \\ &\approx 2b \pi \Re \left(i \left(\mathbf{d}^e \right)^T \tilde{\mathbf{Q}}_x^e \left(\mathbf{d}^e \right)^* \right) \end{aligned} \tag{37}$$

$$\begin{aligned} W_y^e &= \int_e \pi \Re \left(i \left(\mathbf{d}^e \right)^T \mathbf{Q}_y^e \left(\mathbf{d}^e \right)^* \right) dx \\ &\approx 2a \pi \Re \left(i \left(\mathbf{d}^e \right)^T \tilde{\mathbf{Q}}_y^e \left(\mathbf{d}^e \right)^* \right) \end{aligned} \tag{38}$$

where $\tilde{\mathbf{Q}}_x^e$ and $\tilde{\mathbf{Q}}_y^e$ are the element matrices \mathbf{Q}_x^e and \mathbf{Q}_y^e evaluated at the center of the elements. For a fine mesh the error introduced with this simplification is negligible.

A finite subdomain of the plate Ω_s is composed of N_{Ω_s} elements with N_{Ω_x} and N_{Ω_y} elements in the two directions respectively. The energy transported in the two directions averaged over Ω_s , denoted $\bar{\mathbf{W}}$, has the components:

$$\begin{aligned} \bar{W}_x &= \frac{1}{\Delta x} \int_{\Omega_s} W_x d\Omega \\ &= \frac{1}{N_{\Omega_x}} \sum_{e=1}^{N_{\Omega_s}} W_x^e = \frac{2b\pi}{N_{\Omega_x}} \Re \left(\mathbf{id}^T \tilde{\mathbf{Q}}_x \mathbf{d}^* \right) \end{aligned} \tag{39}$$

$$\begin{aligned} \bar{W}_y &= \frac{1}{\Delta y} \int_{\Omega_s} W_y d\Omega \\ &= \frac{1}{N_{\Omega_y}} \sum_{e=1}^{N_{\Omega_s}} W_y^e = \frac{2a\pi}{N_{\Omega_y}} \Re \left(\mathbf{id}^T \tilde{\mathbf{Q}}_y \mathbf{d}^* \right) \end{aligned} \tag{40}$$

the global matrices $\tilde{\mathbf{Q}}_x$ and $\tilde{\mathbf{Q}}_y$ are assembled from the element matrices $\tilde{\mathbf{Q}}_x^e$ and $\tilde{\mathbf{Q}}_y^e$ in the usual way.

5 Optimization problem

We consider two different optimization problems. The first is to minimize the global response of a plate subjected to time-harmonic loading. Different formulations for the dynamic compliance for steady-state response have been suggested, e.g. Ma et al. (1995), Jog (2002). We choose a formulation similar to Du and Olhoff (2007) that ensures that the global response of the plate is minimized. In discretized notation it may be written as

$$\Phi_1 = \mathbf{d}^T \mathbf{M} \mathbf{d}^* \tag{41}$$

in which \mathbf{M} is the mass matrix. The objective function is thus proportional to the kinetic energy of the plate. Alternatively, we could have chosen to consider the potential energy or a weighted average between kinetic and potential energy, but with time-harmonic loading the difference is minimal.

The second optimization problem considered is the maximization of energy transport through a vertical or horizontal line in the structure, Γ , which has the normal vector \mathbf{n} . The objective function is then written in continuous and discretized form as

$$\Phi_2 = \int_{\Gamma} \mathbf{n} \cdot \mathbf{W} d\Gamma \sim \Re \left(\mathbf{id}^T \tilde{\mathbf{Q}}_j \mathbf{d}^* \right) \tag{42}$$

where subscript j indicates either the x-direction or y-direction depending on the orientation of the line Γ and the factor appearing in (39)–(40) has been omitted for simplicity. In the case of lines not aligned with either the x- or y-direction the formulas (39)–(40) can be modified in a straightforward way.

For the gradient-based optimization procedure we need sensitivities of the objective function with respect to the design variables. In the following ϱ_e will denote the element-wise continuous design variable that may take values between 0 and 1. The adjoint method is used (Bendsøe and Sigmund 2003; Sigmund and Jensen 2003) and the sensitivities become

$$\frac{d\Phi_1}{d\varrho_e} = \mathbf{d}^T \frac{\partial \mathbf{M}}{\partial \varrho_e} \mathbf{d}^* + 2\Re \left(\boldsymbol{\lambda}^T \frac{\partial \mathbf{S}}{\partial \varrho_e} \mathbf{d} \right) \tag{43}$$

in which the Lagrange multipliers $\boldsymbol{\lambda}$ are calculated from the equation

$$\mathbf{S}^T \boldsymbol{\lambda} = -\mathbf{M}^T \mathbf{d}^* \tag{44}$$

Since \mathbf{S} is symmetric and already factorized during the solution of the equation of motion $\boldsymbol{\lambda}$ can be computed without much computational effort.

For the second objective function the sensitivities are found as:

$$\frac{d\Phi_2}{d\varrho_e} = -\Re \left(\mathbf{id}^T \frac{\partial \tilde{\mathbf{Q}}_j}{\partial \varrho_e} \mathbf{d}^* \right) + 2\Re \left(\boldsymbol{\lambda}^T \frac{\partial \mathbf{S}}{\partial \varrho_e} \mathbf{d} \right) \tag{45}$$

and

$$\mathbf{S}^T \boldsymbol{\lambda} = -\frac{i}{2} \left(\mathbf{Q}_j^T - \mathbf{Q}_j \right) \mathbf{d}^* \tag{46}$$

In this paper we consider plates built from two different materials so that the design variable ϱ_e determines the fraction of one material in element e . The stiffness and mass density of the material is interpolated between the two materials with stiffness E^0 and E^{min} and mass density ρ^0 and ρ^{min} , respectively, based on the value of ϱ_e . We use the RAMP scheme (Stolpe and Svanberg 2001) for the interpolation of stiffness

$$E(\varrho_e) = E^{min} + \frac{\varrho_e}{1 + q(1 - \varrho_e)} (E^0 - E^{min}) \tag{47}$$

and a linear interpolation for the mass density

$$\rho(\varrho_e) = \rho^{min} + \varrho_e (\rho^0 - \rho^{min}) \tag{48}$$

This formulation is used in order to penalize intermediate densities and at the same time it allows us to use two different materials. If $q = 0$ then (47) reduces to linear interpolation.

In all the examples shown a density filter is used in order to avoid checkerboard structures (Guest et al. 2004; Sigmund 2007). The method of moving asymptotes (Svanberg 1987) is used for the optimization.

6 Examples: vibration response

In this section we show examples of plates optimized with the objective of minimizing the overall response given by (41). The structure to be optimized is a simply supported plate subjected to a harmonic point load in the center. The plate is 0.5×0.5 m, has a thickness of 3 mm and is made from steel and polycarbonate with a maximum allowed fraction of steel of 25%. There is no damping included.

In Fig. 2 the resulting topology and frequency responses based on (41) are shown for three different frequencies which are close to one of the eigenfrequencies of the plate (for the initial homogeneous structure).

In the first example the structure is optimized at the third eigenfrequency, in the second example at the fourth eigenfrequency and in the last example at the seventh eigenfrequency.

When looking at the optimized structures we notice that they all consist of a central steel inclusion of varying size which is surrounded by an array of smaller inclusions. Looking at the frequency responses we see a large reduction in overall response at the optimization frequencies. This reduction has been obtained by changing the structure in such a way that the eigenfrequencies are moved away from the excitation frequencies. The minimum of the response curve is now located close to the optimization frequency and we see that there exists a relative large span around this frequency where the response is low. However in the last case there are response peaks inside this frequency range and close to the optimization frequency. Due to the complex designs the frequency responses for the optimized plates are more irregular than for the original plates. In the examples shown here no damping is included. Adding damping as well as changing the stiffness to mass ratio will change the optimal topology but this has not been investigated in detail.

In Fig. 3 a plot of the displacements of the plate shown in the last plot in Fig. 2 is shown for the frequency $\omega = 9000 \frac{\text{rad}}{\text{s}}$. It is seen that for the optimized plate the largest displacements are located around the plate center where the load is applied. Although no damping is applied to the structure the displacements decay rapidly when moving away from the plate center. This behavior is also characteristic for bandgap structures where the response is localized and decays rapidly

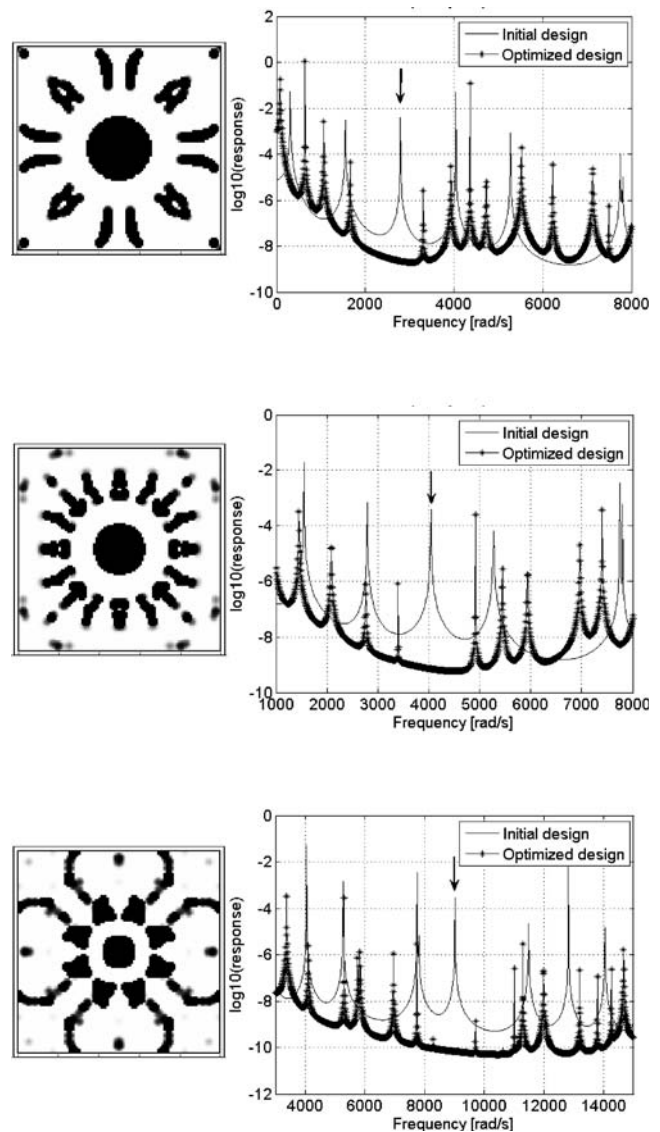


Fig. 2 Minimization of dynamic response [given by (41)] of a simply supported plate subjected to a harmonic point load in the plate center. The optimized topologies and frequency responses are shown. Black represents steel and the arrows in the frequency responses indicate the optimization frequencies. Top: $\omega_{opt} = 2790 \frac{\text{rad}}{\text{s}}$, center: $\omega_{opt} = 4040 \frac{\text{rad}}{\text{s}}$, bottom: $\omega_{opt} = 9000 \frac{\text{rad}}{\text{s}}$

(exponentially) away from the point of excitation (see e.g. Halkjær et al. 2006). In contrast the displacements are large all over the plate for the original plate.

A way of ensuring a low response for larger ranges of frequencies without the computational efforts of doing the full calculations could be through the use of Pade approximants (Jensen and Sigmund 2005; Jensen 2007a).

The results shown here are all for a two-material case such that the structure always has a certain static stiffness. If instead we were using one solid material and void it could be necessary to include a constraint

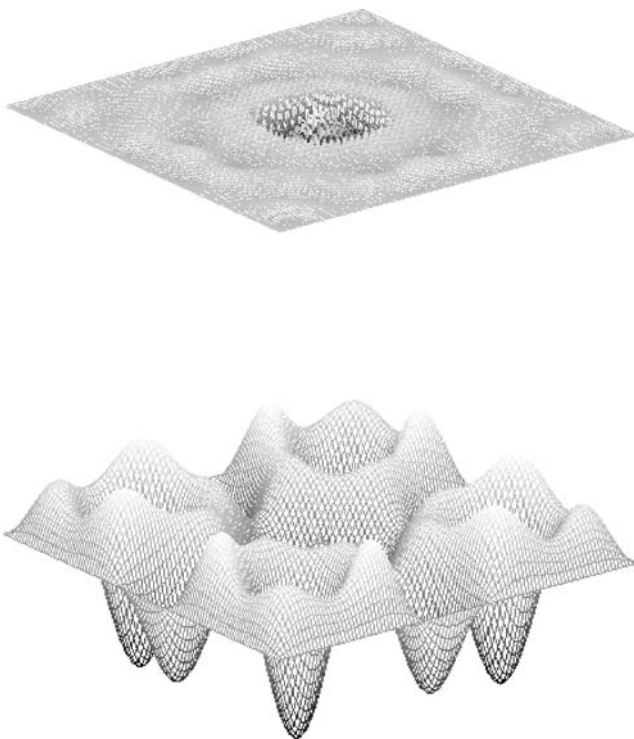


Fig. 3 Displacement of the plate shown in Fig. 2 bottom for the frequency $\omega = 9000 \frac{\text{rad}}{\text{s}}$. *Top*: The optimized plate. The largest displacements are located around the plate center. *Bottom*: The original plate

on static stiffness in order to obtain results that can be used in practice.

7 Examples: energy transport

In this section we look at the optimization of the energy transport in different plates. Although we present academic problems they are relevant for guiding mechanical vibrations in certain direction with the purpose of absorbing them or alternatively harvesting the energy.

First consider the problem sketched in Fig. 4a. The figure shows a plate subjected to a harmonically varying out-of-plane force on the left edge and damped in all degrees of freedom along the remaining edges. The objective is to maximize the energy transport in the horizontal direction through the black part to the right which consists of 4 by 8 elements. The black areas also indicate that the densities are fixed at one, i.e. they represent steel. The frequencies of excitation are $\omega = 11900, 12000, 12100 \frac{\text{rad}}{\text{s}}$. We use three frequencies in order to optimize for a wider frequency span and also it seems to provide more black and white designs. The plate is quite heavily damped with damping coefficients $\alpha = 1 \cdot 10^{-4}$ and $\beta = 1 \cdot 10^{-5}$ and damping applied to

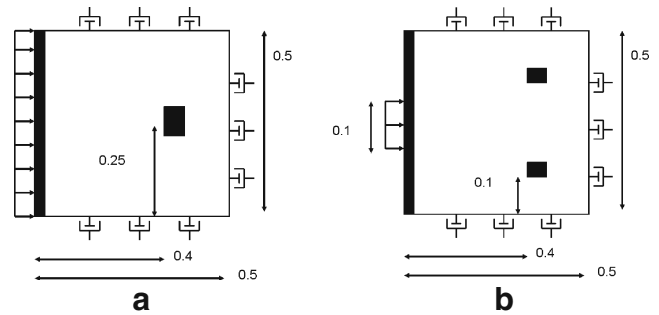


Fig. 4 Sketch of optimization problem. **a** The objective is to maximize the energy in the horizontal direction through the black area to the right which consists of 4x8 elements. **b** The objective is to maximize the energy in the vertical direction towards the edges through the black areas to the right. Each area is made by 4x3 elements

the three edges as well. The plate is discretized into 100 by 100 elements which combined with a wavelength of 0.064m in the pure polycarbonate means that there are approximately 13 elements per wavelength. The wavelength in steel is longer giving more elements per wavelength in steel regions. We will allow at most 50% steel to be used in the design.

In Jensen and Sigmund (2005) artificial damping (pamping) was proposed to penalize intermediate densities and obtain more black and white structures. By adding the term

$$C_p^e = \epsilon_P \rho^e (1 - \rho^e) \omega M^e \tag{49}$$

to the element damping matrix intermediate density elements will act as dampers. In (49) ϵ_P is a parameter controlling the magnitude of damping and M^e is the element mass matrix. When maximizing energy transport this will favor 0-1 designs.

The results are shown in Fig. 5 as a plot of the topology and vectors showing the energy transport.

We see a structure with a cone-like shape that guides the energy from the excitation towards the optimization

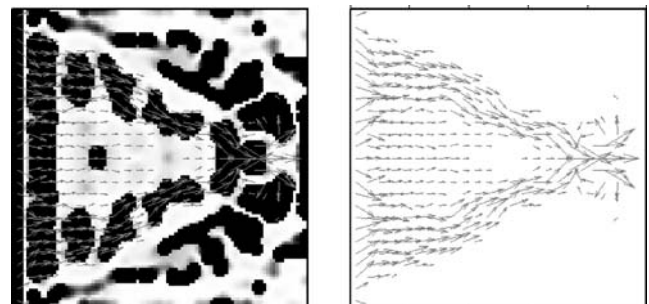


Fig. 5 Topology and energy transport for the problem sketched in Fig. 4a. Only energy vectors larger than 10% of the maximum energy vector are shown for clarity

domain. To the very left the passive elements are seen and immediately to the right of these a thin strip of white (polycarbonate) before a large domain of steel. Further to the right the structure consists of steel inclusions that deflect the energy towards the optimization area and keeps it away from the damped edges. Only energy vectors larger than 10% of the largest vector are shown in order to make the figure more clear. From that we can see that very little energy is transported outside the cone-shaped part. This is partly due to damping and partly due to the optimized design that guides the energy. Right at the optimization area an interesting effect is seen, as the energy after passing these elements follows a circular path back in order to increase the objective value.

A closer look at the results shows that during the optimization the objective energy is increased by a factor of 63 while the energy supplied to the structure is increased by a factor of 5.7. This means that a part of the increase in objective energy is due to a larger energy input to the structure and a part is due to an improved design that is able to guide the energy more efficiently. As we are maximizing the energy through some part of the structure an increase in input energy is an efficient way to obtain a larger objective value.

We now look at a slightly different example as shown in Fig. 4b, consisting of the same plate as before but only loaded along the central part of the left edge. The objective is now to maximize the energy transport in the vertical direction through two symmetrically placed areas near the top and bottom edge. The structure is thus supposed to split the energy and lead it towards the edges. The topology and energy transport is shown in Fig. 6.

We see that the structure is designed in such a way that the energy is kept from going to the edges. Instead it is being led to the right where it bends towards the optimization areas. Looking closely we recognize the same behaviour as before where the energy turns after

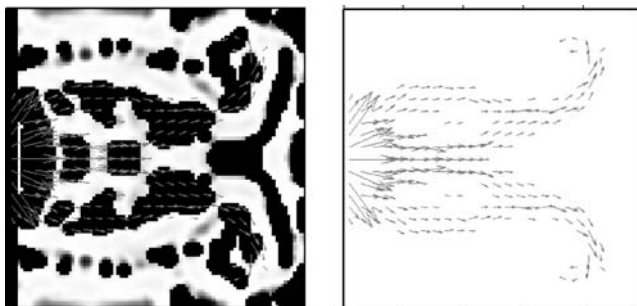


Fig. 6 Topology and energy transport for the problem sketched in Fig. 4b. Only energy vectors larger than 10% of the maximum energy vector are shown for clarity

leaving the optimization area in that way increasing the objective energy.

As in the previous example both the input and objective energies are increased. The input energy is increased by a factor of 5.4 while the objective energy is increased by a factor of 306. This is a very large improvement compared to the input energy and compared to the last example. The large improvement is possible because the objective is to maximize the energy in the vertical direction and for the original plate the energy propagates from the applied force in a way such that the vertical component of the energy through the optimization areas is very small. In this case the increase is therefore mostly due to an improvement in the design of the plate.

In both examples, shown here, it is seen that the material boundaries, i.e. where steel and polycarbonate meet, deflect the energy such that it is guided along the boundary. This effect is clear around the central part of the plates in Figs. 5 and 6. However the energy seems to pass material boundaries if these are perpendicular to the energy vector. This is particularly clear in the left part of Fig. 5.

As stated earlier artificial damping is used in order to penalize intermediate density elements. However it is clear from the two examples shown that some grey elements still exist. This means that the plate is more damped than what is applied as material or external damping. In the next example we therefore omit this penalization and only include material damping.

In the final example the objective is to guide the energy in a circular path in order to create a ring

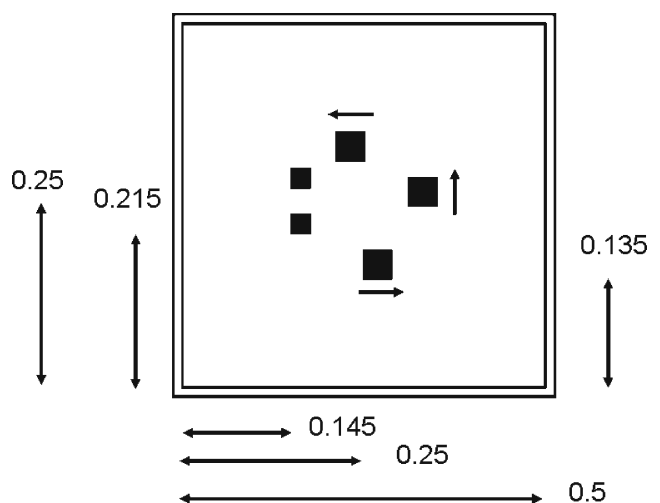


Fig. 7 Sketch of optimization problem for creating a ring wave in a simply supported plate. The black parts indicate fixed steel regions and the arrows indicate in which direction the energy transport is optimized. The two small steel areas indicate where the forces are applied

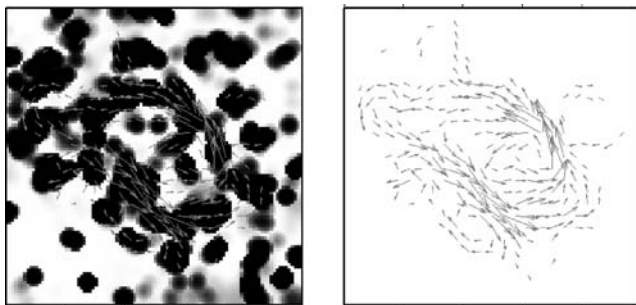


Fig. 8 Topology and energy transport for the optimization problem sketched in Fig. 7. Only energy vectors larger than 10% of the maximum vector are shown

wave device. The simply supported plate is excited by two harmonic forces, where one is phase shifted by a quarter of a period. This will initiate a wave in the plate. The objective function is defined as the energy through three groups of elements as sketched in Fig. 7. This example is inspired by the working principles of piezoelectric ring motors that rely on ring waves and friction between a stator and a rotor, see e.g. Uchino (1998).

In Fig. 8 the optimized structure is shown along with the energy transport. We see that energy is being guided in a near-circular path as defined in the optimization problem but also that some energy escapes this path. This can for instance be seen in the lower right part of the plate. Especially at the lower optimization area we see that the energy vectors have a relatively large vertical component while in the other two areas the energy is more efficiently guided only in the desired direction.

8 Conclusion

We have presented a material layout algorithm based on the method of topology optimization. The algorithm allows for the design of bi-material elastic plates with optimized vibrational suppression and guided energy transport when subjected to harmonic excitation.

The optimization algorithm is based on a finite element model of plate vibration for moderately thick plates using the Mindlin plate theory. Special consideration is given to the derivation of an energy transport measure using the Poynting vector.

The optimization algorithm is based on the FE model combined with analytical sensitivity analysis performed with the adjoint method. An iterative optimization scheme is set up with design updates performed with the method of moving asymptotes.

To demonstrate the capabilities of the method we have presented two sets of examples. The first deals with minimizing the total vibrational response of the plate in response to harmonic excitation at one or several distinct frequencies. The resulting bi-material designs display a low vibrational response at the target frequency range by moving the plate natural frequencies away from these targets.

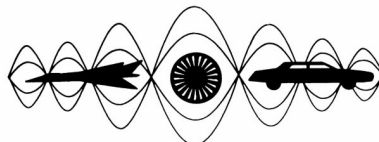
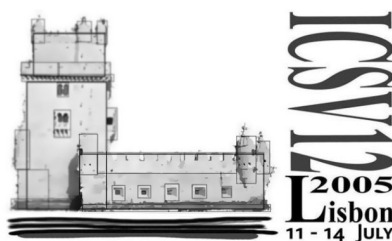
The second, and more challenging, set of examples deals with optimizing the materials distribution in order to direct the vibrational energy flow in specified paths in the plate. It was demonstrated that the specified energy transporting behavior could be realized by a complicated material layout and the rather difficult task of creating a ring wave device that functions by material contrasts was accomplished.

Acknowledgements This work received support from the Eurohorcs/ESF European Young Investigator Award (www.esf.org/euryi) through the grant “Synthesis and topology optimization of optomechanical systems”, the New Energy and Industrial Technology Development Organization project (Japan), and from the Danish Center for Scientific Computing.

References

- Auld BA (1973) *Acoustic fields and waves in solids*, vol I. Wiley, New York
- Bendsøe MP, Kikuchi N (1988) Generating optimal topologies in structural design using a homogenization method. *Comput Methods Appl Mech Eng* 71(2):197–224
- Bendsøe MP, Sigmund O (2003) *Topology optimization - theory, methods and applications*. Springer, Berlin Heidelberg New York
- Cox SJ, Dobson DC (1999) Maximizing band gaps in two-dimensional photonic crystals. *SIAM J Appl Math* 59(6): 2108–2120
- Du J, Olhoff N (2007) Minimization of sound radiation from vibrating bi-material structures using topology optimization. *Struct Multidisc Optim* 33(4–5):305–321
- Guest J, Prevost J, Belytschko T (2004) Achieving minimum length scale in topology optimization using nodal design variables and projection functions. *Int J Numer Methods Eng* 61(2):238–254
- Halkjær S, Sigmund O, Jensen JS (2005) Inverse design of phononic crystals by topology optimization. *Z Kristallogr* 220:895–905
- Halkjær S, Sigmund O, Jensen JS (2006) Maximizing band gaps in plate structures. *Struct Multidisc Optim* 32:263–275
- Hussein MI, Hulbert GM, Scott RA (2007) Dispersive elastodynamics of 1d banded materials and structures: design. *J Sound Vib* 307:865–893
- Jensen JS (2007a) Topology optimization of dynamics problems with Padé approximants. *Int J Numer Methods Eng* 72: 1605–1630
- Jensen JS (2007b) Topology optimization problems for reflection and dissipation of elastic waves. *J Sound Vib* 301:319–340

- Jensen JS, Sigmund O (2005) Topology optimization of photonic crystal structures: a high bandwidth low loss T-junction waveguide. *J Opt Soc Am B* 22(6):1191–1198
- Jog CS (2002) Topology design of structures subjected to periodic loading. *J Sound Vib* 253(3):687–709
- Ma ZD, Kikuchi N, Cheng HC (1995) Topological design for vibrating structures. *Comput Methods Appl Mech Eng* 121:259–280
- Olhoff N, Du J (2008) Topological design for minimum dynamic compliance of continuum structures subjected to forced vibration. *Struct Multidisc Optim* (in press)
- Rupp C, Evgrafov A, Maute K, Dunn ML (2007) Design of phononic materials/structures for surface wave devices using topology optimization. *Struct Multidisc Optim* 34(2): 111–121
- Sigmund O (2007) Morphology-based black and white filters for topology optimization. *Struct Multidisc Optim* 33(4–5): 401–424
- Sigmund O, Jensen JS (2003) Systematic design of phononic band-gap materials and structures by topology optimization. *Philos Trans R Soc Lond Ser A Math Phys Eng Sci* 361: 1001–1019
- Stolpe M, Svanberg K (2001) An alternative interpolation scheme for minimum compliance topology optimization. *Struct Multidisc Optim* 22:116–124
- Svanberg K (1987) The method of moving asymptotes - a new method for structural optimization. *Int J Numer Methods Eng* 24:359–373
- Uchino K (1998) Piezoelectric ultrasonic motors: overview. *Smart Mater Struct* 7:273–285



Twelfth International Congress
on Sound and Vibration

Systematic design of acoustic devices by topology optimization

Jakob Søndergaard Jensen and Ole Sigmund

Department of Mechanical Engineering, Solid Mechanics
Nils Koppels Allé, Building 404, Technical University of Denmark
DK-2800 Kgs. Lyngby, Denmark
jsj@mek.dtu.dk

Abstract

We present a method to design acoustic devices with topology optimization. The general algorithm is exemplified by the design of a reflection chamber that minimizes the transmission of acoustic waves in a specified frequency range.

INTRODUCTION

We treat the problem of designing acoustic devices with prescribed properties by using topology optimization. The method is exemplified by the design of a reflection chamber with minimized acoustic transmission in a designated frequency range.

A recent example of optimization of an acoustic devices, was given in [1], who used a FEM-based shape optimization algorithm to design an acoustic horn with minimal reflection for larger frequency ranges. In general, shape optimization employs a parametrization of the original device geometry as a basis for obtaining an optimized design. Thus, good results rely on the initial geometry as well as a suitable set of design parameters. Contrary to this, topology optimization ([2]) is based on a point-(or element-)wise parametrization of the material properties. This allows for, in principle, unlimited design freedom, regardless of the initial geometry. The method is well suited when good performance is hard to obtain with intuition-based design, which is often the case for wave propagation phenomena. Preliminary studies of using topology optimization to design acoustic devices were presented in [3] and [4], and the present

paper extends on this work. For an outline of the general method as well as examples of various applications see e.g. [5].

We start out by describing the governing equation and discuss the basic material interpolation scheme on the basis of a simple acoustic model. We solve the model equations using a FEM procedure, and move on to illustrating the optimization algorithm for a sample problem. Lastly, we give conclusion and directions for further work.

ACOUSTIC MODEL

We consider a plane model of steady-state acoustic wave propagation, modelled by the 2D Helmholtz equation:

$$\nabla \cdot (\rho^{-1} \nabla p) + \omega^2 \kappa^{-1} p = 0. \quad (1)$$

In Eq. (1), p is a complex pressure amplitude, ρ and κ are the position dependent density and bulk modulus of the acoustic medium. The wave frequency is denoted ω .

The optimization problem is to distribute two materials (air and solid), in a design domain Ω_d , so that some functional $\Phi(\omega, \rho, \kappa, \nabla p, p)$ is extremized. The two materials have the following set of material properties: $(\rho, \kappa) = (\rho_1, \kappa_1)$ (air), and $(\rho, \kappa) = (\rho_2, \kappa_2)$ (solid). It should be emphasized that the present pure-acoustic model neglects any acoustic-structure interaction. For large values of $\rho_2 \kappa_2$ the solid is practically a perfectly rigid and thus fully reflecting, whereas for smaller values it represents an acoustic medium.

We rescale the equations by introducing the new variables:

$$\tilde{\rho} = \frac{\rho}{\rho_1} = \begin{cases} 1, & \text{air} \\ \frac{\rho_2}{\rho_1}, & \text{solid} \end{cases}, \quad \tilde{\kappa} = \frac{\kappa}{\kappa_1} = \begin{cases} 1, & \text{air} \\ \frac{\kappa_2}{\kappa_1}, & \text{solid} \end{cases} \quad (2)$$

and inserting them into Eq. (1):

$$\nabla \cdot (\tilde{\rho}^{-1} \nabla p) + \tilde{\omega}^2 \tilde{\kappa}^{-1} p = 0, \quad (3)$$

where $\tilde{\omega} = \omega/c$ is a scaled wave frequency and $c = \sqrt{\kappa_1/\rho_1}$ is the speed of sound in air. In the following the tildes will be omitted for simplicity.

We may apply different boundary conditions to simulate incoming waves, as well as reflecting and absorbing boundaries. Additionally, perfectly matching layers can be added to the model such that low reflection at radiating boundaries is ensured for all angles of incidence.

DESIGN VARIABLES AND MATERIAL INTERPOLATION

The basis of the topology optimization method is to let the "material" properties ρ and κ take not only the discrete values of air and solid (cf. Eq. (2)), but also any intermediate values. To facilitate this, we introduce a continuous material indicator field $0 \leq \varrho \leq 1$,

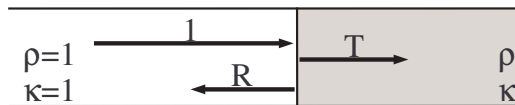


Figure 1 - A one-dimensional acoustic wave in air is partially reflected (R) and transmitted (T) at the interface to an acoustic medium.

and define continuous property interpolation functions $\rho(\varrho)$ and $\kappa(\varrho)$ that fulfill the following conditions:

$$\rho(\varrho) = \begin{cases} 1, & \varrho = 0 \\ \frac{\rho_2}{\rho_1}, & \varrho = 1 \end{cases}, \quad \kappa(\varrho) = \begin{cases} 1, & \varrho = 0 \\ \frac{\kappa_2}{\kappa_1}, & \varrho = 1 \end{cases} \quad (4)$$

The introduction of continuous properties allows us to compute the gradients of the objective functional with respect to the indicator function: $d\Phi/d\varrho$, and we can thus use a gradient based optimization strategy with ϱ as a topological design variable.

Clearly, we are only interested in binary values (0 or 1) of the indicator function in our optimized design, and our optimization formulation must include a strategy to avoid intermediate values of ϱ in the final design. Various strategies exist to ensure a binary design (see e.g. [5]) and in this work we rely on the choice of the functions $\rho(\varrho)$ and $\kappa(\varrho)$. To find suitable candidates we study a simple 1D acoustic system (Fig. 1).

A unit magnitude wave propagating in air is partially transmitted (T) and partially reflected (R) at the interface to an acoustic medium with the material properties $\rho(\varrho)$ and $\kappa(\varrho)$. The amplitudes of the reflected and the transmitted wave are:

$$R = \frac{\sqrt{\kappa\rho} - 1}{\sqrt{\kappa\rho} + 1}, \quad T = \frac{2}{\sqrt{\kappa\rho} + 1}, \quad (5)$$

so that $R \rightarrow 1$, $T \rightarrow 0$ when $\kappa\rho \rightarrow \infty$ (a perfectly rigid solid), and $R = 0$, $T = 1$ when $\kappa\rho = 1$ (air).

We want to choose our interpolation functions so that the reflection from the acoustic medium is a smooth and well-behaved function of ϱ . One possible choice is the polynomial form:

$$\rho(\varrho) = 1 + \varrho^{q_1} \left(\frac{\rho_2}{\rho_1} - 1 \right), \quad \kappa(\varrho) = 1 + \varrho^{q_2} \left(\frac{\kappa_2}{\kappa_1} - 1 \right). \quad (6)$$

The reflection versus ϱ is depicted in Fig. 2(left) for different values of q_1 and q_2 ($\rho_2/\rho_1 = \kappa_2/\kappa_1 = 500$). All curves have vanishing slope at $\varrho = 1$, which turns out to make it difficult to obtain well defined solid regions in the design.

Instead, inspired by the Helmholtz equation, we use polynomial interpolation in ρ^{-1} and κ^{-1} :

$$\rho(\varrho)^{-1} = 1 + \varrho^{q_1} \left(\left(\frac{\rho_2}{\rho_1} \right)^{-1} - 1 \right), \quad \kappa(\varrho)^{-1} = 1 + \varrho^{q_1} \left(\left(\frac{\kappa_2}{\kappa_1} \right)^{-1} - 1 \right). \quad (7)$$

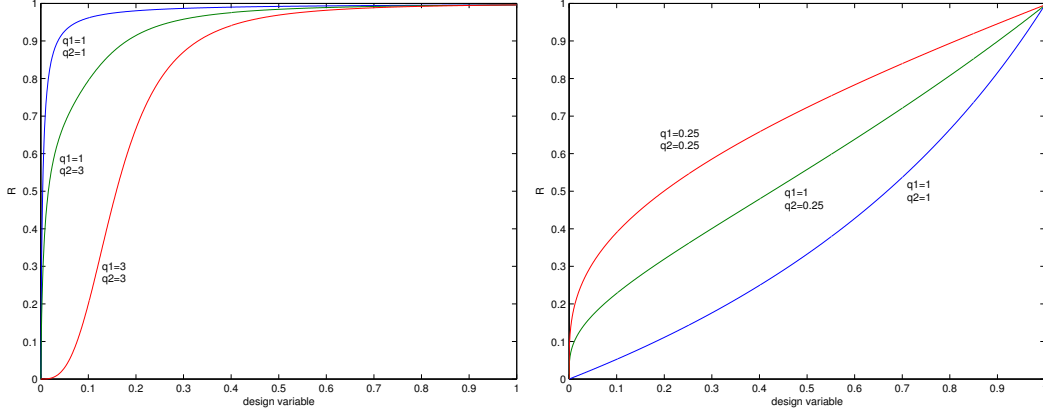


Figure 2 - Reflection, R , versus the design variable ϱ , left: polynomial interpolation (Eq. (6)), right: inverse polynomial interpolation (Eq. (7)), for different values of the parameters q_1 and q_2 . Parameters: $\rho_2/\rho_1 = \kappa_2/\kappa_1 = 500$.

Fig. 2(right) shows reflection versus ϱ for different parameter values. The curves are clearly more well-behaved with a non-vanishing slope for $\varrho \rightarrow 1$. The different parameter combinations have been used in the optimization algorithm and the simplest choice of $q_1 = q_2 = 1$ yields good results with well-defined air and solid regions in the optimized designs. Naturally, a simple 1D model cannot fully account for all necessary properties, and more work should be put into fully understanding the effect of the choice of interpolation functions.

DISCRETIZATION AND SENSITIVITY ANALYSIS

To solve the model equation (with the appropriate boundary conditions) and the optimization problem, we discretize the complex amplitude field p and the design field ϱ using finite elements:

$$p = \sum_{i=1}^N \phi_i p_i, \quad \varrho = \sum_{i=1}^{N_d} \psi_i \varrho_i, \quad (8)$$

where ϕ_i and ψ_i are basis functions, and the vectors $\mathbf{p} = \{p_1 \ p_2 \ \dots \ p_N\}^T$ and $\boldsymbol{\varrho} = \{\varrho_1 \ \varrho_2 \ \dots \ \varrho_{N_d}\}^T$ contain the nodal values of the two fields. We use the commercial FEM package FEMLAB on top of MATLAB for assembling and solving the discretized equation:

$$\mathbf{S}(\boldsymbol{\varrho})\mathbf{p} = \mathbf{f}(\boldsymbol{\varrho}). \quad (9)$$

Throughout this work we use a triangular element mesh, and a quadratic approximation for the pressure field and a linear approximation for the design field.

We now derive the sensitivities of the objective functional $\Phi(\boldsymbol{\varrho}, \mathbf{p})$ with respect to a single design variable. We use the adjoint method and obtain the adjoint equation as:

$$\mathbf{S}^T \boldsymbol{\lambda} = -\frac{1}{2} \left(\frac{\partial \Phi}{\partial \mathbf{p}_R} - i \frac{\partial \Phi}{\partial \mathbf{p}_I} \right)^T, \quad (10)$$

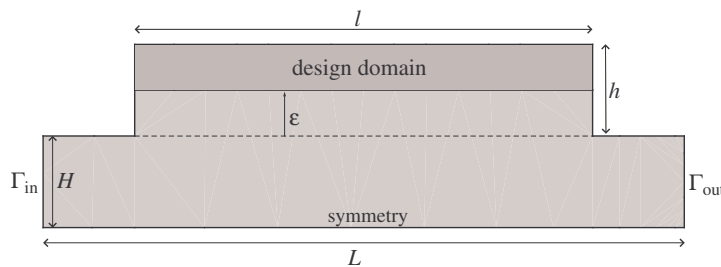


Figure 3 - Half model of a channel with two symmetrically placed reflection chambers.

where \mathbf{p}_R and \mathbf{p}_I are the real and the imaginary parts of the complex pressure. The sensitivities are then found as:

$$\frac{d\Phi}{d\rho_i} = \frac{\partial\Phi}{\partial\rho_i} + 2\Re(\boldsymbol{\lambda}^T (\frac{\partial\mathbf{S}}{\partial\rho_i}\mathbf{p} - \frac{\partial\mathbf{f}}{\partial\rho_i})). \quad (11)$$

The vectors $\frac{\partial\Phi}{\partial\boldsymbol{\rho}}$, $\frac{\partial\Phi}{\partial\mathbf{p}_R}$, $\frac{\partial\Phi}{\partial\mathbf{p}_I}$, and the matrix $(\frac{\partial\mathbf{S}}{\partial\rho_i}\mathbf{p} - \frac{\partial\mathbf{f}}{\partial\rho_i})$ are obtained through the FEMLAB matrix assembly procedure (see e.g. [6]).

OPTIMIZATION OF A REFLECTION CHAMBER

We consider the model problem illustrated in Fig. 3. The goal is to distribute solid material in a chamber in such a way that a propagating wave is reflected. The acoustic waves propagate in air through the main channel of height $2H$ and length L . Two reflection chambers with height h and length l are positioned symmetrically on the main channel. Each chamber consists of an air-filled part and the design domain where a favorable distribution of air and solid is to be found.

We apply the following boundary conditions:

$$\begin{aligned} n \cdot (\rho^{-1}\nabla p) + i\omega\sqrt{\rho^{-1}\kappa^{-1}}p &= 2i\omega\sqrt{\rho^{-1}\kappa^{-1}}p_0, & \Gamma_{\text{in}} \\ n \cdot (\rho^{-1}\nabla p) + i\omega\sqrt{\rho^{-1}\kappa^{-1}}p &= 0, & \Gamma_{\text{out}} \\ n \cdot (\rho^{-1}\nabla p) &= 0, & \text{other boundaries.} \end{aligned} \quad (12)$$

This specifies an incoming plane wave with amplitude p_0 at Γ_{in} (p_0 set to unity in the following), absorbing boundaries at Γ_{in} and Γ_{out} , traction free conditions on the outer boundaries and a symmetry condition at the lower boundary.

As optimization objective we consider the squared amplitude of the acoustic pressure averaged over the output boundary:

$$\Phi(\omega) = \frac{1}{H} \int_{\Gamma_{\text{out}}} |p(\omega)|^2 dS, \quad (13)$$

and minimize the maximum value of $\Phi(\omega_i)$ for a set of frequencies ω_i , $i = 1, \dots, M$. We now state the optimization problem as follows:

$$\begin{aligned} \min \max \quad & \Phi(\omega_i) & i = 1, \dots, M \\ \text{subject to : } & \mathbf{S}(\boldsymbol{\rho})\mathbf{p} = \mathbf{f} \\ & 0 \leq \rho_j \leq 1 & j = 1, \dots, N_d \\ & \frac{1}{N_d} \sum_{j=1}^{N_d} \rho_j \leq V \end{aligned} \quad (14)$$

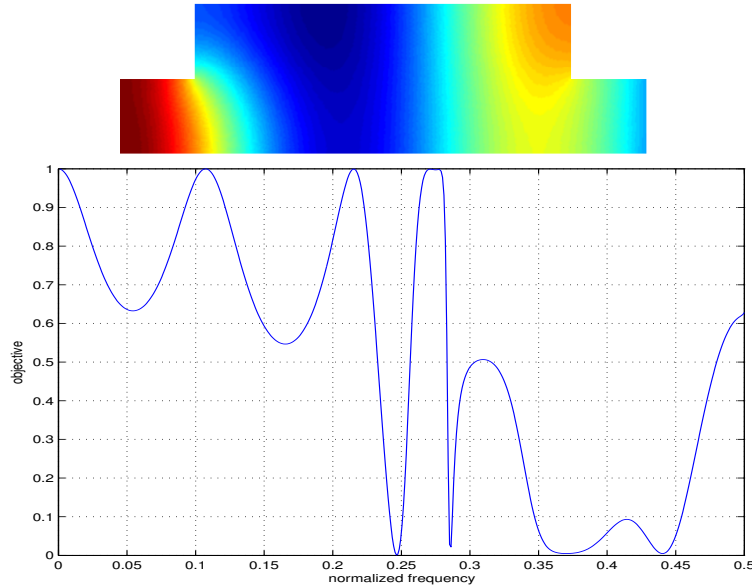


Figure 4 - Objective $\Phi(\omega^*)$ for the air-filled chamber and response for $\omega^* = 0.175$. Parameter values: $L = 7$, $l = 5$, $H = 1$, $h = 1$.

where the third constraint introduces an optional limit on the amount of solid to be distributed ($V = 1$ corresponds to no limit). The optimization problem is solved iteratively by material redistribution steps, using Svanberg's MMA [7] as optimizer and the analytical sensitivities in Eqs. (10)–(11). The optimization formulation considers the objective for a number of discrete frequencies. Since we are interested in minimizing the objective in frequency ranges rather than at discrete frequencies we use frequency sweeps at regular intervals during the optimization in order to identify the most critical frequencies in the desired interval and then update the target frequencies ω_i accordingly. The frequency sweeps are done fast and accurately using Padé expansions [8].

We now optimize the chamber for a specific set of parameters; $L = 7$, $l = 5$, $H = 1$, $h = 1$, $\epsilon = 0.5$. Fig. 4 shows $\Phi(\omega^*)$ for an air-filled reflection chamber and the computed pressure field for $\omega^* = 0.175$. The frequency is here normalized so that $\omega^* = 2\pi c\omega/H$. We choose now to design the chamber so that $\Phi(\omega)$ is minimized in the frequency range $\omega^* = 0.15 - 0.20$ by distributing maximum 15% solid material ($V = 0.15$). The optimized topology, the corresponding response curve, and the pressure field for $\omega^* = 0.175$ are shown in Fig. 5. Clearly, a reduction of Φ is seen in the designated frequency range. Naturally, a larger reduction can be obtained if the chamber dimensions are increased. Fig. 6 shows the results for a double length chamber $l = 10$ and here a further reduction of the objective is noted.

CONCLUSIONS AND FURTHER WORK

We have demonstrated a general design method for acoustic devices based on topology optimization.

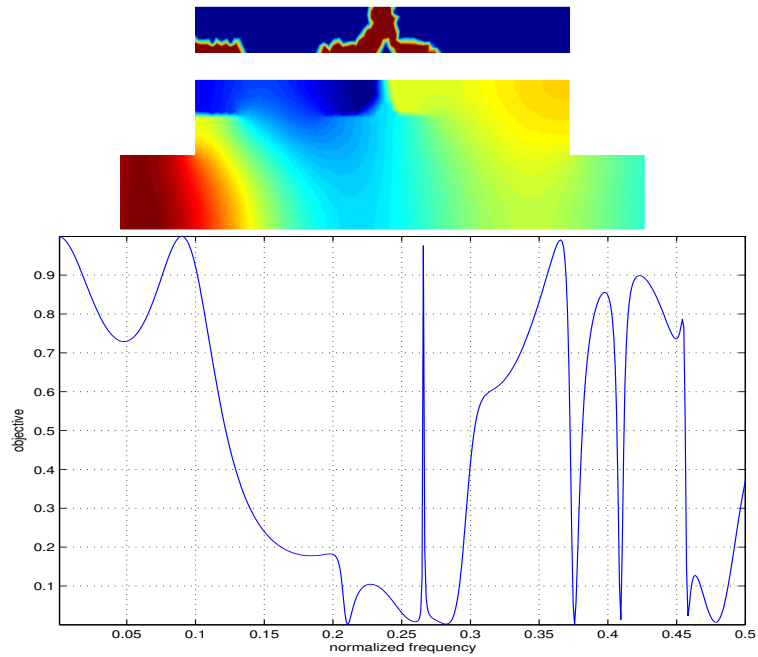


Figure 5 - Optimized topology for $\omega^* = 0.15 - 0.20$ and $V = 0.15$, blue: air, red: solid. Pressure field for $\omega^* = 0.175$ and response curve $\Phi(\omega^*)$. Parameters: $L = 7$, $l = 5$, $H = 1$, $h = 1$, $\epsilon = 0.5$.

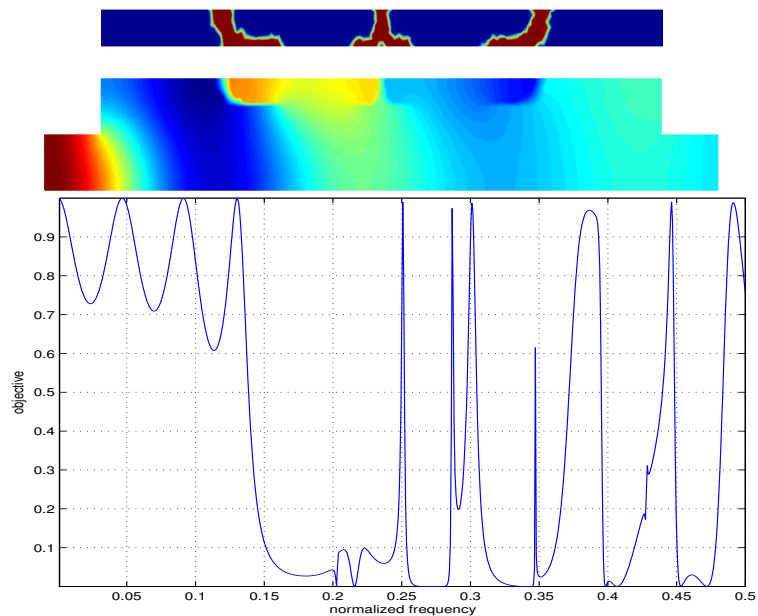


Figure 6 - Optimized topology for $\omega^* = 0.15 - 0.20$ and $V = 0.15$, blue: air, red: solid. Pressure field for $\omega^* = 0.175$ and response curve $\Phi(\omega^*)$. Parameters: $L = 12$, $l = 10$, $H = 1$, $h = 1$, $\epsilon = 0.5$.

The optimization algorithm employs repeated material redistributions based on analytical sensitivity analysis and mathematical programming. In this work we develop continuous material interpolation functions using a simple 1D model, and use the method to design a reflection chamber that minimizes the transmitted wave in a designated frequency range. The frequency range optimization is facilitated by computing fast frequency sweeps to identify the most critical frequencies.

Further work will include multi-physics modelling in order to study coupled problems, e.g. combined fluid flow and acoustic wave propagation or fluid-structure interaction.

This work was supported by the Danish Technical Research Council (FTP).

REFERENCES

- [1] Bängtsson, E., Noreland, D. and Berggren, M., “Shape optimization of an acoustic horn”, *Computer Methods in Applied Mechanics and Engineering*, 2003, **192**:11–12, 1533–1571.
- [2] Bendsøe, M.P. and Kikuchi, N., “Generating optimal topologies in structural design using a homogenization method”, *Computer Methods in Applied Mechanics and Engineering*, 1988, **71**:2, 197–224.
- [3] Sigmund, O. and Jensen, J.S., “Design of acoustic devices by topology optimization”, *Short papers of the 5th World Congress on Structural and Multidisciplinary Optimization WCSMO5*, 2003, 267–268.
- [4] Sigmund, O., Jensen, J.S., Gersborg-Hansen, A. and Haber, R. B., “Topology optimization in wave-propagation and flow problems”, *Proceedings of Warsaw International Seminar on Design and Optimal Modelling WISDOM*, 2004, 45–54.
- [5] Bendsøe, M.P. and Sigmund, O., “Topology Optimization: Theory, Methods and Applications”, *Springer Verlag*, Berlin, 2003.
- [6] Olesen, L.H., Okkels, F. and Bruus, H., “A high-level programming-language implementation of topology optimization applied to steady-state Navier-Stokes flow”, *International Journal for Numerical Methods in Engineering*, 2004, submitted.
- [7] Svanberg, K., “The Method of Moving Asymptotes - A New Method for Structural Optimization”, *International Journal for Numerical Methods in Engineering*, 1987, **24**, 359–373.
- [8] Jensen, J.S., Sigmund, O., “Topology optimization of photonic crystal structures: A high-bandwidth low-loss T-junction waveguide”, *Journal of the Optical Society of America B*, 2005, to appear.

Systematic design of photonic crystal structures using topology optimization: Low-loss waveguide bends

Jakob S. Jensen^{a)} and Ole Sigmund

Department of Mechanical Engineering, Solid Mechanics, Nils Koppels Allé, Building 404, Technical University of Denmark, 2800 Kgs. Lyngby, Denmark

(Received 26 August 2003; accepted 25 January 2004)

Topology optimization is a promising method for systematic design of optical devices. As an example, we demonstrate how the method can be used to design a 90° bend in a two-dimensional photonic crystal waveguide with a transmission loss of less than 0.3% in almost the entire frequency range of the guided mode. The method can directly be applied to the design of other optical devices, e.g., multiplexers and wave splitters, with optimized performance. © 2004 American Institute of Physics. [DOI: 10.1063/1.1688450]

A range of perspectives exist for using photonic crystal (PC) based waveguides in optical components. This has led to a considerable research interest in the design of waveguide bends with low transmission loss.

PCs can be created by periodic arrangements of materials with different dielectric properties such as, e.g., dielectric columns in air or holes in a dielectric base material.¹ Such two-dimensional periodic configurations may forbid the propagation of plane polarized light in specific frequency ranges, i.e., the so-called photonic band gaps (PBGs). A waveguide can be created by removing one or several lines of columns or holes resulting in defects that support guided modes in the PC structure.²

A key advantage of PC waveguides is that bends can be created with very little or no transmission loss even with bend curvatures as small as the wavelength. Although PC waveguides generally offer low losses compared to traditional dielectric waveguides, much effort has been devoted to reducing these losses to a minimum over larger frequency ranges. Waveguides with dielectric columns in a rectangular configuration have been subjected to extensive computations³ and recently waveguides with holes etched in a triangular pattern in a dielectric have been analyzed thoroughly both theoretically and experimentally.⁴

Despite the considerable amount of studies on PC waveguides that have appeared, few papers have dealt with optimization or the inverse problem of obtaining structures with optimal or desired properties. The few papers that have appeared (e.g., Refs. 5 and 6) have considered simple geometry variations like existence/nonexistence of holes or rods or variations of hole or rod diameters. The topology optimization method^{7,8} is a gradient-based optimization method that creates optimized designs with no restrictions on resulting topologies and can thus be used to create designs with previously unattainable properties. The topology optimization method has in the last decade been used to design materials with extremal properties, compliant and multiphysics mechanisms, piezoelectric actuators, and plenty more.⁸ Here, the transmission loss in a column-based waveguide with a 90° bend is systematically minimized by the topology optimization

method. This work applies a gradient-based method to waveguide optimization, thus creating optimized waveguides with much less computational effort and more design freedom than previously used genetic or other heuristic algorithms.

The analyses and optimization presented here are based on a time-harmonic two-dimensional finite element (FE) model. Unwanted reflections from the input and output waveguide ports are eliminated by using anisotropic perfectly matching layers (PML) with the waveguide structure continued into the damping layers. This ensures that reflections from the input and output ports are kept to a minimum.⁹ The loss in the waveguide bend is found by comparing the transmission of energy through the bend waveguide to that of a straight waveguide.

The computational model is shown in Fig. 1 and consists of the actual computational domain and two additional PML areas. For this example we consider propagation of an *E*-polarized wave governed by

$$\nabla^2 E + \omega^2 \left(\frac{n}{c} \right)^2 E = 0, \quad (1)$$

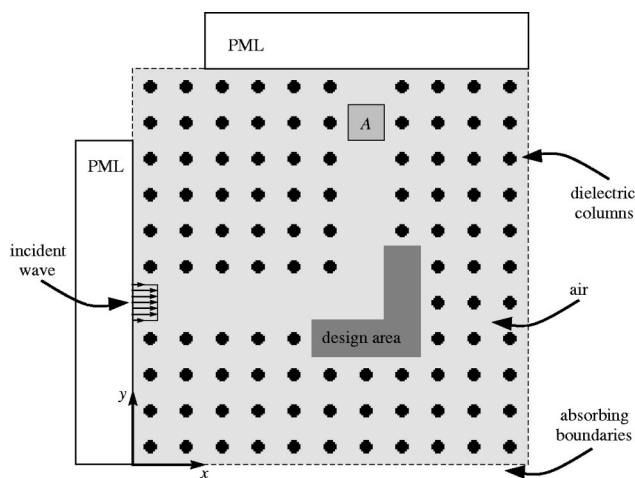


FIG. 1. Waveguide with a 90° bend line defect in a periodic configuration of dielectric columns ($n=3.4$) in air. Unwanted reflections from the input and output waveguide ports are eliminated by using anisotropic PML regions, and the energy transmission through the waveguide is evaluated in the unit cell denoted A.

^{a)}Electronic mail: jsj@mek.dtu.dk

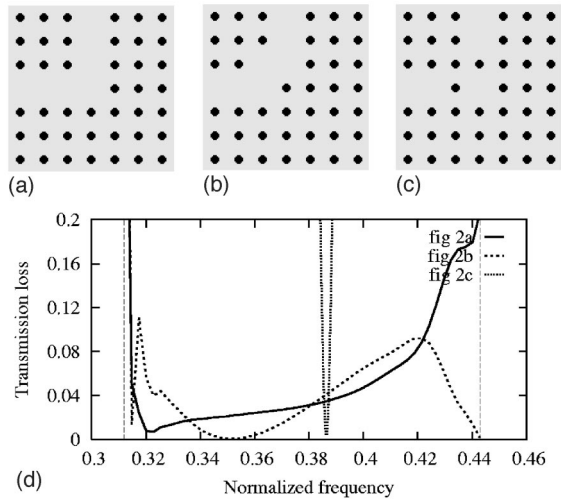


FIG. 2. (a), (b), and (c) Three standard corner designs, and (d) the corresponding transmission losses vs normalized frequency $\omega a/(2\pi c)$ computed in the guided mode frequency range (indicated by vertical dashed lines).

where ω is the wave frequency, $n=n(x,y)$ is the refractive index, c the speed of light, and $E=E(x,y)$ is the electric field. In the PML regions the governing equation is modified to obtain anisotropic damping properties.⁹

An incident wave is specified by the boundary condition: $\mathbf{n}\cdot\nabla E=2i\omega(n/c)$, and on the other boundaries of the computational domain the condition: $\mathbf{n}\cdot\nabla E+i\omega(n/c)E=0$, ensures normal absorbing boundaries. The vector \mathbf{n} is in both cases an outward pointing normal vector.

We use a FE discretization of Eq. (1) (as well as the PML equation and the boundary conditions) with $\approx 115\,000$ rectangular bilinear elements. This leads to a set of linear complex equations:

$$\mathbf{S}(\omega)\mathbf{u}=\mathbf{f}(\omega), \quad (2)$$

where $\mathbf{S}(\omega)$ is a frequency-dependent system matrix, $\mathbf{f}(\omega)$ a frequency-dependent load vector, and Eq. (2) is solved for the vector \mathbf{u} containing the discretized nodal values of the field E .

The energy transmission through the waveguide is found by computing the time-averaged Poynting vector through the area A (Fig. 1):

$$\mathbf{p}=\{p_x p_y\}^T=\frac{\omega}{2a}\int_A \Re(i(\nabla E)E^*)dA, \quad (3)$$

where a is the lattice constant and E^* is the complex conjugate field.

We consider a square configuration of unit cells with centered dielectric columns ($n=3.4$) with a diameter of $d=0.36a$ placed in air. This configuration has been shown to have a PBG for E -polarized waves for $\omega=0.302-0.443(2\pi c/a)$.³ Each unit cell is discretized using 19×19 finite elements which is adequate to reproduce this band gap frequency range. The waveguide model (Fig. 1) consists of 11×11 unit cells with 2 PML regions attached (each having a depth of 11 unit cells). By removing a line of columns a waveguide is created that supports a single guided mode in the frequency range $\omega=0.312-0.443(2\pi c/a)$.³

First we consider three standard corner designs [Figs. 2(a)–2(c)] and compute their corresponding transmission

loss [Fig. 2(d)]. The zero-curvature bend [Fig. 2(a)] displays a loss up to $\approx 20\%$ in the guided mode frequency range. By repositioning a single column [Fig. 2(b)] the loss is reduced and full transmission through the bend is reached for $\omega\approx 0.352(2\pi c/a)$. In Fig. 2(c) the corner is designed with two extra columns in the path and via resonant tunneling nearly full transmission is obtained for $\omega\approx 0.386(2\pi c/a)$, but the loss increases significantly for other frequencies. The losses computed with our FE model have been verified against results previously obtained by using different computational methods, e.g., FDTD simulations.^{3,10}

In order to reduce the bend loss we now apply the topology optimization method to design the corner geometry. We choose a design area in the corner region consisting of five unit cells (Fig. 1) and designate a single design variable x_i to each corresponding finite element in the region:

$$x_i\in\mathbb{R}|0\leq x_i\leq 1 \quad \text{for } i=1,N, \quad (4)$$

that is, in total N design variables where in this case $N=5\times 19^2=1805$. We use a linear interpolation scheme for the dielectric property $\varepsilon=n^2$ of the material in the design region elements:

$$n_i^2=n_1^2+x_i(n_2^2-n_1^2), \quad (5)$$

where $n_1=1$ and $n_2=3.4$ corresponding to air and the dielectric, respectively. That is, for $x_i=0$ the element will take the property of air, for $x_i=1$ the property of the dielectric, and for any intermediate value of x_i we have some intermediate dielectric property. As will appear in the following, these intermediate values practically vanish in the optimized design which may be explained by the fact that a high index contrast is favorable for creating wide band gaps.

In this example we choose as our optimization goal to maximize the y component of the time-averaged Poynting vector p_y in the cell A for a number M of target frequencies $\bar{\omega}_j$, $j=1,M$. Our optimization objective can thus be formulated as

$$\begin{aligned} \max_{x_i} C &= \sum_{j=1}^M p_y(\mathbf{u}_j) \\ \text{subject to: } \mathbf{S}(\bar{\omega}_j)\mathbf{u}_j &= \mathbf{f}(\bar{\omega}_j), \quad j=1,M, \\ 0 &\leq x_i \leq 1, \quad i=1,N. \end{aligned} \quad (6)$$

The optimization problem in Eq. (6) is solved using an iterative procedure (see Ref. 8 for details). Given an initial material distribution x_i [here chosen as the structure in Fig. 2(a)] the objective C is computed along with the sensitivities with respect to the design variables. Using the mathematical programming tool MMA¹¹ this is transformed into an improved design suggestion, i.e., updated values of x_i , and C is again computed. This procedure is repeated until the design x_i no longer changes significantly between successive iterations. The sensitivities are found analytically using the adjoint method,^{8,12} which is computationally very cheap since it only requires solving the system equation (2) for one additional load case. Although we here use a simple objective function it should be emphasized that any numerically quantifiable objective function can be used, and since we are using

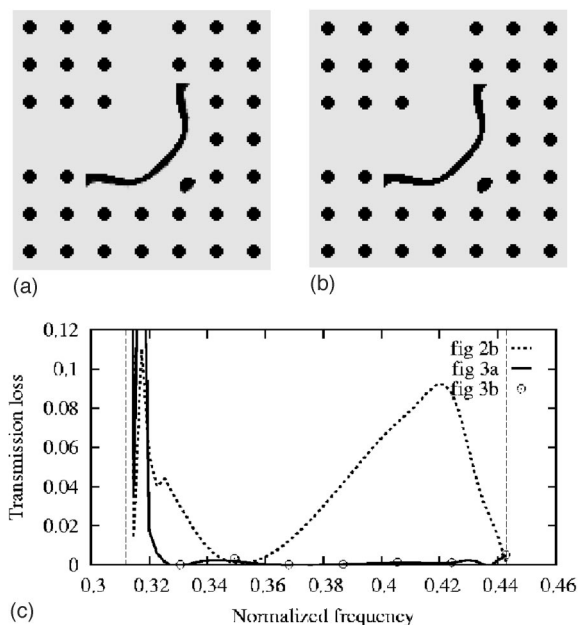


FIG. 3. (a) Optimized corner design, (b) postprocessed design with black and white elements only, and (c) transmission losses for the two designs and for a standard corner design.

ing a mathematical programming solver (MMA) extra geometric or behavioral constraints can easily be added to Eq. (6).

In our example we maximize the output energy for three frequencies $\bar{\omega} = 0.34, 0.38, 0.42(2\pi c/a)$ in order to minimize the loss in a large frequency range. Figure 3(a) shows the optimized design obtained after about 500 iterations of the optimization algorithm (about 20 s per iteration on a 2.66 GHz computer). It is evident that the optimized design is practically “black–white,” i.e., almost free of elements with intermediate x_i values between 0 and 1. In Fig. 3(b) is shown a postprocessed design where the few intermediate values that do appear are forced to either 0 or 1 with a simple filter. Figure 3(c) shows the transmission loss for the optimized and for the postprocessed designs. Noticeable is that a loss

below 0.3% is obtained in the entire frequency range from $\omega \approx 0.325$ to $0.440(2\pi c/a)$.

Although low transmission loss is obtained using a two-dimensional model, the question of out-of-plane losses for the optimized waveguide remains open and should be addressed using a three-dimensional (3D) model (the optimization algorithm can immediately be used with a 3D model). However, the method is naturally also applicable to the design of waveguides based on holes in a dielectric and these are generally known to be less prone to out-of-plane losses. In addition to waveguide bends the method can be applied to systematic design of a large variety of optical devices such as, e.g., wave-splitters, multiplexers, and other more complex objectives. Future work will address these issues and we are also expecting to test optimized devices experimentally in the near future. Previous work by the authors has considered design of similar devices for elastic waves.¹²

This work was supported by the Danish technical research council (STVF).

¹J. D. Joannopoulos, R. D. Meade, and J. N. Winn, *Photonic Crystals* (Princeton University Press, Princeton, NJ, 1995).

²K. Sakoda, *Optical Properties of Photonic Crystals* (Springer, Berlin, 2001).

³A. Mekis, J. C. Chen, I. Kurland, S. Fan, P. R. Villeneuve, and J. D. Joannopoulos, *Phys. Rev. Lett.* **77**, 3787 (1996).

⁴J. Moosburger, M. Kamp, A. Forchel, S. Olivier, H. Benisty, C. Weisbuch, and U. Oesterle, *Appl. Phys. Lett.* **79**, 3579 (2001).

⁵W. S. Mohammed, E. G. Johnson, and L. Vaissie, *Proc. SPIE* **4291**, 65 (2001).

⁶J. Smajic, C. Hafner, and D. Erni, *Opt. Express* **11**, 1378 (2003).

⁷M. P. Bendsøe and N. Kikuchi, *Comput. Methods Appl. Mech. Eng.* **71**, 197 (1988).

⁸M. P. Bendsøe and O. Sigmund, *Topology Optimization* (Springer, Berlin, 2003).

⁹M. Koshiba, Y. Tsuji, and S. Sasaki, *IEEE Microw. Wirel. Compon. Lett.* **11**, 152 (2001).

¹⁰Y. Naka and H. Ikuno, *International Symposium on Antennas and Propagation (ISAP2000)*, Fukuoka, Japan, 2000, p. 787.

¹¹K. Svanberg, *Int. J. Numer. Methods Eng.* **24**, 359 (1987).

¹²O. Sigmund and J. S. Jensen, *Proc. R. Soc. London, Ser. A* **361**, 1001 (2003).

Topology optimization of photonic crystal structures: a high-bandwidth low-loss T-junction waveguide

Jakob S. Jensen and Ole Sigmund

Department of Mechanical Engineering, Technical University of Denmark, Nils Koppels Allé, Building 404, 2800 Kgs. Lyngby, Denmark

Received September 13, 2004; revised manuscript received December 8, 2004; accepted December 29, 2004

A T junction in a photonic crystal waveguide is designed with the topology-optimization method. The gradient-based optimization tool is used to modify the material distribution in the junction area so that the power transmission in the output ports is maximized. To obtain high transmission in a large frequency range, we use an active-set strategy by using a number of target frequencies that are updated repeatedly in the optimization procedure. We apply a continuation method based on artificial damping to avoid undesired local maxima and also introduce artificial damping in a penalization scheme to avoid nondiscrete properties in the design domain. © 2005 Optical Society of America

OCIS codes: 000.4430, 130.1750, 230.7390.

1. INTRODUCTION

Since the primary publications,^{1,2} photonic crystals (PhCs) have attracted much attention owing to the potential applications in integrated optical circuits and communication devices. PhCs rely on the bandgap phenomenon that causes total prohibition of wave propagation for some frequencies in certain periodic media. Future applications of PhC components will inevitably rely on high-level performance, such as ultra-low-loss and high-bandwidth operation. Thus an increased interest has recently been devoted to the possibility of using inverse design techniques in the form of various optimization methods to design such components,³ e.g., to maximize bandgaps of PhCs and to reduce losses in PhC waveguide bends, junctions, inlets, and outlets. In this paper we demonstrate how topology optimization can be used to design low-loss and high-bandwidth two-dimensional (2D) waveguide T junctions.

In a recent paper⁴ a 90-deg bend in a 2D PhC waveguide was designed with topology optimization. The optimization was performed by maximization of the power transmission of *E*-polarized waves through the bend for three wave frequencies simultaneously, and the resulting design, which was rather unconventional, displayed a good performance in a large frequency range. In the present paper the theoretical details behind the optimization algorithm are explained in detail, and a new optimization strategy based on active frequency sets, as well as a new penalization scheme, is introduced to treat the more difficult case of a T-junction waveguide. Although we here consider the case of *E* polarization, the methods described can immediately be applied to *H* polarization with a change of material parameters. In Ref. 5 a double 120-deg bend designed for *H* polarization was fabricated and showed a satisfactory performance of the component in good agreement with numerical simulations.

The T junction in a 2D PhC with circular dielectric rods in a square configuration has previously been studied and subjected to optimization. In Ref. 6, T junctions (and 90-deg bends) were studied by use of a 2D finite-difference time domain simulations, and the performance of the junction was improved by addition of extra rods of various radii in the corner regions. In Ref. 7 the reflection at the T junction was minimized with a combination of genetic-type algorithms and gradient-based optimization with the position and size of a selected number of rods used as design variables. In a related study,⁸ optimization based on simulated annealing was used to optimize a 60-deg junction in a waveguide based on a triangular configuration of holes. In that case the design variables were the radii of a number of holes. Recently researchers performed a similar optimization study⁹ by allowing the radii of selected holes in a 60-deg bend to be varied to maximize the transmission through the bend.

Unlike the aforementioned studies, topology optimization is based on free distribution of material in a design domain and hence does not restrict the design to consist of circular rods, or indeed rods at all. The method was originally developed for use in structural mechanics with the aim of obtaining the stiffest possible structures with a restricted amount of material.¹⁰ This has led to new designs that significantly outperformed structures designed with standard shape- or size-optimization techniques, led to an increasing popularity in aero and automotive industries, and resulted in implementation in commercial optimization tools.¹¹ In the past decade, topology optimization has also been successfully applied in other areas such as fluid mechanics and heat conduction.¹² Recently the method has been applied to optimization of phononic bandgap materials and structures.¹³

In this paper we use topology optimization to design T junctions with high transmission over a large frequency

range. To ensure a high bandwidth of the junction, we maximize the transmission for a number of target frequencies simultaneously and use an active-set strategy to update these frequencies repeatedly. To identify the frequencies with lowest transmission, we use fast frequency sweeps based on Padé approximants. The performance of the junction design obtained with this new method (Section 4) is compared with the performance of designs we get by optimizing the junction for single frequencies (Section 3). In Section 2 we introduce the basic optimization procedure along with the continuation method and a new penalization scheme.

2. TOPOLOGY OPTIMIZATION OF TWO-DIMENSIONAL PHOTONIC CRYSTAL STRUCTURES

Our implementation of topology optimization is based on the finite-element method. We use a frequency-domain method based on a 2D model of plane polarization (2D Helmholtz equation) in domain Ω :

$$\nabla \cdot [A(\mathbf{x}) \nabla u(\mathbf{x})] + \omega^2 B(\mathbf{x})u(\mathbf{x}) = 0 \quad \text{in } \Omega. \quad (1)$$

In Eq. (1), ω is the wave frequency, $u(\mathbf{x})$ is the unknown field in the plane $\mathbf{x}=(x,y)$, and $A(\mathbf{x})$ and $B(\mathbf{x})$ are the position-dependent material coefficients. For E polarization $A=1$ and $B=\varepsilon_r(\mathbf{x})c^{-2}$, and for H polarization $A=\varepsilon_r^{-1}(\mathbf{x})$ and $B=c^{-2}$, where $\varepsilon_r(\mathbf{x})$ is the dielectric constant and c is the speed of light in air. In the following we consider E polarization only.

The 2D computational model of the T junction is shown in Fig. 1. The domain Ω consists of 15×15 square unit cells, each with a centrally placed circular rod with the dielectric constant $\varepsilon_r=11.56$ and diameter $0.36a$, where a is the distance between the individual rods. This configura-

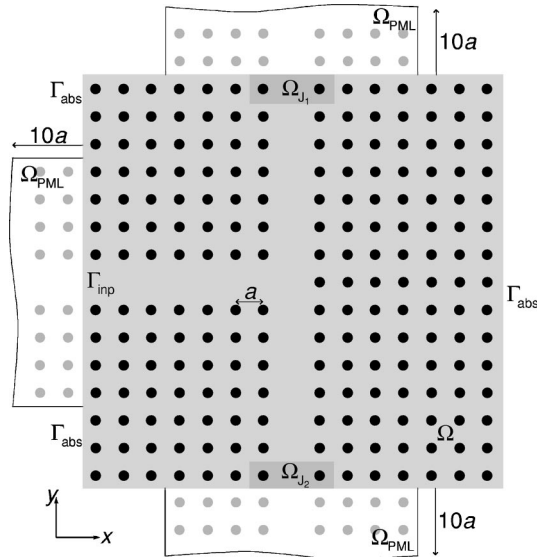


Fig. 1. Computational model consisting of 15×15 unit cells in Ω with centrally placed circular rods of diameter $0.36a$. A wave input is provided on Γ_{inp} , and absorbing boundaries are specified on Γ_{abs} . Perfectly matching layers Ω_{PML} are added to avoid reflections from the input and output waveguide ports. The objective is to maximize the power transmission in the two subdomains near the output ports Ω_{J_1} and Ω_{J_2} .

tion has been shown to have a large bandgap in E polarization in the frequency range $\omega=0.302-0.443 2\pi c/a$, and, with single rows of dielectric columns removed, a guided mode is supported for $\omega=0.312-0.443 2\pi c/a$.¹⁴ One creates T-junction waveguide by removing single rows of rods as shown in Fig. 1.

Incident wave and absorbing boundary conditions are specified on $\Gamma_{\text{inp}} \subset \partial\Omega$ and $\Gamma_{\text{abs}} \subset \partial\Omega$, respectively (Fig. 1),

$$\begin{aligned} \mathbf{n} \cdot (A \nabla u) &= 2i\omega\sqrt{AB}U & \text{on } \Gamma_{\text{inp}}, \\ \mathbf{n} \cdot (A \nabla u) + i\omega\sqrt{AB}u &= 0 & \text{on } \Gamma_{\text{abs}}, \end{aligned} \quad (2)$$

where U is a scaling factor for the wave amplitude (in the following, set to unity). In Eqs. (2), \mathbf{n} is the outward-pointing normal vector at the boundary, and the material coefficients are those of air in E polarization: $A=1$ and $B=B_{\text{air}}=c^{-2}$.

To eliminate reflections from the input and output waveguide ports, we add more anisotropic perfectly matching layers (PMLs) (denoted Ω_{PML} in Fig. 1). The governing equation in these layers is

$$\frac{\partial}{\partial x} \left(\frac{s_y}{s_x} A \frac{\partial u}{\partial x} \right) + \frac{\partial}{\partial y} \left(\frac{s_x}{s_y} A \frac{\partial u}{\partial y} \right) + \omega^2 s_x s_y B u = 0 \quad \text{in } \Omega_{\text{PML}}, \quad (3)$$

where the factors s_x and s_y are complex functions of the position and govern the damping properties of the layers. A standard implementation for PhC waveguides is used with the PhC structure retained in the PMLs.¹⁵

A Galerkin finite-element procedure is applied,¹⁶ leading to the discretized set of equations:

$$(-\omega^2 \mathbf{M} + i\omega \mathbf{C} + \mathbf{K}) \mathbf{u} = \mathbf{f}, \quad (4)$$

where \mathbf{u} is a vector of discretized nodal values of $u(\mathbf{x})$. On the element level the nodal values are interpolated as $u(\mathbf{x}) = \mathbf{N}(\mathbf{x}) \mathbf{u}$, which leads to the following form of the finite-element matrices:

$$\begin{aligned} \mathbf{M} &= \sum_{e \in \Omega} B_e \mathbf{M}^e + \sum_{e \in \Omega_{\text{PML}}} B_e s_{x_e} s_{y_e} \mathbf{M}^e, & \mathbf{M}^e &= \int \mathbf{N}^T \mathbf{N} dV, \\ \mathbf{C} &= \mathbf{C}_{\text{abs}} = \sum_{e \in \Gamma_{\text{abs}}} \sqrt{A_e B_e} \mathbf{C}^e, & \mathbf{C}^e &= \oint \mathbf{N}^T \mathbf{N} dS, \\ \mathbf{K} &= \sum_{e \in \Omega} A_e \mathbf{K}^e + \sum_{e \in \Omega_{\text{PML}}} A_e \left[\begin{pmatrix} s_{y_e} \\ s_{x_e} \end{pmatrix} \mathbf{K}_x^e + \begin{pmatrix} s_{x_e} \\ s_{y_e} \end{pmatrix} \mathbf{K}_y^e \right], \\ \mathbf{K}^e &= \mathbf{K}_x^e + \mathbf{K}_y^e = \int \frac{\partial \mathbf{N}^T}{\partial x} \frac{\partial \mathbf{N}}{\partial x} dV + \int \frac{\partial \mathbf{N}^T}{\partial y} \frac{\partial \mathbf{N}}{\partial y} dV, \\ \mathbf{f} &= 2i\omega \sum_{e \in \Gamma_{\text{inp}}} \sqrt{A_e B_e} \mathbf{f}^e, & \mathbf{f}^e &= \oint \mathbf{N}^T dS, \end{aligned} \quad (5)$$

where A_e , B_e , s_{x_e} , and s_{y_e} are assumed element wise constants.

We discretize the domain by using standard quadratic bilinear elements,¹⁶ with 19×19 elements for each unit

cell. Thus the entire computational domain consists of $(15 \times 15 + 3 \times 9 \times 10) \times 19^2 = 178,695$ elements. On a 2.66-GHz computer with 1-Gbyte RAM, a solution for a single frequency of Eq. (4) takes approximately 10 s. This is sufficiently fast for the model to be used in our iterative optimization algorithm in which several hundred solutions need to be computed in a single optimization procedure.

A. Design Variables and Material Interpolation

The design domain Ω_D is a subdomain of Ω . We assign one design variable x_e to each finite element within Ω_D :

$$0 \leq x_e \leq 1, \quad e \in \Omega_D. \quad (6)$$

It is impossible to solve the discrete combinatorial problem for more than, e.g., 100 design variables. Instead, we use continuous design variables so that we can apply a gradient-based algorithm. We let the design variable govern the distribution of air and dielectric in each element in Ω_D by letting the material coefficients A_e and B_e vary linearly with x_e :

$$\begin{aligned} A_e &= A_1 + x_e(A_2 - A_1), \\ B_e &= B_1 + x_e(B_2 - B_1), \end{aligned} \quad (7)$$

such that, for $x_e=0$, the material in the element will be material 1 (air) and, with $x_e=1$, it will be material 2 (dielectric). It is now the task for the optimization algorithm to identify the values of x_e in Ω_D that optimize our chosen objective function and, additionally, to ensure only discrete values, 0 and 1, of the design variables in the final design in order to obtain a well-defined structure.

B. Objective Function and Sensitivity Analysis

The goal is to maximize the power transmission through the waveguide, thereby minimizing the reflection at the T junction. The power transmission is found from the time-averaged Poynting vector:

$$\mathbf{P}(\mathbf{x}) = \{P_x P_y\}^T = \frac{1}{2} \omega A \Re(i \bar{u} \nabla u). \quad (8)$$

We consider the vertical component of the power transmission, P_y , averaged in two separate domains Ω_{J_1} and Ω_{J_2} near the two output waveguide ports [see Fig. 1]:

$$\begin{aligned} J_1 &= \frac{1}{N_y} \sum_{e \in \Omega_{J_1}} P_y^e, \\ J_2 &= -\frac{1}{N_y} \sum_{e \in \Omega_{J_2}} P_y^e, \end{aligned} \quad (9)$$

where N_y are the number of finite elements in the y direction in Ω_{J_1} and Ω_{J_2} . The vertical component of the time-averaged Poynting vector in each element is given as

$$P_y^e = \frac{1}{2} \omega A_e \Re[i(\mathbf{u}^e)^T \mathbf{Q}_y^e \bar{\mathbf{u}}^e], \quad (10)$$

where $\bar{\mathbf{u}}^e$ denotes the complex conjugate of the element nodal values. \mathbf{Q}_y^e is defined as

$$\mathbf{Q}_y^e = \int \frac{\partial \mathbf{N}^T}{\partial y} \mathbf{N} dS|_{y=0}. \quad (11)$$

We want to maximize the total power transmitted through the output ports for a given frequency ω , which leads to the optimization problem:

$$\max_{x_e} J(\omega),$$

$$J(\omega) = J_1(\omega) + J_2(\omega), \quad (12)$$

in which we additionally enforce a simple symmetry condition to ensure a symmetrical design with $J_1=J_2$. The optimization problem in expressions (12) is solved with the mathematical programming tool, the Method of Moving Asymptotes,¹⁷ in combination with the computed sensitivities of the objective function with respect to the design variables.

Analytical sensitivity analysis is an essential part of a fast optimization method and can be performed, e.g., with the adjoint method,¹² leading to the expression

$$\frac{dJ}{dx_e} = 2\Re \left[\boldsymbol{\lambda}^T \frac{d(-\omega^2 \mathbf{M} + i\omega \mathbf{C} + \mathbf{K})}{dx_e} \mathbf{u} \right], \quad (13)$$

where it has been assumed for simplicity that the design domain Ω_D neither includes the wave input boundary Γ_{inp} nor overlaps Ω_J and where $\boldsymbol{\lambda}$ is the solution to the adjoint problem

$$(-\omega^2 \mathbf{M} + i\omega \mathbf{C} + \mathbf{K})^T \boldsymbol{\lambda} = \frac{i\omega}{4} \sum_{e \in \Omega_{J_1}} A_e [\mathbf{Q}_y^e - (\mathbf{Q}_y^e)^T]^T \bar{\mathbf{u}}^e, \quad (14)$$

where the summation should be understood in the normal finite-element sense. Note that Eq. (14) can be solved essentially without computational effort if the original problem is solved by a direct factorization method. This means that one can obtain all the sensitivities [Eq. (13)] simply by solving the original problem [Eq. (4)] with an extra right-hand side (load case) and inserting the result into Eq. (13).

In structural mechanics the problem of mesh dependency arises when the standard formulation is used. This implies that if the finite-element mesh is refined, finer details will appear in the optimized structure. One can avoid this by introducing a heuristic mesh-independency filter.¹² In optics this dependency is not inherent in the problem, but the filter can nevertheless be applied with advantage to avoid too fine details in the structure. The variant used here is based on filtering the computed sensitivities in the following way:

$$\frac{d\hat{J}}{dx_e} = \frac{\sum \left(\hat{H}_e \frac{dJ}{dx_e} \right)}{\sum \hat{H}_e}, \quad (15)$$

where the summation is performed over all elements in the design domain and where \hat{H}_i is a convolution operator defined as

$$\begin{aligned} \hat{H}_e &= r_{\min} - \text{dist}(k, e), & \{e \in \Omega_D | \text{dist}(k, e) \leq r_{\min}\}, \\ k &= 1, \dots, N_{\Omega_D}. \end{aligned} \quad (16)$$

Thus the filtered sensitivities is a modification of the original sensitivities based on a weighted average of the sensitivities in neighboring elements within a fixed range (specified by r_{\min}). In the examples shown, we have used $r_{\min}=2.5$ times the element size.

C. Continuation Method and Penalization

The solution of the optimization problem turns out to be strongly nonunique, which results in multiple local maxima. Some of these are based on local resonance effects that lead to a poor performance away from the target frequency and to strong out-of-plane scattering and, consequently, to poor transmission for a real three-dimensional structure. A way to reduce the chance of ending up in such a maximum is to apply a continuation method in which we attempt to convexify the object function by changing the original problem into a smoother one. After a converged design is obtained for the smooth problem, we gradually change the problem back into its original form during a continued optimization procedure. As shown for phononic bandgap structures,¹⁸ the presence of strong damping smoothes the dynamic response considerably, and in Ref. 13 this was used with advantage to avoid undesired local extrema in the optimization of these structures.

Similar to the case of phononics (elastic waves), we here add an artificial damping term \mathbf{C}_{art} to the model:

$$\mathbf{C} = \mathbf{C}_{\text{abs}} + \mathbf{C}_{\text{art}}, \quad (17)$$

where \mathbf{C}_{abs} is the damping matrix stemming from the absorbing boundaries. We let the extra damping matrix be proportional to the mass matrix, such that

$$\mathbf{C}_{\text{art}} = \beta \omega \mathbf{M}, \quad (18)$$

where β is a real and positive constant. In a typical optimization procedure we start out with strong damping, say, $\beta=0.1$, and then gradually decrease β until the performance of the structure no longer can be improved.

Even when avoiding the pitfall of resonance-based local maxima, we may still end up with an unfeasible design with elements that have nondiscrete design variables x_e , i.e., values other than strictly 0 or 1. For other applications of topology optimization, various penalization methods have been developed to avoid this problem. For bandgap-type problems, the need for penalization appears to be small¹³ in that the highest possible material contrast is favorable for maximum wave reflection. However, if the problem is not strictly of the reflection type, we may end up with some gray elements.

Here we propose a new scheme inspired by an explicit penalization scheme introduced in Ref. 19. Instead of adding a penalization term directly to the objective, we use an implicit variant by introducing the penalty as an extra damping term for elements in Ω_D :

$$\mathbf{C}_{\text{pen}}^e = 4\epsilon x_e(1-x_e)\omega \mathbf{M}^e, \quad e \in \Omega_D, \quad (19)$$

thereby causing elements with $0 < x_e < 1$ to induce an energy loss and hence be expensive for the objective function. The penalization scheme is typically employed when a converged design is obtained and gray elements have appeared. Then ϵ is gradually increased from, e.g., $\epsilon=0.01$ until the gray elements vanish. However, if a lot of gray elements appear in the design, it can be beneficial to have a nonzero ϵ throughout the optimization procedure. In the following we call ϵ the pamping coefficient as an acronym for penalization damping.

D. Algorithm

The optimization algorithm is outlined in the following:

1. Set up a finite-element model and choose an appropriate design domain Ω_D and target frequency ω .
2. Choose an initial design, i.e., distribution of x_e in Ω_D , and initial values of artificial damping, e.g., $\beta=0.1$.
3. Compute the elementwise material coefficients A_e and B_e .
4. Solve system equations and compute objective function \mathcal{J} and filtered design sensitivities $d\hat{\mathcal{J}}/dx_e$.
5. Update design with the mathematical programming tool, the Method of Moving Asymptotes.¹⁷
6. Repeat steps (3)–(5) until design convergence is $\max|x_{\text{new}}-x_e| < \delta$, where δ is a small positive constant.
7. Decrease artificial damping, e.g., $\beta_{\text{new}}=\beta/2$.
8. Repeat steps (3)–(7) until the performance is no longer improved.
9. If gray elements appear in the design, repeat steps (3)–(5) with increasing values of ϵ , starting from, e.g., $\epsilon=0.01$. Alternatively, carry out the whole optimization procedure with a nonzero ϵ .

3. SINGLE-FREQUENCY OPTIMIZATION

We now use the basic algorithm to design the T junction for maximum transmission at three separate frequencies. Figure 2 shows the design domain. A domain consisting of ten unit cells is chosen, but the choice is arbitrary, and it

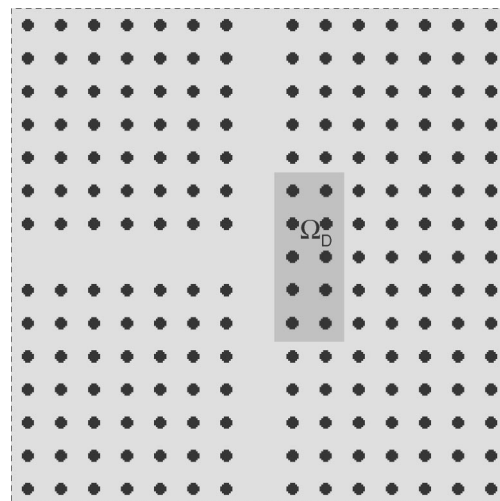


Fig. 2. Design domain Ω_D and initial material distribution.

should be emphasized that the CPU time per iteration is almost independent of the design domain size (for the given discretization).

We optimize the junction for $\tilde{\omega}=0.32$, $\tilde{\omega}=0.38$, and $\tilde{\omega}=0.44$ ($\tilde{\omega}=\omega 2\pi c/a$). This corresponds to two frequencies near the extremal values of the guided-mode frequency range and one center frequency. For an initial design, we choose the unoptimized structure as depicted in Fig. 2.

Figures 3–5 show three optimized designs together with the fields for the corresponding target frequencies. In Figure 6 the transmission spectrum is depicted for the three optimized designs as well as for the initial structure. The spectra have been normalized with the power transmission through a straight waveguide, so that 0.5 corresponds to 50% transmission through both upper and lower output ports of the symmetrical design, and hence there is no reflection at the junction.

For all three designs, practically full transmission is obtained at the specified target frequency. Except for the design obtained for $\tilde{\omega}=0.32$, a good performance is also seen away from the target, which indicates that the continuation approach has been effective in eliminating local maxima that are based on local resonances. These may display high transmission at single frequencies but are normally associated with excessive peaks and valleys in the transmission spectrum. Starting from different initial designs in most cases, we obtain different optimized designs, which indicates the strong nonuniqueness of the optimization problem. However, all designs obtained perform equally well (full transmission) at the target frequency.

Owing to the long wavelength of the guided mode at $\tilde{\omega}=0.32$, the optimized structure for this frequency is not well suited for higher frequencies at which the wavelength is significantly shorter. Similarly, the optimized design for $\tilde{\omega}=0.44$ performs poorly at lower frequencies. However, the design for $\tilde{\omega}=0.38$ gives a good transmission in a large frequency range, and the transmission drops significantly only for frequencies below $\tilde{\omega}=0.35$ and above $\tilde{\omega}=0.41$.

4. FREQUENCY-RANGE OPTIMIZATION BY USE OF ACTIVE SETS

To get a larger bandwidth with high transmission, we need to optimize the junction for several frequencies in the specified frequency range simultaneously. In Ref. 4 the sum of the transmission for a number of target frequencies was considered. With this approach the frequencies should be chosen carefully, and even then the transmission may still drop significantly between these frequencies. This problem could be partially remedied by use of a large number of frequencies. However, this would be CPU time expensive.

Instead, we introduce an active-set strategy in which we no longer keep the target frequencies fixed but let them vary according to the most critical frequencies, i.e., those with minimum transmission.

We now write the objective as

$$\max_{x_e} \sum_{\omega_1, \dots, \omega_N} \min_{\omega_i \in I_i} [J(\omega_i)/J^*(\omega_i)],$$

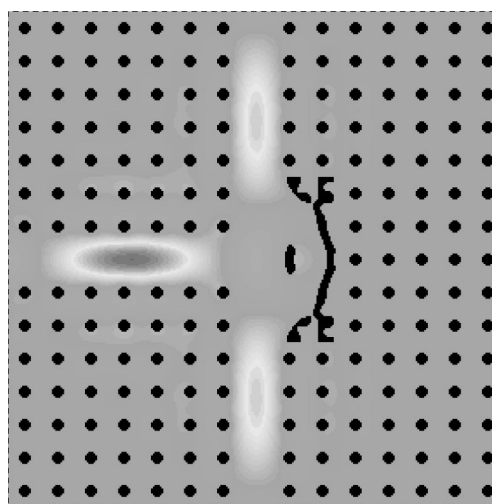


Fig. 3. Optimized T-junction topology for target frequency $\tilde{\omega}=0.32$ and the corresponding field distribution.

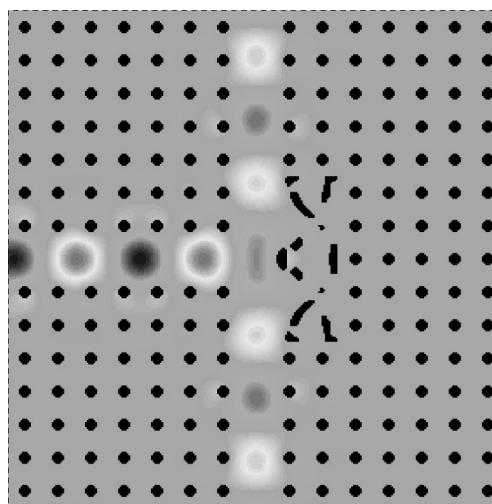


Fig. 4. Optimized T-junction topology for target frequency $\tilde{\omega}=0.38$ and the corresponding field distribution.

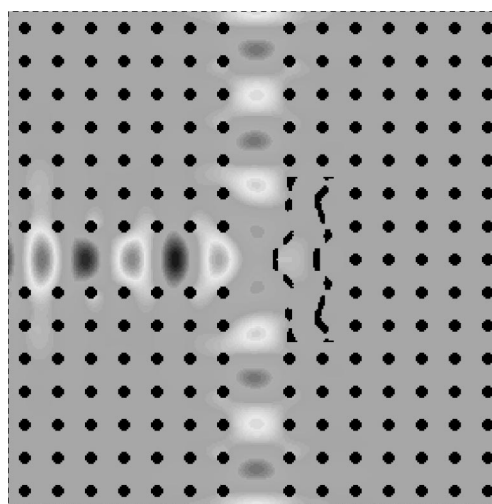


Fig. 5. Optimized T-junction topology for target frequency $\tilde{\omega}=0.44$ and the corresponding field distribution.

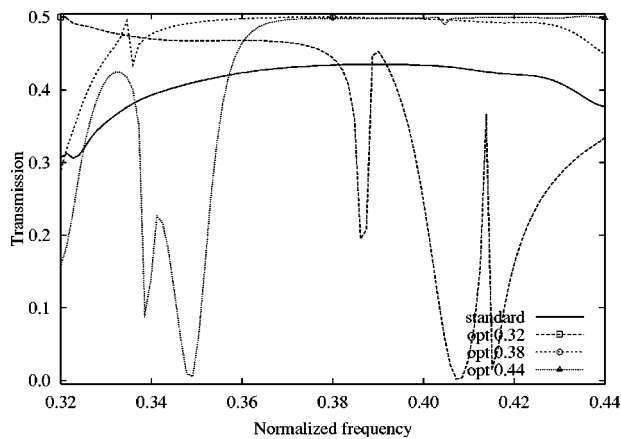


Fig. 6. Transmission through the top and bottom output ports. Results for the standard junction is shown along with three optimized designs for three different frequencies.

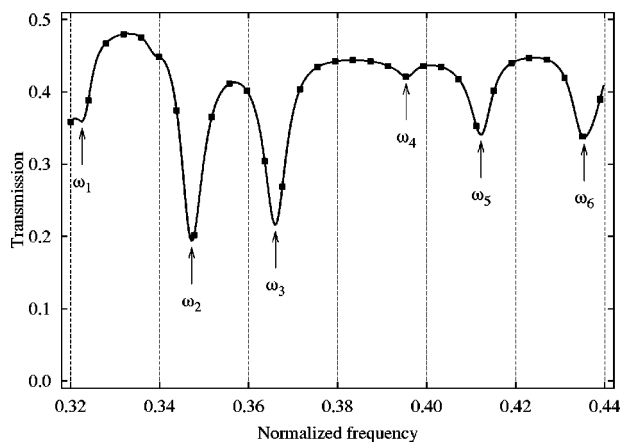


Fig. 7. Illustration of update scheme for target frequencies. The frequency curve is computed with Padé approximations to obtain high frequency resolution at low computational cost. Discrete markers indicate transmission values computed directly.

$$I_1 = [\tilde{\omega}_1; \tilde{\omega}_2[\dots , I_n =]\tilde{\omega}_N; \tilde{\omega}_{N+1}], \quad (20)$$

where N is the number of target frequencies and $\tilde{\omega}_{N+1} - \tilde{\omega}_1$ is the entire frequency range of interest, divided into N equally sized intervals. The power transmission is normalized for each frequency with the corresponding transmission for the straight waveguide J^* . In this way a proper weighting of the different frequencies is ensured.

The implementation of the the active-set strategy is illustrated in Fig. 7. A number N of target frequencies is chosen, and the frequency interval is divided into N equally sized sections. At regular intervals during the optimization, e.g., every 20 or 30 iterations, the transmission spectrum is computed, and the frequency with the lowest transmission is identified in each interval. These frequencies now become the new target frequencies in subsequent iterations. It is important that the spectrum is computed with high frequency resolution to accurately detect the critical frequencies. Unfortunately, this requires solving the direct problem [Eq. (4)] for many frequencies, thus slowing down the optimization procedure significantly. A way to overcome this is to compute the spectrum with a fast-frequency-sweep technique with

Padé approximates.²⁰ We then need to solve Eq. (4) only once for each frequency interval and can then expand the solution in the neighboring frequency range with high accuracy at low computational cost. The transmission spectrum in Fig. 7 is computed with a fast frequency sweep, and the solutions computed by our solving the direct problem, depicted with discrete markers, illustrate the accuracy of the expansion.

In the first example we use the original design domain (Fig. 2) and attempt to design the junction with full transmission in the entire frequency range from $\tilde{\omega}=0.32$ to $\tilde{\omega}=0.44$. We start out with three target frequencies and increase this number to 12 as the continuation parameter β is reduced to its final value at $\beta=0.00625$. Throughout the optimization we keep the pumping parameter $\epsilon=0.1$. Figure 8 shows the final design and the field computed for $\tilde{\omega}=0.38$. Figure 10 shows the corresponding transmission spectrum. However, note that the transmission still drops near the extremal frequencies.

It appears that the chosen design domain is unable to provide a full transmission in the entire frequency range, and therefore the domain is increased by an additional eight unit cells near the corners of the junction. We repeat the optimization procedure described above by using the previous design as the initial design and obtain the structure displayed in Fig. 9 that shows also the field computed for $\tilde{\omega}=0.38$. As can be seen in the transmission diagram (Fig. 10), the transmission is now improved and especially near the limits of the frequency range. By choosing even larger design domains, one can expect further improvements.

5. CONCLUSIONS

We have developed a design method based on topology optimization and used it to design a T junction in a photonic crystal waveguide with high transmission in a large frequency range.

The optimization algorithm is based on a frequency-domain finite-element model of 2D plane polarization. Elementwise constant design variables govern the distribu-

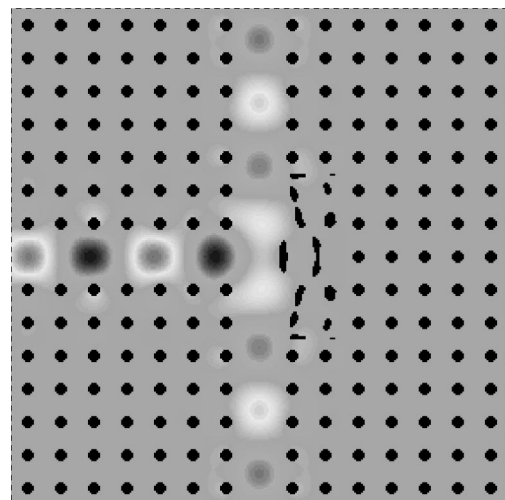


Fig. 8. Design optimized for frequency range $\tilde{\omega}=0.32-0.44$. The field is computed for $\tilde{\omega}=0.38$.

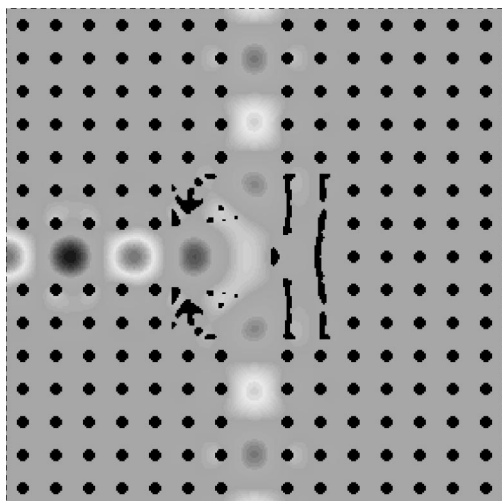


Fig. 9. Design optimized for frequency range $\tilde{\omega}=0.32-0.44$ with an enlarged design domain. The field is computed for $\tilde{\omega}=0.38$.

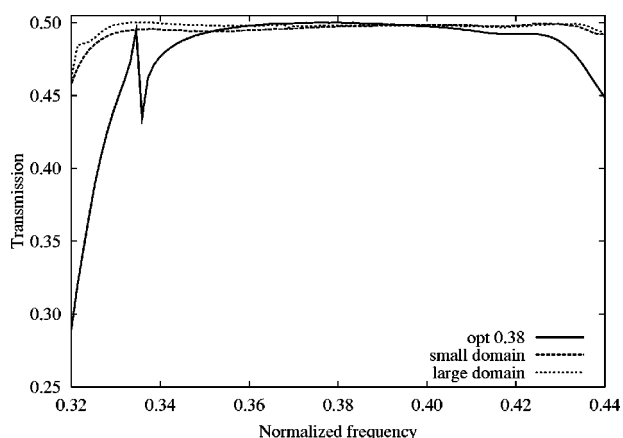


Fig. 10. Transmission spectra for the design optimized for the entire frequency range $\tilde{\omega}=0.32-0.44$. Shown also is the spectrum for the design optimized for $\tilde{\omega}=0.38$.

tion of material in a design domain near the junction. By maximizing the power transmission through the two waveguide output ports, we obtain designs with vanishing reflection at the junction.

We obtained a high transmission locally by performing the optimization for single frequencies. To get a larger bandwidth with high transmission, we introduced an active-set strategy in which the transmission is maximized for several frequencies simultaneously and in which these target frequencies are repeatedly updated with fast frequency sweeps to identify the most critical frequencies with lowest transmission. It was shown that, by increasing the design domain, we obtained a better performance in a larger frequency range, approaching full transmission for the entire frequency range under consideration.

To avoid local maxima based on local resonance effects, we applied a continuation method by convexifying the object and response functions with artificial damping. Additionally, we introduced a scheme to avoid values of the continuous design variable between 0 and 1, correspond-

ing to intermediate material. This was done by penalizing these intermediate values with extra artificial damping.

The algorithm appears to be a robust and efficient design tool for PhC components. Although based on a 2D model, recent experience with manufactured structures⁵ indicates that good performance of the actual devices can be expected, and the optimization scheme can directly be implemented with a three-dimensional computational model to address the important issue of out-of-plane scattering. Additionally, the objective function can easily be modified to deal with other functionalities.

ACKNOWLEDGMENTS

The authors thank Martin P. Bendsøe for valuable comments and suggestions. The work was supported by the Danish Technical Research Council through the grant “Designing bandgap materials and structures with optimized dynamic properties.”

J. S. Jensen, the corresponding author, can be reached by e-mail at jsj@mek.dtu.dk.

REFERENCES

1. E. Yablonovitch, “Inhibited spontaneous emission in solid-state physics and electronics,” *Phys. Rev. Lett.* **58**, 2059–2062 (1987).
2. S. John, “Strong localization of photons in certain disordered dielectric superlattices,” *Phys. Rev. Lett.* **58**, 2486–2489 (1987).
3. M. Burger, S. J. Osher, and E. Yablonovitch, “Inverse problem techniques for the design of photonic crystals,” *IEICE Trans. Electron.* **E87-C**, 258–265 (2004).
4. J. S. Jensen and O. Sigmund, “Systematic design of photonic crystal structures using topology optimization: low-loss waveguide bends,” *Appl. Phys. Lett.* **84**, 2022–2024 (2004).
5. P. I. Borel, A. Harpøth, L. H. Frandsen, M. Kristensen, P. Shi, J. S. Jensen, and O. Sigmund, “Topology optimization and fabrication of photonic crystal structures,” *Opt. Express* **12**, 1996–2001 (2004).
6. K. B. Chung, J. S. Yoon, and G. H. Song, “Analysis of optical splitters in photonic crystals,” in *Photonic Bandgap Material and Devices*, A. Adibi, A. Scherer, and S.-Yu. Lin, eds., *Proc. SPIE* **4655**, 349–355 (2002).
7. J. Smajic, C. Hafner, and D. Erni, “Optimization of photonic crystal structures,” *J. Opt. Soc. Am. A* **21**, 2223–2232 (2004).
8. W. J. Kim and J. D. O’Brien, “Optimization of a two-dimensional photonic-crystal waveguide branch by simulated annealing and the finite-element method,” *J. Opt. Soc. Am. B* **21**, 289–295 (2004).
9. T. Felici and T. F. G. Gallagher, “Improved waveguide structures derived from new rapid optimization techniques,” in *Physics and Simulation of Optoelectronic Devices XI*, M. Osinski, H. Amano, and P. Blood, eds., *Proc. SPIE* **4986**, 375–385 (2003).
10. M. P. Bendsøe and N. Kikuchi, “Generating optimal topologies in structural design using a homogenization method,” *Comput. Methods Appl. Mech. Eng.* **71**, 197–224 (1988).
11. H. L. Thomas, M. Zhou, and U. Schramm, “Issues of commercial optimization software development,” *Struct. Multidiscip. Optim.* **23**, 97–110 (2002).
12. M. P. Bendsøe and O. Sigmund, *Topology Optimization—Theory, Methods and Applications* (Springer, Berlin, 2003).
13. O. Sigmund and J. S. Jensen, “Systematic design of phononic band-gap materials and structures by topology

- optimization,” Proc. R. Soc. London, Ser. A **361**, 1001–1019 (2003).
14. A. Mekis, J. C. Chen, I. Kurland, S. Fan, P. R. Villeneuve, and J. D. Joannopoulos, “High transmission through sharp bends in photonic crystal waveguides,” Phys. Rev. Lett. **77**, 3787–3790 (1996).
 15. M. Koshiba, Y. Tsuji, and S. Sasaki, “High-performance absorbing boundary conditions for photonic crystal waveguide simulations,” IEEE Microw. Wirel. Compon. Lett. **11**, 152–154 (2001).
 16. R. D. Cook, D. S. Malkus, M. E. Plesha, and R. J. Witt, *Concepts and Applications of Finite Element Analysis*, 4th ed. (Wiley, New York, 2002).
 17. K. Svanberg, “The method of moving asymptotes—a new method for structural optimization,” Int. J. Numer. Methods Eng. **24**, 359–373 (1987).
 18. J. S. Jensen, “Phononic band gaps and vibrations in one- and two-dimensional mass-spring structures,” J. Sound Vib. **266**, 1053–1078 (2003).
 19. G. Allaire and G. A. Francfort, “A numerical algorithm for topology and shape optimization,” in *Topology Optimization of Structures*, M. P. Bendsøe and C. A. M. Soares, eds. (Kluwer, Dordrecht, The Netherlands, 1993), pp. 239–248.
 20. J. Jin, *The Finite Element Method in Electromagnetics*, 2nd ed. (Wiley, New York, 2002).

Topology optimization and fabrication of photonic crystal structures

P. I. Borel, A. Harpøth, L. H. Frandsen, M. Kristensen

Research Center COM, Technical University of Denmark, DK-2800 Kgs. Lyngby, Denmark
pib@com.dtu.dk, harpoeth@com.dtu.dk, lhf@com.dtu.dk, mk@com.dtu.dk

<http://www.com.dtu.dk/research/glass/pipe/index.html>

P. Shi

Department of Micro and Nanotechnology, Technical University of Denmark, DK-2800 Kgs. Lyngby, Denmark
pxshi@mic.dtu.dk

J. S. Jensen and O. Sigmund

Department of Mechanical Engineering, Technical University of Denmark, DK-2800 Kgs. Lyngby, Denmark
jsj@mek.dtu.dk, sigmund@mek.dtu.dk

<http://www.topopt.dtu.dk>

Abstract: Topology optimization is used to design a planar photonic crystal waveguide component resulting in significantly enhanced functionality. Exceptional transmission through a photonic crystal waveguide Z-bend is obtained using this inverse design strategy. The design has been realized in a silicon-on-insulator based photonic crystal waveguide. A large low loss bandwidth of more than 200 nm for the TE polarization is experimentally confirmed.

©2004 Optical Society of America

OCIS codes: (000.3860) Mathematical methods in physics; (000.4430) Numerical approximation and analysis; (130.2790) Guided waves; (130.3130) Integrated optics materials; (220.4830) Optical systems design; (230.5440) Polarization-sensitive devices; (230.7390) Waveguides, planar; (999.9999) Photonic crystals.

References and links

1. E. Yablonovitch, "Inhibited spontaneous emission in solid-state physics and electronics," *Phys. Rev. Lett.* **58**, 2059-2062 (1987).
2. S. John, "Strong localization of photons in certain disordered dielectric superlattices," *Phys. Rev. Lett.* **58**, 2486-2489 (1987).
3. T. F. Krauss, R. M. De La Rue, and S. Brand, "Two-dimensional photonic-bandgap structures operating at near-infrared wavelengths," *Nature* **383**, 699-702 (1996).
4. M. Thorhauge, L. H. Frandsen and P. I. Borel, "Efficient Photonic Crystal Directional Couplers," *Opt. Lett.* **28**, 1525-1527 (2003).
5. L. H. Frandsen, P. I. Borel, Y. X. Zhuang, A. Harpøth, M. Thorhauge, M. Kristensen, W. Bogaerts, P. Dumon, R. Baets, V. Wiaux, J. Wouters, and S. Beckx, "Ultra-low-loss 3-dB Photonic Crystal Waveguide Splitter," *Opt. Lett.* (to be published).
6. D. Taillaert, H. Chong, P.I. Borel, L.H. Frandsen, R.M. De La Rue, and R. Baets, "A Compact Two-dimensional Grating Coupler used as a Polarization Splitter," *IEEE Photon. Technol. Lett.* **15**, 1249-1251 (2003).
7. M. P. Bendsøe and N. Kikuchi, "Generating optimal topologies in structural design using a homogenization method," *Comput. Meth. Appl. Mech. Eng.* **71**, 197-224 (1988).
8. M. P. Bendsøe and O. Sigmund, *Topology optimization — Theory, Methods and Applications* (Springer-Verlag, 2003).
9. T. P. Felici and D. F. G. Gallagher, "Improved waveguide structures derived from new rapid optimization techniques," *Proc. SPIE* **4986**, 375-385 (2003).
10. J. Smajc, C. Hafner and D. Erni, "Design and optimization of an achromatic photonic crystal bend," *Opt. Express* **11**, 1378-1384 (2003), <http://www.opticsexpress.org/abstract.cfm?URI=OPEX-11-12-1378>.

11. W. J. Kim and J. D. O'Brien, "Optimization of a two-dimensional photonic-crystal waveguide branch by simulated annealing and the finite element method," *J. Opt. Soc. Am. B* **21**, 289-295 (2004).
12. M. Tokushima, H. Kosaka, A. Tomita and H. Yamada, "Lightwave propagation through a 120° sharply bent single-line-defect photonic crystal waveguide," *Appl. Phys. Lett.* **76**, 952-954 (2000).
13. T. Uusitupa, K. Kärkkäinen and K. Nikoskinen, "Studying 120° PBG waveguide bend using FDTD," *Microwave Opt. Technol. Lett.* **39**, 326-333 (2003).
14. It should be emphasized that the method can readily be implemented in a 3D finite element model where the computational requirements naturally will be significantly higher.
15. K. Svanberg, "The method of moving asymptotes: a new method for structural optimization," *Int. J. Numer. Meth. Engng.* **24**, 359-373 (1987).
16. J. S. Jensen and O. Sigmund, "Systematic design of photonic crystal structures using topology optimization: Low-loss waveguide bends," *Appl. Phys. Lett.* **84**, 2022-2024 (2004).
17. O. Sigmund and J. S. Jensen, "Systematic design of phononic band gap materials and structures by topology optimization," *Phil. Trans. R. Soc. Lond. A* **361**, 1001-1019 (2003).
18. P. I. Borel, L. H. Frandsen, M. Thorhauge, A. Harpøth, Y. X. Zhuang, M. Kristensen, and H. M. H. Chong, "Efficient propagation of TM polarized light in photonic crystal components exhibiting band gaps for TE polarized light," *Opt. Express* **11**, 1757-1762 (2003), <http://www.opticsexpress.org/abstract.cfm?URI=OPEX-11-15-1757>.
19. A. Lavrinenko, P. I. Borel, L. H. Frandsen, M. Thorhauge, A. Harpøth, M. Kristensen, T. Niemi, and H. M. H. Chong, "Comprehensive FDTD modelling of photonic crystal waveguide components," *Opt. Express* **12**, 234-248 (2004), <http://www.opticsexpress.org/abstract.cfm?URI=OPEX-12-2-234>.

1. Introduction

The planar photonic crystal (PhC) is an optical nano-material with periodic modulation of the refractive index. The modulation is designed to forbid propagation of light in certain wavelength ranges, so-called photonic bandgaps (PBGs) [1-3]. Breaking the crystal symmetry by introducing line defects and other discontinuities allows control of the light on a sub-wavelength scale in the PhCs. Therefore, photonic devices based on the PBG effect may be up to one million times smaller than traditional integrated optical devices. PhC structures with 20-40 nm useful optical bandwidths have previously been demonstrated [4-6]. Until now, however, no bandgap-based PhC components have been demonstrated with satisfactory performance in a broad wavelength range. A major reason for this has been the lack of efficient inverse design tools that can be applied irrespectively of the device under consideration. Therefore, most PhC design structures today are obtained either by intuition or by varying one or two design parameters—typically the position or size of a PhC element—using the trial-and-error method.

In this paper we show exceptional transmission through a Z-bend consisting of two successive 120° PhC waveguide bends. The design of the bends is obtained using an efficient inverse design strategy called *topology optimization*. The optimized design is experimentally realized in a silicon-based PhC. Measurements have confirmed a large low-loss bandwidth of more than 200 nm for TE polarized light.

2. Topology optimization

The systematic design method based on topology optimization allows creation of improved PhC components with previously unseen low transmission losses and high operational bandwidths, or with wavelength selective functionalities. The method was originally developed for structural optimization problems [7], but has recently been extended to a range of other design problems [8]. The method is based on repeated finite element analyses where the distribution of material in a given design area is iteratively modified in order to improve a chosen performance measure. The resulting designs are inherently free from geometrical restrictions such as the number of holes, hole shapes etc., thereby allowing the large potentials of PhC components to be exploited to hitherto unseen levels. Previously reported optimization tools for such components have all been restricted to deal with circular holes [9-11].

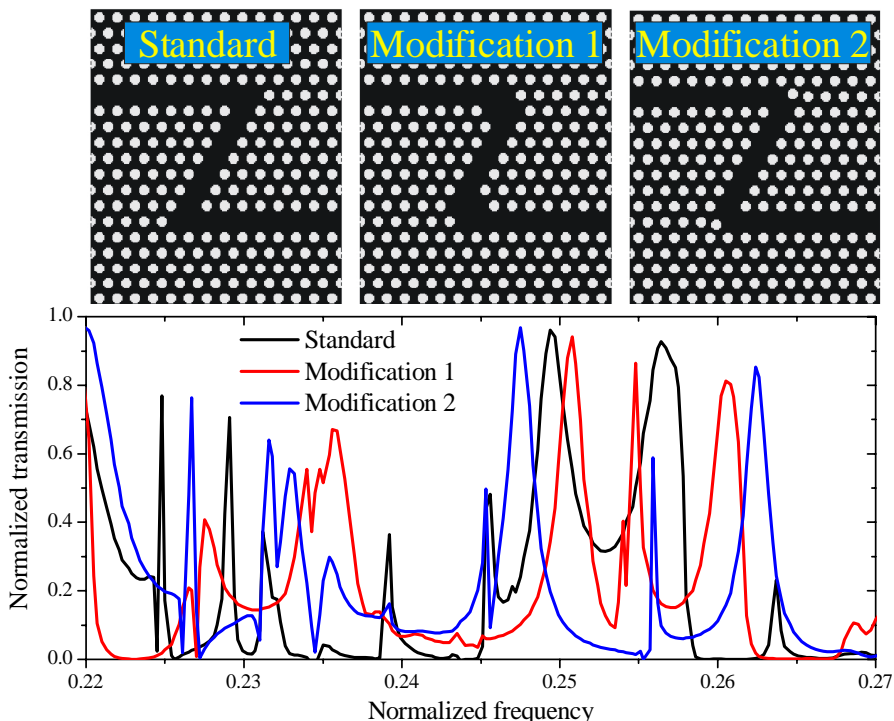


Fig. 1. Top: Standard and two modified Z-bend waveguides. Bottom: Transmission through the bends calculated using a 2D frequency domain finite element model.

To demonstrate the method, we have designed and fabricated an optimized PhC Z-bend consisting of two successive 120° waveguide bends [12]. The un-optimized Z-bend displays high bend losses except in narrow frequency bands. Although a Z-bend PhC may have limited practical applicability, it is a difficult and challenging design problem that serves as an excellent benchmark for our method. Intuitive attempts to improve the design by removing or displacing single holes in the bends do usually not lead to significant reduction of the bend loss as indicated in Fig. 1. Larger bandwidth with high transmission has previously been predicted for two 120° bends by displacing a larger number of holes [13], but this procedure is very time-consuming and does not guarantee acceptable solutions.

We base our optimization procedure on a 2D frequency domain finite element model of the waveguide [14] and choose the outer parts of the two bend regions as design areas wherein the material distribution should be modified (see Fig. 2, Left).

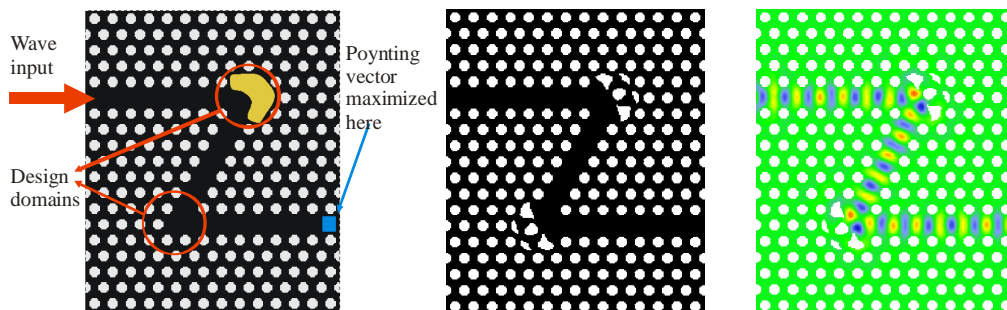


Fig. 2. Left: Schematic illustration of the topology optimization procedure. The yellow area sketches the design domain of one bend. Middle: (149 kB) Movie of how the material is redistributed in the design domain in the optimization procedure. In about 600 iteration steps a final design is obtained that has optimized transmission properties. Right: (482 kB) Movie of TE polarized light propagating through the topology optimized Z-bend.

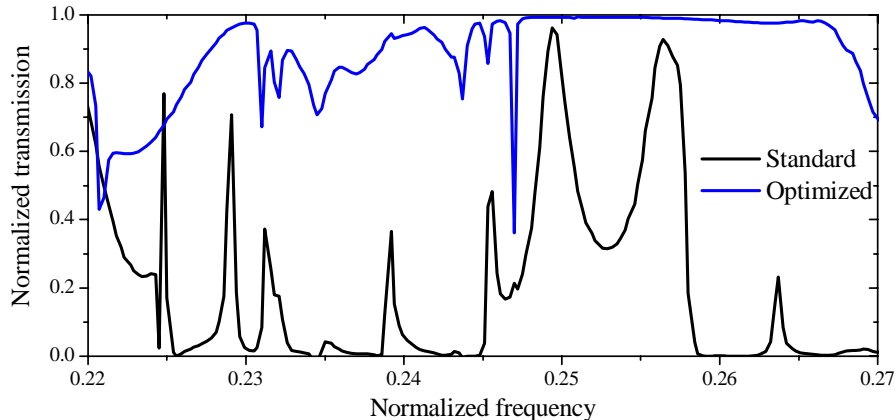


Fig. 3. The transmission for TE polarized light through the un-optimized (standard) design (black) and the optimized design (blue). The transmission spectra are based on a 2D frequency domain finite element model.

Although we could have chosen much larger design areas, the numerical experiments showed that relatively small design areas were enough to yield the wanted improvement in efficiency. Had the efficiency been unsatisfactory, the design areas could have been enlarged in order to introduce more freedom in the design. In order to reduce the bend loss we choose the transmitted energy flow (Poynting vector) through the Z bent waveguide to be maximized (see Fig. 2, left). Relatively short inlet, 120 degree and outlet channels were chosen for CPU time reasons. However, the results have been numerically verified to be insensitive to larger channel lengths.

During the iterative optimization procedure the material distribution is changed based on analytical sensitivity analysis combined with the use of a mathematical programming tool [15]. For more information regarding the procedure we refer to Ref. [16] dealing with optimization of a 90° bend in a pillar-based waveguide. More details regarding sensitivity analysis etc. can be found in Ref. [17] where *phononic* bandgap materials and structures are optimized.

The optimization can be performed for any number of frequencies simultaneously, also with min-max (or max-min) formulations. In the case of the Z-bend we find that the use of a single frequency in the optimization is sufficient to produce a large bandwidth with low loss. The algorithm is run on a personal computer requiring about 5 s per iteration and around 600 iteration steps to reach a converged design.

Figure 2 shows the optimized design along with the iterative material re-distribution in the design domains (middle) and the resulting wave propagation through the optimized waveguide (right). In Fig. 3 the transmission through an un-optimized (black) and an optimized (blue) Z-bend is shown. It is noticed how the operational bandwidth is dramatically improved by applying topology optimization to the design.

3. Fabrication and characterization

The PhC Z-bend has been fabricated in silicon-on-insulator material utilizing e-beam lithography (JEOL JBX-9300FS). The written patterns were transferred into the approximately 300 nm thick top silicon layer employing standard anisotropic reactive-ion etch as described in Ref. [18]. The Z-bend waveguide is realized in a triangular lattice of holes by removing rows of nearest-neighbor holes. The lattice constant $\Lambda=430$ nm and the diameter of the holes $D=260$ nm. A scanning electron micrograph of the fabricated Z-bend is shown in Fig. 4.

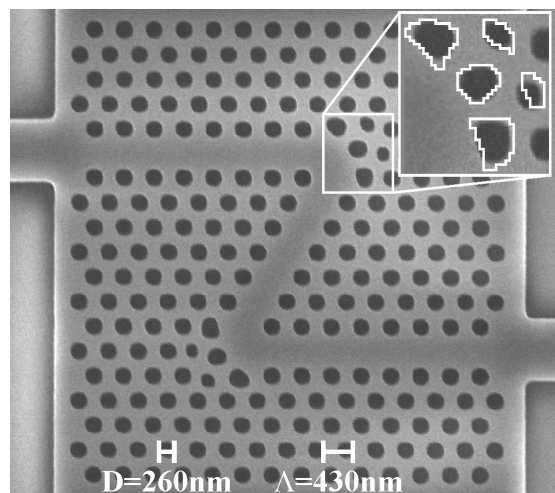


Fig. 4. Scanning electron micrograph of the fabricated Z-bend. The number, shape and size of the holes at each bend are designed using topology optimization. The inset shows a magnified view of the optimized holes as designed (white contour) and actually fabricated.

The e-beam was slightly defocused during the lithography process due to imperfect filament conditions. Corrections to compensate for this deficiency were undertaken by appropriate modifications of the design files. Due to the finite e-beam spot-size, the fabricated structure is slightly different from the optimized design as shown in the inset. No special proximity corrections were applied for the irregular shaped holes.

The fabricated components were characterized using the setup sketched in Fig. 5. Tapered lensed fibers were used to couple light in and out of the ridge waveguides connected to the PhC waveguides. The light sources were broadband light emitting diodes. Three polarization controllers and two polarizer crystals with extinction ratios better than 35 dB were used to control the polarization of the in-coupled light and to analyze the transmitted light from the device under test. The optical spectra for the transmitted light are recorded using an optical spectrum analyzer with a 10 nm resolution (ANDO AQ6315E).



Fig. 5. Experimental setup used to characterize the waveguide samples.

4. Experimental results

The measured loss per bend for TE polarized light sent through the fabricated Z-bend is shown in Fig. 6. The measured transmission spectrum has been normalized to a transmission spectrum for a straight PhC waveguide of the same length. The polarization of the light transmitted through the device containing the Z-bend was analyzed and found to be purely TE polarized. Hence, no significant TE-TM coupling is introduced by the Z-bend.

Also shown in the figure are the calculated losses, obtained by employing 3D finite-difference time-domain (FDTD) calculations [19], for the fabricated and the un-optimized Z-bend. These spectra have also been normalized to spectra for straight PhC waveguides of the same length. The calculated FDTD spectra have been blue-shifted ~4% in wavelength.

The most prominent feature of the spectra is the extremely broad wavelength range of more than 200 nm having a low bend loss of just above ~1 dB. This is to the best of our knowledge by far the largest bandwidth with low bend loss demonstrated for the TE polarization in a PhC waveguide. Without topology optimization 3D FDTD calculations show up to ~10 dB higher loss per bend.

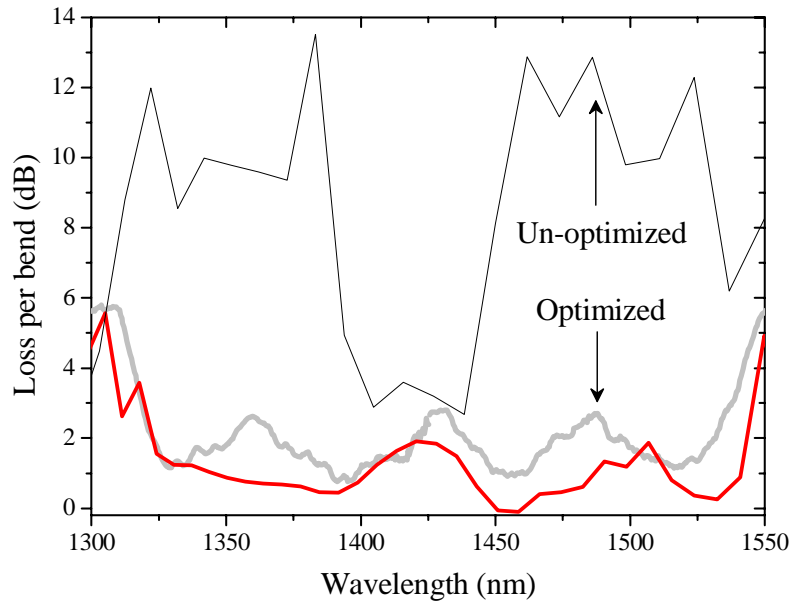


Fig. 6. The measured (gray) and 3D FDTD calculated (red) loss per bend for TE polarized light in the fabricated structure. Also shown is the 3D FDTD calculated bend loss for the un-optimized (black) Z-bend.

It is worth noting that the low bend loss is obtained experimentally even though the fabricated structure deviates slightly from the optimized design shown in Fig. 2 (middle). This fact proves the robustness of the design for experimental fabrication tolerances. Using the min-max formulation, this robustness may also hold for other applications.

5. Conclusion

We have reported the successful experimental realization of a planar photonic crystal component with functionalities that have been enhanced using the inverse design strategy *topology optimization*. As an example application of this new method we have chosen to design and fabricate a topology optimized photonic crystal bend consisting of two successive 120° waveguide bends.

The optimized photonic crystal waveguide Z-bend has experimentally been found to display a low bend loss of just more than ~ 1 dB in a broad wavelength range of more than 200 nm for the TE polarization. The design is proven robust regarding fabrication tolerances. We believe topology optimization can be used as a general inverse design tool to design a wide range of photonic crystal waveguide components irrespectively of the device under consideration.

Broadband photonic crystal waveguide 60° bend obtained utilizing topology optimization

L.H. Frandsen, A. Harpøth, P.I. Borel, M. Kristensen

Research Center COM, Technical University of Denmark, DK-2800 Kgs. Lyngby, Denmark
lhf@com.dtu.dk, harpoeth@com.dtu.dk, pib@com.dtu.dk, mk@com.dtu.dk

<http://www.com.dtu.dk/research/glass/pipe/index.html>

J.S. Jensen and O. Sigmund

Department of Mechanical Engineering, Technical University of Denmark, DK-2800 Kgs. Lyngby, Denmark
jsj@mek.dtu.dk, sigmund@mek.dtu.dk

<http://www.topopt.dtu.dk>

Abstract: Topology optimization has been used to design a 60° bend in a single-mode planar photonic crystal waveguide. The design has been realized in a silicon-on-insulator material and we demonstrate a record-breaking 200nm transmission bandwidth with an average bend loss of 0.43 ± 0.27 dB for the TE polarization. The experimental results agree well with 3D finite-difference-time-domain simulations.

©2004 Optical Society of America

OCIS codes: (000.3860) Mathematical methods in physics; (000.4430) Numerical approximation and analysis; (130.2790) Guided waves; (130.3130) Integrated optics materials; (220.4830) Optical systems design; (230.5440) Polarization-sensitive devices; (230.7390) Waveguides, planar; (999.9999) Photonic crystals.

References and links

1. E. Yablonovitch, "Inhibited spontaneous emission in solid-state physics and electronics," *Phys. Rev. Lett.* **58**, 2059-2062 (1987).
2. S. John, "Strong localization of photons in certain disordered dielectric superlattices," *Phys. Rev. Lett.* **58**, 2486-2489 (1987).
3. T. F. Krauss, R. M. De La Rue, and S. Brand, "Two-dimensional photonic-bandgap structures operating at near-infrared wavelengths," *Nature* **383**, 699-702 (1996).
4. M. Thorhauge, L. H. Frandsen and P. I. Borel, "Efficient Photonic Crystal Directional Couplers," *Opt. Lett.* **28**, 1525-1527 (2003).
5. Y. Sugimoto, Y. Tanaka, N. Ikeda, K. Kanamoto, Y. Nakamura, S. Ohkouchi, H. Nakamura, K. Inoue, H. Sasaki, Y. Watanabe, K. Ishida, H. Ishikawa, K. Asakawa, "Two Dimensional Semiconductor-Based Photonic Crystal Slab Waveguides for Ultra-Fast Optical Signal Processing Devices," *IEICE Trans. Electron.* **E87-C**, 316-327 (2004).
6. L. H. Frandsen, P. I. Borel, Y. X. Zhuang, A. Harpøth, M. Thorhauge, M. Kristensen, W. Bogaerts, P. Dumon, R. Baets, V. Wiaux, J. Wouters, and S. Beckx, "Ultra-low-loss 3-dB Photonic Crystal Waveguide Splitter," *Opt. Lett.* **29**, 1623-1625 (2004).
7. T. Søndergaard, J. Arentoft, and M. Kristensen, "Theoretical Analysis of Finite-Height Semiconductor-on-Insulator-Based Planar Photonic Crystal Waveguides," *J. Lightwave Technol.* **20**, 1619-1626 (2002)
8. C. Jamois, R. B. Wehrspohn, L.C. Andreani, C. Hermann, O. Hess, U. Gösele, "Silicon-based two-dimensional photonic crystal waveguides," *Photonics and Nanostructures – Fundamentals and Applications* **1**, 1-13 (2003).
9. P.I. Borel, L.H. Frandsen, A. Harpøth, J.B. Leon, H. Liu, M. Kristensen, W. Bogaerts, P. Dumon, R. Baets, W. Wiaux, J. Wouters, S. Beckx, "Bandwidth tuning of photonic crystal waveguide bends," *Electron. Lett.* **40**, 1263-1264 (2004).
10. A. Chutinan, M. Okano, S. Noda, "Wider bandwidth with high transmission through waveguide bends in two-dimensional photonic crystal slabs," *Appl. Phys. Lett.* **80**, 1698-1700 (2002).
11. J. Smajic, C. Hafner, D. Erni, "Design and optimization of an achromatic photonic crystal bend," *Opt. Express* **11**, 1378-1384 (2003), <http://www.opticsexpress.org/abstract.cfm?URI=OPEX-11-12-1378>.

12. P.I. Borel, A. Harpøth, L.H. Frandsen, M. Kristensen, P. Shi, J.S. Jensen and O. Sigmund, "Topology Optimization and fabrication of photonic crystal structures," *Opt. Express* **12**, 1996–2001 (2004), <http://www.opticsexpress.org/abstract.cfm?URI=OPEX-12-9-1996>.
13. A. Lavrinenko, P.I. Borel, L.H. Frandsen, M. Thorhauge, A. Harpøth, M. Kristensen and T. Niemi, "Comprehensive FDTD Modelling of Photonic Crystal Waveguide Components," *Opt. Express* **12**, 234-248 (2004), <http://www.opticsexpress.org/abstract.cfm?URI=OPEX-12-2-234>.
14. P.I. Borel, L. H. Frandsen, M. Thorhauge, A. Harpøth, Y. X. Zhuang, M. Kristensen, and H. M. H. Chong, "Efficient propagation of TM polarized light in photonic crystal components exhibiting band gaps for TE polarized light." *Opt. Express* **11**, 1757-1762 (2003), <http://www.opticsexpress.org/abstract.cfm?URI=OPEX-11-15-1757>.
15. A. Talneau, L. Le Gouezigou, N. Bouadma, M. Kafesaki, C.M. Soukoulis, M. Agio, "Photonic-crystal ultrashort bends with improved transmission and low reflection at 1.55 μm ," *Appl. Phys.Lett.* **80**, 547-549 (2002).
16. E. Chow, S. Y. Lin, J. R. Wendt, S. G. Johnson, J. D. Joannopoulos, "Quantitative analysis of bending efficiency in photonic-crystal waveguide bends at $\lambda = 1.55 \mu\text{m}$ wavelengths," *Opt. Lett.* **26**, 286-288 (2001).
17. M. P. Bendsøe and O. Sigmund, *Topology optimization — Theory, Methods and Applications* (Springer-Verlag, 2003).
18. K. Svanberg, "The method of moving asymptotes: a new method for structural optimization," *Int. J. Numer. Meth. Engng.* **24**, 359-373 (1987).
19. J. S. Jensen and O. Sigmund, "Systematic design of photonic crystal structures using topology optimization: Low-loss waveguide bends," *Appl. Phys. Lett.* **84**, 2022-2024 (2004).
20. O. Sigmund and J. S. Jensen, "Systematic design of phononic band gap materials and structures by topology optimization," *Phil. Trans. R. Soc. Lond. A* **361**, 1001-1019 (2003).
21. J. S. Jensen and O. Sigmund, "Topology optimization of photonic crystal structures: A high bandwidth low loss T-junction waveguide," *J. Opt. Soc. Am. B*, accepted (2004).
22. R. L. Espinola, R. U. Ahmad, F. Pizzuto, M. J. Steel, R. M. Osgood, Jr., "A study of high-index contrast 90° waveguide bend structures," *Opt. Express* **8**, 517-528 (2001), <http://www.opticsexpress.org/abstract.cfm?URI=OPEX-8-9-517>.

1. Introduction

Modulating the refractive index profile periodically in an optical material can create photonic bandgaps (PBGs) wherein no optical modes can exist [1-3]. Such structures are often referred to as photonic crystals (PhCs) and have attracted a lot of attention as they potentially allow ultra-compact photonic integrated circuits (PICs) to be realized [4-6]. Planar PhC structures are often defined as triangular arrangements of low dielectric pillars in a high dielectric material. This configuration gives rise to a large PBG for the transverse-electric (TE) polarization [7, 8]. Defects in the PhC can introduce modes in the PBG. In this way, photonic crystal waveguides (PhCWs) can be formed by locally breaking the periodicity along a specific direction of the PhC lattice. Due to the triangular lattice configuration, such PhCWs are naturally bent in steps of 60°, thus, making the 60° PhCW bend a key component in PhC-based PICs.

In the field of planar photonic crystals, research has within the last decade mostly relied on an Edisonian design approach combining physical arguments and experimental/numerical verifications [9, 10]. Further optimizations have typically been done in an iterative trial-and-error procedure to improve a chosen performance measure of the PhC component. Such an approach is very time-consuming and does not guarantee optimal solutions. Recently, Smajic *et al.* [11] have shown that sensitivity analyses can be assistive in choosing the critical PhC rods/holes to be altered. A different approach was suggested in our previous work [12], in which we used an inverse design strategy called topology optimization to optimize the performance of a PhCW containing two consecutive 120° bends. This design method offers an effective and robust optimization of the photonic crystal structure irrespectively of the device under consideration. Here, we apply the topology optimization method to the much more important and commonly used PhCW 60° bend and demonstrate an experimental 1-dB transmission bandwidth of more than 200nm. Experimental transmission spectra are compared to spectra obtained from 3D finite-difference-time-domain (FDTD) calculations [13] and good agreement is found.

2. Design and fabrication

Silicon-on-insulator (SOI) is an excellent choice of material for a monolithic integration of PhC-based PICs and electronic devices. We define the PhC structures in the top silicon layer of a SOI material by utilizing e-beam lithography and standard anisotropic reactive-ion etch [14]. The regular PhCs are defined as air holes arranged in a triangular lattice and the PhCWs are carved out as W1 waveguides by removing one row of holes in the nearest-neighbor direction of the crystal lattice. The lattice pitch is $\Lambda \approx 400\text{nm}$ and the diameter of the holes $D \approx 275\text{nm}$. This configuration gives rise to a broad PBG below the silica-line from $\Lambda/0.3463$ - $\Lambda/0.2592$ and allows TE-like single-mode propagation in the PhCW.

The optimization of the 60° PhCW bend has typically relied on attempts to smooth out the bend by altering, displacing, and/or removing holes in the bend region. However, the useful bandwidth ($\sim 30\text{nm}$) of practical waveguide bends has usually been one order of magnitude smaller than the bandgap [9, 10, 15, 16]. Thus, a careful design, tolerant to fabrication deviations, is very important to utilize the full bandgap of the PhC.

Figure 1 shows schematics of PhCWs defined in a triangular lattice and containing two consecutive 60° bends. The distance between the bends has been chosen arbitrarily, but sufficiently long to achieve steady-state behavior of the PBG mode in the waveguide section separating the bends so that these bends can be treated as separate components. The left image illustrates a PhCW with two simple 60° bends. Such generic bends form severe discontinuities in the PhCW and introduce large reflections and excite higher order modes, which are not necessarily guided in the PhCW.

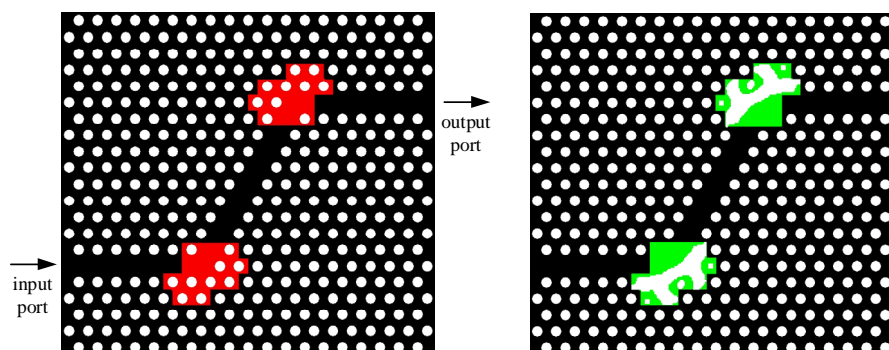


Fig. 1. Schematics of photonic crystal waveguides containing two consecutive 60° bends. Left: Generic bend configuration. The red areas illustrate the chosen design domains in the topology optimization procedure. Right: Topology-optimized bends. The green areas highlight the optimized structures showing that a non-trivial smoothing has been applied to the bend.

We use the method of topology optimization (see e.g. [17]) to optimize the performance of the component. This is done by changing the material distribution in the designated design domains indicated by the two red areas in Fig. 1 (left). No geometrical restrictions are enforced so the resulting design in these domains may consist of an arbitrary number of holes of arbitrary sizes and shapes.

The optimization algorithm is based on a 2D finite-element frequency-domain solver, which produces an accurate 2D field solution. The solver is used repeatedly in an iterative scheme, in which the material distribution is updated every iteration based on analytical sensitivity analysis and use of a mathematical programming tool [18]. On a standard 2.66GHz PC with 1 GB RAM each iteration takes about 10s. More details about the general method can be found in [17] and its application in optimization of photonic/phononic crystal structures in [12, 19, 20].

For the 60° bends in Fig. 1 (left) we optimize the component by modifying the material distribution so that the transmission through the waveguide is *maximized*. The transmission is evaluated as the power flow at the output port. In order to create a *broadband* component the

power flow is evaluated for several frequencies (up to 6) in the chosen frequency range. During the optimization procedure we maximize the output for all frequencies, and update these target frequencies every 10th or 20th iteration in order to eliminate transmission dips in the frequency range [21].

The optimized design is shown in Fig. 1 (right) where the green areas highlight the optimized design domains. This design was obtained after approximately 1000 iterations of the optimization algorithm, however, with the qualitative structure of the design appearing after about 200 iterations. Clearly, the bends have been smoothed by applying a soft curvature in the bend region and one hole has been removed on the inner side of the bend. However, the smoothing is not trivial as the design domain still contains complex structures. Note that the optimized 60° bend mostly resembles an etched mirror [22], whereas the topology-optimized 120° bend [12] retained its original crystal structure with deformed holes. The major strength of the topology optimization method is that the superior type of structure does not need to be known in advance; it will appear from the optimization procedure.

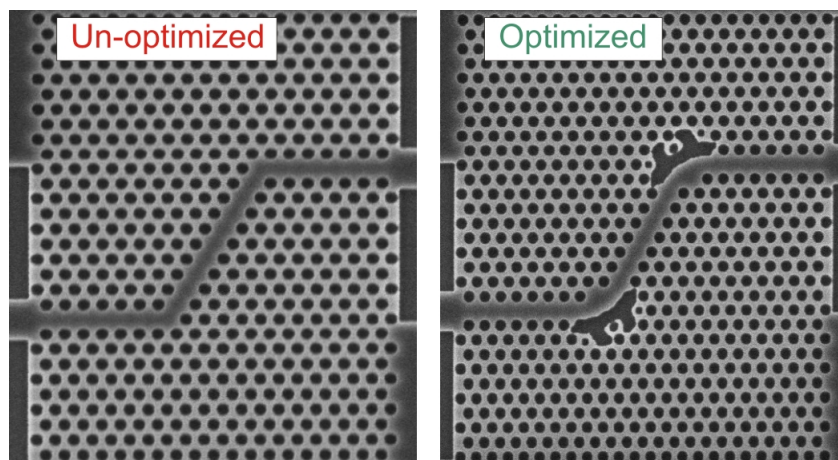


Fig. 2. Scanning electron micrographs of fabricated photonic crystal waveguides containing two consecutive 60° bends. The pitch of the triangular lattice is $\Lambda \approx 400\text{nm}$ with hole diameter $D \approx 275\text{nm}$. Left: Waveguide with generic. Right: Waveguide with topology-optimized bends. The number, shape and size of the holes at each bend are designed using topology optimization. The contrast and brightness of the images have been changed for clarity.

Figure 2 shows scanning electron micrographs of the fabricated PhCWs containing two un-optimized (left) and two topology-optimized (right) 60° bends. The PhC structures have been fabricated without applying any special proximity corrections to the irregular shaped holes during the e-beam patterning. Nonetheless, the fabricated topology-optimized structures nicely resemble those shown in Fig. 1 (right).

3. Simulation and experimental results

Figure 3 shows the steady-state magnetic field distribution for the fundamental PBG mode of the fabricated PhCWs simulated using 2D FDTD. The left image shows the mode behavior for light incident from the bottom-left through the PhCW with the generic bends. It is clearly seen that the generic bend forms a severe discontinuity in the straight PhCW and excite an odd mode, which is not well guided in the PhCW. Moreover, the lower bend introduces large reflections and scattering of light to the PhC structure. In contrast, the right image shows that the topology-optimized bend regions guide the fundamental PBG mode nicely through the two bends without disturbing the mode profile.

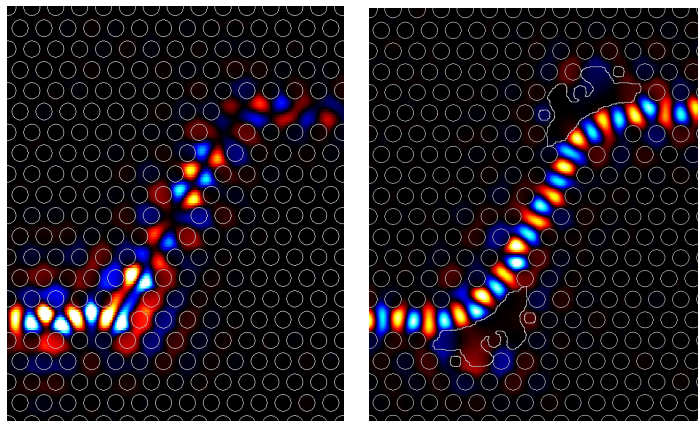


Fig. 3. Steady-state magnetic field distribution for the fundamental PBG mode simulated using 2D FDTD. The mode is incident from the bottom-left part of the waveguide. Left: Mode profile through the generic bends. Right: Mode profile through the topology-optimized bends.

The fabricated PhCWs shown in Fig. 2 have been optically characterized using broadband light emitting diodes (LEDs) as sources. To cover the full bandwidth of the fabricated components we used three different LEDs centered around 1310nm, 1414nm, and 1538nm. Tapered lensed fibers were used to couple light in and out of the ridge waveguides connected to the PhCWs. Two polarization controllers and a polarizer with an extinction ratio better than 35 dB were used to control the polarization of the light sent into the device under test. The optical spectra for the transmitted light were recorded with a spectral resolution of 10nm using an optical spectrum analyzer. To extract the bend loss the transmission spectra have been normalized to the transmission spectrum for a straight PhCW of the same length. Figure 4 shows the measured bend loss of TE polarized light for the un-optimized generic (red curve) and the topology-optimized (green curve) 60° bend.

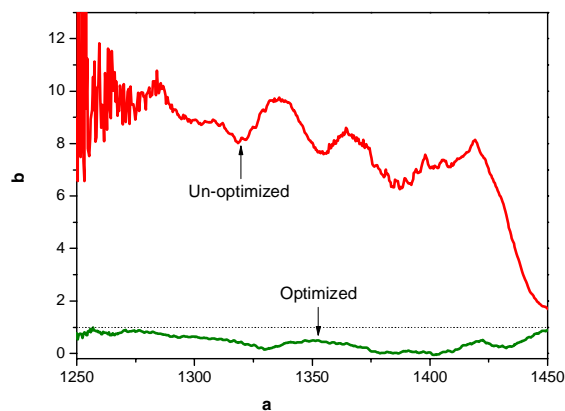


Fig. 4. Measured loss per bend for the un-optimized 60° bends (red) and the topology-optimized 60° bends (green). Both spectra have been normalized to the transmission through straight PhCWs of the same length to eliminate the coupling and the propagation loss in straight waveguides. Dotted line marks a bend loss of 1dB.

The topology-optimized bend displays more than 200nm bandwidth with less than 1dB loss and an average bend loss of 0.43 ± 0.27 dB. In the same wavelength range the un-optimized bend clearly shows a large bend loss, which only reduces in a narrow range near the cut-off of the fundamental mode at longer wavelengths. Thus, applying the two-dimensional topology

optimization method has dramatically boosted the performance of the 60° bend and opened for a practical implementation of the bend without the need for delicately tuning a narrow operational bandwidth of the bend to the bandwidth of the rest of the PhC component. The high transmission bandwidth of the bend is obtained for the fundamental even mode in the PBG of the PhCW. Due to the fundamental properties of the SOI PhCW [7, 8] this bandwidth is above the silica-line but in the PBG and cannot be attributed to the optimization method, as this is a purely two-dimensional algorithm.

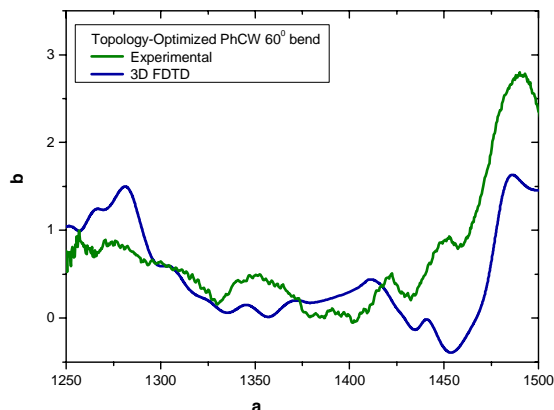


Fig. 5. Experimental bend loss (green) compared to 3D FDTD calculated bend loss (blue). The 3D FDTD curve has been shifted 1.2% in absolute wavelength.

Figure 5 shows a detailed comparison between the experimental and calculated loss of the optimized bend and a good agreement is found. The negative theoretical propagation losses are due to numerical artifacts when calculating near zero losses. The 3D FDTD spectrum has been shifted 1.2% in absolute wavelength and slightly undershoots the experimental values. These deviations are partly due to uncertainties in the experimental hole diameters, but more importantly due to the limited grid resolution in the calculations [13].

4. Conclusion

We have optimized the performance of a 60° planar photonic crystal waveguide bend using a two-dimensional inverse design strategy called topology optimization. The design was fabricated in silicon-on-insulator material and we experimentally obtained a record-high 1-dB transmission bandwidth exceeding 200nm for the TE polarization. The experimental results agree well with 3D finite-difference-time-domain simulations. The broadband topology-optimized 60° waveguide bend solves an important issue in designing planar photonic crystal components and opens for the realization of a wide range of ultra-compact, low-loss, and broadband optical devices.

Acknowledgments

This work was supported in part by the Danish Technical Research Council through the research programs ‘Planar Integrated PBG Elements’ (PIPE) and ‘Designing bandgap materials and structures with optimized dynamic properties’.

Topology optimised broadband photonic crystal Y-splitter

P.I. Borel, L.H. Frandsen, A. Harpøth, M. Kristensen, J.S. Jensen and O. Sigmund

A planar photonic crystal waveguide Y-splitter that exhibits large-bandwidth low-loss 3 dB splitting for TE-polarised light has been fabricated in silicon-on-insulator material. The high performance is achieved by utilising topology optimisation to design the Y-junction and by using topology optimised low-loss 60° bends. The average excess loss of the entire component is found to be 0.44 ± 0.29 dB for a 100 nm bandwidth, and the excess loss due to the Y-junction is found to be 0.34 ± 0.30 dB in a 175 nm bandwidth.

Introduction: A photonic crystal (PhC) is an optical material in which the refractive index is periodically modulated [1, 2]. Planar PhC structures are often defined as triangular arrangements of air holes in a high dielectric material, since this configuration may give rise to a large photonic bandgap (PBG) for the transverse-electric (TE) polarisation. Such PhC structures have recently gained a lot of consideration as they potentially allow for the realisation of ultra-compact photonic integrated components [3–8]. Planar PhC waveguides (PhCWs) are typically formed by locally breaking the periodicity along a specific direction of the PhC lattice. Most of the research within PhCs has hitherto relied on intuitive design approaches based on physical arguments, possibly combined with iterative trial-and-error procedures, to improve the performance of the PhC component. Recently, we have proposed to use a systematic inverse design strategy called topology optimisation [9] to optimise the performance of PhCW 60° and 120° bends [10, 11]. In this Letter, we consider the important and commonly encountered 50/50 Y-splitter and utilise topology optimisation to design a silicon-on-insulator (SOI) based PhCW Y-splitter having a smooth broadband spectral performance. A transmission bandwidth of more than 100 nm with less than 1 dB excess loss is obtained for a fabricated PhCW component with a size smaller than $10 \times 15 \mu\text{m}$.

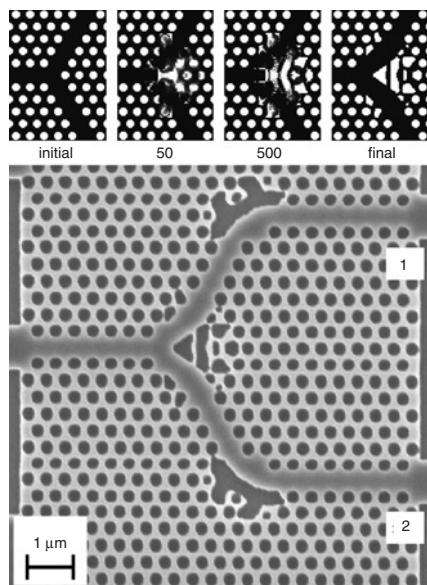


Fig. 1 Scanning electron micrograph of fabricated structure containing topology-optimised Y-junction and 60° bends

Top panel shows material distribution in Y-junction design domain during optimisation procedure after 0, 50, 500 iterations, and for final topology-optimised structure

Design and fabrication: We utilise e-beam lithography and standard anisotropic reactive-ion etch to define the PhC structures in the top silicon layer of a SOI material. The PhC is defined by circular air holes arranged in a triangular lattice and the PhCWs are formed by removing one row of holes in the Γ -K direction of the crystal lattice. The lattice period is $\Lambda \simeq 400$ nm and the diameter of the holes $D \simeq 275$ nm.

Several PhCW based Y-splitters have previously been reported in the literature [4–7]. Attempts have been made to improve the performance by adding, removing and/or resizing holes in the splitting region.

However, the useful bandwidth (~ 30 – 50 nm) of experimentally realised Y-splitters has typically been almost one order of magnitude smaller than the bandgap. The topology optimisation design method implies that the distribution of silicon and air is freely interchanged in the chosen design domain with no geometrically enforced restrictions. The optimisation algorithm is based on a 2D frequency-domain finite-element solver. The solver is used repeatedly in an iterative scheme, in which the material distribution is updated every iteration based on analytical sensitivity analysis and use of a mathematical programming tool [9]. The Y-junction is optimised by modifying the material distribution in such a way that the transmission (power flow) through both output ports of the splitter is *maximised*. The material is only redistributed in a small design area of approximately $1.5 \times 2.5 \mu\text{m}$ as illustrated in the top panel of Fig. 1. During the optimisation procedure the power flow is evaluated for six frequencies in a chosen frequency range so that a broadband component is achieved. The optimised splitter design was obtained after approximately 1200 iterations of the optimisation algorithm. It is seen that the optimised splitter region has been smoothed in both the inner and outer sides of the two waveguide branches of the splitter region. However, the smoothing is not trivial as the splitter region contains several separate complex structures.

Fig. 1 shows a scanning electron micrograph of the fabricated PhCW Y-splitter containing the topology-optimised Y-junction followed by two topology-optimised 60° bends [11]. The PhC structures have been fabricated without applying any special proximity corrections to the irregular shaped holes during the e-beam patterning. The designed structure is symmetric and the minor asymmetries of the fabricated splitter are due to fabrication tolerances.

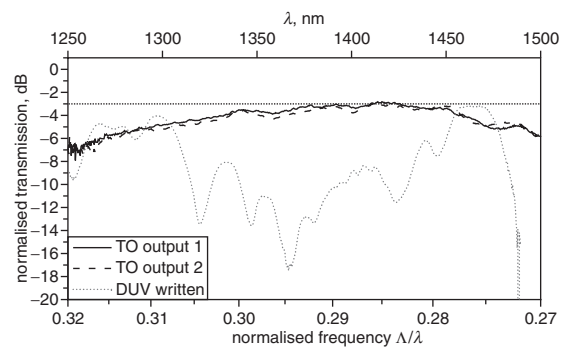


Fig. 2 Measured normalised transmission against normalised frequency from two output ports for topology-optimised (TO) component shown in Fig. 1 (solid and dashed lines, respectively) (in this case, normalised frequency corresponds to wavelength scale at top of graph)

Also shown is measured normalised output against normalised frequency from previously fabricated Y-junction with consecutive 60° bends (dotted lines) [6]. For this component normalised frequency range roughly corresponds to 1350–1600 nm. Horizontal dotted line at -3 dB corresponds to zero excess loss of component

Results: The fabricated Y-splitter has been optically characterised using a setup described in detail in [10, 11]. Fig. 2 shows the normalised transmission for TE polarised light from the two output ports of the complete PhCW structure displayed in Fig. 1. The spectra have been normalised to the transmission spectrum for a straight PhCW of same length in order to extract the performance of the Y-junction and subsequent 60° bend. The topology-optimised splitter displays smooth, low-loss, and nearly indistinguishable transmission spectra for the two output ports. The complete component is experimentally found to have a 100 nm bandwidth with an average loss of 0.44 ± 0.29 dB. This value includes excess losses due to both the Y-junction and the subsequent 60° bend. Also shown in Fig. 2 is the performance of a previously reported low-loss Y-splitter [4] designed using intuitive design ideas and fabricated using deep UV (DUV) lithography. In contrast to the topology-optimised splitter, the spectrum for the DUV written Y-splitter is seen to be rather spiky, indicating resonant and high-loss behaviour often observed for PhCW components.

Fig. 3 displays the normalised transmission of the topology-optimised Y-splitter corrected for the loss introduced by the 60° bend [11]. Hence, this graph presents the excess loss due to the Y-junction itself. The excess loss is found to be 0.18 ± 0.20 and 0.34 ± 0.30 dB for 100 and 175 nm bandwidths, respectively. Hence, the topology optimised design opens up for a practical implementation of the Y-splitter without the need for delicately matching a narrow operational

bandwidth of the Y-junction to the bandwidth of other parts of the PhC component. It should be emphasised that the high transmission bandwidth can be easily shifted to another wavelength range, e.g. around 1550 nm by changing the parameters D and/or Λ of the PhC.

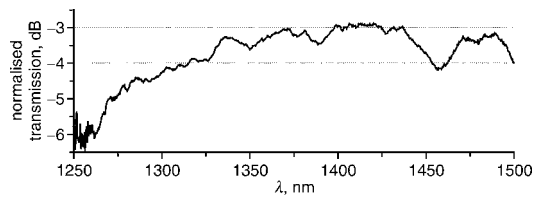


Fig. 3 Normalised transmission (solid line) for Y-splitter corrected for bend loss of subsequent 60° bend

Horizontal lines at -3 dB and -4 dB correspond to zero loss and 1 dB excess loss, respectively

Conclusion: The spectral smoothness and high transmission bandwidth of a 50/50 planar photonic crystal waveguide Y-splitter has been vastly improved by use of the inverse design method called topology optimisation. The Y-splitter was fabricated in silicon-on-insulator material and a record-high 1 dB transmission bandwidth exceeding 100 nm for the TE polarisation of the entire component consisting of a Y-junction and two 60° bends was experimentally obtained.

Acknowledgments: This work was supported in part by the Danish Technical Research Council through the research programmes ‘Planar Integrated PBG Elements’ (PIPE) and ‘Designing bandgap materials and structures with optimised dynamic properties’.

© IEE 2005

5 November 2004

Electronics Letters online no: 20057717

doi: 10.1049/el:20057717

P.I. Borel, L.H. Frandsen, A. Harpøth and M. Kristensen (Research Center COM, Technical University of Denmark, Building 345V, DK-2800 Kgs. Lyngby, Denmark)

E-mail: pib@com.dtu.dk

J.S. Jensen and O. Sigmund (Department of Mechanical Engineering, Solid Mechanics, Technical University of Denmark, Building 404, DK-2800 Kgs. Lyngby, Denmark)

References

- 1 Yablonovitch, E.: ‘Inhibited spontaneous emission in solid-state physics and electronics’, *Phys. Rev. Lett.*, 1987, **58**, pp. 2059–2062
- 2 Krauss, T.F., De La Rue, R.M., and Brand, S.: ‘Two-dimensional photonic-bandgap structures operating at near-infrared wavelengths’, *Nature*, 1996, **383**, pp. 699–702
- 3 Thorhauge, M., Frandsen, L.H., and Borel, P.I.: ‘Efficient photonic crystal directional couplers’, *Opt. Lett.*, 2003, **28**, pp. 1525–1527
- 4 Frandsen, L.H., Borel, P.I., Zhuang, Y.X., Harpøth, A., Thorhauge, M., Kristensen, M., Bogaerts, W., Dumon, P., Baets, R., Wiaux, V., Wouters, J., and Beckx, S.: ‘Ultra-low-loss 3-dB photonic crystal waveguide splitter’, *Opt. Lett.*, 2004, **29**, pp. 1623–1625
- 5 Lin, S.Y., Chow, E., Bur, J., Johnson, S.G., and Joannopoulos, J.D.: ‘Low-loss, wide-angle Y splitter at ~ 1.6 μm wavelengths built with a two-dimensional photonic crystal’, *Opt. Lett.*, 2002, **27**, pp. 1400–1402
- 6 Wilson, R., Karle, T.J., Moerman, I., and Krauss, T.F.: ‘Efficient photonic crystal Y-junctions’, *J. Opt. A, Pure Appl. Opt.*, 2003, **5**, pp. S76–S80
- 7 Inoue, K., Sugimoto, Y., Ikeda, N., Tanaka, Y., Asakawa, K., Sasaki, H., and Ishida, K.: ‘Ultra-small photonic-crystal-waveguide-based Y-splitters useful in the near-infrared wavelength region’, *Jpn. J. Appl. Phys.*, 2004, **4**, pp. L446–L448
- 8 Borel, P.I., Frandsen, L.H., Harpøth, A., Leon, J.B., Liu, H., Kristensen, M., Bogaerts, W., Dumon, P., Baets, R., Wiaux, V., Wouters, J., and Beckx, S.: ‘Bandwidth engineering of photonic crystal waveguide bends’, *Electron. Lett.*, 2004, **40**, pp. 1263–1264
- 9 Bendsoe, M.P., and Sigmund, O.: ‘Topology optimization: theory, methods and applications’ (Springer, 2004)
- 10 Frandsen, L.H., Harpøth, A., Borel, P.I., Kristensen, M., Jensen, J.S., and Sigmund, O.: ‘Broadband photonic crystal waveguide 60° bend obtained utilizing topology optimization’, *Opt. Express*, 2004 (accepted for publication)
- 11 Borel, P.I., Harpøth, A., Frandsen, L.H., Kristensen, M., Shi, P., Jensen, J.S., and Sigmund, O.: ‘Topology optimization and fabrication of photonic crystal structures’, *Opt. Express*, 2004, **12**, pp. 1996–2001

Topology Design and Fabrication of an Efficient Double 90° Photonic Crystal Waveguide Bend

J. S. Jensen, O. Sigmund, L. H. Frandsen, P. I. Borel, A. Harpøth, and M. Kristensen

Abstract—We have designed and fabricated a novel 90° bend in a photonic crystal waveguide. The design was obtained using topology optimization and the fabricated waveguide displays a bend loss for transverse-electric-polarized light of less than 1 dB per bend in a 200-nm wavelength range.

Index Terms—Planar photonic crystals (PhCs), topology optimization, waveguide bends.

I. INTRODUCTION

IN THIS letter, we report on the performance of a fabricated planar photonic crystal (PhC) waveguide with a new type of double 90° bend that we have designed using topology optimization.

Topology optimization is an inverse design method that allows for manipulating the distribution of material in a structure so that a quantified performance is systematically improved. The method was originally developed to obtain the layout of a limited amount of elastic material that gives the stiffest possible structure [1]. Since then, the method has been extended to a variety of applications, such as design of mechanical mechanisms, electrothermomechanical actuators, materials with prescribed properties, conduction problems, and many others [2].

PhCs based on a triangular pattern of holes in a high refractive index material, such as silicon or GaAs, display large photonic bandgaps (PBGs) for transverse-electric (TE)-polarized light [3] and are regarded as possible candidates for components in photonic integrated circuits (PICs) [4]. Thus, the possibility for improving the performance of PhCW bends and splitters has recently received a lot of attention, e.g., [5]–[8]. We have previously reported on topology optimized components, such as a 120° bend [9], a 60° bend [10], and a Y-splitter [11]. All components displayed the important characteristics of low loss and a broad-band performance.

Here, we report on a new type of double 90° waveguide bend, which may be used to provide an offset transition to a waveguide over a very short distance. Such a type of bend is unnatural with a triangular hole configuration due to the inherent lack of 90°

Manuscript received December 9, 2004; revised January 25, 2005. The work of J. S. Jensen and O. Sigmund was supported by the STVF Grant “Designing bandgap materials and structures with optimized dynamic properties,” and the work of L. H. Frandsen, P. I. Borel, A. Harpøth, and M. Kristensen was supported by the STVF Grant “Planar Integrated PBG Elements (PIPE).”

J. S. Jensen and O. Sigmund are with the Department of Mechanical Engineering, Solid Mechanics, Technical University of Denmark, Kgs. Lyngby DK-2800, Denmark (e-mail: jsj@mek.dtu.dk).

L. H. Frandsen, P. I. Borel, and A. Harpøth are with the Research Center COM, Technical University of Denmark, Kgs. Lyngby DK-2800, Denmark.

M. Kristensen is with the Research Center COM, Technical University of Denmark, Kgs. Lyngby DK-2800, Denmark, and also with the Department of Physics and Astronomy, University of Aarhus, Aarhus C DK-8000, Denmark.

Digital Object Identifier 10.1109/LPT.2005.846502

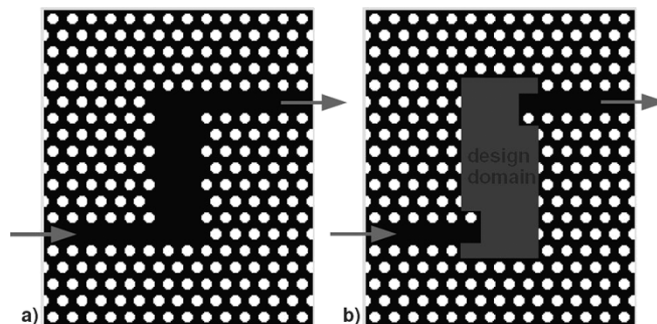


Fig. 1. (a) Initial configuration of the double 90° bend and (b) indication of the design domain where the material distribution is to be modified by the optimization algorithm.

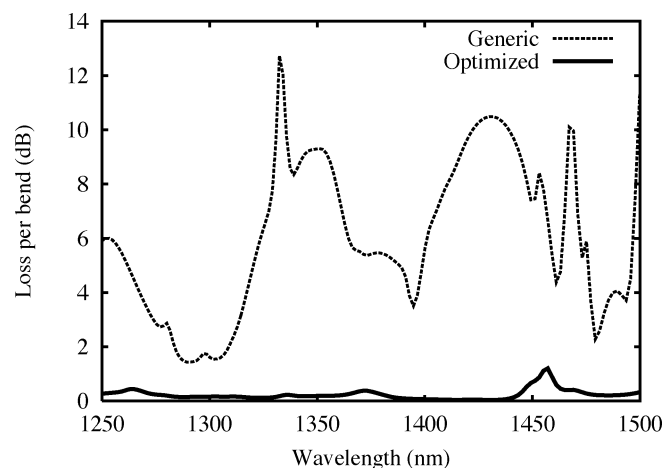


Fig. 2. Loss per bend for the initial structure (dotted) and for the final optimized structure (solid) calculated with the 2-D frequency-domain finite element solver.

symmetry and a satisfactory performance is difficult to obtain. Nevertheless, the component may be a useful supplement to the standard 60° bends if its performance can be improved. We use the initial structure shown in Fig. 1(a) as a basis for the optimization procedure. This generic structure has, as expected, a poor transmission for most wavelengths, as shown in Fig. 2. The key advantage of the topology design method is, however, that there is no geometrical restrictions on the design so the specific performance of the initial structure is of little importance. In order to improve the performance sufficiently, we must allow for the entire bend region to be modified, as indicated by the shaded area in Fig. 1(b). This approach is different from the previous applications of the method [9]–[11], where there was only a need to modify a small part of the waveguide structure. Consequently, the design that we obtain here has a very different appearance compared to conventional PhC waveguide (PhCW) structures.

II. OPTIMIZATION

The method of topology optimization is used to modify the distribution between the dielectric and air in the designated design area shown in Fig. 1(b). The optimization algorithm is based on a two-dimensional (2-D) frequency-domain solver based on a finite element discretization that yields the following equations for TE-polarized light:

$$\mathbf{S}(\varepsilon^{-1}(\mathbf{r}), \omega) \mathbf{u} = \mathbf{f}(\omega) \quad (1)$$

in which \mathbf{f} is a wave input vector, \mathbf{u} is a vector containing the discretized nodal values of the out-of-plane magnetic field H_z , and \mathbf{S} is the system matrix with an explicit dependence on the wave frequency ω , and the position-dependent dielectric constant $\varepsilon(\mathbf{r})$. Here, \mathbf{r} is the plane position vector.

Each unit cell is discretized using 14×12 four-noded quadrilateral elements. This discretization is sufficient for describing the geometry satisfactorily, and for capturing the dynamic behavior with adequate accuracy. The full computational model consists of the domain shown in Fig. 1(a) as well as additional perfectly matching layers [12] and comprises in total about 115 000 elements of which 6720 are within the design domain.

A single design variable x_e is now introduced in each finite element within the design domain, and ε is assumed to be element-wise constant and to depend explicitly on x_e as follows:

$$\varepsilon_e^{-1} = 1 + x_e (\varepsilon_d^{-1} - 1) \quad (2)$$

where

$$x_e \in R, \quad 0 < x_e < 1. \quad (3)$$

Thus, we let the design variable in each element govern the material properties of the element, in such a way that if $x_e = 0$, the dielectric constant of that element is one, and with $x_e = 1$ it takes the value ε_d .

We use continuous design variables to allow for using a gradient-based optimization strategy. The optimization method is described in detail in [2] and [13] and will only be briefly outlined here; as the goal for the optimization algorithm, we wish to find the material distribution that maximizes the transmitted power evaluated at the output port P_{out} , which is computed based on the solution to (1). Based on the sensitivities $\partial P_{\text{out}} / \partial x_e$, computed analytically, a mathematical programming tool MMA [14] is then used to change the material distribution in an iterative process until P_{out} cannot be further improved.

Since the design variables are continuous and not discrete, the possibility for elements in the final design with values between zero and one, so-called “gray” elements, is present. This corresponds to an intermediate “porous” material which is not feasible from a fabrication point of view. Several techniques have been developed to remedy this problem [2], but here we use a method specially designed for photonic waveguides [13], in that we artificially make design variables between zero and one induce additional conduction σ_e , in the following form:

$$\sigma_e \sim \alpha x_e (1 - x_e) \quad (4)$$

which enters (1) as an additional imaginary term in the system matrix \mathbf{S} and causes dissipation of energy. In this way, gray elements will be “un-economical” and will, thus, be forced toward

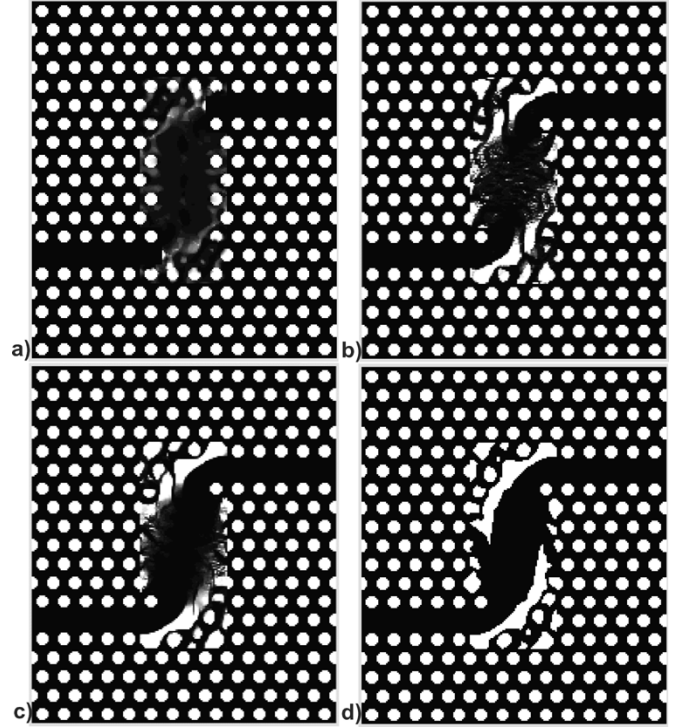


Fig. 3. Snapshots of the material distribution during the optimization process at (a) 25, (b) 1000, and (c) 2300 iterations, and (d) the final design after about 2500 iterations.

either white or black ($x_e = 0$ or $x_e = 1$), if the conduction parameter α is sufficiently large.

The effect is seen in Fig. 3 that shows four snapshots of the optimization iteration process. After about 1000 iterations with $\alpha = 0$, the basic structure is formed [Fig. 3(b)] but many gray elements appear in the design. Then α is slowly increased and the gray elements gradually disappear as the final structure is reached in about 2500 iterations. The computation time per iteration is less than 10 s on a standard PC.

A broad bandwidth operation is ensured by maximizing the transmission through the waveguide for several frequencies simultaneously. We use a technique based on active sets [13] in which we fix a number of target frequencies in the desired frequency interval. During the optimization, these target frequencies are repeatedly changed, according to the most critical frequencies with lowest transmission. The critical frequencies are found every 10th or 20th iteration by performing a fast frequency sweep [15].

The final optimized design is seen in Fig. 3(d). This design is quite different from traditional photonic crystal structures but, nevertheless, shows a very good broad-band performance, as shown in Fig. 2, computed using the 2-D frequency-domain finite element solver.

III. FABRICATION AND CHARACTERIZATION

We have fabricated the designed waveguide structure and tested its performance. Silicon-on-insulator (SOI) is an excellent choice of material with low optical propagation loss and with future possibilities for a monolithic integration of PhC-based PICs and electronic devices. We define the PhC structures in the top silicon layer of an SOI material using

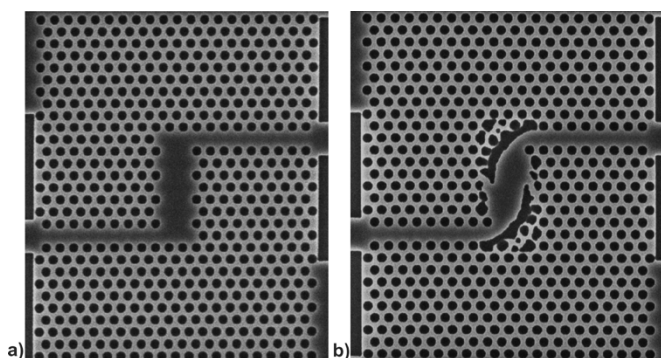


Fig. 4. (a) Fabricated generic structure and (b) the topology optimized double 90° waveguide bend.

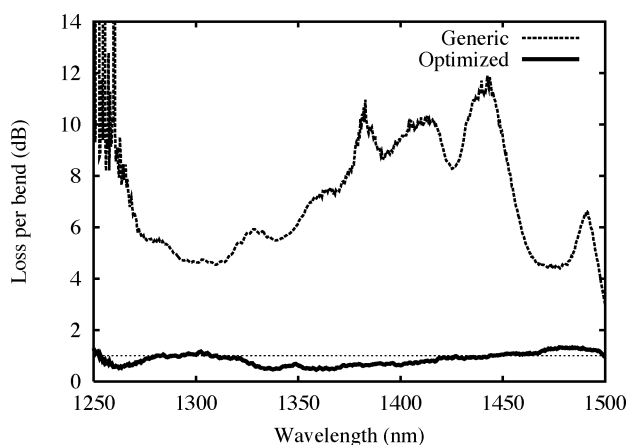


Fig. 5. Measured bend loss for the fabricated generic and optimized waveguide component.

e-beam lithography and standard anisotropic reactive-ion etch. The PhCs are defined as air holes in a triangular lattice and the PhCWs are carved out by removing a single row of holes in the nearest-neighbor direction of the crystal lattice. We use lattice pitch $\Gamma = 400$ nm, diameter of the holes $D = 275$ nm, and thickness of the Si-SiO₂ layers 340 nm/ $1 \mu\text{m}$. This configuration displays a broad PBG below the silica-line from 0.2592 to 0.3436 (normalized frequency) and allows TE-polarized single-mode propagation in the PhCWs. The fabricated topology-optimized structure is shown in Fig. 4(b) and it nicely resembles the designed structure [Fig. 3(d)].

The fabricated PhCWs were optically characterized using broad-band light-emitting diodes (LEDs) as sources. Three different LEDs centered around 1310 , 1414 , and 1538 nm were used to cover the full bandwidth of the fabricated components and tapered lensed fibers were used to couple light in and out of the ridge waveguides connected to the PhCWs. Two polarization controllers and a polarizer with an extinction ratio better than 35 dB were used to control the polarization of the light sent into the device. The optical spectra for the transmitted light were recorded with a spectral resolution of 10 nm using an optical spectrum analyzer. To extract the bend loss, the transmission spectra have been normalized to the transmission spectrum for a straight PhCW of similar length. Fig. 5 shows the measured bend loss of TE-polarized light for

the generic structure and the topology-optimized structure. A transmission loss of <1 dB/bend is obtained for the wavelength range 1250 – 1450 nm.

IV. CONCLUSION

We have used the method of topology optimization to design a double 90° bend in a photonic crystal waveguide based on a triangular configuration of air holes. The waveguide was fabricated in SOI and showed a very low bend loss for TE-polarized light of less than 1 dB per bend in a broad wavelength range of 200 nm.

The fabricated device adds to the existing collection of high-performance photonic crystal building blocks that display low-loss over a broad wavelength. The good performance makes these components natural parts of the realization of PICs based on photonic crystals.

REFERENCES

- [1] M. P. Bendsøe and N. Kikuchi, "Generating optimal topologies in structural design using a homogenization method," *Comput. Methods Appl. Mech. Eng.*, vol. 71, no. 2, pp. 197–224, 1988.
- [2] M. P. Bendsøe and O. Sigmund, *Topology Optimization—Theory, Methods and Applications*. Berlin, Germany: Springer-Verlag, 2003.
- [3] J. D. Joannopoulos, R. D. Meade, and J. N. Winn, *Photonic Crystals*. Princeton, NJ: Princeton Univ. Press, 1995.
- [4] Y. Sugimoto, Y. Tanaka, N. Ikeda, K. Kanamoto, Y. Nakamura, S. Ohkouchi, H. Nakamura, K. Inoue, H. Sasaki, Y. Watanabe, K. Ishida, H. Ishikawa, and K. Asakawa, "Two dimensional semiconductor-based photonic crystal slab waveguides for ultra-fast optical signal processing devices," *IEICE Trans. Electron.*, vol. E87-C, pp. 316–327, 2004.
- [5] A. Chutinan, M. Okano, and S. Noda, "Wider bandwidth with high transmission through waveguide bends in two-dimensional photonic crystal slabs," *Appl. Phys. Lett.*, vol. 80, pp. 1698–1700, 2002.
- [6] A. Talneau, L. L. Gouezigou, N. Bouadma, M. Kafesaki, C. M. Soukoulis, and M. Agio, "Photonic-crystal ultrashort bends with improved transmission and low reflection at $1.55 \mu\text{m}$," *Appl. Phys. Lett.*, vol. 80, pp. 547–549, 2002.
- [7] R. Wilson, T. J. Karle, I. Moerman, and T. F. Krauss, "Efficient photonic crystal Y-junctions," *J. Opt. A, Pure Appl. Opt.*, vol. 5, pp. 76–80, 2003.
- [8] P. I. Borel, L. H. Frandsen, A. Harpøth, J. B. Leon, H. Liu, M. Kristensen, W. Bogaerts, P. Dumon, R. Baets, V. Wiaux, J. Wouters, and S. Beckx, "Bandwidth engineering of photonic crystal waveguide bends," *Electron. Lett.*, vol. 40, pp. 1263–1264, 2004.
- [9] P. I. Borel, A. Harpøth, L. H. Frandsen, M. Kristensen, P. Shi, J. S. Jensen, and O. Sigmund, "Topology optimization and fabrication of photonic crystal structures," *Opt. Express*, vol. 12, no. 9, pp. 1996–2001, 2004.
- [10] L. H. Frandsen, A. Harpøth, P. I. Borel, M. Kristensen, J. S. Jensen, and O. Sigmund, "Broadband photonic crystal waveguide 60° bend obtained utilizing topology optimization," *Opt. Express*, vol. 12, no. 24, pp. 5916–5921, 2004.
- [11] P. I. Borel, L. H. Frandsen, A. Harpøth, M. Kristensen, J. S. Jensen, and O. Sigmund, "Topology optimized broadband photonic crystal Y-splitter," *Electron. Lett.*, vol. 41, no. 2, pp. 69–71, 2005.
- [12] M. Koshiba, Y. Tsuji, and S. Sasaki, "High-performance absorbing boundary conditions for photonic crystal waveguide simulations," *IEEE Microw. Wireless Components Lett.*, vol. 11, no. 4, pp. 152–154, Apr. 2001.
- [13] J. S. Jensen and O. Sigmund, "Topology optimization of photonic crystal structures: a high-bandwidth low-loss T-junction waveguide," *J. Opt. Soc. Amer. B*, to be published.
- [14] K. Svanberg, "The method of moving asymptotes—a new method for structural optimization," *Int. J. Numer. Methods Eng.*, vol. 24, pp. 359–373, 1987.
- [15] J. Jin, *The Finite Element Method in Electromagnetics*, 2nd ed. New York: Wiley, 2002.

Imprinted silicon-based nanophotonics

Peter I. Borel¹, Brian Bilenberg², Lars H. Frandsen¹, Theodor Nielsen²,
Jacob Fage-Pedersen¹, Andrei V. Lavrinenko¹, Jakob S. Jensen³,
Ole Sigmund³, and Anders Kristensen²

¹COM•DTU, Department of Communications, Optics & Materials

²MIC - Department of Micro and Nanotechnology

³MEK, Department of Mechanical Engineering

^{1,2,3} Nano•DTU, Technical University of Denmark, DK-2800 Kgs Lyngby, Denmark

pib@com.dtu.dk, ak@mic.dtu.dk

<http://www.nano.dtu.dk> <http://www.com.dtu.dk> <http://www.mic.dtu.dk/nil>

Abstract: We demonstrate and optically characterize silicon-on-insulator based nanophotonic devices fabricated by nanoimprint lithography. In our demonstration, we have realized ordinary and topology-optimized photonic crystal waveguide structures. The topology-optimized structures require lateral pattern definition on a sub 30-nm scale in combination with a deep vertical silicon etch of the order of ~300 nm. The nanoimprint method offers a cost-efficient parallel fabrication process with state-of-the-art replication fidelity, comparable to direct electron beam writing.

©2007 Optical Society of America

OCIS codes: (000.3860) Mathematical methods in physics; (000.4430) Numerical approximation and analysis; (130.2790) Guided waves; (130.3120) Integrated optics devices; (220.4000) Microstructure fabrication; (220.4830) Optical systems design; (230.3120) Integrated optics devices; 230.4000 Microstructure fabrication; (230.5440) Polarization-sensitive devices; (230.7390) Waveguides, planar; (999.9999) Photonic crystals.

References and links

1. Y. A. Vlasov, and S. J. McNab, "Losses in single-mode silicon-on-insulator strip waveguides and bends," *Opt. Express* **12**, 1622-1631 (2004). <http://www.opticsinfobase.org/abstract.cfm?URI=oe-12-8-1622>
2. E. Dulkeith, F. Xia, L. Schares, W. M. J. Green, and Y. A. Vlasov, "Group index and group velocity dispersion in silicon-on-insulator photonic wires," *Opt. Express* **14**, 3853-3863 (2006). <http://www.opticsinfobase.org/abstract.cfm?URI=oe-14-9-3853>
3. E. Dulkeith, F. Xia, L. Schares, W. M. Green, L. Sekaric, and Y. A. Vlasov, "Group index and group velocity dispersion in silicon-on-insulator photonic wires: errata," *Opt. Express* **14**, 6372-6372 (2006). <http://www.opticsinfobase.org/abstract.cfm?URI=oe-14-13-6372>
4. S. McNab, N. Moll, and Y. Vlasov, "Ultra-low loss photonic integrated circuit with membrane-type photonic crystal waveguides," *Opt. Express* **11**, 2927-2939 (2003). <http://www.opticsinfobase.org/abstract.cfm?URI=oe-11-22-2927>
5. K. K. Lee, D. R. Lim, L. C. Kimerling, J. Shin, and F. Cerrina, "Fabrication of ultralow-loss Si/SiO₂ waveguides by roughness reduction," *Opt. Lett.* **26**, 1888-1890 (2001). <http://www.opticsinfobase.org/abstract.cfm?URI=ol-26-23-1888>
6. W. Bogaerts, D. Taillaert, B. Luyssaert, P. Dumon, J. Van Campenhout, P. Bienstman, D. Van Thourhout, R. Baets, V. Wiaux, and S. Beckx, "Basic structures for photonic integrated circuits in Silicon-on-insulator," *Opt. Express* **12**, 1583-1591 (2004). <http://www.opticsinfobase.org/abstract.cfm?URI=oe-12-8-1583>
7. Y. A. Vlasov, M. O'Boyle, H. F. Hamann, and S. J. McNab, "Active control of slow light on a chip with photonic crystal waveguides," *Nature* **438**, 65-69 (2005)
8. V. R. Almeida, Q. F. Xu, and M. Lipson, "Ultrafast integrated semiconductor optical modulator based on the plasma-dispersion effect," *Opt. Lett.* **30**, 2403-2405 (2005)
9. H. Rong, Y. -H. Kuo, A. Liu, M. Paniccia, and O. Cohen, "High efficiency wavelength conversion of 10 Gb/s data in silicon waveguides," *Opt. Express* **14**, 1182-1188 (2006). <http://www.opticsinfobase.org/abstract.cfm?URI=oe-14-3-1182>
10. H. Rong, R. Jones, A. Liu, O. Cohen, D. Hak, A. Fang, and M. Paniccia, "A continuous-wave Raman silicon laser," *Nature* **433**, 725-728, (2005)

11. P. Debackere, S. Scheerlinck, P. Bienstman, and R. Baets, "Surface plasmon interferometer in silicon-on-insulator: novel concept for an integrated biosensor," *Opt. Express* **14**, 7063-7072 (2006).
<http://www.opticsinfobase.org/abstract.cfm?URI=oe-14-16-7063>
12. D. Erickson, T. Rockwood, T. Emery, A. Scherer, and D. Psaltis, "Nanofluidic tuning of photonic crystal circuits," *Opt. Lett.* **31**, 59-61 (2006).
<http://www.opticsinfobase.org/abstract.cfm?URI=ol-31-1-59>
13. S. Y. Chou, P. R. Krauss, P. J. Renstrom, "Imprint of sub-25 nm vias and trenches in polymers," *Appl. Phys. Lett.* Vol. 67, pp. 3114-3116 (1995)
14. M. D. Austin, H. Ge, W. Wu, M. Li, Z. Yu, D. Wasserman, S. A. Lyon, S. Y. Chou, "Fabrication of 5 nm linewidth and 14 nm pitch features by nanoimprint lithography," *Appl. Phys. Lett.* Vol. 84, pp. 5299-5301, (2004)
15. P.I. Borel, A. Harpøth, L.H. Frandsen, M. Kristensen, P. Shi, J.S. Jensen, and O. Sigmund, "Topology optimization and fabrication of photonic crystal structures," *Opt. Express* **12**, 1996-2001 (2004).
<http://www.opticsinfobase.org/abstract.cfm?URI=oe-12-9-1996>
16. L.H. Frandsen, A. Harpøth, P.I. Borel, M. Kristensen, J.S. Jensen, and O. Sigmund, "Broadband photonic crystal waveguide 60° bend obtained utilizing topology optimization," *Opt. Express* **12**, 5916-5921 (2004).
<http://www.opticsinfobase.org/abstract.cfm?URI=oe-12-24-5916>
17. A. Lavrinenko, P.I. Borel, L.H. Frandsen, M. Thorhauge, A. Harpøth, M. Kristensen, T. Niemi, and H. Chong, "Comprehensive FDTD modelling of photonic crystal waveguide components," *Opt. Express* **12**, 234-248 (2004). <http://www.opticsinfobase.org/abstract.cfm?URI=oe-12-2-234>
18. TEBN-1 by Tokuyama Corp., Tokyo, Japan <http://www.tokuyama.co.jp>
19. B. Bilenberg, M. Schøler, P. Shi, M. S. Schmidt, P. Bøggild, M. Fink, C. Schuster, F. Reuther, G. Gruetzner, and A. Kristensen, "Comparison of High Resolution Negative Electron Beam Resists," *J. Vac. Sci. Technol. B* **24**, 1776-1779 (2006)
20. B. Bilenberg, S. Jacobsen, M. S. Schmidt, L. H. D. Skjolding, P. Shi, P. Bøggild, J. O. Tegenfeldt, and A. Kristensen, "High Resolution 100 kV Electron Beam Lithography in SU-8," *Microelectron. Eng.* **83**, 1609-1612 (2006)
21. A.A. Ayón, D.-Z. Chen, R. Khanna, R. Braff, H.H. Sawin, and M.A. Schmidt, "Novel integrated MEMS process using fluorocarbon films deposited with a deep reactive ion etching (DRIE) tool," *Mat. Res. Soc.* **605**, 141-147 (2000)
22. H. Schulz, F. Osenberg, J. Engemann, and H.-C. Scheer, "Mask fabrication by nanoimprint lithography using anti-sticking layers," *Proc. SPIE* **3996**, 244-249 (2000)
23. micro resist technology GmbH, Berlin, Germany, <http://www.microresist.com>
24. T. Nielsen, D. Nilsson, F. Bundgaard, P. Shi, P. Szabo, O. Geschke, and A. Kristensen, "Nanoimprint lithography in the cyclic olefin copolymer, Topas, a highly UV-transparent and chemically resistant thermoplast," *J. Vac. Sci. Technol. B* **22**, 1770-1775 (2004)
25. J. S. Jensen and O. Sigmund, "Systematic design of photonic crystal structures using topology optimization: low-loss waveguide bends," *Appl. Phys. Lett.*, **84**, 2022-2024 (2004)
26. M. P. Bendsøe and O. Sigmund, *Topology optimization — Theory, Methods and Applications* (Springer-Verlag, 2003)

1. Introduction

Within recent years the development of planar silicon-on-insulator (SOI) based nanophotonic structures such as photonic wires and 2D photonic crystal waveguides (PhCWs) [1-6] has progressed to a level of performance and functionality where technological applications within optical communication [7-10] and sensing [11,12] have become feasible. In the context of transferring SOI-based nanophotonics from research to applications it is of relevance to assess methods of volume manufacture of such components and systems.

The optical performance of SOI-based nanophotonic components is highly sensitive to the nanometer feature size definition of the components. Even small deviations from the design may be devastating for the functionality and/or the target operating frequency. This calls for state-of-the-art nanofabrication technologies, where electron beam lithography (EBL) and deep-ultraviolet lithography (DUVL) have been successfully applied for device demonstration. EBL, in particular, provides nanophotonic structures with extremely high resolution, and this fabrication method is appropriate for many research investigations. However, being a serial fabrication process it is not optimal for mass fabrication of photonic devices. DUVL, on the other hand, is developed for mass fabrication. In this case, however, the production volume must be large enough to support the substantial costs affiliated with the

fabrication method. Furthermore, fabrication tolerances are currently pushed to their limits to obtain acceptable structures, leaving only little room for improvement.

Fabrication of nanophotonic structures using nanoimprint lithography (NIL) [13] is emerging as a cost-efficient alternative capable of nanometer-to-micrometer-scale pattern definition in a parallel process. The resolution of NIL is currently limited by the resolution of the stamp, where e.g. 5-nm linewidth and 14-nm pitch line gratings have been demonstrated [14].

Here, we demonstrate the feasibility of NIL for the fabrication of SOI-based nanophotonic components. In our fabrication process lateral resolution better than 30 nm is achieved on the NIL stamp by high resolution EBL in a thin film of negative resist and subsequent reactive ion etching (RIE). The pattern is imprinted in a thin film of NIL resist with a high etch resistance to silicon RIE, which facilitates device definition with the required high lateral resolution in combination with deep etching into the SOI substrate.

In our device demonstrations, we have realized planar W1 PhCWs, i.e. where the defect is formed by removing one row of holes in the Γ -K direction of the crystal lattice as shown in Fig. 1(left). Furthermore, we demonstrate topology-optimized photonic structures [15,16], see Fig. 2. This type of structure is particular challenging to fabricate with NIL as the frequency response of the device is highly sensitive to the complicated non-circular features of the optimized structures and impose local variations in the pattern density. The pattern replication fidelity is assessed by comparing the measured frequency response with 3D finite-difference time-domain (FDTD) calculations [17].

2. Nanoimprint lithography fabrication

The fabrication of SOI-based nanophotonic devices is based on thermal NIL [13]. The desired pattern is defined as a surface relief on the stamp (a silicon wafer) by EBL and RIE. The pattern is transferred to a thin film of thermoplastic resist on the SOI device wafer by mechanical deformation as the stamp is embossed into the heated resist. Finally, the pattern is transferred into the top silicon layer of the SOI wafer by RIE. High resolution and high aspect ratio of the transferred pattern is obtained by exploiting a high-resolution negative EBL resist for silicon stamp fabrication in combination with NIL in the thermoplastic resist with high etching resistance.

The silicon stamp is fabricated by 100 kV EBL (JEOL JBX9300FS) in a 50 nm thin film of TEBN-1 [18] on a silicon substrate (100 mm diameter and 0.5 mm thick) at an exposure dose of 9 mC/cm² [19]. The written structures are developed in methyl isobutyl ketone (MIBK) for 20 seconds, rinsed in isopropyl alcohol (IPA), and subsequently transferred 100 nm into the silicon substrate by a highly anisotropic RIE [20]. After etching the silicon, any remaining resist is removed in oxygen plasma prior to deposition of an anti-sticking layer formed from a C₄F₈ plasma and imprinting.

The passivation layer deposition capability of a deep reactive ion etching tool is used to plasma deposit an anti-sticking layer on the stamp, as originally suggested by Ayón et al [21]. A few monolayers of PTFE-like fluorocarbon polymer is deposited from C₄F₈ precursor gas, which is dissociated by plasma to form ions and radical species [22]. The dissociated species subsequently polymerize on the surface and form a layer of polymerized nCF₂. The thickness of such a fluorocarbon film has been measured to around 5 nm [22]. Without the anti-sticking layer, the polymer will stick to the stamp, and parts of the polymer pattern are peeled off the substrate when the stamp and substrate are separated.

The nanophotonic devices are fabricated in a SOI wafer from Soitec (100 mm diameter and 340 nm silicon on top of 1 μ m buried oxide). An 80 nm thin film of mr-I T85 (4 wt%) [23] is spin coated onto the SOI substrate at a spin speed of 3000 rpm and baked at 150°C for 5 min on a hotplate. The stamp is imprinted in the mr-I T85 film using a pressure of 13 bar for 10 minutes in a parallel plate imprint tool (EVG 520HE) under vacuum (0.01 mbar) and at a temperature of 140°C. The stamp and the SOI wafer are separated at a lowered temperature of 60°C. The imprint parameters result in a complete filling situation of the stamp in the photonic-crystal structured areas, resulting in 80 nm deep holes in the mr-I T85 resist. The

nanoimprinted patterns are transferred into the top 340 nm thick silicon layer of the SOI wafer by using an optimized SF₆-based inductively coupled plasma (ICP) RIE. The etch-selectivity is 9:1 (silicon:mr-I T85) [24] which allows for pattern transfer of the imprinted holes through the device silicon layer of the SOI wafer.

3. Straight photonic crystal waveguides

Figure 1 (left) shows a scanning electron microscope (SEM) image of the central part of a NIL fabricated SOI device consisting of a W1 PhCW connected to ordinary tapered ridge waveguides. The photonic crystal part of the waveguide is 10 μm long, the pitch of the hexagonal crystal lattice 400 nm, and the hole diameter 250 nm. The width of the ridge waveguides are adiabatically tapered over 450 μm from 4 μm at the end facets of the sample down to 1 μm at the interface to the crystal waveguide. The etch patterns seen to the right and left of the PhCW are caused by the controlled flow of excess polymer during the imprint process. The excess polymer is a result from the large variation in pattern density between the PhCW area and the surrounding un-patterned regions. The polymer flow does not represent an issue in the fabrication of high-quality photonic circuits with more complex design. The excess polymer flow can easily be controlled by adding dummy structures to equalize the pattern density. Also, the fabrication of more complex and/or high-density photonic circuits will typically reduce the variation in the pattern density, and thus simplify the control of the polymer flow.

The fabricated waveguides have been characterized by optical transmission measurements using quasi-transverse electric (TE) polarized light from a laser source in the wavelength region from 1520–1620 nm (ANDO AQ4321D) and broadband light emitting diodes (ANDO AQ4222) covering the wavelength range 1360–1620 nm. Figure 1 (right) shows the resulting laser transmission spectrum. The spectrum exhibits the characteristics of a W1 PhCW having a sharp and well-defined transition (around 1590 nm) between the low-loss guided defect mode and the photonic band gap. The observed sharp cut-off and the high and uniform transmission level below the cut-off wavelength of the spectrum are similar to results obtained for PhCWs of similar designs fabricated by EBL [17] and DUVL [6]. The ripples in the spectrum (zoom-in shown in the inset) are due to Fabry-Pérot oscillations caused by reflections from the end facets of the sample.

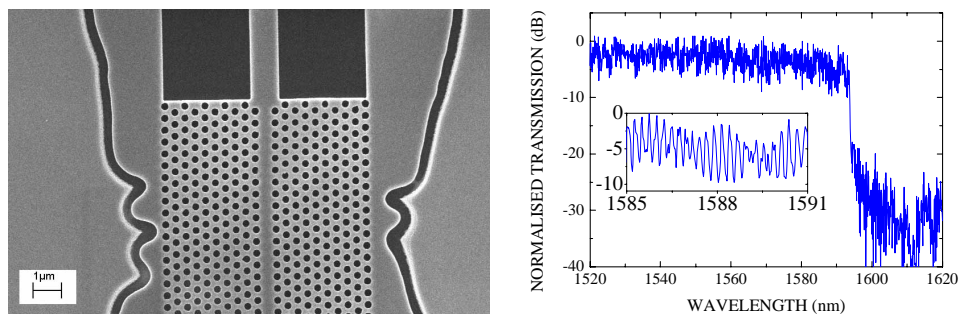


Fig. 1. (Left) SEM image of a photonic wire adjacent to a 10 μm long W1 PhCW fabricated in SOI by NIL. The etch patterns seen on the outer sides are caused by the controlled flow of excess polymer during the imprint process. (Right): Measured transmission spectrum for quasi-TE polarized laser light through the structure. Inset shows a zoom-in on the spectrum.

4. Topology optimized nanophotonic devices

Recently, we have proposed a novel inverse design strategy called topology optimization (TO), which allows for designing nanophotonic structures with enhanced functionalities [25]. In some cases, this inverse design method proposes optimized designs with feature sizes down to ~ 30 nm. Hence, such structures are very challenging to fabricate even with EBL and will serve as excellent benchmarks for pattern replication fidelity in the NIL fabrication process.

In our demonstrations, we have chosen a topology-optimized PhCW coarse wavelength selective Y-splitter as shown in Fig. 2 (right). Such a device is challenging for NIL fabrication since the frequency response of the device is highly sensitive to small variations in the complex structures in the central part of the Y-branch. These structures also impose local variations in the pattern density, which complicate the polymer flow during imprint.

The device optimization is illustrated in Fig. 2. The topology optimization methods redistribute material in a given design domain in order to maximize a certain objective function [25,26]. This method has successfully been applied within mechanical and electrical engineering and, recently, also in fabrication of nanophotonic structures [15,16]. Figure 2 illustrates the evolution of the iterative optimization process, where the material in the design domain (the central Y-branch) is redistributed using the simulated spectral features of the signals transmitted in the upper and lower arms as feedback. The initial structure (Fig. 2 (leftmost)) has the same frequency response in the upper and lower output arms. The optimization criterion was that the longer wavelengths are transmitted through the upper arm whereas the shorter wavelengths are transmitted through the lower arm, see also Fig. 3.

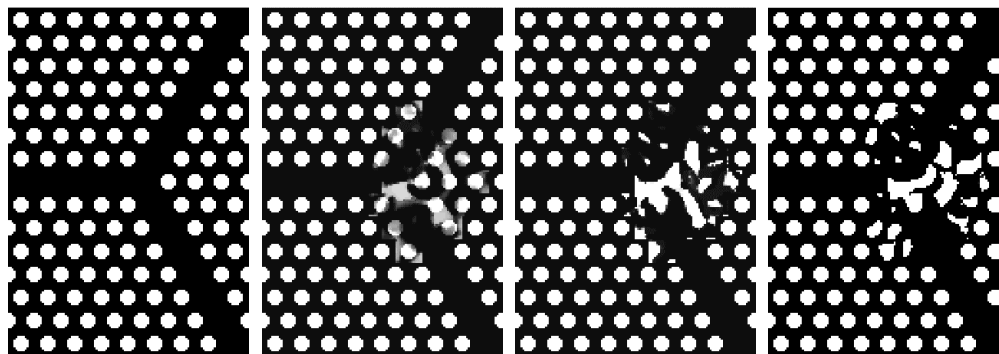


Fig. 2. Leftmost: (587 kB) Movie of how the material is redistributed in the design domain during the topology optimization procedure. The figure shows four frames from the movie of the topology optimization process. The leftmost frame shows the initial un-optimized structure and the rightmost frame the final topology-optimized design obtained after 760 iterations. The two middle frames show intermediate stages (iteration steps 10 and 200, respectively) before the optimization process has converged.

Figure 3 shows the fabrication results and optical performance of the NIL fabricated TO PhCW wavelength selective Y-splitter.

Figure 3 (left) shows the design layout of the converged TO structure. The red and blue arrows indicate the wavelength-selective transmission of longer (red) and shorter (blue) wavelengths to the upper and lower arms, respectively. The circles and squares in the right panel of the figure show the 3D FDTD simulations of a perfectly fabricated device, i.e. the black and white structure in Fig. 3 (leftmost). The middle panel shows a SEM image of the fabricated structure, which closely resembles the TO design. Deviations between the fabricated and designed structures are partly caused by limitations in the resolution of the lithography and partly caused by line broadening in the RIE. The solid red and blue lines in the right panel show the measured optical transmission performance of the fabricated structure for the upper and lower arms, respectively. The transmission in the upper and lower arms of the Y-splitter is normalized to the measured transmission level of a straight PhCW of same length. The measured spectra are seen to closely resemble to the 3D FDTD simulations both regarding transmission levels and spectral distributions.

The optical response of the structure critically depends on the precise fabrication of small features of sizes down below 30 nm. This was underlined by a series of 3D FDTD calculations, where an increasing number of the ~30-50 nm sized oddly shaped holes in succession were removed from the optimized Y-splitter region. The transmission levels changed typically 1-2 dB in the corresponding pass band when only two features were

removed and the spectra changed drastically when nearly all the details were removed. In general the transmission level in the upper arm of the Y-splitter was more affected than in the lower arm. Furthermore, we observed that absence of the small details in the splitter region did not lead to improvement of the transmission in the pass bands. Hence, the small details in the design do not contribute significantly in scattered losses of the Y-splitter. From the above observations and comments, we infer that these small details play an important role in the optimized structure and that they cannot be removed without hampering the performance of the splitter in spite of their negligible size.

The good agreement between the calculated spectra of the designed structure and the optical measurements on the fabricated structure confirms that the NIL fabrication of the challenging nanophotonic TO design has been successful. It should be noted though that the crosstalk is less suppressed in the fabricated structure, illustrating that there still is room for improvement in the fabrication process.

Finally, it is remarked that the TO compact wavelength splitter functions as designed, namely as a fairly efficient and coarse high-pass/low-pass wavelength filter.

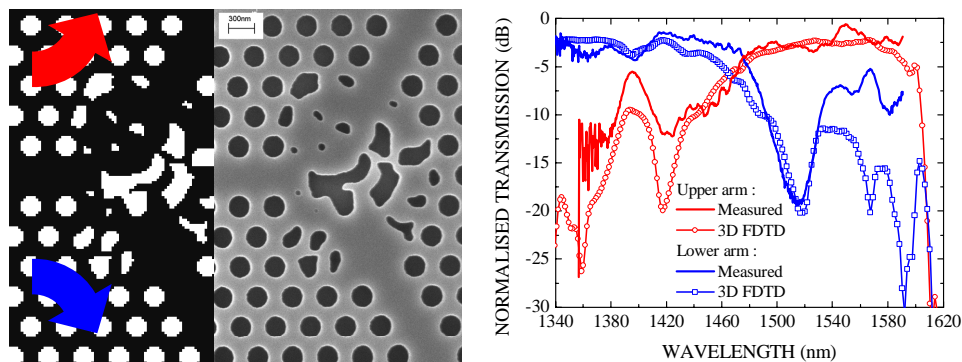


Fig. 3. (Left) The original TO design. Light enters the component from the left side and is split into the two arms dependent on the wavelength. (Middle) SEM image of the fabricated splitter using NIL. (Right) Normalized measured transmission below the cut-off wavelength for quasi-TE polarized light from the two output arms. Also shown are 3D FDTD calculations for the transmission through the output arms of the originally designed structure. The 3D FDTD calculations have been blue-shifted by 0.5% in wavelength to match the experimental wavelength scale.

5. Conclusions

We have used NIL to fabricate SOI-based nanophotonic structures with feature sizes down below 30 nm. The NIL fabricated devices perform comparably to the direct EBL defined devices and the obtained results are in good agreement with 3D FDTD calculations. Thus, we have demonstrated the feasibility of NIL as a cost-efficient fabrication technique for silicon-based nanophotonics.

Acknowledgments

This project was supported in parts by the European network of excellence Epixnet, the Danish Research Council for Technology and Production Sciences via the PIPE project, and by the New Energy and Industrial Technology Development Organization (NEDO) via the Japanese Industrial Technology Research Area. The partial support of the EC-funded project NaPa (Contract no. NMP4-CT-2003-500120) is gratefully acknowledged. OS and JSJ received support from the Eurohorcs/ESF European Young Investigator Award (EURYI) through the grant "Synthesis and topology optimization of optomechanical systems". Finally, the authors would like to thank Peixiong Shi, Danchip, DTU, for his technical assistance.

Topology Optimization of Building Blocks for Photonic Integrated Circuits

Jakob Søndergaard Jensen and Ole Sigmund

Department of Mechanical Engineering, Solid Mechanics
Nils Koppels Allé, Building 404, Technical University of Denmark
DK-2880 Kgs. Lyngby, Denmark
jsj@mek.dtu.dk

1. Abstract

Photonic integrated circuits are likely candidates as high speed replacements for the standard electrical integrated circuits of today. However, in order to obtain a satisfactory performance many design problems that up until now have resulted in too high losses must be resolved. In this work we demonstrate how the method of topology optimization can be used to design a variety of high performance building blocks for the future circuits.

2. Keywords: photonic crystals and wires, integrated circuits, topology optimization.

3. Introduction

A key component in photonic integrated circuits (PICs) [1] is the photonic crystal (PhC). A PhC is an optical material that has a periodic modulation of the refractive index, e.g. obtained by a dielectric base material such as silicon perforated with circular air holes in a triangular pattern. Such materials may display large band gaps, i.e. frequency ranges for which light cannot propagate. Functional components can be created from the PhCs, e.g. by removing a single hole to form a resonating cavity, removing a line of holes to create a waveguide, and by combining cavities and waveguides in order to design more advanced functionality such as frequency selective components, dispersion compensators, etc. Basic PhC waveguide components such as various bends and splitters have recently been designed using topology optimization (e.g. [2]), which led to a significant (up to orders of magnitude) increase in component performance. Another candidate for basic signal transmission is photonic wires (PhWs), created by making simple waveguide strips of high refractive material surrounded by air. These PhWs have been reported to have superior loss characteristics for straight waveguides compared to PhC straight waveguides [3].

In this paper we demonstrate new topology optimized splitters based on PhWs that display a good performance compared to the optimized bend and splitters in PhC waveguides. Additionally we demonstrate a new optimized PhC-based component with advanced functionality that includes bends, splitters and crossings. The optimization is based on a topology optimization algorithm [4] using a SIMP-like material model to distribute two material phases (dielectric and air), using analytical sensitivity analysis and the mathematical programming software MMA [5]. As the objective we wish to distribute the two materials in a designated design domain at various trouble spots in the component, such that the energy flow through the component is maximized. In order to create broadband components we can maximize for several wave frequencies simultaneously using a strategy in which we repeatedly update the target frequencies to be the most critical ones. The update is based on using Padé approximants to facilitate fast frequency sweeps with high resolution. In order to avoid gray elements in the final design we introduce a penalization method (PAMPING) in which elements with densities between 0 and 1 artificially cause dissipation and thus cause undesired loss of energy. Although developed for photonics [6] the methods directly apply to elastic vibration and wave propagation problems as well.

4. Photonic Crystal Waveguides: Bends and Splitters

Since the primary publications ([7], [8]), PhCs have received large attention primarily due to their potential application in photonic integrated circuits.

PhCs are optical materials that have a periodic modulation of their refractive indices [9]. The periodicity gives rise to gaps in the band structure that characterizes the wave propagation in the material, i.e. the so-called band gaps. Within the band gap frequency range, light cannot propagate regardless of direction so that the material acts as a perfect omnidirectional mirror.

Photonic crystals that consist of dielectric columns placed in a rectangular or triangular pattern display large band gaps and have been subjected to numerous theoretical investigations [9]. However,

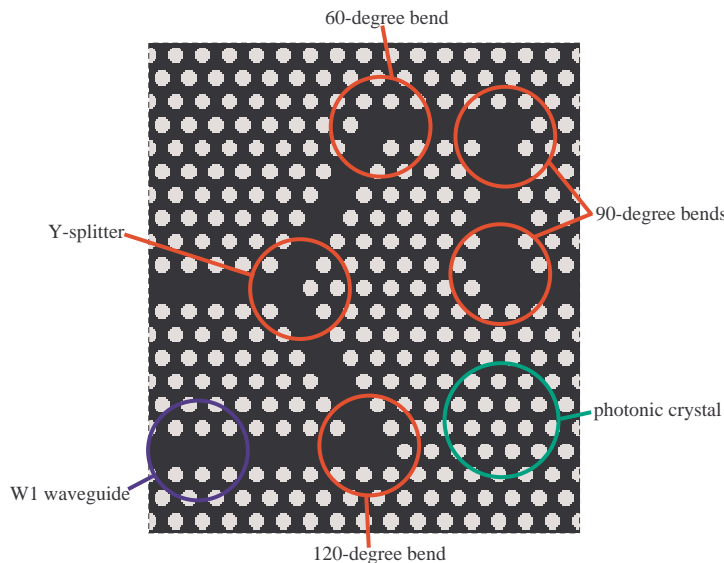


Figure 1: Schematic overview of a photonic circuit made from a photonic crystal with circular air holes in a dielectric including W1 waveguides and various bends and splitters.

due to a large out-of-plane loss of light, these structures seem to be less efficient than structures that are based on photonic crystals with air holes drilled in a periodic pattern in a dielectric material.

Figure 1 shows a schematic photonic circuit created from a PhC base material consisting of circular air holes in a triangular pattern in the dielectric. With a sufficiently high refractive index of the dielectric and sufficiently large diameter of holes this configuration gives rise to a large band gap for plane TE-polarized waves. The basic circuit component in the PhC is the waveguide, exemplified in the figure in form of so-called W1-waveguides. This means that the waveguide is created by removing a single row of air holes. The behavior of PhC waveguides is intricate [10], but most importantly the W1 waveguide with this PhC configuration supports wave propagation in a certain frequency interval within the band gap range. However, dealing only with straight waveguides is not enough to enable sufficient manipulation of the light in a circuit and additional building blocks like bends and splitters are needed. In Figure 1 examples of bends (60-, 90-, and 120-degree) as well as a Y-splitter are shown. Without modification of the straightforward material distribution shown in the figure, these bends and splitters display huge excess losses due wave reflection at the discontinuities. This difficulty has been tried solved by introducing various geometry modifications, such as changed radius and displacement of holes near the highly reflective bend regions - however, with limited success [11].

In recent publications ([2], [12], [13], [14]) it has been shown how the excess loss of such building blocks can be minimized by using topology optimization to redistribute the material in the critical regions. The topology optimized designs have odd-shaped holes and are qualitatively very different looking than the usual designs, but they nevertheless display a very good performance also for the actual fabricated structures.

Here, we demonstrate the design of a complicated photonic crystal circuit that possesses many of the basic building blocks that can be encountered in real circuits; bends, splittes and crossings - the PP component*.

4.1. The PP component (dedicated to Professor Pauli Pedersen)

Figure 2 illustrates the desired functionality for the PP component. A single mode wave is sent into the component at the lower portion of the left boundary. The energy flow direction inside the structure is

*The PP component was designed (and later fabricated) in honor of Professor Pauli Pedersen's retirement from the Department of Mechanical Engineering, Technical University of Denmark in April 2005. The PP symbolizes Pauli's initials.

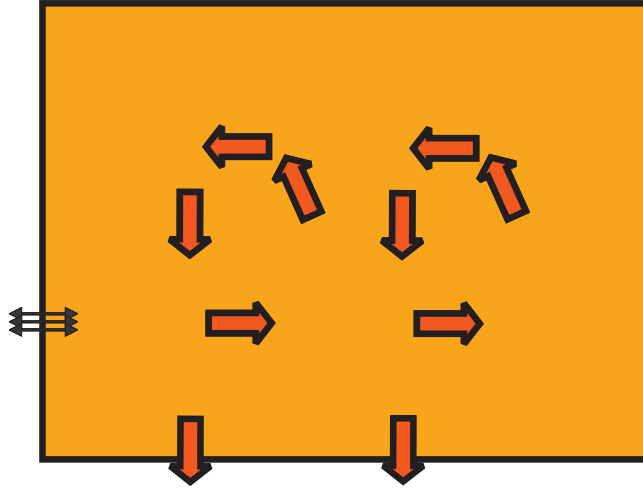


Figure 2: The desired functionality for the PP component.

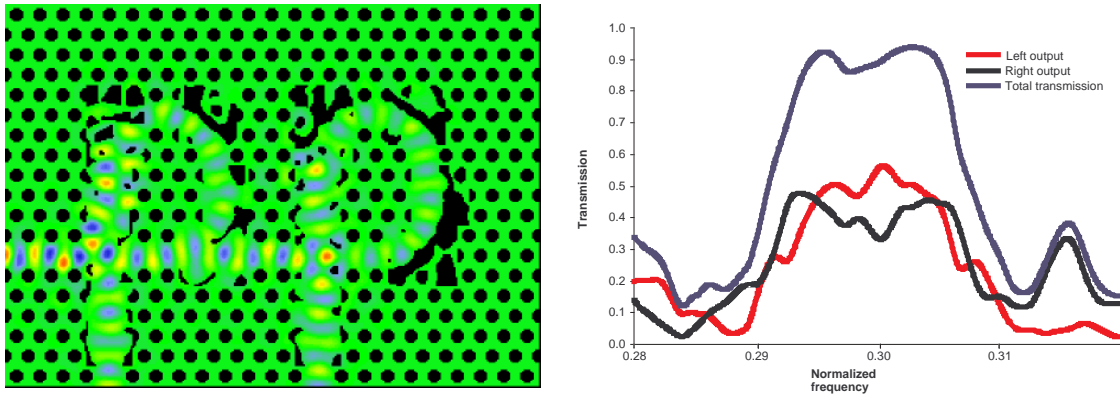


Figure 3: Left: the designed structure and the wave pattern for a single frequency, right: the transmitted energy through the output ports relative to the input wave energy.

designated to follow the arrows and two output wave ports are specified at the lower boundary. The desired performance is to have 50% transmitted energy in each output port measured relative to the input wave energy.

The designed component and the wave pattern is shown in Figure 3(left) and the corresponding performance is shown in Figure 3(right). In order to obtain a high performance in a broad frequency range the transmission is maximized for several frequencies in the range $\Omega = 0.295 - 0.305$ (normalized frequencies) by using a max-min formulation. The 2D performance of the designed structure is seen to have a high total transmission of more than 90% of the input energy and a fairly even distribution between the two output channels.

But, even when the excess loss at various waveguide discontinuities are minimized, as in the case of the PP component, PhC waveguides still display large propagation losses. These losses are e.g. due to out-of-plane scattering in the air holes. It has been shown that with respect to pure propagation loss (usually measured in dB/cm or dB/mm) PhC waveguides are inferior to the performance of photonic wires (PhW) [3] which are simple strip or ridge waveguides that can be created from the same high refractive dielectric as used in the PhCs.

In the following sections we show examples of the design of a basic building block for PhW waveguides: the T-splitter.

5. Photonic Wire Waveguides

Figure 4 shows a schematic setup of a PhW waveguide T-splitter. A straight waveguide with width w and of dielectric constant $\varepsilon = n^2$, carries an incoming wave that propagates from left towards right. The input signal is to be split into two equal waves so that 50% of the incoming wave energy is transmitted through both the upper and lower output ports. We use a two-dimensional model of plane polarized light that for time-harmonic waves is governed by the Helmholtz equation:

$$\nabla \cdot (A \nabla u) + B \omega^2 u = 0, \quad (1)$$

where $A = \varepsilon^{-1}$ and $B = c^{-2}$ for TE-polarized waves, and $A = 1$ and $B = \varepsilon c^{-2}$ for TM-polarized waves. The frequency of the wave is denoted ω and the unknown magnetic or electric field is u .

The boundary condition specifies an incoming wave at the left waveguide port:

$$n \cdot (A \nabla u) = 2i\omega \sqrt{AB} u_0, \quad (2)$$

where u_0 is the specified amplitude of the incoming wave. In addition to the wave source, the computational domain in Figure 4 is embedded in a perfectly matched layer (PML) [15] that ensures a minimized reflection of outgoing waves. The governing equation in the PML is:

$$\frac{\partial}{\partial x} \left(\frac{s_y}{s_x} A \frac{\partial u}{\partial x} \right) + \frac{\partial}{\partial y} \left(\frac{s_x}{s_y} A \frac{\partial u}{\partial y} \right) + B \omega^2 s_x s_y u = 0, \quad (3)$$

where the two complex functions s_x and s_y specify the absorbing properties in the x - and y -direction, respectively. At the interface to the computational domain, $s_x = s_y = 1$ which transforms Eq. (3) into the original Eq. (1), thus creating a perfectly matching interface.

5.1. Topology optimization

We use the method of topology optimization [4] to find a suitable material distribution in the design domain (the area indicated with a question mark in Figure 4).

The optimization problem is formulated as:

$$\begin{cases} \max \min & \Phi_1, \Phi_2 \\ \text{subject to:} & \mathbf{S}(\boldsymbol{\rho}, \omega) \mathbf{p} = \mathbf{f}(\omega) \\ & 0 \leq \rho_e \leq 1 \quad e = 1, \dots, N_d. \end{cases} \quad (4)$$

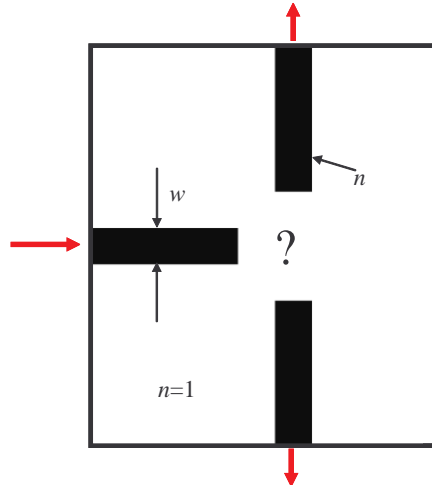


Figure 4: Design problem for a photonic wire waveguide T-splitter. The material distribution in the area indicated with a question mark is found using topology optimization. The objective is to distribute 50% of the input energy into the top and bottom output ports and thus eliminate reflection and radiation at the waveguide junction.

The optimization problem in Eq. (4) is based on a Galerkin finite element discretization of Eqs. (1)-(3) which leads to the system equation consisting of a set of linear complex equations. A single design variable ϱ_e is assigned to each finite element within the chosen design domain (N_d elements). This design variable is then used with a SIMP-like model to control the material properties in the corresponding elements:

$$\begin{aligned} A_e &= A_1 + \varrho_e(A_2 - A_1) \\ B_e &= B_1 + \varrho_e(B_2 - B_1). \end{aligned} \quad (5)$$

The optimization problem is formulated as a max-min problem aiming to maximize both objectives Φ_1 and Φ_2 . As objective we wish to maximize the wave transmission at the two output ports, so we specify the two objectives as the time-averaged Poynting vector integrated over these ports, which quantifies the corresponding energy flux. The point-wise time-averaged Poynting vector is given as:

$$\mathbf{P}(\mathbf{x}) = \{P_x \ P_y\}^T = \frac{1}{2}\omega A \Re(i\bar{u}\nabla u). \quad (6)$$

For further details regarding the discretization of Eq. (6) see [6]. Analytical sensitivity analysis is facilitated by the adjoint method ([4], [6]), and the optimization problem stated in Eq. (4) is solved using the mathematical programming software MMA [5].

5.2. Penalization - PAMPING

We relate the element design variables to the element material properties using Eq. (5). Since we do not impose a volume constraint, which does not make sense in this problem, we cannot rely on using a penalization factor as in the usual SIMP model to ensure a well defined binary structure. Thus, we use a simple linear interpolation (Eq. (5)) and introduce instead a penalization of intermediate design variables based on artificial dissipation [6].

This is done by adding an extra conduction (or dissipation) term in each element within the design domain:

$$\sigma_e \sim \alpha \varrho_e(1 - \varrho_e), \quad (7)$$

where α is a scaling factor. Thus, elements with intermediate values of ϱ_e dissipate energy and consequently reduce the objective function. In this way the element design variables will be forced towards 0 and 1, if α is sufficiently large.

We now exemplify results of applying the optimization algorithm to the model problem in Figure 4.

5.3. T-splitter - TM polarization

The first example is for TM-polarized waves. We use the setup described in [16], using straight waveguides of width $w = 200nm$ and a dielectric material with refractive index $n = 3.2$. A similar system was recently studied in [17]. As previously reported the reflection in the wavelength range around $1.55\mu m$ is about 25% for a plain simple T-junction.

Figure 5 shows the optimized waveguide for a single frequency corresponding to a wavelength of $1.55\mu m$. In this case we have chosen a very small design domain allowing only for small modifications of the material distribution and thus giving limited possibilities for improving the performance. In Figure 5 two different designs are shown along with the corresponding wave patterns. The structure at the top (structure 1) has the better performance and has been obtained by a straightforward implementation of the optimization algorithm. It is noticeable that the designed waveguide is discontinuous and the waves has to cross an air bridge. In the 2D loss-free model this leads to a good performance (see Figure 7), but for a real 3D structure large out-of-plane scattering losses can be expected. To avoid this, we have designed the bottom structure (structure 2) with simulated dissipation in the air. Consequently discontinuities are less favorable since the waves have to travel a distance in the lossy medium. The resulting structure performs worse with the loss-free 2D model, but we anticipate that it will perform better than structure 1 using 3D simulations and also in experiments. This is ongoing work.

We now attempt to improve the performance by increasing the design domain. Figure 6 shows two examples of optimized structures with larger design domains. Both designs have been obtained with dissipation in the air. Figure 6 (top) (structure 3) has been obtained by enlarging the design domain in a straightforward manner with a very good performance as a results (see Figure 7), showing practically full transmission near the target frequency. In Figure 6 (bottom) (structure 4) the design domain from

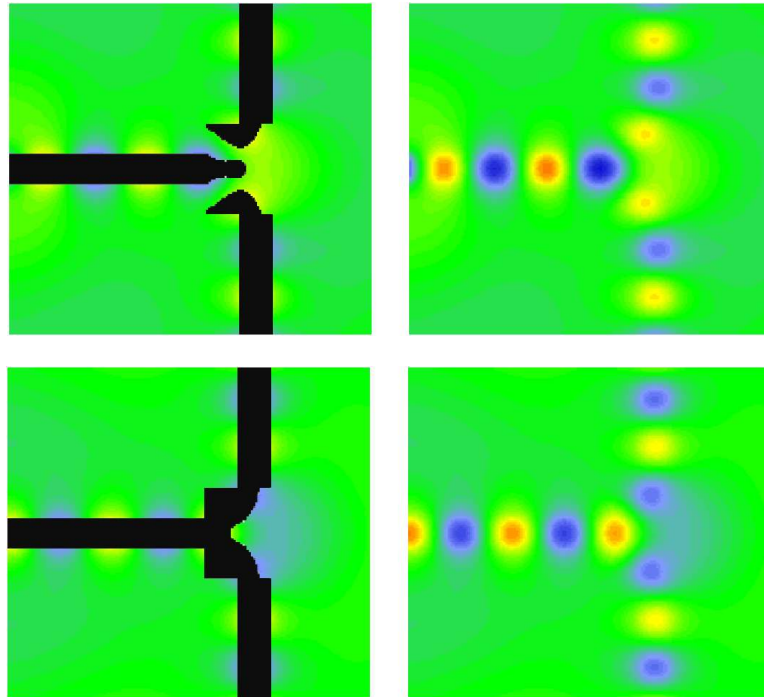


Figure 5: Optimized designs and corresponding wave patterns for a small design domain. Top: structure 1 obtained with straightforward optimization and bottom: structure 2 obtained by simulating dissipation in the air.

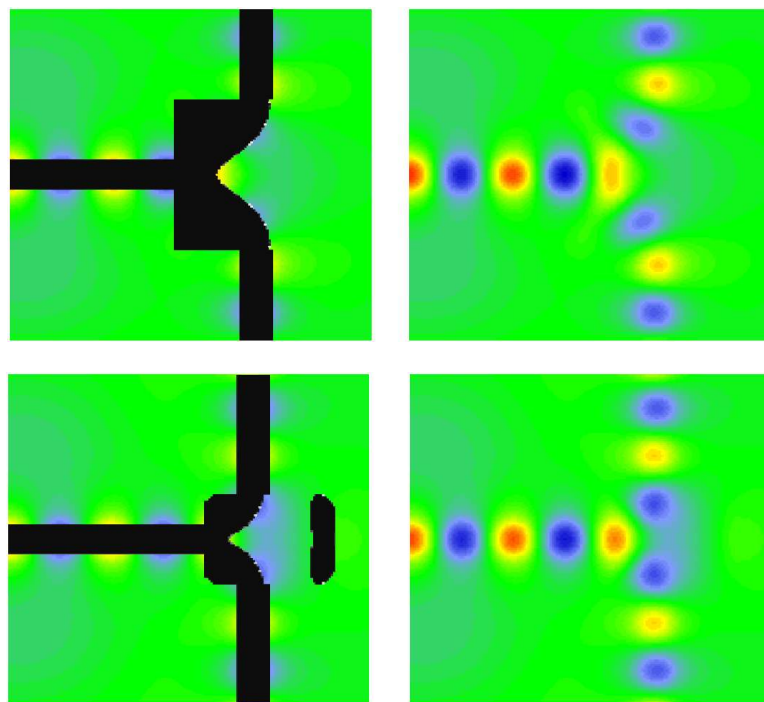


Figure 6: Optimized designs and corresponding wave patterns with enlarged design domains. Top: structure 3 and bottom: structure 4.

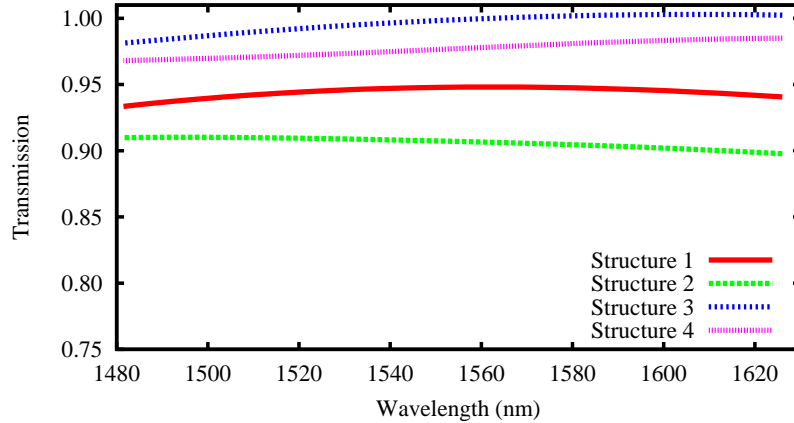


Figure 7: Total energy transmitted through top and bottom output ports relative to the input wave energy for the 4 structures in Figures 5 and 6.

the first two structures is basically kept but enlarged aft of the structure. As can be seen this allows for placing an extra reflector aft of the waveguide at a distance commensurable with the wavelength. By comparing the response for structure 4 and structure 2 in Figure 7, it is noticed that this difference of the otherwise quite similar structures has caused a considerable improvement of the 2D transmission.

5.4. T-splitter - TE polarization

The second example is for TE-polarized waves. The basic system dimensions and material properties are taken from [3] in which propagation losses in straight waveguides with simple bends were studied experimentally. In this case $w = 445nm$ and $n = 3.5$. The optimized structures in Figure 8 are both obtained by simulating dissipation in the air.

Figure 8 (top) (structure 1) shows the optimized structure obtained by maximizing the transmission for a wavelength of $1.55\mu m$. For TE waves this corresponds to a significantly shorter wavelength compared to the width of the waveguide than for the TM wave example. This difference is noticeable in the optimized structures which possess structural details at a corresponding smaller scale. It is noted that the transmission is almost 100% near the target frequency. The design shown in Figure 8 (bottom) (structure 2) was obtained by attempting to get a high transmission for a broader frequency range. This was done by modifying the objective in the optimization problem (Eq. (4)) to include the transmission at two distinct frequencies:

$$\max \min \quad \Phi_1(\omega_1), \Phi_1(\omega_2), \Phi_2(\omega_1), \Phi_2(\omega_2). \quad (8)$$

The two target frequencies ω_1 and ω_2 are not kept fixed during the optimization procedure, but are repeatedly updated (e.g. every 10-20 iterations) so that they correspond to the critical frequencies with minimum transmission. The critical frequencies are identifying by fast-frequency-sweeps using Padé approximants [6]. Naturally, the number of frequencies in Eq. (8) can be increased which is necessary if a larger frequency range is considered.

Figure 9 shows a comparison of the performance of the two designs. As noted the bandwidth of structure 2 is slightly better than that of structure 1, but this has been obtained at the expense of the high transmission near $1.55\mu m$. Including more frequencies in the optimization does not change this significantly.

6. Conclusions

We have demonstrated the use of topology optimization to design low-loss photonic circuit components such as bends and splitters.

Previously it has been shown that such components in photonic crystal waveguides can effectively be designed with topology optimization, leading to low losses in large frequency ranges. In this paper we have demonstrated design of similar low loss components also in photonic wire waveguides. These

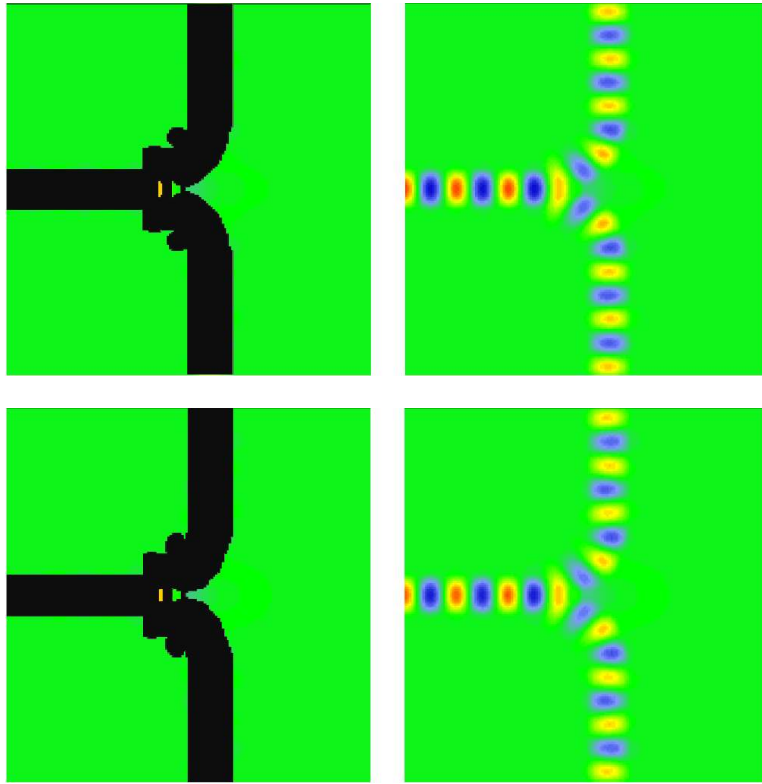


Figure 8: Optimized designs and corresponding wave patterns for TE-polarized waves. Top: structure 1 obtained by maximizing transmission for a single frequency and bottom: structure 2 obtained by maximizing transmission for two distinct frequencies that are repeatedly updated during the optimization procedure.

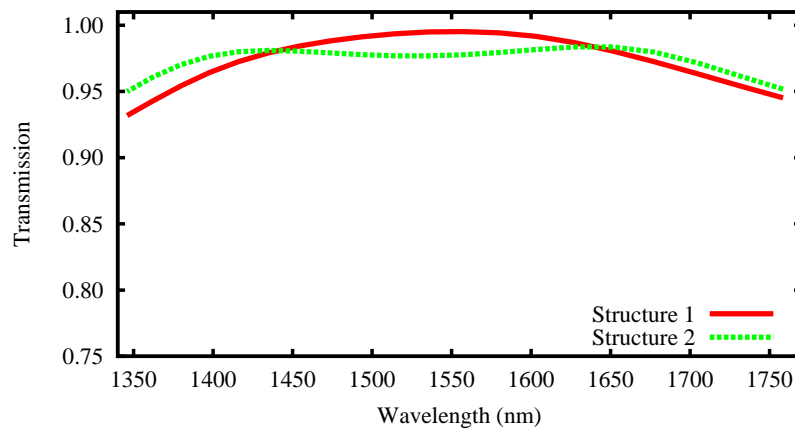


Figure 9: Transmission for the two optimized structures in Figure 8.

waveguides have inherently lower propagation losses than the photonic crystal waveguides, and may be alternatives/supplements to these in future photonic integrated circuits.

Our topology optimization algorithm is based on a two-dimensional finite element model of the Helmholtz equation that models propagation of plane polarized light. The finite element model is used to compute the energy transmission through the waveguides and the optimization algorithm is used to redistribute air and dielectric in the trouble regions in order to maximize the transmission. A SIMP-like material model is used together with analytical sensitivity analysis and the mathematical programming software MMA. We use a penalization method based on artificial damping (PAMPING) to ensure a feasible binary design, and perform optimization for several frequencies by exploiting fast-frequency-sweeps using Padé approximants.

The photonic wire components are currently being analyzed using a 3D finite-difference-time-domain code and will soon be tested experimentally. Additionally, other components such as a wavelength splitters in photonic crystal and photonic wire waveguides are currently being developed as well as directional couplers. Future research include also optimization based on 3D finite element models.

7. References

- [1] Sugimoto Y, Tanaka Y, Ikeda N, Kanamoto K, Nakamura Y, Ohkouchi S, Nakamura H, Inoue K, Sasaki H, Watanabe Y, Ishida K, Ishikawa H and Asakawa K. Two dimensional semiconductor-based photonic crystal slab waveguides for ultra-fast optical signal processing devices, *IEICE Trans. Electron.*, 2004, E87-C, 316-327.
- [2] Borel P I, Harpøth A, Frandsen L H, Kristensen M, Shi P, Jensen J S and Sigmund O. Topology optimization and fabrication of photonic crystal structures, *Optics Express*, 2004, 12(9), 1996-2001.
- [3] Vlasov Y A and McNab S J. Losses in single-mode silicon-on-insulator strip waveguides and bends, *Optics Express*, 2004, 12(8), 1622-1631.
- [4] Bendsoe M and Sigmund O. Topology Optimization - Theory, Methods and Applications. *Springer Verlag, Berlin Heidelberg*, 2003.
- [5] Svanberg K. The method of moving asymptotes - a new method for structural optimization, *International Journal for Numerical Methods in Engineering*, 1987, 24, 359-373.
- [6] Jensen J S and Sigmund O. Topology optimization of photonic crystal structures: A high-bandwidth low-loss T-junction waveguide, *J. Opt. Soc. Am. B*, 2005, 22(6), to appear.
- [7] Yablonovitch E. Inhibited spontaneous emission in solid-state physics and electronics, *Physical Review Letters*, 1987, 58, 2059-2062.
- [8] John S. Strong localization of photons in certain disordered dielectric superlattices, *Physical Review Letters*, 1987, 58, 2486-2489.
- [9] Joannopoulos J D, Meade R D and Winn J N. Photonic Crystals. *Princeton University Press, New Jersey*, 1995.
- [10] Ammari H. and Santosa F. Guided waves in a photonic bandgap structure with a line defect, *SIAM J. Appl. Math.*, 2004, 64(6), 2018-2033.
- [11] Borel P I, Frandsen L H, Harpøth A, Leon J B, Liu H, Kristensen M, Bogaerts W, Dumon P, Baets R, Wiaux V, Wouters J and Beckx S. Bandwidth engineering of photonic crystal waveguide bends, *Electron. Lett.*, 2004, 40, 1263-1264.
- [12] Frandsen L H, Harpøth A, Borel P I, Kristensen M, Jensen J S and Sigmund O. Broadband photonic crystal waveguide 60-degree bend obtained using topology optimization, *Optics Express*, 2004, 12(24), 5916-5921.

- [13] Borel P I, Frandsen L H, Harpøth A, Kristensen M, Jensen J S and Sigmund O. Topology Optimised Broadband Photonic Crystal Y-Splitter, *Electron. Lett.*, 2005, 41(2), 69-71.
- [14] Jensen J S, Sigmund O, Frandsen L H, Borel P I, Harpøth A and Kristensen M. Topology design and fabrication of an efficient double 90-degree photonic crystal waveguide bend, *IEEE Photonics Technology Letters*, 2005, 17(6), to appear.
- [15] Koshiha M, Tsuji Y and Sasaki S. High-performance absorbing boundary conditions for photonic crystal waveguide simulations, *IEEE Microwave Wireless Components Lett.*, 2001, 11, 152-154.
- [16] Manolatou C, Johnson S G, Fan S, Villeneuve P R, Haus H A and Joannopoulos J D. High-density integrated optics, *Journal of Lightwave Technology*, 1999, 17(9), 1682-1692.
- [17] Sakai A, Fukazawa T and Baba T. Low loss ultra-small branches in a silicon photonic wire waveguide, *IEICE Trans. Electron.*, 2002, E85-C, 1033-1038.

Topology optimization of dynamics problems with Padé approximants

Jakob S. Jensen^{*,†}

Department of Mechanical Engineering, Solid Mechanics, Technical University of Denmark, Nils Koppels Allé, Building 404, Denmark

SUMMARY

An efficient procedure for topology optimization of dynamics problems is proposed. The method is based on frequency responses represented by Padé approximants and analytical sensitivity analysis derived using the adjoint method. This gives an accurate approximation of the frequency response over wide frequency ranges and a formulation that allows for design sensitivities to be computed at low computational cost also for a large number of design variables. Two examples that deal with optimization of forced vibrations are included. Copyright © 2007 John Wiley & Sons, Ltd.

Received 30 October 2006; Revised 1 February 2007; Accepted 2 March 2007

KEY WORDS: Padé approximants; topology optimization; forced vibrations

1. INTRODUCTION

The solution to a discretized linear vibration problem with harmonic excitation can be expressed in the exact form

$$\mathbf{u} = \frac{\sum_{i=0}^{2N_d-2} \tilde{\mathbf{a}}_i (\Omega - \Omega_0)^i}{\sum_{i=0}^{2N_d} \tilde{\mathbf{b}}_i (\Omega - \Omega_0)^i} \quad (1)$$

in which N_d is the number of degrees of freedom in the model, $\tilde{\mathbf{a}}_i$ and $\tilde{\mathbf{b}}_i$ are expansion coefficients, Ω is the excitation frequency, and Ω_0 is an arbitrary expansion frequency. This representation of the solution is rarely used except for systems with only few degrees of freedom for which the corresponding small number of expansion coefficients can be found analytically. Solutions for larger problems are usually obtained numerically with a factorization method or an iterative method.

*Correspondence to: Jakob S. Jensen, Department of Mechanical Engineering, Solid Mechanics, Technical University of Denmark, Nils Koppels Allé, Building 404, Denmark.

†E-mail: jsj@mek.dtu.dk

To compute a frequency response with a fine frequency resolution can be computationally costly since a numerical solution must be obtained for each considered frequency. Furthermore, if the analysis is the basis for an iterative optimization procedure this approach will in most cases be unfeasible. In this work, an efficient approach for obtaining the frequency response based on the solution form in Equation (1) is used and applied in a topology optimization procedure. Other methods can be used to reduce computational costs, e.g. the modal expansion technique which is especially applicable to lower frequency ranges where only a few modes influence the response [1]. However, optimization of eigenvalues and eigenvectors often leads to non-smooth problems that might pose difficulties for optimization algorithms. Thus, the investigation of alternatives seems justified.

In the proposed procedure, the expression in Equation (1) is used with fewer expansion terms in the numerator and denominator so that a good approximation for \mathbf{u} is obtained only in a neighbourhood of Ω_0 . It will be demonstrated how the coefficients $\tilde{\mathbf{a}}_i$ and $\tilde{\mathbf{b}}_i$ can be computed by performing only a single factorizing of the system matrix $\mathbf{S} = -\Omega^2\mathbf{M} + i\Omega\mathbf{C} + \mathbf{K}$ for a chosen expansion frequency $\Omega = \Omega_0$, followed by relatively inexpensive forward-/back substitution in order to obtain gradients at Ω_0 . The rational polynomial expansion in Equation (1) can be recognized as the Padé approximant (PA) associated with an infinite power series of the form $\sum_{i=0}^{\infty} \mathbf{c}_i (\Omega - \Omega_0)^i$ [2]. This paper will not go into the theory behind the PA. But due to the connection between the solution form in Equation (1) and a PA, the term PA is used throughout this work to describe the approximation and to characterize the proposed method.

PA approximants have been popular as means for computing the frequency response of different dynamic systems at a low computational cost. They are the backbone of the so-called asymptotic waveform evaluation (AWE) methods [3], used for circuit analysis and for electromagnetic wave scattering problems, e.g. [4, 5]. In [6] the application to electromagnetic problems was extended to treat problems in bounded and open domains and in [7] PAs were used to obtain the response of vibro-acoustic systems over wide ranges of frequencies.

The pure acoustic problem was considered by Djellouli *et al.* [8]. They used the PA to compute scattering of acoustic fields and compared the results to those obtained by a standard Taylor expansion. The PA algorithm was shown to outperform the Taylor expansion and give a good approximation over wide frequency ranges. The acoustic problem was treated also by Malhotra and Pinsky [9] and the work was extended in [10] by using a Krylov subspace projection method. In fact, the Krylov method has a strong link to matrix-valued PAs [11], also referred to as the Padé-*via*-Lanczos connection (PVL) [12].

The possibility for using PA approximants to compute frequency responses with a high-frequency resolution was utilized in a previous optimization study by the author [13]. In that work, a photonic crystal waveguide was designed with a topology optimization approach. The PAs were used to accurately pinpoint a number of the most critical frequencies in the operational frequency range at a low computational cost. The optimization considered the performance for these critical frequencies which were repeatedly updated during the optimization process. Another optimization study was reported in [14], in which a PA was used to approximate the dynamic response for large variations of a design variable and used as a basis for finite element-based size optimization

Only few works have considered direct optimization of the frequency response based on its PA. In [15] a procedure was developed for sensitivity analysis of PAs for 3-D microwave device applications. The formulation was suitable for shape/size optimization with a few design variables and was implemented in [16] to optimize microwave devices with up to four geometry design

variables. The present paper is related to these works [15, 16] but focuses on optimization problems with a large number of design variables such as found in topology optimization.

In Section 2 it is shown how the PA is computed and the validity of the approximation is demonstrated with simple examples along with a discussion of the importance of numerical precision. In Section 3 the sensitivity analysis of a PA response function with respect to a set of design variables is treated in detail. The approach is based on adjoint analysis which makes the method suitable for the case of many design variables. Two examples of topology optimization of forced vibration problems with PAs are presented in Section 4. Finally, conclusions are given in Section 5.

2. FREQUENCY RESPONSES WITH PADÉ APPROXIMANTS

The basis of the proposed method is the computation of the frequency response using a PA. The proposed procedure differs slightly from what appears to be the standard implementation of method (see e.g. [5]). The difference will be pointed out in the following.

Time-harmonic motion of a linear damped dynamic system is governed by the discretized set of equations

$$\mathbf{S}\mathbf{u} = \mathbf{f} \quad (2)$$

in which the system matrix \mathbf{S} is defined as

$$\mathbf{S} = -\Omega^2\mathbf{M} + i\Omega\mathbf{C} + \mathbf{K} \quad (3)$$

\mathbf{M} is the mass matrix, \mathbf{C} the damping matrix, \mathbf{K} the stiffness matrix, and \mathbf{f} is the loading vector. The frequency of excitation is denoted Ω and \mathbf{u} is a vector containing the discretized nodal values of the complex amplitude function.

An approximate solution for \mathbf{u} is now sought in the vicinity of some expansion frequency Ω_0 . The de-tuning parameter:

$$\sigma = \Omega - \Omega_0 \quad (4)$$

is used to define the closeness of the excitation frequency Ω to this expansion frequency. Equation (2) is rewritten as

$$(\mathbf{P}_0 + \mathbf{P}_1\sigma + \mathbf{P}_2\sigma^2)\mathbf{u} = \mathbf{f} \quad (5)$$

in which the new matrices are defined as

$$\mathbf{P}_0 = \mathbf{S}(\Omega_0) = -\Omega_0^2\mathbf{M} + i\Omega_0\mathbf{C} + \mathbf{K} \quad (6)$$

$$\mathbf{P}_1 = \frac{\partial\mathbf{S}}{\partial\Omega}(\Omega_0) = -2\Omega_0\mathbf{M} + i\mathbf{C} \quad (7)$$

$$\mathbf{P}_2 = \frac{1}{2} \frac{\partial^2\mathbf{S}}{\partial\Omega^2}(\Omega_0) = -\mathbf{M} \quad (8)$$

Cramer's rule [17] is applied to Equation (5):

$$\mathbf{u} = \frac{\sum_{i=0}^{2N_d-2} \tilde{\mathbf{a}}_i \sigma^i}{\sum_{i=0}^{2N_d} \tilde{b}_i \sigma^i} \quad (9)$$

where N_d is the total number of degrees of freedom in the discretized model. It should be noted that Equation (9) is an exact representation of \mathbf{u} . But for normal finite element models this formulation requires the computation of a large number of expansion coefficients. This is not only inconvenient but also practically impossible due to numerical errors (as will be discussed in Section 2.3). However, an accurate approximation in the vicinity of the expansion frequency ($\sigma=0$) can be obtained with series containing fewer expansion terms in both the numerator and the denominator:

$$\mathbf{u} \approx \frac{\sum_{i=0}^N \tilde{\mathbf{a}}_i \sigma^i}{\sum_{i=0}^N \tilde{b}_i \sigma^i} = \frac{\tilde{\mathbf{a}}_0 + \tilde{\mathbf{a}}_1 \sigma + \cdots + \tilde{\mathbf{a}}_N \sigma^N}{\tilde{b}_0 + \tilde{b}_1 \sigma + \cdots + \tilde{b}_N \sigma^N} \quad (10)$$

where N terms have been used in the expansion. It should be noted that the choice of retaining the same number of terms in the numerator and denominator is not the only possible one. For further details the reader is referred to a separate publication on PAs, e.g. [2].

Finite response for $\sigma=0$ ensures that $\tilde{b}_0 \neq 0$ (can be ensured by non-zero damping in the system). Hence, all coefficients can be divided by \tilde{b}_0 to obtain a new set of coefficients b_1, \dots, b_N and $\mathbf{a}_1, \dots, \mathbf{a}_N$

$$\mathbf{u} = \frac{\mathbf{a}_0 + \mathbf{a}_1 \sigma + \cdots + \mathbf{a}_N \sigma^N}{1 + b_1 \sigma + \cdots + b_N \sigma^N} \quad (11)$$

in which the approximation sign has now been replaced by an equality sign for simplicity. Thus, \mathbf{u} now represents the expansion in Equation (11) and not the exact solution of the original equation.

The coefficient \mathbf{a}_0 is easily determined by considering the system at the expansion frequency ($\sigma=0$). Equation (11) reduces for $\sigma=0$ to

$$\mathbf{u}(\sigma=0) = \mathbf{a}_0 \quad (12)$$

so that this coefficient is recognized as the solution at the expansion frequency Ω_0 (for clarity referred to as \mathbf{u}_0). Thus, the final expression for the expansion is

$$\mathbf{u} = \frac{\mathbf{u}_0 + \sum_{i=1}^N \mathbf{a}_i \sigma^i}{1 + \sum_{i=1}^N b_i \sigma^i} \quad (13)$$

2.1. Gradients at $\sigma=0$

The gradients at $\sigma=0$ are used to determine the unknown coefficients. To do this \mathbf{u} is written in form of its truncated Taylor series (with N_t terms)

$$\mathbf{u} = \mathbf{u}_0 + \mathbf{u}'_0 \sigma + \frac{1}{2!} \mathbf{u}''_0 \sigma^2 + \cdots + \frac{1}{N_t!} \mathbf{u}^{(N_t)}_0 \sigma^{N_t} \quad (14)$$

A set of Taylor expansion coefficients are defined: $\mathbf{u}_i = (1/i!) \mathbf{u}_0^{(i)}$, so that Equation (14) can be written as

$$\mathbf{u} = \mathbf{u}_0 + \sum_{i=1}^{N_t} \mathbf{u}_i \sigma^i \quad (15)$$

In order to find \mathbf{u}_i , Equation (15) is inserted into Equation (5)

$$(\mathbf{P}_0 + \mathbf{P}_1 \sigma + \mathbf{P}_2 \sigma^2) \left(\mathbf{u}_0 + \sum_{i=1}^{N_t} \mathbf{u}_i \sigma^i \right) = \mathbf{f} \quad (16)$$

and the terms are matched by the order of the de-tuning parameter σ . This gives the following set of equations:

$$\mathbf{P}_0 \mathbf{u}_0 = \mathbf{f} \quad (17)$$

$$\mathbf{P}_0 \mathbf{u}_1 = -\mathbf{P}_1 \mathbf{u}_0 \quad (18)$$

$$\mathbf{P}_0 \mathbf{u}_i = -\mathbf{P}_1 \mathbf{u}_{i-1} - \mathbf{P}_2 \mathbf{u}_{i-2}, \quad i = 2, N_t \quad (19)$$

The zeroth order equation (Equation (17)) is equivalent to the original Equation (5) for $\sigma = 0$. It is assumed that this equation is solved by a factorization method so that \mathbf{P}_0 is available in factorized form. The benefit of this is evident from Equations (18)–(19) since the coefficients \mathbf{u}_1 , \mathbf{u}_2 and so forth can be computed simply by forward-/back substitutions. The factorized \mathbf{P}_0 will be used also to compute design sensitivities.

2.2. Coefficients \mathbf{a}_i and b_i

The combination of Equations (15) and (13) can now be utilized to find the unknown PA coefficients:

$$\mathbf{u}_0 + \sum_{i=1}^{N_t} \mathbf{u}_i \sigma^i = \frac{\mathbf{u}_0 + \sum_{i=1}^N \mathbf{a}_i \sigma^i}{1 + \sum_{i=1}^N b_i \sigma^i} \quad (20)$$

Both sides of Equation (20) are multiplied with the denominator

$$\left(\mathbf{u}_0 + \sum_{i=1}^{N_t} \mathbf{u}_i \sigma^i \right) \left(1 + \sum_{i=1}^N b_i \sigma^i \right) = \mathbf{u}_0 + \sum_{i=1}^N \mathbf{a}_i \sigma^i \quad (21)$$

and terms are matched by the order of σ^i

$$\mathbf{a}_1 = \mathbf{u}_1 + b_1 \mathbf{u}_0 \quad (22)$$

$$\mathbf{a}_i = \mathbf{u}_i + \sum_{j=1}^{i-1} b_j \mathbf{u}_{i-j} + b_i \mathbf{u}_0, \quad i = 2, \dots, N \quad (23)$$

from which the \mathbf{a}_i coefficients can be computed if the b_i coefficients are known. Equating the terms of order σ^{N+1} gives

$$\mathbf{0} = \mathbf{u}_{N+1} + \sum_{j=1}^N b_j \mathbf{u}_{N+1-j} \quad (24)$$

in which the b_i coefficients are the only unknowns.

The following procedure used to obtain b_i is limited to the case where the number of degrees of freedom N_d is higher than the chosen number of expansion terms N . As mentioned previously, this is a practical necessity when dealing with large finite element models and hence poses no real limitation on the method. With this assumption the equation system in Equation (24) is over-determined and can be used to find a common set of b_i coefficients for all degrees of freedom in the model. This approach differs from many previous implementations (e.g. [5]) where additional equations of the form in (24) are created by matching terms of order σ^{N+2} up to σ^{2N} .

Equation (24) can be written as

$$[\mathbf{u}_N \ \mathbf{u}_{N-1} \ \cdots \ \mathbf{u}_1] \begin{pmatrix} b_1 \\ b_2 \\ \vdots \\ b_N \end{pmatrix} = -\mathbf{u}_{N+1} \quad (25)$$

and is solved by finding the least-squares solution with the use of the pseudoinverse matrix [17]:

$$\begin{pmatrix} b_1 \\ b_2 \\ \vdots \\ b_N \end{pmatrix} = - \begin{bmatrix} \mathbf{u}_1^+ \\ \mathbf{u}_2^+ \\ \vdots \\ \mathbf{u}_N^+ \end{bmatrix} \mathbf{u}_{N+1} \quad (26)$$

in which \mathbf{u}_i^+ denotes a row vector in the pseudoinverse matrix. The pseudoinverse matrix can in this case be explicitly computed as

$$\begin{bmatrix} \mathbf{u}_1^+ \\ \mathbf{u}_2^+ \\ \vdots \\ \mathbf{u}_N^+ \end{bmatrix} = \mathbf{Q} \begin{bmatrix} \mathbf{u}_N^* \\ \mathbf{u}_{N-1}^* \\ \vdots \\ \mathbf{u}_1^* \end{bmatrix} \quad (27)$$

in which $\mathbf{Q} = \mathbf{P}^{-1}$ and

$$\mathbf{P} = \begin{bmatrix} \mathbf{u}_N^* \\ \mathbf{u}_{N-1}^* \\ \vdots \\ \mathbf{u}_1^* \end{bmatrix} [\mathbf{u}_N \ \mathbf{u}_{N-1} \ \cdots \ \mathbf{u}_1] \quad (28)$$

with \mathbf{u}_i^* denoting the conjugate transpose of the \mathbf{u}_i vector. The procedure is justified by numerical experiments showing that \mathbf{P} is of full rank so that the matrix inversion is possible.

However, \mathbf{P} turns out to be ill-conditioned if N is large setting a limit to the order of approximation that can be constructed. As pointed out in [10], this problem can be circumvented by using the

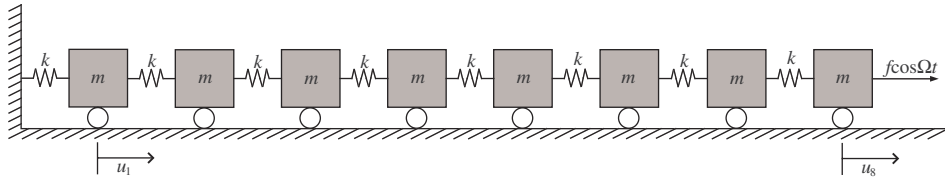


Figure 1. A simple mass–spring chain with a harmonic load.

related Krylov subspace projection method since the b_i coefficients are not directly computed with this method. To determine if the Krylov method is suitable for a design optimization procedure is left for future studies. The problems with ill-conditioning can be significantly reduced if the computations are carried out with higher precision numerics (e.g. quad precision as available on some 64-bit platforms). Apart from the simple test case analysed in Section 2.3, the use of higher precision numerics is also left for future work.

To conclude the analysis the individual steps involved in constructing the PA are listed:

- Solve the original equation at the chosen expansion frequency ($\sigma=0$) by a factorization method (Equation (17)) and compute $N + 1$ gradients (w.r.t. σ at $\sigma=0$) by forward-/back substitutions (Equations (18)–(19)).
- Compute the b_i coefficients by solving the over-determined system of equations in Equation (25).
- Compute the coefficients \mathbf{a}_i with Equations (22)–(23).

2.3. Analytical example: forced vibrations of a mass–spring chain

In this example the accuracy of the numerical scheme is demonstrated and the issue of numerical precision is addressed. The simple mass–spring chain in Figure 1 is considered which allows for analytical computation of the PA.

The steady-state vibration amplitudes of the masses are governed by a set of equations of the form Equations (2)–(3), in which the load vector is

$$\mathbf{f} = \{0 \ 0 \ 0 \ 0 \ 0 \ 0 \ 0 \ f\}^T \tag{29}$$

if the harmonic load of magnitude f acts on the rightmost mass.

In order to compare with the numerical scheme, the de-tuning parameter $\sigma = \Omega - \Omega_0$ (cf. Equation (4)) is introduced. With σ introduced, \mathbf{S} can be written as

$$\mathbf{S} = (-\Omega_0^2 \mathbf{M} + i\Omega_0 \mathbf{C} + \mathbf{K}) + (-2\Omega_0 \mathbf{M} + i\mathbf{C})\sigma + (-\mathbf{M})\sigma^2 \tag{30}$$

in which simple mass-proportional damping $\mathbf{C} = c\mathbf{M}$ is assumed.

The solution is written as

$$\mathbf{u} = \mathbf{H}\mathbf{f} \tag{31}$$

in which $\mathbf{H} = \mathbf{S}^{-1}$. The amplitude of the rightmost mass is

$$u_8 = H_{88}f \tag{32}$$

Table I. Coefficients a_i and b_i computed for $m = k = f = 1$, $c = 0.01$ and for the centrefrequency $\Omega_0 = 1$.

i	b_i	a_i
0	—	$-0.997905 - 0.0598893i$
1	$5.98175 + 0.628924i$	$6.00628 - 0.209591i$
2	$-45.0048 + 0.449545i$	$38.9141 + 2.42528i$
3	$-119.742 - 9.18382i$	$-84.0400 + 2.49613i$
4	$280.119 - 9.43850i$	$-250.510 - 13.2525i$
5	$712.978 + 32.9055i$	$230.125 - 11.5939i$
6	$-385.688 + 46.9032i$	$616.065 + 20.4211i$
7	$-1670.33 - 30.2742i$	$-56.4125 + 23.7608i$
8	$-493.363 - 79.0623i$	$-636.239 - 5.67282i$
9	$1428.97 - 21.4553i$	$-297.395 - 16.6529i$
10	$1285.16 + 38.5100i$	$154.880 - 6.12446i$
11	$-0.339896 + 32.7067i$	$195.702 + 1.25137i$
12	$-545.314 + 6.37730i$	$76.8638 + 1.39493i$
13	$-349.447 - 3.13286i$	$13.9728 + 0.348890i$
14	$-104.813 - 1.94300i$	$0.997905 + 0.0299102i$
15	$-15.9689 - 0.398731i$	—
16	$-0.997905 - 0.0299102i$	—

and by inserting the found expression for H_{88} this leads to the exact form of u_8

$$u_8 = \frac{a_0 + a_1\sigma + a_2\sigma^2 + \dots + a_{14}\sigma^{14}}{1 + b_1\sigma + b_2\sigma^2 + \dots + b_{16}\sigma^{16}} \quad (33)$$

in which the solution a_0 at the expansion frequency and the 30 additional expansion coefficients $a_1 - a_{14}$ and $b_1 - b_{16}$ are complicated functions of the system parameters and Ω_0 . The expressions are formidable even for this simple system so only numerical approximate values are given in Table I for a specific set of parameters ($m = k = f = \Omega_0 = 1$ and $c = 0.01$).

The vibration amplitude of the rightmost mass is illustrated in Figure 2. The response $\ln(u_8 \bar{u}_8)$, in which the bar denotes the complex conjugate, is plotted *versus* the excitation frequency Ω . The response shows the eight peaks that correspond to the natural frequencies of the system as well as seven anti-resonances. For $\Omega > 2$ the response drops off rapidly.

In Figure 2 the exact response is also compared to results obtained with the proposed numerical scheme. Even with a small number of expansion terms ($N = 3$) the accuracy of the approximation is remarkably good in a large frequency interval and visually indistinguishable from the exact solution in the range from $\Omega = 0.75 - 1.25$. With two additional terms in the numerator and denominator the high-accuracy frequency range is increased and three anti-resonances and 3–4 resonances are well captured. However, with $N = 7$ the accuracy significantly deteriorates. The reason is that the \mathbf{P} matrix in Equation (28) becomes severely ill-conditioned.

The problem with ill-conditioning can be overcome if higher precision numerical procedures are available. In Figure 2 the response with $N = 7$ is shown when computed with quad precision numerics (32 significant digits). The accuracy of the approximation is significantly improved, whereas for $N = 3$ and 5 the responses are practically unchanged (not shown in the figure). The

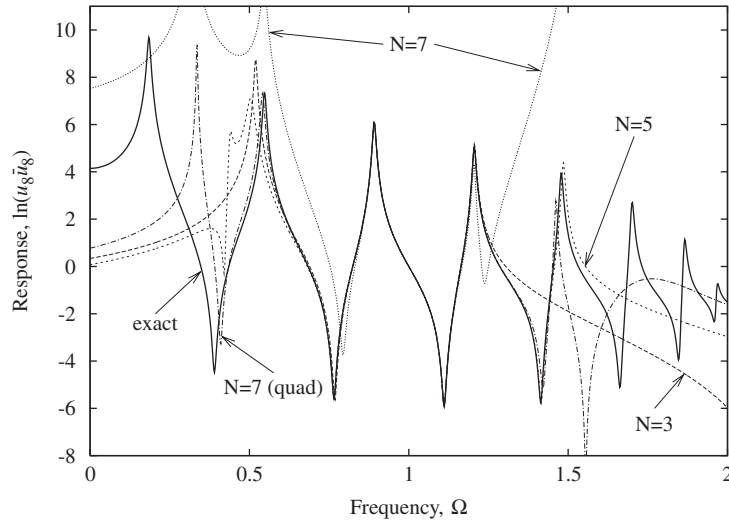


Figure 2. Comparison between exact response and Padé approximant with different numbers of expansion terms N .

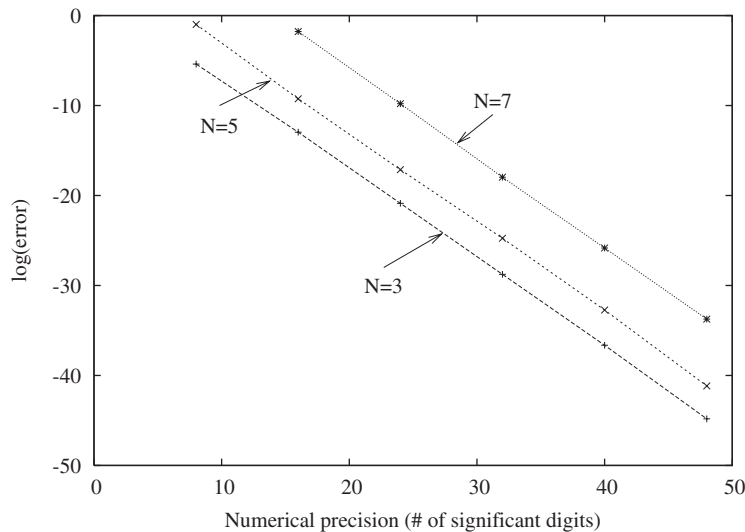


Figure 3. Error of the b_i coefficients versus the numerical precision in the computations.

approximation with $N = 7$ is generally superior to lower-order approximations but it is noted that the improvement when going from $N = 5$ to 7 is limited.

The error introduced by insufficient numerical precision is illustrated in Figure 3. The ill-conditioning of the \mathbf{P} matrix leads to inaccurate computations of the b_i coefficients. This

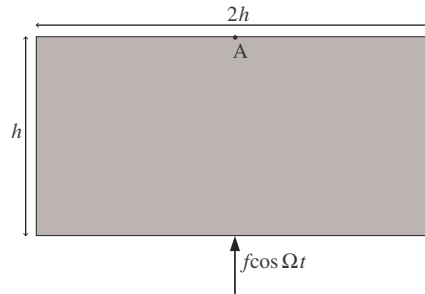


Figure 4. An unsupported 2-D elastic body (plane stress) subjected to a harmonic load.

error is measured as

$$\text{error} = \sqrt{\frac{1}{N} \sum_{i=1}^N \left(\frac{b_i - (b_i)_{\text{ref}}}{(b_i)_{\text{ref}}} \right)^2} \quad (34)$$

in which the reference values have been computed with 100 significant digits in the computations.

Figure 3 reveals a close to direct relation between the choice of numerical precision and $\log(\text{error})$ of the b_i coefficients. For this specific system and choice of parameters the high-order expansion ($N = 7$) leads to a significant error also for computations with standard double-precision variables (16 significant digits). If quad precision variables (32 significant digits) are used, the error is seen to be reduced to a sufficiently small level.

2.4. Numerical example: 2-D forced vibration

The second example demonstrates the numerical scheme for a structure with many degrees of freedom. An unsupported 2-D elastic body (Figure 4) is subjected to a harmonic load in the middle point of the lower boundary and the response is computed in the middle point A of the upper boundary. The following material parameters are used for the elastic body:

$$E = 1, \quad \rho = 1, \quad \nu = 0.3$$

with a plane stress model and unit thickness. A Rayleigh damping model is assumed so that the damping matrix \mathbf{C} is a linear combination of the mass- and the stiffness-matrices:

$$\mathbf{C} = \alpha \mathbf{M} + \beta \mathbf{K} \quad (35)$$

with damping coefficients $\alpha = 0.5$ and $\beta = 0.005$.

The body is discretized with 40×20 bi-linear quadratic elements and the size of the body is normalized so that the total mass is unity. All computations are carried out with standard double-precision numerics.

The response $\ln(u_A \bar{u}_A)$ is plotted in Figure 5 versus the excitation frequency Ω . The expansion frequency is $\Omega_0 = 1$. As reference, the direct solution is computed for a high number of frequencies and shown with a thick solid line. As appears from the figure an accurate approximation of the response is obtained in the frequency range from $\Omega \approx 0.7$ to 1.3 if a sufficient number of expansion terms are included ($N = 9$). However, if N is chosen larger than 9, the accuracy can be shown

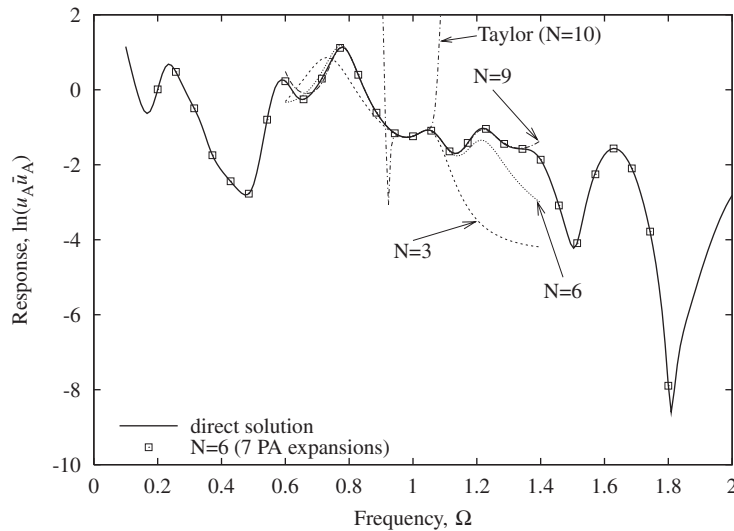


Figure 5. The response of point A in Figure 4 using direct computation of the frequency response (solid line) and PAs with different numbers of expansion coefficients.

to deteriorate, again due to an ill-conditioned \mathbf{P} matrix. To demonstrate the accuracy of the PA a standard Taylor-expansion with 10 terms has been included in the figure for comparison.

As mentioned in Section 2.3 the problem with ill-conditioning can be overcome with higher precision numerics. Another possibility is to construct the frequency response with several PAs each with a different expansion frequency. This is illustrated in Figure 5 in which seven separate PA expansions (with $N = 6$) have been computed with equidistant frequency spacing and then patched together. This multiplies the computational time accordingly, but offers an implicit control of the accuracy of the PA expansions by requiring that two patches should coincide at their midpoint frequency.

3. DESIGN SENSITIVITY ANALYSIS

The core of this work is to use the PA directly for optimization of the dynamic response. The first step is to compute the sensitivity of a chosen objective function, denoted c , w.r.t. a set of design variables. Analytical expressions for the sensitivities are obtained using the adjoint method.

A real-valued objective function with the general form

$$c = c(\mathbf{u}, \mathbf{x}) \quad (36)$$

is considered. The function depends on the PA (\mathbf{u}) and may also explicitly depend on the set of design variables defined in the vector $\mathbf{x} = \{x_1, x_2, \dots, x_{N_x}\}^T$.

In the general case with non-zero damping \mathbf{u} is complex and conveniently split up in the real and imaginary parts

$$c = c(\mathbf{u}_R, \mathbf{u}_I, \mathbf{x}) \quad (37)$$

The derivative of c w.r.t. a single design variable x_i is then

$$c' = \frac{\partial c}{\partial x_i} + \frac{\partial c}{\partial \mathbf{u}_R} \mathbf{u}'_R + \frac{\partial c}{\partial \mathbf{u}_I} \mathbf{u}'_I \quad (38)$$

in which $()' = d/dx_i$ and the scalar $\partial c/\partial x_i$ and the row vectors $\partial c/\partial \mathbf{u}_R$, $\partial c/\partial \mathbf{u}_I$ can be found directly for a given objective function.

To facilitate the computation of \mathbf{u}'_R and \mathbf{u}'_I it is exploited that \mathbf{u}' can be expressed in terms of the derivative of the Taylor expansion coefficients \mathbf{u}_i in the following form:

$$\mathbf{u}' = \sum_{i=0}^{N+1} (\mathbf{D}_i \mathbf{u}'_i + \mathbf{E}_i \bar{\mathbf{u}}'_i) \quad (39)$$

The derivation of the matrices \mathbf{D}_i and \mathbf{E}_i is lengthy and given in the Appendix.

Equation (39) is written out in terms of the real and imaginary parts \mathbf{u}'_R and \mathbf{u}'_I

$$\mathbf{u}'_R = \frac{1}{2} \sum_{i=0}^{N+1} ((\mathbf{D}_i + \bar{\mathbf{E}}_i) \mathbf{u}'_i + (\bar{\mathbf{D}}_i + \mathbf{E}_i) \bar{\mathbf{u}}'_i) \quad (40)$$

$$\mathbf{u}'_I = -\frac{i}{2} \sum_{i=0}^{N+1} ((\mathbf{D}_i - \bar{\mathbf{E}}_i) \mathbf{u}'_i - (\bar{\mathbf{D}}_i - \mathbf{E}_i) \bar{\mathbf{u}}'_i) \quad (41)$$

and Equations (40)–(41) are inserted into Equation (38):

$$c' = \frac{\partial c}{\partial x_i} + \frac{\partial c}{\partial \mathbf{u}} \sum_{i=0}^{N+1} (\mathbf{D}_i \mathbf{u}'_i + \bar{\mathbf{D}}_i \bar{\mathbf{u}}'_i) + \frac{\partial c}{\partial \bar{\mathbf{u}}} \sum_{i=0}^{N+1} (\bar{\mathbf{E}}_i \mathbf{u}'_i + \mathbf{E}_i \bar{\mathbf{u}}'_i) \quad (42)$$

in which the derivative-like terms $\partial c/\partial \mathbf{u}$ and $\partial c/\partial \bar{\mathbf{u}}$ are defined as

$$\frac{\partial c}{\partial \mathbf{u}} = \frac{1}{2} \left(\frac{\partial c}{\partial \mathbf{u}_R} - i \frac{\partial c}{\partial \mathbf{u}_I} \right) \quad (43)$$

$$\frac{\partial c}{\partial \bar{\mathbf{u}}} = \frac{1}{2} \left(\frac{\partial c}{\partial \mathbf{u}_R} + i \frac{\partial c}{\partial \mathbf{u}_I} \right) \quad (44)$$

The adjoint approach [18] is now used to replace the terms \mathbf{u}'_i and $\bar{\mathbf{u}}'_i$ in Equation (42) with terms that are easier to compute. The expression for c' is augmented with two series of additional terms

$$c'_0 = c' + \sum_{i=0}^{N+1} \lambda_i^T \mathbf{R}'_i + \sum_{i=0}^{N+1} \bar{\lambda}_i^T \bar{\mathbf{R}}'_i \quad (45)$$

where λ_i^T are vectors of Lagrangian multipliers and \mathbf{R}_i are the residuals defined from Equations (17)–(19) as

$$\mathbf{R}_0 = \mathbf{P}_0 \mathbf{u}_0 - \mathbf{f} \quad (46)$$

$$\mathbf{R}_1 = \mathbf{P}_0 \mathbf{u}_1 + \mathbf{P}_1 \mathbf{u}_0 \quad (47)$$

$$\mathbf{R}_i = \mathbf{P}_0 \mathbf{u}_i + \mathbf{P}_1 \mathbf{u}_{i-1} + \mathbf{P}_2 \mathbf{u}_{i-2}, \quad i = 2, N + 1 \quad (48)$$

that all vanish at equilibrium so that $c'_0 = c'$. Equation (45) is rewritten with Equations (46)–(48) inserted

$$\begin{aligned} c'_0 = c' &+ \sum_{i=0}^{N+1} (\lambda_i^T \mathbf{P}_0 + \lambda_{i+1}^T \mathbf{P}_1 + \lambda_{i+2}^T \mathbf{P}_2) \mathbf{u}'_i + \sum_{i=0}^{N+1} (\lambda_i^T \mathbf{P}'_0 + \lambda_{i+1}^T \mathbf{P}'_1 + \lambda_{i+2}^T \mathbf{P}'_2) \mathbf{u}_i \\ &+ \sum_{i=0}^{N+1} (\bar{\lambda}_i^T \bar{\mathbf{P}}_0 + \bar{\lambda}_{i+1}^T \bar{\mathbf{P}}_1 + \bar{\lambda}_{i+2}^T \bar{\mathbf{P}}_2) \bar{\mathbf{u}}'_i + \sum_{i=0}^{N+1} (\bar{\lambda}_i^T \bar{\mathbf{P}}'_0 + \bar{\lambda}_{i+1}^T \bar{\mathbf{P}}'_1 + \bar{\lambda}_{i+2}^T \bar{\mathbf{P}}'_2) \bar{\mathbf{u}}_i \end{aligned} \quad (49)$$

where $\lambda_{N+2} = \lambda_{N+3} = \mathbf{0}$ have been introduced for simplicity and it has been assumed that the load \mathbf{f} is independent of the design.

Inserting Equation (42) into Equation (49) yields

$$\begin{aligned} c'_0 = \frac{\partial c}{\partial x_i} &+ \frac{\partial c}{\partial \mathbf{u}} \sum_{i=0}^{N+1} (\mathbf{D}_i \mathbf{u}'_i + \bar{\mathbf{D}}_i \bar{\mathbf{u}}'_i) + \frac{\partial c}{\partial \bar{\mathbf{u}}} \sum_{i=0}^{N+1} (\bar{\mathbf{E}}_i \mathbf{u}'_i + \mathbf{E}_i \bar{\mathbf{u}}'_i) \\ &+ \sum_{i=0}^{N+1} (\lambda_i^T \mathbf{P}_0 + \lambda_{i+1}^T \mathbf{P}_1 + \lambda_{i+2}^T \mathbf{P}_2) \mathbf{u}'_i + \sum_{i=0}^{N+1} (\lambda_i^T \mathbf{P}'_0 + \lambda_{i+1}^T \mathbf{P}'_1 + \lambda_{i+2}^T \mathbf{P}'_2) \mathbf{u}_i \\ &+ \sum_{i=0}^{N+1} (\bar{\lambda}_i^T \bar{\mathbf{P}}_0 + \bar{\lambda}_{i+1}^T \bar{\mathbf{P}}_1 + \bar{\lambda}_{i+2}^T \bar{\mathbf{P}}_2) \bar{\mathbf{u}}'_i + \sum_{i=0}^{N+1} (\bar{\lambda}_i^T \bar{\mathbf{P}}'_0 + \bar{\lambda}_{i+1}^T \bar{\mathbf{P}}'_1 + \bar{\lambda}_{i+2}^T \bar{\mathbf{P}}'_2) \bar{\mathbf{u}}_i \end{aligned} \quad (50)$$

The Lagrangian multipliers are now chosen so that the terms that involve \mathbf{u}'_i and $\bar{\mathbf{u}}'_i$ vanish. This condition is fulfilled if

$$\frac{\partial c}{\partial \mathbf{u}} \sum_{i=0}^{N+1} \mathbf{D}_i \mathbf{u}'_i + \frac{\partial c}{\partial \bar{\mathbf{u}}} \sum_{i=0}^{N+1} \bar{\mathbf{E}}_i \mathbf{u}'_i + \sum_{i=0}^{N+1} (\lambda_i^T \mathbf{P}_0 + \lambda_{i+1}^T \mathbf{P}_1 + \lambda_{i+2}^T \mathbf{P}_2) \mathbf{u}'_i = 0 \quad (51)$$

which assures that the complex conjugate of this equation is also fulfilled and consequently that all terms in Equation (50) with \mathbf{u}'_i and $\bar{\mathbf{u}}'_i$ disappear. The terms in Equation (51) are collected

$$\sum_{i=0}^{N+1} \left(\frac{\partial c}{\partial \mathbf{u}} \mathbf{D}_i + \frac{\partial c}{\partial \bar{\mathbf{u}}} \bar{\mathbf{E}}_i + \lambda_i^T \mathbf{P}_0 + \lambda_{i+1}^T \mathbf{P}_1 + \lambda_{i+2}^T \mathbf{P}_2 \right) \mathbf{u}'_i = 0 \quad (52)$$

which holds if the following conditions for λ_i are satisfied:

$$\lambda_i^T \mathbf{P}_0 + \lambda_{i+1}^T \mathbf{P}_1 + \lambda_{i+2}^T \mathbf{P}_2 = -\frac{\partial c}{\partial \mathbf{u}} \mathbf{D}_i - \frac{\partial c}{\partial \bar{\mathbf{u}}} \bar{\mathbf{E}}_i, \quad i = 0, N + 1 \quad (53)$$

Equation (53) is conveniently solved for λ_i by starting with $i = N + 1$

$$\mathbf{P}_0^T \lambda_{N+1} = -\left(\frac{\partial c}{\partial \mathbf{u}} \mathbf{D}_{N+1} \right)^T - \left(\frac{\partial c}{\partial \bar{\mathbf{u}}} \bar{\mathbf{E}}_{N+1} \right)^T \quad (54)$$

which is solved for λ_{N+1} , and then carrying on to solve the remaining equations

$$\mathbf{P}_0^T \lambda_N = - \left(\frac{\partial c}{\partial \mathbf{u}} \mathbf{D}_N \right)^T - \left(\frac{\partial c}{\partial \bar{\mathbf{u}}} \bar{\mathbf{E}}_N \right)^T - \mathbf{P}_1 \lambda_{N+1} \quad (55)$$

$$\mathbf{P}_0^T \lambda_i = - \left(\frac{\partial c}{\partial \mathbf{u}} \mathbf{D}_i \right)^T - \left(\frac{\partial c}{\partial \bar{\mathbf{u}}} \bar{\mathbf{E}}_i \right)^T - \mathbf{P}_1 \lambda_{i+1} - \mathbf{P}_2 \lambda_{i+2}, \quad i = N - 1, 0 \quad (56)$$

It is noted that with \mathbf{P}_0 already factorized all Lagrangian multipliers can be computed by forward/back-substitutions.

With λ_i given from Equations (54)–(56) the final expression for c' becomes

$$c' = c'_0 = \frac{\partial c}{\partial x_i} + 2 \operatorname{Re} \left(\sum_{i=0}^{N+1} (\lambda_i^T \mathbf{P}'_0 + \lambda_{i+1}^T \mathbf{P}'_1 + \lambda_{i+2}^T \mathbf{P}'_2) \mathbf{u}_i \right) \quad (57)$$

4. TOPOLOGY OPTIMIZATION OF FORCED VIBRATIONS

A formulation has been developed that allows for the design sensitivities to be computed without overwhelming computational effort regardless of the number of design variables. This makes the present method well suited for optimization problems with many design variables such as in topology optimization [19]. In a standard topology optimization implementation with the density approach, a single design variable is used for each finite element in the model, typically leading to thousands of variables. Therefore, a fast sensitivity analysis procedure is essential for practical applications.

Two forced vibration problems are considered as application examples. Topology optimization of forced vibrations has been studied previously, e.g. by [1, 19–22]. All studies considered the dynamic performance at single or multiple excitation frequencies. With the proposed method the performance of the structure can be optimized in entire frequency ranges at little extra cost.

The average response in the frequency range from Ω_1 to Ω_2 is considered:

$$c = \frac{1}{\Omega_2 - \Omega_1} \int_{\Omega_1}^{\Omega_2} \mathbf{u}^T \mathbf{L} \bar{\mathbf{u}} \, d\Omega \approx \frac{1}{N_\Omega} \sum_{k=1}^{N_\Omega} \mathbf{u}^T \mathbf{L} \bar{\mathbf{u}} \quad (58)$$

in which \mathbf{L} is a diagonal matrix that is used to indicate the degrees of freedom that are considered in the optimization. The integral is well approximated by the sum if a sufficient number of evaluation points N_Ω is used (50–100 points are typically used in the examples). The objective function is written in terms of real and imaginary parts:

$$c = \frac{1}{N_\Omega} \sum_{k=1}^{N_\Omega} (\mathbf{u}_R^T \mathbf{L} \mathbf{u}_R + \mathbf{u}_I^T \mathbf{L} \mathbf{u}_I) \quad (59)$$

so that the complex derivatives can be computed

$$\frac{\partial c}{\partial \mathbf{u}} = \frac{1}{2} \left(\frac{\partial c}{\partial \mathbf{u}_R} - i \frac{\partial c}{\partial \mathbf{u}_I} \right) = \frac{1}{N_\sigma} \sum_{k=1}^{N_\sigma} \bar{\mathbf{u}}^T \mathbf{L} \quad (60)$$

$$\frac{\partial c}{\partial \bar{\mathbf{u}}} = \frac{1}{2} \left(\frac{\partial c}{\partial \mathbf{u}_R} + i \frac{\partial c}{\partial \mathbf{u}_I} \right) = \frac{1}{N_\sigma} \sum_{k=1}^{N_\sigma} \mathbf{u}^T \mathbf{L} \quad (61)$$

which leads to the expressions

$$\frac{\partial c}{\partial \mathbf{u}} \mathbf{D}_i = \frac{1}{N_\Omega} \sum_{k=1}^{N_\Omega} \bar{\mathbf{u}}^T \mathbf{L} \mathbf{D}_i \quad (62)$$

$$\frac{\partial c}{\partial \bar{\mathbf{u}}} \bar{\mathbf{E}}_i = \frac{1}{N_\Omega} \sum_{k=1}^{N_\Omega} \mathbf{u}^T \mathbf{L} \bar{\mathbf{E}}_i \quad (63)$$

Large savings in computational time and memory use are obtained if \mathbf{D}_i and $\bar{\mathbf{E}}_i$ are not explicitly computed. Instead, the formulas for \mathbf{D}_i and $\bar{\mathbf{E}}_i$ are inserted into Equations (62)–(63)

$$\frac{\partial c}{\partial \mathbf{u}} \mathbf{D}_0 = \frac{1}{N_\Omega} \sum_{k=1}^{N_\Omega} \bar{\mathbf{u}}^T \mathbf{L} \quad (64)$$

$$\frac{\partial c}{\partial \mathbf{u}} \mathbf{D}_{N+1} = -\frac{1}{N_\Omega} \sum_{k=1}^{N_\Omega} \left(\frac{1}{B} \sum_{j=1}^N (\bar{\mathbf{u}}^T \mathbf{L} \tilde{\mathbf{u}}_j) \mathbf{u}_j^+ \right) \quad (65)$$

in which $B = 1 + \sum_{i=1}^N b_i \sigma^i$ is the denominator of the PA and

$$\frac{\partial c}{\partial \mathbf{u}} \mathbf{D}_i = \frac{1}{N_\Omega} \sum_{k=1}^{N_\Omega} \frac{1}{B} (\tilde{b}_i (\bar{\mathbf{u}}^T \mathbf{L}) + \mathbf{u}_{N+1-i}^+ \mathbf{u}_{N+1} \sum_{j=1}^N (\bar{\mathbf{u}}^T \mathbf{L} \tilde{\mathbf{u}}_j) \tilde{\mathbf{Q}}_j^T) \quad (66)$$

$$\frac{\partial c}{\partial \bar{\mathbf{u}}} \bar{\mathbf{E}}_i = -\frac{1}{N_\Omega} \sum_{k=1}^{N_\Omega} \frac{1}{B} \sum_{j=1}^N \bar{\mathbf{Q}}_{j,N+1-i} (\overline{\mathbf{u}^T \mathbf{L} \tilde{\mathbf{u}}_j}) \bar{\mathbf{h}}^T \quad (67)$$

for $i = 1, N$. In Equation (66)–(67) the following symbols have been introduced

$$\mathbf{h}^T = \mathbf{u}_{N+1}^T - \sum_{l=1}^N \mathbf{u}_l^+ \mathbf{u}_{N+1} \mathbf{u}_{N+1-l}^T \quad (68)$$

$$\tilde{\mathbf{Q}}_j^T = \sum_{l=1}^N \mathbf{Q}_{j,N+1-l} \mathbf{u}_l^* \quad (69)$$

which are independent of the frequency and must be computed only once for each optimization iteration. This is also the case for the scalar $\mathbf{u}_{N+1-i}^+ \mathbf{u}_{N+1}$. The following quantities that appear in Equations (64)–(67) should be computed for each frequency evaluation point k :

$$\tilde{b}_i = \sum_{j=i}^N b_{j-i} \sigma^j \quad (70)$$

$$\tilde{\mathbf{u}}_j = \sum_{l=j}^N \mathbf{u}_{l-j} \sigma^l - \mathbf{u} \sigma^j \quad (71)$$

Based on the expressions given in Equations (64)–(67) the adjoint fields can be computed from Equations (54)–(56) and finally the design sensitivities from Equation (57).

4.1. Optimized reinforcement of a 2-D elastic body

As the first example, the dynamic response of the 2-D elastic body in Figure 4 (with material properties $E = 1$, $\rho = 1$, $\nu = 0.3$) is optimized by distributing a maximum amount of 25% reinforcement material. The material properties of the reinforcement material are:

$$E = 2, \quad \rho = 2, \quad \nu = 0.3$$

and the plane stress model with unit thickness is considered. The structure is discretized using 80×40 bi-linear quadratic elements and the load is applied in three nodes in the middle of the lower boundary.

A standard Matlab implementation of the topology optimization algorithm is used. Specific details are not included here and the reader is referred to [23] for implementation details and to [19] for a general presentation of the method. Design updates are found with the method of moving asymptotes (MMA) [24]. As material interpolation the RAMP-model [25] is implemented with penalization parameter $p = 5$. A sensitivity filter is not used and the symmetry of the designs is explicitly enforced by averaging the left–right sensitivities. In the initial design the 25% reinforcement material is uniformly distributed in the entire body and 100–150 iterations have been used in the examples.

The damping coefficients $\alpha = 0.5$ and $\beta = 0.005$ are reused from the analysis example in Section 2.4 with the important note that the damping is kept independent of the design by being proportional only to the constant part of the mass- and stiffness-matrix.

The first objective is to minimize the response in point A (Figure 4), averaged over a finite frequency range. Equation (58) becomes

$$c_1 = \frac{1}{N_\Omega} \sum_{k=1}^{N_\Omega} u_A \bar{u}_A \quad (72)$$

by specifying \mathbf{L} to have one unit entry in the diagonal that corresponds to the vertical amplitude in A.

Figure 6 shows four examples of optimized material distribution. Figure 6(a) shows the distribution when the response is minimized for a single frequency $\Omega = 1$, whereas the designs in Figure 6(b)–(d) are obtained when the response is minimized for larger frequency ranges. The number of PA expansion terms is $N = 7$ and the number of frequency evaluation points for the objective function is $N_\Omega = 100$. For the smallest optimization interval ($\Omega = 0.9 - 1.1$) a single PA is used but in order to obtain good approximations for the larger intervals the number of patched PA expansions is increased to two and three for the intervals $\Omega = 0.8 - 1.2$ and $\Omega = 0.7 - 1.3$, respectively.

Figure 7 shows the PA for the initial structure and the PA for the optimized body corresponding to the optimization interval $\Omega = 0.9 - 1.1$ (Figure 6(b)). A low response is seen in the entire optimization interval, which is accomplished by the creation of several closely spaced anti-resonances. The frequency responses for the initial and the optimized designs are also computed using a standard direct approach for a high number of frequencies (thin solid lines) to illustrate the validity of the PA approximations.

Figure 8 shows the response for the other optimized designs in Figure 6. The structures and their corresponding responses are very dependent on the optimization interval. The structure optimized

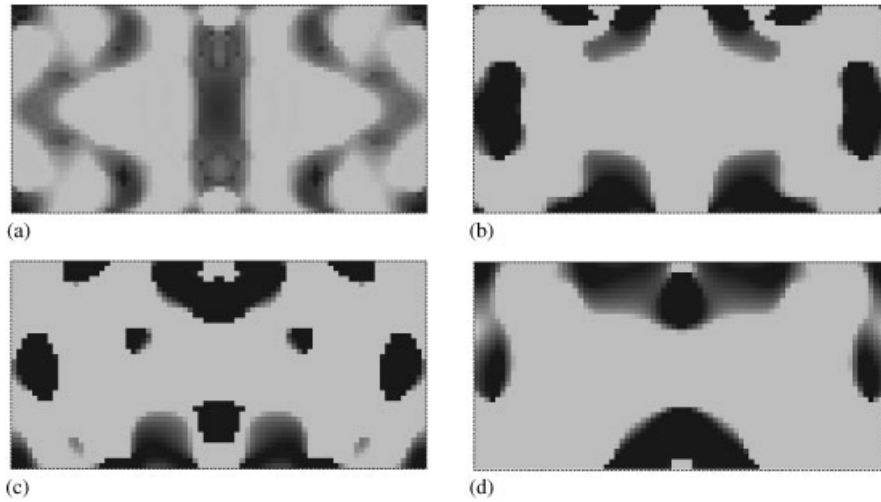


Figure 6. Optimized distribution of base material (grey) and 25% reinforcement material (black) for minimized response in point A for: (a) $\Omega = 1$ and for 3 different frequency intervals; (b) $\Omega = 0.9\text{--}1.1$; (c) $\Omega = 0.8\text{--}1.2$; and (d) $\Omega = 0.7\text{--}1.3$.

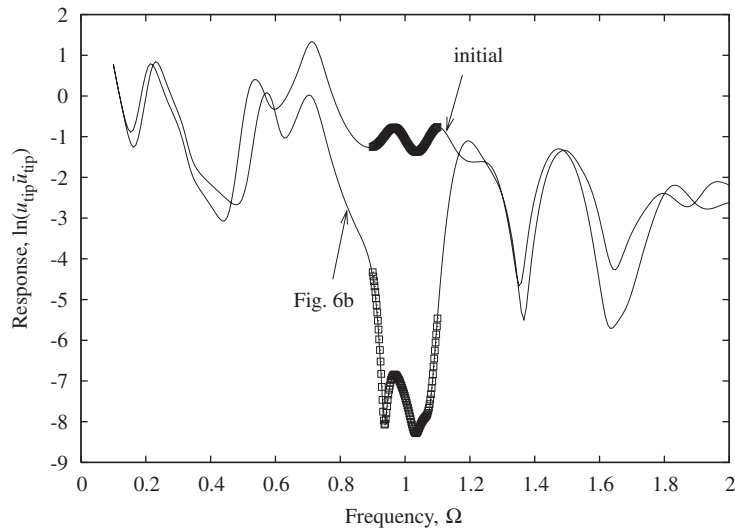


Figure 7. Response in point A for the initial structure and the structure in Figure 6(b) optimized for $\Omega = 0.9\text{--}1.1$. The PAs are indicated by discrete markers and directly computed responses are plotted as thin solid lines.

for the single excitation frequency $\Omega = 1$ (Figure 6(a)) has a very low response exactly at the target frequency but a high response if the frequency is only slightly de-tuned from that target. Much more robust designs with broadband low response are obtained when the response is minimized

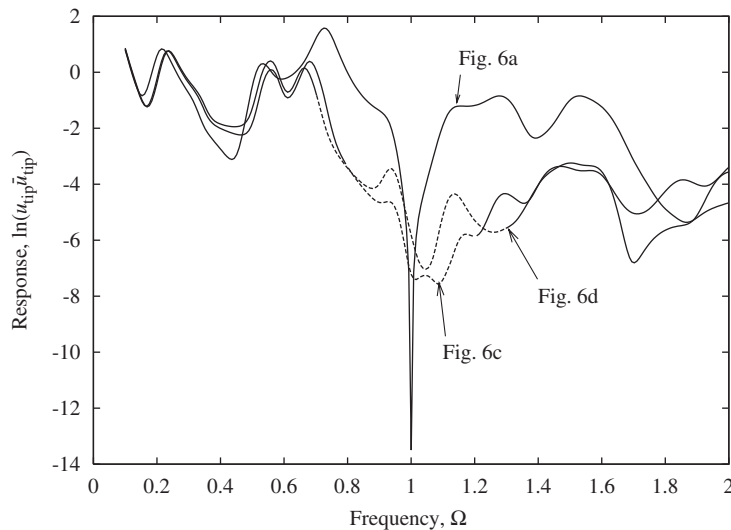


Figure 8. Response in point *A* for the optimized structures in Figure 6(a), (c), (d). Dashed lines indicate the optimization frequency interval.

in larger frequency ranges. Additionally, it is evident that the optimized material distribution for the single frequency optimization is dominated by intermediate material properties. Not all of the allowed reinforcement material is used in this case. The designs in Figure 6(b)–(d) show a much more well-defined material distribution, and all of the allowed reinforcement material is utilized to create the best possible performance.

All optimized designs have been obtained from an initial design with a uniform material distribution. Different optimized designs (local optima) appear with other initial designs. Actually, by using the structures in Figures 6(c) and (d) as the initial design for the optimization problem with the frequency interval $\Omega = 0.9\text{--}1.1$, designs with a slightly better performance were obtained.

The same optimization set-up is now used to minimize the response in the entire body instead of just in a single output point. The second objective function

$$c_2 = \frac{1}{N_\Omega} \sum_{k=1}^{N_\Omega} \mathbf{u}^T \bar{\mathbf{u}} \quad (73)$$

is obtained by setting \mathbf{L} to be the unit matrix. Figure 9 shows the optimized designs for two different optimization frequency intervals and Figure 10 shows the responses for the two designs as well as for the initial design. In this case, the anti-resonance mechanism cannot be used since this is a local phenomenon. Instead, a low response is created by moving resonances away from the optimization interval. For the small interval it is seen that all resonances have been removed and a very low response is obtained in the entire interval. For the large interval, not all resonances are removed and two response peaks remain near $\Omega = 1$. However, all other nearby resonances are moved either below or above the interval and consequently a low average response is obtained.

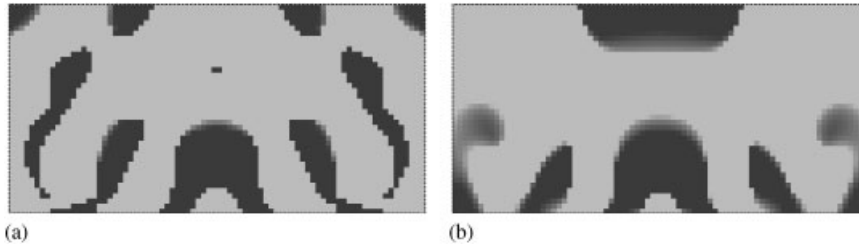


Figure 9. Optimized material distribution (25% reinforcement material) for minimized response of the entire body for two different frequency intervals: (a) $\Omega = 0.9\text{--}1.1$ and (b) $\Omega = 0.7\text{--}1.3$.

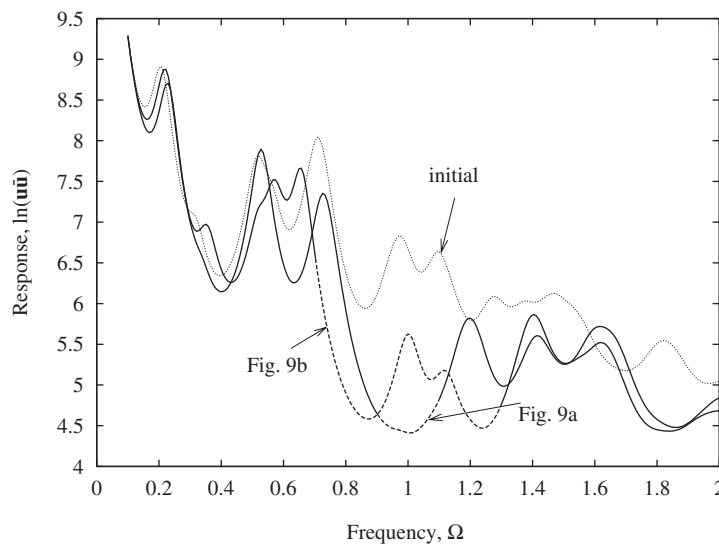


Figure 10. Total response for the body for the two different optimized structures in Figure 9 and for the initial structure with 25% material uniformly distributed in the domain. Dashed lines indicate the optimization interval.

4.2. Structural optimization of a tip-loaded cantilever

The tip-loaded cantilever shown in Figure 11 is a classical benchmark problem in structural topology optimization with static loads [19]. A few works have considered similar optimization problems for harmonic loads [20, 22] but only for single frequencies. Here, the proposed method is used to optimize the distribution of solid and void in the cantilever so that the dynamic compliance in the lower frequency range is minimized.

The problem is defined as a standard structural topology optimization problem in which a limited amount of material (50%) with material parameters:

$$E = 1, \quad \rho = 1, \quad \nu = 0.3$$

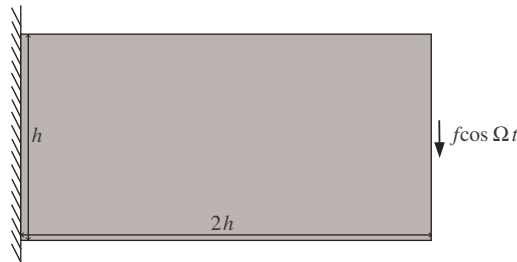


Figure 11. A short cantilever subjected to a harmonic tip-load with frequency Ω .

is to be distributed so that a chosen objective function is minimized. The objective function is

$$c_3 = \frac{1}{N_\Omega} \sum_{k=1}^{N_\Omega} u_{\text{tip}} \bar{u}_{\text{tip}} \quad (74)$$

so that the response of the tip is chosen as a measure of the dynamic compliance.

A plane stress model with unit thickness is considered and the cantilever is discretized using 80×40 bi-linear quadratic elements. The load is applied in three nodes in middle of the right boundary. Damping coefficients are $\alpha = 0.05$ and $\beta = 0.002$. The Matlab implementation from Section 4.1 is used, and a sensitivity filter (filter-size: $1.5 \times$ element-size) is included to avoid mesh-dependent solutions and checkerboard formation [23]. The initial design has 50% material uniformly distributed in the domain.

Figure 12 shows the cantilever optimized for four different frequency intervals. If the frequency interval is in the low range ($\Omega = 0-0.02$) well below the first resonance frequency of the initial design, then the optimized cantilever (Figure 12(a)) resembles the structure that is obtained for a static tip-load. The increased static and low-frequency dynamic stiffness is obtained by moving the first resonance frequency up in the frequency range. Figure 12(b) shows that if the frequency range is increased to $\Omega = 0-0.04$, the material is slightly redistributed so that the first resonance frequency is further increased and the high stiffness frequency range broadened. If the optimization interval is increased to higher frequency ranges, the optimized structures (Figure 12(c), (d)) change qualitatively.

Figure 13 shows the corresponding responses for the four optimized structures as well as for the initial design. As mentioned before, the structures in Figure 12(a) and (b) have responses in which the first resonance frequency is moved up in the frequency range. Similar observations were made in [22]. However, the structures in Figure 12(c) and (d) obtain a low average response by a different mechanism: the static and low-frequency stiffness is lower (higher response) but an anti-resonance is introduced in the optimization interval. At the anti-resonance the tip response is small whereas the response of the rest of the structure is high. Thus, if a different measure of the dynamic compliance had been used, e.g. the total energy, these designs would not be optimal.

It should be mentioned that the choice of N (number of expansion terms) is critical for this example. The initial problem in which the structure is homogeneous is very ill-conditioned and if $N > 2$ the errors introduced in the PA computation and the corresponding sensitivities become too large with a double-precision implementation. Therefore, in the shown examples the first iterations are done with $N = 2$ and up to eight PA expansions. After a few iterations, say 15–20, N is increased (up to $N = 5$) and the number of expansions reduced to one or two.

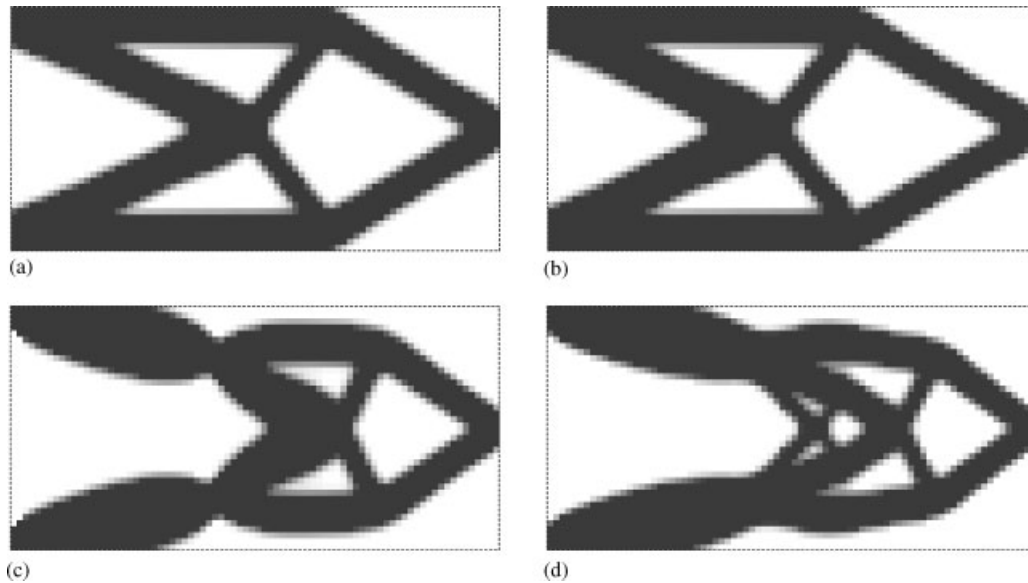


Figure 12. Optimized distribution of 50% solid (black) for four different frequency intervals: (a) $\Omega = 0-0.02$; (b) $\Omega = 0-0.04$; (c) $\Omega = 0-0.06$; and (d) $\Omega = 0-0.08$.

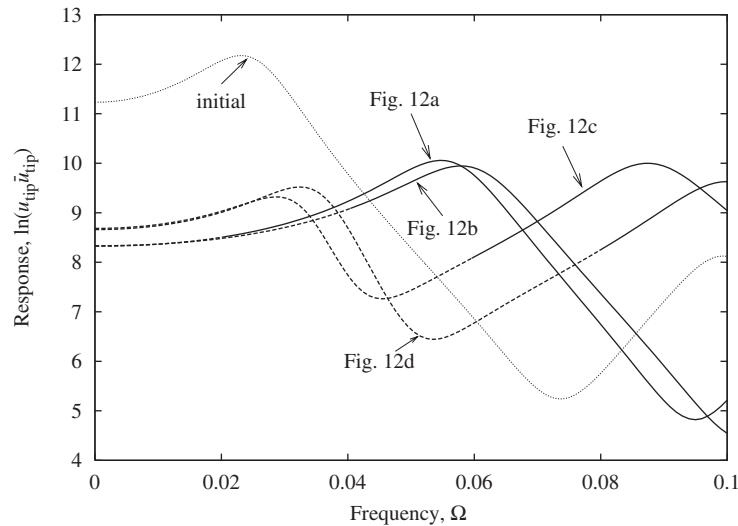


Figure 13. Tip response of the four different optimized structures in Figure 12 and for the initial structure with 50% material uniformly distributed in the domain. Dashed lines indicate optimization frequency intervals.

Additionally, it appears that many local optima exist for this optimization problem especially for larger optimization intervals. Different optima are obtained with variations in the optimization procedure, e.g. the small differences due to the choice of N and number of PA expansions (see paragraph above) and also the choice of initial design. However, the designs differ only in structural

details and have a similar overall appearance and performance. The presented designs are the best that could be obtained with the specific initial design, however, it is perfectly possible that these are not global optima.

5. CONCLUSIONS

This paper proposes an alternative approach to topology optimization of dynamics problems. The method addresses the need for considering the response in frequency ranges rather than for single frequencies. With a traditional approach the system matrix needs to be factorized for each considered frequency which leads to high computational costs and the alternative modal approach typically leads to non-smooth optimization problems.

The proposed method uses PAs to rapidly compute frequency response functions with high accuracy over a wide range of frequencies. Formulas for the sensitivity of the response with respect to design variables are derived using analytical methods. The derivation is based on the adjoint approach which provides the design sensitivities for a large number of design variables at low computational cost. This makes the formulation particularly suited for topology optimization that typically involves thousands of design variables.

The accuracy of the PAs is studied for simple 1-D and 2-D systems. It is shown that the numerical procedure yields an accurate approximation to the frequency response also for a relatively a small number of terms in the Padé expansion. Due to ill-conditioning the effect of numerical precision in the computations is critical and if many terms are included in the expansion an implementation of the algorithm with higher precision numerics (e.g. quad precision) should be considered.

Two examples of topology optimization of forced vibrations are included to demonstrate the proposed optimization procedure. In the first example, a 2-D elastic body is optimized by distributing a limited amount of reinforcement material so that the average response in medium-range frequency intervals is minimized. By optimizing for frequency intervals rather than single frequencies a good broadband performance can be obtained rather than a narrow band performance that is very sensitive to slight frequency de-tuning. In the second example, structural optimization of a tip-loaded cantilever is considered and the distribution of solid and void optimized so that the average dynamic response is minimized in the low-frequency range. Different optimization frequency intervals result in qualitatively different optimized designs that rely on qualitatively different mechanisms to obtain a low value of the objective function.

APPENDIX A

In this Appendix it is shown that \mathbf{u}' can be expressed in the following form:

$$\mathbf{u}' = \sum_{i=0}^{N+1} (\mathbf{D}_i \mathbf{u}'_i + \mathbf{E}_i \bar{\mathbf{u}}'_i) \quad (\text{A1})$$

where $()'$ is the derivative w.r.t. a design variable.

To determine \mathbf{D}_i and \mathbf{E}_i the PA is written as

$$\mathbf{u} = \frac{\mathbf{A}}{B} \quad (\text{A2})$$

in which

$$\mathbf{A} = \mathbf{u}_0 + \sum_{i=1}^N \mathbf{a}_i \sigma^i \quad (\text{A3})$$

$$B = 1 + \sum_{i=1}^N b_i \sigma^i \quad (\text{A4})$$

Equation (A2) is differentiated w.r.t. a design variable

$$B\mathbf{u}' = \mathbf{A}' - B'\mathbf{u} \quad (\text{A5})$$

and by differentiating the expressions for \mathbf{A} and B

$$B\mathbf{u}' = \sum_{i=0}^N \mathbf{a}'_i \sigma^i - \left(\sum_{i=1}^N b'_i \sigma^i \right) \mathbf{u} \quad (\text{A6})$$

in which the notation $\mathbf{u}'_0 = \mathbf{a}'_0$ is used for simplicity.

From Equations (22)–(23) \mathbf{a}'_i can be expressed as

$$\mathbf{a}'_i = \sum_{j=0}^i b_j \mathbf{u}'_{i-j} + \sum_{j=1}^i b'_j \mathbf{u}_{i-j} \quad (\text{A7})$$

and this expression is inserted into Equation (A6) to yield

$$B\mathbf{u}' = \sum_{i=0}^N \left(\sum_{j=0}^i b_j \mathbf{u}'_{i-j} + \sum_{j=1}^i b'_j \mathbf{u}_{i-j} \right) \sigma^i - \left(\sum_{i=1}^N b'_i \sigma^i \right) \mathbf{u} \quad (\text{A8})$$

which after reorganizing terms is given as

$$B\mathbf{u}' = \sum_{i=0}^N \left(\sum_{j=0}^i b_j \mathbf{u}'_{i-j} \right) \sigma^i + \sum_{i=1}^N \left(\left(\sum_{j=1}^i b'_j \mathbf{u}_{i-j} \right) - b'_i \mathbf{u} \right) \sigma^i \quad (\text{A9})$$

After some index manipulation we can write this expression as

$$B\mathbf{u}' = \sum_{i=0}^N \tilde{b}_i \mathbf{u}'_i + \sum_{i=1}^N \tilde{\mathbf{u}}_i b'_i \quad (\text{A10})$$

with

$$\tilde{b}_i = \sum_{j=i}^N b_{j-i} \sigma^j \quad (\text{A11})$$

$$\tilde{\mathbf{u}}_i = \sum_{j=i}^N \mathbf{u}_{j-i} \sigma^j - \mathbf{u} \sigma^i \quad (\text{A12})$$

Equation (A10) contains terms that depend on b'_i . By differentiating Equation (26) b'_i can be expressed in terms of \mathbf{u}'_i

$$\begin{pmatrix} b'_1 \\ b'_2 \\ \vdots \\ b'_N \end{pmatrix} = - \begin{bmatrix} (\mathbf{u}_1^+)' \\ (\mathbf{u}_2^+)' \\ \vdots \\ (\mathbf{u}_N^+)' \end{bmatrix} \mathbf{u}_{N+1} - \begin{bmatrix} \mathbf{u}_1^+ \\ \mathbf{u}_2^+ \\ \vdots \\ \mathbf{u}_N^+ \end{bmatrix} \mathbf{u}'_{N+1} \tag{A13}$$

An expression for $(\mathbf{u}_i^+)'$ is now needed. Differentiating Equation (27) gives

$$\begin{aligned} \mathbf{P} \begin{bmatrix} (\mathbf{u}_1^+)' \\ (\mathbf{u}_2^+)' \\ \vdots \\ (\mathbf{u}_N^+)' \end{bmatrix} &= \begin{bmatrix} (\mathbf{u}_N^*)' \\ (\mathbf{u}_{N-1}^*)' \\ \vdots \\ (\mathbf{u}_1^*)' \end{bmatrix} - \begin{bmatrix} (\mathbf{u}_N^*)' \\ (\mathbf{u}_{N-1}^*)' \\ \vdots \\ (\mathbf{u}_1^*)' \end{bmatrix} [\mathbf{u}_N \ \mathbf{u}_{N-1} \ \dots \ \mathbf{u}_1] \begin{bmatrix} \mathbf{u}_1^+ \\ \mathbf{u}_2^+ \\ \vdots \\ \mathbf{u}_N^+ \end{bmatrix} \\ &\quad - \begin{bmatrix} \mathbf{u}_N^* \\ \mathbf{u}_{N-1}^* \\ \vdots \\ \mathbf{u}_1^* \end{bmatrix} [\mathbf{u}'_N \ \mathbf{u}'_{N-1} \ \dots \ \mathbf{u}'_1] \begin{bmatrix} \mathbf{u}_1^+ \\ \mathbf{u}_2^+ \\ \vdots \\ \mathbf{u}_N^+ \end{bmatrix} \end{aligned} \tag{A14}$$

where it is recalled that \mathbf{P} is defined as

$$\mathbf{P} = \begin{bmatrix} \mathbf{u}_N^* \\ \mathbf{u}_{N-1}^* \\ \vdots \\ \mathbf{u}_1^* \end{bmatrix} [\mathbf{u}_N \ \mathbf{u}_{N-1} \ \dots \ \mathbf{u}_1] \tag{A15}$$

and $()^*$ is the conjugate transpose vector.

Thus, if both sides of Equation (A14) is multiplied by $\mathbf{Q} = \mathbf{P}^{-1}$ an expression for $(\mathbf{u}_i^+)'$ is obtained which can be inserted into Equation (A13) to find b'_i . This is then used to build an expression for $\tilde{\mathbf{u}}_i b'_i$

$$\tilde{\mathbf{u}}_i b'_i = -\tilde{\mathbf{u}}_i \mathbf{u}_i^+ \mathbf{u}'_{N+1} - \left(\sum_{j=1}^N \mathbf{Q}_{j,N+1-i} \tilde{\mathbf{u}}_j \right) \tilde{\mathbf{h}}^T \tilde{\mathbf{u}}'_i + \mathbf{u}_{N+1-i}^+ \mathbf{u}_{N+1} \left(\sum_{j=1}^N \tilde{\mathbf{u}}_j \tilde{\mathbf{Q}}_j^T \right) \mathbf{u}'_i \tag{A16}$$

in which

$$\mathbf{h}^T = \mathbf{u}_{N+1}^T - \sum_{k=1}^N \mathbf{u}_k^+ \mathbf{u}_{N+1} \mathbf{u}_{N+1-k}^T \tag{A17}$$

$$\tilde{\mathbf{Q}}_j^T = \sum_{k=1}^N \mathbf{Q}_{j,N+1-k} \mathbf{u}_k^* \quad (\text{A18})$$

Equation (A16) is inserted into Equation (A10)

$$\begin{aligned} B\mathbf{u}' &= B\mathbf{u}'_0 - \left(\sum_{j=1}^N \tilde{\mathbf{u}}_j \mathbf{u}_j^+ \right) \mathbf{u}'_{N+1} \\ &+ \sum_{i=1}^N \left(\left(\tilde{b}_i \mathbf{I} + \mathbf{u}_{N+1-i}^+ \mathbf{u}_{N+1} \sum_{j=1}^N \tilde{\mathbf{u}}_j \tilde{\mathbf{Q}}_j^T \right) \mathbf{u}'_i - \left(\sum_{j=1}^N \mathbf{Q}_{j,N+1-i} \tilde{\mathbf{u}}_j \right) \mathbf{h}^T \tilde{\mathbf{u}}'_i \right) \end{aligned} \quad (\text{A19})$$

in which it has been used that $\tilde{b}_0 = B$.

Equation (A19) can now be used to identify the components of the matrices \mathbf{D}_i and \mathbf{E}_i

$$\mathbf{D}_0 = \mathbf{I}, \quad \mathbf{E}_0 = \mathbf{0} \quad (\text{A20})$$

$$\mathbf{D}_{N+1} = -\frac{1}{B} \sum_{j=1}^N \tilde{\mathbf{u}}_j \mathbf{u}_j^+, \quad \mathbf{E}_{N+1} = \mathbf{0} \quad (\text{A21})$$

and

$$\mathbf{D}_i = \frac{1}{B} \left(\tilde{b}_i \mathbf{I} + \mathbf{u}_{N+1-i}^+ \mathbf{u}_{N+1} \sum_{j=1}^N \tilde{\mathbf{u}}_j \tilde{\mathbf{Q}}_j^T \right) \quad (\text{A22})$$

$$\mathbf{E}_i = -\frac{1}{B} \left(\sum_{j=1}^N \mathbf{Q}_{j,N+1-i} \tilde{\mathbf{u}}_j \right) \mathbf{h}^T \quad (\text{A23})$$

for $i = 1, N$.

ACKNOWLEDGEMENTS

The author wishes to thank Professors M. P. Bendsøe, Department of Mathematics and P. C. Madsen, Department of Informatics and Mathematical Modelling at the Technical University of Denmark for helpful suggestions and discussions.

REFERENCES

1. Tcherniak D. Topology optimization of resonating structures using SIMP method. *International Journal for Numerical Methods in Engineering* 2002; **54**:1605–1622.
2. Baker GA, Graves-Morris P. *Padé Approximants* (2nd edn). Cambridge University Press: Cambridge, 1996.
3. Pillage LT, Rohrer RA. Asymptotic waveform evaluation for timing analysis. *IEEE Transactions on Computer-Aided Design* 1990; **9**:352–366.
4. Gong J, Volakis L. Awe implementation for electromagnetic fem analysis. *Electronics Letters* 1996; **32**:2216–2217.
5. Zhang J-P, Jin J-M. Preliminary study of awe method for fem analysis of scattering problems. *Microwave and Optical Technology Letters* 1998; **17**:7–12.
6. Kuzuoglu M, Mittra R. Finite element solution of electromagnetic problems over a wide frequency range via the Padé approximation. *Computer Methods in Applied Mechanics and Engineering* 1999; **169**:263–277.

7. Coyette J-P, Lecomte C, Migeot J-L. Calculation of vibro-acoustic frequency response functions using a single frequency boundary element solution and a Padé expansion. *Acta Acoustica* 1999; **85**:371–377.
8. Djellouli R, Farhat C, Tezaur R. A fast method for solving acoustic scattering problems in frequency bands. *Journal of Computational Physics* 2001; **168**:412–432.
9. Malhotra M, Pinsky PM. Efficient computation of multi-frequency far-field solutions of the Helmholtz equation using Padé approximation. *Journal of Computational Acoustics* 2000; **8**:223–240.
10. Wagner MM, Pinsky PM, Oberai AA, Malhotra M. A Krylov subspace projection method for simultaneous solution of Helmholtz problems at multiple frequencies. *Computer Methods in Applied Mechanics and Engineering* 2003; **192**:4609–4640.
11. Xu GL, Bultheel A. Matrix Padé-approximation—definitions and properties. *Linear Algebra and its Applications* 1990; **137**:67–136.
12. Freund RW. Computation of matrix Padé approximations of transfer functions via a Lanczos-type process. *Approximation and Interpolation of Approximation Theory VIII*, vol. 1. World Scientific: Singapore, 1995; 215–222.
13. Jensen JS, Sigmund O. Topology optimization of photonic crystal structures: a high-bandwidth low-loss T-junction waveguide. *Journal of the Optical Society of America B* 2005; **22**(6):1191–1198.
14. Kwon SK, Bernard JE. Design optimization based on Padé expansions. *Finite Elements in Analysis and Design* 1992; **11**:235–246.
15. Webb JP. Design sensitivity of frequency response in 3-d finite-element analysis of microwave devices. *IEEE Transactions on Magnetics* 2002; **38**:1109–1112.
16. Nair D, Webb JP. Optimization of microwave devices using 3-D finite elements and the design sensitivity of the frequency response. *IEEE Transactions on Magnetics* 2003; **39**:1325–1328.
17. Strang G. *Linear Algebra and its Applications* (3rd edn). Hartcourt Brace Jovanovich: Orlando, FL, 1986.
18. Tortorelli DA, Michaleris P. Design sensitivity analysis: overview and review. *Inverse Problems in Engineering* 1994; **1**:71–105.
19. Bendsoe MP, Sigmund O. *Topology Optimization—Theory, Methods and Applications*. Springer: Berlin, Heidelberg, 2003.
20. Ma Z-D, Kikuchi N, Hagiwara I. Structural topology and shape optimization for a frequency response problem. *Computational Mechanics* 1993; **13**:157–174.
21. Jog CS. Topology design of structures subjected to periodic loading. *Journal of Sound and Vibration* 2002; **253**(3):687–709.
22. Olhoff N, Du J. Topological design for minimum dynamic compliance of continuum structures subjected to forced vibration. *Structural and Multidisciplinary Optimization* 2007, to appear.
23. Sigmund O. A 99 line topology optimization code written in matlab. *Structural and Multidisciplinary Optimization* 2001; **21**:120–127.
24. Svanberg K. The method of moving asymptotes—a new method for structural optimization. *International Journal for Numerical Methods in Engineering* 1987; **24**:359–373.
25. Stolpe M, Svanberg K. An alternative interpolation scheme for minimum compliance optimization. *Structural and Multidisciplinary Optimization* 2001; **22**:116–124.

OPTIMIZATION OF NON-LINEAR MASS DAMPER PARAMETERS FOR TRANSIENT RESPONSE

Jakob S. Jensen

Department of Mechanical Engineering
Nils Koppels Allé, Building 404
Technical University of Denmark
jsj@mek.dtu.dk

Boyan S. Lazarov

Department of Mechanical Engineering
Nils Koppels Allé, Building 404
Technical University of Denmark
bsl@mek.dtu.dk

Abstract

We optimize the parameters of multiple non-linear mass dampers based on numerical simulation of transient wave propagation through a linear mass-spring carrier structure. Topology optimization is used to obtain optimized distributions of damper mass ratio, natural frequency, damping ratio and nonlinear stiffness coefficient. Large improvements in performance is obtained with optimized parameters and it is shown that nonlinear mass dampers can be more effective for wave attenuation than linear mass dampers.

Key words

Non-linear mass dampers, wave propagation, topology optimization.

1 Introduction

In this paper we report on a systematic approach for optimizing the individual parameters of local non-linear oscillators attached to a linear mass-spring chain. The optimization procedure is based on transient simulation of wave propagation through the linear carrier structure. The work follows a recent theoretical and numerical study (Lazarov and Jensen, 2007) of band gap formation in this non-linear system.

Band gaps are frequency ranges in which waves cannot propagate through the structure (Brillouin, 1953). They occur in infinite periodic systems and also in mass-spring chains with attached oscillators (Liu *et al.*, 2000). In a finite structure excitation with a frequency within the band gap results in a localized response near the point of excitation or at the boundary of the structure (Jensen, 2003). The attached oscillators act as multiple mass dampers (Strasberg and Feit, 1996) that "absorb" waves that propagate in the main chain and can thus be used to reduce the transmission of waves in the chain.

In (Lazarov and Jensen, 2007) it was demonstrated that non-linear oscillators can be used to shift band

gap frequencies and control the propagation of waves in the main chain. Additionally, it was demonstrated that a non-uniform distribution of non-linear coefficients could be used to improve the attenuation properties of the structure. In this paper we apply a systematic design procedure based on the method of topology optimization (Bendsøe and Sigmund, 2003) to find optimized sets of oscillator parameters that minimize the transmission of waves.

The paper is organized as follows. In Section 2 we introduce the physical and numerical model. Typical transient behavior is illustrated in Section 3. Section 4 presents the optimization algorithm including sensitivity analysis. In Section 5 we show examples of optimized oscillator parameters for mono-frequency steady-state behavior as well as full transient behavior. In Section 6 we give conclusions.

2 A mass-spring chain with attached nonlinear oscillators

Fig. 1 illustrates the basic unit cell. The coupled equations for the displacement of a mass in the chain, denoted u_j , and the displacement of the attached oscillator read:

$$\begin{aligned} \ddot{u}_j + 2u_j - u_{j-1} - u_{j+1} &= \beta(\omega^2 q + \gamma q^3 + 2\zeta\omega\dot{q}) \quad (1) \\ \ddot{q} + 2\zeta\omega\dot{q} + \omega^2 q + \gamma q^3 &= -\ddot{u}_j \quad (2) \end{aligned}$$

Non-dimensional parameters in (1)–(2) are $\beta = M/m$ which is the ratio between the mass of the oscillator and the mass to which it is attached, ω is the natural frequency of the oscillator relative to a characteristic frequency of the main chain denoted $\omega_0 = \sqrt{k/m}$, ζ is the damping ratio of the oscillator and γ is the non-linear stiffness coefficient. Additionally, the non-dimensional time measure $\tau = \omega_0 t$ has been introduced.

We consider a finite system based on the building block unit cell in Fig. 1. Fig. 2 shows this finite system.

The number of masses in the chain that carry an oscillator is denoted N . Additionally, a number of masses without attached oscillators are connected to the chain at both ends; N_{in} to the left, and N_{out} to the right of the section with oscillators. All oscillators may have different parameters, denoted β_i , ω_i , γ_i and ζ_i , whereas the main chain consist of equal springs with stiffness k and equal masses m . By setting both end masses to $m/2$ and adding viscous dampers ($c = \sqrt{mk}$) we mimic transparent boundaries at both ends of the chain.

Wave motion is imposed by a time-dependent force $f(t)$ acting on the leftmost mass in the chain. The specific force is to be specified in the forthcoming example sections.

Eqs. (1)–(2) are rewritten in matrix form. We introduce a vector of the unknown displacements:

$$\mathbf{u} = \{u_1 \ u_2 \ \dots \ u_{N+N_{\text{in}}+N_{\text{out}}} \ q_1 \ q_2 \ \dots \ q_N\}^T \quad (3)$$

and can write the model equations as:

$$\ddot{\mathbf{u}} + \mathbf{C}\dot{\mathbf{u}} + \mathbf{K}\mathbf{u} + \mathbf{F}_{\text{non}}(\mathbf{u}) = \mathbf{F}_{\text{ext}} \quad (4)$$

In (4) \mathbf{C} is a damping matrix, \mathbf{K} is a stiffness matrix, \mathbf{F}_{non} is a vector of nonlinear forces and the vector \mathbf{F}_{ext} contains the external load.

3 Numerical simulation of system behavior

The optimization algorithm is based on repeated analyses of (4), sometimes several hundred, thus a fast and robust numerical solver is essential. We use a central-difference explicit scheme (Cook *et al.*, 2002) that is very fast and stable with a sufficiently small time step.

In all numerical simulations we use trivial initial conditions $\mathbf{u} = \dot{\mathbf{u}} = \mathbf{0}$ and the total simulation time is denoted \mathcal{T} .

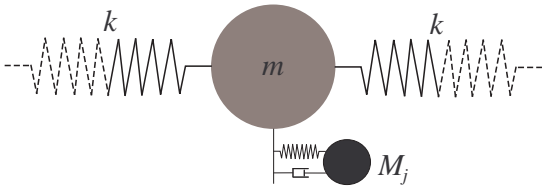


Figure 1. Basic unit cell with a mass in the linear main chain and an attached non-linear oscillator.

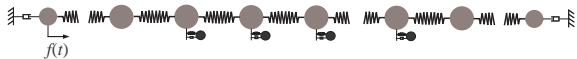


Figure 2. Finite chain consisting of N masses with attached oscillators, N_{in} and N_{out} masses without oscillators in the left and right end. Viscous dampers are added in the ends to simulate transparent boundaries.

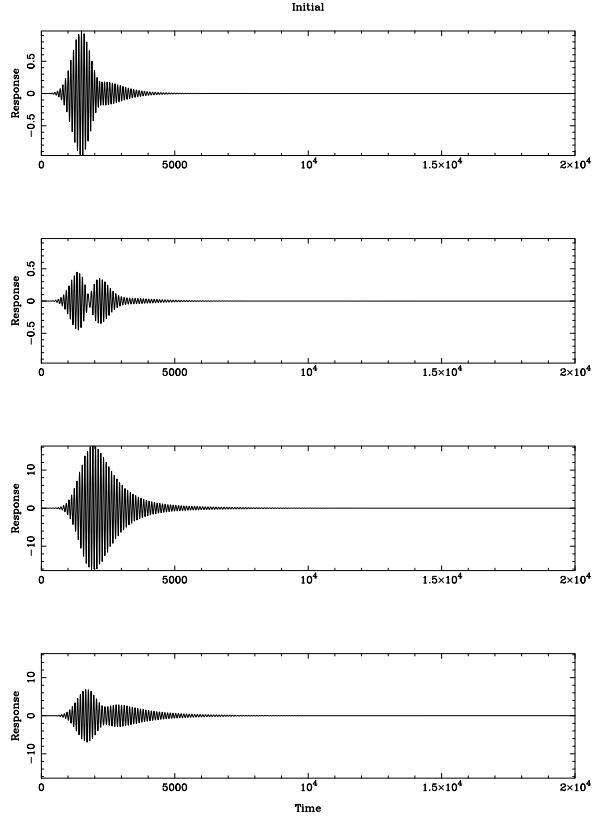


Figure 3. Typical transient response. Figures shows (from top and down): Response of the leftmost and rightmost mass in the chain, response of the first and last attached oscillator.

Fig. 3 shows typical simulation results for transient response of the system – here for the following set of system parameters:

$$\begin{aligned} \beta &= 0.1, \zeta = 0.01, \omega = \Omega = 0.0625, \gamma = 0 \\ N &= 26, N_{\text{in}} = N_{\text{out}} = 1 \\ f(t) &= \sin(\Omega(t - t_0))e^{-\delta(t-t_0)^2} \\ t_0 &= 1500, \delta = 0.000004 \end{aligned}$$

In Fig. 3 the response of the rightmost mass in the chain is depicted (second plot from top). This illustrates the signal actually transmitted through the chain. It is seen that the transmitted signal is composed of a main signal transmitted instantly followed by a trailing signal due to reflections in the structure.

4 Optimization of mass damper parameters

We will in the following quantify the mass damper performance by considering the response of the rightmost mass in the chain integrated over a certain time interval. We consider the general objective function:

$$\Phi = \int_{T_1}^{T_2} c(\mathbf{u})dt \quad (5)$$

in which $c(\mathbf{u})$ is a positive real function of the displacement vector. The smaller Φ is, the more effective the attached mass dampers.

We wish to minimize the functional Φ by manipulating the parameters of each of the N attached oscillators. We may vary all 4 parameters β_i , ω_i , γ_i and ζ_i and have in total $4 \times N$ design variables which are defined by the following relations:

$$\beta_i = \beta_{\min} + x_i^\beta (\beta_{\max} - \beta_{\min}) \quad (6)$$

$$\omega_i = \omega_{\min} + x_i^\omega (\omega_{\max} - \omega_{\min}) \quad (7)$$

$$\gamma_i = \gamma_{\min} + x_i^\gamma (\gamma_{\max} - \gamma_{\min}) \quad (8)$$

$$\zeta_i = \zeta_{\min} + x_i^\zeta (\zeta_{\max} - \zeta_{\min}) \quad (9)$$

in which the subscript min and max refer to upper and lower bounds on the parameters that are specified *a priori*. Thus, continuous design variables varying between 0 and 1 let the material parameters take any value between these min and max values.

A higher mass of the oscillators generally leads to increased wave attenuation. In order to give a fair comparison between the performance of different structures we therefore introduce a limit on the maximum average mass ratio $\tilde{\beta}$, such that:

$$\frac{1}{N} \sum_{i=1}^N \beta_i < \tilde{\beta} \quad (10)$$

The continuous design variables allow us to apply a gradient-based optimization algorithm to optimize the performance of the structure. In order to do this we need to compute the gradient of Φ with respect to x_i^β , x_i^ω , x_i^γ and x_i^ζ . Let x denote any design variable, then by using the chain rule we obtain:

$$\begin{aligned} \frac{d\Phi}{dx} &= \int_{\mathcal{T}_1}^{\mathcal{T}_2} \frac{dc}{d\mathbf{u}} \frac{d\mathbf{u}}{dx} dt = \\ &\int_0^{\mathcal{T}_2} \frac{dc}{d\mathbf{u}} \frac{d\mathbf{u}}{dx} dt - \int_0^{\mathcal{T}_1} \frac{dc}{d\mathbf{u}} \frac{d\mathbf{u}}{dx} dt \end{aligned} \quad (11)$$

In order to eliminate the term $\frac{d\mathbf{u}}{dx}$ we use the adjoint method that has previously been applied to transient design problems (Bendsøe and Sigmund, 2003). We rewrite (11) as:

$$\begin{aligned} \frac{d\Phi}{dx} &= \int_0^{\mathcal{T}_2} \left(\frac{dc}{d\mathbf{u}} \frac{d\mathbf{u}}{dx} + \boldsymbol{\lambda}_1^T \frac{d\mathbf{R}}{dx} \right) dt \\ &\quad - \int_0^{\mathcal{T}_1} \left(\frac{dc}{d\mathbf{u}} \frac{d\mathbf{u}}{dx} + \boldsymbol{\lambda}_2^T \frac{d\mathbf{R}}{dx} \right) dt \end{aligned} \quad (12)$$

in which

$$\mathbf{R} = \ddot{\mathbf{u}} + \mathbf{C}\dot{\mathbf{u}} + \mathbf{K}\mathbf{u} + \mathbf{F}_{\text{non}}(\mathbf{u}) - \mathbf{F}_{\text{ext}} \quad (13)$$

is the residual that vanishes at equilibrium.

We compute

$$\begin{aligned} \frac{d\mathbf{R}}{dx} &= \frac{d\ddot{\mathbf{u}}}{dx} + \frac{d\mathbf{C}}{dx} \ddot{\mathbf{u}} + \mathbf{C} \frac{d\dot{\mathbf{u}}}{dx} + \frac{d\mathbf{K}}{dx} \mathbf{u} + \mathbf{K} \frac{d\mathbf{u}}{dx} \\ &\quad + \frac{d\mathbf{F}_{\text{non}}}{dx} + \frac{d\mathbf{F}_{\text{non}}}{d\mathbf{u}} \frac{d\mathbf{u}}{dx} \end{aligned} \quad (14)$$

since we assume that the external force (wave input) is independent of the design. By inserting (14) and performing partial integration we rewrite (12) into:

$$\begin{aligned} \frac{d\Phi}{dx} &= \int_0^{\mathcal{T}_2} \left(\left(\frac{dc}{d\mathbf{u}} + \ddot{\boldsymbol{\lambda}}_1^T - \dot{\boldsymbol{\lambda}}_1^T \mathbf{C} + \boldsymbol{\lambda}_1^T (\mathbf{K} + \frac{d\mathbf{F}_{\text{non}}}{d\mathbf{u}}) \right) \frac{d\mathbf{u}}{dx} \right. \\ &\quad \left. + \boldsymbol{\lambda}_1^T \left(\frac{d\mathbf{C}}{dx} \ddot{\mathbf{u}} + \frac{d\mathbf{K}}{dx} \mathbf{u} + \frac{d\mathbf{F}_{\text{non}}}{dx} \right) \right) dt \\ &- \int_0^{\mathcal{T}_1} \left(\left(\frac{dc}{d\mathbf{u}} + \ddot{\boldsymbol{\lambda}}_2^T - \dot{\boldsymbol{\lambda}}_2^T \mathbf{C} + \boldsymbol{\lambda}_2^T (\mathbf{K} + \frac{d\mathbf{F}_{\text{non}}}{d\mathbf{u}}) \right) \frac{d\mathbf{u}}{dx} \right. \\ &\quad \left. + \boldsymbol{\lambda}_2^T \left(\frac{d\mathbf{C}}{dx} \ddot{\mathbf{u}} + \frac{d\mathbf{K}}{dx} \mathbf{u} + \frac{d\mathbf{F}_{\text{non}}}{dx} \right) \right) dt \\ &+ \left[\boldsymbol{\lambda}_1^T \mathbf{C} \frac{d\mathbf{u}}{dx} + \boldsymbol{\lambda}_1^T \frac{d\dot{\mathbf{u}}}{dx} - \dot{\boldsymbol{\lambda}}_1^T \frac{d\mathbf{u}}{dx} \right]_0^{\mathcal{T}_2} \\ &\quad - \left[\boldsymbol{\lambda}_2^T \mathbf{C} \frac{d\mathbf{u}}{dx} + \boldsymbol{\lambda}_2^T \frac{d\dot{\mathbf{u}}}{dx} - \dot{\boldsymbol{\lambda}}_2^T \frac{d\mathbf{u}}{dx} \right]_0^{\mathcal{T}_1} \end{aligned} \quad (15)$$

By choosing the following conditions:

$$\boldsymbol{\lambda}_1(\mathcal{T}_2) = \dot{\boldsymbol{\lambda}}_1(\mathcal{T}_2) = 0 \quad (16)$$

$$\boldsymbol{\lambda}_2(\mathcal{T}_1) = \dot{\boldsymbol{\lambda}}_2(\mathcal{T}_1) = 0 \quad (17)$$

and by requiring the initial response of the structure to be independent of the design the terms in the square brackets vanish.

We now require the terms inside the integration terms that are coefficients to $\frac{d\mathbf{u}}{dx}$ to vanish:

$$\ddot{\boldsymbol{\lambda}}_1^T - \dot{\boldsymbol{\lambda}}_1^T \mathbf{C} + \boldsymbol{\lambda}_1^T (\mathbf{K} + \frac{d\mathbf{F}_{\text{non}}}{d\mathbf{u}}) = -\frac{dc}{d\mathbf{u}} \quad (18)$$

$$\ddot{\boldsymbol{\lambda}}_2^T - \dot{\boldsymbol{\lambda}}_2^T \mathbf{C} + \boldsymbol{\lambda}_2^T (\mathbf{K} + \frac{d\mathbf{F}_{\text{non}}}{d\mathbf{u}}) = -\frac{dc}{d\mathbf{u}} \quad (19)$$

These two new transient problems are solved for $\boldsymbol{\lambda}_1$ and $\boldsymbol{\lambda}_2$ and we can compute the sensitivities by the final expression:

$$\begin{aligned} \frac{d\Phi}{dx} &= \int_0^{\mathcal{T}_2} \boldsymbol{\lambda}_1^T \left(\frac{d\mathbf{C}}{dx} \ddot{\mathbf{u}} + \frac{d\mathbf{K}}{dx} \mathbf{u} + \frac{d\mathbf{F}_{\text{non}}}{dx} \right) dt \\ &\quad - \int_0^{\mathcal{T}_1} \boldsymbol{\lambda}_2^T \left(\frac{d\mathbf{C}}{dx} \ddot{\mathbf{u}} + \frac{d\mathbf{K}}{dx} \mathbf{u} + \frac{d\mathbf{F}_{\text{non}}}{dx} \right) dt \end{aligned} \quad (20)$$

Our strategy for optimizing the oscillator parameters can be summarized as: perform repeated analyses of (4), with each analysis followed by a computation of the sensitivities by solving (18), (19) and (20), and the sensitivities provided to a mathematical programming software MMA (Svanberg, 1987) to obtain a design update. This iterative procedure is continued until design converges within a specified threshold.

5 Results

The optimization algorithm is demonstrated by two examples where we consider steady-state and transient response. In both examples we find optimized sets of oscillator parameters that minimize the transmitted wave.

5.1 Steady-state mono-frequency behavior

As the first example we optimize the system parameters for mono-frequency steady-state behavior. The system parameters and excitation is:

$$\begin{aligned} N &= 26, N_{\text{in}} = N_{\text{out}} = 1, \Omega = 0.0625 \\ f(t) &= \sin(\Omega(t - t_0))e^{-\delta(t-t_0)^2}, t < t_0 \\ f(t) &= \sin(\Omega(t - t_0)), t > t_0 \\ t_0 &= 2500, \delta = 0.000002 \end{aligned}$$

and the objective function is evaluated in the time interval specified by $\mathcal{T}_1 = 15000$ and $\mathcal{T}_2 = 20000$. In this way we ensure that the response has reached steady state.

First we consider linear oscillators ($\gamma_i = 0$) and optimize the distribution of natural frequencies and mass ratios. The damping ratio is fixed at $\zeta = 0.01$. We allow the parameters to vary as follows:

$$\begin{aligned} \omega_{\text{min}} &= 0.0615, \omega_{\text{max}} = 0.0630 \\ \beta_{\text{min}} &= 0.0, \beta_{\text{max}} = 0.2 \end{aligned}$$

and keep the maximum average mass ratio at $\tilde{\beta} = 0.1$. Fig. 4 shows the oscillator parameters for the optimized design and Fig. 5 displays the response of the leftmost and rightmost mass in the chain (two top plots) as well as the response of the first and last oscillator (two bottom plots). An almost uniform distribution of natural frequencies is obtained, close to the excitation frequency. This is expected for mono-frequency excitation (cf. working principles of standard mass dampers). The slight detuning between the excitation and natural frequencies is due to the presence of damping. The optimized design is composed mainly of oscillators with the maximum mass ratio ($\beta = 0.2$) and minimum mass ratio ($\beta = 0$ - corresponding to no oscillator). A physical interpretation of the effects of this mass distribution is difficult due to the complexity of the wave motion, but the effect is a reduction of the objective with about 22% compared to an optimized design with a fixed uniform mass ratio of $\beta = 0.1$.

If we allow the non-linear stiffness coefficients to vary the performance of the mass dampers can be further improved. The minimum and maximum coefficients are chosen as:

$$\gamma_{\text{min}} = -0.00006, \gamma_{\text{max}} = 0.00006$$

As seen in Fig. 6 the the distribution of natural frequencies and mass ratios is qualitatively similar to the linear case. However, the distribution is no longer symmetric around the chain center and more irregular. The natural frequencies are lower than for the linear case but this is combined with positive (hardening) non-linear

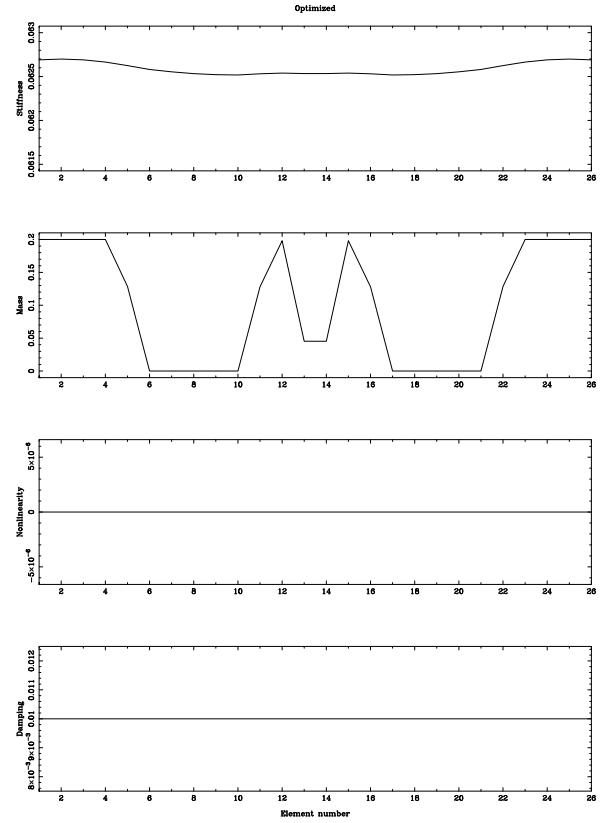


Figure 4. Optimized distribution of natural frequencies and mass ratios for steady-state response. Zero nonlinearity and uniform damping ratio.

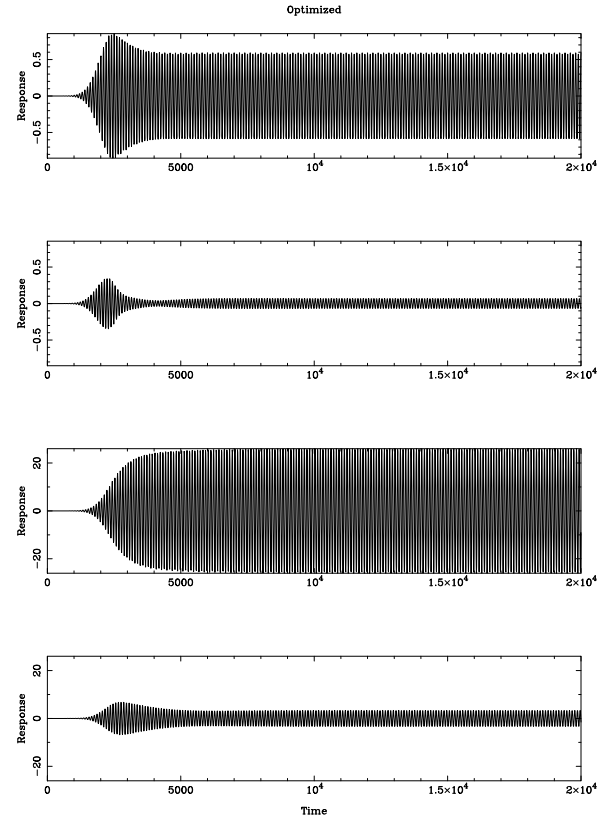


Figure 5. Response for optimized design shown in Fig. 4.

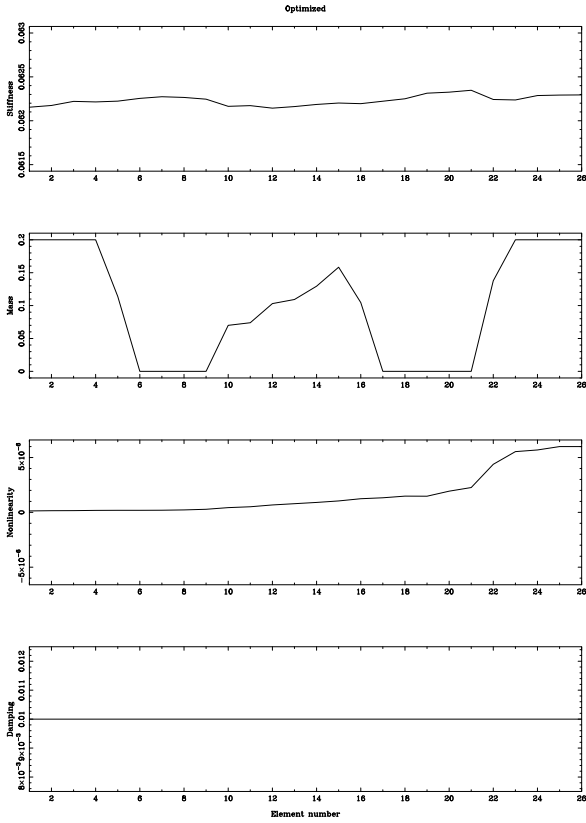


Figure 6. Optimized distribution of natural frequencies, mass ratios and non-linear coefficients for steady-state response. Uniform damping ratio.

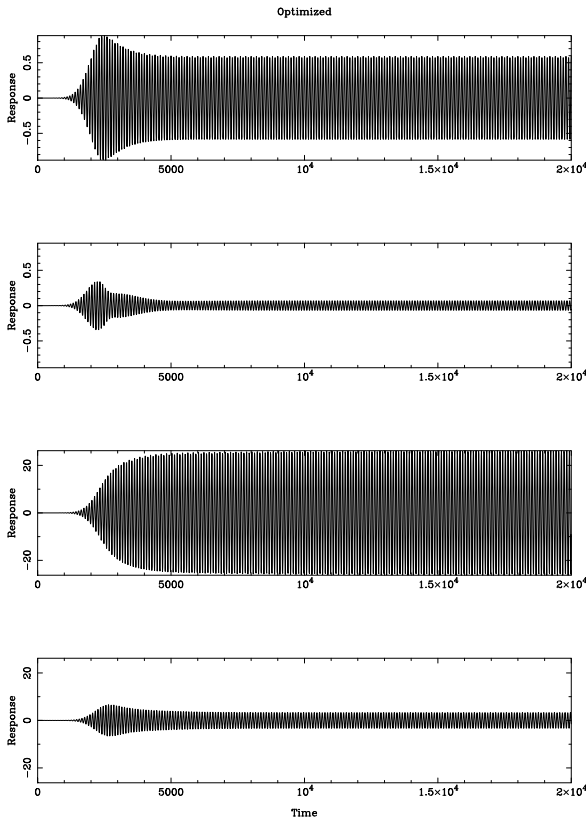


Figure 7. Response for optimized design shown in Fig. 6.

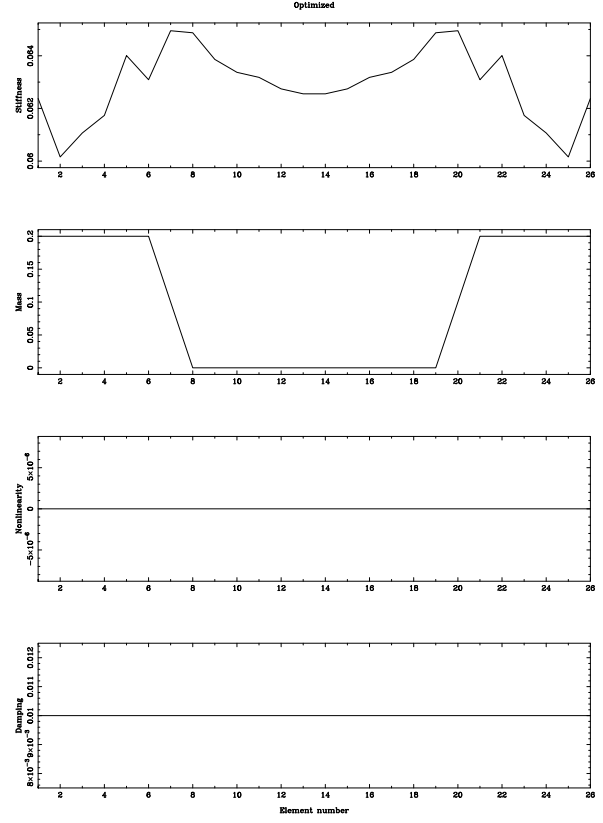


Figure 8. Optimized distribution of natural frequencies and mass ratios for transient response. Zero nonlinearity and uniform damping ratio.

stiffness that increases along the chain length. The objective function is reduced by 2.4% compared to the linear case.

It should be noted that a reduction of the damping ratio ζ always cause a further reduction of Φ . No beneficial effects of a non-uniform damping distribution has been observed.

5.2 Transient response

We now consider the full transient response of the chain. The system parameters and excitation are:

$$\begin{aligned} N &= 26, N_{\text{in}} = N_{\text{out}} = 1, \Omega = 0.0625 \\ f(t) &= \sin(\Omega(t - t_0))e^{-\delta(t-t_0)^2} \\ t_0 &= 2500, \delta = 0.000002 \end{aligned}$$

and the objective function evaluates the response in the entire simulation time interval: $\mathcal{T}_1 = 0$ and $\mathcal{T}_2 = 20000$.

Fig. 8 shows the optimized design with zero nonlinearity and uniform damping ratio $\zeta = 0.01$. The minimum and maximum values of the natural frequency and mass ratio are:

$$\begin{aligned} \omega_{\min} &= 0.060, \omega_{\max} = 0.064 \\ \beta_{\min} &= 0.0, \beta_{\max} = 0.2 \end{aligned}$$

with a constraint on the average mass ratio of $\bar{\beta} = 0.1$.

Fig. 8 shows a larger variation of the natural frequen-

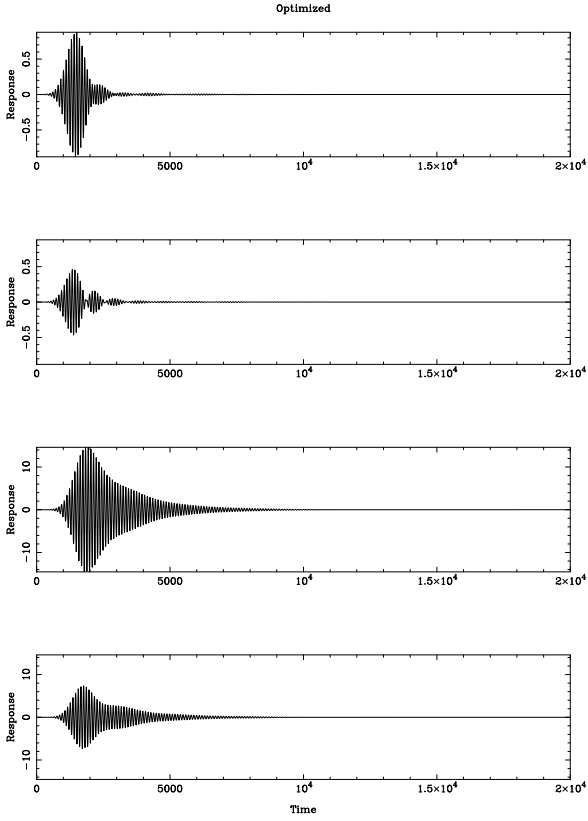


Figure 9. Response for optimized design shown in Fig. 8.

cies than for the steady-state case. This is a results of the broader frequency content of the wave pulse, and thus a broader spectrum of oscillator frequencies are needed to quench the signal effectively. The response shown in Fig. 9 reveals that the output signal consists of a main signal followed by smaller trailing pulses.

We now allow the nonlinear stiffness to vary between:

$$\gamma_{\min} = -0.00006, \gamma_{\max} = 0.00006$$

Interestingly, the γ -distribution shows alternating sections of softening and hardening non-linearities in the optimized design. This is combined with an irregular ω -distribution. As a result the trailing pulses in the output signal (Fig. 11) are now significantly reduced in magnitude, leading to a further reduction of the objective function by 21%. Thus, adding nonlinearities allow for a significant extra reduction of the transmission of a pulse, whereas for the steady-state response the effect was smaller.

6 Conclusion

We have used topology optimization based on transient simulation to design the individual parameters of nonlinear oscillators attached to linear mass-spring chain. The optimized parameters minimize the transmission of wave pulses through the main chain.

The natural frequency, mass ratio, nonlinear stiffness and damping ratio of each oscillator were optimized.

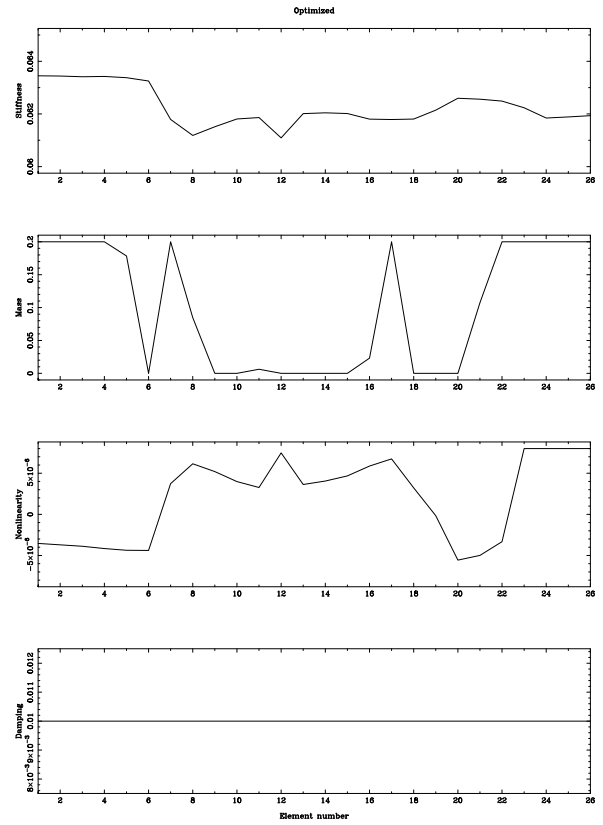


Figure 10. Optimized distribution of natural frequencies, mass ratios and non-linear coefficients for transient response. Zero nonlinearity and uniform damping ratio.

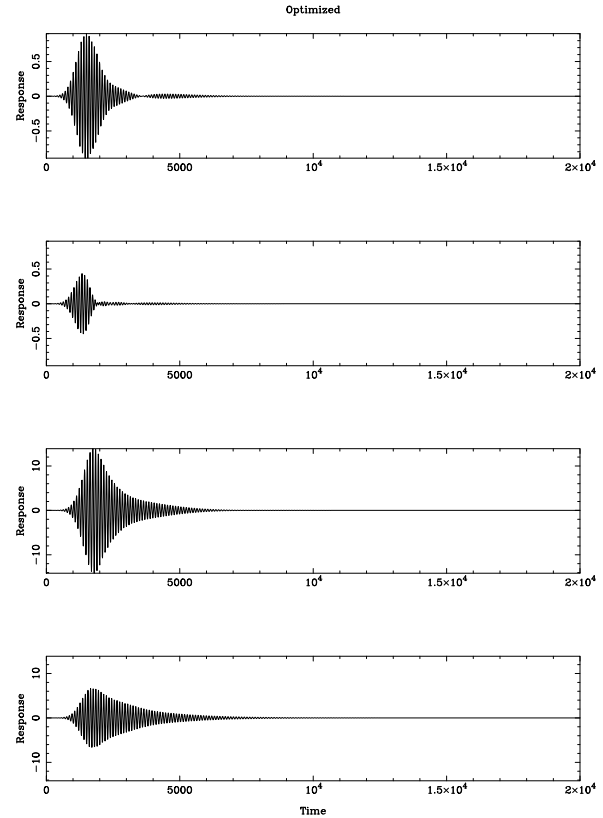


Figure 11. Response for optimized design shown in Fig. 10.

Non-trivial parameter distributions were obtained leading to a significant reduction of the transmitted wave signal. Two examples were considered. For a mono-frequency steady-state response it was noted that a hardening but non-uniform nonlinearity was favored whereas for a full transient simulation combinations of softening and hardening nonlinearities appeared in the optimized design. It was shown also that including non-linear stiffness was beneficial compared to having only a linear oscillator. This was most pronounced for when considering the full transient response.

Acknowledgement

This work was supported by grant 274-05-0498 from the Danish Research Council for Technology and Production Sciences.

References

- Bendsøe, M. P. and O. Sigmund (2003). *Topology Optimization - Theory, Methods and Applications*. Springer Verlag, Berlin Heidelberg.
- Brillouin, L. (1953). *Wave propagation in periodic structures*. 2 ed.. Dover Publications.
- Cook, R. D., D. S. Malkus, M. E. Plesha and R. J. Witt (2002). *Concepts and applications of finite element analysis, 4th Ed.*. Wiley, New York.
- Jensen, J. S. (2003). Phononic band gaps and vibrations in one- and two-dimensional mass-spring structures. *Journal of Sound and Vibration* **266**(5), 1053–1078.
- Lazarov, B. S. and J. S. Jensen (2007). Low-frequency band gaps in chains with attached non-linear oscillators. *International Journal of Non-Linear Mechanics* **42**(10), 1186–1193.
- Liu, Z., X. Zhang, Y. Mao, Y. Y. Zhu, Z. Yang, C. T. Chan and P. Sheng (2000). Locally resonant sonic materials. *Science* **289**, 1734–1736.
- Strasberg, M. and D. Feit (1996). Vibration damping of large structures induced by attached small resonant structures. *Journal of the Acoustical Society of America* **99**(1), 335–344.
- Svanberg, K. (1987). The method of moving asymptotes - a new method for structural optimization. *International Journal for Numerical Methods in Engineering* **24**, 359–373.



Contents lists available at ScienceDirect

Comput. Methods Appl. Mech. Engrg.

journal homepage: www.elsevier.com/locate/cma

Space–time topology optimization for one-dimensional wave propagation

Jakob S. Jensen *

Department of Mechanical Engineering, Solid Mechanics, Nils Koppels Allé, Building 404, Technical University of Denmark, 2800 Lyngby, Denmark

ARTICLE INFO

Article history:

Received 11 March 2008
 Received in revised form 30 September 2008
 Accepted 3 October 2008
 Available online 29 October 2008

Keywords:

Topology optimization
 Wave propagation
 Transient loading
 Dynamic materials

ABSTRACT

A space–time extension of the topology optimization method is presented. The formulation, with design variables in both the spatial and temporal domains, is used to create structures with an optimized distribution of material properties that can vary in time. The method is outlined for one-dimensional transient wave propagation in an elastic rod with time dependent Young's modulus. By two simulation examples it is demonstrated how dynamic structures can display rich dynamic behavior such as wavenumber/frequency shifts and lack of energy conservation. The optimization method's potential for creating structures with novel dynamic behavior is illustrated by a simple example; it is shown that an elastic rod in which the optimized stiffness distribution is allowed to vary in time can be much more efficient in prohibiting wave propagation compared to a static bandgap structure. Optimized designs in form of spatio-temporal laminates and checkerboards are generated and discussed. The example lays the foundation for creating designs with more advanced functionalities in future work.

© 2008 Elsevier B.V. All rights reserved.

1. Introduction

Topology or material layout optimization has gained popularity as a design tool in academics and industry. This is mainly due to the large design freedom and the use of adjoint sensitivity analysis that allows for efficient handling of the many element design variables usually appearing in the discretized models. Topology optimization was originally introduced to design stiff lightweight mechanical structures [2] and has since been extended to a variety of different settings. A fairly recent overview of applications can be found in [4] and new applications appear regularly, e.g. the recent works on optimization of ferromagnetic materials [9], incompressible materials [7], electrostatically actuated devices [38], acousto-structural interaction [37], and damage detection [20].

A number of papers have considered optimization of structures based on its transient response, see, e.g. [17] for a review, and recently there has been an increasing interest in using topological design variables for these transient problems, e.g. in structural dynamics [27,34], for thermal problems [33,21], crashworthiness [29], electromagnetics [10,28], and structural wave propagation [13]. In this paper, the topology optimization concept for transient loads is extended with design variables in the temporal domain, in order to allow for the optimized material properties to vary in time. The extended method is demonstrated for wave propagation in a one-dimensional (1D) model of an elastic rod with time dependent Young's modulus. The present study is closely related to recent works [25,26] that present a solid mathematical foundation

for spatio-temporal design problems for the 1D and 2D wave equation.

By including design variables in the time domain the optimization problem becomes equivalent to the classical problem of optimal control [18]. Holtz and Arora [14] solved an optimal control problem by using adjoint sensitivity analysis and mathematical programming and exemplified the method with obtaining optimized trajectories for a scalar control force. The contribution of the present work can be viewed as an extension to [14] by considering the material layout problem with topological design variables.

The dynamics of structures with time varying material parameters have been studied in a number of works. Clark [11] demonstrated numerically the possibility for vibration control by using stiffness switching induced by piezoelectric materials, Ramaratnam and Jalili [30] considered a bi-stiffness spring setting and demonstrated vibration control theoretically and experimentally, and Issa et al. [16] considered a similar problem with stiffness switching induced by a controllable hinge and showed vibration attenuation numerically and experimentally. Other examples of geometric stiffness control have been demonstrated in [19,31] and alternatively magneto- or electro-rheological fluids can be used to obtain a similar control of the stiffness in the temporal domain. Recently reported is the possibility for using a combination of non-linear materials and external high-frequency excitation that results in an effective change of the material stiffness [6].

General properties of space–time varying materials (denoted “dynamic materials”) has been studied, e.g. in [22,5]. The recent monograph [24] gives an extensive coverage of the subject with a special emphasis on space–time variation of electromagnetic

* Tel.: +45 45 25 42 50; fax: +45 45 93 14 75.
 E-mail address: jsj@mek.dtu.dk

material properties. Means for realization of time varying properties (such as the dielectric constant) is the use of non-linear optic material or with the use of ferroelectric/ferromagnetic materials.

In order to keep the derivations simple and at the same time consider structures that are realizable as mechanical systems, it is chosen to consider the case of time varying stiffness and a constant material density. The starting point is a dynamic FE model:

$$\mathbf{M}\ddot{\mathbf{u}} + \mathbf{C}\dot{\mathbf{u}} + \mathbf{K}(t)\mathbf{u} = \mathbf{f}(t), \tag{1}$$

in which \mathbf{M} and \mathbf{C} are constant mass and damping matrices and $\mathbf{K}(t)$ is the time dependent stiffness matrix. The vector \mathbf{u} contain the nodal displacements and $\mathbf{f}(t)$ is the time dependent load.

The paper is organized as follows. Section 2 introduces the space–time design variables and the basic notation is defined. In Section 3, the time integration algorithm is described and basic simulation results are presented and compared to exact results from literature. Section 4 covers sensitivity analysis w.r.t. space–time design variables. In Section 5, an example of an optimized dynamic structure is given. The space–time distribution of stiffness in a 1D elastic rod is optimized in order to minimize wave transmission; a so-called dynamic bandgap structure. In Section 6, the results are summarized and conclusions are given.

2. Space–time design variables for a one-dimensional problem

In traditional topology optimization with the density approach [1], a single design variable is introduced for each element in the finite element model. This is illustrated in Fig. 1 for a single spatial dimension.

The design variables are denoted x_1, x_2, \dots, x_N where N is the number of elements in the model. The design variables are collected in the vector \mathbf{x} . The value of x_i governs the material properties of the corresponding element according to a specified material interpolation model [3].

In the proposed formulation, we extend the traditional approach by allowing the material properties in a spatial element to change in time. This is facilitated by introducing a two-dimensional design element grid (for one spatial dimension), see Fig. 2.

An array of design variable vectors is introduced:

$$\mathbf{X} = \{\mathbf{x}_1, \mathbf{x}_2, \dots, \mathbf{x}_M\}, \tag{2}$$

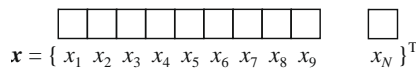


Fig. 1. Traditional design variable concept for topology optimization with the density approach for one spatial dimension.

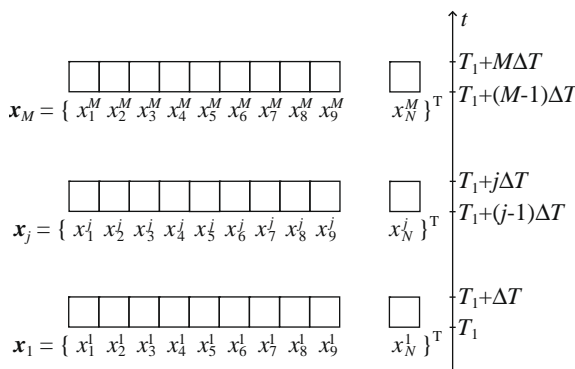


Fig. 2. Extended topology optimization approach with space–time design variables for one spatial dimension.

in which each design vector in the array contains the element-wise design variables for a specific time interval. For time interval j , the design vector components are specified as

$$\mathbf{x}_j = \{x_1^j, x_2^j, \dots, x_N^j\}^T. \tag{3}$$

In (2) M is the number of time intervals in which the material properties can attain different values. The temporal design starts at $t = \mathcal{T}_1$ and continues to $t = \mathcal{T}_2 = \mathcal{T}_1 + M\Delta\mathcal{T}$. For simplicity, uniform intervals $\Delta\mathcal{T}$ are specified but non-uniform intervals can readily be used by the presented formulation.

The choice of $\Delta\mathcal{T}$ should depend on the specific problem considered, such as the frequency of the wave, but should also take into account the temporal discretization used in the time integration algorithm. In the present work a central-difference explicit scheme with a fixed time step Δt is applied. In this case it is necessary that $\Delta t \ll \Delta\mathcal{T}$ in order for the numerical results to be accurate. Another and perhaps more natural choice, could be to use a space–time finite element formulation, e.g. [15]. This will be subject for future work.

3. Numerical simulation of dynamic structures

A standard central-difference explicit scheme is used to solve (1) (see, e.g. [12]). Based on the displacement vector \mathbf{u}_n at the current time step and at the previous time step \mathbf{u}_{n-1} , the displacement vector at the next time step \mathbf{u}_{n+1} is approximated as

$$\frac{1}{(\Delta t)^2} \mathbf{M} \mathbf{u}_{n+1} \approx \mathbf{f}_n - \mathbf{K}_n \mathbf{u}_n + \left(\frac{2}{(\Delta t)^2} \mathbf{M} - \frac{1}{\Delta t} \mathbf{C} \right) \mathbf{u}_n - \left(\frac{1}{(\Delta t)^2} \mathbf{M} - \frac{1}{\Delta t} \mathbf{C} \right) \mathbf{u}_{n-1}, \tag{4}$$

in which \mathbf{f}_n and \mathbf{K}_n is the load vector and stiffness matrix at the current time step. The scheme in (4) is efficient, especially if \mathbf{M} is diagonal (this simplification is made throughout the examples in this paper). However, one has to ensure that the time step Δt is sufficiently small (CFL-condition [12]) to ensure stability of the scheme.

In the following sections, (4) is used to simulate the behavior of structures with a time dependent stiffness matrix. The examples will serve both as an illustration of typical behavior observed when the material properties vary in time, as well as documentation for the applicability (and limitations) of the proposed time integration scheme.

3.1. Instant change of material properties

The propagation of a wave in a medium that experiences an instant change of the material parameters was studied theoretically in [36], in which it is shown that a forward travelling wave splits up in a “transmitted” forward travelling wave and a “reflected” backward travelling wave, and that they both retain the shape of the original wave. Fig. 3 shows a 1D elastic rod in which the material properties for $t < t_0$ are $\rho = E = 1$ and for $t = t_0$ the stiffness is changed to $E = E_0$ whereas the density is unchanged. Shown also are snapshots of the simulated wave motion.

Weekes [36] predicts the amplitudes of the forward travelling wave, T , and the backward travelling wave, R :

$$T = \frac{\sqrt{E_0} + 1}{2\sqrt{E_0}}, \quad R = \frac{\sqrt{E_0} - 1}{2\sqrt{E_0}}. \tag{5}$$

In Fig. 4 the amplitude of the forward and backward travelling waves are estimated based on simulation of the wave propagation with (4). The amplitudes are given relative to the input amplitude and are computed for different values of E_0 . The results are compared to the exact values in (5) and the agreement is seen to be very

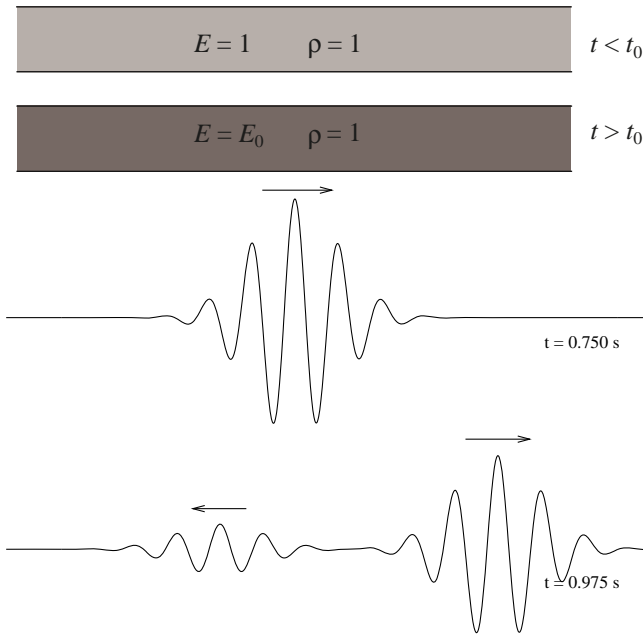


Fig. 3. Top: one-dimensional medium with an instant change in the stiffness for $t = t_0$. Bottom: two snapshots of the wave motion with indication of the propagation direction.

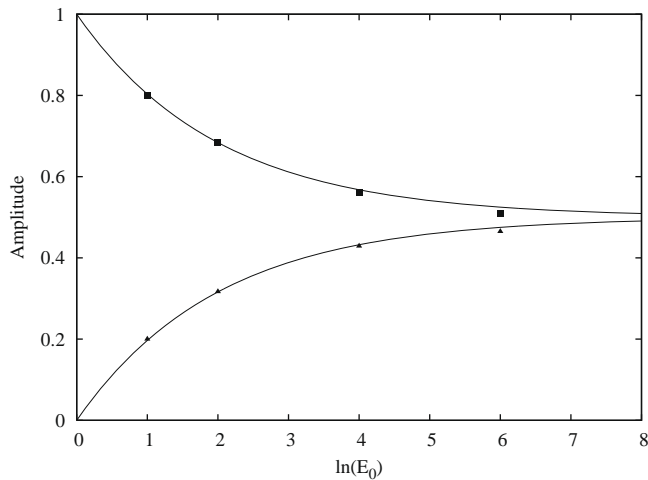


Fig. 4. Amplitude of the forward and backward travelling waves versus the stiffness E_0 . Comparison between exact (solid lines) and numerical results (discrete markers).

good for low to moderate stiffness contrasts ($E_0 < 50$). Interestingly, as the material contrast grows to infinity the wave splits up in a forward and backward travelling wave of equal magnitude.

An external force is generally required to change the material properties, hence the mechanical energy in the wave is not conserved. Based on the formulas for the forward and backward travelling waves in [36] the relative change of mechanical energy occurring at $t = t_0$ is found as

$$\frac{\Delta E_{\text{mek}}}{E_{\text{mek}}} = \frac{1}{2}(E_0 - 1), \quad (6)$$

thus, if the stiffness of the medium is increased ($E_0 > 1$) energy is supplied to the wave, whereas for $E_0 < 1$ energy is taken out of the wave. Simulation results show excellent agreement with the analytical result.

Fig. 7 shows simulated values for E_{mek} and also E_{kin} and E_{pot} versus time for the case of $E_0 = 3$. The instant doubling of the mechanical energy is noted at the time of instant material property change – as predicted by (6). Furthermore, oscillations in the kinetic and potential energy are seen in the short time interval after the material change for which the forward and backward travelling waves have a spatial overlap.

Thus, it has been demonstrated that the simple time integration algorithm produces accurate results in the case of instant material properties changes, at least in the case of low to moderate stiffness contrasts.

3.2. Moving material interface

Weekes [35] studied wave propagation in structures with a moving material interface. Exact results were provided for the example illustrated in Fig. 5.

Here, the interface between a material with stiffness $E = 1$ and a material with stiffness $E = E_0$ moves with constant speed V towards left. A wave that propagates towards right meets the moving interface and is partly transmitted and partly reflected at the interface. It was shown in [35] that the relative amplitudes of the transmitted wave T and the reflected wave R are independent of the material interface speed

$$T = \frac{2}{\sqrt{E_0} + 1}, \quad R = \frac{\sqrt{E_0} - 1}{\sqrt{E_0} + 1}, \quad (7)$$

which correspond to the known results for transmission and reflection of waves at an immovable interface.

However, the interface speed V causes a shift in the wavenumber (or frequency) of the transmitted and reflected waves (Doppler shift). The relative wavenumber shift of the reflected wave is found as

$$\left(\frac{\Delta\gamma}{\gamma_0}\right)_R = \frac{1 + V}{1 - V}, \quad (8)$$

i.e. the shift depends only on the interface speed. Here, it should be noted that V is given relative to the wave speed in the material in which the incoming wave propagates ($c = \sqrt{E/\rho} = 1$). The shift

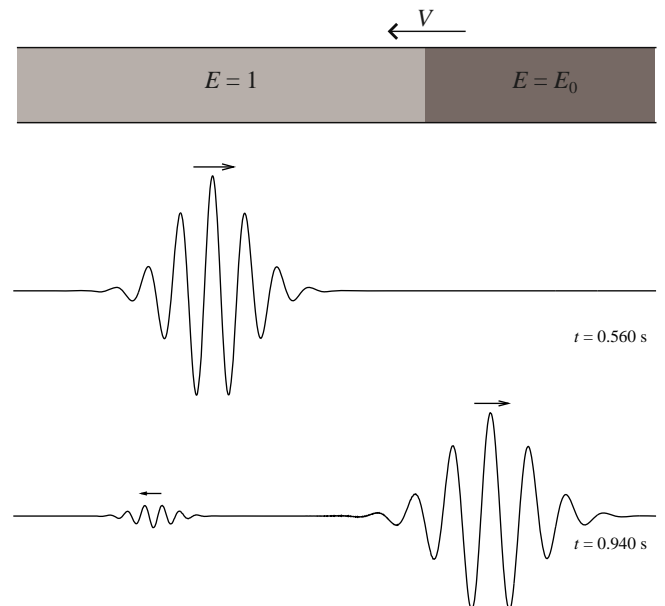


Fig. 5. Top: one-dimensional elastic rod with a moving material interface. Bottom: two snapshots of the wave motion indicating the propagation direction.

does not depend on the material properties of the second material (i.e. E_0).

Fig. 6 shows the computed wavenumber shift compared to the exact value (8). A good accuracy of the numerical results is noted for values of the interface speed up to about $V = 0.5$, but for higher values the numerical simulations overestimate the shift. This is due to an insufficient number of elements per wavelength resulting from the increase in wavenumber (decrease in wavelength). The presented results have been computed with 80 elements per wavelength in material 1 (for $V = 0$). For $V = 0.6$ this has decreased to only 20 elements per wavelength thereby leading to inaccurate results. The shift in wavenumber is seen to approach infinity when $V \rightarrow 1$. This corresponds to the case when the interface speed approaches the wave speed.

Similarly to the previous example, the energy in the wave is not conserved and the increase in energy can be computed based on the results in [35]. The exact results are shown in Fig. 8 (the lengthy but explicit formula is not given) and compared to the numerical results for four different values of E_0 . As seen in Fig. 8 the results deviate significantly even for relative small values of E_0 (such as $E_0 = 1.25$) also for $V \ll 0.5$. Thus, the reason for this discrepancy is not insufficient discretization of the wave.

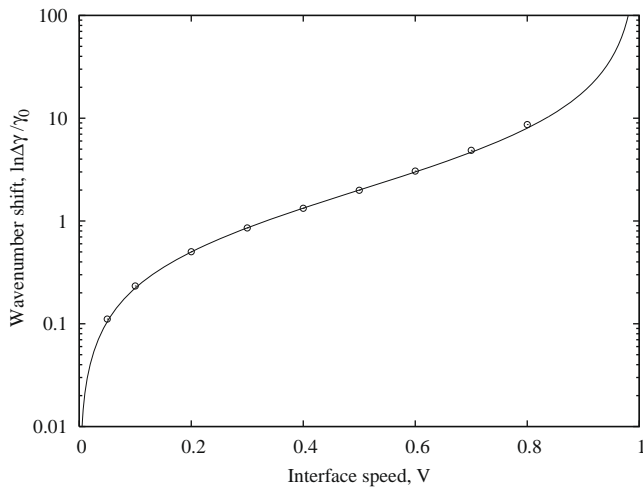


Fig. 6. Shift in the wavenumber of the reflected wave versus the interface speed V . Comparison between exact results (solid line) and numerical simulation (discrete markers).

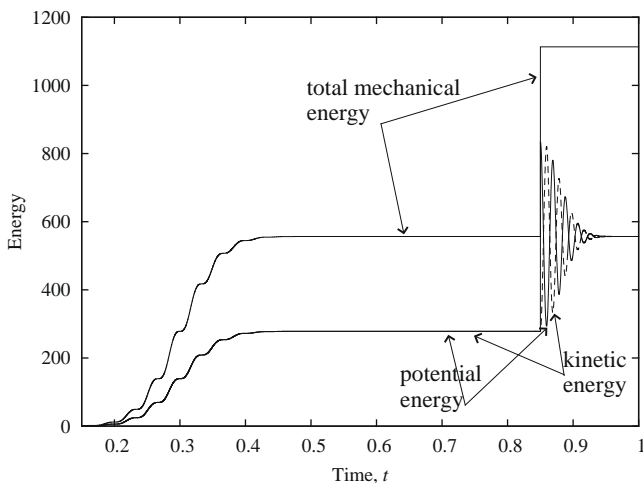


Fig. 7. Total mechanical, potential, and kinetic energy versus time. Instant change of stiffness to $E_0 = 3$ at $t = 0.85$ s.

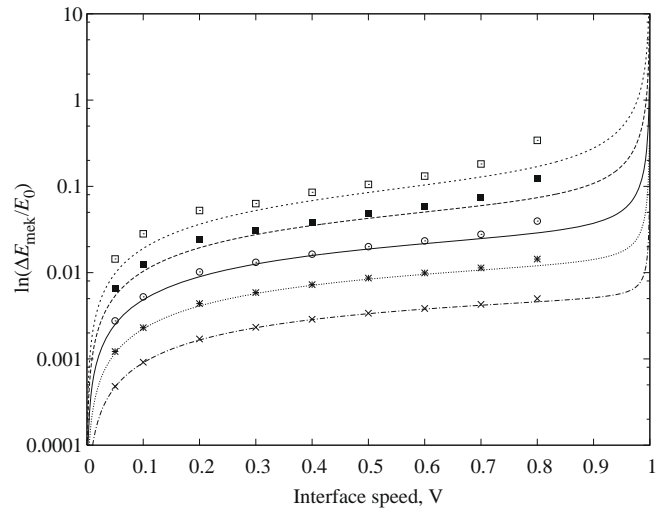


Fig. 8. The relative jump in the total mechanical energy versus the interface speed V for $E_0 = 1.5, E_0 = 1.25, E_0 = 1.11, E_0 = 1.05, E_0 = 1.02$ (top-down). Comparison between exact results (lines) and numerical simulation (markers).

The reason for the overestimation of the energy increase is the time integration scheme and the origin of the problem is illustrated in Fig. 9. The plots show the computed wave velocities for

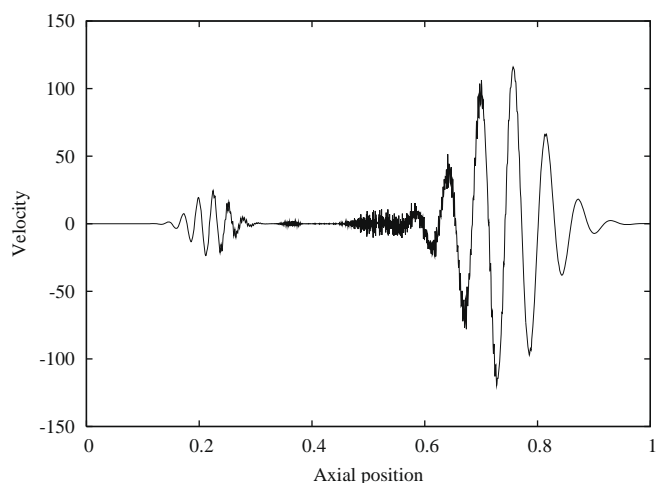
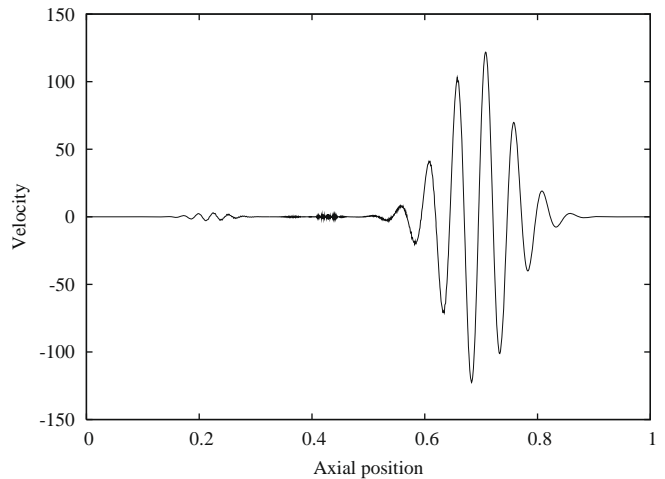


Fig. 9. Wave velocities for $V = 0.3$ for two different values of E_0 , left: $E_0 = 1.05$ and right: $E_0 = 1.5$.

$V = 0.3$ at a given time instant for two values of E_0 . Spurious high-frequency oscillations in the velocities are noted which add substantially to the computed energies and these grow stronger with increasing stiffness contrast E_0 . The oscillations are a result of the fact that the simple time integration scheme is incapable of treating finite time-discontinuous materials properties properly.

The oscillations not only lead to inaccurate predictions of the energy change, but more importantly, to instabilities in the optimization algorithm. Thus, the problem should be resolved. A natural way is to use a more advanced time integration scheme. Specialized schemes have been developed for temporal laminates in [36] and for structures with moving material interfaces in [35], but these cannot be directly applied in this case since the appearance of the structure is not known a priori. Alternatively, the use of a space–time finite element scheme could probably overcome this problem. Another, simpler, way to reduce the presence of spurious oscillations, while still preserving the overall behavior, is to add stiffness dependent damping that dissipates mainly the high-frequency oscillations

$$\mathbf{C} = \frac{\beta}{\omega_0^2} \tilde{\mathbf{K}}, \quad (9)$$

in which β is a damping coefficient, ω_0 is the center-frequency of the wave and $\tilde{\mathbf{K}}$ is a constant stiffness matrix corresponding to the normalized background material. The scaling of the damping coefficient with ω_0^{-2} gives β the unit $(\text{kg m})^{-1}$.

In Fig. 10, the effect of adding damping with $\beta = 0.1$ is illustrated. As noted the overall behavior is retained while the spurious

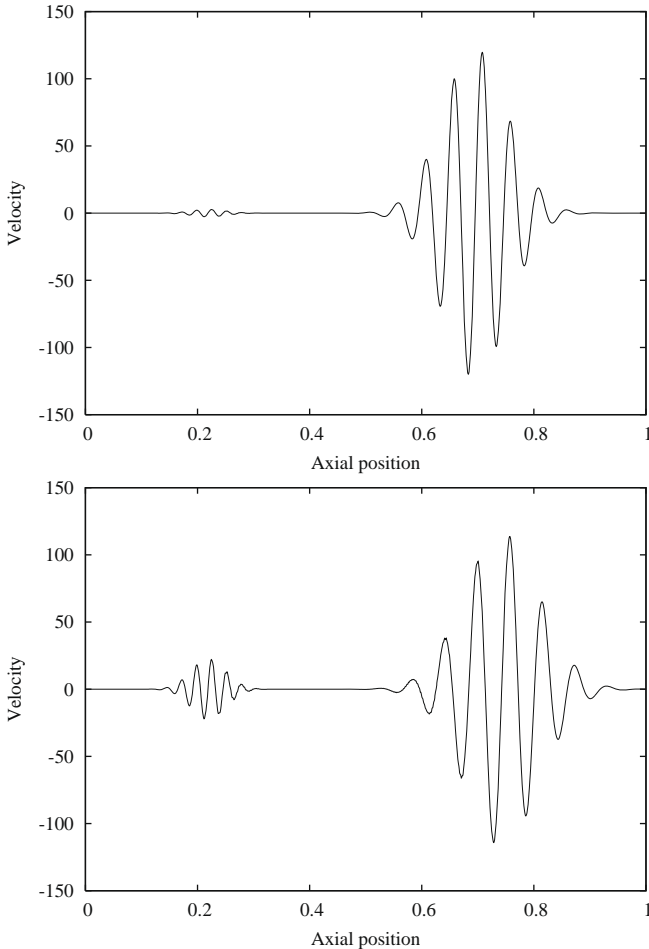


Fig. 10. Wave velocities for $V = 0.3$ and $\beta = 0.1$ for two different values of E_0 , left: $E_0 = 1.05$ and right: $E_0 = 1.5$.

oscillations are eliminated. Still, for higher values of E_0 the problem persists and only a better numerical procedure will allow for simulation and optimization of dynamic structures with higher material contrasts. But for a basic illustration of the method and its potentials, the simple fix will suffice.

4. Design sensitivity analysis

After these examples, illustrating the rich dynamic behavior of structures with space–time varying properties, focus is now put on the design problem. For this purpose analytical expressions for the design sensitivities are derived.

The optimization scheme is based on the minimization of an objective function that is assumed to be written on the following form:

$$\Phi = \int_0^{\mathcal{T}} c(\mathbf{u}, \mathbf{X}, t) dt. \quad (10)$$

The derivative of a given quantity w.r.t. a single design variable that corresponds to the j 'th time interval and the i 'th spatial variable is denoted

$$(\cdot)_i^j = \frac{\partial}{\partial x_i^j} \quad (11)$$

and thus the sensitivity of Φ w.r.t. the design variable x_i^j is

$$\Phi_i^j = \int_0^{\mathcal{T}} \left(\frac{\partial c}{\partial \mathbf{u}} \mathbf{u}_i^j + c_i^j \right) dt. \quad (12)$$

Eq. (12) involves the term \mathbf{u}_i^j and since \mathbf{u} is an implicit function of the design variables the term is not easily evaluated. To overcome this difficulty, the adjoint method can be used to replace this term with one that is more easily computed. For this purpose, the residual vector \mathbf{R} is introduced

$$\mathbf{R} = \mathbf{M}\ddot{\mathbf{u}} + \mathbf{C}\dot{\mathbf{u}} + \mathbf{K}\mathbf{u} - \mathbf{f} = \mathbf{0} \quad (13)$$

and differentiated w.r.t. x_i^j

$$\mathbf{R}_i^j = \mathbf{M}\ddot{\mathbf{u}}_i^j + \mathbf{C}\dot{\mathbf{u}}_i^j + \mathbf{K}_i^j \mathbf{u} + \mathbf{K} \mathbf{u}_i^j = \mathbf{0}, \quad (14)$$

in which it has been used that \mathbf{M} , \mathbf{C} , and \mathbf{f} are assumed to independent of the design.

With the aid of (14) and (12) is reformulated as

$$\Phi_i^j = \int_0^{\mathcal{T}} \left(\frac{\partial c}{\partial \mathbf{u}} \mathbf{u}_i^j + c_i^j + \lambda_j^T \mathbf{R}_i^j \right) dt, \quad (15)$$

in which λ_j is an arbitrary Lagrangian vector belonging to j 'th time interval.

Eq. (14) is inserted into (15)

$$\Phi_i^j = \int_0^{\mathcal{T}} \left(\lambda_j^T \mathbf{M}\ddot{\mathbf{u}}_i^j + \lambda_j^T \mathbf{C}\dot{\mathbf{u}}_i^j + \left(\lambda_j^T \mathbf{K} + \frac{\partial c}{\partial \mathbf{u}} \right) \mathbf{u}_i^j + \lambda_j^T \mathbf{K}_i^j \mathbf{u} + c_i^j \right) dt. \quad (16)$$

The terms involving $\ddot{\mathbf{u}}_i^j$ and $\dot{\mathbf{u}}_i^j$ are rewritten using integration by parts

$$\begin{aligned} \int_0^{\mathcal{T}} \lambda_j^T \mathbf{M}\ddot{\mathbf{u}}_i^j dt &= [\lambda_j^T \mathbf{M}\dot{\mathbf{u}}_i^j]_0^{\mathcal{T}} - \int_0^{\mathcal{T}} \dot{\lambda}_j^T \mathbf{M}\dot{\mathbf{u}}_i^j dt \\ &= [\lambda_j^T \mathbf{M}\dot{\mathbf{u}}_i^j]_0^{\mathcal{T}} - [\dot{\lambda}_j^T \mathbf{M}\mathbf{u}_i^j]_0^{\mathcal{T}} + \int_0^{\mathcal{T}} \ddot{\lambda}_j^T \mathbf{M}\mathbf{u}_i^j dt, \end{aligned} \quad (17)$$

$$\int_0^{\mathcal{T}} \lambda_j^T \mathbf{C}\dot{\mathbf{u}}_i^j dt = [\lambda_j^T \mathbf{C}\mathbf{u}_i^j]_0^{\mathcal{T}} - \int_0^{\mathcal{T}} \dot{\lambda}_j^T \mathbf{C}\mathbf{u}_i^j dt.$$

All boundary contributions in (17) vanish if we impose the following terminal conditions for λ :

$$\lambda_j(\mathcal{T}) = \dot{\lambda}_j(\mathcal{T}) = \mathbf{0} \quad (18)$$

and further require that the initial response at $t = 0$ is independent of the design such that

$$\mathbf{u}_i^j(0) = \dot{\mathbf{u}}_i^j(0) = \mathbf{0}. \quad (19)$$

Inserting (17)–(19) into (16) yields

$$\Phi_i^j = \int_0^{\mathcal{T}} \left(\left(\dot{\lambda}_j^T \mathbf{M} - \dot{\lambda}_j^T \mathbf{C} + \dot{\lambda}_j^T \mathbf{K} + \frac{\partial \mathcal{C}}{\partial \mathbf{u}} \right) \mathbf{u}_i^j + \dot{\lambda}_j^T \mathbf{K}_i^j \mathbf{u} + c_i^j \right) dt. \quad (20)$$

The arbitrary adjoint vectors λ_j are now chosen so that the first parenthesis in (20) vanishes

$$\ddot{\lambda}_j^T \mathbf{M} - \dot{\lambda}_j^T \mathbf{C} + \dot{\lambda}_j^T \mathbf{K} + \frac{\partial \mathcal{C}}{\partial \mathbf{u}} = \mathbf{0}, \quad (21)$$

which, after transposing, can be rewritten as

$$\mathbf{M}^T \ddot{\lambda}_j + \mathbf{C}^T \dot{\lambda}_j + \mathbf{K}^T \lambda_j = - \left(\frac{\partial \mathcal{C}}{\partial \mathbf{u}} \right)^T. \quad (22)$$

As appears from (22) all adjoint equations are identical since the r.h.s. does not depend on j . Thus only one equation needs to be solved and the substitution $\lambda_j = \lambda$ is made.

Eq. (22) is conveniently rewritten by introducing the new time variable $\tau = \mathcal{T} - t$

$$\mathbf{M}^T \ddot{\lambda} + \mathbf{C}^T \dot{\lambda} + \mathbf{K}^T \lambda = - \left(\frac{\partial \mathcal{C}}{\partial \mathbf{u}} \right)^T_{\mathcal{T}-\tau}. \quad (23)$$

Thus, with symmetric matrices, $\mathbf{M}^T = \mathbf{M}$, $\mathbf{C}^T = \mathbf{C}$, $\mathbf{K}^T = \mathbf{K}$, the l.h.s. of (23) is identical to that of the original model equation (1), the only difference being the new adjoint load that appears on the r.h.s. However, it should be noted that the two equations cannot be solved simultaneously due the r.h.s. of (23) that requires an evaluation of $\partial \mathcal{C} / \partial \mathbf{u}$ at time $\mathcal{T} - \tau$.

When λ fulfills (23) the expression for the sensitivities reduces to

$$\Phi_i^j = \int_0^{\mathcal{T}} (\lambda^T (\mathcal{T} - t) \mathbf{K}_i^j \mathbf{u} + c_i^j) dt, \quad (24)$$

in which it is specified that λ should be evaluated at $\tau = \mathcal{T} - t$. The term \mathbf{K}_i^j denotes the derivative of the stiffness matrix w.r.t. the i 'th element design variable in the j 'th time interval, thus

$$\mathbf{K}_i^j = \mathbf{0} \text{ for } t < \mathcal{T}_j^- \text{ and } t > \mathcal{T}_j^+, \quad (25)$$

in which \mathcal{T}_j^- and \mathcal{T}_j^+ is the start and finish point for the j 'th time interval. Thus,

$$\Phi_i^j = \int_0^{\mathcal{T}} c_i^j dt + \int_{\mathcal{T}_j^-}^{\mathcal{T}_j^+} \lambda^T (\mathcal{T} - t) (\mathbf{K}_j)_i' \mathbf{u} dt, \quad (26)$$

in which \mathbf{K}_j is the stiffness matrix in the j 'th time interval.

It is assumed that the stiffness matrix $\mathbf{K}(t)$ can be written in the following form:

$$\mathbf{K}(t) = \sum_{i=1}^N E_i(t) \mathbf{K}^i, \quad (27)$$

in which $E_i(t)$ is the element-wise and time dependent Young's modulus and \mathbf{K}^i is a local element matrix. With the temporal discretization of the design space

$$\mathbf{K}_j = \sum_{i=1}^N E(x_i^j) \mathbf{K}^i \quad (28)$$

such that

$$(\mathbf{K}_j)_i' = \frac{dE}{dx_i^j} \mathbf{K}^i \quad (29)$$

and the expression for the sensitivities becomes

$$\Phi_i^j = \int_0^{\mathcal{T}} c_i^j dt + \frac{dE}{dx_i^j} \int_{\mathcal{T}_j^-}^{\mathcal{T}_j^+} (\lambda^T (\mathcal{T} - t) \mathbf{K}^i \mathbf{u}^i) dt, \quad (30)$$

in which λ^i and \mathbf{u}^i are local element vectors.

4.1. Material interpolation and optimization algorithm

The material properties in the design elements are interpolated linearly based on the design variables. Thus, the stiffness of element i in time interval j is

$$E = 1 + x_i^j (E_0 - 1), \quad (31)$$

in which the stiffness of the “background” material is set to unity as in the numerical examples in Section 3. Thus, the expression in (30) can be further reduced to

$$\Phi_i^j = \int_0^{\mathcal{T}} c_i^j dt + (E_0 - 1) \int_{\mathcal{T}_j^-}^{\mathcal{T}_j^+} (\lambda^T (\mathcal{T} - t) \mathbf{K}^i \mathbf{u}^i) dt. \quad (32)$$

Thus, sensitivities w.r.t. all design variables are obtained by solving the additional problem (23) followed, for each variable, by the integration in (32) which is carried out numerically. If the objective function does not depend explicitly on the design variables the first integral in (32) vanishes and no extra computational effort is required to handle the space–time design variables compared to the case of static design variables. However, the need to store \mathbf{u} and λ at each time step can be a significant computational burden, but has been solved previously for a 3D problem in [28].

Optimized space–time structures are generated on the basis of the computed sensitivities by using a gradient-based algorithm. A mathematical programming software, MMA [32], is used to obtain the design updates and forward analysis, sensitivity analysis and design updates are continued in an iterative fashion until the design converges. See, e.g. [4] for a detailed description of the iterative optimization algorithm.

5. Optimization example: dynamic bandgap structures

The design problem is illustrated in Fig. 11.

A sinusoidal Gauss-modulated pulse is sent through a one-dimensional elastic rod and the transmitted wave is recorded at the output point. The purpose of the study is to design the structure so that the transmission is minimized. The following objective function is considered:

$$\min \Phi = \int_0^{\mathcal{T}} u_{\text{out}}^2 dt, \quad (33)$$

in which u_{out} is the displacement of the output point and \mathcal{T} is the total simulation time. Thus, the considered objective function is proportional to the total transmitted wave energy.

The wave pulse is generated by applying the the following force at the input point:

$$f_1(t) = -2u_0 \omega_0 \sin(\omega_0(t - t_0)) e^{-\delta(t-t_0)^2}, \quad (34)$$

in which u_0 is the amplitude of the generated pulse, ω_0 is the center-frequency of excitation and δ determines the width of the pulse.

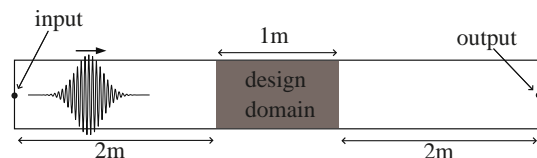


Fig. 11. Design problem. The transmission of a sinusoidal Gauss-modulated pulse is minimized.

The parameters used in this example are given as

$$\begin{aligned} \mathcal{T} &= 10 \text{ s}, \quad u_0 = 1 \text{ m}, \quad t_0 = 2.5 \text{ s}, \quad N = 150, \\ \omega_0 &= 15.7 \text{ rad/s}, \quad \Delta t = 0.06 \text{ s}, \quad \beta = 0.1 (\text{kg m})^{-1}, \\ \delta &= 1.5 \text{ s}^{-2}, \quad E_0 = 1.25 \text{ N/m}^2. \end{aligned}$$

To be able to clearly separate input and reflected waves in the time series, inlet and outlet sections of 2 m with constant material properties are added on each side of the design domain of length 1 m. The material properties of the inlet and outlet sections are normalized to $E = 1 \text{ N/m}^2$ and $\rho = 1 \text{ kg/m}^3$, so that the incoming wave propagates with the speed $c = 1 \text{ m/s}$. In order to simulate wave propagation in this finite structure, fully absorbing boundaries are added at the input and output points by appropriate viscous dampers.

Two materials can be distributed in the design domain: the normalized material used for the the inlet and output sections, and a material with a slightly higher stiffness $E_0 = 1.25$. The relatively small stiffness contrast is used in order to avoid problems with spurious oscillations (cf. Section 3.2). The presence of oscillations leads to incorrect sensitivity calculations that destabilize the optimization process. A small stiffness contrast combined with added stiffness proportional damping ($\beta = 0.1$ used throughout this example) eliminate these problems while still displaying the main qualitative features.

5.1. Static bandgap structure

For comparison the structure is optimized for the static case, i.e. a spatial material distribution is obtained which cannot change in time. Similar design problems were considered recently for transient loading in [13]. Fig. 12 shows the optimized design and Fig. 13 shows the nodal displacements as a function of time at the input and the output points. In the time plots one can easily identify the input and reflected waves at the input point (top figure) and the transmitted wave at the output point (bottom figure).

The optimized structure in Fig. 12 is a bandgap structure [8] with periodically layered inclusions of the stiffer material. Such a structure reflects the waves maximally and reduces the objective function to 76% compared to the undisturbed wave. For comparison it can be mentioned that in the case in which the design domain is completely filled with the stiffer material the objective function is only reduced to 93%. These computations have been performed with stiffness proportional damping corresponding to $\beta = 0.1$. Without damping ($\beta = 0$) the transmissions are 81% and 99%, respectively.

With a static structure the only way to further reduce Φ would be to either increase the material contrast or to increase the length of the design domain relative to the wavelength of the pulse. The latter choice would result in more inclusion layers that lead to an increased reflection of the wave.

5.2. Space–time bandgap structure

The design is now allowed to change in time as well as in space. The optimized static bandgap structure in Fig. 12 is used as a starting point for the dynamic structure. This is illustrated in Fig. 14 where the space–time design domain is indicated. A temporal design interval of $\Delta\mathcal{T} = 1.5 \text{ s}$ is chosen, which is sufficiently long to

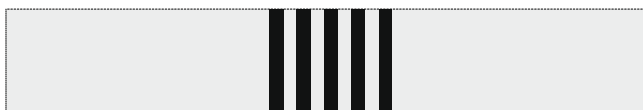


Fig. 12. Optimized structure for the “static” wave propagation problem.

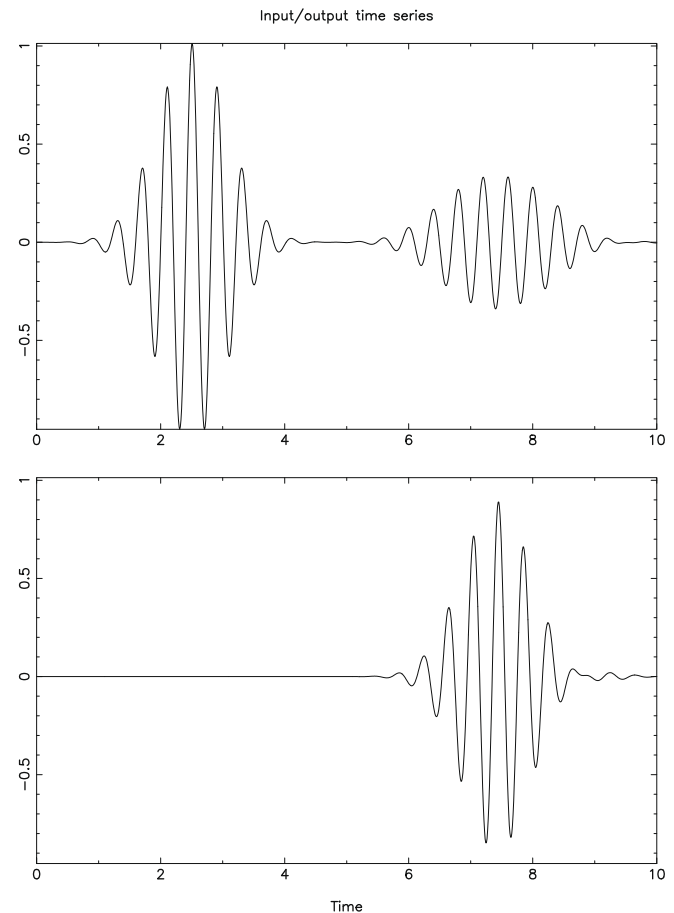


Fig. 13. Response for the optimized structure shown in Fig. 12. Top: input point displacement showing the input and reflected wave, bottom: output point displacement showing the transmitted wave.

significantly modify the wave motion but still keeps the total number of design variables at a manageable level. The start and finish point for the optimization is chosen as $\mathcal{T}_1 = 4.25 \text{ s}$ and $\mathcal{T}_2 = 5.75 \text{ s}$ and the number of sub-intervals is $M = 225$, thus the material properties in each element are allowed to change 150 times per second. The spatial discretization is unchanged from the static case with 150 elements in the design domain. Thus, the two-dimensional design grid is composed of “square” elements with the dimensions $\frac{1}{150} \text{ s} \times \frac{1}{150} \text{ m}$ and a total of 33750 design variables.

The initial value of all design variables is chosen as $x_e = 0.5$, implying that the stiffness in all design elements is initially $E = 1.125 \text{ N/m}^2$. The optimized design is obtained after about 100 iterations and is shown in Fig. 15. The structure is seen to be a kind of spatio-temporal laminate with space–time layered inclusions. Properties of spatio-temporal laminates are discussed, e.g. in [22,35,24].

At each time instance the structure is layered in a similar way as the static bandgap structure. However, the inclusion layers move with a constant speed corresponding to the wave speed in the layered medium so that the wave peaks and valleys actually move together with the front of the inclusions. This is illustrated in Fig. 16, in which the material distribution is shown together with the wave motion at the two time instances $t = 5.0 \text{ s}$ and $t = 5.4 \text{ s}$.

Fig. 17 shows the input and output point time responses. The objective is reduced to 23% relative to the undisturbed input signal – thus, a significant reduction is noted compared to the static case (76%). The large reduction is not a consequence of an increased

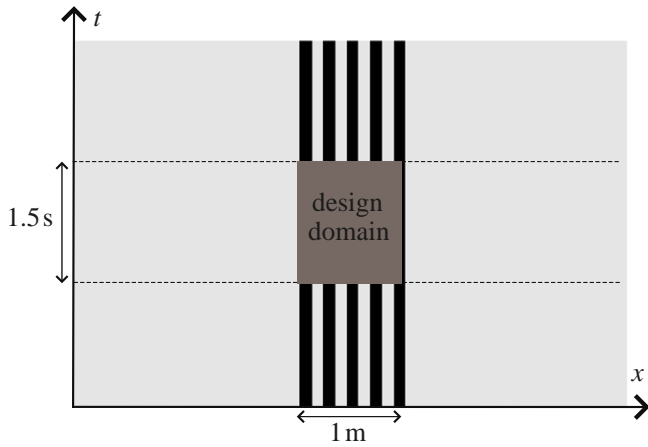


Fig. 14. Design domain for the space-time optimization problem.

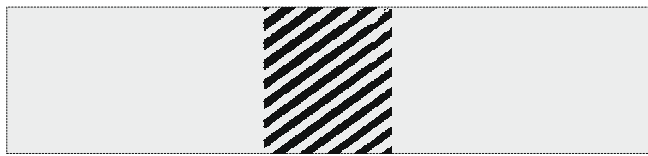


Fig. 15. Optimized space-time structure for minimum transmission of the wave pulse.

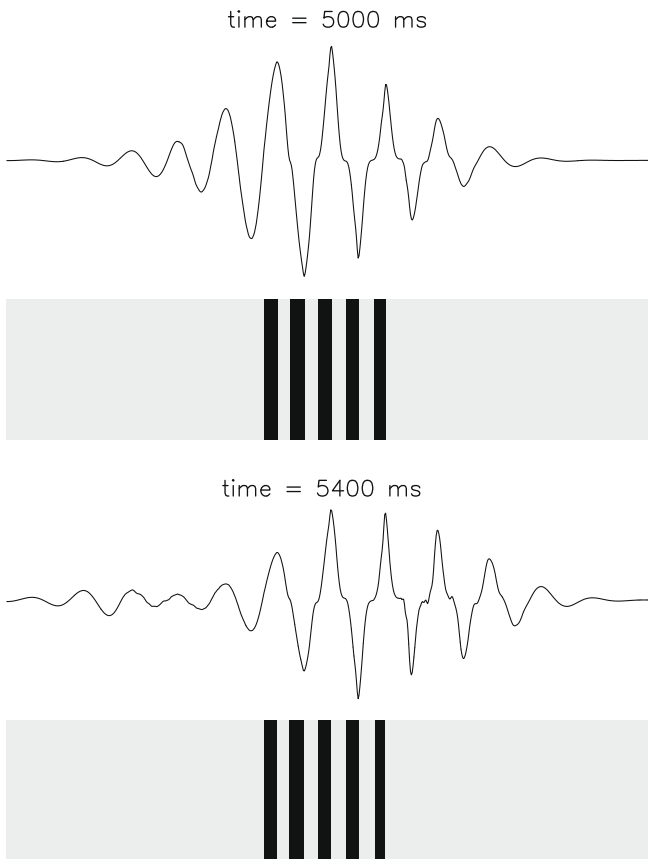


Fig. 16. Instantaneous material distribution and wave motion at $t = 5.0$ s and $t = 5.4$ s for the structure in Fig. 15.

reflection (as appears from the input point response). Actually, the reflected energy is reduced to only about 1% of the input compared

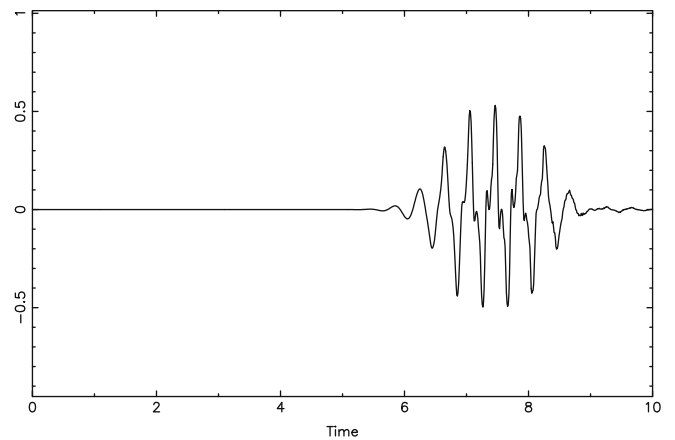
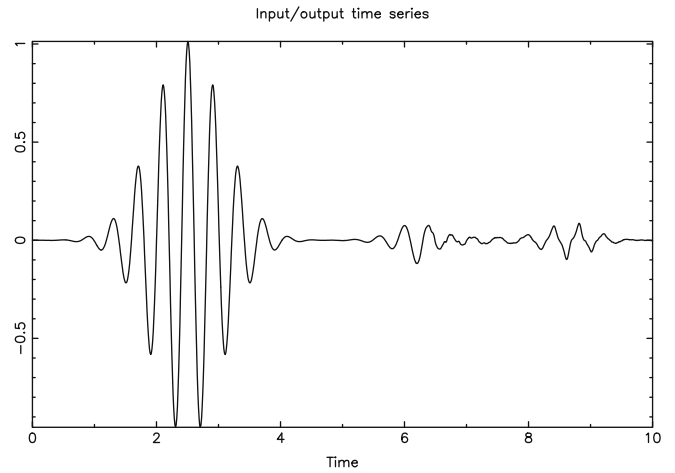


Fig. 17. Response for the optimized structure shown in Fig. 15. Top: displacement of input point, bottom: displacement of output point.

to about 17% for the static bandgap structure. Instead the main part of the energy (about 75%) is extracted from the system via the time dependent force that is needed to change the stiffness in time (cf. the discussion on energy conservation in Section 3). Only a small fraction (about 1%) is dissipated by the stiffness proportional damping. However, without the presence of damping the optimization procedure becomes unstable after only a few iterations.

The output time response in Fig. 17 indicates that the frequency content of the wave has changed. This is confirmed by an FFT-analysis shown in Fig. 18. In addition to the main frequency component $\omega_0 = 15.7\text{rad/s}$, higher order components at $\approx 3\omega_0$ and $\approx 5\omega_0$ (and more further up in the spectrum) are seen as well. This might seem surprising since the system is completely linear. However, as mentioned, the material properties can only be changed in time with a time dependent external force acting on the system, and this force contributes to the signal with these higher order frequency components.

Similar structures as the one shown, can be obtained with different values of the material contrast E_0 . Only the wave speed in the layered medium changes and thereby also the speed of the bandgap material front which leads to a different “slope” of the spatio-temporal laminates. Additionally, the ratio of the two materials in the structure depends on the choice of E_0 in such a way that the inclusion layers become thicker with increasing contrast.

5.3. Realizable structures – patches and checkerboards

The optimized structure in the previous section would be a challenge if it came to a practical realization. In order to generate

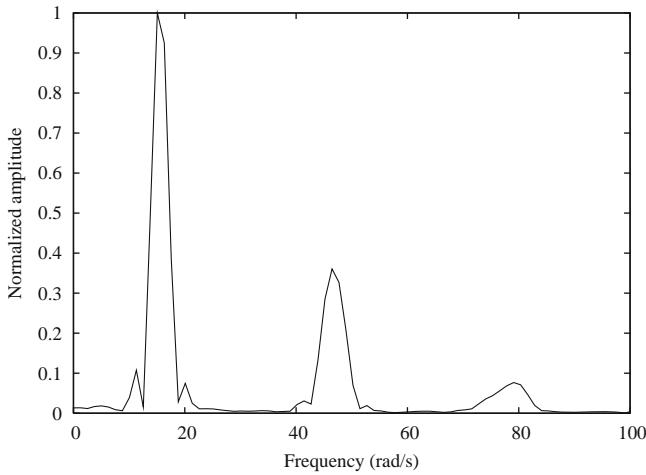


Fig. 18. FFT-analysis of the output point time response shown in Fig. 17.

structures that could more easily be realized, the number of design variables is reduced. This is done by lumping spatial elements together in patches and reducing the number of temporal design intervals as well.

Fig. 19 shows two examples of simplified optimized structures. Both structures have 30 spatial design elements (patches of 5 elements). Using fewer design variables than this, makes it impossible to resolve the layered structures adequately. The two structures have $M = 45$ and $M = 15$ time design intervals, respectively. The finer structure (1350 design variables in total) displays the same spatio-temporal laminate structure as the fully discretized structure in Fig. 15 and the corresponding objective function is only marginally higher (27% compared to 23%). For the coarse design with only 15 time design variables (total of 450 design variables) the laminated structure can no longer be created. Instead the structure has a checkerboard appearance. The objective is increased to 45% which is significantly higher than for the laminated structure, but still much better than for the static bandgap structure.

The checkerboard structure is an example of a space–time material pattern that is easier to realize in practice than the spatio-temporal laminate. A detailed analysis of the properties of such structures can be found in [23,24]. A design parametrization is now constructed that ensures a checkerboard structure as outcome. This is done by replacing the material interpolation model in (31) by

$$E = 1 + (\tilde{x}_i - \tilde{x}_j)^2 (E_0 - 1), \tag{35}$$

in which \tilde{x}_i is a vector of spatial design variables and \tilde{x}_j is a vector of temporal design variables. The computation of the design sensitivities should now be done directly based on (24) since the simplification in (25) no longer holds. This increases the computation time for

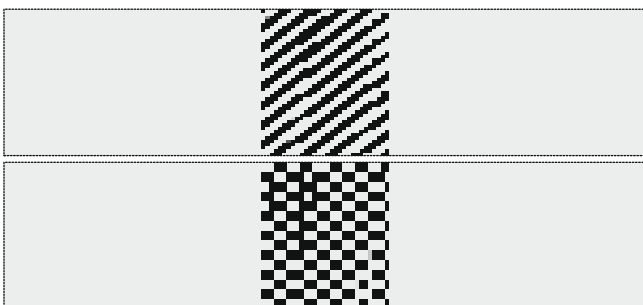


Fig. 19. Simplified optimized structures with a reduced number of design variables. Top: 30×45 and bottom 30×15 variables.

each design variable but the number of variables is correspondingly smaller. The fully discretized optimized structure in Fig. 15 has $150 \times 225 = 33\,750$ variables, but with the new parametrization, the same discretization results in $150 + 225 = 375$ variables. The resulting checkerboard structure is seen in Fig. 20 and the resulting response in Fig. 21. The structure is seen to qualitatively resemble the structure in Fig. 19(bottom) with the same number (15) of temporal inclusions. The objective is also similar (40% compared to 45%). Compared to the response for the fully discretized structure in Fig. 17 the response peaks are now higher but the qualitative nature of the response is unchanged.

5.4. Long wavelengths – temporal laminates

The appearance of the optimized spatio-temporal laminates depends strongly on the frequency and wavelength contents of the wave. In the previous examples the main wavelength of the wave was $\lambda = 0.4$ m for a wave with center frequency $\omega_0 = 15.7$ rad/s

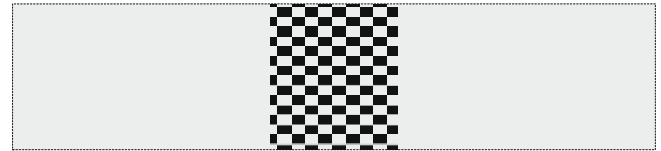


Fig. 20. Optimized checkerboard structure with checkerboard design variable model.

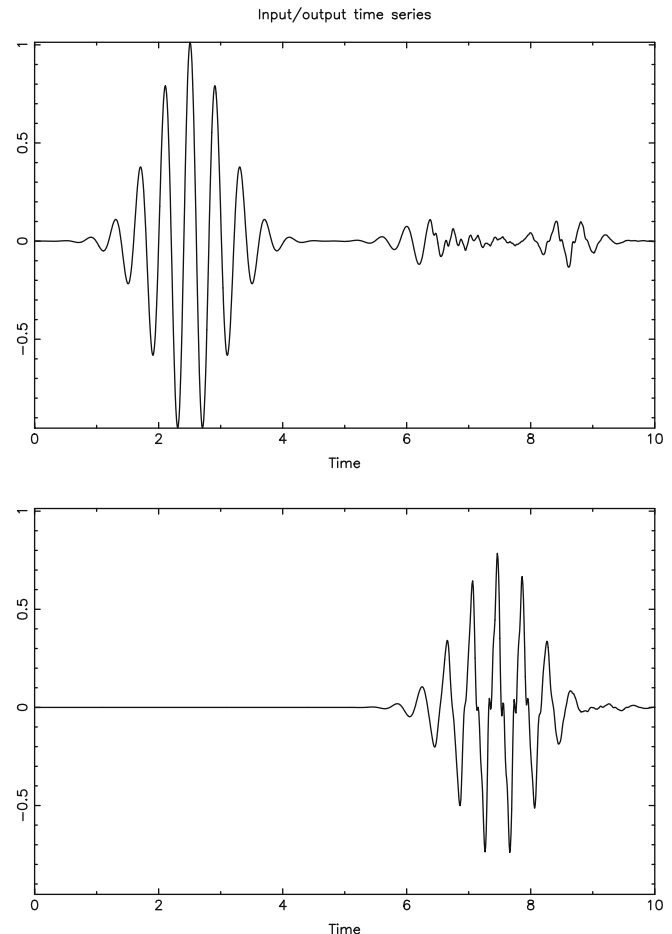


Fig. 21. Response for the optimized structure shown in Fig. 20. Top: displacement of input point, bottom: displacement of output point.

propagating in the material with $c = 1$ m/s. Thus, the design domain had a spatial extent corresponding to 2.5 wavelengths.

If the design domain length is short compared to the main wavelength, a spatially layered structure is no longer efficient for minimizing the wave transmission. Fig. 22 shows two optimized structures for $\lambda = 2.5$ m and $\lambda = 10$ m, respectively. The temporal design intervals have been increased accordingly to 5 s and 10 s. As appears, longer wavelengths result in structures that are spatially more homogeneous at any given time. In the long wavelength limit, the optimized structure approaches that of a pure temporal laminate with instant simultaneous switching of the material properties in the entire rod (cf. the analysis in Section 3.1). For a discussion of temporal laminates see [36,24].

5.5. Stability of structural response – shifted wave pulses

The optimized dynamic bandgap structures have been demonstrated to be effective in prohibiting the propagation of waves. But a significant drawback compared to the static structures is that they are sensitive to the operating conditions and rely on a timely activation of the spatio-temporal material variation.

This is illustrated by simulating the response of the structure with an input pulse that is delayed compared to the reference pulse for which the structure is optimized. Fig. 23 shows the instantaneous material distribution and wave motion as in Fig. 16(top), but with the wave pulse delayed 0.1 s, so that the wave peaks and valleys follow the rear side of the inclusions instead of the inclusion fronts. The effect on the response is significant and the resulting output wave pulse is actually magnified compared to the input pulse.

A shifted (delayed or advanced) pulse will in general cause the structure to perform worse than optimal. However, the deteriora-



Fig. 22. Optimized structures for long wavelengths. Top: $\lambda = 2.5$ m and bottom: $\lambda = 10$ m.

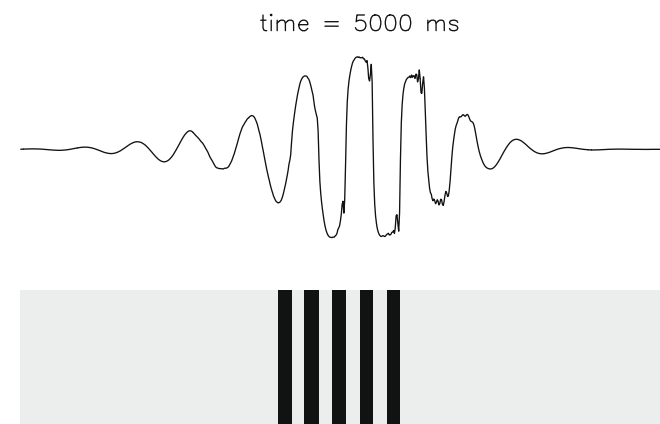


Fig. 23. Instantaneous material distribution and wave motion at $t = 5.0$ s for the optimized structure in Fig. 15 with the input pulse delayed 0.1 s.

tion occurs smoothly with small perturbations only resulting in small changes in the performance and with maximum deterioration for this example occurring with the 0.1 s shift shown in Fig. 23. If the pulse is delayed another 0.1 s (0.2 s in total) the waves will again follow the inclusion fronts and the optimal situation is reestablished.

6. Summary and conclusions

This paper describes an extension of the topology optimization method to facilitate optimization of material distributions in space and time.

The established topology optimization formulation is extended with design variables in the temporal domain that allows the point-wise optimized material properties to change in time. The extended method is described for one-dimensional wave propagation in elastic rods with time dependent Young's modulus and subjected to transient loading.

A gradient-based optimization algorithm is applied based on explicit time integration of the discretized model equation. Gradients are obtained using the adjoint method which requires just one additional transient problem to be solved irrespectively of the number of design variables.

A simulation study of two simple problems illustrate the rich behavior of structures with dynamic material distributions. Instant changes in Young's modulus or a moving interface between two material phases, result in phenomena such as increase or decrease in the total mechanical wave energy and shifts in the wavenumber/frequency of waves. The shortcomings of the numerical integration scheme are outlined and a simple remedy in form of stiffness proportional damping is proposed.

These dynamic phenomena are reflected in the optimization example. The objective is to design a structure that minimizes the transmission of a sinusoidal Gauss-modulated pulse. The best static structure is a bandgap structure with periodically placed inclusion layers of the stiffer material. It is demonstrated that structures in which the inclusion layers move with the propagating waves, so-called spatio-temporal laminates, can be much more effective in minimizing the transmission. The improvement is facilitated by removal of mechanical energy via the external force that is required to change the stiffness.

Additionally, it is demonstrated that if we allow the stiffness to change less often, the optimized design change qualitatively and attain a checkerboard appearance. A special design parametrization was constructed that ensures a checkerboard structure and the resulting design was compared to the other designs. The performance of the checkerboard structure is not a good as the laminated structure but still significantly better than the static bandgap structure.

The sensitivity of the optimized designs were analyzed with respect to changes in the operating conditions. It was demonstrated that the performance depends on a timely activation of the space-time material pattern and if the pulse is delayed w.r.t. the optimization conditions the performance is significantly deteriorated.

The ability of supply/extract energy and change the frequency contents of the wave opens up for more advanced pulse manipulation than demonstrated in this relatively simple example. Currently, the possibility to compress pulses is being investigated and will be reported elsewhere.

Acknowledgements

The work was supported by the Danish Research Council for Technology and Production Sciences (Grant 274-05-0498). The author wishes to thank Jon J. Thomsen and Boyan S. Lazarov (both

at the Department of Mechanical Engineering at the Technical university of Denmark) for inspiring discussions.

References

- [1] M.P. Bendsøe, Optimal shape design as a material distribution method, *Struct. Optim.* 10 (1989) 193–202.
- [2] M.P. Bendsøe, N. Kikuchi, Generating optimal topologies in structural design using a homogenization method, *Comput. Methods Appl. Mech. Engrg.* 71 (1988) 197–224.
- [3] M.P. Bendsøe, O. Sigmund, Material interpolations in topology optimization, *Arch. Appl. Mech.* 69 (1999) 635–654.
- [4] M.P. Bendsøe, O. Sigmund, *Topology Optimization – Theory, Methods and Applications*, Springer-Verlag, Berlin, 2003.
- [5] I.I. Blekhman, K.A. Lurie, On dynamic materials, *Proc. Russian Acad. Sci. (Doklady)* 37 (2000) 182–185.
- [6] I.I. Blekhman, Vibrational dynamic materials and composites, *J. Sound Vib.* 317 (2008) 657–663.
- [7] M. Bruggi, P. Venini, Topology optimization of incompressible media using mixed finite elements, *Comput. Methods Appl. Mech. Engrg.* 196 (2007) 3151–3164.
- [8] L. Brillouin, *Wave Propagation in Periodic Structures*, second ed., Dover Publications, 1953.
- [9] J.S. Choi, J. Yoo, Structural optimization of ferromagnetic materials based on the magnetic reluctivity for magnetic field problems, *Comput. Methods Appl. Mech. Engrg.* 197 (2008) 4193–4206.
- [10] Y.-S. Chung, C. Cheon, S.-Y. Hahn, Reconstruction of dielectric cylinders using FDTD and topology optimization technique, *IEEE Trans. Magnetics* 36 (2000) 956–959.
- [11] W.W. Clark, Vibration control with state-switched piezoelectric materials, *J. Intel. Mater. Syst. Struct.* 11 (2000) 263–271.
- [12] R.D. Cook, D.S. Malkus, M.E. Plesha, R.J. Witt, *Concepts and Applications of Finite Element Analysis*, fourth ed., Wiley, New York, 2002.
- [13] J. Dahl, J.S. Jensen, O. Sigmund, Topology optimization for transient wave propagation problems in one dimension, *Struct. Multidiscipl. Optim.* 36 (2008) 585–595.
- [14] D. Holtz, J.S. Arora, An efficient implementation of adjoint sensitivity analysis for optimal control problems, *Struct. Optim.* 13 (1997) 223–229.
- [15] G.M. Hulbert, Time finite element methods for structural dynamics, *Int. J. Numer. Methods Engrg.* 33 (1992) 307–331.
- [16] J. Issa, R. Mukherjee, A.R. Diaz, S.W. Shaw, Modal disparity and its experimental verification, *J. Sound Vib.* 311 (2008) 1465–1475.
- [17] B.-S. Kang, G.-J. Park, J.S. Arora, A review of optimization of structures subjected to transient loads, *Struct. Multidiscipl. Optim.* 31 (2006) 81–95.
- [18] D.E. Kirk, *Optimal Control Theory: An Introduction*, Prentice-Hall, New Jersey, 1970.
- [19] V. Krylov, S.V. Sorokin, Dynamics of elastic beams with controlled distributed stiffness parameters, *Smart Mater. Struct.* 6 (1997) 573–582.
- [20] J.S. Lee, J.E. Kim, Y.Y. Kim, Damage detection by the topology design formulation using modal parameters, *Int. J. Numer. Methods Engrg.* 69 (2007) 1480–1498.
- [21] Y. Li, K. Saitou, N. Kikuchi, Topology optimization of thermally actuated compliant mechanisms considering time-transient effect, *Finite Elem. Anal. Des.* 11 (2004) 1317–1331.
- [22] K.A. Lurie, Effective properties of smart elastic laminates and the screening phenomenon, *Int. J. Solids Struct.* 34 (1997) 1633–1643.
- [23] K.A. Lurie, S.L. Weekes, Wave propagation and energy exchange in a spatio-temporal material composite with rectangular microstructure, *J. Math. Anal. Appl.* 314 (2006) 286–310.
- [24] K.A. Lurie, *An Introduction to Mathematical Theory of Dynamic Materials*, Springer-Verlag, 2007.
- [25] F. Maestre, A. Münch, P. Pedregal, A spatio-temporal design problem for a damped wave equation, *SIAM J. Appl. Math.* 68 (2007) 109–132.
- [26] F. Maestre, P. Pedregal, Dynamic materials for an optimal design problem under the two-dimensional wave equation, *Discrete Contin. Dyn. Syst. – Ser. A*, in press.
- [27] S. Min, N. Kikuchi, Y.C. Park, S. Kim, S. Chang, Optimal topology design of structures under dynamic loads, *Struct. Optim.* 17 (1999) 208–218.
- [28] T. Nomura, K. Sato, K. Taguchi, T. Kashiwa, S. Nishiwaki, Structural topology optimization for the design of broadband dielectric resonator antennas using the finite difference time domain technique, *Int. J. Numer. Methods Engrg.* 71 (2007) 1261–1296.
- [29] C.L.W. Pedersen, Crashworthiness design of transient frame structures using topology optimization, *Comput. Methods Appl. Mech. Engrg.* 193 (2004) 653–678.
- [30] A. Ramaratnam, N. Jalili, A switched stiffness approach for structural vibration control: theory and real-time implementation, *J. Sound Vib.* 291 (2006) 258–274.
- [31] S.V. Sorokin, O.A. Ershova, S.V. Grishina, The active control of vibrations of composite beams by parametric stiffness modulation, *Eur. J. Mech. A – Solids* 19 (2000) 873–890.
- [32] K. Svanberg, The method of moving asymptotes – a new method for structural optimization, *Int. J. Numer. Methods Engrg.* 24 (1987) 359–373.
- [33] S. Turteltaub, Optimal material properties for transient problems, *Struct. Multidiscipl. Optim.* 22 (2001) 157–166.
- [34] S. Turteltaub, Optimal non-homogeneous composites for dynamic loading, *Struct. Multidiscipl. Optim.* 30 (2005) 101–112.
- [35] S.L. Weekes, Numerical computation of wave propagation in dynamic materials, *Appl. Numer. Math.* 37 (2001) 417–440.
- [36] S.L. Weekes, A stable scheme for the numerical computation of long wave propagation in temporal laminates, *J. Comput. Phys.* 176 (2002) 345–362.
- [37] G.H. Yoon, J.S. Jensen, O. Sigmund, Topology optimization of acoustic-structure interaction problems using a mixed finite element formulation, *Int. J. Numer. Methods Engrg.* 70 (2007) 1049–1075.
- [38] G.H. Yoon, O. Sigmund, A monolithic approach for topology optimization of electrostatically actuated devices, *Comput. Methods Appl. Mech. Engrg.* 197 (2008) 4062–4075.

Control and Cyberneticsvol. **39** (2010) No. 3**Optimization of space-time material layout for 1D wave propagation with varying mass and stiffness parameters***

by

Jakob S. Jensen

Department of Mechanical Engineering, Solid Mechanics
Technical University of Denmark
Nils Koppels Allé, Building 404, Denmark
e-mail: jsj@mek.dtu.dk

Abstract: Results are presented for optimal layout of materials in the spatial and temporal domains for a 1D structure subjected to transient wave propagation. A general optimization procedure is outlined including derivation of design sensitivities for the case when the mass density and stiffness vary in time. The outlined optimization procedure is exemplified on a 1D wave propagation problem in which a single gaussian pulse is compressed when propagating through the optimized structure. Special emphasis is put on the use of a time-discontinuous Galerkin integration scheme that facilitates analysis of a system with a time-varying mass matrix.

Keywords: dynamic structures, topology optimization, wave propagation, transient analysis.

1. Introduction

The method of topology optimization is a popular method for obtaining the optimal layout of one or several material constituents in structures and materials (Bendsøe and Kikuchi, 1988; Bendsøe and Sigmund, 2003). The methodology has within the last two decades evolved into a mature and diverse research field involving advanced numerical procedures and various application areas such as fluids (Borrvall and Petersson, 2003), waves (Sigmund and Jensen, 2003), electromagnetism (Cox and Dobson, 1999), as well as various coupled problems such as e.g. fluid-structure interaction (Yoon, Jensen and Sigmund, 2007). Additionally, industrial applications in the automotive and aerospace industries are established and widespread. The success has been facilitated by the large design freedom inherently associated with the concept, but also by efficient numerical techniques such as adjoint sensitivity analysis for rapid computation of gradients (Tortorelli and Michaleris, 1994), various penalization and regularization

*Submitted: June 2009; Accepted: June 2010.

techniques for obtaining both meaningful and useful designs (Sigmund and Petersson, 1998) and the close integration with mathematical programming tools, such as the method of moving asymptotes (MMA) (Svanberg, 1987).

Recently it was suggested to apply (and somewhat extend) the standard topology optimization framework to design a 1D structure in which the stiffness could change both in space and time (Jensen, 2009). As an example, an optimized “dynamic structure” that prohibits wave propagation was designed and manifested itself as a moving bandgap structure with layers of stiff inclusions moving with the propagating wave. The dynamic structure was demonstrated to reduce the transmission of a wave pulse by about a factor of three compared to an optimized static structure. The present paper extends the described work by allowing materials that have not only time-varying stiffness but also a time-varying mass density. This extension requires special attention to the choice of time-integration scheme since many standard schemes fail. However, it allows for extended manipulation of the wave propagation as illustrated in the example in the present paper, in which a single gaussian wave pulse is compressed when propagating through the optimized structure. Preliminary results for this design problem in the case of time-varying stiffness were presented in Jensen (2008).

The basic setting for obtaining optimal space and time distributions of materials for problems governed by the wave equation was first presented in Maestre, Münch and Pedregal (2007), Maestre and Pedregal (2009). These papers analyze 1D and 2D problems with a strong focus on the mathematical aspects of the optimization problem. Both the present paper and the aforementioned works root in the fundamental concept of dynamic materials. This concept was introduced by Lurie and Blekhman (Lurie, 1997; Blekhman and Lurie, 2000; Blekhman, 2008) who unfolded the rich and complex behavior of materials with properties that vary in space and time. The dynamics of structures with space and time varying properties was also studied in the work by Krylov and Sorokin (Krylov and Sorokin, 1997) and later in Sorokin, Ershova and Grishina (2000), Sorokin and Grishina (2004).

The basis for the presented optimization problem is time-integration of the transient model equation coupled with adjoint sensitivity analysis. Thus, the problem closely resembles previous studies that have been carried out for topology optimization of static structures using a transient formulation, e.g. Min et al., (1999), Turteltaub (2005), Dahl, Jensen and Sigmund (2008).

The outline of the paper is as follows. In Section 2 the governing equation is presented and the basic setup defined. In Section 3 the design parametrization is defined and design sensitivities are derived. Section 4 is devoted to numerical analysis of the transient direct and adjoint equations and numerical simulation results are presented. In Section 5 an optimization problem is defined and examples of optimized designs are presented. Section 6 summarizes and gives conclusions.

2. Governing equation

The starting point for the analysis and subsequent optimization study is a time-dependent FE model in which the mass matrix ($\mathbf{M}(t)$) and the stiffness matrix ($\mathbf{K}(t)$) are allowed to vary in time:

$$\frac{\partial}{\partial t}(\mathbf{M}(t)\mathbf{v}) + \mathbf{C}\mathbf{v} + \mathbf{K}(t)\mathbf{u} = \mathbf{f}(t) \quad (1)$$

in which \mathbf{C} is a constant damping matrix and $\mathbf{f}(t)$ is the transient load. The vector $\mathbf{u}(t)$ contains the unknown nodal displacements and the notation $\mathbf{v} = \partial\mathbf{u}/\partial t$ has been used to denote the unknown velocities. It is assumed that the mass matrix is diagonal, e.g. obtained by a standard lumping procedure. This will be of importance when choosing a proper time-integration routine but it should be emphasized that all formulas derived in the following hold also for the case of \mathbf{M} being non-diagonal.

The governing equation is solved in the time domain with the trivial initial conditions:

$$\mathbf{u}(t) = \mathbf{v}(t) = \mathbf{0} \quad (2)$$

which imposes only limited loss of generality and facilitates the sensitivity analysis as shown later.

It should be noted that although the terms mass matrix/mass density and stiffness matrix/stiffness are used here and in the following presentation, the equations could just as well apply to an electromagnetic or an acoustic problem with proper renaming of involved parameters. However, the terminology from elasticity will be kept throughout this paper.

3. Parameterization and sensitivities

The density approach to topology optimization (Bendsøe, 1989) is adapted to the present problem. With this approach a single design variable x_e ("density") is assigned to each element in the FE model. As in Jensen (2009) this is expanded to the space-time case by defining a vector of continuous design variables:

$$\mathbf{x}_j = \{x_j^1, x_j^2, \dots, x_j^N\}^T \quad (3)$$

for each of a predefined number M of time intervals (such that $j \in [1, M]$), for which the design will be allowed to change. In Eq. (3) N is the number of spatial elements in the FE model. Thus, for a 1D spatial structure, as considered in the example in Section 5, the corresponding design space is two-dimensional with dimension $N \times M$.

The value of the density variable x_j^e will determine the material properties of that space-time element by an interpolation between two predefined materials

1 and 2, where the variable is allowed to take any value from 0 to 1 ($x_j^e \in [0; 1]$). By rescaling the equations with respect to the material properties of material 1, the mass and stiffness matrices can be written as:

$$\mathbf{M}_j = \sum_{e=1}^N (1 + x_j^e(\rho - 1))\mathbf{M}^e \quad (4)$$

$$\mathbf{K}_j = \sum_{e=1}^N (1 + x_j^e(E - 1))\mathbf{K}^e \quad (5)$$

such that ρ, E denote the *contrast* between the two materials for the mass density and stiffness, respectively. In Eqs. (4)–(5), \mathbf{M}^e and \mathbf{K}^e are local mass and stiffness matrices expressed in global coordinates.

Analytical expressions for the design sensitivities are now derived. The optimization is based on an objective that is assumed to be written as:

$$\phi = \int_0^{\mathcal{T}} c(\mathbf{u})dt \quad (6)$$

in which c is a real scalar function of the time-dependent displacement vector and \mathcal{T} is the total simulation time. It should be emphasized that more complicated objective functions, e.g. with a dependence on the velocities or an integration different from the total simulation time, can be treated with minor modification of the following derivation.

The derivative wrt. a single design variable in the j 'th time-interval and e 'th spatial variable is denoted $()' = \partial/\partial x_j^e$ and thus the sensitivity of ϕ wrt. to x_j^e is:

$$\phi' = \int_0^{\mathcal{T}} \frac{\partial c}{\partial \mathbf{u}} \mathbf{u}' dt \quad (7)$$

Eq. (7) involves the term \mathbf{u}' which is difficult to evaluate explicitly. However, the adjoint method can be used to circumvent this problem in an efficient way (Arora and Holtz, 1997). For this purpose the residual vector \mathbf{R} :

$$\mathbf{R} = \frac{\partial}{\partial t}(\mathbf{M}\mathbf{v}) + \mathbf{C}\mathbf{v} + \mathbf{K}\mathbf{u} - \mathbf{f}(t) \quad (8)$$

is differentiated wrt. x_j^e :

$$\mathbf{R}' = \frac{\partial}{\partial t}(\mathbf{M}'\mathbf{v} + \mathbf{M}\mathbf{v}') + \mathbf{C}\mathbf{v}' + \mathbf{K}'\mathbf{u} + \mathbf{K}\mathbf{u}' \quad (9)$$

in which it has been used that \mathbf{f} (the transient load) and \mathbf{C} (the damping matrix) are both independent of the design.

With the aid of Eq. (9), Eq. (7) is reformulated as:

$$\phi' = \int_0^T \left(\frac{\partial c}{\partial \mathbf{u}} \mathbf{u}' + \boldsymbol{\lambda}^T \mathbf{R}' \right) dt \quad (10)$$

in which $\boldsymbol{\lambda}$ denote an unknown vector of Lagrangian multipliers to be determined in the following.

Expanding the expression in Eq. (10) and using integration by parts leads to the following equation:

$$\begin{aligned} \phi' = \int_0^T (\boldsymbol{\lambda}^T \mathbf{K}' \mathbf{u} - \boldsymbol{\gamma}^T \mathbf{M}' \mathbf{v}) dt + \int_0^T \left(\frac{\partial c}{\partial \mathbf{u}} + \frac{\partial}{\partial t} (\boldsymbol{\gamma}^T \mathbf{M}) - \boldsymbol{\gamma}^T \mathbf{C} + \boldsymbol{\lambda}^T \mathbf{K} \right) \mathbf{u}' dt \\ + [\boldsymbol{\lambda}^T (\mathbf{M}' \mathbf{v} + \mathbf{M} \mathbf{v}' + \mathbf{C} \mathbf{u}') - \boldsymbol{\gamma}^T \mathbf{M} \mathbf{u}']_0^T \end{aligned} \quad (11)$$

in which the notation $\boldsymbol{\gamma} = \partial \boldsymbol{\lambda} / \partial t$ has been introduced.

Now the unknowns $(\boldsymbol{\lambda}, \boldsymbol{\gamma})$ can be chosen so that the last integral in expression (11) vanishes along with the bracketed term that originates in the boundary contribution from integrating by parts (if the trivial initial conditions in Eq. (2) are applied as well). This leads to the following adjoint equation:

$$\frac{\partial}{\partial t} (\mathbf{M}^T \boldsymbol{\gamma}) - \mathbf{C}^T \boldsymbol{\gamma} + \mathbf{K}^T \boldsymbol{\lambda} = - \left(\frac{\partial c}{\partial \mathbf{u}} \right)^T \quad (12)$$

along with the following terminal conditions:

$$\boldsymbol{\lambda}(T) = \boldsymbol{\gamma}(T) = \mathbf{0}. \quad (13)$$

The sensitivities can then be computed from the remaining expression:

$$\phi' = \int_0^T (\boldsymbol{\lambda}^T \mathbf{K}' \mathbf{u} - \boldsymbol{\gamma}^T \mathbf{M}' \mathbf{v}) dt = \int_{\mathcal{T}_j^-}^{\mathcal{T}_j^+} (\boldsymbol{\lambda}^T \mathbf{K}' \mathbf{u} - \boldsymbol{\gamma}^T \mathbf{M}' \mathbf{v}) dt \quad (14)$$

in which the integral can be reduced to the j 'th time interval ranging from \mathcal{T}_j^- to \mathcal{T}_j^+ simply because \mathbf{K}' and \mathbf{M}' vanish outside the interval belonging to the specific design variable.

The expression can be further reduced to element level as follows:

$$\phi' = \int_{\mathcal{T}_j^-}^{\mathcal{T}_j^+} \left((E - 1) (\boldsymbol{\lambda}^e)^T \mathbf{K}^e \mathbf{u}^e - (\rho - 1) (\boldsymbol{\gamma}^e)^T \mathbf{M}^e \mathbf{v}^e \right) dt \quad (15)$$

by using the material interpolations defined in Eqs. (4)–(5).

4. Numerical analysis

Special care has to be taken to solve the direct and adjoint problems in Eqs. (1)–(2) and Eqs. (12)–(13) in the case where \mathbf{M} is not constant. In this case, \mathbf{v} and γ are not continuous and the numerical integration scheme must be able to handle this difficulty. A time-discontinuous Galerkin procedure (Wiberg and Li, 1999) allows for discontinuous field variables in time domain and is applicable for this case. An explicit version of the scheme is applied. The choice of an explicit solver (in combination with a lumped mass matrix) is essential for an efficient solution of the equations.

The basic numerical procedure is described shortly in the following for the direct problem of solving for $\mathbf{u}(t), \mathbf{v}(t)$. The adjoint problem for $\lambda(t), \gamma(t)$ is solved in a similar way. The total simulation time \mathcal{T} is divided into N_t equidistant intervals and a discrete set of displacement and velocity vectors $\mathbf{u}_i, \mathbf{v}_i$ is obtained for $i \in [1, N_t + 1]$ including the initial conditions. Each time interval ($k \in [1, N_t]$) is treated as a time element and an inner-loop iterative procedure is used to obtain a velocity vector at the beginning of the interval denoted \mathbf{v}_1^k and one at the end of the interval denoted \mathbf{v}_2^k . For the n^{th} inner-loop iteration the updates of \mathbf{v}_1^k and \mathbf{v}_2^k are:

$$\begin{aligned} \mathbf{M}(\mathbf{v}_1^k)^n &= (\mathbf{M}\mathbf{v}_2)^{k-1} + \frac{\Delta t}{6}(\mathbf{f}_1 - \mathbf{f}_2) \\ &+ \frac{(\Delta t)^2}{18}\mathbf{K}(\mathbf{v}_1^k - 2\mathbf{v}_2^k)^{n-1} - \frac{\Delta t}{6}\mathbf{C}(\mathbf{v}_1^k - \mathbf{v}_2^k)^{n-1} \end{aligned} \quad (16)$$

$$\begin{aligned} \mathbf{M}(\mathbf{v}_2^k)^n &= ((\mathbf{M}\mathbf{v}_2)^{k-1} - \Delta t(\mathbf{K}\mathbf{u})^{k-1}) + \frac{\Delta t}{2}(\mathbf{f}_1 + \mathbf{f}_2) \\ &- \frac{(\Delta t)^2}{6}\mathbf{K}(2\mathbf{v}_1^k - \mathbf{v}_2^k)^{n-1} - \frac{\Delta t}{2}\mathbf{C}(\mathbf{v}_1^k + \mathbf{v}_2^k)^{n-1} \end{aligned} \quad (17)$$

in which \mathbf{f}_1 and \mathbf{f}_2 is the load vector evaluated at the beginning and end of the time interval, respectively. The values of $(\mathbf{v}_1^k)^{n-1}$ and $(\mathbf{v}_2^k)^{n-1}$ for the initial iteration ($n = 1$) are taken to be equal to the value of \mathbf{v}_2^{k-1} . These inner loop iterations are continued until \mathbf{v}_1^k and \mathbf{v}_2^k do not change more than some predefined small tolerance (usually 2-3 iterations are performed).

Based on the converged time element values the recorded velocity and displacement vector at discrete time i is then:

$$\mathbf{v}^i = \mathbf{v}_2^k \quad (18)$$

$$\mathbf{u}^i = \mathbf{u}^{i-1} + \frac{\Delta t}{2}(\mathbf{v}_1^k + \mathbf{v}_2^k). \quad (19)$$

4.1. Test problem

The explicit time-discontinuous Galerkin formulation is now compared to a standard explicit central difference scheme as previously employed in Jensen (2009). The model problem is depicted in Fig. 1 and the setting is described in the following. A sine-modulated gaussian pulse propagates in a homogeneous medium with material properties $\rho = E = 1$ and at $t = t_0$ the material properties change instantaneously to $\rho = \rho_0$ and $E = E_0$. As a result the propagating wave splits

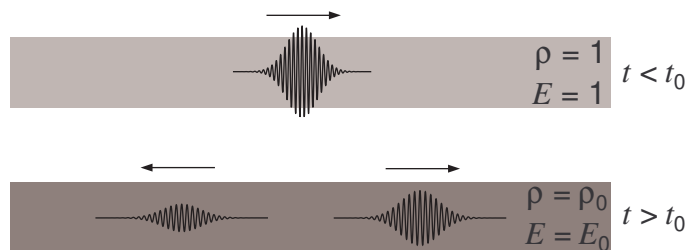


Figure 1. Propagation of a sine-modulated Gaussian pulse in a homogeneous medium with an instant change of material properties at $t = t_0$.

up into a forward and a backward travelling wave. It can be shown analytically that the relative change in wave energy at the moment of change of material properties is given as:

$$\frac{\Delta E}{E} = \frac{1}{2} \left(E_0 + \frac{1}{\rho_0} \right) - 1. \quad (20)$$

In Fig. 2 the wave energy is plotted as a function of time. Both plots in the figure correspond to the case where the material properties are changed at $t_0 = 0.85$ s. In the first plot the material properties are $\rho_0 = 1$ and $E_0 = 1.5$, which correspond to a relative energy jump of 0.25 and as appears from the plot, this jump is accurately predicted by the time-discontinuous Galerkin procedure but also with a normal central difference scheme. In the second plot $\rho_0 = 2$ and $E_0 = 1.5$ are chosen and thus zero energy jump should occur. From the plot we can see that the time-discontinuous scheme correctly captures the behavior as opposed to the central difference scheme.

It should be mentioned that the time-discontinuous scheme is computationally more expensive than the straightforward central-difference scheme, since it involves inner loop iterations. The computational overhead depends on the specific value of the tolerance set for the inner-loop iterations (see Wiberg and Li, 1999, for more details). It is possible that more efficient schemes could be developed.

5. Example: pulse compression

The optimization algorithm is now demonstrated on the particular design problem illustrated in Fig. 3. A single Gaussian pulse is sent through a one-dimensional structure and the transmitted wave is recorded. Wave propagation in the bar is simulated by applying a time-dependent load at the left boundary and adding absorbing boundary conditions in the form of simple dampers at both ends.

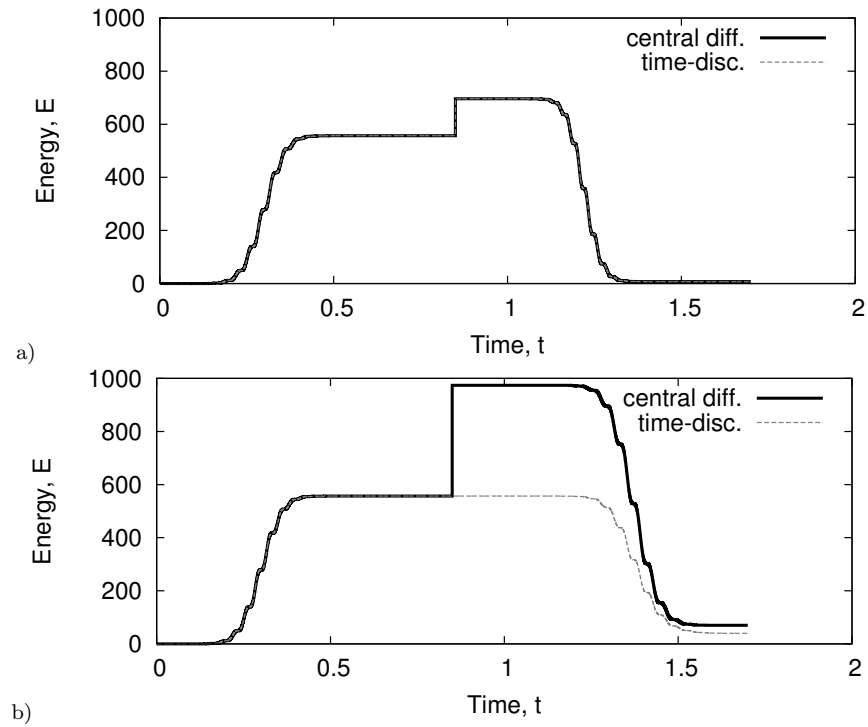


Figure 2. Simulation values of the wave energy in the homogeneous structure with an instantaneous change of material properties at $t_0 = 0.85$ s. a) $\rho_0 = 1$ and $E_0 = 1.5$ and b) $\rho_0 = 2$ and $E_0 = 1.5$.



Figure 3. Design problem. A single gaussian pulse is to be compressed when propagating through the design domain by a suitable stiffness and mass density distribution in space and time.

The purpose of the optimization problem is to design the structure so that that the difference between the recorded output and a specified target is minimized. Thus, the following objective function is considered:

$$\phi = \int_0^{\mathcal{T}} (u_{\text{out}} - u_{\text{out}}^*)^2 dt \quad (21)$$

in which u_{out} is the displacement history of the output point, u_{out}^* is the output point target, and \mathcal{T} is the total simulation time.

The wave pulse is generated by applying the following force at the input point:

$$f(t) = -4u_0\delta(t - t_0)e^{-\delta(t-t_0)^2} \quad (22)$$

in which δ determines the width of the pulse, t_0 is the time center for the pulse, and u_0 is the amplitude of the resulting input wave pulse:

$$u(t) = u_0e^{-\delta(t-t_0)^2}. \quad (23)$$

As the target output pulse we choose

$$u_{\text{out}}^*(t) = \tilde{u}_0e^{-\tilde{c}\delta(t-\tilde{t}_0)^2} \quad (24)$$

in which \tilde{c} represents the specified compression of the pulse.

5.1. Auxiliary design variables

In Eq. (24) the pulse time center at the output point is specified as \tilde{t}_0 and the amplitude of the output wave is specified to be \tilde{u}_0 . Instead of fixing these values, they are included in the optimization problem via extra design variables.

It is obvious that a reshaping of the wave leads to some delay of the pulse and the best value of \tilde{t}_0 is not known *a priori* and it is thus natural to include it in the design problem. The value of \tilde{t}_0 is given as:

$$\tilde{t}_0 = (\tilde{t}_0)_{\min} + x_1((\tilde{t}_0)_{\max} - (\tilde{t}_0)_{\min}) \quad (25)$$

so that the corresponding extra design variable x_1 takes values from 0 to 1. The minimum and maximum values are simply chosen large enough so that the value of x_1 does not reach the 0 or 1 limit during the optimization process.

The extra design variable x_2 associated with the output wave amplitude \tilde{u}_0 is defined as follows:

$$\tilde{u}_0 = (\tilde{u}_0)_{\min} + x_2((\tilde{u}_0)_{\max} - (\tilde{u}_0)_{\min}) \quad (26)$$

where the minimum and maximum values are specified as values close to u_0 , e.g. $(\tilde{u}_0)_{\min} = 0.8u_0$ and $(\tilde{u}_0)_{\max} = 1.2u_0$. In this way the optimization problem is

relaxed somewhat in order to allow the optimization algorithm to find an optimal compression of the pulse without a too strict constraint on the pulse amplitude. It should be emphasized that obtaining an output pulse with an amplitude larger than the input pulse is possible also for an uncompressed pulse, since the energy is not conserved due to the external control of the material properties.

The sensitivities with respect to the auxiliary design variables can be obtained in a straightforward manner from Eqs. (21), (24)–(26).

5.2. Optimization problem

The optimization problem can now be written as:

$$\begin{aligned}
 \min_{\mathbf{x}_j, x_1, x_2} \quad & \phi = \int_0^T (u_{\text{out}} - u_{\text{out}}^*)^2 dt \\
 \text{s.t. :} \quad & \frac{\partial}{\partial t} (\mathbf{M}(t)\mathbf{v}) + \mathbf{C}\mathbf{v} + \mathbf{K}(t)\mathbf{u} = \mathbf{f}(t) \\
 & t \in [0; T] \\
 & \mathbf{u}(0) = \mathbf{v}(0) = \mathbf{0} \\
 & 0 \leq \mathbf{x}_j \leq 1, \quad j \in [1, M] \\
 & 0 \leq x_1 \leq 1 \\
 & 0 \leq x_2 \leq 1
 \end{aligned} \tag{27}$$

and is solved using the derived expressions for the design sensitivities in combination with the method of moving asymptotes (Svanberg, 1987).

5.3. Results and discussion

In the following, results are presented for the optimization problem described above. The model and simulation details are as follows. A unit length design domain is split into $N = 500$ spatial elements. The total simulation time is chosen to be $\mathcal{T} = 1.8$ s and the numerical time-integration is performed using $N_t = 9000$ time steps. The input pulse is defined via the parameters $u_0 = 1$, $\delta = 100 \text{ s}^{-2}$ and $t_0 = 0.3$ s.

The optimization problem is defined by specifying the target pulse with a compression corresponding to $\tilde{c} = 3.5$. The limits for the auxiliary design variables are chosen to be $(\tilde{t}_0)_{\min} = 1.2$ s, $(\tilde{t}_0)_{\max} = 1.35$ s, $(\tilde{u}_0)_{\min} = 0.8u_0$ and $(\tilde{u}_0)_{\max} = 1.2u_0$. The design is allowed to change $M = 36$ times during the simulation time and in order to keep the designs simpler, the spatial elements are grouped into 20 patches. Thus, the total number of design variables in the model becomes $20 \times 36 + 2 = 722$.

Fig. 4 shows an example of a pulse that is compressed when propagating through a space-time optimized structure obtained with material parameters $\rho = 1$ and $E = 1.75$. The curves in Fig. 4 additionally illustrate how the pulse, apart from being compressed, is delayed in the optimized structure when compared to the pulse propagating in the homogeneous structure. In this case the optimized value of the delay parameter is $\tilde{t}_0 \approx 1.25$ s, whereas the optimized

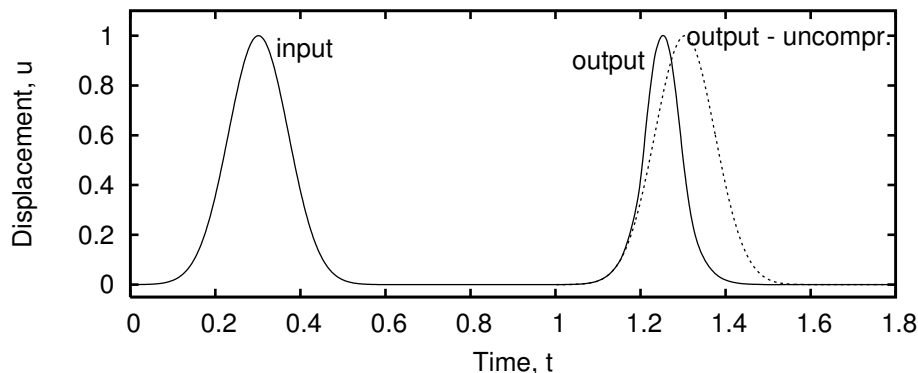


Figure 4. Left: input wave pulse. Right: optimized compressed wave pulse and for comparison the uncompressed output wave pulse.

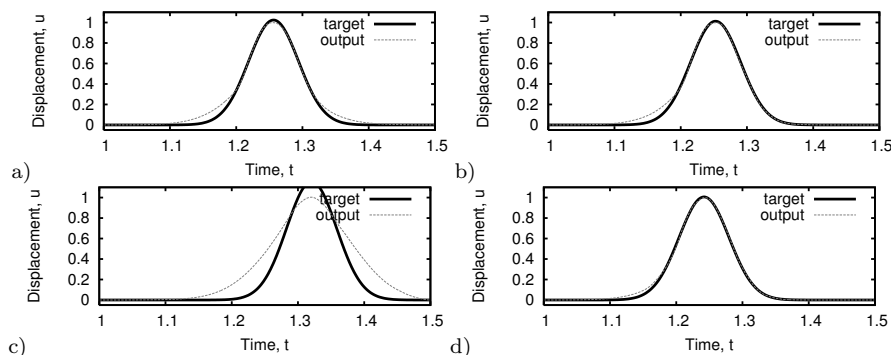


Figure 5. Four examples of output pulse through the optimized structure and the corresponding target pulse. The material parameters are: a) $\rho = 1$, $E = 1.25$, b) $\rho = 1$, $E = 1.75$, c) $\rho = 1.33$, $E = 1.25$, d) $\rho = 0.75$, $E = 1.25$.

value of the output pulse amplitude \tilde{u}_0 is very close to the input pulse amplitude $u_0 = 1$.

In Fig. 5 four plots are presented, each showing a compressed output pulse compared to the target output pulse, each for a different set of material parameter contrasts ρ and E . Note that the targets are different for the four plots since they depend on the optimized values of the auxiliary design variables x_1 and x_2 .

Figs. 5a,b are obtained for structures that are optimized with a constant value of $\rho = 1$ but two different values of E (stiffness contrast). For low E ($E = 1.25$) it is evident that the target compression of the pulse cannot be obtained. There is a discrepancy between the curves near the tip and at the pulse front and tail where the pulse has not been compressed enough. However,

when the contrast is increased ($E = 1.75$), a much better match to the target is obtained. The pulse front (corresponding to the part of the curve near $t = 1.1$ s) is still somewhat off the target.

In Figs. 5c,d the stiffness contrast is kept at the lower value ($E = 1.25$), but now the mass density contrast is changed to $\rho = 1.33$ and $\rho = 0.75$, respectively. It is evident from Fig. 5c that for this material property combination ($\rho = 1.33$) the targeted pulse compression is not possible at all, whereas for $\rho = 0.75$ the compression of the pulse is nearly perfect (with the pulse front still being slightly off). Thus, it is clear that the combined effect of the two material parameters is very important and they should be chosen carefully in order to obtain the desired compression effect.

In the examples shown, the corresponding design variables range broadly from 0 to 1 (see Fig. 6a) which implies that the corresponding material properties in the structure should be interpolations of material 1 and material 2. There is nothing in the optimization formulation as stated that forces a binary 0-1 design that could be created with only the two materials available. If it is required that the structure can be fabricated with only the two specified sets of material properties, an explicit penalization scheme can be employed (e.g. Borrvall and Petersson, 2001). Hence, the objective is appended with a penalizing term:

$$\phi = \int_0^T (u_{\text{out}} - u_{\text{out}}^*)^2 dt + \epsilon \sum_{j=1}^M \sum_{e=1}^N x_j^e (1 - x_j^e) \quad (28)$$

and in this way intermediate values of the design variables (between 0 and 1) are expensive and the design will inevitably be pushed toward a binary 0-1 design if the parameter ϵ is sufficiently large.

In Fig. 6a the space-time design variables in the optimized designs are plotted for the case of $\rho = 0.75$, $E = 1.25$, and in Fig. 6b the design variables are plotted with the optimization performed on the new objective function with explicit penalization from Eq. (28). The penalization has been employed by using the non-penalized structure as a starting point and increasing the value of ϵ in a number of steps using a continuation approach until most of the design variables take values that are 0 or 1. As it appears from the figure only a few of the design variables are now intermediate. However, Fig. 7 shows that the almost perfect 0-1 design has been obtained at some cost in terms of performance of the structure. Especially, near the pulse tail the output pulse for the 0-1 optimized structure is quite different from the target.

Finally, in order to further illustrate the space-time distribution of the material properties, Fig. 8 show snapshots of the design variables along with the wave profile at four different time instances. The plots are for the non-penalized structure of Fig. 6a.

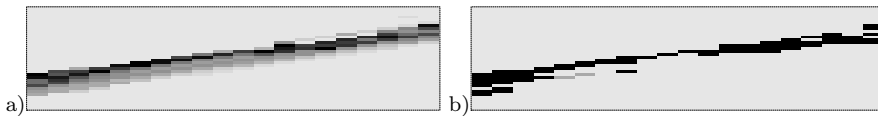


Figure 6. Space-time plot of the material distribution in the optimized structure. a) without penalization of intermediate densities, b) with penalization of intermediate densities.

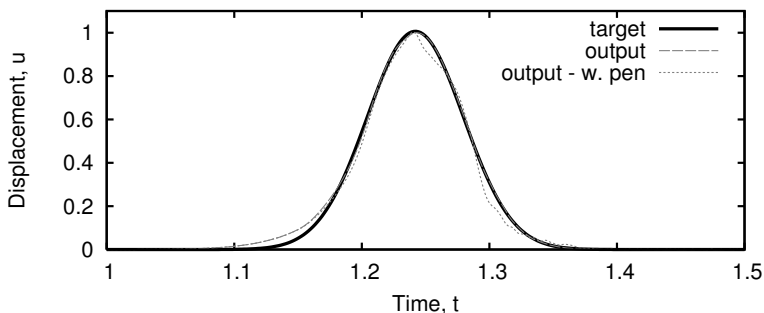


Figure 7. Target output pulse and output pulse for the optimized design without and with penalization of intermediate design variables.

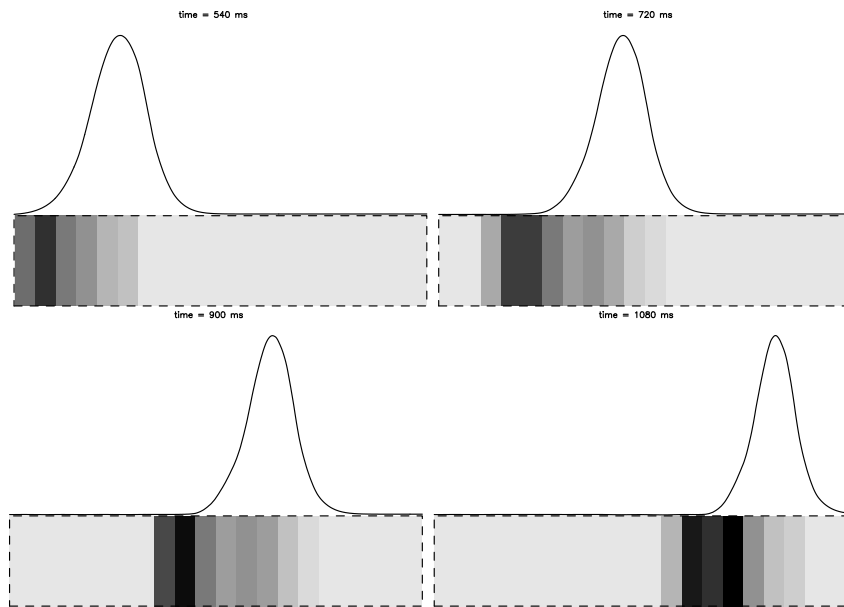


Figure 8. Illustration of pulse compression as the pulse propagates through the optimized dynamic structure corresponding to Fig. 6a.

6. Summary and conclusions

This paper reports on a topology optimization procedure for the distribution of material in space and time. The procedure is applied to a 1D transient wave propagation problem in which a gaussian wave pulse is compressed when propagating through the structure which is composed of materials with different mass and stiffness parameters.

Expressions for the design sensitivities are derived using the adjoint method. This leads to a terminal value transient problem. The direct and the adjoint discretized equations are solved using a time-discontinuous Galerkin procedure. This allows for the correct simulation of the system when the mass matrix is not constant in time, however, at the expense of extra computational effort. The performance of the numerical scheme is demonstrated on a wave propagation problem in which the material properties change instantly. It is shown that the time-discontinuous scheme correctly simulates the problem, whereas a standard central difference scheme fails if the mass matrix is not constant in time.

The optimization procedure is demonstrated on a 1D wave propagation problem in which a single gaussian pulse is compressed through an optimized space and time distribution of two materials with different mass density and stiffness. The optimization problem is formulated as a minimization problem in which the difference between the output pulse and a specified target output is minimized. Two auxiliary design parameters are introduced to relax the problem. They control the temporal location of the output pulse and its amplitude, which are allowed to vary within some predefined limits. The optimization problem is solved with the mathematical programming tool MMA.

It is shown that it is possible to compress the pulse depending on the specific values of mass and stiffness contrasts but that the designs will be composed of material properties that are mixtures of two predefined materials. An explicit penalization scheme is finally introduced in order to eliminate intermediate design variables so that the designs are primarily composed of the two available materials. This is shown to compromise the performance to some extent. The example clearly demonstrates that the pulse compression can be accomplished by using the presented scheme and indicates promising perspectives for using space-time topology optimization to create devices for more complex pulse shaping.

References

- ARORA, J.S. and HOLTZ, D. (1997) An efficient implementation of adjoint sensitivity analysis for optimal control problems. *Structural Optimization* **13**, 223–229.
- BENDSØE, M.P. (1989) Optimal shape design as a material distribution method. *Structural Optimization* **10**, 193–202.
- BENDSØE, M.P. and KIKUCHI, N. (1988) Generating optimal topologies in

- structural design using a homogenization method. *Computer Methods in Applied Mechanics and Engineering* **71** (2), 197–224.
- BENDSØE, M.P. and SIGMUND, O. (2003) *Topology Optimization - Theory, Methods and Applications*. Springer-Verlag, Berlin Heidelberg New York.
- BLEKHMEN, I.I. (2008) Vibrational dynamic materials and composites. *Journal of Sound and Vibration* **317**, 657–663.
- BLEKHMEN, I.I. and LURIE, K.A. (2000) On dynamic materials. *Proceedings of the Russian Academy of Sciences (Doklady)* **37**, 182–185.
- BORRVALL, T. and PETERSSON, J. (2001) Topology optimization using regularized intermediate density control. *Computer Methods in Applied Mechanics and Engineering* **190**, 4911–4928.
- BORRVALL, T. and PETERSSON, J. (2003) Topology optimization of fluids in Stokes flow. *International Journal for Numerical Methods in Fluids* **41**, 77–107.
- COX, S.J. and DOBSON, D.C. (1999) Maximizing band gaps in two-dimensional photonic crystals. *SIAM Journal for Applied Mathematics* **59** (6), 2108–2120.
- DAHL, J., JENSEN, J.S. and SIGMUND, O. (2008) Topology optimization for transient wave propagation problems in one dimension. *Structural and Multidisciplinary Optimization* **36**, 585–595.
- JENSEN, J.S. (2008) Time-space topology optimization. In: B.H.V. Topping and M. Papadrakakis, eds., *Proceedings of the Ninth International Conference on Computational Structures Technology*. Civil-Comp Press, Stirlingshire, United Kingdom. Paper 72.
- JENSEN, J.S. (2009) Space-time topology optimization for one-dimensional wave propagation. *Computer Methods in Applied Mechanics and Engineering* **198**, 705–715.
- KRYLOV, V. and SOROKIN, S.V. (1997) Dynamics of elastic beams with controlled distributed stiffness parameters. *Smart Materials and Structures* **6**, 573–582.
- LURIE, K.A. (1997) Effective properties of smart elastic laminates and the screening phenomenon. *International Journal of Solids and Structures* **34**, 1633–1643.
- LURIE, K.A. (2006) *An Introduction to Mathematical Theory of Dynamic Materials*. Springer-Verlag, Berlin Heidelberg New York.
- MAESTRE, F., MÜNCH, A. and PEDREGAL, P. (2007) A spatio-temporal design problem for a damped wave equation. *SIAM Journal of Applied Mathematics* **68**, 109–132.
- MAESTRE, F. and PEDREGAL, P. (2009) Dynamic materials for an optimal design problem under the two-dimensional wave equation. *Discrete and Continuous Dynamical Systems - Series A* **23**, 973–990.
- MIN, S., KIKUCHI, N., PARK, Y.C., KIM, S. and CHANG, S. (1999) Optimal topology design of structures under dynamic loads. *Structural Optimization* **17**, 208–218.

- SIGMUND, O. and JENSEN, J.S. (2003) Systematic design of phononic band-gap materials and structures by topology optimization. *Philosophical Transactions of the Royal Society London, Series A (Mathematical, Physical and Engineering Sciences)* **361**, 1001–1019.
- SIGMUND, O. and PETERSSON, J. (1998) Numerical instabilities in topology optimization: A survey on procedures dealing with checkerboards, mesh-dependencies and local minima. *Structural Optimization* **16**, 68–75.
- SOROKIN, S.V., ERSHOVA, O.A. and GRISHINA, S.V. (2000) The active control of vibrations of composite beams by parametric stiffness modulation. *European Journal of Mechanics A - Solids* **19**, 873–890.
- SOROKIN, S.V. and GRISHINA, S.V. (2004) Analysis of wave propagation in sandwich beams with parametric stiffness modulation. *Journal of Sound and Vibration* **271**, 1063–1082.
- SVANBERG, K. (1987) The method of moving asymptotes - a new method for structural optimization. *International Journal for Numerical Methods in Engineering* **24**, 359–373.
- TORTORELLI, D.A. and MICHALERIS, P. (1994) Design sensitivity analysis: overview and review. *Inverse Problems in Engineering* **1**, 71–105.
- TURTELTAUB, S. (2005) Optimal non-homogeneous composites for dynamic loading. *Structural and Multidisciplinary Optimization* **30**, 101–112.
- WIBERG, N.E. and LI, X.D. (1999) Adaptive finite element procedures for linear and non-linear dynamics. *International Journal for Numerical Methods in Engineering* **46**, 1781–1802.
- YOON, G.H., JENSEN, J.S. and SIGMUND, O. (2007) Topology optimization of acoustic-structure interaction using mixed finite elements. *International Journal for Numerical Methods in Engineering* **70**, 1049–1075.